
MAGNETIC, ELECTRICAL AND OPTICAL PROPERTIES AND APPLICATIONS OF INTERMETALLIC COMPOUNDS

Edited by

J. H. Westbrook

Brookline Technologies, Ballston Spa, New York, USA

and

R. L. Fleischer

Union College, Schenectady, New York, USA

JOHN WILEY & SONS, LTD

Chichester · New York · Weinheim · Brisbane · Singapore · Toronto

Copyright © 2000 by John Wiley & Sons Ltd,
Baffins Lane, Chichester,
West Sussex PO19 1UD, England

National 01243 779777
International (+44) 1243 779777
e-mail (for orders and customer service enquiries): cs-books@wiley.co.uk
Visit our Home Page on <http://www.wiley.co.uk>
or <http://www.wiley.com>

All Rights Reserved. No part of this publication may be reproduced, stored in a retrieval system, or transmitted, in any form or by any means, electronic, mechanical, photocopying, recording, scanning or otherwise, except under the terms of the Copyright, Designs and Patents Act 1988 or under the terms of a licence issued by the Copyright Licensing Agency, 90 Tottenham Court Road, London W1P 9HE, without the permission in writing of the Publisher

Other Wiley Editorial Offices

John Wiley & Sons, Inc., 605 Third Avenue,
New York, NY 10158-0012, USA

WILEY-VCH Verlag GmbH, Pappelallee 3,
D-69469 Weinheim, Germany

Jacaranda Wiley Ltd, 33 Park Road, Milton,
Queensland 4064, Australia

John Wiley & Sons (Asia) Pte Ltd, 2 Clementi Loop #02-01,
Jin Xing Distripark, Singapore 129809

John Wiley & Sons (Canada) Ltd, 22 Worcester Road,
Rexdale, Ontario M9W 1L1, Canada

Library of Congress Cataloging-in-Publication Data

Crystal structures in intermetallic compounds / edited by J. H. Westbrook and R. L. Fleischer.
p. cm.

'This volume is one of four now being published, each of which consists of reprints of chapters from the 1995 comprehensive two-volume set—Intermetallic compounds, principles and practice . . . selected sets of chapters are collected, each set being on a single theme . . . reprint volume 4'—Pref.

Includes bibliographical references and index.

ISBN 0-471-61261-8 (pbk. : alk. paper)—ISBN 0-471-60814-9 (set)

1. Intermetallic compounds—Magnetic properties. 2. Intermetallic compounds—Electric properties. 3. Intermetallic compounds—Optical properties. 4. Alloys. 5. Physical metallurgy. I. Westbrook, J. H. (Jack Hall), 1924– II. Fleischer, R. L. (Robert Louis), 1930– III. Title: Intermetallic compounds.

TA483.M26 2000
620.1'697—dc21

99-052443

British Library Cataloguing in Publication Data

A catalogue record for this book is available from the British Library

ISBN 0 471 61261 8
ISBN 0 471 60814 9 (set)

Typeset by Dobbie Typesetting Ltd, Tavistock, Devon
Printed and bound in Great Britain by Antony Rowe, Chippenham, Wiltshire
This book is printed on acid-free paper responsibly manufactured from sustainable forestry, in which at least two trees are planted for each one used for paper production.

Dedication

To the memory of
John Herbert Hollomon
1919–1985

Wise, vigorous, effective advocate of the relevance and value of scientific research in industry.

His strong belief in the synergetic interaction of Principles and Practice in the field of metallurgy impelled him to assemble an innovative, diverse staff at General Electric, and to inspire independent exploration that benefited both science and engineering.

Contributors

Edward T Arakawa
Life Sciences Division,
Oak Ridge, National Laboratory,
Oak Ridge, TN 37831-6123,
USA



Akinori Katsui
School of High Technology for
Human Welfare, Department of
Materials Science and
Technology, Tokai University,
317 Nishino, Numazu,
Shizuoka, 410-0321, Japan



Milenko M. Brannović
5975 Place de l'Authion,
Suite 503,
Montreal, QC,
Canada H1M 2W3



James S. Kouvel
Department of Physics,
University of Illinois at Chicago,
Chicago, IL 60680, USA



M. Wendy (England) Williams
Life Sciences Division,
Oak Ridge National Laboratory,
Oak Ridge, TN 37831-6123,
USA



William A. McGahan,
Center for Microelectronic and
Optical Materials Research,
Department of Electrical Engineering,
University of Nebraska at Lincoln,
NE 68508-0511,
USA



Rodeny D. Greenough
Department of Applied Physics,
University of Hull, Hull,
HU6 7RX, UK



Katashi Masumoto
The Research Institute for
Electric and Magnetic Materials,
2-1-1 Yagiyaama
Minami,
Taihaku-ku Sendai 982-0807, Japan



Eric Gregory
Intermagetics General Corporation,
6 Eastern Road,
Acton, MA 01720, USA



Takashi Matsuoka
NFT
Laboratories, Nippon Telegraph
and Telephone Corporation,
301 Wakamiya Marinosato,
Atsugi, Kanagawa
Japan



Bernd Reinsch

Institut für Werkstoffwissenschaft,
Max-Planck-Institut für
Metallforschung,
D-70569 Stuttgart, Germany

**Hans H. Stadeimaier**

Department of Materials Science
and Engineering, North Carolina
State University,
Raleigh, NC 27695-7907, USA

**Roger de Reus**

Mikroelektronik Centret,
Ørstedes Plads, DTU,
Bldg 345-East, DK-2300 Lyngby,
Denmark

**Z. J. John Stekly**

Intermagnetics General Corporation,
6 Eastern Road,
Acton, MA 01720, USA

**Michael P. Schulze**

Department of Applied Physics
University of Hull,
Hull HU6 7RX, UK

**Matrat V. Vedernikov,**

A. P. Ioffe Physico-Technical
Institute, Russian Academy of
Sciences, 26 Polytechnicheskaya,
194 021 St. Petersburg, Russia



Preface to the 1995 Edition

Intermetallic compounds were last comprehensively reviewed in 1967 in a volume that was edited by one of us (JHW). At that time the field was described as of special interest because it was undergoing 'exponential proliferation'. That trend continues to the present. The number of intermetallic entries in the Permuterm Subject Index shows a doubling period of less than nine years, having reached roughly 1800 entries per year in 1993. Apart from scholarly interest, intermetallics have now become of substantial commercial significance; for some, such as Ni_3Al , world-wide use is in the 1000s of tons; for others, for example III-V semiconducting compounds, although the quantities employed are not in tonnage numbers, their value as vital components of electronic circuits is in the billions of dollars.

From the 1967 book we remind the reader that 'The first published paper dealing with intermetallic compounds appeared in 1839, and more than sixty years elapsed before . . . the first review paper by Neville in 1900. However, new results were then appearing so rapidly that fifteen years later two books were printed, devoted exclusively to this subject, one by Desch in England and one by Giua and Giua in Italy'. More recently, conference volumes that deal exclusively with intermetallics but typically only within specific, limited sub-topical subject areas have become common. The scope of the present work is as broad as that of its 1967 predecessor. However, the increased volume of activity in intermetallics and the increased significance of their applications have necessitated an expansion from the 27 chapters of the earlier work to the 75 chapters of the present treatise.

First, what are intermetallic compounds? Generally, such a compound is a structure in which the two or more metal constituents are in relatively fixed abundance ratios and are usually ordered on two or more sublattices, each with its own distinct population of atoms. Often substantial or complete disorder may obtain, as a result of low ordering energy or the intervention of some external agency, for example extreme cooling rates, radiation, etc. Deviations from precise stoichiometry are frequently permitted on one or both sides of the nominal ideal atomic ratios, necessitating a partial disorder. Here we include as intermetallic compounds all metal-metal compounds, both ordered and disordered, binary and multicomponent. Even the metal-metal aspect of the definition is often relaxed by including some metal-metalloid compounds, such as silicides, tellurides, and semiconductors. We believe this inclusion is appropriate since the phenomenology of many such compounds is nearly identical to metal-metal ones, and they provide useful examples of principles, properties, and practices.

The burgeoning literature on intermetallics and the lack of a comprehensive single source of up-to-date descriptions of where we are, what we need to know, and what we can do with intermetallics created the incentive for the present pair of volumes. This work was planned to provide state-of-the-art assessments of theory, experiment, and practice that will form a solid base for workers who wish to know more than their own particular area. Each author was asked to set forth the principles of his or her subject in terms that are meaningful to scientists and engineers who are not specialists in the author's field, and then to progress to include knowledge that workers in their own areas would wish to have. Concluding sections of most chapters give the authors' critical assessment of the state of their subject and of where they believe further effort is merited.

This work is divided into two volumes in order that each be of manageable size. The first, on the theme Principles, is directed at the science of intermetallics—how do we understand their formation, structure and properties? The Practice volume considers commercial production and engineering applications of intermetallic compounds. The reader who browses carefully will recognize that the immediacy of the practice described ranges from hoped-for use, to beginnings of use, to actual commercial application—depending on the specific subject. Some of the hoped-for uses are fated never to be realized, but the authors have aimed to reveal what the obstacles are so that the reader may make his or her own assessment (and possibly provide a solution!).

We conferred carefully with many people in order to identify authorities for each subject; having recruited contributors for the project, we then strove to assist them in achieving clarity and thoroughness from outline to draft to final manuscript. The contributors cooperated superbly, and we thank them for their hard work and high achievement. We sought experts wherever they were to be found, and our international set of nearly 100 authors turned out to be almost equally divided between the United States and 14 other countries. Manuscripts have in fact come from all inhabited continents.

We planned this work as an aid to both scientists and engineers. It can serve as a base for those who wish to know about intermetallics as an area in which to begin research. Equally it is a resource to workers who are already active in the field and need, or wish, to expand their knowledge of related science or practical technology. We expect that many chapters are appropriate source matter for special topic or seminar courses at the advanced undergraduate and various graduate school levels. It is hoped that passage of the next 25 years will reveal some influence of this treatise on the further development of this field.

As an assist to readers we have provided in the following pages a consolidated acronym list and some crystallographic tables. Nomenclature for crystal structure types is often complex, and some of the authors have introduced their own. Generally we have asked authors to include both of two commonly used types of symbols as they introduce structures. The two-part table following this preface lists many of the common types—by Strukturbericht symbol, prototype name (termed a *structure type*), and Pearson symbol. Strukturbericht symbols are only partly significant and systematic: A's are not compound structures but consist of a single lattice of atoms (except for A15!); B's are equiatomic ordered structures; C's have 2-to-1 atomic abundance ratios, D0's 3-to-1. Structure type compounds are the specific ones used to designate a particular structure. Thus B2 compounds are also referred to as CsCl compounds. Many structures are better known to metallurgists and mineralogists by names other than the formula of the structure type chosen by crystallographers, e.g. Laves, fluorite, Heusler, etc. Such names have been added in selected cases. The Pearson symbols tell the crystal symmetry and the number of atoms per unit cell. Thus, B2, CsCl has a primitive (P) cubic (c) structure with 2 atoms per cell and hence the Pearson symbol (cP2). The Pearson designation is informative, but it is not necessarily unique. Although there is only one cP2 structure, Villars and Calvert list two cP4s, three cF12s and twenty-two hP9s. Thus to be definitive, both the structure type and the Pearson symbol need to be given, or the Pearson and the Strukturbericht symbol.

The index in each volume includes the subjects in *both* volumes of this work, in order that the reader may be able to locate any subject that is addressed. Although the purpose of such combined indices is not to induce the owner of a single volume to purchase the other, it possibly may help to reduce the barrier to such action.

We have benefited from outstanding secretarial help during the three years of this project, first by Phillis Liu, then Constance Remscheid at General Electric, finally Mary Carey at Rensselaer Polytechnic Institute. We appreciate the hospitality of the General Electric Research and Development Center during the inception and middle period of preparing these volumes. Assembling the final product has been eased for us by the continuing efforts and cheerful good counsel at John Wiley of Jonathan Agbenyega, Irene Cooper, Philip Hastings, Vanessa Lutman and Cliff Morgan.

J. H. WESTBROOK, *Ballston Spa, New York*

R. L. FLEISCHER, *Schenectady, New York*

Upon these considerations, we have been induced to undertake the present extensive work, the purpose of which is to instruct rather than to amuse; in which nothing will be omitted that is elegant or great; but the principal regard will be shown to what is necessary and useful.

—Isaac Ware, 1756

Preface to the Reprint Volumes from Intermetallic Compounds: Principles and Practice

This volume is one of four now being published, each of which consists of reprints of chapters from the 1995 comprehensive two-volume set *Intermetallic Compounds: Principles and Practice*. In the present volumes selected sets of chapters are collected, each set being on a single theme. In this format readers who are interested in a particular aspect of intermetallic compounds can have a less weighty volume specific to their subject; a volume that can be produced more economically than the full, original 1900-page set; and that includes a modest updating of the subject matter.

The subjects in most cases are taken from one or more chapter groupings of the original Volume 1 or 2: Hence reprint volume 1, *Crystal Structures of Intermetallic Compounds*, contains the ten chapters from the original work under the heading Crystal Structures; reprint volume 2, *Basic Mechanical Properties and Lattice Defects of Intermetallic Compounds*, contains three from Property Fundamentals, four chapters from Defect Structures, and two from Kinetics and Phase Transformations; reprint volume 3, *Structural Applications of Intermetallic Compounds* contains the thirteen chapters that were under that same topic; and finally reprint volume 4, *Magnetic, Electrical, and Optical Properties and Applications of Intermetallic Compounds*, contains two chapters from the section on Property Fundamentals, seven from Electromagnetic Applications and one from Miscellaneous. Although each chapter is reprinted nearly intact (only typographic and factual errors corrected), the author or authors were given the option of adding a brief addendum in order to add whatever new perspective has arisen over the intervening few years. Some have chosen to do so; some have not, either in the preferred case because they felt none was needed or because the four-month window of opportunity they were given to satisfy our and the publisher's desire for promptness did not fit their work schedule. Corrections to the original chapters that were so lengthy that they would upset the original pagination are to be found in the addenda at the end of each relevant chapter.

Where an addendum is particularly relevant to a portion of the original chapter being reproduced, a margin mark (*) alerts the reader to refer to the added pages at the end of the chapter. Cross-references to other chapters relate to the original 1995 two-volume work, the tables of contents of which appear at the end of this volume.

JHW
RLF

Acronyms

| | | | |
|---------|--|--------|---|
| 2D | two-dimensional | BH | buried heterostructure |
| 3D | three-dimensional | BIS | bremsstrahlung isochromat spektroskopie |
| 6D | six-dimensional | BM | Bowles–Mackenzie (theory of martensitic transformation) |
| ACAR | angular correlation of annihilation radiation | BSCCO | bismuth–strontium–calcium–copper oxide |
| ACPAR | angular correlation of positron annihilation radiation | BSE | back-scattered electrons |
| AE | atomic environment | BT | Bhatia–Thornton (partial structure factor for liquid alloys) |
| AES | Auger electron spectroscopy | BW | Bragg–Williams (theory of ordering) |
| AET | atomic environment type | BZ | Brillouin zone |
| AIM | argon induction melting | | |
| ALCHEMI | atom location by channeling enhanced microanalysis | CAM | c-axis modulated |
| ALE | atomic layer epitaxy | CANDU | Canadian deuterium–uranium (power reactor) |
| AM | air mass | CAP | consolidated under atmospheric pressure |
| AMT | Advanced Materials Technology, Inc. | CAT | computer-assisted tomography |
| AN | atomic number | CBLM | cluster Bethe lattice method |
| AP | atom probe | CC | cluster center |
| AP | atomic property | CCD | charge-coupled device |
| APB | antiphase boundary | CCGSE | concentric-circle grating surface- emitting (laser) |
| APD | antiphase domain | CCIC | cabled conductor in conduit |
| APD | avalanche photodetector | CCMAI | crystal chemical model of atomic interactions |
| APE | atomic property expression | c.c.p. | cubic close-packed |
| APW | augmented plane wave | CCT | continuous cooling transformation |
| AR | antireflection | CD | compact disc |
| ARIPES | angle-resolved inverse photoemission spectroscopy | CD | climb dislocation |
| ARPES | angle-resolved photoemission spectroscopy | CEBAF | continuous electron-beam accelerator facility |
| ASA | atomic-sphere approximation | CEF | crystalline electric field |
| ASW | augmented spherical wave | CERN | Centre Européenne Recherche Nucléaire |
| BC | bond charge | CFT | concentration-functional theory |
| b.c.c. | body-centered cubic | CMC | ceramic–matrix composite |
| BCS | Bardeen–Cooper–Schrieffer (theory of superconductivity) | CN | coördination number |
| b.c.t. | body-centered tetragonal | | |

| | | | |
|----------|---|--------|--|
| CO | cubo-octahedron | ESR | electroslag refined |
| CP | coördination polyhedron | ETP | electrolytic tough pitch (copper) |
| CPA | coherent-potential approximation | EXAFS | extended X-ray absorption fine structure |
| CRSS | critical resolved shear stress | | |
| CS | chemisorption | f.c.c. | face-centered cubic |
| CSF | complex stacking fault | f.c.t. | face-centered tetragonal |
| CSL | coincidence-site lattice | FENIX | Fusion Engineering International Experimental Magnet Facility |
| CSRO | chemical short-range order | | |
| CT | chisel toughness | FET | field effect transistor |
| CTE | coefficient of thermal expansion | FIM | field ion microscopy |
| CVD | chemical vapor deposition | FLAPW | full-potential linearized augmented plane wave |
| CVM | cluster variation method | | |
| CW | cold worked | FLASTO | full-potential linearized augmented Slater-type orbital |
| CW | concentration wave | FLMTO | full-potential linearized muffin-tin orbital |
| CWM | Connolly-Williams method (theory of phase transformations) | FOM | figure of merit |
| | | FP | Fabry-Perot (laser) |
| D-A | donor-acceptor | FT | phase transformation |
| DB | diffusion bonding | FZ | floating zone |
| DBTT | ductile-brittle transition temperature | | |
| DC | direct chill (casting) | GB | gain \times bandwidth (product) |
| DC | direct current | GB | grain boundary |
| DCA | direct configurational averaging | GFT | glass-forming tendency |
| DF | density functional | GGA | generalized gradient approximation |
| DFB | distributed feedback | GITT | galvanostatic intermittent titration technique |
| DFT | density-functional theory | | |
| DH | double heterojunction | GPM | generalized perturbation method |
| d.h.c.p. | double hexagonal close-packed | GRPA | generalized random-phase approximation |
| dHvA | de Haas-van Alphen (effect) | | |
| DLZR | directional levitation zone melting | GS | ground state |
| DOS | density of states | GT | Goody-Thomas (electronegativity) |
| DPA | displacement per atom | | |
| DPC | demonstration poloidal coil | HB | horizontal Bridgman |
| DRP | dense random packing | HBT | heterojunction bipolar transistor |
| DS | directional solidification | HCF | high-cycle fatigue |
| DSC | displacement shift complete | h.c.p. | hexagonal close-packed |
| | | HEMT | high-electron-mobility transistor |
| e/a | electron/atom (ratio) | HIP | hot isostatic pressing |
| EAM | embedded-atom method | HPT | heterojunction phototransmitter |
| EBPVD | electron beam physical vapor deposition | HR | high resolution |
| ECI | effective cluster interaction | HREM | high-resolution electron microscopy |
| ECM | embedded-cluster method | HRTEM | high-resolution transmission electron microscopy |
| EDC | electro-optic directional coupler | HSCT | high-speed civil transport |
| EDM | electrodischarge machining | HTS | high-temperature superconductor |
| EDX | energy-dispersive X-ray (spectroscopy) | HVEM | high-voltage electron microscopy |
| | | HVTEM | high-voltage transmission electron microscopy |
| EELS | electron energy-loss spectroscopy | | |
| EMF | electromotive force | | |
| EPI | effective pair interaction | IAE | irregular atomic environment |
| ESF | extrinsic stacking fault | IAET | irregular atomic environment type |

| | | | |
|---------|---|----------|--|
| IC | integrated circuit | LO | longitudinal optical (wave) |
| IC | investment cast | LPCVD | low-pressure chemical vapor deposition |
| IDOS | integrated density of states | LPE | liquid-phase epitaxy |
| IEM | interstitial-electron model | LPPS | low-pressure plasma spraying |
| IGC | Intermagetics General | LPS | long-period superstructure |
| IHP/TET | integrated high-performance turbine engine technology | LRO | long-range order |
| ILS | invariant line strain | LSDA | local spin-density approximation |
| IMC | intermetallic compound | LSI | large-scale integration |
| IMC | intermetallic matrix composite | μ SR | muon spin relaxation |
| IMC | inverse Monte Carlo (method) | MA | mechanical alloying |
| IPM | independent-particle method (approximation) | MAPW | modified augmented plane wave |
| IPS | invariant plan strain | MB | Martinov-Basanov (electronegativity) |
| IQC | icosahedral quasicrystal | MBE | molecular beam epitaxy |
| IR | infrared | MBT | metal-base transistor |
| ISF | intrinsic stacking fault | MC | Monte Carlo |
| IT | (positive) inner tetrahedron | MCS | Monte Carlo simulation |
| ITER | International Thermonuclear Experimental Reactor | MD | molecular dynamics |
| IV | intermediate valence | MEE | migration-enhanced epitaxy |
| JFET | junction field-effect transistor | MESFET | metal Schottky field-effect transistor |
| KKR | Korringa-Kohn-Rostoker (bond-calculation method) | MFTF | Mirror Fusion Test Facility |
| KSV | Khantha-Cserti-Vitek (deformation model) | MISFET | metal-insulator-semiconductor field effect transistor |
| KTP | potassium titanyl phosphate | MJR | McDonald jelly roll (superconducting cable construction) |
| KW | Kear-Wilsdorf (dislocation locking mechanism) | MLR | multi-layer reflector |
| LA | longitudinal acoustic (wave) | MMC | metal-matrix composite |
| LAPW | linearized augmented plane wave | MN | Mendeleev number |
| LASTO | linearized augmented Slater-type orbital | MO | magneto-optical |
| LCAO | linear combination of atomic orbitals | MOCVD | metal-organic chemical vapor deposition |
| LCF | low-cycle fatigue | MOS | metal-oxide-semiconductor |
| LCT | large coil task | MOSFET | metal-oxide-semiconductor field effect transistor |
| LCW | Lock-Crisp-West (radiation analysis) | MOVPE | metal-organic vapor phase epitaxy |
| LD | laser diode | MQW | multiple quantum well |
| LDA | local-density approximation | MRI | magnetic resonance imaging |
| LEC | liquid-encapsulated Czochralski | MRSS | maximum resolved shear stress |
| LED | light-emitting diode | MRT | orthodontic NiTi alloy |
| LEED | Low-energy electron diffraction | MT | muffin tin |
| LEISS | low-energy ion scattering spectroscopy | MTD | martensitic transformation diagram |
| LHC | Large Hadron Collider | MVA | million volt-amperes |
| LKKR | Layered KKR (structure calculation) | NASP | National AeroSpace Plane |
| LME | liquid metal embrittlement | NET | Next European Torus (fusion device) |
| LMTO | linearized muffin-tin orbital | NHE | normal hydrogen electrode |
| LNT | liquid nitrogen temperature | NMI | National Maglev Initiative |
| | | NMR | nuclear magnetic resonance |
| | | NN | nearest neighbor |
| | | NNH | nearest-neighbor histogram |

| | | | |
|-------------------|--|---------|---|
| NNN | next nearest neighbor | RDS | rate-determining step |
| NOR | negative OR (logic operator) | RE | rare earth (metal) |
| NSR | notch/strength ratio | RF | radiofrequency |
| OAZ | oxidation-affected zone | RHE | reversible hydrogen electrode |
| ODR | oxygen dissolution reaction | RIM | rigid-ion model |
| ODS | oxide dispersion-strengthened | RKKY | Ruderman-Kittel-Kasuya-Yoshida (electron interactions) |
| OEIC | optoelectronic integrated circuit | r.m.s. | root mean square |
| OH | octahedron | RRR | residual resistivity ratio |
| ORNL | Oak Ridge National Laboratory | RS | rapidly solidified |
| OT | (negative) outer tetrahedron | RSP | rapid solidification processing |
| OTMC ¹ | orthorhombic Ti-matrix composites | RSS | resolved shear stress |
| PAS | positron annihilation spectroscopy | RT | room temperature |
| PBC | periodic bond chain | RUS | resonance ultrasound spectroscopy |
| PBT | permeable-base transistor | | |
| PCM | phase-change material | SAD | selected-area diffraction |
| PCT | pressure-composition-temperature | SAED | selected-area electron diffraction |
| PD | phase diagram | SAGBO | stress-assisted grain-boundary oxidation |
| PDF | pair distribution function | SAM-APD | separate absorption and multiplication avalanche photodetector |
| PDOS | phonon density of states | | |
| PFC | planar flow casting | s.c. | simple cubic |
| PH | <i>Pearson's Handbook</i> | SC | semiconductor |
| PHACOMP | phase computation | SCE | standard colomel electrode |
| PKA | primary knock-on atom | SCH | separate confinement heterostructures |
| PL | photoluminescence | SDC | specific damping capacity |
| PM | powder metallurgy | SDW | spin-density wave |
| PMTC | phenomenological martensite transformation concept | SEM | scanning electron microscopy |
| PN | periodic number | SESF | superlattice extrinsic stacking fault |
| pnpn | type of photothyristor | SF | stacking fault |
| PPDF | partial pair distribution function | SG | spin glass |
| PPM | path-probability method | SHS | self-propagating high-temperature synthesis |
| PPV | Paidar-Pope-Vitek (L1 ₂ hardening model) | SI/VLSI | semi-insulating very large-scale integration |
| PS | Pearson symbol | SIA | self-interstitial atom |
| PT | phase transformation | SIC | self-interaction correlation |
| PTMC | phenomenological theory of martensite crystallography | SIM | stress-induced martensite |
| PVD | physical vapor deposition | SIMS | secondary-ion mass spectrometry |
| PZT | lead zirconate titanate (ceramic) | SIS | superconductor-insulator- superconductor |
| QC | quasicrystal(line) | SISF | superlattice intrinsic stacking fault |
| QCSE | quantum confined Stark effect | SIT | static inductance transistor |
| QFD | quantum formation diagram | SM | semimetal |
| QN | quantum number | SMA | second-moment approximation |
| QSD | quantum structural diagram | SMA | shape-memory alloy |
| QW | quantum well | SME | shape-memory effect |
| | | SPF | superplastic forming |
| | | SQUID | superconducting quantum interference device |
| RBS | Rutherford back scattering | | |
| RC | ribbon comminution | SRO | short-range order |
| RCS | replacement-collision sequence | SSAR | solid-state amorphizing reaction |
| RDF | radial distribution function | SSD | structural stability diagram |

| | | | |
|------|--|------------------|--|
| SSF | superlattice stacking fault | ULSI | ultra large-scale integration |
| STA | <i>Atlas of Crystal Structure Types</i> | USW | ultrasonic wave |
| STEM | scanning transmission electron microscopy | UTS | ultimate tensile strength |
| STM | scanning tunneling microscopy | UV | ultraviolet |
| SV | Sodani-Vitole change of Paidar <i>et al.</i> model | VAR | vacuum arc refined |
| | | VCSEL | vertical-cavity surface-emitting laser |
| TA | transverse acoustic (wave) | VEC | valence-electron concentration |
| TB | tight binding | VGf | vertical gradient freezing |
| TCP | topologically close-packed | VHF | very high frequency |
| TD | thoria dispersion | VIM | vacuum induction melting |
| TDFS | temperature dependence of flow stress | VLS | vapor-liquid-solid |
| TE | thermoelectric | VLSI | very large-scale integration |
| TE | transverse electric (field) | VPE | vapor phase epitaxy |
| TEC | thermoelectric cooler | VPS | vacuum plasma spraying |
| TEG | thermoelectric generator | VUV | vacuum ultraviolet |
| TEM | transmission electron microscopy | WB | weak beam |
| TEP | triethylphosphene | WGPD | waveguide photodetector |
| TGW | Teatum-Gschneidner-Waber (atomic radius) | WLR | Wechsler-Lieberman-Read (theory of martensitic transformation) |
| TIP | thermally induced porosity | WS | Wigner-Seitz (cell) |
| TK | Takeuchi-Kuramoto (dislocation locking mechanism) | WSS | Winterbon-Sigmund-Sanders (model of irradiation damage) |
| TM | transition metal | wt.ppm | weight parts per million |
| TM | transverse magnetic (field) | | |
| TMA | titanium-molybdenum-aluminum (alloy) | XC | exchange-correlation |
| TO | transverse optical (wave) | XD TM | exothermic dispersion (synthesis process) |
| TPA | two-photon absorption | XIM | X-ray inspection module |
| TSRO | topological short-range ordering | XPS | X-ray photoelectron spectroscopy |
| TT | truncated tetrahedron | XRD | X-ray diffraction |
| TTS | tubular tin source | XUV | extreme ultraviolet |
| TTT | time-temperature-transformation | YAG | yttrium aluminum garnet |
| UHF | ultra-high frequency | ZIF | zero insertion force |
| UHV | ultra-high vacuum | | |

Crystal Structure Nomenclature*

Arranged Alphabetically by Pearson-Symbol Designation

| Pearson symbol | Prototype | Strukturbericht designation | Space group | Pearson symbol | Prototype | Strukturbericht designation | Space group |
|----------------|---|-----------------------------|-------------------|----------------|---|-----------------------------|----------------------|
| cF4 | Cu | A1 | Fm $\bar{3}m$ | cP6 | Ag ₂ O | C3 | Pn $\bar{3}m$ |
| cF8 | C (diamond) | A4 | Fd $\bar{3}m$ | cP7 | CaB ₆ | D2 ₁ | Pm $\bar{3}m$ |
| | NaCl (rock salt) | B1 | Fm $\bar{3}m$ | cP8 | Cr ₃ Si (β W) | A15 | Pm $\bar{3}n$ |
| | ZnS (sphalerite) | B3 | F $\bar{4}3m$ | | FeSi | B20 | P2 ₁ 3 |
| cF12 | CaF ₂ (fluorite) | C1 | Fm $\bar{3}m$ | | Cu ₃ VS ₄ (sulfvanite) | H2 ₄ | P4 ₃ m |
| | MgAgAs | C1 _h | F $\bar{4}3m$ | cP12 | FeS ₂ (pyrite) | C2 | Pa3 |
| cF16 | AlCu ₂ Mn (Heusler) | L2 ₁ | Fm $\bar{3}m$ | | NiSbS (ullmanite) | F0 ₁ | P2 ₁ 3 |
| | BiF ₃ (AlFe ₃) | D0 ₃ | Fm $\bar{3}m$ | cP20 | β Mn | A13 | P4 ₃ 2 |
| | NaTi | B32 | Fd $\bar{3}m$ | cP36 | BaHg ₁₁ | D2 ₂ | Pm $\bar{3}m$ |
| cF24 | AuBe ₃ | C15 _h | F $\bar{4}3m$ | cP39 | Mg ₂ Zn ₁₁ | D8 ₂ | Pm $\bar{3}$ |
| | SiO ₂ (β cristobalite) | C9 | Fd $\bar{3}m$ | cP52 | Cu ₉ Al ₄ (γ brass) | D8 ₃ | P4 ₃ m |
| | Cu ₂ Mg (Laves) | C15 | Fd $\bar{3}m$ | hP1 | HgSn ₆₋₁₀ | A ₁ | P6 ₃ /mmm |
| cF32 | CuPt ₃ | L1 ₁ | Fm $\bar{3}c$ | hP2 | Mg | A ₃ | P6 ₃ /mmc |
| cF52 | UB ₁₂ | D2 ₇ | Fm $\bar{3}m$ | | WC | B ₄ | P6 ₃ m2 |
| cF56 | Al ₂ MgO ₄ (spinel) | H1 ₁ | Fd $\bar{3}m$ | hP3 | AlB ₂ | C32 | P6 ₃ /mmm |
| | Co ₃ S ₄ | D7 ₂ | Fd $\bar{3}m$ | | CdI ₂ | C6 | P3m1 |
| cF68 | Co ₃ S ₈ | D8 ₉ | Fm $\bar{3}m$ | | Fe ₂ N | L'3 | P6 ₃ /mmc |
| cF80 | Sb ₂ O ₃ (senarmontite) | D5 ₄ | Fd $\bar{3}m$ | | LiZn ₂ | C ₄ | P6 ₃ /mmc |
| cF112 | Fe ₃ W ₃ C (η carbide) | E9 ₃ | Fd $\bar{3}m$ | | γ Se | A8 | P3 ₂ 1 |
| | NaZn ₁₃ | D2 ₃ | Fm $\bar{3}c$ | hP4 | α La | A3' | P6 ₃ /mmc |
| cF116 | Cr ₂₃ C ₆ | D8 ₄ | Fm $\bar{3}m$ | | BN | B ₄ | P6 ₃ /mmc |
| | Mn ₂₃ Th ₆ Cu ₁₆ Mg ₄ Si ₇ (G-phase) | D8 ₅ | Fm $\bar{3}m$ | | C (graphite) | A9 | P6 ₃ /mmc |
| cI2 | W | A2 | Im $\bar{3}m$ | | NiAs | B8 ₁ | P6 ₃ /mmc |
| cI16 | CoU | B ₂ | I2 ₃ | | ZnS (wurtzite) | B4 | P6 ₃ mc |
| cI28 | Th ₃ P ₄ | D7 ₃ | I4 ₃ d | hP5 | La ₂ O ₃ | D5 ₂ | P3m1 |
| cI32 | CoAs ₃ (skutterudite) | D0 ₂ | Im $\bar{3}$ | | Ni ₂ Al ₃ | D5 ₁₃ | P3m1 |
| cI40 | Ge ₇ Ir ₃ | D8 ₇ | Im $\bar{3}m$ | hP6 | CaCu ₅ | D2 ₄ | P6 ₃ /mmm |
| | Pu ₂ C ₃ | D5 ₅ | I4 ₃ d | | CoSn | B35 | P6 ₃ /mmm |
| cI52 | Cu ₂ Zn ₈ (γ brass) | D8 ₂ | I4 ₃ m | | Cu ₂ Te | C ₄ | P6 ₃ /mmm |
| | Fe ₃ Zn ₁₀ (γ brass) | D8 ₁ | Im $\bar{3}m$ | | HgS | B9 | P3 ₂ 1 |
| cI54 | Sb ₂ Tl ₇ | L2 ₂ | Im $\bar{3}m$ | | MoS ₂ | C7 | P6 ₃ /mmc |
| cI58 | α Mn (χ -phase) | A12 | I4 ₃ m | | Ni ₂ In | B8 ₂ | P6 ₃ /mmc |
| cI76 | Cu ₁₅ Si ₄ | D8 ₆ | I4 ₃ d | hP8 | Na ₃ As | D0 ₁₈ | P6 ₃ /mmc |
| cI80 | Mn ₂ O ₃ | D5 ₃ | Ia $\bar{3}$ | | Ni ₃ Sn | D0 ₁₉ | P6 ₃ /mmc |
| cI96 | AlLi ₃ N ₃ | E9 ₄ | Ia $\bar{3}$ | | TiAs | B ₁ | P6 ₃ /mmc |
| cI162 | Mg ₃₂ (Al,Zn) ₄₉ | D8 ₈ | Im $\bar{3}$ | hP9 | CrSi ₂ | C40 | P6 ₃ 22 |
| cP1 | α Po | A ₄ | Pm $\bar{3}m$ | | Fe ₂ P | C22 | P6 ₃ 2m |
| cP2 | CsCl | B2 | Pm $\bar{3}m$ | | γ AgZn | B ₃ | P3 |
| cP4 | AuCu ₃ | L1 ₂ | Pm $\bar{3}m$ | | SiO ₂ (high quartz) | C8 | P6 ₃ 22 |
| | ReO ₃ | D0 ₃ | Pm $\bar{3}m$ | hP10 | Pt ₂ Sn ₃ | D5 ₈ | P6 ₃ /mmc |
| cP5 | AlFe ₃ C (perovskite) | L1' ₂ | Pm $\bar{3}m$ | hP12 | CuS | B18 | P6 ₃ /mmc |
| | CaTiO ₃ (perovskite) | E2 ₁ | Pm $\bar{3}m$ | | MgZn ₂ (Laves) | C14 | P6 ₃ /mmc |
| | Fe ₄ N | L1' | P4 ₃ m | | SiO ₂ (β tridymite) | C10 | P6 ₃ /mmc |

continued

*Adapted (with additions and corrections) from ASM Handbook, Vol. 3, 10th ed, ASM International, Materials Park, OH.

Arranged Alphabetically by Pearson-Symbol Designation (*continued*)

| Pearson symbol | Prototype | Strukturbericht designation | Space group | Pearson symbol | Prototype | Strukturbericht designation | Space group |
|----------------|---|-----------------------------|---------------------------------------|----------------|---|-----------------------------|---------------------------------------|
| <i>hP</i> 14 | W ₂ B ₃ | D8 _h | <i>P</i> 6 ₃ / <i>mmc</i> | <i>oP</i> 8 | βCu ₃ Ti | D0 ₈ | <i>Pmmn</i> |
| <i>hP</i> 16 | Mn ₃ Si ₃ | D8 _h | <i>P</i> 6 ₃ / <i>mc</i> m | | FeB | B27 | <i>Pnma</i> |
| | Ni ₃ Ti | D0 ₂₄ | <i>P</i> 6 ₃ / <i>mmc</i> | | GeS | B16 | <i>Pnma</i> |
| <i>hP</i> 18 | Al ₃ C ₃ Si | E9 ₄ | <i>P</i> 6 ₃ / <i>mc</i> | | SnS | B29 | <i>Pm̄cn</i> |
| | Al ₃ FeMg ₃ Si ₆ | E9 ₆ | <i>P</i> 6 ₂ / <i>m</i> | | MnP | B31 | <i>Pnma</i> |
| | Mg ₂ Ni | C ₆ | <i>P</i> 6 ₂ 22 | | TiB | B ₂ | <i>Pnma</i> |
| <i>hP</i> 20 | Fe ₃ Th ₃ | D10 ₂ | <i>P</i> 6 ₃ / <i>mc</i> | <i>oP</i> 12 | Co ₂ Si, NiSiTi (E-phase) | C23 | <i>Pnma</i> |
| | Th ₃ Si ₂ | D8 _k | <i>P</i> 6 ₃ / <i>m</i> | | Co ₂ Si | C37 | <i>Pbnm</i> |
| <i>hP</i> 24 | Cu ₃ P | D0 ₂₁ | <i>P</i> 6 ₃ / <i>cm</i> | | HgCl ₂ | C28 | <i>Pm̄nb</i> |
| | MgNi ₂ (Laves) | C36 | <i>P</i> 6 ₃ / <i>mmc</i> | <i>oP</i> 16 | Al ₃ Ni | D0 ₂₀ | <i>Pnma</i> |
| <i>hP</i> 28 | Co ₂ Al ₃ | D8 ₁₁ | <i>P</i> 6 ₃ / <i>mmc</i> | | AsMn ₃ | D0 ₄ | <i>Pm̄mn</i> |
| <i>hR</i> 1 | αHg | A10 | <i>R</i> 3̄m | | BaS ₃ | D0 ₁₇ | <i>P</i> 42 ₁ / <i>m</i> |
| | βPo | A ₁ | <i>R</i> 3̄m | | CdSb | B ₂ | <i>Pbca</i> |
| <i>hR</i> 2 | αAs | A7 | <i>R</i> 3̄m | | CuS ₂ Sb (wolfsbergite) | F ₂ ₆ | <i>Pnma</i> |
| <i>hR</i> 3 | αSm | C19 | <i>R</i> 3̄m | | Fe ₃ C (cementite) | D0 ₁₁ | <i>Pnma</i> |
| <i>hR</i> 4 | NaCrS ₂ | F5 ₁ | <i>R</i> 3̄m | <i>oP</i> 20 | Cr ₂ C ₂ | D5 ₁₀ | <i>Pnma</i> |
| <i>hR</i> 5 | Bi ₂ Te ₃ | C33 | <i>R</i> 3̄m | | Sb ₂ S ₃ | D5 ₅ | <i>Pnma</i> |
| | Ni ₃ S ₂ | D5 ₂ | <i>R</i> 32 | <i>oP</i> 24 | Sb ₂ O ₃ (valentinite) | D5 ₁₁ | <i>Pccn</i> |
| <i>hR</i> 6 | CaSi ₂ | C12 | <i>R</i> 3̄m | | AuTe ₂ (krennerite) | C46 | <i>Pma</i> 2 |
| | NiS (millerite) | B13 | <i>R</i> 3̄m | | CuFe ₂ S ₃ (cubanite) | E9 ₂ | <i>Pnma</i> |
| <i>hR</i> 7 | Al ₄ C ₃ | D7 ₁ | <i>R</i> 3̄m | | TiO ₂ (brookite) | C21 | <i>Pbca</i> |
| | Mo ₂ B ₃ | D8 ₁ | <i>R</i> 3̄m | <i>oP</i> 40 | Cr ₂ C ₃ | D10 ₁ | <i>Pnma</i> |
| <i>hR</i> 10 | αAl ₂ O ₃ (corundum) | D5 ₁ | <i>R</i> 3̄c | <i>1I</i> 2 | αPa | A ₂ | <i>14</i> / <i>mmm</i> |
| <i>hR</i> 12 | BaPb ₃ | | <i>R</i> 3̄m | | In | A ₆ | <i>14</i> / <i>mmm</i> |
| <i>hR</i> 13 | Fe ₇ W ₆ (μ-phase) | D8 ₅ | <i>R</i> 3̄m | <i>1I</i> 4 | βSn | A5 | <i>14</i> / <i>amd</i> |
| <i>hR</i> 15 | B ₄ C | D1 ₈ | <i>R</i> 3̄m | <i>1I</i> 6 | CaC ₂ | C11 ₁ | <i>14</i> / <i>mmm</i> |
| <i>hR</i> 20 | HoAl ₃ | | <i>R</i> 3̄m | | MoSi ₂ | C11 ₂ | <i>14</i> / <i>mmm</i> |
| <i>hR</i> 26 | Cr ₃ Al ₈ | D8 ₁₀ | <i>R</i> 3̄m | <i>1I</i> 8 | ThH ₂ | L ₂ ₆ | <i>14</i> / <i>mmm</i> |
| <i>hR</i> 32 | CuPt | L1 ₁ | <i>R</i> 3̄m | <i>1I</i> 10 | Al ₃ Ti | D0 ₂₂ | <i>14</i> / <i>mmm</i> |
| <i>mC</i> 6 | AuTe ₂ (calaverite) | C34 | <i>C</i> 2/ <i>m</i> | | Al ₃ Ba | D1 ₃ | <i>14</i> / <i>m</i> |
| <i>mC</i> 8 | CuO (tenorite) | B26 | <i>C</i> 2/ <i>c</i> | <i>1I</i> 12 | MoNi ₄ | D1 ₂ | <i>14</i> / <i>m</i> |
| <i>mC</i> 12 | ThC ₂ | C ₂ | <i>C</i> 2/ <i>c</i> | | Al ₃ Cu | C16 | <i>14</i> / <i>mc</i> m |
| <i>mC</i> 14 | δNi ₃ Sn ₄ | D7 ₂ | <i>C</i> 2/ <i>m</i> | <i>1I</i> 14 | ThSi ₃ | C ₂ | <i>14</i> / <i>amd</i> |
| <i>mC</i> 16 | FeKS ₂ | F5 ₂ | <i>C</i> 2/ <i>c</i> | <i>1I</i> 16 | Al ₂ CdS ₄ | E3 | <i>14</i> |
| <i>mP</i> 12 | AgAuTe ₄ (sylvanite) | E1 ₆ | <i>P</i> 2/ <i>c</i> | | Al ₂ Zr | D0 ₁₃ | <i>14</i> / <i>mmm</i> |
| | ZrO ₂ | C43 | <i>P</i> 2/ <i>c</i> | | CuFeS ₄ (chalcopyrite) | E ₁₁ | <i>14</i> 2d |
| <i>mP</i> 20 | As ₂ S ₃ | D5 ₇ | <i>P</i> 2/ <i>c</i> | | Cu ₂ FeSnS ₄ (stannite) | H2 ₂ | <i>14</i> 2m |
| <i>mP</i> 22 | Co ₂ Al ₃ | D8 ₄ | <i>P</i> 2 ₁ / <i>c</i> | | Ir ₂ Si | D0 ₇ | <i>14</i> / <i>mc</i> m |
| <i>mP</i> 24 | FeAsS | E0 ₇ | <i>P</i> 2 ₁ / <i>c</i> | | MoB | B ₂ | <i>14</i> / <i>amd</i> |
| <i>mP</i> 32 | AsS (realgar) | B ₁ | <i>P</i> 2 ₁ / <i>c</i> | <i>1I</i> 18 | SiU ₃ | D0 ₆ | <i>14</i> / <i>mc</i> m |
| | βSe | A ₁ | <i>P</i> 2 ₁ / <i>c</i> | | TiSe | B37 | <i>14</i> / <i>mc</i> m |
| <i>mP</i> 64 | αSe | A ₂ | <i>P</i> 2 ₁ / <i>c</i> | <i>1I</i> 26 | Fe ₃ N | D2 ₂ | <i>14</i> / <i>mmm</i> |
| <i>oC</i> 4 | αU | A20 | <i>Cmcm</i> | <i>1I</i> 28 | Mn ₁₂ Th | D2 ₆ | <i>14</i> / <i>mmm</i> |
| <i>oC</i> 8 | CaSi | B ₂ | <i>Cm̄mc</i> | <i>1I</i> 32 | MnU ₆ | D2 ₂ | <i>14</i> / <i>mc</i> m |
| | αGa | A11 | <i>Cmca</i> | | Cr ₂ B ₃ | D8 ₁ | <i>14</i> / <i>mc</i> m |
| | CrB | B33 | <i>Cm̄cm</i> | | Ni ₃ P | D0 ₈ | <i>14</i> |
| | I ₂ | A14 | <i>Cmca</i> | | W ₂ Si ₃ | D8 ₂ | <i>14</i> / <i>mc</i> m |
| | P (black) | A17 | <i>Cmca</i> | <i>1P</i> 2 | δCuTi | L2 ₂ | <i>P</i> 4/ <i>mmm</i> |
| <i>oC</i> 12 | ZrSi ₂ | C49 | <i>Cm̄cm</i> | <i>1P</i> 4 | βNp | A ₂ | <i>P</i> 42 ₂ |
| <i>oC</i> 16 | BRe ₃ | E1 ₂ | <i>Cm̄cm</i> | | AuCu | L1 ₉ | <i>P</i> 4/ <i>mmm</i> |
| <i>oC</i> 20 | PdSn ₄ | D1 ₂ | <i>A</i> ba2 | | CuTi ₃ | L6 ₆ | <i>P</i> 4/ <i>mmm</i> |
| <i>oC</i> 24 | PdSn ₂ | C ₂ | <i>A</i> ba2 | | γCuTi | B11 | <i>P</i> 4/ <i>nm̄m</i> |
| <i>oC</i> 28 | Al ₂ Mn | D2 ₂ | <i>Cm̄cm</i> | | PbO | B10 | <i>P</i> 4/ <i>nm̄m</i> |
| <i>oF</i> 24 | TiSi ₂ | C54 | <i>F</i> ddd | | Pb ₃ Sr | | <i>P</i> 4/ <i>nm̄m</i> |
| <i>oF</i> 40 | Mn ₂ B | D1 ₇ | <i>F</i> ddd | <i>1P</i> 6 | PtS | B17 | <i>P</i> 4 ₂ / <i>mmc</i> |
| <i>oF</i> 48 | CuMg ₂ | C ₆ | <i>F</i> ddd | | Cu ₂ Sb | C38 | <i>P</i> 4/ <i>nm̄m</i> |
| <i>oF</i> 72 | GeS ₂ | C44 | <i>F</i> dd2 | | PbFCl | E0 ₁ | <i>P</i> 4/ <i>nm̄m</i> |
| <i>oF</i> 128 | αS | A16 | <i>F</i> ddd | <i>1P</i> 10 | TiO ₂ (rutile) | C4 | <i>P</i> 4 ₂ / <i>nm̄m</i> |
| <i>oI</i> 12 | SiS ₂ | C42 | <i>I</i> bam | | Pb ₂ Pt | D1 ₄ | <i>P</i> 4/ <i>nbm</i> |
| <i>oI</i> 14 | Ta ₃ B ₄ | D7 ₂ | <i>I</i> mmm | <i>1P</i> 16 | Si ₂ U ₃ | D5 ₂ | <i>P</i> 4/ <i>mbm</i> |
| <i>oI</i> 20 | Al ₃ U | D1 ₂ | <i>I</i> mma | <i>1P</i> 20 | PdS | B34 | <i>P</i> 4 ₂ / <i>m</i> |
| <i>oI</i> 28 | Ga ₂ Mg ₃ | D8 ₂ | <i>I</i> bam | <i>1P</i> 30 | B ₂ Th | D1 ₁ | <i>P</i> 4/ <i>mbm</i> |
| <i>oP</i> 4 | AuCd | B19 | <i>P</i> nma | | βU | A ₂ | <i>P</i> 4 ₂ / <i>nm̄m</i> |
| <i>oP</i> 6 | FeS ₂ (marcasite) | C18 | <i>P</i> nnm | <i>1P</i> 40 | αCrFe | D8 ₆ | <i>P</i> 4 ₂ / <i>nm̄m</i> |
| | CaCl ₂ | C35 | <i>P</i> nnm | | Al ₃ Cu ₂ Fe | E9 ₂ | <i>P</i> 4/ <i>mc</i> m |
| <i>oP</i> 8 | αNp | A ₂ | <i>P</i> nma | <i>1P</i> 50 | Zn ₃ P ₂ | D5 ₃ | <i>P</i> 4 ₂ / <i>nm̄c</i> |
| | γNiSi | B ₂ | <i>P</i> bnm | | γB | A ₂ | <i>P</i> 4 ₂ / <i>nm̄m</i> |

Arranged Alphabetically by Strukturbericht Designation

| Struktur- bericht designation | Prototype | Pearson symbol | Space group | Struktur- bericht designation | Prototype | Pearson symbol | Space group |
|-------------------------------------|--------------------------|-------------------|--------------------------------------|-------------------------------------|--------------------------------------|-------------------|--------------------------------------|
| A _a | αPa | <i>tI</i> 2 | <i>I</i> 4/ <i>mmm</i> | B20 | FeSi | <i>cP</i> 8 | <i>P</i> 2 ₁ 3 |
| A _b | βU | <i>tP</i> 30 | <i>P</i> 4 ₂ / <i>mmn</i> | B26 | CuO (tenorite) | <i>mC</i> 8 | <i>C</i> 2/ <i>c</i> |
| A _c | αNp | <i>oP</i> 8 | <i>Pnma</i> | B27 | FeB | <i>oP</i> 8 | <i>Pnma</i> |
| A _d | βNp | <i>tP</i> 4 | <i>P</i> 4 ₂ 2 | B29 | SnS | <i>oP</i> 8 | <i>Pm</i> <i>cn</i> |
| A _f | HgSn ₆₋₁₀ | <i>hP</i> 1 | <i>P</i> 6/ <i>mmm</i> | B31 | MnP | <i>oP</i> 8 | <i>Pnma</i> |
| A _g | γB | <i>tP</i> 50 | <i>P</i> 4 ₂ / <i>nnm</i> | B32 | NaTl | <i>cF</i> 16 | <i>Fd</i> 3 <i>m</i> |
| A _h | αPo | <i>cP</i> 1 | <i>Pm</i> 3 <i>m</i> | B33(=B _f) | CrB | <i>oC</i> 8 | <i>Cmcm</i> |
| A _i | βPo | <i>hR</i> 1 | <i>R</i> 3 <i>m</i> | B34 | PdS | <i>tP</i> 16 | <i>P</i> 4 ₂ / <i>m</i> |
| A _k | αSe | <i>mP</i> 64 | <i>P</i> 2 ₁ / <i>c</i> | B35 | CoSn | <i>hP</i> 6 | <i>P</i> 6/ <i>mmm</i> |
| A _l | βSe | <i>mP</i> 32 | <i>P</i> 2 ₁ / <i>c</i> | B37 | TiSe | <i>tI</i> 16 | <i>I</i> 4/ <i>mcm</i> |
| A1 | Cu | <i>cF</i> 4 | <i>Fm</i> 3 <i>m</i> | C _a | Mg ₂ Ni | <i>hP</i> 18 | <i>P</i> 6 ₂ 2 |
| A2 | W | <i>cI</i> 2 | <i>Im</i> 3 <i>m</i> | C _b | CuMg ₂ | <i>oF</i> 48 | <i>Fdd</i> |
| A3 | Mg | <i>hP</i> 2 | <i>P</i> 6 ₃ / <i>mmc</i> | C _c | ThSi ₂ | <i>tI</i> 12 | <i>I</i> 4 ₁ / <i>amd</i> |
| A3' | αLa | <i>hP</i> 4 | <i>P</i> 6 ₃ / <i>mmc</i> | C _e | PdSn ₂ | <i>oC</i> 24 | <i>Aba</i> 2 |
| A4 | C (diamond) | <i>cF</i> 8 | <i>Fd</i> 3 <i>m</i> | C _f | ThC ₂ | <i>mC</i> 12 | <i>C</i> 2/ <i>c</i> |
| A5 | βSn | <i>tI</i> 4 | <i>I</i> 4 ₁ / <i>amd</i> | C _g | Cu ₂ Te | <i>hP</i> 6 | <i>P</i> 6/ <i>mmm</i> |
| A6 | In | <i>tI</i> 2 | <i>I</i> 4/ <i>mmm</i> | C _h | LiZn ₂ | <i>hP</i> 3 | <i>P</i> 6 ₃ / <i>mmc</i> |
| A7 | αAs | <i>hR</i> 2 | <i>R</i> 3 <i>m</i> | C1 | CaF ₂ (fluorite) | <i>cF</i> 12 | <i>Fm</i> 3 <i>m</i> |
| A8 | γSe | <i>hP</i> 3 | <i>P</i> 3 ₂ 1 | C1 _b | MgAgAs | <i>cF</i> 12 | <i>F</i> 43 <i>m</i> |
| A9 | C (graphite) | <i>hP</i> 4 | <i>P</i> 6 ₃ / <i>mmc</i> | C2 | FeS ₂ (pyrite) | <i>cP</i> 12 | <i>P</i> 4 ₃ |
| A10 | αHg | <i>hR</i> 1 | <i>R</i> 3 <i>m</i> | C3 | Ag ₂ O | <i>cP</i> 6 | <i>Pn</i> 3 <i>m</i> |
| A11 | αGa | <i>oC</i> 8 | <i>Cmca</i> | C4 | TiO ₂ (rutile) | <i>tP</i> 6 | <i>P</i> 4 ₂ / <i>mmn</i> |
| A12 | αMn (χ-phase) | <i>cI</i> 58 | <i>I</i> 43 <i>m</i> | C6 | CdI ₂ | <i>hP</i> 3 | <i>P</i> 3 <i>m</i> 1 |
| A13 | βMn | <i>cP</i> 20 | <i>P</i> 4 ₃ 2 | C7 | MoS ₂ | <i>hP</i> 6 | <i>P</i> 6 ₃ / <i>mmc</i> |
| A14 | I ₂ | <i>oC</i> 8 | <i>Cmca</i> | C8 | SiO ₂ (high quartz) | <i>hP</i> 9 | <i>P</i> 6 ₂ 2 |
| A15 | Cr ₂ Si (β-W) | <i>cP</i> 8 | <i>Pm</i> 3 <i>n</i> | C9 | SiO ₂ (β cristobalite) | <i>cF</i> 24 | <i>Fd</i> 3 <i>m</i> |
| A16 | αS | <i>oF</i> 128 | <i>Fdd</i> | C10 | SiO ₂ (β tridymite) | <i>hP</i> 12 | <i>P</i> 6 ₃ / <i>mmc</i> |
| A17 | P (black) | <i>oC</i> 8 | <i>Cmca</i> | C11 _a | CaC ₂ | <i>tI</i> 6 | <i>I</i> 4/ <i>mmm</i> |
| A20 | αU | <i>oC</i> 4 | <i>Cmcm</i> | C11 _b | MoSi ₂ | <i>tI</i> 6 | <i>I</i> 4/ <i>mmm</i> |
| B _a | CoU | <i>cI</i> 16 | <i>I</i> 2 ₃ | C12 | CaSi ₂ | <i>hR</i> 6 | <i>R</i> 3 <i>m</i> |
| B _b | {AgZn} | <i>hP</i> 9 | <i>P</i> 3 | C14 | MgZn ₂ | <i>hP</i> 12 | <i>P</i> 6 ₃ / <i>mmc</i> |
| B _c | CaSi | <i>oC</i> 8 | <i>Cmcm</i> | C15 | Cu ₂ Mg } Laves | <i>cF</i> 24 | <i>Fd</i> 3 <i>m</i> |
| B _d | ηNiSi | <i>oP</i> 8 | <i>Pbnm</i> | C15 _b | AuBe ₃ | <i>cF</i> 24 | <i>F</i> 43 <i>m</i> |
| B _e | CdSb | <i>oP</i> 16 | <i>Pbca</i> | C16 | Al ₂ Cu | <i>tI</i> 12 | <i>I</i> 4/ <i>mcm</i> |
| B _f (=B33) | CrB | <i>oC</i> 8 | <i>Cmcm</i> | C18 | FeS ₂ (marcasite) | <i>oP</i> 6 | <i>Pnnm</i> |
| B _g | MoB | <i>tI</i> 16 | <i>I</i> 4 ₁ / <i>amd</i> | C19 | αSm | <i>hR</i> 3 | <i>R</i> 3 <i>m</i> |
| B _h | WC | <i>hP</i> 2 | <i>P</i> 6 <i>m</i> 2 | C21 | TiO ₂ (brookite) | <i>oP</i> 24 | <i>Pbca</i> |
| B _i | TiAs | <i>hP</i> 8 | <i>P</i> 6 ₃ / <i>mmc</i> | C22 | Fe ₂ P | <i>hP</i> 9 | <i>P</i> 6 <i>m</i> 2 |
| B _k | BN | <i>hP</i> 4 | <i>P</i> 6 ₃ / <i>mmc</i> | C23 | Co ₂ Si, NiSiTi (E-phase) | <i>oP</i> 12 | <i>Pnma</i> |
| B _l | AsS (realgar) | <i>mP</i> 32 | <i>P</i> 2 ₁ / <i>c</i> | C28 | HgCl ₂ | <i>oP</i> 12 | <i>Pmnb</i> |
| B _m | TiB | <i>oP</i> 8 | <i>Pnma</i> | C32 | AlB ₂ | <i>hP</i> 3 | <i>P</i> 6/ <i>mmm</i> |
| B1 | NaCl (rock salt) | <i>cF</i> 8 | <i>Fm</i> 3 <i>m</i> | C33 | Bi ₂ Te ₃ | <i>hR</i> 5 | <i>R</i> 3 <i>m</i> |
| B2 | CsCl | <i>cP</i> 2 | <i>Pm</i> 3 <i>m</i> | C34 | AuTe ₂ (calaverite) | <i>mC</i> 6 | <i>C</i> 2/ <i>m</i> |
| B3 | ZnS (sphalerite) | <i>cF</i> 8 | <i>F</i> 43 <i>m</i> | C35 | CaCl ₂ | <i>oP</i> 6 | <i>Pnnm</i> |
| B4 | ZnS (wurtzite) | <i>hP</i> 4 | <i>P</i> 6 ₃ <i>mc</i> | C36 | MgNi ₂ (Laves) | <i>hP</i> 24 | <i>P</i> 6 ₃ / <i>mmc</i> |
| B8 ₁ | NiAs | <i>hP</i> 4 | <i>P</i> 6 ₃ / <i>mmc</i> | C37 | Co ₂ Si | <i>oP</i> 12 | <i>Pbnm</i> |
| B8 ₂ | Ni ₂ In | <i>hP</i> 6 | <i>P</i> 6 ₃ / <i>mmc</i> | C38 | Cu ₂ Sb | <i>tP</i> 6 | <i>P</i> 4/ <i>nnm</i> |
| B9 | HgS (cinnabar) | <i>hP</i> 6 | <i>P</i> 3 ₂ 1 | C40 | CrSi ₂ | <i>hP</i> 9 | <i>P</i> 6 ₂ 2 |
| B10 | PbO | <i>tP</i> 4 | <i>P</i> 4/ <i>nnm</i> | C42 | SiS ₂ | <i>oI</i> 12 | <i>Ibam</i> |
| B11 | γCuTi | <i>tP</i> 4 | <i>P</i> 4/ <i>nnm</i> | C43 | ZrO ₂ | <i>mP</i> 12 | <i>P</i> 2 ₁ / <i>c</i> |
| B13 | NiS (millerite) | <i>hR</i> 6 | <i>R</i> 3 <i>m</i> | C44 | GeS ₂ | <i>oF</i> 72 | <i>Fdd</i> 2 |
| B16 | GeS | <i>oP</i> 8 | <i>Pnma</i> | C46 | AuTe ₂ (krennerite) | <i>oP</i> 24 | <i>Pma</i> 2 |
| B17 | PtS (cooperite) | <i>tP</i> 4 | <i>P</i> 4 ₂ / <i>mmc</i> | C49 | ZrSi ₂ | <i>oC</i> 12 | <i>Cmcm</i> |
| B18 | CuS (rovelite) | <i>hP</i> 12 | <i>P</i> 6 ₃ / <i>mmc</i> | C54 | TiSi ₂ | <i>oF</i> 24 | <i>Fddd</i> |
| B19 | AuCd | <i>oP</i> 4 | <i>Pnma</i> | D0 _a | βCu ₂ Ti | <i>oP</i> 8 | <i>Pmnn</i> |
| | | | | D0 _c | SiU ₃ | <i>tI</i> 16 | <i>I</i> 4/ <i>mcm</i> |

continued

Arranged Alphabetically by Strukturbericht Designation (*continued*)

| Struktur- bericht designation | Prototype | Pearson symbol | Space group | Struktur- bericht designation | Prototype | Pearson symbol | Space group |
|-------------------------------------|---|-------------------|---------------------------|-------------------------------------|--|-------------------|---------------------------|
| D0 _c | Ir ₂ Si | <i>tI</i> 16 | <i>I4/mcm</i> | D8 _d | Co ₂ Al ₉ | <i>mP</i> 22 | <i>P2₁/c</i> |
| D0 _d | AsMn ₃ | <i>oP</i> 16 | <i>Pmmn</i> | D8 _e | Mg ₃₂ (Al,Zn) ₄₉ | <i>cl</i> 162 | <i>Im</i> 3 |
| D0 _e | Ni ₃ P | <i>tI</i> 32 | <i>I</i> 4 | D8 _f | Ge ₂ Ir ₃ | <i>cl</i> 40 | <i>Im</i> 3m |
| D0 _f | CoAs ₃ (skutterudite) | <i>cl</i> 32 | <i>Im</i> 3 | D8 _g | Ga ₂ Mg ₃ | <i>ol</i> 28 | <i>Ibam</i> |
| D0 _g | BiF ₃ , AlFe ₃ | <i>cF</i> 16 | <i>Fm</i> 3m | D8 _h | W ₂ B ₃ | <i>hP</i> 14 | <i>P6₃/mmc</i> |
| D0 _h | ReO ₃ | <i>cP</i> 4 | <i>Pm</i> 3m | D8 _i | Mo ₂ B ₃ | <i>hR</i> 7 | <i>R</i> 3m |
| D0 _i | Fe ₃ C (cementite) | <i>oP</i> 16 | <i>Pnma</i> | D8 _k | Th ₃ Si ₂ | <i>hP</i> 20 | <i>P6₃/m</i> |
| D0 _j | BaS ₃ | <i>oP</i> 16 | <i>P4₂/m</i> | D8 _l | Cr ₃ B ₃ | <i>tI</i> 32 | <i>I4/mcm</i> |
| D0 _k | Na ₂ As | <i>hP</i> 8 | <i>P6₃/mmc</i> | D8 _m | W ₂ Si ₃ | <i>tI</i> 32 | <i>I4/mcm</i> |
| D0 _l | Ni ₃ Sn | <i>hP</i> 8 | <i>P6₃/mmc</i> | D8 _n | Fe ₃ Zn ₁₀ | <i>cl</i> 52 | <i>Im</i> 3m |
| D0 _m | Al ₃ Ni | <i>oP</i> 16 | <i>Pnma</i> | D8 _o | Cu ₃ Zn ₈ | <i>cl</i> 52 | <i>I</i> 43m |
| D0 _n | Cu ₃ P | <i>hP</i> 24 | <i>P6₃/cm</i> | D8 _p | Cu ₃ Al ₄ | <i>cP</i> 52 | <i>P</i> 43m |
| D0 _o | Al ₃ Ti | <i>tI</i> 8 | <i>I4/mmm</i> | D8 _q | Cr ₂₃ C ₆ | <i>cF</i> 116 | <i>Fm</i> 3m |
| D0 _p | Al ₃ Zr | <i>tI</i> 16 | <i>I4/mmm</i> | D8 _r | Fe ₂ W ₆ (μ -phase) | <i>hR</i> 13 | <i>R</i> 3m |
| D0 _q | Ni ₃ Ti | <i>hP</i> 16 | <i>P6₃/mmc</i> | D8 _s | Cu ₁₅ Si ₄ | <i>cl</i> 76 | <i>I</i> 43d |
| D1 _a | MoNi ₄ | <i>tI</i> 10 | <i>I4/m</i> | D8 _t | Mn ₂ Si ₃ | <i>hP</i> 16 | <i>P6₃/mcm</i> |
| D1 _b | Al ₄ U | <i>ol</i> 20 | <i>Imma</i> | D8 _u | Co ₃ S ₈ | <i>cF</i> 68 | <i>Fm</i> 3m |
| D1 _c | PdSn ₄ | <i>oC</i> 20 | <i>Aba</i> 2 | D8 _v | Cr ₃ Al ₈ | <i>hR</i> 26 | <i>R</i> 3m |
| D1 _d | Pb ₃ Pt | <i>tP</i> 10 | <i>P4/nbm</i> | D8 _w | Co ₂ Al ₃ | <i>hP</i> 28 | <i>P6₃/mmc</i> |
| D1 _e | B ₄ Th | <i>tP</i> 20 | <i>P4/mbm</i> | D10 ₁ | Cr ₇ C ₃ | <i>oP</i> 40 | <i>Pnma</i> |
| D1 _f | Mn ₄ B | <i>oF</i> 40 | <i>Fddd</i> | D10 ₂ | Fe ₃ Th ₇ | <i>hP</i> 20 | <i>P6₃/mc</i> |
| D1 _g | B ₃ C | <i>hR</i> 15 | <i>R</i> 3m | E0 ₁ | PbFCl | <i>tP</i> 6 | <i>P4/nmm</i> |
| D1 _h | Al ₃ Ba | <i>tI</i> 10 | <i>I4/mmm</i> | E0 ₂ | FeAsS | <i>mP</i> 24 | <i>P2₁/c</i> |
| D2 _a | Mn ₁₂ Th | <i>tI</i> 26 | <i>I4/mmm</i> | E1 _a | MgCuAl ₂ | <i>oC</i> 16 | <i>Cmcm</i> |
| D2 _b | MnU ₆ | <i>tI</i> 28 | <i>I4/mcm</i> | E1 _b | AgAuTe ₄ (sylvanite) | <i>mP</i> 12 | <i>P2/c</i> |
| D2 _c | CaCu ₅ | <i>hP</i> 6 | <i>P6₃/mmm</i> | E1 _c | CuFeS ₂ (chalcopyrite) | <i>tI</i> 16 | <i>I</i> 42d |
| D2 _d | BaHg ₁₁ | <i>cP</i> 36 | <i>Pm</i> 3m | E2 ₁ | CaTiO ₃ (perovskite) | <i>cP</i> 5 | <i>Pm</i> 3m |
| D2 _e | UB ₁₂ | <i>cF</i> 52 | <i>Fm</i> 3m | E3 | Al ₂ CdS ₄ | <i>tI</i> 14 | <i>I</i> 4 |
| D2 _f | Fe ₉ N | <i>tI</i> 18 | <i>I4/mmm</i> | E9 _a | Al ₃ Cu ₄ Fe | <i>tP</i> 40 | <i>P4/mnc</i> |
| D2 _g | Al ₆ Mn | <i>oC</i> 28 | <i>Cmcm</i> | E9 _b | Al ₃ FeMg ₃ Si ₆ | <i>hP</i> 18 | <i>P</i> 62m |
| D2 _h | CaB ₆ | <i>cP</i> 7 | <i>Pm</i> 3m | E9 _c | Mn ₃ Al ₂ Si | <i>hP</i> 26 | <i>P6₃/mmc</i> |
| D2 _i | NaZn ₁₃ | <i>cF</i> 112 | <i>Fm</i> 3c | E9 _d | AlLi ₃ N ₂ | <i>cl</i> 96 | <i>Ia</i> 3 |
| D5 _a | Si ₃ U ₃ | <i>tP</i> 10 | <i>P4/mbm</i> | E9 _e | CuFe ₂ S ₃ (cubanite) | <i>oP</i> 24 | <i>Pnma</i> |
| D5 _b | Pt ₂ Sn ₃ | <i>hP</i> 10 | <i>P6₃/mmc</i> | E9 _f | Fe ₃ W ₃ C (η carbide) | <i>cF</i> 112 | <i>Fd</i> 3m |
| D5 _c | Pu ₃ C ₃ | <i>cl</i> 40 | <i>I</i> 43d | E9 _g | Al ₄ C ₄ Si | <i>hP</i> 18 | <i>P6₃/mc</i> |
| D5 _d | Ni ₃ S ₂ | <i>hR</i> 5 | <i>R</i> 32 | F0 ₁ | NiSbS (ullmannite) | <i>cP</i> 12 | <i>P2₁/c</i> |
| D5 _e | As ₂ S ₃ | <i>mP</i> 20 | <i>P2₁/c</i> | F5 _a | FeKS ₂ | <i>mC</i> 16 | <i>C2/c</i> |
| D5 _f | α -Al ₂ O ₃ (corundum) | <i>hR</i> 10 | <i>R</i> 3c | F5 _b | NaCrS ₂ | <i>hR</i> 4 | <i>R</i> 3m |
| D5 _g | La ₂ O ₃ | <i>hP</i> 5 | <i>P</i> 3m1 | F5 _c | CuS ₂ Sb (wolfsbergite) | <i>oP</i> 16 | <i>Pnma</i> |
| D5 _h | Mn ₂ O ₃ | <i>cl</i> 80 | <i>Ia</i> 3 | H1 ₁ | Al ₂ MgO ₄ (spinel) | <i>cF</i> 56 | <i>Fd</i> 3m |
| D5 _i | Sb ₂ O ₃ (senarmontite) | <i>cF</i> 80 | <i>Fd</i> 3m | H2 ₁ | Cu ₃ VS ₃ (sylvanite) | <i>cP</i> 8 | <i>P</i> 43m |
| D5 _j | Sb ₂ S ₃ | <i>oP</i> 20 | <i>Pnma</i> | H2 ₂ | Cu ₂ FeSnS ₄ | <i>tI</i> 16 | <i>I</i> 42m |
| D5 _k | Zn ₃ P ₂ | <i>tP</i> 40 | <i>P4₂/nmc</i> | L1 ₁ | Fe ₂ N | <i>cP</i> 5 | <i>Pm</i> 3m |
| D5 _l | Cr ₃ C ₂ | <i>oP</i> 20 | <i>Pnma</i> | L1 ₂ | CuPt ₃ | <i>cF</i> 32 | <i>Fm</i> 3c |
| D5 _m | Sb ₂ O ₃ (valentinite) | <i>oP</i> 20 | <i>Pccn</i> | L1 ₃ | AuCu | <i>tP</i> 4 | <i>P4/mmm</i> |
| D7 _a | Ni ₃ Al ₃ | <i>hP</i> 5 | <i>P</i> 3m1 | L1 ₄ (M) | AuCuII | <i>ol</i> 40 | <i>Imma</i> |
| D7 _b | δ -Ni ₃ Sn ₄ | <i>mC</i> 14 | <i>C2/m</i> | L1 ₅ | CuPt | <i>hR</i> 32 | <i>R</i> 3m |
| D7 _c | Ta ₃ B ₄ | <i>ol</i> 14 | <i>Immm</i> | L1 ₆ | AuCu ₃ | <i>cP</i> 4 | <i>Pm</i> 3m |
| D7 _d | Al ₃ C ₃ | <i>hR</i> 7 | <i>R</i> 3m | L1 ₇ | AlFe ₃ C (perovskite) | <i>cP</i> 5 | <i>Pm</i> 3m |
| D7 _e | Co ₃ S ₄ | <i>cF</i> 56 | <i>Fd</i> 3m | L2 ₁ | δ -CuTi | <i>tP</i> 2 | <i>P4/mmm</i> |
| D7 _f | Th ₃ P ₄ | <i>cl</i> 28 | <i>I</i> 43d | L2 ₂ | ThH ₃ | <i>tI</i> 6 | <i>I4/mmm</i> |
| D8 _a | Mn ₂₃ Th ₆ , Cu ₁₆ Mg ₆ Si ₇ (G-phase) | <i>cF</i> 116 | <i>Fm</i> 3m | L2 ₃ | AlCu ₂ Mn (Heusler) | <i>cF</i> 16 | <i>Fm</i> 3m |
| D8 _b | σ -CrFe | <i>tP</i> 30 | <i>P4₂/nmm</i> | L2 ₄ | Sb ₂ Tl ₃ | <i>cl</i> 54 | <i>Im</i> 3m |
| D8 _c | Mg ₂ Zn ₁₁ | <i>cP</i> 39 | <i>Pm</i> 3 | L3 ₁ | Fe ₂ N | <i>hP</i> 3 | <i>P6₃/mmc</i> |
| | | | | L6 ₀ | CuTi ₃ | <i>tP</i> 4 | <i>P4/mmm</i> |

Contents

Contributors ix

Preface to the 1995 Edition xi

Preface to Reprint Volumes xiii

Acronyms xv

Crystal Structure Nomenclature xxi

1. Magnetic Principles **1**

1.1 Introduction 1

1.2 Basic Magnetic Concepts 2

1.3 Categories of Magnetic Behavior 3

1.4 References 6

2. Electrical and Electronic Behavior **7**

2.1 Introduction 7

2.2 Electrical Conduction in Metals 8

2.3 Electrical Conduction in Intermetallic Compounds 11

2.4 Summary 26

2.5 References 27

3. Magnetic Applications **31**

3.1 Introduction 31

3.2 Magnetically Soft Materials 34

3.3 Permanent Magnets 35

| | | |
|-----------|---|-----------|
| 3.4 | Applications | 45 |
| 3.5 | Conclusions | 47 |
| 3.6 | References | 47 |
| 4. | Semiconductor Applications | 51 |
| 4.1 | Introduction | 51 |
| 4.2 | Compound Semiconductors for Device Applications | 54 |
| 4.3 | Electrical Applications | 60 |
| 4.4 | Optical Applications | 64 |
| 4.5 | Other Applications | 72 |
| 4.6 | Conclusions | 74 |
| 4.7 | References | 76 |
| | Addendum | 78 |
| 5. | Superconductor Applications | 83 |
| 5.1 | Introduction – Characteristics of A15 Superconductors | 83 |
| 5.2 | Intrinsic Properties | 84 |
| 5.3 | Extrinsic Properties | 87 |
| 5.4 | General – Applications of A15 Superconductors | 96 |
| 5.5 | Comparison with Other Superconductors | 98 |
| 5.6 | High-Field Magnets | 99 |
| 5.7 | Nuclear Magnetic Resonance (NMR) | 102 |
| 5.8 | Hybrid Magnet Facilities | 103 |
| 5.9 | Magnetic Fusion | 103 |
| 5.10 | Particle Accelerators | 108 |
| 5.11 | Magnetic Resonance Imaging (MRI) | 109 |
| 5.12 | Magnetically Levitated High-Speed Vehicles | 111 |
| 5.13 | Power Applications | 112 |
| 5.14 | Electronics | 115 |
| 5.15 | Conclusions | 116 |
| 5.16 | References | 116 |

| | |
|---|------------|
| 6. Magnetostriction: Materials and Applications | 121 |
| 6.1 Introduction | 121 |
| 6.2 History of Magnetostrictive Materials | 122 |
| 6.3 Magnetostriction | 123 |
| 6.4 Binary REFe Compounds | 126 |
| 6.5 Properties of Terfenol-D for Devices | 127 |
| 6.6 Recent Developments | 132 |
| 6.7 Magnetostrictive Actuators | 133 |
| 6.8 Summary | 135 |
| 6.9 Acknowledgements | 135 |
| 6.10 References | 136 |
| 7. Optical Applications | 139 |
| 7.1 Introduction | 139 |
| 7.2 Applications Based Principally on Optical Properties | 140 |
| 7.3 Single-Stage Applications Based on Photon-Electron Interactions | 150 |
| 7.4 Integrated Circuits and Other Multicomponent Systems | 164 |
| 7.5 Summary | 164 |
| 7.6 Acknowledgement | 164 |
| 7.7 References | 164 |
| Addendum | 167 |
| 8. Magneto-Optical Applications | 169 |
| 8.1 Introduction | 169 |
| 8.2 Phenomenological Description of Magneto-Optical Effects | 169 |
| 8.3 Physical Origins of Magneto-Optical Effects | 172 |
| 8.4 Materials Requirements for Magneto-Optical Applications | 175 |
| 8.5 Magneto-Optical Properties of Intermetallic Compounds | 176 |
| 8.6 Summary | 184 |
| 8.7 Acknowledgements | 184 |
| 8.8 References | 184 |

| | |
|---|------------|
| 9. Thermoelectric and Electrical Applications | 187 |
| 9.1 Introduction | 187 |
| 9.2 Thermoelectricity: Physical Phenomena and Terminology | 188 |
| 9.3 Thermoelectric Applications: Principles | 189 |
| 9.4 Thermoelectric Applications: Practice | 190 |
| 9.5 Thermoelectrics (TE Materials) | 194 |
| 9.6 General Discussion of the Art in TE Applications | 199 |
| 9.7 Electrical Applications | 203 |
| 9.8 Conclusion | 204 |
| 9.9 References | 205 |
| Addendum | 205 |
| 10. Diffusion Barriers | 207 |
| 10.1 Introduction | 207 |
| 10.2 Types of Diffusion Barriers | 208 |
| 10.3 Prediction of the Phase Formation Sequence: The Effective Heat of Formation Model | 210 |
| 10.4 Stability of Amorphous Metal Alloys | 213 |
| 10.5 Interactions between Binary Alloys and Semiconductor Substrates | 218 |
| 10.6 Diffusion Barriers in Metallization Schemes | 226 |
| 10.7 Preparation and Use | 232 |
| 10.8 Summary | 233 |
| 10.9 Acknowledgements | 234 |
| 10.10 References | 234 |
| Addendum | 239 |
| Index | 241 |

Chapter 1

Magnetic Principles

James S. Kouvel

Department of Physics, University of Illinois at Chicago, Chicago, IL 60680, USA

1. Introduction

Intermetallic compounds containing one or more of the iron-group, rare-earth, or actinide metals continue to provide an arena for enormous advances in the understanding and applications of many aspects of magnetism. The years since the publication of the original edition of *Intermetallic Compounds* (Westbrook, 1967) have seen many important unanticipated developments. Foremost examples include: the compounds of rare earths with transition metals that are extraordinarily strong permanent magnets; the so-called heavy-fermion compounds of cerium or uranium; the magnetic intermetallics with partial chemical disorder that exhibit spin-glass properties; and (in a related area) the superconducting intermetallic compounds of niobium, whose critical temperatures were a record high until the more recent discovery of the superconducting oxides.

These recent developments simply extend the long and distinguished history of intermetallic compounds as magnetic materials. It is now almost a century ago that Heusler (1903, 1904) discovered that certain ternary alloys containing none of the common ferromagnetic metals (iron, cobalt, or nickel) were nevertheless ferromagnetic, and it was later found by X-ray diffraction that many of these alloys were chemically ordered at specific stoichiometries. However, the prototypical Heusler compounds, Cu_2MnSn and Cu_2MnAl , do contain manganese, which is in the same transition-metal series as iron and is therefore similarly capable of deriving an atomic magnetic moment from its unfilled 3d-electron shell. Analogous examples,

discovered more recently, are the weakly ferromagnetic compounds Au_4V , Sc_3In , and ZrZn_2 , where vanadium and scandium are also in the iron-group series while zirconium is in the heavier transition-metal series characterized by a partially filled 4d electron shell. Indeed, as the magnetic implications of the electronic basis of the periodic table of elements came to be understood with the advent of quantum mechanics in the 1920s, it became increasingly puzzling as to why so few of the intermetallic (or ionic) compounds of the transition-group elements (even of iron) showed any evidence of ferromagnetism.

This puzzle was largely resolved in the early 1930s through the intuition of Néel (1932), who conceived of the antiferromagnetic state, in which the magnetic moments of neighboring atoms are aligned antiparallel to each other and thus produce no magnetization in the material as a whole, in contrast to the parallel moments in the case of ferromagnetism. The existence of antiferromagnetism has subsequently been confirmed in numerous intermetallic compounds of transition metals, e.g. MnAu (Bacon and Street, 1958; Bacon, 1962), and of rare earths, e.g. TbAg (Cable *et al.*, 1964), by means of neutron diffraction measurements, the experimental technique of prime importance in determining atomic magnetic configurations (see Chapter 19 by Roth in this volume). In various other intermetallics, e.g. Mn_2Sb (Wilkinson *et al.*, 1957), as well as in the ionic ferrites and garnets, this technique has also established the existence of the ferrimagnetic state, where the antiparallel atomic moments are unequal in size, which Néel (1948) had postulated as an extension to the antiferromagnetic case. In such a case, there is a net

bulk magnetization, though smaller, of course, than if the atomic moments were aligned parallel.

Even in a ferromagnetic material, the bulk magnetization in zero field is normally smaller than the saturation magnetization in large fields. Demagnetization effects associated with the shape of the sample cause the material to subdivide into macroscopic regions called ferromagnetic domains, which have magnetizations of the same magnitude (per unit volume) but different orientations. When the material is subjected to a magnetic field \mathbf{H} , the domains with magnetizations oriented closest to the direction of \mathbf{H} will grow in size at the expense of the others by means of domain-wall motion. Moreover, the domain magnetizations will all turn by various amounts toward the direction of \mathbf{H} . The ease with which these processes can occur separates the 'soft' from the 'hard' magnetic materials, the extremes of the latter being the strong permanent magnets.

2. Basic Magnetic Concepts

Certain general features of the ordered magnetic states found in intermetallic compounds have had profound theoretical implications pertinent to all magnetic materials. Their significance can best be appreciated with reference to various interpretations of the basic magnetic parameters: (i) the magnitude of the atomic moments and (ii) the strength and sign of the coupling between these moments. (Conventionally, a positive (ferromagnetic) or negative (antiferromagnetic) coupling favors a parallel or antiparallel alignment of magnetic moments, respectively.) All modern theories of magnetism agree that the origin of both (i) and (ii) lies in the quantum-mechanical part of the electron Coulomb energy known as the exchange energy, but they differ in the approximations made in their application to different types of materials.

At one extreme, in the atomistic theories, the viewpoint is taken that (i) and (ii) can be considered quite separately. This approach is especially valid for ionic crystals, in which all the electrons are tightly bound to the ion cores. The energy levels of the unfilled d- or f-electron shell of a transition-metal or rare-earth ion in such a crystal, though modified in their spacing by interactions with the electrostatic fields of neighboring ions, are nevertheless fairly discrete and are therefore occupied, if at all, by an integral number of electrons (per ion). Consequently, the magnetic moment per ion equals a certain number of individual electron moments (or Bohr magnetons). In most cases, in which the electrostatic interactions between adjacent ions are

rather weak, the ionic moment in a crystal is nearly the same as that of the free ion. Consistent with this approximation, the exchange coupling between the moments of magnetic ions in such a crystal is a minor perturbation and does not appreciably affect the size of the ionic moments. These considerations continue to apply to rare-earth atoms in a metallic system, where the f electrons are still tightly bound and do not participate significantly in the structural binding. However, the same cannot be said for the d electrons in transition-metal systems.

At the other extreme is the collective electron theory. As applied to the transition metals, this approach has strong interactions among the d and s (conduction) electrons, giving rise to a broadening of their energy levels into bands. Furthermore, because the d and s bands overlap in energy and are both occupied up to the same maximum (Fermi) energy level, the number of electrons in each band will not be integral. If, in addition, a sufficiently strong exchange coupling favors a parallel alignment of the electron moments, the energies of those with moments parallel or antiparallel to a reference direction will be lowered or raised, respectively, relative to the Fermi energy, and their numbers will adjust further. As a result, there will be a net bulk magnetization corresponding in general to a non-integral number of Bohr magnetons per atom, which agrees qualitatively with the situation for elemental iron, cobalt, and nickel. However, since this theory handles all the d and s electrons collectively, it makes no distinction between the constituent elements of disordered transition-metal alloys and has therefore enjoyed only a limited success in explaining their basic magnetic properties.

It is with respect to the magnetic properties of ordered alloys or intermetallic compounds that the limitations of these extreme theoretical viewpoints are particularly evident. As neutron diffraction experiments have revealed, the magnetic moment of a transition-metal atom such as iron varies appreciably from one compound to another and even among crystallographically different sites in the same compound. Such a variability in magnetic moment testifies against the validity of the collective electron model in the simple form described above. On the other hand, the fact that the magnetic moments of transition-metal atoms in intermetallic compounds are usually not integral in Bohr magnetons tells us that the simple atomistic model also is not valid. Indeed, as theoretical work has shown (White, 1970), the appropriate magnetic model is a complicated (but solvable) intermediate between these two extremes. Moreover, in intermetallic systems, the exchange

interactions between the atoms with magnetic moments do not derive entirely from a direct process involving the d or f electrons that are responsible for the atomic moments. There is also an indirect exchange process in which the conduction electrons act as intermediary agents, and this process predominates in cases where the moment-bearing atoms are separated by large distances, as they often are in compounds with large unit cells.

Another type of variability of magnetic moment is seen in certain intermetallic compounds containing prototypically cerium or uranium, the lightest of the lanthanide (rare-earth) and actinide elements with electrons in the 4f or 5f shell. In these compounds (e.g. CeCu_2Si_2 and UPt_3 , whose antiferromagnetism is accompanied by superconductivity at very low temperatures), the number of electrons in these shells, which defines the effective valence, is not a stable quantity but fluctuates rapidly with time, resulting in a fluctuating magnetic moment. These so-called heavy-fermion systems are of considerable current interest (see Chapter 10 by Aronson and Coles in this volume).

More generally, an appropriate model must also explain the origin of magnetocrystalline anisotropy, the phenomenon defined by the orientational preference of atomic moments in a crystal for certain crystallographically equivalent directions. It is broadly understood that the anisotropy associated with any magnetic atom derives from the coupling between the spin and orbital moments of its d or f electrons. The orbital electronic motion interacts, in turn, with the electrostatic fields produced by the local crystalline environment. For rare-earth atoms, the interactions of the nearly localized f electrons with the crystal fields are not very strong and can be readily calculated. In the case of transition-metal atoms, whose d electrons are much more extended spatially, the crystal-field interactions are correspondingly stronger and they restrict the degrees of freedom associated with the orbital states. This 'orbital quenching' results in an atomic moment that reflects primarily the electronic spin state and which, paradoxically as it may seem, has a much weaker anisotropy than in the case of the rare earths. In all cases, the magnetocrystalline anisotropy also depends on the crystalline symmetry and is weakest when the symmetry is highest (i.e. cubic).

3. Categories of Magnetic Behavior

3.1 Intrinsic Properties

The intrinsic magnetic properties of an intermetallic compound (or any other system) are most easily

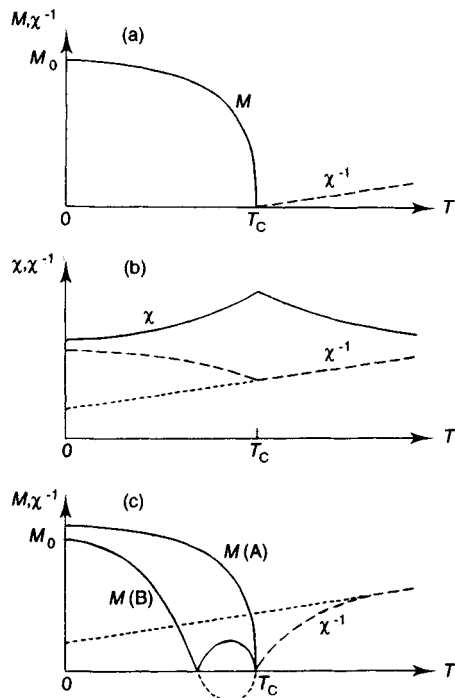


Figure 1. Typical variation with temperature of the magnetization (M) or susceptibility (χ) below the Curie point (T_C) and of χ^{-1} above T_C for (a) a ferromagnet, (b) an antiferromagnet, and (c) a ferrimagnet. In (c), M versus T is shown for cases A and B, as described in the text

described within the framework of the molecular-field theory, in which the net exchange coupling between a given atom and all its neighbors is approximated by the interaction of its magnetic moment with an effective 'molecular' field. The situation is particularly simple for a *ferromagnetic* system when all the exchange interactions are positive, in which case the spontaneous magnetization corresponds at 0° K to a parallel alignment of all the atomic moments and diminishes monotonically with increasing temperature as the moments fluctuate in direction. The manner in which the magnetization decreases from its value M_0 at 0° K and finally vanishes at the Curie temperature (T_C) is represented in Figure 1(a). Above T_C , where the system is magnetically disordered (i.e. paramagnetic), the magnetic susceptibility (χ) decreases with rising temperature according to the following relation known as the Curie-Weiss law:

$$\chi = C/(T - \theta) \quad (1)$$

where C is the Curie constant. Thus, as shown in the figure, $1/\chi$ versus temperature T describes a straight line

intersecting the temperature axis at $T = \theta$. When all the atomic moments of the system are the same, the theory predicts that θ and T_C will be identical. However, in ferromagnetic systems whose magnetic atoms are of different elements and/or are not crystallographically equivalent, θ and T_C will not be equal and equation (1) will not be strictly valid except at very high temperatures. Deviations from equation (1) can also arise from short-range magnetic ordering, which is ignored in the molecular-field theory.

In the simplest *antiferromagnetic* system, all the magnetic atoms are chemically and crystallographically alike and, as a result of negative exchange interactions between them, subdivide in equal numbers into two groups (or sublattices) having moments of opposite direction. Hence, the spontaneous magnetization of the system is zero at all temperatures. Instead, as shown in Figure 1(b), there is a susceptibility that (for a randomly oriented polycrystal) increases as the temperature rises from 0 K, reaching a peak value at the magnetic disordering temperature T_C (which for an antiferromagnet is usually referred to as the Néel temperature). The susceptibility decrease above T_C again follows equation (1), except that θ will be negative, roughly equal to $-T_C$. Any inequality between θ and $-T_C$ is accounted for by the theory as evidence of interatomic interactions within (in addition to those between) the magnetic sublattices.

The simplest *ferrimagnetic* system is also characterized by two magnetic sublattices with antiparallel magnetizations. Here, however, the sublattices are not equivalent and the magnitudes of their magnetizations are not the same. Consequently, the system will have a net spontaneous magnetization, whose variation with temperature will often resemble that of a ferromagnet, as illustrated by curve A in Figure 1(c). More unusual forms for the magnetization-temperature behavior of a ferromagnet are theoretically possible and indeed have been encountered experimentally. The most exotic example perhaps is that demonstrated by curve B in Figure 1(c), which is readily understood in terms of the magnetization of one sublattice being larger at low temperatures but decreasing more rapidly with temperature than that of the other sublattice. Since the two sublattice magnetizations are opposite in direction, the net bulk magnetization (when measured in a small field) may actually reverse in polarity, as shown by the dotted curve, and the initial temperature at which it goes through zero is called the *compensation point*. Regardless of their magnetization behavior below T_C , all ferrimagnetic systems are expected to show a similar

temperature dependence of susceptibility above T_C . As indicated in Figure 1(c), the theoretical $1/\chi$ versus T curve follows a complicated hyperbolic variation before it ultimately approaches a straight line that obeys equation (1) at high T , usually with a negative value of θ . Again, as in the antiferromagnetic case, θ will deviate from $-T_C$ owing to any magnetic interactions between atoms of the same sublattice.

A more general statement regarding θ in equation (1) is that it represents an algebraic sum of all the positive (ferromagnetic) and negative (antiferromagnetic) interactions in the system, in contrast to T_C , which is increased or decreased depending on whether a given interaction helps or hinders the atomic-moment alignment that describes the ordered magnetic state. Hence, in an intermetallic compound of any complexity, a deviation of θ from $\pm T_C$ is to be expected and, in fact, can be used in determining the magnitudes and signs of the different interactions. Another important distinction is that between the *ferromagnetic moment* μ_F and the 'effective' *paramagnetic moment* μ_P of a magnetic atom in a simple ferromagnetic system. The latter is derived from the following expression for the Curie constant C in equation (1):

$$C = N\mu_P^2/3k \quad (2)$$

where N is the number of magnetic atoms per unit volume and k is the Boltzmann constant. For transition-metal atoms, it is defined by

$$\mu_P = g[S(S+1)]^{1/2}\mu_B \quad (3)$$

where g is the spectroscopic splitting factor (with a value close to 2), S is the spin quantum number (the orbital momentum being quenched), and μ_B is the Bohr magneton. On the other hand, μ_F is simply the low-temperature spontaneous magnetization M_0 divided by N , and it is defined by

$$\mu_F = gS\mu_B \quad (4)$$

In the case of rare-earth atoms, the distinction between equation (3) and (4) persists, but S is replaced by J , the total angular momentum (spin plus orbital) quantum number, and g has various values of order unity.

An interesting phenomenon arises when the exchange interactions between magnetic atoms are conflicting with regard to the orientations of the atomic moments. Such a situation obviously cannot exist when all the interactions are ferromagnetic, but it is a distinct possibility when some or all of the interactions are

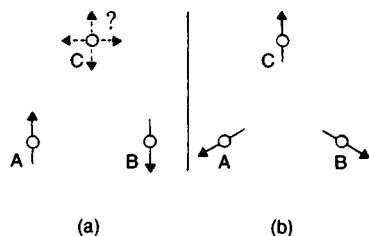


Figure 2. Magnetization vectors of antiferromagnetically interacting sublattices A, B, and C in an apparent dilemma (a) and in a stable but frustrated configuration (b)

antiferromagnetic. In a simple example of the latter, cleverly provided by Nature in the hexagonal compound Mn_3Sn , (D_{019} , Ni_3Sn type (hP8)) the magnetic (Mn) atoms lie in equal numbers on three different but related crystallographic sites (A, B, C), where each atom interacts antiferromagnetically with its magnetic nearest neighbors, which are of equal number on the other two sites. Schematically, in Figure 2(a), we see that if the magnetic moments of atoms A and B are aligned antiparallel to each other, thus completely satisfying the antiferromagnetic A–B interaction, then the magnetic moment of atom C is in a dilemma as to how to satisfy both the antiferromagnetic A–C and B–C interactions simultaneously. Energetically, the resolution of this problem is a compromise, whereby the magnetic moments of atoms A, B, and C are oriented at 120° relative to each other, such that their vector sum is zero, as shown in Figure 2(b). This triangular magnetic configuration has in fact been found in Mn_3Sn , and also in the related Mn_3Ge and Mn_3Rh compounds, by means of neutron diffraction (Kouvel and Kasper, 1964). This phenomenon, in which the exchange interactions are not totally satisfied, is aptly called *frustration*. It is known to occur in many stoichiometric intermetallic compounds, where it often produces complicated but periodic magnetic configurations that may or may not be commensurate with the spatial periodicity of the atomic structure.

In non-stoichiometric compounds, the atomic disorder on one or more of the crystallographic sites can combine with any magnetic frustration to give rise to magnetic properties characteristic of a spin glass (SG). These properties include pronounced irreversibilities such as the differences in the magnetization-field behavior after cooling to below the SG ordering temperature with and without a magnetic field. Such properties, for example, have been observed in the cubic pseudobinary compounds $\text{Tb}_{1-x}\text{Y}_x\text{Ag}$ as clear departures from the simple antiferromagnetism of

stoichiometric TbAg (Said *et al.*, 1988, 1990). In the SG state, the combination of magnetic frustration and atomic disorder produces a nearly random orientational arrangement of atomic moments, and its occurrence in partially disordered intermetallic compounds has further expanded the study of this intriguing subject. (Magnetic structures are discussed in Roth, Chapter 19 in this volume.)

3.2 Soft and Hard Ferromagnets

In order that a strong magnetocrystalline anisotropy in a ferromagnet may be useful as a permanent magnetic property, it is necessary in response to a reversing magnetic field that the magnetization be constrained to rotate against the anisotropy forces. If this constraint is absent, the magnetization may reverse at much lower reverse fields by means of the motion of the domain walls that separate adjacent ferromagnetic domains. The result, as shown schematically in Figure 3(a), will be a thin hysteresis loop with a very small intrinsic coercive

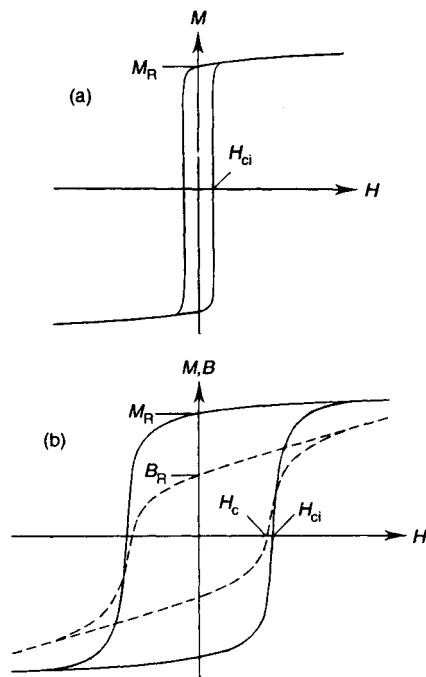


Figure 3. Typical hysteresis loops of magnetization (M) or magnetic induction (B) versus applied field (H) for a soft magnetic material (a) and a hard magnetic material (b). M_R and B_R are remanent values at $H=0$; H_{ci} and H_c are coercive fields at $M=0$ and $B=0$, respectively

field H_{ci} , which characterizes many homogeneous bulk materials that are soft ferromagnets, especially those with weak anisotropy. However, if a ferromagnetic material with strong anisotropy is subdivided into small particles of dimensions comparable to the thickness of a domain wall (typically of the order of 1000 Å), it becomes energetically unfavorable for any domain walls to exist in the particles. Each particle is then a single domain, whose magnetization can reverse only by a rotation process requiring a reverse external field equal to the so-called anisotropy field. Since the anisotropy fields of known materials range up to several thousand oersteds, the hysteresis loop of a compact of single-domain particles can be extremely wide, as shown in Figure 3(b). It is not this hysteresis loop of M versus H , however, but the loop of the magnetic flux density B versus H (shown as broken curves in the figure) that sets the quality of a material as a practical permanent magnet. Because $B = H + 4\pi M$, the coercive field H_c defined at $B = 0$ is generally smaller than H_{ci} defined at $M = 0$ and, in fact, is limited to a maximum value equal to B_R , the remanent flux density, regardless of how large H_{ci} may be. Thus, the magnetization as well as the anisotropy of a material must be fairly large for it to qualify as a hard ferromagnet capable of use as a permanent magnet.

Many intermetallic systems have atomically ordered phases that are strongly ferromagnetic with a large anisotropy, where the atomic ordering process is inhomogeneous and can be easily controlled. A suitable thermal treatment of such a system produces very small regions of the ordered phase in a matrix of a weakly magnetic disordered phase, which is magnetically analogous to a compact of single-domain particles with desirable permanent-magnet properties. Moreover, there

are now several known ferromagnetic intermetallics—notably, the compounds $R_2T_{14}B$, where R is a rare earth and T is iron and/or cobalt whose magneto-crystalline anisotropies are so extraordinarily large that, when a bulk homogeneous sample is driven to its saturation magnetization, it stays in this condition (i.e. without subdividing into domains) even when very sizable reverse fields are applied. The discovery of these compounds has had an enormous impact on the permanent-magnet industry. (Applications of magnetic IMCs are reviewed in Stadelmaier and Rausch, Chapter 14 in Volume 2, and by McGahan, Chapter 19 in Volume 2.)

4. References

- Bacon, G. E. (1962). *Proc. Phys. Soc.*, **79**, 938.
- Bacon, G. E., and Street, R. (1958). *Proc. Phys. Soc.*, **72**, 470.
- Cable, J. W., Koehler, W. C., and Wollan, E. O. (1964). *Phys. Rev.*, **136**, A240.
- Heusler, F. (1903). *Verh. Dtsch. Phys. Ges.*, **5**, 219.
- Heusler, F. (1904). *Z. Angew. Chem.*, **17**, 260.
- Kouvel, J. S., and Kasper, J. S. (1964). *Proc. Intl. Conf. on Magnetism*, Nottingham. Institute of Physics, London, p. 169.
- Néel, L. (1932). *Ann. Physique*, **17**, 5.
- Néel, L. (1948). *Ann. Physique*, **3**, 137.
- Said, M. R., Kouvel, J. S., and Brun, T. O. (1988). *J. Appl. Phys.*, **63**, 4340.
- Said, M. R., Kouvel, J. S., and Brun, T. O. (1990). *J. Appl. Phys.*, **67**, 5961.
- Westbrook, J. H. (ed.) (1967). *Intermetallic Compounds*. Wiley, New York.
- White, R. M. (1970). *Quantum Theory of Magnetism*. McGraw-Hill, New York.
- Wilkinson, M. K., Gingrich, N. S., and Shull, C. G. (1957). *J. Phys. Chem. Solids*, **2**, 289.

This chapter was originally published in 1995 as Chapter 40 in *Intermetallic Compounds*, Vol. 1: *Principles*, edited by J. H. Westbrook and R. L. Fleischer.

Chapter 2

Electrical and Electronic Behavior

M. Braunović

IREQ, Institut de Recherche d'Hydro-Québec, Varennes, Québec, Canada J3X 1S1

1. Introduction

The great technological and scientific importance of intermetallic compounds and the nature of their crystallographic structure have captivated an unprecedented interest from both theoretical and practical points of view. The past 40 or so years has been a period of amassing structural, constitutional, and property data, and of empirical systematization of intermetallic compounds aimed at understanding the basis for the occurrence of certain compounds and the nature of bonding in these structures.

In recent years, there has been growing interest in theoretical calculations of structure, bonding, and properties of intermetallic compounds using the ever-increasing computing power that is becoming available. The rapid growth of experimental research activity in this field can be attributed to the many diverse and novel properties possessed by these materials. However, despite such concentrated research activity in this field, there are still unanswered questions concerned with the crystal structure, bonding, and chemical composition of intermetallic compounds, as well as the effect of various structural defects on the physical, chemical, and mechanical properties of these compounds.

Electrical resistivity was often used in the early days as an exploratory tool to detect the existence of intermetallics because the composition and temperature dependences were distinctive (see Chapter 1 by Westbrook in this volume). More recently, the electrical and electronic properties of intermetallic compounds have attracted considerable interest because of the vast

list of practical applications of these compounds. The prospect of these applications led to a large number of theoretical and experimental studies of these properties over recent decades. Nevertheless, the question as to whether the attractive electrical and electronic properties of intermetallic compounds arise from certain structures and bond types or from their composition, independent of crystal structure and bonding, awaits an answer. On the other hand, at the risk of overstating the case, knowledge of both atomic and electronic structure is essential to an understanding of practically all properties of intermetallic compounds. It is also to be remarked that, interestingly, the intermetallic compound family embraces instances of metallic, semiconducting, and superionic conductors, and even some (e.g. Mg_3Bi_2 compounds) whose conduction mechanism differs in the solid (metallic) and liquid (semiconducting) states.

In this chapter an attempt is made to present an up-to-date survey of the basic principles underlying the electrical and electronic properties of intermetallic compounds and hence to provide the fundamentals for understanding practical developments based on electrical and electronic properties of intermetallics (see Chapters 15, 16, 18, and 20 in Volume 2 by Masumoto *et al.*, Stekly and Gregory, England and Arakawa, and Vedernikov, respectively). Furthermore, whenever possible, a phenomenological description of the transport processes as affected by the common metallurgical variables is given. As a means of maintaining clarity of presentation while attempting comprehensive coverage, a brief, non-rigorous, review of the theory of the electrical conduction in metals is

presented. This review is followed by a discussion of the parameters relating the electrical properties (electrical resistivity) to the structure (electronic and crystallographic) of the compounds. Particular attention is given to the effects of order-disorder phase transitions and of lattice defects on the resistivity in selected compounds. The discussion is concluded with some general remarks concerning future developments in our understanding of the electrical and electronic properties of intermetallic compounds.

Although the electrical resistivity is, in general, less spectacular than the other properties of intermetallic compounds, such as magnetic, optical or thermoelectric ones, it nevertheless remains a powerful tool for the investigation of microstructural and physical phenomena in metallic systems, raising many questions of considerable importance in our understanding of basic electrical and electronic processes.

2. Electrical Conduction in Metals

2.1 Basic Concepts

The foundations of the modern electron theory of metals were laid at the beginning of this century when the existence of a gas of free electrons was postulated by Drude to explain the conducting properties of metals. The behavior of the electrons was subsequently analyzed by Lorentz by means of the dynamic theory of gases. The main successes of this theory were expressing Ohm's law in an analytical form and predicting the Wiedemann-Franz law, which connects electrical and thermal conductivities. However, later developments revealed an increasing number of difficulties, which could not be resolved until the advent of quantum mechanics, when Pauli and Sommerfeld applied Fermi-Dirac statistics to the free electrons in a metal, thus reconciling most of the contradictions.

The present theories on electron conduction in metals are based on quantum-mechanical principles recognized by Bloch. However, with the present state of the theory of metals, it is impossible to work out a theory that fully takes into account the electronic structure peculiar to a particular metal. Rather than introduce a large number of parameters of doubtful physical significance, it is best to work with the simplest model that gives reasonable results. The simple Sommerfeld theory of the free electrons in metals and their mean free path may be used to discuss the conduction phenomenon.

When an electrical field (E) is applied to a metal that has a free-electron distribution given by Fermi statistics, the whole Fermi distribution is displaced in the direction

of the field. Initially, the conduction electrons accelerate, but an equilibrium state resulting in a steady current is quickly reached because of the interaction with lattice vibrations (phonons) and with lattice imperfections.

If this model is utilized, one can explain the resistivity by means of collisions of the drifting electrons with lattice atoms. The more collisions encountered, the higher is the resistance. This concept qualitatively describes the increase in resistivity with increasing density of lattice imperfections, e.g. grain boundaries, dislocations, foreign atoms, etc. It also explains the observed increase in resistance with increasing temperature: the thermal energy causes the lattice atoms to oscillate about their equilibrium positions, thus increasing the probability for collisions with the drifting electrons. Hence, electrical conductivity (σ) according to the Sommerfeld theory can be summarized as

$$\sigma = N_F e^2 \tau / m \quad (1)$$

in which N_F is the number of free electrons per unit volume, e is the charge of the electron, m is the mass of the electron, and τ is the relaxation time, defined as the characteristic time to reach a static equilibrium and related through the electron velocity v to the mean free path l between two consecutive collisions as

$$l = v \tau \quad (2)$$

The relaxation time is generally expressed as

$$\tau = m v_f / e E \quad (3)$$

where v_f is the final average electron drift velocity (steady state).

In the classical picture, one would assume that all conduction electrons drift, under the influence of an electric field, with a modest velocity. Quantum mechanics, instead, shows that only specific electrons participate in conduction and that these electrons drift with a high velocity. i.e. the Fermi velocity v_F . Furthermore, the maximum energy that the electrons can assume in a metal at $T = 0$ K is the Fermi energy E_F . A large number of electrons actually possess this energy, since the density of states and thus the population density is highest around E_F . Hence, raising a substantial number of electrons from the Fermi level into slightly higher states requires very little extra energy. As a consequence, the energy (or the velocity) of electrons accelerated by the electric field E is only slightly larger than the Fermi energy E_F (or the Fermi

velocity v_F), so that for all practical purposes the mean velocity v_f can be approximated by the Fermi velocity v_F . Hence, the quantum-mechanical approach yields for the conductivity the following expression:

$$\sigma = \frac{1}{3} e^2 v_F^2 \tau N(E_F), \quad (4)$$

where $N(E_F)$ is the number of electrons per unit energy at the Fermi energy.

This quantum-mechanical equation reveals that the conductivity depends on the Fermi velocity, the relaxation time, and the electron population density (per unit volume), which is proportional to the density of states. Equation (4) is more meaningful than the expression derived from the classical electron theory (equation (1)), since it contains the information that not all free electrons N_F are responsible for conduction, i.e. the conductivity in metals depends to a large extent on the population density of the electrons near the Fermi surface: For example, monovalent metals (such as copper, silver, or gold) have partially filled valence bands and their electron population densities near their Fermi energy are high, which results in a large conductivity. Bivalent metals, on the other hand, are distinguished by an overlapping of the upper bands and by a small electron concentration near the bottom of the valence band. As a consequence, the electron population near the Fermi energy is small, leading to a comparatively low conductivity. Finally, insulators and semiconductors have, under certain conditions, completely filled electron bands, which result in a virtually zero population density near the top of the valence band; thus, the conductivity in these materials is extremely small.

It is often stated that metallic and semiconducting materials can be clearly distinguished by the temperature coefficient of resistance in the absence of knowledge of the specific resistivity. However, it should be noted that this is by no means always true and that the sign of the temperature coefficient of resistivity is not always determinative. The best examples are Bi_2Te_3 , a semiconductor with a positive temperature coefficient of resistivity, and the alloy $\text{Pd}(40\text{Ag})$, a clearly metallic conductor but with a negative temperature coefficient over some temperature ranges (Coles, 1967).

Recognition that the use of electrical resistance measurements alone could not be used to monitor all changes occurring in the intermetallics stimulated investigations on the behavior of the galvanomagnetic coefficients, magnetoresistance coefficient (B), thermoelectric power (Q), and Hall effect (R). The galvano-

magnetic coefficient is sensitive to splitting of Brillouin zones altered during ordering, while the magnetoresistive coefficient allows the detection and measurement of Fermi-surface distortion, resulting from ordering. The thermoelectric power is sensitive to the detailed nature of the electron scattering process responsible for the electrical resistivity. Hall-constant (R) measurements allow detection of the changes in the relative concentrations of hole and electron conduction. Combined measurements of the above properties provide an almost complete description of the relation between electron state changes and the structure, and hence lead to a true characterization of conduction mechanism.

2.2 Factors Affecting Electrical Conductivity

An important contribution of wave mechanics is the result that τ tends to infinity as the imperfections and lattice vibrations tend to zero, so that a very small number of metallic electrons per atom will confer a high conductivity on a well-ordered solid, even when they give only a small contribution to the total bonding energy. Conversely, large changes in conductivity (by a factor of 10^5) can be produced in a metal with negligible change in the number and nature of the conduction electrons.

If the lattice is truly perfect, with no imperfections whatever, the electrons, or rather electron waves, will be scattered only coherently and will propagate through the lattice without any loss of energy, i.e. there will be no resistance to the motion of the electrons. However, in practice, the lattice is not perfect and the electron waves will be incoherently scattered, losing energy in the process. Hence, the resistance to electron wave motion arises from the following sources:

- Atoms of different size that alter the lattice parameter locally.
- Atoms having different valences that introduce a local charge difference, thus increasing the scattering probability.
- Solutes with a different electron concentration compared to the host element that alter the position of the Fermi energy, thus changing the population density $N(E_F)$.
- The vibration of the lattice ions due to the thermal energy increasing with temperature.
- The presence of chemical or physical imperfections in the lattice, such as foreign atoms, vacancies, dislocations or grain boundaries.

An experimental fact, known for a long time, is that the contributions to the electrical resistivity (defined as

the reciprocal of conductivity) from these sources of electron scattering are additive. This is known as Matthiessen's rule, which may be summarized as:

$$\rho = \rho_0 + \rho_i(T) + \rho_R(T) \quad (5)$$

The first part of equation (5) is temperature-independent. The second term is temperature-dependent and known variously as the 'ideal', the intrinsic, the lattice or the phonon resistivity. At low temperatures this part is, in general, proportional to T^5 , but is linear at higher temperatures. The third part of the equation, usually called the 'residual' resistivity, arises from the electron scattering by lattice imperfections and is generally independent of temperature.

Although Matthiessen's rule gives good agreement with experimental data, particularly at higher temperatures, there is increasing evidence that the rule is not strictly valid. It is therefore of interest to mention some of the assumptions on which this rule is based

- Scattering of the conduction electrons by impurities, and by phonons, are two independent processes.
- The effective number of conduction electrons is not changed by the introduction of solute atoms having a different valency from the solvent.
- The temperature must be high enough to justify treating all thermal scattering as elastic.

None of these assumptions is likely to be strictly valid, and according to Sondheimer (1950) some deviations are to be expected at lower temperatures and are indeed found (Alley and Serin, 1959; Klemens and Lowenthal, 1961; Das and Gerritsen, 1964) in multivalent metals describable by a two-band model. In such cases, if each conduction band depends in a different way on the scattering, then, although Matthiessen's rule may apply separately to each band, deviations occur when the total resistivity is evaluated. Also, accurate experimental studies made of the conformance of this rule in dilute alloy systems have shown that $d\rho/dT$ varies systematically with the impurity concentration (Campbell *et al.*, 1967). The nature of these deviations depends on the type of impurity atom or other defect present as well as on their quantity; this is particularly evident when transition-metal impurity atoms are present (Gerritsen, 1956). Deviations from Matthiessen's rule found experimentally may be generally expressed as a temperature-dependent quantity (Jones, 1956; Ziman, 1960; Bass, 1972).

So far we have excluded from discussion the resistivity of ferromagnetic materials. We have done so because, apart from the conditions that control the conductivity of non-magnetic metals, ferromagnetic materials are

characterized by numerous unusual properties arising from the presence of magnetic ions in a conductor influencing the resistivity, irrespective of the external field (see Chapter 40 by Kouvel in this volume). In addition to the components of resistivity included in equation (5), another important contribution to the resistivity occurs only in ferromagnetic and anti-ferromagnetic metals below their magnetic transition temperatures and is due to the scattering from disordered spin arrangements (ρ_M). The magnitude of this effect varies according to the element, but it is very great indeed in Mn and many rare earths, and is largely responsible for their high resistivities. This magnetic disorder term, temperature-dependent below the Curie (Néel) temperature, may to a first approximation be considered additive to the residual and ideal resistivities in these metals. Hence, for these materials,

$$\rho = \rho_0 + \rho_i(T) + \rho_R(T) + \rho_M(T) \quad (6)$$

Common features possessed by all the ferromagnetic metals are partially filled sub-lying electron shells, which in first, second, and third long-period transition elements are the 3d, 4d, and 5d shells respectively. Mott (1936) constructed a detailed theory of the properties of the transition elements on the assumption that the valence electrons are shared between a wide, low density of states (s band) and a narrow, high density of states (d band). This high density of states arises because the spatial extension of the d-electron wavefunction is much less than that of the s-electron one, with consequently less overlap from atom to atom. Hence, the d band is narrower, although it accommodates 10 electrons compared to two electrons in the s band. Because of this, and their large effective mass, the d band electrons contribute very little to the conductivity. Nevertheless, the d band plays an important part in resistivity, since the conduction s-electrons can be scattered not only into energy states in the s band but also into vacant states in the d band. Because the density of the latter is so high, these s-d transitions will contribute most to the scattering probability and thus to the resistivity. It should be pointed out, however, that the collective electron theory treats all the d-electrons of a material collectively and makes practically no distinction between the constituent elements of disordered transition-group alloys, and therefore has had only a limited success in explaining the basic electrical and magnetic properties.

Recently, electrical resistivity of disordered binary alloys was calculated within the framework of the coherent-potential approximation (CPA) (Brouers and Vedyayev, 1972; Granovskii *et al.*, 1991). It was shown

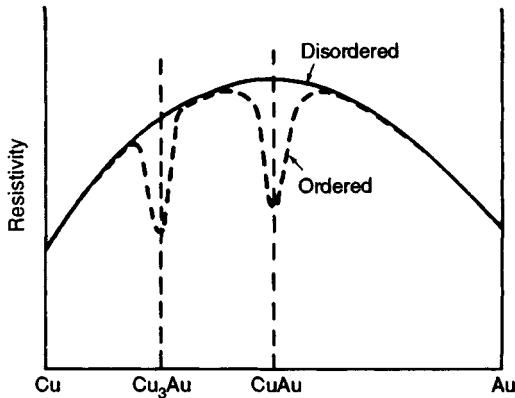


Figure 1. Schematic representation of the resistivity of ordered and disordered copper-gold alloys

that in a 'two s-d band' alloy model that is appropriate to transition-metal alloys, the energy spectrum and the electrical conductivity are determined by the scattering of s-d hybridized electrons by random d levels.

In recent years a rival concept to the collective band model has been developed to explain the resistivities of ferromagnetic and antiferromagnetic metals (Meaden, 1965). This new approach is based on the so-called spin-disorder scattering effect, which results from exchange interactions taking place between conduction electrons and certain unpaired ('magnetic') electrons called magnons localized on a particular atom. The energy of interaction depends on the relative orientations of the spins of the electrons involved. Conduction electrons progressing through such a disordered exchange field receive scattering from the field, which adds to that of the conventional impurities and lattice imperfections, and this contribution to the resistivity can be very large. This spin-disorder component is essentially constant above the Curie (Néel) point, where the spins are totally disordered, but becomes zero at low enough temperatures that all the localized spins are aligned.

The above indirect exchange interaction is of the Ruderman-Kittel type that takes place between nuclear spins on different ions via the hyperfine interaction, which couples ionic spins on neighboring ions. The basic theory of this interaction is known as the Ruderman-Kittel-Kasuya-Yoshida (RKKY) theory, as a tribute to the major theoretical extensions of Kasuya (1956) and Yoshida (1958). The spin-disorder concept has had a particular success in the case of rare-earth metals and alloys, which owe their characteristic magnetic properties to a partially empty 4f shell. In these substances the scattering originates from an s-f

exchange interaction between s conduction electrons and spins localized on f electrons (Meaden, 1965).

The transition elements display more complicated behavior than do non-transition metals; this is reflected in the change of the temperature exponents of resistivity, found experimentally to range from 2.0 to 5.3. The latest experimental and theoretical work explains such behavior of transition elements, in particular the ferromagnetic metals, by the existence of two or more scattering mechanisms operating simultaneously. According to this, the effect of impurities appears to disguise the true temperature dependence that would otherwise be obtained.

3. Electrical Conduction in Intermetallic Compounds

3.1 Effect of Ordering and Formation of Antiphase Domains

The electrical properties of many intermetallic compounds are altered by ordering, which usually involves a substantial decrease in resistivity, as seen in Figure 1. This decrease in resistivity is caused by coherent scattering of electron waves entering a lattice with periodically arranged solute atoms (for example, in a 50/50 alloy of $L1_0$ (tP4) structure, the A and B atoms in some directions alternately occupy successive lattice sites). To understand fully the properties of these alloys, it is necessary to consider the effects of long-range order (LRO), short-range order (SRO), domain size, and structural changes caused by ordering. These effects can be best and most accurately evaluated by electrical resistivity measurements, which can allow ready determination of the order-disorder kinetics, and, thus, provide insight into the diffusion process and thermally induced changes in compound characteristics.

The effect of LRO on electrical resistivity has been treated both theoretically and experimentally. Rossiter (1980) developed a theoretical approach describing the overall dependence of the resistivity on the LRO parameter (η) in a non-magnetic, stoichiometric compound and above the Debye temperature Θ_D . The effect of LRO is treated by a pseudopotential method in the Bragg-Williams approximation in a nearly-free-electron model, which yields for the resistivity

$$\rho = (m^*/n_{\text{eff}})/e^2\tau \quad (7)$$

where m^* is the effective mass, n_{eff} is effective density of conduction electrons per unit volume, and τ is the

relaxation time. Both n_{eff} and τ are order-dependent and given as

$$\begin{aligned}\tau^{-1} &= \tau_0^{-1} [1 - \eta^2(T)] \\ n_{\text{eff}} &= n_0 [1 - A\eta^2(T)]\end{aligned}\quad (8)$$

where τ_0 is the relaxation time corresponding to the disordered state. The constant A depends on the relative positions of the Fermi surface and the superlattice Brillouin-zone boundaries. Its sign determines the evolution of the electronic band structure near the Fermi level while the LRO structure is forming. Hence, if the Debye temperature Θ_D is approximately independent of the degree of order, the total resistivity of a non-magnetic stoichiometric compound for a given concentration is given as:

$$\rho(\eta, T) = \rho_0(\eta) + \rho_P(T) \quad (9)$$

where ρ_0 is the temperature-dependent residual resistivity and ρ_P is the phonon contribution, also temperature-dependent. The final expression for the resistivity of a non-magnetic LRO phase is given as

$$\rho(\eta, T) = \rho_0 [1 - \eta^2(T)] / [1 - A\eta^2(T)] + BT/n_0 [1 - A\eta^2(T)] \quad (10)$$

This simple expression for the LRO dependence of electrical resistivity has been applied by Rossiter (1980) to the cases of Cu_3Au and Fe_3Al . A very good general agreement was found with the limited experimental data.

This model has been extended recently by Cadeville *et al.* (1992) to the case of ferromagnetic compounds

by adding a term for the spin-disorder scattering ρ_m defined as

$$\rho_m(\eta, T) = \rho_m^D [1 - \sigma^2(T)] / [1 - A\eta^2(T)] \quad (11)$$

where σ is the ferromagnetic LRO parameter, which equals 1 at $T=0$ K and zero at the Curie temperature; ρ_m^D is the value of ρ_m in the paramagnetic state above the order-disorder transition temperature. The spin-disorder scattering term $\rho_m(\eta, T)$ is expected to increase from zero at low temperature to its maximum value at the Curie temperature, and to remain constant in the paramagnetic state. Since antiphase boundaries (APB) are always present in the totally ordered compound (see Chapter 21 by Sun in this volume), an additional term (ρ_{APB}) due to scattering by the APB must be added. The expression (9) for the total resistivity of a stoichiometric intermetallic compound in the ferromagnetic state and for a given concentration must thus be expanded to include these additional terms, and is given as

$$\rho(\eta, T) = \rho_0(\eta, T) + \rho_P(T) + \rho_m(\eta, T) + \rho_{\text{APB}} \quad (12)$$

This expression has been tested in the case of paramagnetic (NiPt and $\text{Fe}_{0.7}\text{Al}_{0.3}$) and ferromagnetic (CoPt and $\text{Co}_{0.3}\text{Pt}_{0.7}$) compounds. Comparisons between experimental values for resistivity and the curves fitted to equation (12) are shown in Figures 2 and 3. On the whole the experimental data and the calculated data for the residual resistivity $\rho_0(\eta, T)$ (i.e. $\rho_{4\text{K}}$) and $\rho(\eta, T)$ (i.e. ρ_{total}) agree very well. It is also interesting to note that calculated values for the contribution of the antiphase boundaries to the resistivity (ρ_{APB}) agree quite well with

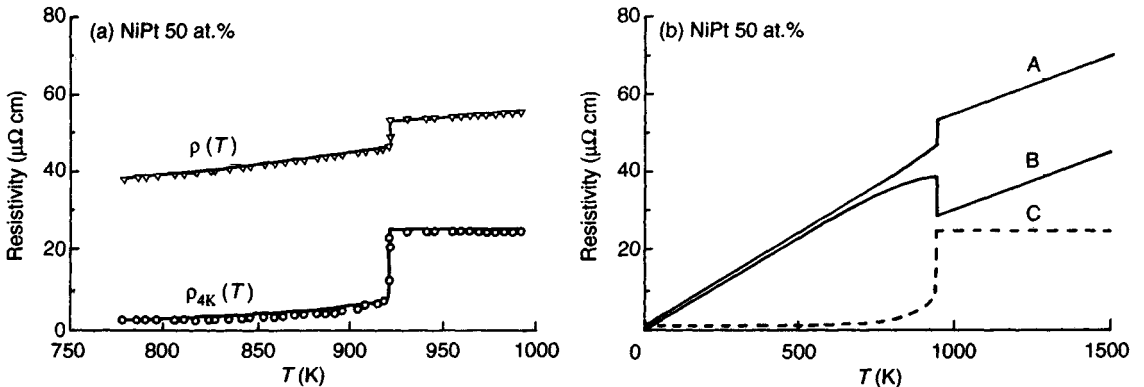


Figure 2. (a) Comparison between experimental values of $\rho_{4\text{K}}$ (○) and ρ_{total} (▽) and the fitted curves over the temperature range of experiment, for NiPt. The discontinuity occurs at the order-disorder temperature. (b) Calculated values of ρ_{total} (A), phonon (B) and $\rho_{4\text{K}}$ (C) between 0 and 150 K (After Cadeville *et al.*, 1992)

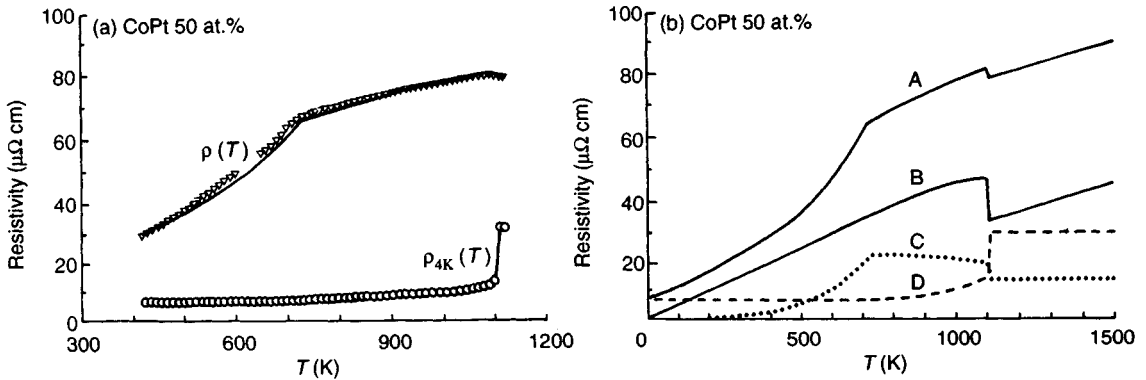


Figure 3. (a) Same as Figure 2(a), for CoPt. (b) Same as Figure 2(b) but with magnetic contribution ρ_{mag} (D). Note that with this contribution the ordered state now has a higher resistivity than the disordered state at the order-disorder temperature (After Cadeville *et al.*, 1992)

Table 1. Comparison of observed and calculated values for the resistivity contribution arising from antiphase boundaries

| Alloy | Structure | ρ_{APB} ($\mu\Omega \text{ cm}$) | | | Reference |
|----------------------------------|----------------------|--|------|--|--------------------------------|
| | | Calc. | Exp. | | |
| CoPt | L1_0 (tP4) | 6.6 | 5 | | Leroux <i>et al.</i> (1989) |
| $\text{Co}_{0.3}\text{Pt}_{0.7}$ | L1_2 (cP4) | 10.2 | 12 | | Leroux <i>et al.</i> (1989) |
| NiPt | L1_0 (tP4) | 1.1 | 2 | | Leroux <i>et al.</i> (1989) |
| $\text{Fe}_{0.7}\text{Al}_{0.3}$ | D0_3 (cF16) | 0 | 2 | | Cadeville <i>et al.</i> (1992) |

the experimental values measured in stoichiometric phases. The results of calculated (fitted) values of ρ_{APB} with the experimental values are shown in Table 1.

This model permits description of the LRO dependence of chemical, magnetic, and electron-phonon scattering contributions to the resistivity of non-magnetic and magnetic intermetallic compounds. The sign and the extent of the variations of resistivity at the order-disorder transition temperature are governed by the electronic structure effects associated with the formation of the LRO structure.

Rossiter (1979) pointed out that, although the comparison of the predicted behavior with that determined experimentally yielded quite good agreement, the tendency of such systems to order by inhomogeneous nucleation and growth of ordered domains or spinodal ordering (Kornilov, 1974) imposes serious restrictions to wider application of this model. A more rigorous test of the model would require experimental determination of both long-range and short-range order, antiphase domain size, and the volume fraction of domains in each specimen for which the residual electrical resistivity has been determined (see Chapter 21 by Sun in this volume for further discussion of antiphase domains).

The effect of antiphase domain boundaries on electrical resistivity deserves more attention because of the subtle but important effects of electronic behavior on antiphase domain stabilization. The importance of the effect of the antiphase boundaries on the electrical resistivity has been recognized by Sykes and Jones (1938), who found that in Cu_3Au the electrical resistance decreased as the antiphase domain (APD) size increased:

$$\rho = (\hbar/e^2) (3/\pi n^2)^{1/3} (1/\Lambda + r/\epsilon) \quad (13)$$

where \hbar is Planck's constant, e is the electronic charge, n is the number of conduction electrons per unit volume, r is the probability of a conduction electron being scattered at an APD boundary, Λ is the electron mean free path, and ϵ is the average APD diameter. A considerable amount of information on the interaction between antiphase boundaries and domains and the electronic structure of an alloy, and their essential role during ordering, has been obtained by measurements of electrical resistance, galvanomagnetic coefficients, thermoelectric power, and Hall coefficients. Most of this work has been done on CuAu (L1_0 (tP4) and Cu_3Au (L1_2 (cP4)). An extensive coverage of work in this area has been given by Beeler (1967).

Another important consequence of the order-disorder transition in intermetallic compounds is the occurrence of a sharp anomalous increase in the residual resistivity. Indeed, a change of $\sim 200 \mu\Omega \text{ cm}$ has recently been reported by Shcherbakov *et al.* (1993) in an L1_2 (cP4) FePd_2Au alloy. The characteristic feature of this alloy is that its ferromagnetic-paramagnetic transition is caused by ordering rather than by a change in the

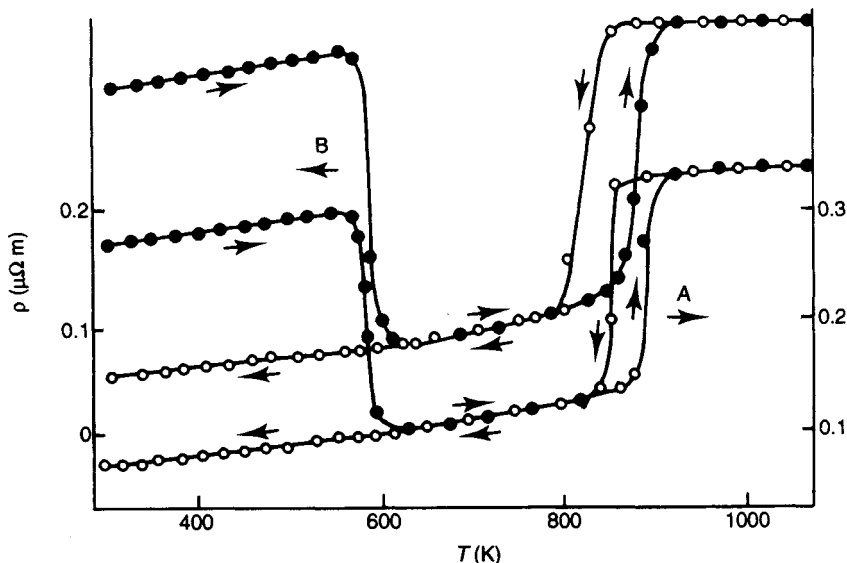


Figure 4. Temperature dependence of electrical resistivity of deformed alloys $\text{Pd}_{0.40}\text{Cu}_{0.60}$ (A) and $\text{Pd}_{0.45}\text{Cu}_{0.55}$ (B) taken during heating (●) and cooling (○) (After Senchenko *et al.*, 1991)

relative concentration of the components. The increase in the residual resistivity was attributed to the formation of a pseudogap in the vicinity of the Fermi level as long-range order increases. A minimum at $T \leq 20$ K was also observed in the resistivity–temperature dependence and was attributed to the structural instability of the alloy in the intermediate ordering stage.

The resistance anomaly, manifested by a higher resistivity in the ordered than in the disordered state, has also been found in Cu_2NiZn and CoPt (Phillips, 1961). The anomaly in this case was attributed to a decrease in the effective electrons associated with splitting of the Brillouin zone during ordering and to the presence of antiphase boundaries or to the latter phenomenon alone.

The effect of ordering on the electrical and magnetic properties of $\text{Pd}_x\text{Cu}_{1-x}$ ($0.4 \leq x \leq 0.48$) alloys, which are promising resistor and contact materials, has been investigated by Senchenko *et al.* (1991). It was shown that these alloys order in the temperature range 580–850 K. The A1→B2 phase transformation at ~800 K is accompanied by compression of the lattice and precipitation hardening and also by a substantial decrease in the resistivity, as seen in Figure 4. The observed resistivity change at the lower temperatures (<600 K) upon initial heating is due to annealing of work-hardened material, which, in turn, accelerates the development of the phase transformation. The ordering process in the alloys was associated with a reduction of

the density of states of d-electrons at the Fermi level, thus causing weakening of the s–d scattering. Increasing the palladium content in the alloys was found to increase the density of states at the Fermi level and thus both magnetic susceptibility and electrical resistivity.

Ordering and disordering kinetics in $\text{Pd}_{45}\text{Cu}_{55-x}\text{M}_x$ ($\text{M} = \text{Co}, \text{Ga}$) have been investigated using resistivity measurements by Balina *et al.* (1991). It was shown that adding small quantities of Co and Ga substantially accelerates the ordering process and slows down disordering. The addition of 1 and 3 at.% Co or 1 at.% Ga to the base alloy $\text{Pd}_{45}\text{Cu}_{55}$ expands the range of homogeneity of the B2 phase and improves its thermal stability. This is reflected in the sharp increase in the critical cooling rate (by almost 3 and 50 for $\text{Pd}_{45}\text{Cu}_{55}\text{Co}_1$ and $\text{Pd}_{45}\text{Cu}_{55}\text{Co}_3$ respectively), which suppresses the ordering process. The activation energy of ordering decreased from 90 kJ mol^{-1} for $\text{Pd}_{45}\text{Cu}_{55}$ to 18 kJ mol^{-1} for $\text{Pd}_{45}\text{Cu}_{55}\text{Ga}_1$ and increased abruptly from 150 to 420 kJ mol^{-1} during disordering. These changes in the activation energy of ordering and disordering were attributed to the greater stability of the ordered solid solution (see Chapter 33 by Dimitrov in this volume for further discussion of order–disorder phenomena).

3.2 Other Effects of Presence of Magnetic Species

In an extensive coverage of magnetic properties of intermetallic compounds, Kouvel (1967) concluded that

the appropriate model for all intermetallic compounds is most likely intermediate between the simple collective electron and spin-disorder models. Effects due to critical fluctuations of the magnetization, which produce their own type of resistivity anomaly at the magnetic order-disorder transition by a process of local ordering are to be expected and differ from one intermetallic compound to another, depending sensitively on the crystal structure and composition. On the other hand, Kouvel showed that, although intermetallic compounds cannot be adequately explained by a simple atomistic model, it is still possible to classify their intrinsic magnetic properties within the framework of the molecular-field theory, providing allowance is made for non-integral atomic moments and other deviations from this model. In this theory, the net exchange coupling between a given atom and all its neighbors is approximated by the interaction of its magnetic moment with an effective 'molecular' field. The consequences of the molecular-field theory are particularly simple when all the interactions in the system are positive (i.e. ferromagnetic), in which case the spontaneous magnetization at 0 K corresponds to a parallel alignment of all the atomic moments and decreases at higher temperatures as the moment directions undergo thermal fluctuation.

The electrical and electronic properties of intermetallic compounds containing magnetic species are strongly affected by the structure and the chemistry of the compound. These effects are manifested by modification of the conduction-electron concentration, which, in turn, increases the negative reactions, leading to a change from ferromagnetic to antiferromagnetic behavior. These changes usually occur at a critical concentration and are reflected through a clearly expressed anomaly in the resistivity-concentration dependence. Such anomalous behavior of the resistivity was recently observed in $(\text{Pd}_x\text{Pt}_{1-x})_3\text{Fe}$ (Kourov *et al.*, 1987), $\text{GdZn}_x\text{Cu}_{1-x}$ (Kourov, 1991), and $\text{GdNi}_{1-x}\text{Cu}_x$ (Blanco *et al.*, 1992).

In the case of $(\text{Pd}_x\text{Pt}_{1-x})_3\text{Fe}$ the anomaly in the resistivity behavior was observed at $x = x_{\text{cr}} \sim 0.5$, which is the concentration where the ferromagnetic-paramagnetic transition occurs. It was shown that the main scattering mechanisms responsible for the observed sharp increase in resistivity when $x \sim x_{\text{cr}}$ is not associated with the magnetic state of the alloys but rather with s-d exchange polarization of conduction electrons in those regions where there are more palladium atoms near spatial fluctuations, causing the fluctuations of the charge and spin density.

For $\text{GdZn}_x\text{Cu}_{1-x}$ alloys, replacing the monovalent Cu atoms by bivalent Zn atoms stabilizes the unstable binary GdCu (B2(cP2)) structure and is accompanied by an anomalous change in the electronic and electrical properties of this alloy in the vicinity of $x \leq 0.07$. The concentration dependence of these properties was explained by the coexistence of a narrow d band and a broad, practically unchanged, s band near the Fermi surface, with the corresponding density of states $N_d \gg N_s$. Under these conditions the resistivity is determined by the transfer of light s carriers to the narrow d band. The observed changes in the electronic parameters occurred at rather high values of the density of states $N(E_F)$, indicating the presence of a narrow (~ 0.01 eV) band near the Fermi surface formed by the d states of Gd^{3+} ions.

In the case of $\text{GdNi}_{1-x}\text{Cu}_x$, substitution for Ni by Cu in GdNi modifies the conduction-electron concentration and causes a ferromagnetic change. This change, which appears at about $x = 0.35$, is manifested by the anomalous resistivity peak at or around the Curie temperature (T_C). This behavior, coupled with the magnetic resistivity variation $\rho_{\text{mag}} \sim T^{3/2}$, indicates that the magnetic fluctuations play an important role even at temperatures much below T_C .

The effect of deviations from stoichiometry on the electronic structure is best illustrated in the case of $\text{CeM}_{2-x}\text{Si}_{2+x}$ ($M = \text{Fe, Co, Ni, Cu}$) alloys (Levin *et al.*, 1992). It was shown that, in the case of $\text{CeCo}_{2-x}\text{Si}_{2+x}$, the temperature dependence of the thermo-EMF (α) varies linearly with composition, reaching its maximum value at a composition close to stoichiometric CeCo_2Si_2 . This behavior is clearly illustrated in Figure 5. In the case of $\text{CeCu}_{2-x}\text{Si}_{2+x}$, the temperature dependence of the thermo-EMF is characterized by the presence of two extrema: a positive maximum at $T = 150$ K and a negative extremum at low temperatures, as seen in Figure 6. The authors concluded that, depending on the electronic structure of the 3d element, a deviation from the stoichiometric composition can result in: (1) the preservation of crystal structure and constancy of lattice spacings with simultaneous displacement of the excess components into the intergranular space (grain boundaries); (2) formation of a multiphase region separating stoichiometric compounds with different effective volumes for Ce ions; and (3) smooth changes of lattice periodicity of $\text{CeM}_{2-x}\text{Si}_{2+x}$ compounds existing in a homogeneous region of considerable extent. The situations (2) and (3) are characterized by changes of the effective valence of Ce and electronic structure parameters close to the Fermi level defined by the f electrons of Ce.

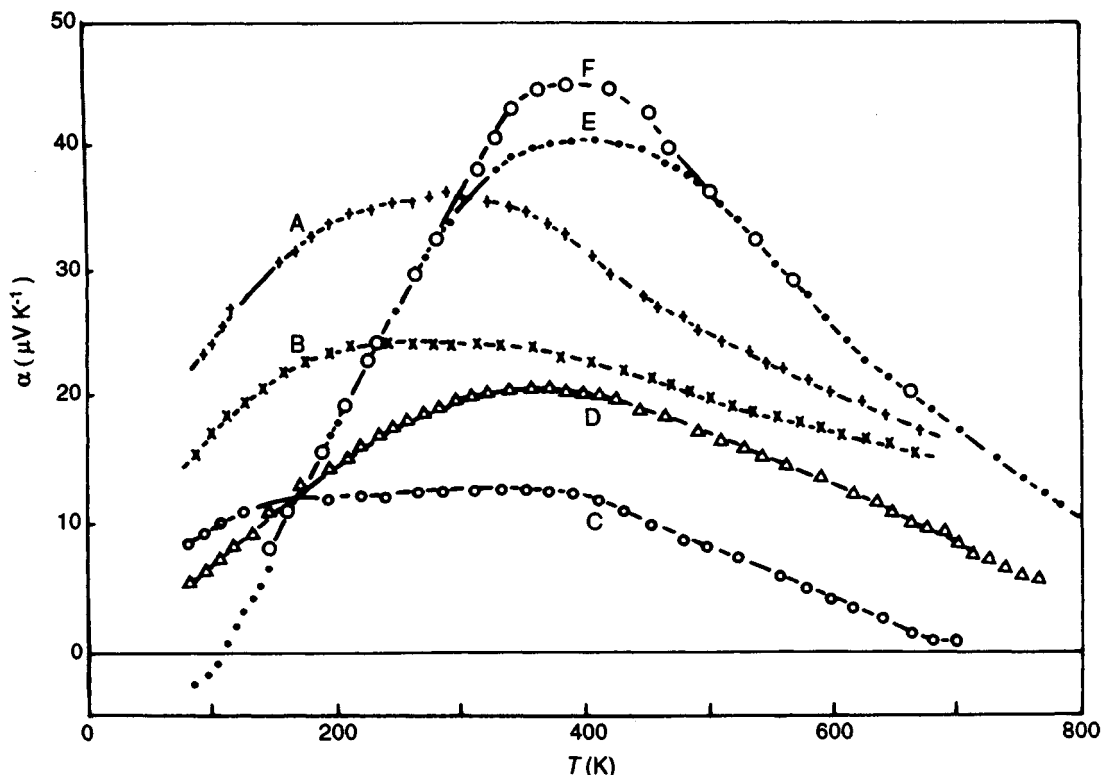


Figure 5. Temperature dependence of the differential thermal EMF (α) of $\text{CeCo}_{2-x}\text{Si}_{2+x}$ alloys with (A) 60, (B) 55, (C) 50, (D) 45, (E) 40 and (F) 38 at.% Si (After Levin *et al.*, 1992)

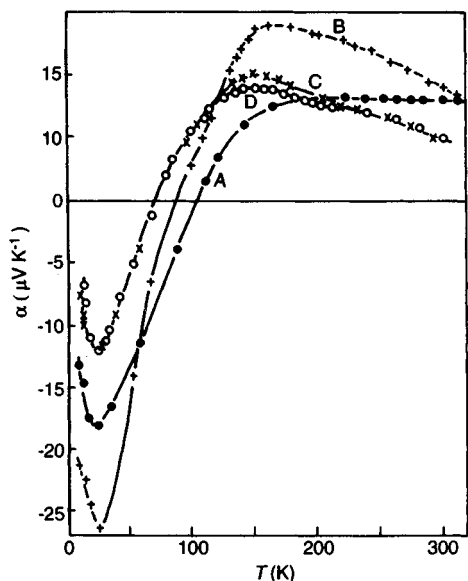


Figure 6. Temperature dependence of the differential thermal EMF (α) of $\text{CeCu}_{2-x}\text{Si}_{2+x}$ alloys with (A) 44, (B) 42, (C) 38 and (D) 36 at.% Si (After Levin *et al.*, 1992)

Otto *et al.* (1987) have measured the electrical resistivity and the Hall effect of the L_{21} (cF16) Heusler alloys Ni_2MnSb , Pt_2MnSb , Co_2MnSb , Au_2MnSb , Cu_2MnSb and Pt_2MnSn . Using the strong-coupling model, they have shown that there are two contributions to the disorder resistivity of Ni_2MnSb alloys: one is due to fluctuations in the energy of a hole in an orbital on an Sb site, while the other comes from the transfer integral between Sb 5p orbitals on neighboring sites. The temperature dependence of the electronic structure was found to be best described by a local band model with complete spin polarization of charge carriers parallel to the local magnetization at all temperatures.

The effects of an applied magnetic field on altering the resistivity of a semiconductor are exploited with III-V intermetallics in so-called magnetoresistive devices as described in Chapter 15 by Masumoto *et al.* in volume 2. It is notable that this effect can be obtained in devices with a very wide range of resistivities ($\sim 10^5$).

3.3 Superconductivity in Intermetallic Compounds

Among the attractive properties characterizing intermetallics, superconductivity is certainly the most

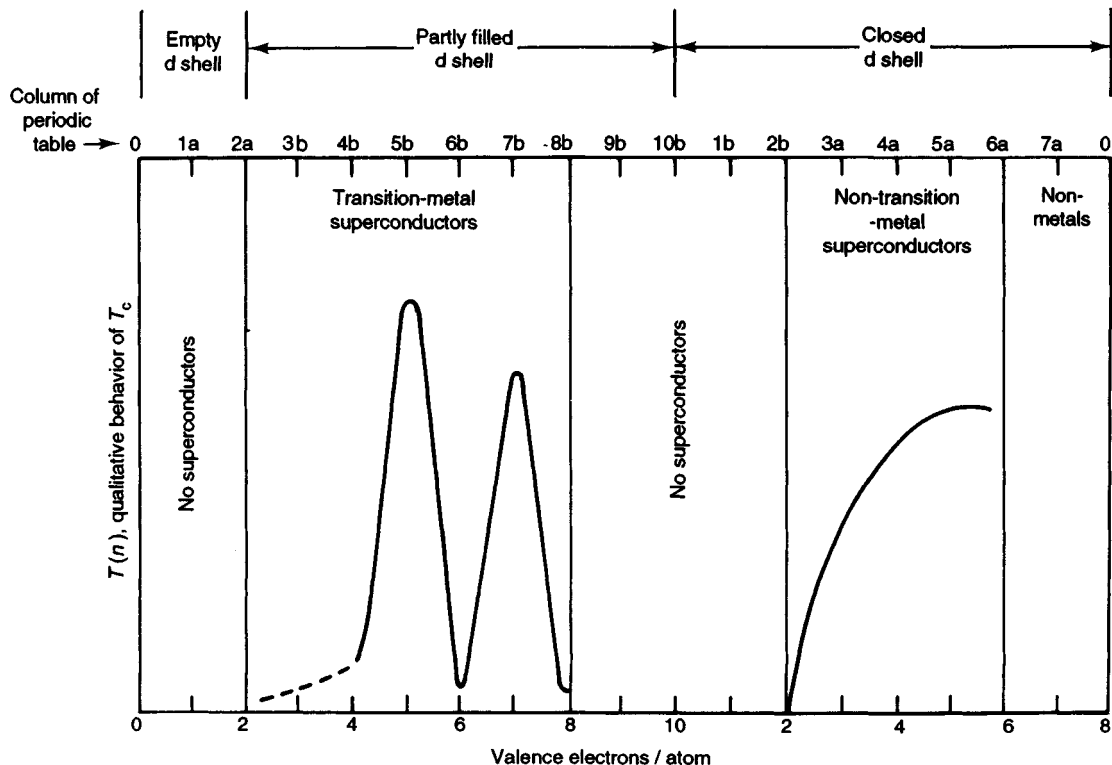


Figure 7. Qualitative behavior of critical temperature (T_c) as a function of the average number of valence electrons per atom as proposed by Matthias (1957)

remarkable. The intermetallic superconductors based on A_3B compounds in the cubic A15 (cP8) structure are the most favorable group. The A15 structure contains chains of closely spaced A atoms running parallel to the cubic axes, with the cavities between the chains occupied by B atoms (see Chapter 15 by Gladyshevskii and Bodak in this volume). The most important physical phenomena characterizing superconducting compounds are the complete loss of electrical resistance below a critical temperature T_c and, while in this superconductive state, the exclusion of magnetic flux up to a value H_c . At the field H_c the superconducting state is quenched, and the compound returns to the normal state. The experimental results and different superconductivity models clearly indicate that the magnetic and electrical properties may be controlled by composition and crystal structure, impurities, dislocations, grain boundaries, strains, or sample size, shape, and configuration. The critical temperature has become very important in utilizing high-field superconductive properties because H_c increases with T_c . Thus materials with large T_c are sought when conductors of supercurrents are needed to produce large

magnetic fields (see Chapter 16 by Stekly and Gregory in volume 2).

An important step in establishing the criteria for the superconductive state in elements, alloys, and compounds was developed by Matthias (1957) from empirical considerations. In Figure 7 is sketched Matthias' function $T(n)$ describing the qualitative variance of T_c with the average number of valence electrons per atom in an element, alloy, or compound. The average number of valence electrons per atom for alloys and compounds is the simple average of the valence (counting all electrons outside a filled shell) for each element in the pure state, weighted as to composition. For example, the A15 (cP8) compound Nb_3Sn has 4.75 valence electrons/atom (3 Nb at 5, plus 1 Sn at 4, equals 19, divided by total number of Nb + Sn, i.e. 4). For the non-transition-metal elements, $T(n)$ was suggested to be a smooth function of the valence electrons/atom, whereas for transition metals a peaked function was given with maxima at three, five, and seven valence electrons/atom. The limiting valences for the occurrence of superconductivity have been extended from two and eight to appreciably greater than

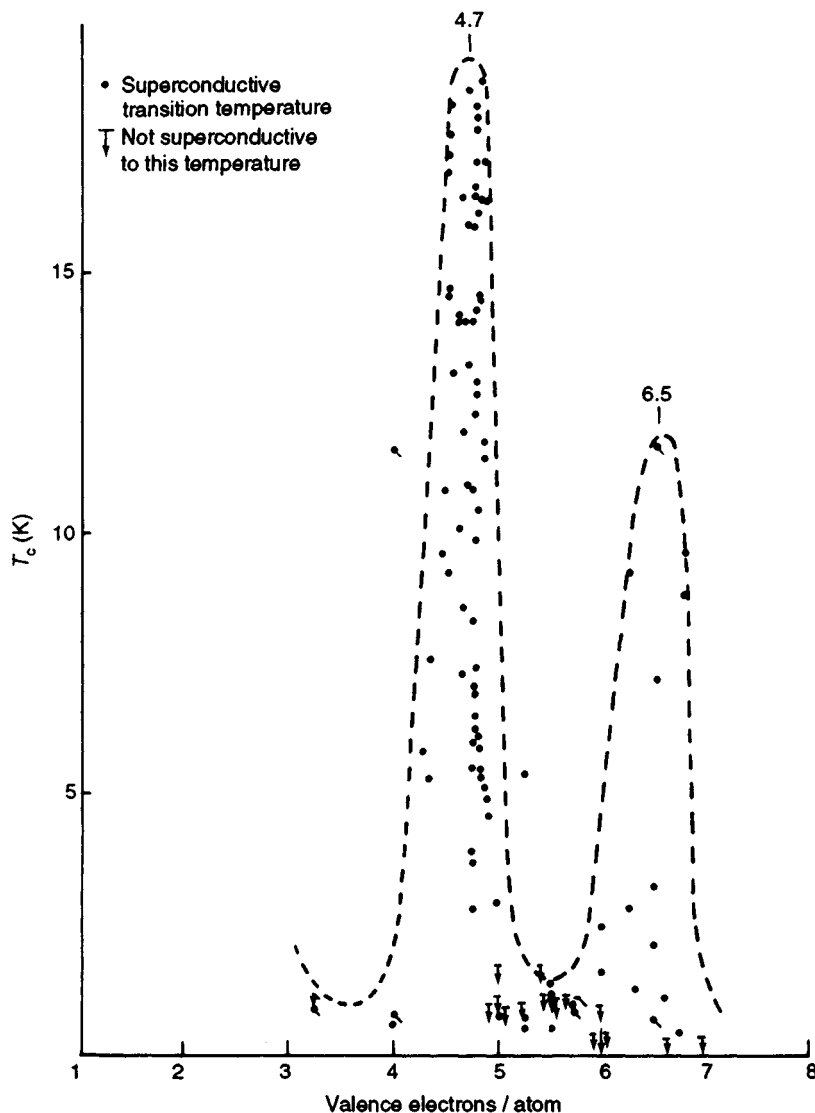


Figure 8. Dependence of critical temperature (T_c) on average number of valence electrons per atom for A15 (Cr_3O) compounds (After Roberts, 1967)

one or less than 10, and the maximum at three valence electrons/atom has since been eliminated. The experimentally determined T_c as a function of the average number of valence electrons/atom for A15 compounds is plotted in Figure 8. This is the most striking correlation for any compound series, illustrating very clearly the importance of the density of states in controlling the critical temperature, and thus confirming Matthias' empirical correlation distinctly.

The electron-phonon coupling mechanism so far seems always to be the essential concept for the interpretation of superconductivity, and in the very best conductors, where this interaction must be small, superconductivity is not found at low temperatures. This would explain why the noble metals with small electron-phonon interactions are not superconducting, while poor conductors in the normal state are potential candidates for high- T_c superconductors. Indeed, in the

metallic superconductors with the highest T_c such as Nb_3Sn , the high temperature resistivity is large ($> 100 \mu\Omega \text{ cm}$) and only weakly temperature-dependent. The origin of this resistivity saturation is under active discussion. One plausible explanation is the existence of a metallic resistivity minimum marked by a reduction of the mean free path to magnitudes comparable with lattice periodicities or interatomic distances (Coles, 1986).

It is of interest to note that an anomalous behavior in the temperature dependence of electrical resistivity was found in the intermetallic compounds with the A15 (cP8) (Nb_3Sn , V_3Si) or C15 (cF24) (ZrV_2) crystallographic phases (Weger *et al.*, 1984). The resistivity of these compounds rises steeply with temperature up to a certain temperature T_0 and less steeply above it. For temperatures below T_0 , this anomalous temperature dependence was associated with hybridized s-like and d-like states by a small electronic matrix element J_{sd} ($J_{sd} = 0.5 \text{ eV}$) and a large electron-phonon coupling constant. Above T_0 the electron-phonon scattering rate (\hbar/τ) exceeds J_{sd} and the s-like and d-like states are decoupled. The electrical conductivity is then due mainly to the s-like states, which possess a smaller electron-phonon coupling constant, giving rise to a smaller electron-phonon coupling and hence to a smaller value of $d\rho/dT$. The anomaly occurs when the mean free path (l) is about an order of magnitude larger than the interatomic spacing (i.e. $l \approx 10d$).

3.4 Effect of Chemical Composition

Intermetallic compounds show a wide range of behavior, which can sometimes be used to elucidate their nature. For instance, the well-ordered intermetallic compound $CuMg_2$ (C_b , cF48) has a resistivity-temperature dependence similar to that of a slightly impure metal. In other words, this compound has a structure governed by the size of the atoms and has a strictly limited stoichiometry (see Chapter 15 by Gladyshevskii and Bodak in this volume); its resistivity is due to deviations from perfect stoichiometry or order. However, intermetallic compounds stabilized by particular conduction-electron concentrations (Hume-Rothery phases) can exist over more extended ranges of composition and may not show a sharp distinction between the sites occupied by the two types of atoms. Consequently, their electrical resistivity resembles that of a concentrated random solid solution. This is particularly the case in transition-metal alloys where d electrons are involved in the metallic bonding and, thus, rationalization of their electrical conductivity cannot be made in terms only of size factors.

Furthermore, some other intermetallic compounds are totally distinct from simple size-factor compounds like $MgCu_2$, or e/a ratio compounds as with Hume-Rothery phases, and owe their existence to normal valency rules. The presence of non-overlapping full valence bands and empty conduction bands yields semiconducting behavior in their electrical properties. Examples are $InSb$, $GaAs$, $CdTe$ (B3 (cF8)), and Mg_2Sn (C1 (cF12)) (see Chapter 14 by Parthé in this volume). The very poor electrical conductivity of these compounds is easily recognized from their resistance-composition dependence, which is sharply distinct from those systems containing size-factor compounds, even when the alloy phase diagrams are similar. The numerous applications of this family of compounds are reviewed in Chapter 15 by Masumoto *et al.* in volume 2.

A clear example is provided by the distinction between two magnesium alloys, each of which exhibits a limited composition range in the phase diagram and possesses an atomic ratio that would seem to follow from 'normal' chemical valences. $MgCu_2$ (C15 (cF24)) has a conductivity close to that of pure magnesium, whereas that of Mg_2Sn (C1 (cF12)) is a factor of at least 10^5 smaller. The semiconducting character of Mg_2Sn does not, however, of itself allow us to decide whether extended or ionic wavefunctions should be used to describe the bonding electrons. It seems likely that a compound of elements differing so strongly in electronegativity would have more ionic character than, for example, $InSb$, another intermetallic semiconductor; but it is difficult to find any simple way of defining a quantitative measure of this difference.

Another example is the compound $CsAu$ (B2 (cP2)) in which both components are monovalent. However, the great difference in electronegativity and significant separation in energy of $6s^2$ and $6s6p$ configurations for Au^- leads to the existence of semiconducting behavior in $CsAu$, in which the highest filled band is based on $6s^2$ electrons on Au atoms, while the conduction band derived from the $6s$ state on Cs atoms is empty (Coles, 1986).

The effect of stoichiometry on the electrical resistivity was investigated by Ikeda and Nakamichi (1975) in a series of Laves phases of Fe_2A ($A = Sc, Y, Nb, Ta, Ti, Zr, Hf$, and U). It was shown that in the C14 (hP12) compounds $Fe_{2+x}Nb_{1-x}$, $Fe_{2+x}Ti_{1-x}$, and $Fe_{2+x}Ta_{1-x}$, the residual resistivity shows a minimum near the stoichiometric composition as seen in Figure 9. A fast increase in the single-phase region and a slow increase in the two-phase region with increased deviations from stoichiometry is evident. In addition, it was also shown that the magnetic resistivity of these alloys is governed

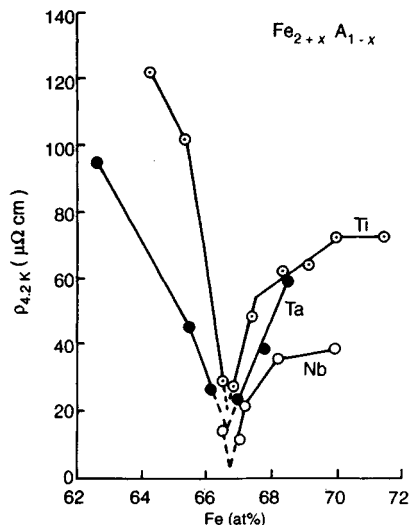


Figure 9. Effect of stoichiometry on the composition dependence of the electrical resistivity at 4.2 K in $\text{Fe}_{2+x}\text{Nb}_{1-x}$, $\text{Fe}_{2+x}\text{Ta}_{1-x}$, and $\text{Fe}_{2+x}\text{Ti}_{1-x}$ (After Ikeda and Nakamichi, 1975)

by the magnitude of the magnetic moments. The resistivity of the paramagnetic compounds $\text{Fe}_{2+x}\text{Nb}_{1-x}$ and $\text{Fe}_{2+x}\text{Ta}_{1-x}$ with $x=0$ showed a fairly large temperature variation and was attributed to paramagnon scattering. The resistivity-temperature dependence in the iron-rich compounds ($x>0$), however, indicated that the appearance of ferromagnetism is caused by the presence of the excess iron atoms occupying wrong atomic sites.

3.5 Effect of Impurities and Vacancies

A small concentration of impurity atoms may not by themselves produce as large an effect on electrical properties in an intermetallic compound as they do in a pure metal. However, in an ordered structure the introduction of an impurity atom may be concomitant with the introduction of a vacancy (see Chapter 23 by de Novion in this volume). Such an impurity-vacancy combination might have a far greater electrical effect than that of the isolated impurity alone, but experimental data are missing.

On the other hand, we have some information on the effects of isolated vacancies on electrical properties. Systematic studies (Otani *et al.*, 1986) of electrical properties of IVa and Va group carbides (in which metal-rich off-stoichiometric compositions are realized by formation of vacancies at carbon sites) have clearly

shown that carbon vacancy concentrations exert a strong influence on the electrical resistivity of these compounds. Recently, Ishizawa *et al.* (1992) have studied the electrical resistivity and Hall effect in NbC_x and TiC_x single crystals. The resistivity increase due to the carbon vacancy in NbC_x was found to be $8\ \mu\Omega\text{ cm/at.}\% V_C$ and $24\ \mu\Omega\text{ cm/at.}\% V_C$ in the TiC_x single crystal, where V_C is the carbon vacancy concentration. A maximum resistivity of $160\ \mu\Omega\text{ cm}$ was observed at $x=0.7$ for NbC_x and of $210\ \mu\Omega\text{ cm}$ for TiC_x at $x=0.8$. The vacancy concentration dependences of the room-temperature resistivity and of the resistivity difference between 4.2 K and room temperature for these systems are shown in Figure 10. The effect of carbon vacancy concentration on the resistivity of TiC_x and NbC_x was explained in terms of both the concentration-dependent carrier densities and the electron-vacancy interaction. The difference in resistivity between 4.2 K and room temperature has also been interpreted as caused by additional concentration-dependent Debye temperature and temperature-dependent anisotropy constants for the relaxation time. The possible influence of short-range order of vacancies at low C/M ratios was also suggested. The marked decrease in resistivity below $x=0.8$ in TiC_x is due to a substantial increase in carrier density compared with that of the stoichiometric composition. This effect is smaller in NbC_x because of a smaller change in carrier density with increasing vacancy concentration in that case.

3.6 Effects of Grain Boundaries

Grain boundaries in polycrystalline metals contribute an additional scattering mechanism for electrical conductivity, and hence resistivity increases with decreasing grain size. There are, however, subtleties beyond the mere change in lattice orientation that constitute the grain boundary. Electrical and electronic properties of grain boundaries ultimately depend on the arrangements of atoms in the boundary, changes in electron bonding, and the existence of point, line, and planar defects in the boundary structure. Considerable experimental and theoretical evidence has been presented to suggest that the structures and properties of grain boundaries in metals depend on the orientation of the boundary plane in addition to the other factors cited. A number of models have been proposed that minimize the energy associated with the grain boundary. These models were based on the dislocation description of low-angle tilt and twist boundaries (Read, 1953) and the coincidence-site lattice model of low-energy, high-angle boundaries. These models are limited almost

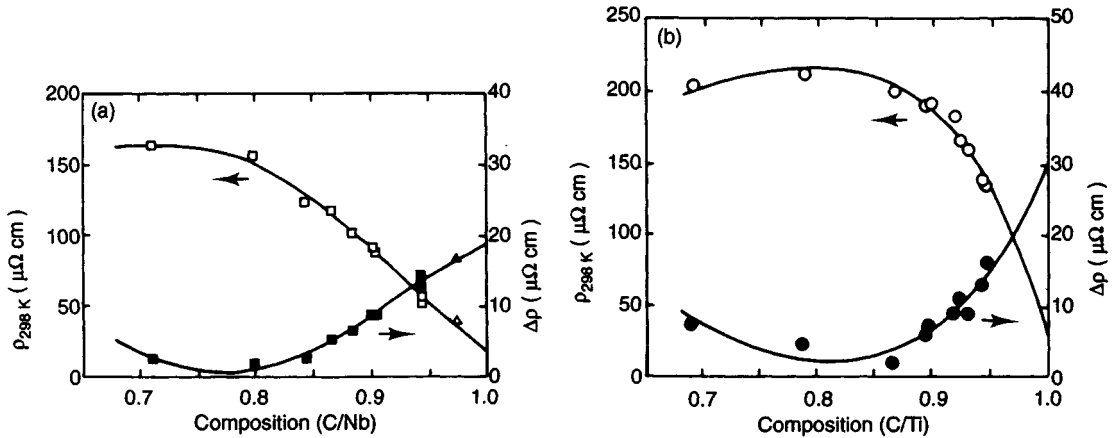


Figure 10. Vacancy concentration dependence of the room-temperature resistivity and the resistivity difference between 4.2 K and room temperature of (a) NbC_x and (b) TiC_x . Full curves are calculated and least-squares fitted to the experimental data (After Ishizawa *et al.*, 1992)

entirely to descriptions of low-temperature structure.

However, grain-boundary models based purely on geometrical considerations may not be sufficient for understanding the real structure and properties of grain boundaries (Hermann *et al.*, 1976), and the electronic structure (bonding) and chemical composition at the boundaries must also be considered along with the geometrical factors. Electronic effects may be small in low-energy boundaries that require little atomic relaxation to achieve a densely packed grain-boundary structure, but these effects are probably important in most other (high-angle) boundaries. Bonding effects rather than geometrical effects in the determination of grain-boundary energies may be particularly important in intermetallics where there are solute and defect gradients associated with the grain boundary (see Chapter 24 by Takasugi in this volume).

Recently, Masuda-Jindo (1991) has developed a model based on LCAO (linear combination of atomic orbitals) recursion electronic theory (Masuda-Jindo, 1988, 1990; Singh, 1991) to describe the atomic configuration and cleavage strength of grain boundaries in the Li_2 (cP4) compound Ni_3Al . It was shown that the increase in d-electron bonding, due to enriched Ni or segregated Fe, Mn atoms, improves the ideal grain-boundary cleavage strength significantly.

Relatively recently it has been realized that grain boundaries are, in principle, capable of existing in more than one distinct phase structure and that a grain boundary may undergo phase transformations with temperature or composition in much the same way as

can bulk phases (Hart, 1972). Such phase transformations can produce discontinuities in the structure, strength, and chemical and kinetic properties of grain boundaries. On the basis of thermodynamic arguments, it has been shown that grain-boundary phase transformations are thermodynamically possible and should be reversible.

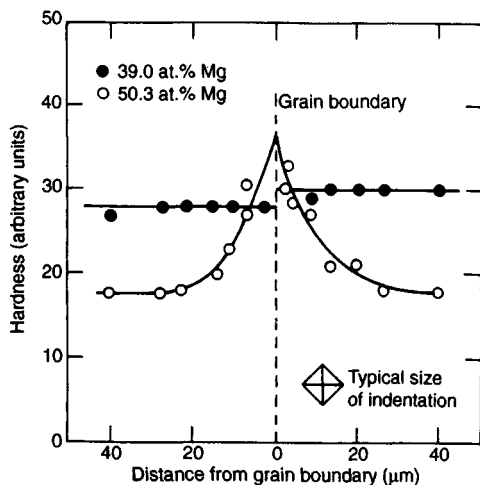
Those properties and effects of grain boundaries observed at high temperatures which differ from those at low temperatures may be due to the existence of distinct high- and low-temperature phase structures. Grain-boundary phase transformations can be revealed by discontinuities, such as a rapid change of slope in equilibrium properties and in non-equilibrium or kinetic properties of grain boundaries (Aust, 1969; Gleiter, 1970; Lagarde and Biscondi, 1974). There is also some indirect evidence, based on grain-boundary mobility (Demianczuk and Aust, 1975), grain-boundary hardening (Arkharov *et al.*, 1973; Braunović, 1974a,b), grain-boundary sliding (Watanabe *et al.*, 1984), and electrical resistivity (Braunović, 1988), that the occurrence of such transformations is dependent upon both the grain-boundary structure and solute segregation.

The effect of grain boundaries and grain-boundary segregation on electrical and thermoelectrical properties has been observed in many pure metals and alloys (Aleksandrov, 1962; Arkharov *et al.*, 1960, 1967; Braunović and Haworth, 1969; Kasen, 1972; Panko *et al.*, 1981). There have been but few attempts to calculate the contribution of grain boundaries to the residual resistivity of polycrystalline metals. Of all the models so far found in the literature, that of Brown (1977) and

Table 2. Comparison of calculated and experimental data for the specific electrical resistivity ρ_B/N_B^a ($10^{-12} \Omega \text{ cm}^2$) of grain boundaries in different metals

| Metal | Brown (1977) | Karolik and Luhvich (1993) | Temp. (K) | Experiment | Reference |
|-------|------------------|----------------------------|-----------|-------------------|----------------------------------|
| Al | 2.7 | 2.6 | 4.2 | 1.35 | Kasen (1972) |
| | | | 4.2 | 2.45 | Andrews <i>et al.</i> (1969) |
| Au | 2.8 | 2.6 | 4.2 | 4.8 | Andrews (1965) |
| | | | 300 | | Chavineau <i>et al.</i> (1969) |
| Be | — | 27.8 | | | |
| Bi | 15×10^4 | | 300 | 1.3×10^4 | Neuman and Ko (1965) |
| | | | 77 | 6.9×10^4 | Ivanov and Papov (1963) |
| Cd | 32.6 | 23.5 | 4.2 | 15.9–19 | Aleksandrov <i>et al.</i> (1974) |
| Co | 2.4 | 6.0 | 77 | 5.0 | van Gorp (1975) |
| Cu | 2.2 | 2.1 | 4.2 | 3.1 | Andrews <i>et al.</i> (1969) |
| | | | 300 | 1.8 | Mannan and Karim (1975) |
| Fe | 6.2 | 15.8 | 4.2 | 60–160 | Arajs <i>et al.</i> (1967) |
| Mo | — | 22.0 | | | |
| Ni | 17 | — | 300 | 5.9 | Mayadas and Shatzke (1970) |
| | | | 77 | 14.0 | Wissmann (1970) |
| Pb | 1.4 | — | 5–20 | 1.3 | Morgner and Pompe (1975) |
| Pt | — | 9.1 | | | |
| Ti | — | 310 | | | |
| W | 22.0 | 21.2 | 300 | 20 | Sun <i>et al.</i> (1973) |
| | | | 77 | 20 | Gaal <i>et al.</i> (1975) |
| Zn | 27.1 | 19.5 | 4.2 | 50 | Aleksandrov <i>et al.</i> (1974) |
| Zr | — | 321 | | | |

^a N_B is the number of grain boundaries per unit length

**Figure 11.** Microhardness traverses using 1 g load across grain boundaries in Ag-rich and Mg-rich AgMg compounds (After Westbrook and Wood, 1963)

Karolik and Luhvich (1991) based on the scattering of conduction electrons by the line defects constituting the grain boundary seems most attractive. The results of these calculations are shown in Table 2, along with the experimental values found for pure metals.

It is surprising, however, that the only significant accumulation of property data on grain-boundary effects in intermetallics appears to be on hardness. Grain-boundary hardening has been found to exist generally in the intermetallic compounds AgMg (Westbrook and Wood, 1963), NiGa (Seybolt and Westbrook, 1964), NiAl (Seybolt and Westbrook, 1965), and Cu-based intermetallics (Shashkov, 1970; Khalim *et al.*, 1970). It was observed that compounds having an excess of the electropositive element over that of the stoichiometric composition showed grain-boundary hardening, whereas those with concentrations of that component below the stoichiometric composition did not show this effect. This is illustrated in Figure 11, showing the hardness profiles of two AgMg compositions. Note that the range of the gradient is in micrometers rather than the ångström range of structural variation alone. Although the specific mechanism for the observed grain-boundary hardening in these systems is not clear, it is believed that it is the result of a concentration of oxygen and/or nitrogen at or near the grain boundary. It has also been shown that the effect can be modified by ternary solute additions and, to some extent, by appropriate annealing treatment.

A model based on a grain-boundary vacancy gradient combined with an oxygen–vacancy interaction has been invoked to account for the extensive hardening effect

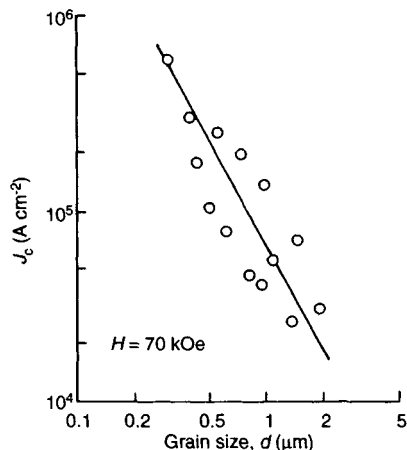


Figure 12. Critical current density of V_3Ga at 4.2 K as a function of reciprocal average grain size ($1/d$) (After Tanaka *et al.*, 1976)

in intermetallic compounds (Seybolt *et al.*, 1964). According to this model, the hardening at grain boundaries results from the dissociation of oxygen-vacancy complexes in the vicinity of grain boundaries or free surfaces; hence the gradient range reflects a kinetic effect. This increases the oxygen concentration and leads to an increase in hardening.

Excessive grain-boundary hardening was also observed in Cu_3Al , Cu_5Ge , and Cu_5Si (Khalim *et al.*, 1970). Segregation of gaseous impurities, primarily hydrogen, at grain boundaries is believed to be the cause for the observed hardening. Indeed, using a local spectral gas analysis, Shashkov (1970) has shown that, in Cu_3Si , Cu_5Si , and Ni_3Sn_2 compounds, the grain boundaries are enriched in oxygen and hydrogen, which are thus the most likely cause for the observed hardening.

In view of these observations, one point of view is to assume that the presence of a wide boundary-affected region (10–50 μm) would equally exert a strong influence on the thermal and electrical properties of intermetallic compounds. Unfortunately, judging from the lack of relevant data in the literature, this effect is virtually unknown in conducting intermetallic compounds. It should be pointed out, however, that grain boundaries exert a very strong influence on the superconducting properties of intermetallic compounds. There is a growing recognition that flux pinning by grain boundaries is an important determinant of the critical current density (J_c) in the A15 superconducting compounds such as Nb_3Sn (West and Rawlings, 1977), V_3Si (Livingston, 1977), and V_3Ga (Tanaka *et al.*,

1976; Livingston, 1977). The effect of grain boundaries on superconducting properties is manifested by an enhancement of the critical currents (J_c) with decreasing grain size, particularly in high-field superconductors such as V_3Ga , as seen in Figure 12.

Grain-boundary flux pinning has been reviewed and treated theoretically (Kramer, 1982; Wilson *et al.*, 1982) and experimentally in the case of Pb–Bi alloy films (Wilson and Kramer, 1982). The elementary pinning force arising from the electron scattering is found to be the most important pinning mechanism, which alone can account for the general magnitude of pinning by grain boundaries in a wide variety of diverse superconductors, such as Pb–Bi alloys, impure Nb or A15 compounds. The model developed predicts that the impurity level in the boundary may be adjusted to optimize pinning. The impurity effect is of significant importance for the enhancement of flux pinning in commercial materials, such as Nb_3Sn , in which inadequate grain-boundary pinning seems to be the limiting factor in performance.

Measurements of the grain-boundary flux pinning at 4.2 K in Pb–Bi alloys over a range of grain sizes (0.4–2.6 μm) show a strong grain-size dependence. The flux pinning force varies inversely with the grain size, as seen in Figure 13, from which a specific flux pinning strength per effective grain-boundary area was found to be roughly 40 $N m^{-2}$.

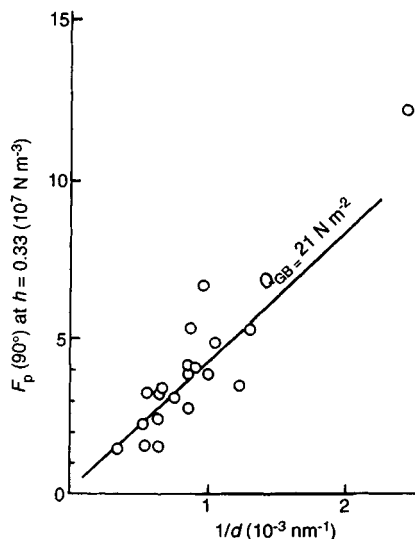


Figure 13. Pinning force as a function of reciprocal grain size ($1/d$) in Pb–18% Bi evaporated films; $h = H/H_{c2}$, the normalized magnetic field (After Wilson *et al.*, 1982)

It is of interest to note that in the case of some of the new high-temperature ceramic superconductors, grain boundaries conversely represent weak links that can severely limit the flow of electrical current. Although the exact nature of the grain-boundary weak links is still unknown, it is believed that a deviation in the chemistry, altered boundary structure or impurity segregation are most likely the causes for the observed detrimental effect.

Before closing this section, it should be stressed that the effects of grain boundaries and solute (impurity) segregation at grain boundaries in semiconductors such as Si and Ge and also in the semiconducting compounds GaAs, InSb, and HgTe is of large practical significance and has attracted exceptional attention because of their ever-increasing use in devices such as solar cells, photo-conduction devices, ultrasonic transducers, photoelectric Hall-effect devices, etc. (see Chapters 15 and 18 by Masumoto *et al.* and England and Arakawa in volume 2). Since detailed analysis of the grain-boundary effects on electrical and electronic properties in semiconductors is beyond the scope of this work, reference is made to excellent reviews by Matare (1971) and Seager (1989), where this topic was treated in great detail, both theoretically and experimentally.

3.7 Effect of Dislocations

As in the case of grain boundaries, there is a general lack of information on the effect of dislocations on the electrical properties of intermetallic compounds as for metallic elements and solid solutions. Hence, in the absence of readily available data on the effect of dislocations in intermetallics, it will be of interest to review briefly this situation in pure metals.

It is common knowledge that, in general, the resistivity of a deformed metal is greater than that of a well-annealed one. All, or at least an appreciable fraction, of this increase is due to the scattering of conduction electrons by dislocations. The resistivity increase $\Delta\rho$ due to the plastic strain ϵ can be expressed by the following empirical equation (Showaki *et al.*, 1968):

$$\Delta\rho/\rho = \alpha\epsilon^n$$

where α and n are constants depending on various conditions of the sample such as grain size. The exponent n can take values of 1/2 or 3/4 (Tanaka and Watanabe, 1972) or 3/2 (Kapička and Polák, 1972) depending on the temperature at which the material was

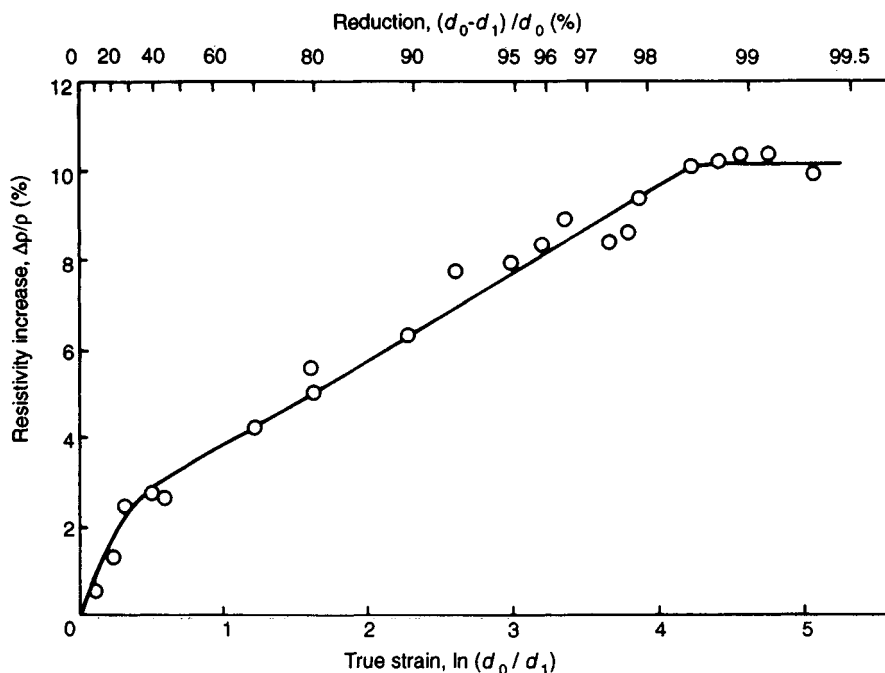


Figure 14. Increase of electrical resistivity of pure aluminum as a function of the true strain and reduction (After Schrank *et al.*, 1980)

deformed. These authors have also found that, under limited conditions, there is a relationship between the shear stress and the strain-induced (dislocation) resistivity $\Delta\rho$ expressed as

$$\sigma = \sigma_g + K(\Delta\rho)^{1/2}$$

where σ_g depends on the grain size and K is a constant. The effect of high deformation on electrical resistivity of high-purity aluminum has been investigated by Schrank *et al.* (1980), who have shown that the increase of electrical resistivity is proportional to the increase of mean dislocation density, i.e. $\Delta\rho \sim \Delta N$, and that below 40% deformation $\Delta\rho$ increases rapidly with true strain and then with a slower linear dependence for 40–98% deformation, reaching saturation above 98% deformation. The resistivity increase as a function of true strain is shown in Figure 14.

The problem of high electrical resistivity of dislocations has been treated theoretically for some time, but as yet there is no satisfactory detailed explanation for this phenomenon. A detailed account of different models developed over the years to calculate the dislocation resistivity is beyond the scope of this work. However, recent advancements in this field and pertinent experimental data warrant some discussion.

Endo (1983) has investigated the temperature dependence of the electrical resistivity due to dislocations in pure Al–0.012 at. % Mg alloys and also in pure Au and Au–0.003 at. % Sn. The most interesting result of this work is the existence of a resistivity minimum in deformed samples at low temperatures in the region 10–20 K, as seen in Figure 15. The temperature at which the resistivity minimum was observed was found to be very sensitive to the presence of solute atoms and the dislocation density of the samples. Annealing of deformed samples eliminated the resistivity minimum. At higher temperatures, resistivity sharply increased and attained a saturation at 50 K and 80 K for gold and aluminium, respectively. An attempt has been made to explain the presence of the resistivity minimum in terms of tunneling, between two parallel dislocations, of electrons localized around the dislocations.

Initial calculations of the dislocation contribution to resistivity based on the straightforward scattering by dislocation strain fields gave values one or two orders of magnitude below the measured values even for the relatively simple noble metals. Significant progress in calculating the dislocation resistivity was made by Brown (1977, 1978), who introduced the resonance scattering of conduction electrons at quasistationary

states, lying near the Fermi level. Watts (1988) showed that dislocation resistivity can be understood in terms of scattering from an assembly of displaced atoms in a region within a few atomic lengths of dislocation lines. Karolik and Golub (1993) developed a dislocation model

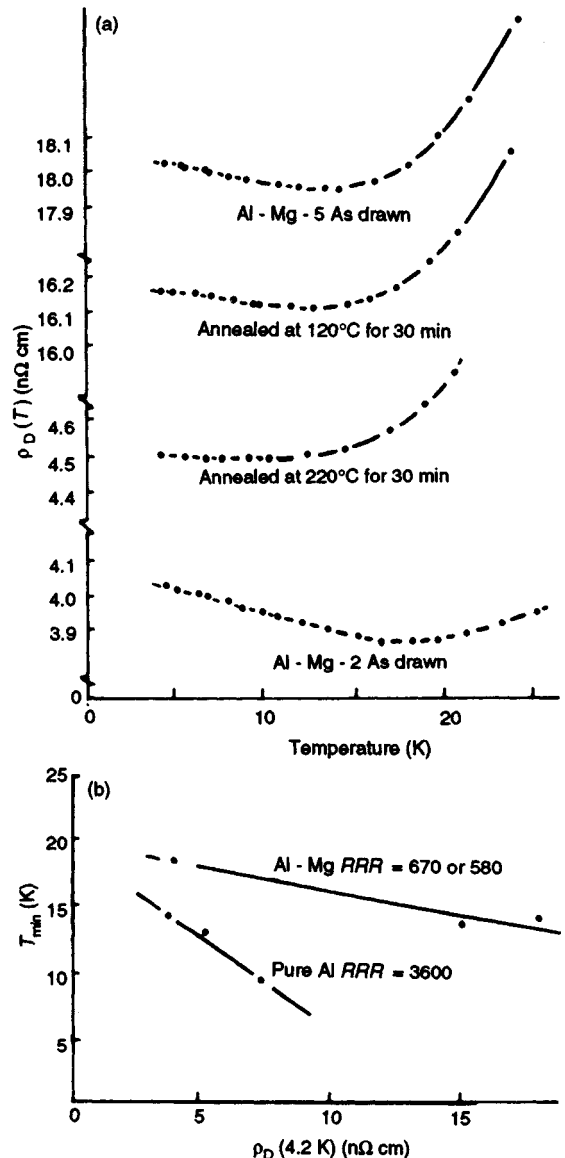


Figure 15. (a) Temperature dependence of resistivity of Al–0.012 at. % Mg, $RRR = 580$, $\rho_D(4.2\text{ K}) = 4.745\ \mu\Omega\text{ cm}$. The samples were step-annealed. (b) Dependence of minimum resistivity on $\rho_D(4.2)$ for pure Al and dilute Al–Mg alloys (After Endo, 1983)

Table 3. Comparison of calculated and experimental data for the specific electrical resistivity ρ_D/N_D^a ($10^{-19} \Omega \text{ cm}^3$) of dislocations in different metals

| Metal | Brown (1977) | Watts (1988) | Karolik and Luhvich (1991) | Temp. (K) | Experiment | Reference |
|-------|-------------------|-----------------|-------------------------------|-----------|-----------------|--------------------------------------|
| Ag | 1.9 | 1.2 | 2.7 | 4.2 | 1.9 | Basinski <i>et al.</i> (1963) |
| Al | 1.8 | 1 | 2.7 | 4.2 | 4.2 | Kino <i>et al.</i> (1974) |
| Au | 1.9 | 1.2 | 2.6 | 4.2 | 2.6 | Basinski <i>et al.</i> (1963) |
| Be | 28 | 22 | 21.7 | 80 | 34 | Papirov <i>et al.</i> (1972) |
| Bi | 1.7×10^5 | 7×10^4 | | 1.3 | 4×10^3 | Bronevoi (1990) |
| Cd | 25 | 7.3 | 21.5 | 80 | 24 | Bever <i>et al.</i> (1973) |
| Co | | | 4.5 | | | |
| Cu | 1.3 | 0.78 | 1.7 | 4.2 | 1.3 | Rider and Foxon (1967) |
| Fe | 1.9 | 9.1 | 12.6 | 80 | 10 | Tanaka and Watanabe (1972) |
| Mo | 3.7 | 3.8 | 17.3 | 4.2 | 5.8 | Whitmire and Brotzen (1967) |
| Ni | 1.1 | 3 | 5.4 | 80 | 10 | Kressel and Brown (1967) |
| Pb | 4.2 | 3.5 | | 80 | 1.1 | Bever <i>et al.</i> (1973) |
| Pt | 4 | 2.5 | 9.0 | 80 | 9 | Basinski <i>et al.</i> (1963) |
| Rh | 1.3 | 2.8 | | 4.2 | 2 | Anderson and Mackintosh (1968) |
| Ti | 29 | | 301 | 4.2 | 100 | Holz and Gould (1972) |
| W | 7.4 | 6.1 | 17.8 | 4.2 | 7.5 | Warlimont-Meier <i>et al.</i> (1967) |
| Zn | | | 15.8 | | | |
| Zr | 40 | 15 | 330 | 80 | 100 | Basinski <i>et al.</i> (1963) |

^a N_D is the density of dislocations per unit volume.

taking into account the presence of quasistationary states and the lattice dilation in the region of a dislocation core. The results of calculations of electrical resistivity of dislocations according to these models are shown in Table 3.

Another interesting model for the dislocation resistivity has been proposed by Molotskiy (1982). His model is based on the assumption that uncompensated spins develop on the broken bonds of edge dislocations and that their interaction leads to antiferromagnetic ordering along the dislocation axis. The observed rapid growth of dislocation resistivity with temperature in a narrow temperature range was attributed to resonance scattering of the conduction electrons by fluctuations of the magnetic moment at dislocations.

It is clear that, in view of the important effect that dislocations, and strain in general, exert on the electrical properties of metals, further studies (both theoretical and experimental) are needed to elucidate the effects of dislocations. This is of particular importance in the case of intermetallic superconductors, the properties of which are significantly affected by the presence of dislocations (Dimos *et al.*, 1988) (see also Chapter 16 by Stekly and Gregory in volume 2).

4. Summary

This review has described the role played by crystal structure, bonding, and chemical composition as well

as structural defects in determining the electronic behavior of intermetallic compounds. Emphasis was directed at systems whose resistivity behavior has become better understood during the last decade as a result of improved understanding of spin-disorder scattering, anomalous resistivities of certain compounds in the vicinity of the order-disorder transition, and effects of lattice defects.

Some of the important aspects of electrical and electronic behavior of intermetallic compounds were discussed generally in terms of the factors that affect the stability of these properties. There is no doubt that the electronic factor is very important, and more detailed knowledge of the electronic state in these materials is required. Recent literature indicates increased activity in the application of a large number of versatile and very powerful experimental techniques to metallic compounds. For some of these measurements, single-crystal specimens with high resistance ratios are needed to obtain meaningful information. High resistance ratios (low resistivity at liquid He temperatures) imply high chemical purity and low defect content, so that the electrons have a large mean free path.

Considerable progress has been made during the past several decades in improving the existing experimental techniques and developing new methods to study the dynamic aspects of intermetallic compounds. However, our understanding of the structure-dependent properties of intermetallic compounds remains more qualitative,

in large part because of difficulties in characterizing the microstructure, both theoretically and experimentally. Nevertheless, efforts are now being made toward quantifying many of the recently developed models and applying them to understand the role of bonding and microstructure-properties relations of compounds.

Much theoretical work is still required in all branches of the subject. Such work is specially important at the present time in view of the widespread desire, common to all physics and chemistry, to expand our knowledge of the microscopic processes involved, in particular, in critical phenomena and to achieve a more complete understanding of the effect of critical fluctuations on the electrical resistance and on transport properties in general. Hence, by recognizing the importance of certain principles and factors, rules can be developed that will help in predicting the constitution and properties of alloy systems not yet investigated. Improved understanding of fundamental electrical behavior of intermetallics can contribute not only to our knowledge of their bonding but also to the identification and exploitation of particular intermetallics with attractive electrical properties.

As Laves (1967) pointed out, every structure type, in principle, can be discussed by considering which of the principles and which of the factors appear to be the dominant ones. On the basis of such a discussion, certain rules emerge, the value of which can be checked by preparing new mixtures of metals that should conform to such rules. In many cases 'predictions' have been verified, thus adding to our confidence in a certain rule. In other cases compounds are formed that do not conform to the predicted result. If this is the case, a new window is usually opened that sheds light on new directions of knowledge concerning the strange relations between chemical composition and the structure and properties of metallic compounds.

In addition, it should be pointed out that, despite our knowledge of the structure of the atom, the laws of quantum mechanics, and our ever-increasing computing capabilities, no compound has as yet been predicted by using such more sophisticated approaches (still less can we succeed in a quantitative prediction of properties). On the other hand, many unknown compounds and their structures have been predicted and verified using past experience, expressed as 'rules' and by the intuition of persons like Hume-Rothery. It appears, to paraphrase Einstein, that 'Imagination is more important than knowledge.' How, true indeed.

5. References

- Aleksandrov, B. N. (1962). *Fiz. Met. Metalloved.*, **14**, 434.
- Aleksandrov, B. N., Kan, Ya. S., and Tatishvilli, D. G. (1974). *Phys. Met. Metall.*, **37**, 22.
- Alley, P., and Serin, B. (1959). *Phys. Rev.*, **116**, 334.
- Andersen, O. K., and Mackintosh, A. R. (1968). *Solid State Commun.*, **6**, 285.
- Andrews, P. V. (1965). *Phys. Lett.*, **19**, 558.
- Andrews, P. V., West, M. B., and Robenson, C. R. (1969). *Phil. Mag.*, **19**, 887.
- Arajs, S., Oliver, B. F., and Michalak, J. T. (1967). *J. Appl. Phys.*, **38**, 1676.
- Arkharov, V. I., Borisov, B. S., Vangenheim, S. D., and Sokolova, G. K. (1960). *Fiz. Met. Metalloved.*, **9**, 81.
- Arkharov, V. I., Vangenheim, S. D., Klyuyeva, I. B., and Serikova, V. P. (1967). *Fiz. Met. Metalloved.*, **24**, 289.
- Arkharov, V. I., Krysov, V. I., and Shumko, A. A. (1973). *Phys. Met. Metalloved.*, **36**, 120.
- Aust, K. T. (1969). *Can. Met. Q.*, **8**, 173.
- Balina, Ye. A., Geld, P. V., Andreyeva, L. P., and Zelenin, L. P. (1991). *Phys. Met. Metall.*, **72**, 113.
- Basinski, M. B., Dugdale, J. S., and Howie, A. (1963). *Phil. Mag.*, **8**, 1989.
- Bass, J. (1972). *Adv. Phys.*, **21**, No. 91.
- Beeler, J. R. (1967). In *Intermetallic Compounds* (ed. J. H. Westbrook). Wiley, New York, p. 233.
- Bever, M. B., Holt, D. L., and Titchener, A. L. (1973). *Prog. Mater. Sci.*, **17**, 1.
- Blanco, J. A., Gómez-Sal, J. C., Rodriguez-Fernandez, J., Gignoux, D., Schmitt, D., and Rodriguez-Carvajal, J. (1992). *J. Phys.: Condens. Matter*, **4**, 8233.
- Braunović, M. (1974a). In *Grain Boundaries in Engineering Materials* (eds J. L. Water, J. H. Westbrook, and D. A. Woodford). Claitor's, Baton Rouge, LA, p. 193.
- Braunović, M. (1974b). *Can. Met. Q.*, **13**, 211.
- Braunović, M. (1988). In *Strength of Metals and Alloys (ICSMA 8)* (eds P. O. Kettunen, K. T. Lepisto, and M. E. Lehtonen). Pergamon, New York, p. 1383.
- Braunović, M., and Haworth, C. W. (1969). *J. Appl. Phys.*, **40**, 3459.
- Bronevoi, I. L. (1980). *Sov. Phys.—JETP*, **52**, 977.
- Brouers, F., and Vedyayev, A. V. (1972). *Phys. Rev.*, **B5**, 348.
- Brown, R. A. (1977). *J. Phys.*, **F7**, 1283.
- Brown, R. A. (1978). *J. Phys.*, **F8**, 1467.
- Cadeville, M. C., Pierron-Bohnes, V., and Sanchez, J. M. (1992). *J. Phys.: Condens. Matter.*, **4**, 9053.
- Campbell, I. A., Fert, A., and Pomeroy, A. R. (1967). *Phil. Mag.*, **15**, 977.
- Chavineau, J. P., Croce, P., Devant, G., and Verhaeghe, M. F. (1969). *J. Vac. Sci. Technol.*, **6**, 776.
- Coles, B. R. (1967). In *Intermetallic Compounds* (ed. J. H. Westbrook). Wiley, New York, p. 79.
- Coles, B. R. (1986). In *Encyclopedia of Materials Science and Engineering* (ed. M. B. Bever). Pergamon, New York, p. 1354.
- Das, S. B., and Gerritsen, A. N. (1964). *Phys. Rev.*, **135**, A1081.
- Demianczuk, D. W., and Aust, K. T. (1975). *Acta Metall.*, **23**, 1149.

- Dimos, D., Chaudari, P., Mannhart, J., and LaGoues, F. K. (1988). *Phys. Rev. Lett.*, **61**, 219.
- Endo, T. (1983). *J. Sci. Hiroshima Univ., Ser. A.*, **46**, 195.
- Gaal, I., Neugebauer, J. M., and Uray, L. (1975). *Acta Tech. Acad. Sci. Hung.*, **80**, 109.
- Gerritsen, A. N. (1956). *Handbuch der Physik*, Vol. 19, Springer-Verlag, Berlin, p. 137.
- Gleiter, H. (1970). *Z. Metallk.*, **1**, 282.
- Granovskii, A. B., Imamnazarov, D. Kh., and Kahilov, I. Kh. (1991). *Phys. Met. Metall.*, **72**, 24.
- Hart, E. W. (1972). In *The Nature and Behaviour of Grain Boundaries* (ed. H. Hu). Plenum, New York, p. 155.
- Hermann, G., Gleiter, H., and Baro, G. (1976). *Acta Metall.*, **24**, 353.
- Holz, A., and Gould, G. (1972). *Thin Solid Films*, **14**, 35.
- Ikeda, K., and Nakamichi, T. (1975). *J. Phys. Soc. Japan.*, **39**, 963.
- Ishizawa, Y., Otani, S., Nozaki, H., and Tanaka, T. (1992). *J. Phys.: Condens. Matter*, **4**, 8593.
- Ivanov, G. A., and Papov, A. M. (1963). *Sov. Phys—Solid State*, **5**, 1040.
- Jones, H. (1956). *Handbuch der Physik*, Vol. 19. Springer-Verlag, Berlin, p. 227.
- Kapička, A., and Polák, J. (1972). *Czech. J. Phys.*, **B22**, 476.
- Karolik, A. S., and Luhvich, A. A. (1991). *J. Phys., Cond. Matter*, **6**, 873.
- Kasen, M. B. (1972). *Acta Metall.*, **20**, 105.
- Kasuya, T. (1958). *Prog. Theor. Phys. (Kyoto)*, **16**, 58.
- Khalim, A. A. R., Ageeva, G. N., Zolotorevskii, V. S., and Novikov, I. I. (1970). *Izv. VUZ. Svetnaya Met.*, No. 3, p. 120.
- Kino, T., Endo, T., and Kawata, S. (1974). *J. Phys. Soc. Japan*, **36**, 698.
- Klemens, P. G., and Lowenthal, G. C. (1961). *Aust. J. Phys.*, **14**, 351.
- Kornilov, I. I. (1974). In *Order-Disorder Transformation in Alloys* (ed. H. Warlimont). Springer-Verlag, Berlin, p. 132.
- Kourou, N. I. (1991). *Phys. Met. Metall.*, **72**, 131.
- Kourou, N. I., Tsioukin, Yu N., and Karpov, Yu. G. (1987). *Phys. Met. Metall.*, **64**, 199.
- Kouvel, J. S. (1967). In *Intermetallic Compounds* (ed. J. H. Westbrook). Wiley, New York, p. 529.
- Kramer, E. J. (1982). In *Advances in Cryogenic Engineering Materials*, Vol. 28 (eds R. P. Clark, and R. P. Reed). Plenum, New York, p. 307.
- Kressel, H., and Brown, N. (1967). *J. Appl. Phys.*, **38**, 1618.
- Lagarde, P., and Biscondi, M. (1974). *Can. Met. Q.*, **13**, 245.
- Laves, F. (1967). In *Intermetallic Compounds* (ed. J. H. Westbrook). Wiley, New York, p. 129.
- Leroux, C., Cadeville, M. C., and Kozubski, R. (1989). *J. Phys.: Condens. Matter*, **1**, 6403.
- Levin, E. M., Bodak, O. I., Gladyshevskii, E. I., and Sinyushko, V. G. (1992). *Phys. Status Solidi*, **a134**, 107.
- Livingston, J. D. (1977). *Phys. Status Solidi*, **a44**, 295.
- Mannan, Kh. M., and Karim, Kh. R. (1975). *J. Phys.*, **F5**, 1687.
- Masuda-Jindo, K. (1988). *J. Physique*, **49**, C5, 557.
- Masuda-Jindo, K. (1990). *Phys. Rev.*, **B41**, 8407.
- Masuda-Jindo, K. (1991). *Intermetallic Compounds: Structure and Mechanical Properties*. Japan Institute of Metals, Sendai, p. 111.
- Matate, H. F. (1971). *Defect Electronics in Semiconductors*. Wiley, New York.
- Matthias, B. T. (1957). *Progress in Low Temperature Physics*, Vol. II. Interscience, New York, p. 138.
- Mayadas, A. F., and Shatzke, M. (1970). *Phys. Rev.*, **B1**, 1382.
- Meaden, G. T. (1965). *Electrical Resistance of Metals*. Heywood, London.
- Molotskiy, M. I. (1982). *Phys. Met. Metall.*, **54**, 24.
- Morgner, H., and Pompe, G. (1975). *Phys. Status Solidi*, **29**, 459.
- Mott, F. R. (1936). *Proc. R. Soc.*, **A153**, 699.
- Neuman, M. R., and Ko, W. H. (1966). *J. Appl. Phys.*, **37**, 3327.
- Otani, S., Tanaka, T., and Ishizawa, Y. (1986). *J. Mater. Sci.*, **21**, 1011.
- Otto, M. J., Feil, H., van Woerden, R. A. M., Wijngaard, J., van der Valk, P. J., van Bruggen, C. F., and Haas, C. (1987). *J. Magn. Magn. Mater.*, **70**, 33.
- Panko, T. I., Zaikovskaya, L. V., and Vangenheim, S. D. (1981). *Metallfizika*, **3**, 113.
- Papirov, I. I., Stoyev, P. I., and Taranenko, I. A. (1972). *Phys. Met. Metall.*, **34**, 1022.
- Phillips, V. A. (1961). *Acta Metall.*, **9**, 876.
- Read, W. T. (1953). *Dislocations in Crystals*. McGraw-Hill, New York.
- Rider, J. G., and Foxon, C. T. B. (1967). *Phil. Mag.*, **16**, 1133.
- Roberts, B. W. (1967). In *Intermetallic Compounds* (ed. J. H. Westbrook). Wiley, New York, p. 501.
- Rossiter, P. L. (1979). *J. Phys.*, **F9**, 891.
- Rossiter, P. L. (1980). *J. Phys.*, **F10**, 1459.
- Schrank, J., Zehetbauer, M., Pfeiler, W., and Trieb, L. (1980). *Scripta Metall.*, **14**, 1125.
- Seager, C. H. (1989). *Annu. Rev. Mater. Sci.*, **15**, 271.
- Senchenko, A. A., Piratinska, I. I., Zelenin, L. P., and Vereshchagin, Yu. A. (1991). *Phys. Met. Metall.*, **72**, 105.
- Seybolt, A. U., and Westbrook, J. H. (1964). *Acta Metall.*, **12**, 449.
- Seybolt, A. U., and Westbrook, J. H. (1965). *5th Plansee Seminar* (ed. F. Benesovsky). Metallwerk Plansee AG, Reute/Tyrol, p. 845.
- Seybolt, A. U., Westbrook, J. H., and Turnbull, D. (1964). *Acta Metall.*, **12**, 1456.
- Shashkov, D. P. (1970). *Fiz. Khim. Obrab. Mater.*, No. 6, p. 31.
- Shcherbakov, A. S., Kourou, N. I., Vereshchagin, Yu. A., and Alekseeva, M. A. (1993). *Phys. Met. Metall.*, **76**, 469.
- Showaki, K., Takamura, M., and Kojim, K. (1968). *Mem. Inst. Sci. Ind. Res. Osaka Univ.*, **25**, 100.
- Singh, P. P. (1991). *Phys. Rev.*, **B43**, 3975.
- Sondheimer, E. H. (1950). *Proc. R. Soc.*, **A203**, 79.
- Sun, R. C., Tisonier, T. C., and Cruzan, P. D. (1973). *J. Appl. Phys.*, **44**, 1009.

- Sykes, C., and Jones, F. W. (1938). *Proc. R. Soc.*, **A166**, 376.
- Tanaka, K., and Watanabe, T. (1972). *Japan. J. Appl. Phys.*, **11**, 1429.
- Tanaka, Y., Ito, K., and Tachikawa, K. (1976). *J. Japan. Inst. Metals*, **40**, 514.
- van Gorp, G. J. (1975). *J. Appl. Phys.*, **46**, 1922.
- Warlimont-Meier, B., Beardmore, P., and Hull, D. (1967). *Acta Metall.*, **15**, 1399.
- Watanabe, T., Kimura, S. -I., and Karashima, S. (1984). *Phil. Mag.*, **A49**, 845.
- Watts, B. R. (1988). *J. Phys.*, **F18**, 1197.
- Weger, M., de Groot, R. A., Mueller, F. M., and Kaveh, M. (1984). *J. Phys.*, **F14**, L207.
- West, A. W., and Rawlings, R. D. (1977). *J. Mater. Sci.*, **12**, 1862.
- Westbrook, J. H., and Wood, D. L. (1963). *J. Inst. Metals*, **91**, 174.
- Whitmire, L. D., and Brotzen, F. R. (1967). *Trans. AIME*, **239**, 824.
- Wilson, E. Y., and Kramer, E. J. (1982). *Phil. Mag.*, **46**, 221.
- Wilson, E. Y., Thomas, D. A., and Kramer, E. J. (1982). *Phil. Mag.*, **46**, 523.
- Wissmann, P. (1970). *Thin Solid Films*, **5**, 329.
- Yoshida, K. (1958). *Phys. Rev.*, **107**, 396.
- Ziman, J. M. (1960). *Electrons and Phonons*. Oxford University Press, Oxford.

This chapter was originally published in 1995 as Chapter 41 in *Intermetallic Compounds*, Vol. 1: *Principles*, edited by J. H. Westbrook and R. L. Fleischer.

Chapter 3

Magnetic Applications

Hans H. Stadelmaier

*Department of Materials Science and Engineering, North Carolina State University,
Raleigh, NC 27695-7907, USA*

Bernd Reinsch

Institut für Werkstoffwissenschaft, Max-Planck-Institut für Metallforschung, D-70569 Stuttgart, Germany

1. Introduction

The development of metallic magnet materials has in a way followed a path similar to that taken by structural alloys, i.e. it has drawn on the solid solutions between elements and the properties of multiphase microstructures before turning its attention directly to intermetallic compounds. The continuous variation of properties in the face-centered cubic Fe–Ni solid solutions has provided a fertile ground for testing theories and tailoring magnetic alloys without specific reference to compounds. Intermetallic compounds, as well as other materials that have permanent magnetic moments of sufficient magnitude for applications, fall broadly into two categories, ‘soft’ and ‘hard’. Magnetically soft alloys have high permeabilities (μ) and low coercivities (H_c) and are applied in situations where they conduct or concentrate a magnetic flux and are magnetic only in the presence of an external field. The hard magnets have a permanent moment in the absence of an applied field. They have a high coercive force and are used in many configurations to provide a constant field in an air gap or, in some instances, to provide an attractive or repulsive mechanical force. Magnetic principles are reviewed more extensively by Kouvel (Chapter 40 in Volume 1) and the often exotic magnetic structures are described by Roth (Chapter 19 in Volume 1).

Intermetallic compounds are among the softest and hardest known magnetic materials. Some soft magnets have permeability maxima at alloy compositions known

to show ordering (FeCo, FeNi₃), but the heat treatment for the highest permeability may require either optimizing the long-range order, as in FeCo, or removing it, as in FeNi₃. To add to the confusion, ordered FeCo is found in both soft and hard magnets. In the best permanent magnets, suitable alloys are invariably ordered and have a very high magnetocrystalline anisotropy that locks the spins in a direction parallel to a unique crystal axis, the direction of easy magnetization. This preferred spin orientation can also be transferred to a polycrystalline magnet by special processing, such as directional solidification or magnetic alignment of small crystallites prior to sintering. Soft magnets are based on the magnetic transition elements Fe, Co and Ni often in combination with other elements such as Al or Si. Hard magnets also contain one or several of the elements Fe, Co and Ni (and sometimes Mn), again in combination with other elements. The Alnicos, which long dominated the permanent magnet applications, are alloys of Fe with varying amounts of Ni, Co and Al. In one permanent magnet, MnAl, the magnetic moment is supplied by the normally nonmagnetic element Mn and, in that sense, it is an offshoot of the ferromagnetic Heusler alloys based on the compounds Cu₂MnAl and Cu₂MnSn (L2₁, cF16) that were known around the turn of the century (Heusler, 1904). The strongest known permanent magnets are formed by alloying Fe or Co with the lanthanides Ce, Pr, Nd, or Sm. The source of magnetic hardness in these ‘rare-earth permanent magnets’ is always an intermetallic compound that

provides the high crystal anisotropy. The physical mechanism that is responsible for the coercivity of these high-performance permanent magnets also depends on the properties and distribution of minor phases. The rapid expansion of rare-earth permanent magnet research has generated an abundance of information that is too voluminous to include in detail; however, the major compound types that have found applications or have been suggested for them will be discussed. An earlier account of the magnetic properties of intermetallic compounds, not all of which are suitable for applications, is found in the article by Kouvel (1967) which includes 369 references.

1.1 Magnet Characterization

1.1.1 Units and Hysteresis Loop

Quantitative data will be expressed in SI units in the following fashion. Both the induction and the magnetic field strength will be given in tesla (T) because in this way they are most easily converted to the c.g.s. units gauss (G) and oersted (Oe), which are firmly entrenched in the older literature and widely used even today. With the vacuum permeability $\mu_0 = 4\pi \times 10^{-7} \text{ T m A}^{-1}$, the field is $\mu_0 H$ T. The intensity of magnetization M is expressed through the polarization (or intrinsic induction) $J = \mu_0 M$ T, and the induction is $B = \mu_0 H + J$. At ambient temperatures the polarization J rarely exceeds the saturation value of Fe, which is 2.2 T at 0 K. The field-dependent relative permeability $\mu = B/\mu_0 H$ is dimensionless, and H and M are expressed in A m^{-1} , but that unit will not be shown in explicit form. The use of J T in preference to $M \text{ A m}^{-1}$ corresponds to the Kennelly system of SI units. The energy density BH for permanent magnets, which was traditionally reported in GOe, is now in $\text{TA m}^{-1} (\equiv \text{J m}^{-3})$. For B , J , and $\mu_0 H$ the conversion is simple: to obtain gauss or oersted in c.g.s., multiply tesla by 10^4 or millitesla by 10 so that an induction B or field $\mu_0 H$ of 1 T represents 10 kG or 10 kOe, respectively. To convert the energy density BH from J m^{-3} to GOe, multiply by 40π .

The hysteresis loop of a ferromagnetic material, in this case a strong permanent magnet, is shown in Figure 1. The polarization J reaches a saturation value J_s after a certain field is attained, but the induction B continues to rise because of the added term $\mu_0 H$. The negative field that reduces the induction B to zero after saturation of J at $+\mu_0 H$ is the coercivity $H_c \text{ A m}^{-1}$ or $\mu_0 H_c \text{ T}$. A different value, known as the intrinsic coercivity $(\mu_0)_i H_c$, marks the field at which J , not B , becomes

zero. In high-performance permanent magnets the intrinsic coercivity is often considerably larger than the simple induction coercivity, as seen in Figure 1. In soft magnets the best materials have intrinsic (J) hysteresis loops that degenerate into a step function, appearing to jump from $-J_s$ to $+J_s$ at $H=0$, when the coercivity $\mu_0 H_c$ is several orders of magnitude smaller than the saturation polarization J_s . Then the abscissa must be rescaled to allow depicting a loop with a finite width. Rectangular ('square') intrinsic hysteresis loops result when a pronounced uniaxial anisotropy is combined with a preferred orientation. In high-performance permanent magnets this is owing to magnetocrystalline anisotropy, and rectangular loops are desirable because they yield the highest energy density (Section 1.1.3) for given values of B_r and H_c . In magnetically soft materials rectangular loops can lead to easy saturation of the polarization, a feature desired in some applications such as DC-to-DC converters and magnetic amplifiers. In some alloys rectangular loops

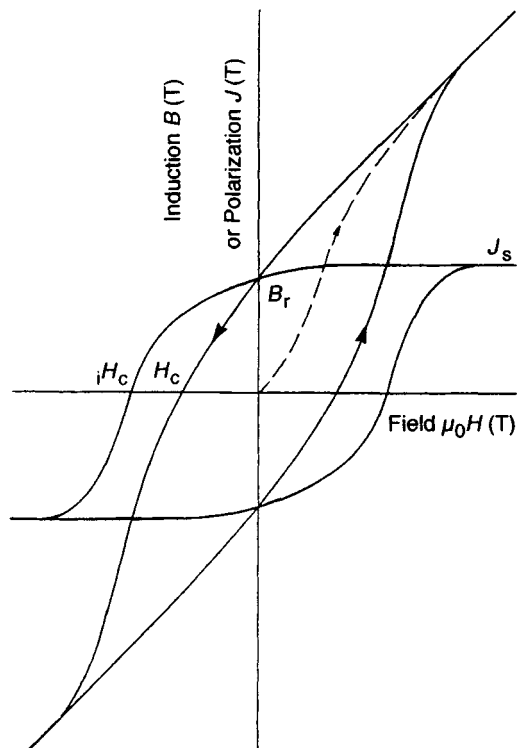


Figure 1. Hysteresis loop of a typical ferromagnet. Magnetic polarization J reaches saturation value J_s , whereas induction B continues to rise with increasing field. The scales of the abscissa and ordinate are identical. The dashed line is the virgin curve of demagnetized material

can be induced by heat treatment in a longitudinal magnetic field (see also Section 2.2). In such a loop the maximum permeability and the remanence B_r are increased and the coercivity H_c is decreased relative to that of the alloy annealed without a field. Annealing the same alloy in a transverse field has the opposite effect and shears the hysteresis loop, making it nearly linear as a function of the field so that the permeability is constant but lower, and the remanence is reduced substantially. Loop shearing can also be achieved by the magnetic separation of particles, as in powdered-iron cores. Therefore inductors made of powdered-iron particles that are separated by a nonmagnetic binder avoid operation in the nonlinear range because higher fields are required for their saturation.

Magnetically soft materials have coercive fields $\mu_0 H_c$, where $B = 0$, that are measured in fractional millitesla (or in oersteds), whereas permanent magnets have intrinsic coercivities $(\mu_0)_i H_c$, where $J = 0$, that begin with tens of millitesla (or hundreds of oersteds) and can run as high as several tesla. At $H = 0$, the residual induction (remanence) B_r and the residual polarization J_r have identical values in the units used here. The area inside either the B or the J hysteresis loop represents the energy (per unit volume) dissipated during one complete cycle. In alternating fields it represents the hysteresis loss, and it increases proportionally as the frequency.

1.1.2 Magnetically Soft Alloys

In soft magnets other parameters of interest are the maximum value of the relative permeability $\mu = B/\mu_0 H$, the initial permeability $\mu_i = (1/\mu_0) dB/dH$ for $B = H = 0$, and the saturation polarization J_s , all of which should be high. When the crystal anisotropy is very low, the effects of mechanical stress or internal stress dominate, so that an additional requirement for soft magnets is the vanishing of magnetostriction. It is axiomatic that all types of magnets with extreme properties are responsive to heat treatment, i.e. are 'structure sensitive'. For many AC applications the B versus H curves of a soft magnet are not treated as loops but are assumed to be single valued and linear and are described by an effective permeability μ_e . In such alternating field applications, eddy current losses are added to the hysteresis losses. They increase with the square of the frequency, and the electrical resistivity should be high to keep them low.

1.1.3 Hard Magnets

Permanent magnets require large values of both residual magnetization B_r and coercivity H_c . A related means of

characterizing a permanent magnet is to determine the largest magnitude of the product BH in the second quadrant ($B > 0$, $H < 0$) of the hysteresis loop B versus H . When a magnetic circuit containing a permanent magnet and an air gap is operated at the point (B, H) of maximum energy density $|BH|$, the field in the gap will have the highest attainable value. This product $|BH|_{\max}$ is loosely referred to as the 'energy product' and is a figure of merit for permanent magnets. If the remanence B_r is less than the intrinsic coercivity $(\mu_0)_i H_c$, the energy product cannot exceed $(0.5B_r)^2 \times 10^4 / 4\pi \text{ kJ m}^{-3}$, where B_r is in tesla, and larger intrinsic coercivities will not raise $|BH|_{\max}$ any further. Large intrinsic coercivities are nevertheless desirable because they improve the stability of a magnet against accidental demagnetization. Typical values of $|BH|_{\max}$ are 10^7 GOe , or 80 kJ m^{-3} in SI units, found in the best Alnicos, and $5 \times 10^7 \text{ GOe}$, or 400 kJ m^{-3} , the current limit attained in rare-earth permanent magnets. A useful means of identifying a potential permanent magnet material, short of measuring the anisotropy coefficients K_i , is the so-called anisotropy field. When the preferred direction of magnetization ('easy axis') of a single crystal or highly oriented magnet is set perpendicular to an applied field, the field magnitude at which the magnetization vector is fully forced into the field direction is the anisotropy field H_a . It is readily measured directly or by extrapolation and provides a theoretical limit for the coercivity, which itself usually reaches no more than a few tenths of H_a . The anisotropy field $\mu_0 H_a$ of a compound that is a potential high-performance permanent magnet will usually approach or exceed 10 T . When the magnetocrystalline anisotropy is specified, often as K_1 , the largest coefficient, its dimension is based on the product $JH \text{ J m}^{-3}$. The relation to older data reported in c.g.s. units is $1 \text{ J m}^{-3} = 10 \text{ ergs cm}^{-3}$. When K_1 is of the order of zero to 10 J m^{-3} , the material is magnetically soft; for hard magnets K_1 is around 10^4 to 10^7 J m^{-3} . Positive K_1 means that the magnetization is parallel to the unique crystallographic axis (the c axis in hexagonal, rhombohedral, and tetragonal crystals); for negative K_1 it lies in the basal plane. Even when the magnitude of negative K_1 is large, it contributes nothing to magnetic hardness because the plane of easy magnetization has an infinite number of allowable directions that are not separated by barriers against directional change.

1.1.4 Composition

In the older magnet literature, compositions were invariably given in wt%. The recent permanent magnet

literature leans toward at% but compositions are often expressed in chemical formulas when they do not represent single-phase alloys at all. We will attempt to keep designations of composition simple, but the problems occasioned by strange notations in the original literature cannot always be avoided.

2. Magnetically Soft Materials

2.1 Roll (Slip-induced) Anisotropy—Isoperm

A form of ordering that is one-dimensional and leads to a single preferred magnetic axis is based on the interaction of dislocations with an ordered structure, which may itself be cubic. When this form of uniaxial anisotropy is significant, it may outweigh any anisotropy that might result from preferred orientation alone. The theory of this behavior has been given by Chikazumi (1964). The anisotropy coefficient K_u that is attached to the phenomenon may be >0 or <0 ; if $K_u > 0$ the preferred magnetic axis is in the rolling direction of a polycrystalline sheet. Roll anisotropy was first observed in Fe–Ni (Six *et al.*, 1934; Dahl and Pfaffenberger, 1934), where it peaks at 48 wt% Ni and 75 wt% Ni (Rathenau and Snoek, 1941), compositions at which the alloys are known to order. Roll anisotropy also occurs in Fe_3Al , Ni–Co, and Ni–Mn. Reduced to a simple description, this form of uniaxial anisotropy that results from plastic deformation is based on an unbalanced distribution of like-atom pairs that favor a single direction. In a low-anisotropy phase such as FeNi_3 , it increases the anisotropy and spoils the high permeability, even though the deformation destroys the higher-anisotropy long-range order. This can be seen with the following numbers for Permalloy consisting of Fe–78 wt% Ni: quenched (disordered), $K_1 \approx -200 \text{ J m}^{-3}$ (Bozorth, 1951); slowly cooled (partially ordered), $K_1 \approx -1800 \text{ J m}^{-3}$ (Bozorth, 1951); polycrystal rolled to 33% reduction in thickness, uniaxial $K_u = 15\,000 \text{ J m}^{-3}$ (Rathenau and Snoek, 1941). In an Fe–Ni alloy of equiatomic composition capable of ordering to the AuCu (tP4) structure (Petersen *et al.*, 1977; Clarke and Scott, 1980), a useful application of roll anisotropy has been described (Rathenau and Snoek, 1941). It has been called Isoperm, a label of uncertain origin, for the fact that its permeability μ is constant over a range of fields H extending to near saturation. The permeability, which is in the range 30 to 100, is not comparable to that of the very soft magnetic alloys. The heat treatment requires two steps, one to form a (100)[001] texture by a reduction in thickness of 98–99% followed by an

anneal at 1000–1200 °C, then a 50% reduction in thickness to introduce the roll anisotropy with $K_u \approx -20\,000 \text{ J m}^{-3}$ (Rathenau and Snoek, 1941). As a result of the negative K , the easy axis lies in the transverse direction, and the rolling direction has become the magnetically harder one. Consequently, magnetizing in the rolling direction flattens the hysteresis loop to the desired shape and, in doing so, provides a lower but nearly constant permeability.

2.2 Permalloy

Permalloy is a generic name for very soft Fe–Ni alloys. The prototype 78-Permalloy with 78 wt% Ni has a composition near the L1_2 (cP4) FeNi_3 phase, but, as mentioned in Section 2.1, the ordered structure does not have the lowest anisotropy. What makes permalloys so outstanding is the fact that their magnetostriction is also near zero so that coercivity and permeability are not very sensitive to mechanical strain. The optimum heat treatment requires cooling from 600 °C at a rate of $\sim 25 \text{ K s}^{-1}$, and the results of other heat-treating schedules discussed by Bozorth (1951) suggest that long-range order, below 517 °C (Massalski, 1992), contributes only insignificantly to the soft magnetic properties of 78-Permalloy. Typical permeabilities are $\mu_i = 10^4$ and $\mu_{\text{max}} = 10^5$ (Bozorth, 1953). The permalloy problem has been discussed in detail by Bozorth (1953).

Magnetic annealing of permalloy (65 wt% Fe) has been shown to produce rectangular hysteresis loops when the properties were measured in the direction of the field that was applied during annealing (Bozorth, 1951). Annealing the same material in a transverse field produces a B versus H loop that is nearly linear up to saturation. The effective permeability can still be quite high, yielding a value of 4000 in this particular alloy. Annealing in a transverse field has the same effect as the roll anisotropy in Isoperm that was described in Section 2.1. The interpretation of the magnetic annealing phenomenon has been proposed by several authors independently and is described in the book by Chikazumi (1964). It is based on directional order whose pair distribution has a symmetry that is lower than cubic and results in the uniaxial anisotropy.

2.3 Fe_3Al (Alfenol); $\text{Fe}_3(\text{Al}, \text{Si})$ (Sendust)

The anisotropy coefficient K of ordered Fe_3Al (DO_{19} , cF16) is -8000 J m^{-3} at 300 K, and the disordered alloy (A2, cI2) has a small positive value (Puzi, 1960). The saturation polarization of Fe_3Al , converted to SI units, is 1.14 T at 250 K, and its Curie point is 441 °C

(Fallot, 1936). The fabrication and properties of the Fe–Al alloys 12-Alfenol and 16-Alfenol (12 and 16 wt% Al) have been described by Nachman and Buehler (1955), and they straddle the Fe_3Al composition. For 15.8 wt% Al, Puzei (1960) states that room-temperature isotropy ($K \approx 0$) is observed in the ‘hardened’ condition, whereas at 11.6 wt% Al it is obtained by annealing. This agrees with the statement by Nachman and Buehler (1955) that alfenols with 13% or less Al yield the best magnetic properties in the ordered state, whereas those with more than 14% Al are best in the disordered condition. 16-Alfenol has $\mu_i = 2800$ and $\mu_{\text{max}} = 115\,000$. Because of its higher Fe content, 12-Alfenol has a higher saturation polarization but its maximum permeability is lower, $\mu_i = 4500$ and $\mu_{\text{max}} = 45\,000$ (Nachman and Buehler, 1955). Ordered Fe_3Si has a saturation polarization at 290 K of 1.17 T and a Curie point of 534 °C (Fallot, 1936). It has the same structure as Fe_3Al and is completely miscible with it. The composition (wt%) 5Al, 10Si, 85Fe was named Sendust by Masumoto (1936) because of the extreme brittleness that made it easy to pulverize. The heat treatment for high permeability, 1 h at 1000 °C followed by slow cooling (Masumoto, 1936), indicates that some ordering is required for optimum properties, which can run as high as $\mu_i = 30\,000$ and $\mu_{\text{max}} = 120\,000$.

2.4 FeCo (Permendur)

The high magnetic moment in Fe–Co alloys has generated interest for application to magnetic cores. In the particular case of FeCo with the B2 CsCl (cP2) structure, a product named ‘Permendur’ by Elmen (1929) has been developed based on the permeability peak at the equiatomic composition. The first anisotropy coefficient K_1 of FeCo is $-17\,000\text{ J m}^{-3}$ in the disordered state but zero when ordered (Hall, 1960). The sequence of phases at the equiatomic composition is, with decreasing temperature, f.c.c. γ above 985 °C, b.c.c. α , followed by ordered α' (B2, cP2) below 725 °C (Massalski, 1992). The best heat treatment consists of furnace cooling from 850 °C out of the α region. Cooling in a weak magnetic field further increases B_r and decreases H_c producing a nearly rectangular hysteresis loop (Libsch *et al.*, 1950). Typical values obtained this way are $B_r = 1.9\text{ T}$ and $\mu_0 H_c = 0.068\text{ mT}$ (Libsch *et al.*, 1950). A modification to improve the properties of Permendur is the addition of 2 wt% V. Since the required ordering lowers the electrical resistivity, an element that raises it efficiently was found in vanadium, which has the added benefit of improving the workability and machinability of the disordered alloy (Bozorth, 1951).

2.5 Borides Based on $\text{Co}_{20}\text{Al}_3\text{B}_6$

Cobalt borides with the structure of the chromium carbide Cr_{23}C_6 (D8₄, cF116) are usually stabilized by including a second metallic element (Stadelmaier, 1969). An example is $\text{Co}_{20}\text{Al}_3\text{B}_6$ in which the stabilizing atom aluminium is ordered. These phases are mechanically hard and typically show a Vickers hardness > 1000 . By replacing some of the Co with Fe, mechanically hard but magnetically soft materials to be used as recording heads were described by Hirota (1969), who patented a single-phase alloy of the type $\text{Co}_{20-x-y}\text{Fe}_x\text{Mo}_y\text{Al}_3\text{B}_6$. At the composition $\text{Co}_{15.72}\text{Fe}_{4.2}\text{Mo}_{0.08}\text{Al}_{2.8}\text{B}_6$ a Curie temperature of 350 °C and an effective permeability of 3200 at 100 Hz were observed.

3. Permanent Magnets

3.1 Lanthanide-free Magnets

3.1.1 Cunife, Cunico, Alnico and Vicalloy

Intermetallic compounds found in these magnets appear to have conflicting functions. In Cunife and Vicalloy, the magnetic phase is actually the same as in the soft magnets Isoperm and Permendur, demonstrating the importance of heat treatment (and composition). In Alnico the intermetallic compound (Ni-rich (Fe, Ni) Al) that survives the heat treatment is not the prominent magnetic phase. In fact, it is only weakly magnetic, and the magnetic moment is supplied by an Fe-rich solid solution. Magnets with the mentioned names have considerable variations in composition, and all have been offered as commercial products for several decades (Underhill, 1952). Adequate descriptions of their technology can be found in the book by Bozorth (1951). The more recent magnets based on Fe–Cr–Co, which can be cold worked or machined, involve no intermetallic compounds but instead consist of a mixture of Fe-rich and Cr-rich solid solutions (Kaneko *et al.*, 1971).

Good permanent magnets usually require a phase with high uniaxial magnetocrystalline anisotropy, which excludes cubic phases, yet early magnets did, in fact, employ cubic phases. This includes the magnets known as Cunife (in wt%, 60Cu, 20Ni, 20Fe) and Cunico (60Cu, 20Ni, 20Co). In both cases heat treatment causes the single-phase f.c.c. alloys to separate into low-Cu and Cu-rich f.c.c. phases, the latter being nonmagnetic. The magnetic phases $\sim \text{NiFe}$ and $\sim \text{NiCo}$ are not inherently hard but derive their anisotropy from the distortion associated with the separation of a single, high-temperature phase into two phases at lower temperatures.

With critical tempering, the coherency strains exceed any residual strain as might be derived from cold work, and have a direct effect in boosting an otherwise low anisotropy. The locations of the coercivity maxima in the composition triangles Cu–Ni–Fe and Cu–Ni–Co near a line Ni:Fe or Ni:Co = 1:1 suggest that the compounds NiFe and NiCo are involved, but the heat treatment cannot be contributing to a large degree of long-range order.

In the case of Alnico both the solid-solution precursor and the final matrix phase following heat treatment are intermetallic compounds. One of the original (Co-free) alloys was, in wt%, 12Al, 30Ni, 58Fe. This is essentially the compound AlFe_2Ni that has the L_{21} (cF16) structure (Buschow and van Engen, 1981) of the Heusler alloy AlCu_2Mn . At the solution treatment temperature $> 1200^\circ\text{C}$ it is single phase, but at low temperatures or in slowly cooled alloys a separation into two phases occurs, one of which is essentially α -Fe that bears the magnetic moment. The other phase moves in the direction toward binary NiAl (B2, cP2 type) and is only weakly magnetic or paramagnetic; it serves to separate the α -Fe particles magnetically. The precipitates of (otherwise soft) α -Fe derive their anisotropy from their rodlike shape, typically $30 \times 30 \times 300$ nm, which forces the magnetic vector into the direction of the rod axis that is also a cubic $\langle 100 \rangle$ direction. Modifications of this basic magnet are numerous and have been made by including the additional elements Co, Cu, Ti and Nb. Although they have moderate coercivities, usually $\mu_0 H_c < 200$ mT, alnicos are still used in designs that call for high remanence, 1 to 1.3 T, good temperature stability, and operating temperatures up to several hundred degrees centigrade. The high remanence is achieved by orienting the grains with the help of directional solidification.

Vicalloy is an Fe–Co–V alloy that is similar to magnetically soft Permendur. Its most useful feature is that it can be obtained as a ductile alloy before the final heat treatment for magnetic hardness. Though a definitive description of the hardening mechanism has never been given, its main features can be understood with some knowledge of the ternary system (Köster and Schmid, 1955; Raynor and Rivlin, 1988). A typical composition is, in wt%, 37Fe, 53Co, 9.4V, 0.6Si, and its heat treatment is oil quenching from 1200°C followed by aging for 8 h at 600°C . The magnetic properties achieved by this treatment are modest: $B_r = 0.9$ T, $\mu_0 H_c = 30$ mT and $|BH|_{\text{max}} = 8$ kJ m $^{-3}$. In the aged condition, the alloy has high hardness, Rockwell C 60. At 1200°C it is single-phase, non-magnetic f.c.c. γ , and held at 600°C for many months it consists of Co-rich ($\sim 20\%$ Fe) f.c.c. γ and Fe-rich

($\sim 55\%$ Fe) b.c.c. α . This condition is not realized after only a few hours at 600°C . Instead, one obtains a non-equilibrium state of partially ordered α_1 (FeCo, CsCl type) plus retained γ , which has an Fe content near that of the original alloy and is nonmagnetic. This results from the very sluggish γ to α transformation reported by Martin and Geisler (1952). Since the crystal anisotropy of ordered α_1 is known to be zero (Section 2.4) and that of disordered α is not expected to be high, the coercivity may be owing to shape anisotropy of the emerging α_1 particles or, possibly, to the anisotropy associated with coherency strains. By preceding the 600°C aging step with cold reduction (presumably to accelerate the γ to α transformation), one obtains properties that are improved over those of the simple heat treatment: $B_r = 1$ T, $\mu_0 H_c = 53$ mT and $|BH|_{\text{max}} = 28$ kJ m $^{-3}$.

3.1.2 AuCu $\text{L}1_0$ (tP4) Structure Type: FePt, CoPt, MnAl and Ag–Mn–Al (Silmanal)

That this tetragonal structure type can support high coercivities has been known since the mid-1930s in the cases of FePt (Graf and Kussmann, 1935) and CoPt (Jellinghaus, 1936) and since 1958 for MnAl (Kono, 1958). If the tP4 description of the structure (derived from the f.c.c. cF4 type) is used, ordering leads to a contraction of the c axis with axial ratios c/a of FePt 0.94, CoPt 0.97 and MnAl 0.91. In a way, MnAl is the oldest of these magnetic compounds because it is also found in Silmanal (in wt%, 86.8Ag, 8.8Mn, 4.4Al). This magnet was first described by Potter (1931), who had earlier identified Cu_2MnAl as the magnetic compound in one of the Heusler alloys (Potter, 1929). However, the magnetic phase in Silmanal was not identified correctly until 1972 (McCurrie and Hawkrige, 1972). These magnets have what were then considered extremely high intrinsic coercivities and were valued for their excellent stability against accidental demagnetization. Silmanal, because of its high silver content, has high ductility but low remanence.

The residual inductions of the Pt-based magnets are comparatively low (580 mT for FePt and 600 mT for CoPt), but the coercivities $\mu_0 H_c$ are considerable (157 and 430 mT, respectively) (Underhill, 1952). FePt, which is f.c.c. at high temperatures, orders below $\sim 1100^\circ\text{C}$ and has a Curie temperature of 480°C (Graf and Kussmann, 1935). The highest coercivities are obtained by quenching from 1200°C so that the structure is only partly ordered. It is assumed that large coherency strains contribute to the coercivity (Lipson *et al.*, 1941). CoPt orders below 825°C and has a magnetic ordering

temperature of $\sim 560^\circ\text{C}$ (Hansen and Anderko, 1958). A heat treatment for optimum properties always involves aging below the ordering temperature, e.g. 3 h at 650°C (Jellinghaus, 1936). The magnet contains a two-phase mixture: retained f.c.c. solid solution plus high-anisotropy, ordered CoPt.

The processing of τ -MnAl ($L1_0$, tP4) to a viable magnet material progressed in stages. The phase relations in Mn–Al were described by Köster and Wachtel (1960) who assumed that tetragonal MnAl is metastable and showed it forming from quenched high-temperature ϵ , hexagonal A3 (hP2) type, by isothermal annealing in a temperature window between 300 and $\sim 600^\circ\text{C}$. For example, half the microstructure of Al–56 at% Mn was MnAl after 60 h at 300°C (Köster and Wachtel, 1960). Hot forming to make a dense magnet was introduced by Koch *et al.* (1960) who also coined the name τ for the phase. The stability of τ is increased by adding carbon, which reduces the Curie temperature from (binary) 365°C to (ternary) 300°C (Yamamoto, 1972), but there are still problems with cracking of the hot-formed material. The final step to a successful magnet was achieved by hot extrusion of gas-atomized powder to obtain full density in a crack-free material (Yamaguchi *et al.*, 1989). At the preferred composition of 55.5 at% Mn there is a slight imbalance of atoms on the two atomic sites causing the magnetic order to be ferrimagnetic (Braun and Goedkoop, 1963). The room-temperature anisotropy coefficient K_1 is $\sim 10^6\text{ J m}^{-3}$ and the saturation polarization is 620 mT (Koch *et al.*, 1960); these translate to permanent magnet properties $(\mu_0)_s H_c = 460\text{ mT}$ and $B_r = 428\text{ mT}$ (Koch *et al.*, 1960).

Silmanal has a coercivity of 630 mT, higher than that of MnAl itself, but the remanence is very modest owing to the high silver content, and it amounts to only 59 mT (Underhill, 1952). The Curie point of 360°C and composition near 'Ag₅MnAl' suggest that the magnetic phase is MnAl, which was verified when it was extracted and its structure found to be the AuCu type (McCurrie and Hawkrigge, 1972). The heat treatment of Silmanal requiring, for example, 300 h at 280°C (Köster and Anantha Swamy, 1962) is compatible with the temperature window reported for τ -MnAl (Köster and Wachtel, 1960). An observation supporting the metastability of τ -MnAl is that at times beyond 300 h at 280°C the saturation magnetization of Silmanal drops again and eventually reaches zero, showing that magnetic τ -MnAl has been replaced by more stable nonmagnetic phases (Köster and Anantha Swamy, 1962).

3.1.3 Cu₂Sb C38 (tP6) Structure Type: MnAlGe

Based on its magnetic moment, which is low owing to the

low Mn content, MnAlGe cannot become a high energy product magnet. It is nevertheless interesting because its structure (tP6) is related to that of MnAl. If one AlGe layer is removed from the unit cell containing two formula units of MnAlGe, one is left with Mn₂AlGe that fits the tP4 description of the AuCu type. The room-temperature anisotropy field of MnAlGe is 3.6 T, from which the anisotropy constant is calculated as $5 \times 10^5\text{ J m}^{-3}$; the saturation polarization is 370 mT (Wernick *et al.*, 1961). The Curie temperature is known for thin films and is only 230°C (Sherwood *et al.*, 1971). Coercive fields at 150–220 mT were measured in powdered specimens (Satya Murthy *et al.*, 1969).

3.1.4 NiAs Type: MnBi (Bismanol)

MnBi has the hexagonal NiAs B8₁ structure type (hP4) and has been known since the early part of the century to be ferromagnetic (Heusler, 1904). It has high magneto-crystalline anisotropy, reported as $K_1 = 8.9 \times 10^5\text{ J m}^{-3}$ and $K_2 = 2.7 \times 10^5\text{ J m}^{-3}$ (Guillaud, 1943). The magnetization drops abruptly above 630 K where the structure transforms to a related orthorhombic type that is pseudo-hexagonal with a b axis of $a\sqrt{3}$ (Andresen *et al.*, 1972); 630 K is therefore the equivalent of a Curie point. The intrinsic coercivity $(\mu_0)_s H_c$ can rise as high as 1.2 T in a powder. Although this material has been offered as a commercial product named 'Bismanol', a sintered magnet with $B_r = 480\text{ mT}$, $\mu_0 H_c = 365\text{ mT}$ and $|BH|_{\text{max}} = 43\text{ kJ m}^{-3}$ (Underhill, 1952), it has not been successful because it corrodes too easily and has an abnormal temperature dependence of anisotropy leading to a loss of coercivity with decreasing temperature.

3.1.5 Co–Zr–B

This development is an offshoot of the research in rare-earth permanent magnets with the goal of eliminating the lanthanide component in favor of Zr. The boride Co₃ZrB₂ is the structural equivalent of hexagonal (hP6) Co₃RB₂ described in Section 3.2.1.2 (Stadelmaier and Schöbel, 1969). A more precise structure determination shows a rhombohedral displacement superstructure resulting in a nine-fold increase of the unit cell volume over hP6 Co₃RB₂ (Voroshilov *et al.*, 1970). With Zr replacing the lanthanide, this phase can have varying boron contents, but it does not break up into the discrete compounds discussed in Section 3.2.1.2. The continuous replacement of boron by the larger Co atom follows the general scheme Co_{3+x}ZrB_{2–x} but before the binary composition Co₅Zr ($x = 2$) is reached, a structural change occurs to another derivative of the Co₅Sm type

which is actually orthorhombic ($a=0.48$, $b=0.82$, $c=3.6$ nm), but the exact atomic arrangement is unknown. These lattice parameters are related to those of the hP6 Co_5Sm type (a , c)_{hex} through $a=a_{\text{hex}}$, $b=a_{\text{hex}}/\sqrt{3}$ and $c=9c_{\text{hex}}$ (Stadelmaier *et al.*, 1991). Both the binary and ternary phases crystallize from the melt and are magnetically hard with $\mu_0 H_a > 3$ T and $T_C \approx 480$ °C. A significant difference between the binary and the ternary phase is the greater stability of the latter. By annealing at 800 °C, binary Co_5Zr decomposes into Co plus cubic (cF116) $\text{Co}_{23}\text{Zr}_6$, whereas ternary $\text{Co}_{3+x}\text{ZrB}_{2-x}$ continues to exist (Stadelmaier *et al.*, 1991). Best coercivities are obtained with rapid solidification, for which values > 300 mT have been reported (Mitra Ghemawat *et al.*, 1989; Stroink *et al.*, 1990). The substitution of Si for some of the Co has increased the coercivity to 670 mT in an alloy (at%) 76Co, 18Zr, 3B, 3Si that was melt spun and annealed for 20 min at 650 °C (Gao *et al.*, 1990). Co_5Zr was already known (as ' Co_4Zr ') in 1938 (Köster and Mulfinger, 1938), and its Curie point was given as 490 °C in agreement with the above value, but no attempt was made to utilize it as a magnet.

3.2 Transition Metal–Lanthanide Magnetic Compounds

3.2.1 Structure and Alloying

There has been a veritable explosion of information on multicomponent magnetic compounds based on alloys of transition metals and rare-earth atoms, and a large number of the important ones have been reviewed by Li and Coey (1991). Several of the magnetic compounds discussed below have structure types that are elaborated by Gladyshevskii and Bodak (Chapter 17 in Volume 1).

3.2.1.1 Binary T–R That alloys of the rare-earth metals (R) with Co or Ni can form many intermetallic compounds was shown by Vogel (1947). One of the reasons for this proliferation of compounds is that they can be formed by new arrangements that are created by combining structural layers of the simpler Cu_5Ca type and the Laves type T_2R (T = transition metal), whose similarity was recognized as early as 1933 (Tarschisch, 1933). The structure and composition of the new phases can be represented by a simple homologous series formula. Fe can form similar compounds, though fewer of them. The structural relations between these compounds have been reviewed by Stadelmaier (1984) and Stadelmaier and El-Masry (1985). A cell of the hexagonal Co_5R structure type (D_{2d} , hP6) consists of

only two atomic layers, one containing 1 R and 2 Co atoms, the other containing 3 Co atoms. Its unit cell constant a results directly from the Co–Co contacts and is four times the Co radius (125 pm), i.e. very near $a=0.5$ nm. The hexagonal c parameter is 0.4 nm. The fundamental building block of the Laves phase has the same dimensions and also contains six atoms ($=\text{T}_4\text{R}_2$); it can be described as a double layer represented either by half of the (001) interplanar spacing of the hexagonal (C14, hP12) type or an equivalent {111} interplanar spacing of the cubic (C15, cF24) type. For compositions between 16.7 and 33.3 at% R, the compounds can be constructed by stacking n hexagonal double layers of the type T_5R (hP6) upon one comparable double layer taken from the Laves phases (T_4R_2). This leads to a simple series formula also mentioned by Gladyshevskii and Bodak, namely $\text{T}_{5n+4}\text{R}_{n+2}$ ($n=0, 1, 2, \dots$). For $n=0$, one gets the Laves phase and for $n \rightarrow \infty$ the T_5R phase. The most common intermediate types are shown in Table 1. The hexagonal sheets that are stacked and shifted within the basal plane to create the above formula always have a c axis height of ~ 0.4 nm, so that the ultimate hexagonal c parameter is always a multiple of 0.4 nm. Depending on the stacking sequence, the final symmetry is either hexagonal (e.g. AA' etc., in Table 1) or rhombohedral (AA'A" etc.). The entry with $n=0$ is represented by the two Laves types, hexagonal MgZn_2 (C14, hP12) and cubic MgCu_2 (C15, cF24; formally hR6 for which c/a is exactly $\sqrt{6}$). Examples of binary compounds that conform to the rhombohedral scheme are Co_2Pr (cF24 = hR6), Co_3Pr (hR12), Co_7Pr_2 (hR18) and $\text{Co}_{19}\text{Pr}_5$ (hR24) (Ray, 1974). A slightly distorted C14 type (hR6, $c/a \sqrt{6}$) is found in low-temperature Co_7Tb (Yoshimoto *et al.*, 1983).

For compositions between 16.7 and 0 at% R, structures are derived from T_5R by replacing some of the R atoms by T–T atom pairs ('dumbbell' pairs) that are coaxial with the hexagonal c axis and have a T–T spacing that is shorter than the usual distance in T_5R . When this replacement is disordered, the structure type is essentially that of T_5R , but the composition is allowed to become more T-rich. A formal description of a phase in which 22% of the R atoms in T_5R are replaced randomly by T–T pairs has become known as the hP8 structure type of Cu_7Tb (Buschow and van der Groot, 1971). The ratio T:R = 7:1 resulting from $(5+2 \times 0.22)/(1-0.22)$ is actually not unique, and others do occur, for example, in the high-temperature phase Co_{5+x}Sm with variable composition (Khan, 1974) and the phases mentioned in Section 3.2.6. The replacement of R atoms by T–T pairs always causes the c axis to expand relative to that of the stoichiometric

Table 1. Hexagonal and rhombohedral structures of $T_{5m+4}R_{n+2}$ formed by the stacking of six-atom hexagonal units of $a=0.5$ nm and $c=0.4$ nm. A represents T_3R_2 and B is T_3R . Primed and double-primed layers are shifted against their equivalent predecessor, and italicization depicts the extent of a single unit cell. AA' represents the $MgZn_2$ (C14, hP12) type and AA'A'' the cubic $MgCu_2$ (C15, cF24) type. Rhombohedral hR6 becomes cubic cF24 when c/a is exactly $\sqrt{6}$

| <i>n</i> | Composition | Stacking sequence | | | | <i>c</i> (nm) | |
|----------|-------------|-------------------|--------|-------------------------|--------|---------------|--------------|
| | | Hexagonal | Symbol | Rhombohedral | Symbol | Hexagonal | Rhombohedral |
| 0 | T_4R_2 | AA'AA'AA'... | hP12 | AA'A"AA'A"AA'A"... | hR6 | 0.8 | 1.2 |
| 1 | T_3R | ABA'B'ABA'B'... | hP24 | ABA'B'A"B'ABA'B'A"B"... | hR12 | 1.6 | 2.4 |
| 2 | T_7R_2 | ABBA'B'B'... | hP36 | ABBA'B'B'A"B'B"... | hR18 | 2.4 | 3.6 |
| 3 | $T_{19}R_5$ | ABBBB'A'B'B'... | hP48 | ABBBB'A'B'B'A"B'B"B"... | hR24 | 3.2 | 4.8 |
| . | . | . | . | . | . | . | . |
| . | . | . | . | . | . | . | . |
| . | . | . | . | . | . | . | . |
| ∞ | T_3R | BBBBB... | hP6 | — | — | 0.4 | — |

T_3R . When the T-T atom pairs replace the R atoms in an ordered fashion, the possible compounds must satisfy the formula (Stadelmaier, 1984) $T_{5m+2n}R_{m-n}$. Therein m denotes the number of unit cells of T_3R that make up the new cell and n is the number of dumbbell pairs in the new cell. The ordering between the pairs and the remaining R atoms tends to occur within layers of the thickness of T_3R (~ 0.4 nm). It follows that, because there is only one R atom in the original T_3R cell, the basal area of the derivative structure must be enlarged, usually twofold or threefold. Then the original hexagonal base in hP6 with lattice constant a becomes rectangular, $a' = a\sqrt{3}$, $b' = a$ for doubling of the area, and trigonal $a' = a\sqrt{3}$ for tripling. Of the large number of structures implied in $T_{5m+2n}R_{m-n}$, only a few have been recognized, and prominent among them are the magnetic compounds hexagonal (hP38 type) $T_{17}R_2$ ($m=6$, $n=2$), $a' \approx 0.5\sqrt{3} = 0.867$ nm, $c' \approx 2c > 0.8$ nm, and rhombohedral (hR19 type) $T_{17}R_2$ ($m=9$, $n=3$), $a' \approx 0.5\sqrt{3} = 0.867$ nm, $c' \approx 3c > 1.2$ nm. A hexagonal unit cell with eight double layers instead of the two in hP38 was described by Fidler *et al.* (1990) and would correspond to $m=24$, $n=8$. A less obvious compound in this series is rhombohedral 'Fe₁₄Dy₂C_x' (here with interstitial carbon, see Section 3.2.3) reported recently (Sanchez *et al.*, 1989). There $m=9$, $n=2$, leading to a ratio Fe:Dy = 7:1 and a structure accommodating, at random, two in place of the usual three dumbbell pairs in (the hexagonal setting of) the rhombohedral cell of $T_{17}R_2$. For this structure Pearson (1972) has suggested the symbol hR18.7 instead of hR19 to reflect the reduced Fe content (56 versus 57 atoms) of the unit cell. Thus the stoichiometry of the Fe₁₄Dy₂C_x phase is better referred to as Fe₇DyC_x because the metal content of the (hexagonal) cell, Fe₄₉Dy₇, is not a multiple of Fe₁₄Dy₂. Long before it was recognized that this unit

cell could support a ratio T:M = 7:1, several rhombohedral '17:2' types were actually reported to have R contents higher than the 10.5 at% prescribed for stoichiometric 17:2, among them not only the original hR19 prototype 'Zn₁₅₋₁₇Th₂' (Makarov and Vinogradov, 1956) but also compounds in the systems Fe-Gd (Kripyakevich *et al.*, 1963; Stadelmaier and Park, 1981) and Fe-Y (El-Masry and Stadelmaier, 1989). Another magnetically interesting compound in this series is $T_{12}R$ ($m=4$, $n=2$). It has the tetragonal tI26 structure of Mn₁₂Th (Florio *et al.*, 1952) that is derived from the orthorhombic cell $c' = a$, $a' = a\sqrt{3}$ and $b' = 2c$ by a slight shift of some atoms, which increases the twofold symmetry about the c' axis to fourfold and, coincidentally, makes $a' = b'$. Properties are discussed in Section 3.2.5.

Substitution of T atoms has been practiced in early permanent magnets and recommends itself in T-R compounds. Partial replacement of Co by Fe (and vice versa) is often used to increase the magnetic moment and/or raise the Curie point without affecting the structure. When a nontransition element replaces T, the moment and magnetic ordering temperature are expected to drop. This loss may be compensated by microstructural features that improve coercivity. From a structural viewpoint, rare-earth atoms are largely interchangeable and continuous replacement between them is usually possible. Since the magnetic properties are quite sensitive to the rare-earth atom type, they can be controlled by alloying with these species.

3.2.1.2 Alloying with metalloids One method of obtaining new compounds from T-R compounds is by alloying with B, C or N. This can lead to new ternary compounds as in Fe₁₄Nd₂B and Fe₁₄Nd₂C (Section 3.2.4), or give a continuous inclusion of interstitial

Table 2. Stacking schemes in the boride homologous series $\text{Co}_{3n+5}\text{R}_{n+1}\text{B}_{2n}$. A is Co_5R and B is Co_3RB_2 . One hexagonal unit cell is italicized

| <i>n</i> | Composition | Stacking sequence | Symbol | <i>c</i> (nm) |
|----------|--|-------------------|--------|---------------|
| 0 | Co_5R | AAAAAA. . . | hP6 | 0.40 |
| 1 | $\text{Co}_8\text{R}_2\text{B}_2 = \text{Co}_4\text{RB}$ | ABABAB. . . | hP12 | 0.68 |
| 2 | $\text{Co}_{11}\text{R}_3\text{B}_4$ | ABBABBABBB. . . | hP18 | 0.98 |
| 3 | $\text{Co}_{14}\text{R}_4\text{B}_6 = \text{Co}_7\text{R}_2\text{B}_3$ | ABBBABBABBB. . . | hP24 | 1.29 |
| . | . | . | . | . |
| . | . | . | . | . |
| . | . | . | . | . |
| ∞ | Co_3RB_2 | BBBBBB. . . | hP6 | 0.30 |

atoms in a binary compound as in $\text{Fe}_{17}\text{Sm}_2\text{N}_x$ (Section 3.2.3). These compounds will be discussed in connection with their high magnetic hardness. Boron atoms are normally considered too small to replace transition metal atoms, yet a series of derivatives of Co_5Sm is formed in just that way (Kuz'ma and Bilonizhko, 1974). The replacement of Co is not continuous but discrete, and the highest boron content is found in Co_3SmB_2 (hP6), where all of the Co atoms in Co_5Sm that are coplanar to Sm have been replaced, with the result that each Sm atom is now surrounded by three boron atoms that lie in the hexagonal basal plane. Additional compounds are obtained by stacking *n* units of Co_3SmB_2 on one unit of Co_5Sm in the manner illustrated by the homologous series formula $\text{T}_{3n+5}\text{R}_{n+1}\text{B}_{2n}$ (*n* = 0, 1, 2, . . .) and shown in Table 2 (El-Masry *et al.*, 1983). The atomic arrangement of these compounds has been described by Gladyshevskii and Bodak (Chapter 17 in Volume 1). The lattice constant *a* of the new hexagonal unit cell is governed by the Co atom size and is therefore that of the parent Co_5R cell, but the *c* dimension is contracted because of the smaller diameter of the boron atom. The final value of *c* shown in the last column of Table 2 is that of Co_5R (0.4 nm) plus *n* times that of Co_3RB_2 (0.3 nm). The substitution of B for Co in Co_5R dilutes the magnetic moment and lowers the Curie point, as seen in the ferromagnetic series Co_5Sm to Co_3SmB_2 , where *T_c* drops from 1021 to 40 K, or in ferrimagnetic Co_5Gd to Co_3GdB_2 with *T_c* ranging from 1083 (or 1014) to 58 K (El-Masry *et al.*, 1983; Smit *et al.*, 1988). When the metalloid atoms are interstitial, they expand the lattice and tend to increase the moment and magnetic ordering temperature (see Section 3.2.3). The loss of moment and Curie temperature in the borides derived from Co_5Sm is unfortunate for applications because the magnetocrystalline anisotropy actually increases with increasing boron content, as evidenced by the increasing coercivity of the as-cast alloys (El-Masry *et al.*, 1983). The anisotropy increase is linked with the progressive

contraction of the subcell axis *c*/(1 + *n*) along the series. For Co_3SmB_2 an extreme coercivity of 5 T at 4.2 K has been reported (Oesterreicher *et al.*, 1977). Similar compounds do not form with Fe and the light rare-earth elements that couple ferromagnetically with Fe; however, partial replacement of Co by Fe is feasible. Therefore some of the magnetization and Curie temperature lost by adding boron can be regained by replacing half the Co in Co_4SmB with Fe (El-Masry and Stadelmaier, 1983). Fe substitution in binary Co_5Sm is very small but can be driven to full Co replacement in the A layers of Table 2 (El-Masry and Stadelmaier, 1983). The possibility of thus reducing the Co content in magnets derived from Co_5Sm has not been exploited commercially, though more recently a sintered magnet has been synthesized that is based on $\text{Co}_7\text{R}_2\text{B}_3$, namely $\text{Fe}_5\text{Co}_2\text{Pr}_2\text{B}_3$ (Huang *et al.*, 1991). Its $|BH|_{\text{max}} = 82 \text{ kJ m}^{-3}$ is less than half that of the best Co_5Sm magnets (see Section 3.2.2).

3.2.2 Magnets Based on Co_5Sm and $\text{Co}_{17}\text{Sm}_2$

The magnets utilizing the high crystal anisotropy of cobalt-lanthanide compounds have been reviewed repeatedly (Becker, 1970; Strnat, 1978; Strnat, 1988; Strnat and Strnat, 1991). Of the compounds discussed in Section 3.2.1, those of the type Co_5R (hP6) were the first to be applied as permanent magnets. Among them Co_5Sm stands out as the most consistently used representative which is preferred for its relative ease of fabrication. Its high anisotropy field, which exceeds 20 T, originates in an equally high *K₁* of at least $7.7 \times 10^6 \text{ J m}^{-3}$ and has been reported to be as high as 44 T (Strnat, 1978). Permanent magnet properties are *B_r* = 1.14 T, *T_c* = 1000 K and $|BH|_{\text{max}}$ up to 260 kJ m^{-3} (Strnat, 1978). The coercivities of Co_5Sm , which easily exceed 1 T in a sintered magnet, have negligible values in the as-cast material, emphasizing the importance of processing. Very high coercivities can be achieved in

Table 3. Microstructural features and properties contributed by the component elements in magnets based on rhombohedral $\text{Co}_{17}\text{Sm}_2$. The magnets are multiphase, and the compositional parameters x , y and z are written to describe the deviation from the stoichiometric composition. Phases are designated by ratios of transition metal to Sm, and Zr is assumed to be the equivalent of Sm

| Elements | Composition | Effect |
|------------|--|--|
| Co, Sm | $\text{Co}_{17}\text{Sm}_2$ | The 17:2 phase has the magnetic moment, anisotropy and high T_C |
| Excess Sm | $\text{Co}_{17}\text{Sm}_{2+z}$ | Causes Co_5Sm to precipitate as cell wall |
| Cu | $\text{Co}_{17-x}\text{Cu}_x\text{Sm}_{2+z}$ | The 5:1 cell wall is enriched in Cu, the Co content is reduced, lowering B_r , but H_c is improved by spinodal decomposition of 5:1 and precipitation of 17:2, both in the cell wall |
| Fe | $\text{Co}_{17-y}\text{Fe}_y\text{Sm}_{2+z}$ | Replaces Co in the 17:2 matrix, increases B_r , reduces H_c by introducing dendrites of free (Co, Fe). Stabilizes 17:2 and 3:1, but not 5:1 |
| Cu, Fe | $\text{Co}_{17-x-y}\text{Cu}_x\text{Fe}_y\text{Sm}_{2+z}$ | The features of Cu and Fe are combined |
| Cu, Fe, Zr | $\text{Co}_{17-x-y}\text{Cu}_x\text{Fe}_y(\text{Sm}, \text{Zr})_{2+z}$ | Effect of Zr is complex; it contributes moderately to the anisotropy of 17:2. Zr promotes phases 19:5, 7:2 and 3:1. It causes formation of platelets inside 17:2, adding to H_c , and prevents formation of free Co (and loss of H_c) caused by excess Cu or Fe |

cast alloys by replacing some of the Co by Cu (Nesbitt *et al.*, 1968) to form solid solutions of Co_5Sm and Cu_5Sm . The enhancement of the coercivity results from a separation into Cu-rich and Co-rich regions of the 5:1 phase at low temperatures, e.g. 4 h at 400 °C (Nesbitt, 1965), and properties reported for $\text{Co}_{3.5}\text{Cu}_{1.5}\text{Sm}$ are ($\mu_0 H_c = 2\text{ T}$ and $J_s = 600\text{ mT}$ (Nesbitt *et al.*, 1968). The subject of cast magnets based on Co–Cu–Sm and also Co–Cu–Ce has been reviewed extensively by Nesbitt and Wernick (1973). The magnetization loss owing to the alloying with Cu is considerable, and a further disadvantage relative to sintered magnets results from the essentially random orientation of the grains that keeps the magnetization at half its potential value. A small increase in moment can be gained by alloying with Fe, but its ability to replace Co is limited, as mentioned in Section 3.2.1. A method of directional solidification to achieve remanence and energy products comparable to those of sintered magnets has not been devised, so that castable magnets based on Co_5Sm have not become a reality.

Replacing Sm by Y or Ce is feasible from a standpoint of anisotropy for which the room-temperature values are Co_5Y , $K_1 = 5.5 \times 10^6\text{ J m}^{-3}$ and Co_5Ce , $K_1 = 6.4 \times 10^6\text{ J m}^{-3}$ (Strnat and Strnat, 1991). Though yttrium magnets are among the first reported, they are not being used. Cerium is found in magnets based on (Co, Fe, Cu)₅Ce or (Co, Fe, Cu)₅(Ce, Sm) and, finally, in the form of Co_3MM (Strnat and Strnat, 1991), where MM is cerium ‘mischmetal’, a mixture of about half Ce plus unspecified fractions of La, Pr, Nd and Sm. The Co_3MM magnets are less expensive than Co_5Sm but have a lower Curie temperature (typically 500 °C) and remanence ($\sim 900\text{ mT}$). Another variant of Co_5Sm is

$\text{Co}_5(\text{Pr}, \text{Sm})$. In it a higher remanence and energy product are obtained at the expense of coercivity when a large fraction of Sm is replaced by Pr (Strnat and Strnat, 1991). Recovery of coercivity to levels found in Co_5Sm magnets has been reported by Ghandehari and Fidler (1985) who doped $\text{Co}_5\text{Pr}_{0.8}\text{Sm}_{0.2}$ with the oxide Cr_2O_3 to inhibit the formation of the Co_7R_2 and Co_{19}R_5 phases, which are considered to be magnetically soft and reduce the coercivity.

The compositions of Cu-containing magnets have tended to shift toward lower Sm contents, as in magnets designated (Co, Fe, Cu)₅₋₇Sm (Strnat and Strnat, 1991). This introduces the additional phase rhombohedral (hR19) $\text{Co}_{17}\text{Sm}_2$ which, because it is isostructural with $\text{Fe}_{17}\text{Sm}_2$, permits unlimited replacement of Co by Fe. $\text{Co}_{17}\text{Sm}_2$ with its high Co content has a higher Curie point (920 °C; Strnat and Strnat, 1991) and moment than Co_5Sm and promises to produce a magnet with a higher energy product. Its anisotropy, $\mu_0 H_a = 6.5\text{ T}$ (Strnat and Strnat, 1991), is considerably lower than that of Co_5Sm ; so successful magnet fabrication has to overcome that deficiency. The magnet types that have evolved rely on several element substitutions to bring about the desired coercivity without sacrificing Curie temperature and remanence. They are generally referred to as precipitation hardened (Menth, 1976) owing to the effect of Cu, and their overall composition is sometimes described as (Co, Fe, Cu, Zr)_xSm with x variously given as $7.2 < x < 8.5$ or $6.8 < x < 8$. For the latter, a commercial composition range, in wt%, would be 48–52 Co, 12–18 Fe, 4–12 Cu, 2–3 Zr, 24–27 Sm. Sintering and annealing above 1100 °C lead to a dense alloy, but the coercivity is developed only after a complex heat-treating schedule below 900 °C in which

a cellular, or honeycomb, microstructure is formed. The cell walls consist of Co_5Sm that results from the excess Sm in the composition. They pin the advancing domain walls because they contain most of the Cu as Cu_5Sm precipitates, as mentioned above for cast Co_5Sm magnets. The complexity of the interaction of the several components is hinted at in Table 3 (Stadelmaier *et al.*, 1988). Typical properties of a $\text{Co}_{17}\text{Sm}_2$ -based magnet are $B_r = 1.0$ T, $(\mu_0)H_c = 1.88$ T and $|BH|_{\max} = 200$ kJ m⁻³. They have temperature coefficients of the magnetic properties that are superior to those of plain Co_5Sm magnets and, of course, they use less Sm.

3.2.3 $\text{Fe}_{17}\text{Sm}_2\text{C}_x$ and $\text{Fe}_{17}\text{Sm}_2\text{N}_x$

The compounds based on the inclusion of carbon or nitrogen in $\text{Fe}_{17}\text{Sm}_2$ differ in two respects from the boride derivatives of Co_5Sm described in Section 3.2.1.2: (i) the metalloid atoms do not replace metal atoms but are interstitial; and (ii) the uptake of metalloid atoms is continuous up to the solubility limit and does not lead to new stoichiometries. An extended account of the status of these materials as of 1991 was given by Li and Coey (1991). Carbon was first shown to dissolve in a structure derived from Fe_{17}R_2 in Fe–Gd–C (Stadelmaier and Park, 1981). The location of the interstitial carbon atom was described by Block and Jeitschko (1986) for rhombohedral $\text{Mn}_{17}\text{Pr}_2\text{C}_{1.77}$ and other compounds $\text{Mn}_{17}\text{R}_2\text{C}_x$. For $\text{Mn}_{17}\text{R}_2\text{C}_x$ it was shown that the carbon expands the lattice continuously, and that the Curie point increases significantly with increasing carbon content (Sheng *et al.*, 1987). The position of the interstitial carbon atom in rhombohedral $\text{Fe}_{17}\text{Nd}_2\text{C}_{0.4}$ was verified with the help of neutron diffraction (Helmholdt and Buschow, 1989). The carbon site is surrounded by six Fe and two R neighbors, and the maximum value of x in this arrangement is 3 (Pearson symbol hR22). For the composition $\text{Fe}_{17}\text{Sm}_2\text{C}_{0.9}$ a room-temperature anisotropy field $H_a = 7$ T and a maximum Curie point of 251 °C have been reported (Grössinger *et al.*, 1991). A coercivity approaching 2 T was obtained by mechanical alloying (Schultz *et al.*, 1991). The carbon was first introduced into the molten alloys through Fe_3C , but $\text{Fe}_{17}\text{Sm}_2\text{C}_x$ can also be formed by carburizing in methane, acetylene, or butane at 550 °C. In this way a higher carbon index $x \approx 2$ is attained, and the Curie point is raised to 400 °C (Coey *et al.*, 1991b). Nitrogen is a more effective interstitial atom. It can be introduced through gaseous NH_3 or N_2 (Coey and Sun, 1990). Sm is the only lanthanide for which the nitride shows easy axis anisotropy. The room-temperature anisotropy field is 22 T (Katter *et al.*,

1992), larger than that of any other Fe–lanthanide compound. The Curie temperature is 476 °C for $\text{Fe}_{17}\text{Sm}_2\text{N}_{2.3}$ (Sun *et al.*, 1990), up from 116 °C for binary $\text{Fe}_{17}\text{Sm}_2$. With mechanical alloying, followed by heat treatment at 650–800 °C and nitriding at 400–550 °C, a coercivity of 3.0 T was achieved when the alloy was off-stoichiometric with 13.5 instead of 10.5 at% Sm (Schnitzke *et al.*, 1990). The present drawback of this material is its tendency to decompose into Fe + SmN above 650 °C so that it cannot be sintered to form a dense magnet. Consolidation has been attempted by cold pressing and by bonding the particles with a polymer or soft-metal matrix.

3.2.4 $\text{Fe}_{14}\text{Nd}_2\text{B}$ Type with Boron and Carbon

The hope of eliminating Co from the very high energy product rare-earth permanent magnets was realized with the development of magnets based on the new tetragonal (tP68) compound $\text{Fe}_{14}\text{Nd}_2\text{B}$ that is stoichiometric. Sagawa *et al.* (1984a) made magnets by powder metallurgical processing of nonstoichiometric alloys containing excess Nd and B and achieved an energy product of 278 kJ m⁻³, soon to be followed by 400 kJ m⁻³ (Sagawa *et al.*, 1986). Simultaneously, a method for fabricating these magnets by rapid solidification (melt spinning) was disclosed by Croat *et al.* (1984), which was followed by a process to consolidate and orient the melt-spun flakes by hot forming, resulting in $|BH|_{\max} = 318$ kJ m⁻³ (Lee, 1985). In addition, further reports of the properties of comparable melt-spun alloys were given by Koon and Das (1984), Becker (1984), and Sellmyer *et al.* (1984), the latter two also including Pr as the lanthanide component. The literature on this subject is still growing, and several reviews give a comprehensive picture of developments up to 1991 (Sagawa *et al.*, 1987; Herbst and Croat, 1991; Herbst, 1991a, b). The high energy product has its basis in the high saturation polarization (1.6 T) and anisotropy ($\mu_0 H_a = 7$ T) of $\text{Fe}_{14}\text{Nd}_2\text{B}$ (Herbst, 1991a). The compound freezes incongruently, and the additional phases that form during cooling detract from or contribute to coercivity, depending upon the alloy composition. General information on the phase equilibria between Fe and boron and the lanthanides can be found in a review by Rogl (1984). The structure of $\text{Fe}_{14}\text{Nd}_2\text{B}$ (tP68, $P4_2/\text{mmn}$, $a = 0.880$ nm, $c = 1.220$ nm) has been determined independently by several laboratories (Herbst, 1991a). It appears complex but contains familiar structural elements, so that the underlying skeleton of Fe atoms is found in the tetragonal σ phase (CrFe, tP30) (Herbst, 1991a). The coordination around the

boron atom is that of Co_3RB_2 discussed in Section 3.2.1, namely three coplanar Nd atoms and a trigonal prism of six Fe atoms. There is also a very close resemblance to the cubic $\text{Mn}_{23}\text{Th}_6$ type (cF116), which is found in alloys of Fe with the heavier lanthanides. This has been demonstrated by Marusin *et al.* (1985), who determined the crystal structure of the carbide $\text{Fe}_{14}\text{La}_2\text{C}$. Not surprisingly, the borides and carbides with this structure are completely miscible (Liu *et al.*, 1987). The compound forms with most lanthanides, but the combination of high anisotropy, high magnetic moment and acceptable Curie temperature required for a permanent magnet is limited to those containing Pr and Nd (Sagawa *et al.*, 1984b). Even there, the Curie temperatures are marginal, 312 °C for $\text{Fe}_{14}\text{Nd}_2\text{B}$ and 292 °C for $\text{Fe}_{14}\text{Pr}_2\text{B}$ (Sellmyer *et al.*, 1984), but can be increased by adding Co, as suggested by Sagawa *et al.* (1984a).

The carbides have magnetic properties that are comparable to those of the borides. Unlike $\text{Fe}_{14}\text{Nd}_2\text{B}$ they do not crystallize from the melt but are transformed from the phase $\text{Fe}_{17}\text{R}_2\text{C}_x$ described in Section 3.2.3. In the case of $\text{Fe}_{14}\text{Nd}_2\text{C}$, the transformation is extremely slow, and the compound only forms in a narrow temperature window (Gueramian *et al.*, 1987; Buschow *et al.*, 1988). The transformation can be accelerated by adding a small amount of boron, which increases the nucleation rate of $\text{Fe}_{14}\text{Nd}_2\text{C}$, or copper, which increases dramatically the interfacial mobility of the growing grains (Jang and Stadelmaier, 1990a). While the crystal anisotropy of the carbides is comparable to that of the borides, the Curie temperatures are lower, 240 °C for $\text{Fe}_{14}\text{Pr}_2\text{C}$ and 262 °C for $\text{Fe}_{14}\text{Nd}_2\text{C}$ (Sellmyer *et al.*, 1984). The small grain size of the boron-doped compound can be utilized to obtain high coercivities without powder metallurgical processing (Stadelmaier and Liu, 1989), though the lack of grain orientation leaves the remanence at lower levels than desirable.

3.2.5 Mn_{12}Th (tI26) Structure Type

An extensive review of these magnetic compounds is given by Li and Coey (1991). Other useful data compilations on the phases are by Buschow (1991) and Schultz and Katter (1991). Early reports of magnetic properties of the structure type (tI26) date from 1987 (Buschow, 1987; Ohashi *et al.*, 1987), beginning a lively research activity with the goal of exploring another family of Fe-based permanent magnets that might compete with $\text{Fe}_{14}\text{Nd}_2\text{B}$. The magnetically interesting compounds have high Fe contents, as high as 85 at% for $(\text{Fe}, \text{Ti})_{12}\text{Sm}$, in contrast to the earlier compounds

such as $\text{T}_4\text{Al}_8\text{R}$ (also discussed in Li and Coey, 1991) in which the structure was stabilized by high Al contents. The large magnetic hardness of RF-sputtered (RF = radio frequency) alloys of Fe–Ti–Sm near a ratio $(\text{Fe}, \text{Ti}): \text{R} = 12:1$ was reported by Cadieu *et al.* (1984) before the systematic studies were under way. The room-temperature saturation polarization of 1.14 T (Coey, 1989) is lower than that of $\text{Fe}_{14}\text{Nd}_2\text{B}$ (1.6 T) but the anisotropy field of 10.5 T is quite adequate for a permanent magnet. Elements that stabilize the Mn_{12}Th structure type with Fe include Ti, V, Cr, Mo, W, Re and Si, but it is mainly Ti and V that have been considered for permanent magnet applications. It had long been believed that binary Fe_{12}R does not form, but Fe_{12}Sm has in fact been obtained by RF sputtering (Hegde *et al.*, 1991). Fe_{12}Sm has a saturation polarization of 1.45 T and a respectable anisotropy field of 13 T at room temperature (Hegde *et al.*, 1991). As in the case of Fe_{17}R_5 (Section 3.2.7), Sm is the rare-earth atom providing the highest anisotropy in these compounds. Difficulties in making sintered magnets of $\text{Fe}_{11}\text{TiSm}$ stem from the presence of neighboring magnetically soft phases that spoil the coercivity mechanism. A sintered alloy with (at%) 83Fe, 9Ti, 8Sm has a saturation polarization of 1.01 T and achieves a coercivity of only 80 mT, whereas a melt-spun ribbon that is heat treated at 800–850 °C can attain 560 mT (Wang *et al.*, 1990). The Curie temperature of $\text{Fe}_{11}\text{TiSm}$ is 311 °C (Li and Coey, 1991). Adding vanadium improves the coercivity: an alloy (at%) 76Fe, 8Ti, 8V, 8Sm shows a $\mu_0 H_c$ of 200 mT by sintering and 1.02 T in melt-spun ribbons (Wang *et al.*, 1990). The vanadium alloy (at%) 70Fe, 15V, 15Sm has produced a comparable coercivity of 1.17 T when prepared by mechanical alloying followed by heat treatment between 600 and 900 °C (Schultz *et al.*, 1990a).

The compounds $\text{T}_{12-x}\text{M}_x\text{R}$ absorb considerable quantities of nitrogen when they are exposed to N_2 gas at temperatures around 500 °C. It is assumed that one N atom per formula unit can enter as an interstitial (Liao *et al.*, 1991), leading to a volume expansion of 1 to 3%. This corresponds to a structure with full occupancy of the interstitial sites as determined by neutron diffraction (Yang *et al.*, 1991), described by Pearson symbol tP28. The nitrogen uptake has two significant effects: (i) it increases the Curie temperature of Fe_{11}TiR (Coey *et al.*, 1991a), by 140 K in the case of $\text{R} = \text{Sm}$ (Yang *et al.*, 1991); and (ii) it modifies the anisotropy. In Fe–Ti–Sm and Fe–V–Sm it is changed from uniaxial to undesirable, easy plane anisotropy (Yang *et al.*, 1991; Wang and Hadjipanayis, 1991). On the other hand, $\text{Fe}_{11}\text{TiNd}$, which has a very low uniaxial anisotropy

$\mu_0 H_a$ equal to 1 T (Jang and Stadelmaier, 1990b) or 2.4 T (Wang and Hadjipanayis, 1991) (making it useless as a permanent magnet material), can be improved dramatically by adding nitrogen. Then $\mu_0 H_a$ of $\text{Fe}_{11}\text{TiNdN}_x$ becomes 9.5 T and its Curie temperature is 723 K, up from 551 K in the nitrogen-free compound (Wang and Hadjipanayis, 1991). The problems attending the fabrication of a fully dense magnet with this nitrided material are similar to those discussed in Section 3.2.3.

3.2.6 Fe_7R Type

The hP8 structure type of Cu_7Tb readily permits a variable composition, as explained in Section 3.2.1. In Fe–Nd it is formed by rapid solidification (Stadelmaier *et al.*, 1986), and it can also be stabilized by adding Ti or V to Fe–Sm (Jang and Stadelmaier, 1990b). Cadieu *et al.* (1991) have shown that this structure also forms in sputtered films of Fe–Sm with added Zr. Because of the high Sm content of 20 at% in the specimen, it must be assumed that the composition is closer to Fe_5Sm than to Fe_7Sm . The coercivity at 293 K for a sputtered film of composition (at%) 72.0Fe, 8.1Zr, 19.9Sm is 670 mT, but the polarization is low, measuring only 620 mT in a field of 1.8 T (Cadieu *et al.*, 1991). The same structure has been observed in binary Fe–Sm by Katter *et al.* (1991) and has a higher Fe content with an assumed composition Fe_5Sm . It was obtained by melt spinning at high wheel velocities, and has a Curie temperature of 210 °C and a saturation polarization of 1.25 T (Katter *et al.*, 1991), twice that of sputtered Fe–Sm–Zr.

3.2.7 Fe_{17}R_5 Type ($\text{Fe}_{17}\text{Sm}_5$, Fe–Ti–Sm)

The first phase of this type to be structurally characterized, magnetically soft $\text{Fe}_{17}\text{Nd}_5$ (hP264), was long overlooked because it exists only at low temperatures and decomposes above 1050 K (Landgraf *et al.*, 1990). It has a large hexagonal unit cell containing 12 formula units, or 264 atoms, with $a = 2.0214$ nm and $c = 1.2329$ nm (Moreau *et al.*, 1990). It was quickly recognized that the magnetically hard phase found at the composition (at%) 70Fe, 10Ti, 20Sm also had this structure (Stadelmaier *et al.*, 1991). The compound was observed to produce a very high coercivity of 3.85 T in an RF sputter-deposited and annealed film of the composition (at%) 73Fe, 8Ti, 19Sm (Kamprath *et al.*, 1988). Preparation methods leading to even higher room-temperature coercivities are (i) mechanical alloying followed by a short anneal above 500 °C, yielding an extraordinary 6.4 T (Schultz *et al.*, 1990b); and (ii) rapid

solidification to form melt-spun ribbons, giving 5.8 T (Katter *et al.*, 1990b). In a sputtered vanadium alloy (at%) 73.5Fe, 6.9V, 19.6Sm the intrinsic coercivity was 1.58 T at 293 K and 3.1 T at 6 K, and the high-field (9 T) polarization at 293 K was 620 mT (Cadieu *et al.*, 1991). Combining Ti and V in an unspecified ratio produced a coercivity of 4.6 T at 293 K in a sputtered film identified with this hP264 structure (Cadieu *et al.*, 1991). Finally, though such a phase was not previously recorded in the binary system Fe–Sm (Massalski, 1992), it was recognized that Ti or V did not need to be added to stabilize the Fe_{17}R_5 type with R = Sm. In a sputtered film of $\text{Fe}_{17}\text{Sm}_5$ a coercivity of 1.47 T has been obtained at 293 K, rising to 3.11 T at 15 K (Rani *et al.*, 1992). Unlike the Sm compound, $\text{Fe}_{17}\text{Nd}_5$ has easy plane anisotropy (Landgraf *et al.*, 1991). This switch in spin orientation is owing to a sign change in the so-called second-order Stevens factor that controls the anisotropy. It is the same preference for Sm over the other lanthanides in achieving high uniaxial anisotropy that is observed in the nitride $\text{Fe}_{17}\text{Sm}_2\text{N}_x$ (Section 3.2.3). The anisotropy field of the Fe–Ti–Sm phase is very large at 25 T, whereas the magnetic polarization is so low that a remanence of only 300 mT is reported for the alloy (at%) 70Fe, 10Ti, 20Sm (Katter *et al.*, 1990a). As a consequence, one obtains energy products of only 18 kJ m^{-3} in spite of the outstanding coercivities, which rank among the highest ever observed.

3.2.8 Fe_3Sm

The rhombohedral structure of Fe_3Sm (hR12, $a = 0.5187$ nm, $c = 2.4910$ nm) (Buschow, 1971) has already been described in Table 1, Section 3.2.1, and it is sometimes referred to by one of its prototypes Be_3Nb or Ni_3Pu . Fe_3Sm has a high uniaxial anisotropy that can be utilized to create high coercivities in alloys near the stoichiometric composition by melt spinning or by mechanical alloying (Wecker *et al.*, 1990). The highest reported coercivity of 1.48 T was obtained in a resin-bonded magnet prepared from a mechanically alloyed powder (Schultz *et al.*, 1990b). In it some Sm was replaced by Zr. The remanence in such a magnet is comparatively low because it lacks crystallite orientation, and the best value (0.5 T) is obtained at a sacrifice in coercivity (now below 1 T) at a composition reported as $\text{Fe}_{3-\delta}\text{Sm}_{0.57}\text{Zr}_{0.43}$ (Wecker *et al.*, 1990). The energy product of 50 kJ m^{-3} for this magnet does not match that achievable with other compounds; its obvious advantage is that it is Co free. Isostructural Co_3Sm has not been suggested as a permanent magnet material

because its magnetic moment and potential energy product cannot reach the values of the very successful magnets based on Co_5Sm .

3.2.9 Laves Phases; Fe_2Tb

Because the Curie temperature of Fe-R compounds increases with increasing R content (unlike Co-R compounds, where it decreases), the magnetic properties of the Laves phases have been of interest. By annealing rapidly sputtered amorphous Fe_2Tb above 300 °C, a microcrystalline state was created that produced room-temperature coercivities as high as 340 mT (Clark, 1973). The assumption that the magnetically hard phase Fe_2Tb is truly cubic cannot be supported because a rhombohedral distortion (elongation along cubic (111)) has been observed (Dwight and Kimball, 1974). In view of the superior permanent magnet properties attainable in Fe-R compounds with higher Fe contents, the Laves phases are noteworthy chiefly for their giant room-temperature magnetostriction (Clark and Belson, 1972; Greenough and Schulze, Chapter 17 in this volume) and for the early indication that Fe-R alloys could become permanent magnet materials.

4. Applications

In the practical application of magnets we pay less attention to the source of magnetism than to their ability to meet our technological needs. Ferromagnets and ferrimagnets, metals as well as magnetic oxides serve as both magnetically soft and hard materials, and in applying a metallic alloy the user is most likely to be unaware of the presence or absence of an intermetallic compound. The ability of the material to be fashioned into its final form is an obvious concern, and the fact that some magnetic materials are hard and brittle and cannot be shaped by plastic deformation limits their end use. In that case casting and grinding or sintering to near net shape may be the method of choice. In fact, most rare-earth permanent magnets are made by sintering because they are brittle intermetallics, and because that method has the additional advantage of permitting magnetic alignment of the powder before sintering, which increases the remanence and energy product. Castings that develop a preferred orientation by directional solidification, as exploited in Alnico, cannot be realized in rare-earth magnets. Another method of forming magnets from powders is found in both soft magnets and permanent magnets and consists in mixing the powder with a polymeric binder and pressing or

injection molding the mix to yield a bonded magnet. This method is used with powdered iron in soft magnet cores of moderate permeability, and also in permanent magnets that require intricate configurations. In the former, the binder provides the electrical insulation that keeps the eddy currents low. In permanent magnets the dilution of the magnetic polarization resulting from the presence of the binder is undesirable because it reduces the remanence and energy product. A rare case of a fully machinable permanent magnet of fairly high coercivity ($\mu_0 H_c = 460$ mT) is found in the compound MnAl, described in Section 3.1.2. Magnets of the Vicalloy type (Section 3.1.1) can be shaped by rolling or drawing, but their coercivities are modest, remaining below 50 mT. The magnetically soft Fe-Ni alloys (Section 2) are readily shaped by cold work. Vanadium-containing Permendur (Section 2.2) is likewise ductile, and has found application in earphone membranes.

Magnetic cores are used in wire-wound devices to increase the inductance, which is proportional to the effective permeability μ_e . The largest tonnage of soft materials is used as cores of transformers, motors, inductors and generators. There electrical steels dominate and they are not compounds but mostly solid solutions of Si in Fe. Whereas a pure inductance is loss free, the magnetic core has hysteresis and eddy current losses, as noted in Section 1.1.2. Though the core losses at frequencies of 50 or 60 Hz may appear to be insignificant, the overall effect in power generation and distribution is high. One of the main uses of magnetically soft materials is in motors, which use over 60% of the electricity in the United States, and the current annual cost of the core losses alone is estimated to exceed $\text{US\$}7.5 \times 10^9$ (Werner and Jaffee, 1992). The economic value of electrical steels is now surpassed by information-storing materials, magnetic tapes and disks, which are mostly oxide based. An equally important application of magnetic materials is in telephone, radio and television communications. Because of the high frequencies involved, high resistivities are required to reduce the eddy current losses which rise with the square of the frequency. This requirement is best met in the large family of magnetic oxides known as ferrites which show values of electrical resistivity that lie in the insulating or semiconducting range. For lower frequencies, such as 50 or 60 Hz, and in the audio-frequency range, the higher-conductivity electrical steels dominate, and they are preferably grain oriented to optimize the permeability. In them eddy current losses are reduced by lamination or by winding toroidal cores from tape and, in either case, the layers are separated by insulating material. A broad overview of the metallurgy of soft magnetic

Table 4. Typical permanent magnet applications

| Action | Manner of application | Device |
|--|---|---|
| Mechanical forces | Attraction between permanent magnet and other magnet or soft magnet | Holding devices (magnetic chucks), door latches, magnetic couplings, switches, thermostats, magnetic separators (for ore concentration) |
| | Magnet to magnet repulsion | Magnetic bearings |
| | Induced repulsion | Steel sheet separation |
| | Alignment with respect to field | Compass, stepping motors |
| Lorentz force (electrical to mechanical energy conversion) | Moving coil | DC motors, loudspeakers, meter movements, disk drive head positioners |
| | Moving permanent magnet | Brushless motors, stepping motors |
| | Moving soft magnet | Telephone receivers, polarized relays |
| Mechanical to electrical energy conversion | Relative motion of coil and magnet | Dynamos, alternators, magnetos, microphones, phonograph pickups |
| Lorentz forces on moving charge carriers | Beam focusing | Some cathode ray tubes, klystrons, traveling wave tubes |
| | Crossed field | Magnetohydrodynamics generator, ion pump, mass spectrometer, vacuum gauge |

materials has been given by Chen (1977), and a more recent introduction to the applications of soft ferro-magnets can be found in the book by Jiles (1991).

A permanent magnet provides a constant magnetic field when it is stationary, and a variable field when it moves or when the element sensing the field moves relative to it. The obvious advantage of the permanent magnet over an electromagnet providing the same static field is that the permanent magnet does not carry the extra burden of ohmic ('copper') losses because the field is sustained without windings. The permanent magnets described in Section 3 are either intermetallic compounds or generally connected with them. On the other hand, a considerable share of the permanent magnet market is taken by the inexpensive hexaferrites based on $\text{SrO} \cdot 6\text{Fe}_2\text{O}_3$. They have values of remanence B_r and intrinsic coercivity $(\mu_0)H_c$ that are both near 400 mT, and therefore they do not compete with the rare-earth permanent magnets. When the ferrite permanent magnets replace Alnico, as in loudspeakers, a significant redesign of the magnetic circuit is required to accommodate the modified magnetic properties (lower B_r , higher H_c), leading to a smaller length to cross section ratio in the ferrites. This and the general subject of the volume and mass efficiencies of the various permanent magnet types have been discussed by Stäblein (1982). The applications of permanent magnets are numerous, as shown in Table 4. Motors using permanent magnets

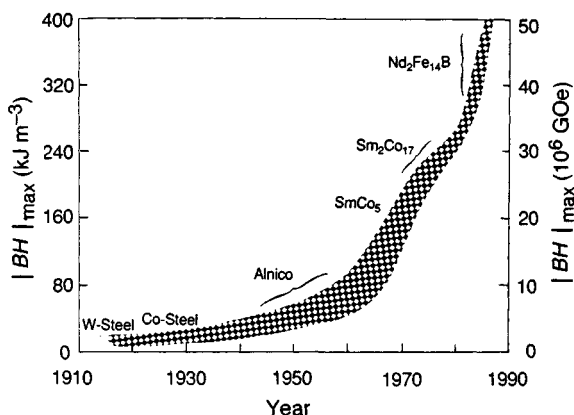


Figure 2. Progress in the development of the energy product (figure of merit) of permanent magnets. The present limit is about 400 kJ m^{-3} ($50 \times 10^6 \text{ GOe}$)

to replace electromagnets in the stator or rotor are becoming increasingly popular because they not only reduce the copper losses but also bring a marked reduction in size. A recent high-volume application of the Fe–Nd–B permanent magnets, which are described in Section 3.2.4, is found in the actuators for the read/write heads of computer disk drives. The push for higher performance in permanent magnets has led to a steep rise in energy products in recent decades, as illustrated

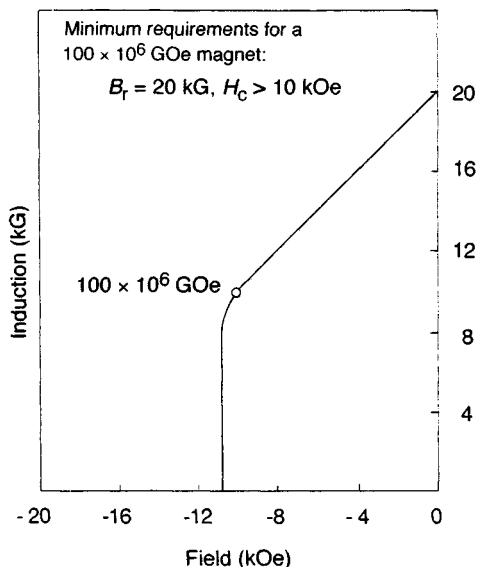


Figure 3. Second quadrant of the hysteresis loop (de-magnetization curve) of a hypothetical permanent magnet with an energy product of 800 kJ m^{-3} ($100 \times 10^6 \text{ GOe}$). To convert B kG to T and H kOe to $\mu_0 H$ T, multiply by 10^{-1}

in Figure 2. The goal of 800 kJ m^{-3} ($100 \times 10^6 \text{ GOe}$) has eluded us to date, and Figure 3 shows the de-magnetization curve that would be needed to attain it. Actually, the required remanence of 2 T (20 kG) is not unrealistic, as seen in the intermetallic compound Fe_3Pt (L1_2 type, cP4), which has a saturation polarization of 2.4 T (Krén and Szabó, 1965). Unlike the related compound FePt (Section 3.1.2), however, it does not have the high magnetocrystalline anisotropy that is imperative if the coercivity is to approach 1 T.

Two special applications of the magnetic properties of intermetallics, magnetostrictive and magneto-optical, are discussed in this volume by Greenough and Schulze (Chapter 17) and McGahan (Chapter 19).

5. Conclusions

Intermetallic compounds are central to applications of magnetic materials, especially in high-performance permanent magnets. Though they are not usually the source of high permeability in soft magnets, they do play a role in many of the intricate mechanisms that lead to desirable properties. In magnetically hard materials, one essentially looks for a compound that has a unique crystallographic axis with a strong tendency to lock in the spins. After such a compound has been identified, a magnet is still not realized until a metallurgical process

has been found that creates magnetically isolated small crystallites, or entities that pin domain walls. Furthermore, the polycrystalline aggregate should be given a preferred orientation to maximize the remanence and energy product. The growing body of permanent magnet literature appears driven by the quest for supermagnets with energy products over 400 kJ m^{-3} and, in the case of ordinary magnets, by economic concerns, i.e. the need for materials that are cheaper or do not have to rely on scarce resources. A study of the cited review papers will show that there is also a trend to characterize compound types systematically once they have been recognized. Not only are $\text{Fe}_{14}\text{Nd}_2\text{B}$ and $\text{Fe}_{14}\text{Pr}_2\text{B}$ now familiar compounds, but the properties of the isostructural phases in which Nd and Pr are replaced by the other lanthanides, and Fe by Co, have also become known. Magnet conferences continue to present a steady flow of information on new phases, and applications employing their magnetic properties will remain a fruitful area of investigation for some time to come.

6. References

- Andresen, A. F., Engbreetsen, J. E., and Refsnes, J. (1972). *Acta Chem. Scand.*, **26**, 175.
- Becker, J. J. (1970). *J. Appl. Phys.*, **41**, 1055.
- Becker, J. J. (1984). *J. Appl. Phys.*, **55**, 2067.
- Block, G., and Jeitschko, W. (1986). *Inorg. Chem.*, **25**, 279.
- Bozorth, R. M. (1951). *Ferromagnetism*. Van Nostrand, Princeton.
- Bozorth, R. M. (1953). *Rev. Mod. Phys.*, **25**, 42.
- Braun, P. B., and Goedkoop, J. A. (1963). *Acta Cryst.*, **16**, 737.
- Buschow, K. H. J. (1971). *J. Less-Common Met.*, **25**, 131.
- Buschow, K. H. J. (1987). *Mater. Res. Soc. Symp. Proc.*, **96**, 1–16.
- Buschow, K. H. J. (1991). *J. Magn. Magn. Mater.*, **100**, 79.
- Buschow, K. H. J., de Mooij, D. B., and Denissen, C. J. M. (1988). *J. Less-Common Met.*, **141**, L15.
- Buschow, K. H. J., and van der Groot, A. S. (1971). *Acta Crystallogr.*, **B27**, 1085.
- Buschow, K. H. J., and van Engen, P. G. (1981). *J. Magn. Magn. Mater.*, **25**, 90.
- Cadieu, F. J., Cheung, T. D., Wickramasekara, L., and Aly, S. H. (1984). *J. Appl. Phys.*, **55**, 2611.
- Cadieu, F. J., Kamprath, N., Hegde, H., Chen, K., Navarathna, A., and Rani, R. (1991). *J. Appl. Phys.*, **59**, 5608.
- Chen, C. W. (1977). In *Selected Topics in Solid State Physics*, Vol. 15 (ed. E. P. Wohlfarth). North-Holland, Amsterdam.
- Chikazumi, S. (1964). *Physics of Magnetism*. Wiley, New York, pp. 373–387.
- Clark, A. E. (1973). *Appl. Phys. Lett.*, **23**, 642.

- Clark, A. E., and Belson, H. S. (1972). *Phys. Rev. B*, **5**, 3642.
- Clarke, Jr, R. S. and Scott, E. R. D. (1980). *Am. Miner.*, **65**, 624.
- Coey, J. M. D. (1989). *J. Magn. Magn. Mater.*, **80**, 9.
- Coey, J. M. D., and Sun, H. (1990). *J. Magn. Magn. Mater.*, **87**, L251.
- Coey, J. M. D., Sun, H., and Hurley, D. P. F. (1991a). *J. Magn. Magn. Mater.*, **101**, 310.
- Coey, J. M. D., Sun, H., Otani, Y., and Hurley, D. P. F. (1991b). *J. Magn. Magn. Mater.*, **98**, 76.
- Croat, J. J., Herbst, J. F., Lee, R. W., and Pinkerton, F. E. (1984). *J. Appl. Phys.*, **55**, 2078.
- Dahl, O., and Pfaffenberger, J. (1934). *Z. Tech. Phys.*, **15**, 99.
- Dwight, A. E., and Kimball, C. W. (1974). *Acta Crystallogr.*, **B30**, 2791.
- El-Masry, N. A., and Stadelmaier, H. H. (1983). *Z. Metallk.*, **74**, 86.
- El-Masry, N. A., and Stadelmaier, H. H. (1989). *Z. Metallk.*, **80**, 723.
- El-Masry, N. A., Stadelmaier, H. H., Shahwan, C. J., and Jordan, L. T. (1983). *Z. Metallk.*, **74**, 33.
- Elmen, G. W. (1929). *U.S. Pat.*, 1 739 752.
- Fallot, M. (1936). *Ann. Physique (11)*, **6**, 305.
- Fidler, J., Bernardi, J., Ohashi, K., and Tawara, Y. (1990). *IEEE Trans. Magn.*, **26**, 1385.
- Florio, J. V., Rundle, R. E., and Snow, A. I. (1952). *Acta Crystallogr.*, **5**, 449.
- Gao, C., Wang, H., and Hadjipanayis, G. C. (1990). *J. Appl. Phys.*, **67**, 4960.
- Ghandehari, H. H., and Fidler, J. (1985). *IEEE Trans. Magn.*, **21**, 1973.
- Graf, L., and Kussman, A. (1935). *Physikal. Z.*, **36**, 544.
- Grössinger, R., Kou, X. C., Jacobs, T. H., and Buschow, K. H. J. (1991). *J. Appl. Phys.*, **69**, 5596.
- Gueramian, M., Bezing, A., Yvon, K., and Muller, J. (1987). *Solid-State Commun.*, **64**, 639.
- Guillaud, C. (1943). Thesis, Strasbourg.
- Hall, R. C. (1960). *J. Appl. Phys.*, **31**, 157S.
- Hansen, M., and Anderko, K. (1958). *Constitution of Binary Alloys*, 2nd edn. McGraw-Hill, New York, p.492.
- Hegde, H., Rani, R., Navarathna, A., Chen, K., and Cadieu, F. J. (1991). *J. Appl. Phys.*, **70**, 6345.
- Helmholdt, R. B., and Buschow, K. H. J. (1989). *J. Less-Common Met.*, **155**, 15.
- Herbst, J. F. (1991a). *Rev. Mod. Phys.*, **63**, 819.
- Herbst, J. F. (1991b). In *Supermagnets, Hard Magnetic Materials* (eds G. J. Long and F. Grandjean). Kluwer, Dordrecht, pp. 69–91.
- Herbst, J. F., and Croat, J. J. (1991). *J. Magn. Magn. Mater.*, **100**, 57.
- Heusler, F. (1904). *Z. Angew. Chem.*, **17**, 260.
- Hirota, H. (1969). *U.S. Pat.*, 3 433 630.
- Huang, M. Q., Ma, B. M., Cheng, S. F., and Wallace, W. E. (1991). *J. Appl. Phys.*, **69**, 5599.
- Jang, T. S., and Stadelmaier, H. H. (1990a). *Mater. Lett.*, **9**, 483.
- Jang, T. S., and Stadelmaier, H. H. (1990b). *J. Appl. Phys.*, **67**, 4957.
- Jellinghaus, W. (1936). *Z. Tech. Phys.*, **17**, 33.
- Jiles, D. (1991). *Introduction to Magnetism and Magnetic Materials*. Chapman and Hall, London, pp. 269–298.
- Kamprath, H., Liu, N. C., Hegde, H., and Cadieu, F. J. (1988). *J. Appl. Phys.*, **64**, 5720.
- Kaneko, H., Homma, M., and Nakamura, K. (1971). *AIP Conf. Proc.*, No. 5, 1088.
- Katter, M., Wecker, J., Kuhrt, C., Schultz, L., Kou, X. C., and Grössinger, R. (1992). *J. Magn. Magn. Mater.*, **111**, 293.
- Katter, M., Wecker, J., and Schultz, L. (1990a). *IEEE Trans. Magn.*, **26**, 1379.
- Katter, M., Wecker, J., and Schultz, L. (1991). *J. Appl. Phys.*, **70**, 3188.
- Katter, M., Wecker, J., Schultz, L., and Grössinger, R. (1990b). *Appl. Phys. Lett.*, **56**, 1377.
- Khan, Y. (1974). *Z. Metallk.*, **65**, 489.
- Koch, A. J. J., Hokkeling, P., van der Steeg, M. G., and de Vos, K. J. (1960). *J. Appl. Phys.*, **31**, 75S.
- Kono, H. (1958). *J. Phys. Soc. Jpn.*, **13**, 1444.
- Koon, N. C., and Das, B. N. (1984). *J. Appl. Phys.*, **55**, 2063.
- Köster, W., and Anantha Swamy, N. K. (1962). *Z. Metallk.*, **53**, 299.
- Köster, W., and Mulfinger, W. (1938). *Z. Metallk.*, **30**, 348.
- Köster, W., and Schmid, H. (1955). *Arch. Eisenhüttenw.*, **26**, 345.
- Köster, W., and Wachtel, E. (1960). *Z. Metallk.*, **51**, 271.
- Kouvel, J. S. (1967). In *Intermetallic Compounds* (ed. J. H. Westbrook). Wiley, New York, pp. 529–568.
- Krén, E., and Szabó, P. (1965). *Solid-State Commun.*, **3**, 371.
- Kripyakevich, P. I., Terekhova, V. F., Zarechnyuk, O. S., and Burov, I. V. (1963). *Kristallografiya*, **8**, 268.
- Kuz'ma, Yu. B., and Bilonizhko, N. S. (1974). *Sov. Phys. Crystallogr.*, **18**, 447.
- Landgraf, F. J. G., Missell, F. P., Rechenberg, H. R., Schneider, G., Villas-Boas, V., Moreau, J. M., Paccard, L., and Nozières, J. P. (1991). *J. Appl. Phys.*, **70**, 6125.
- Landgraf, F. J. G., Schneider, G., Villas-Boas, V., and Missell, F. P. (1990). *J. Less-Common Met.*, **163**, 169.
- Lee, R. W. (1985). *Appl. Phys. Lett.*, **46**, 790.
- Li, H.-S., and Coey, J. M. D. (1991). In *Handbook of Magnetic Materials*, Vol. 6 (ed. K. H. J. Buschow). North-Holland, Amsterdam, pp. 1–83.
- Liao, L. X., Altounian, Z. A., and Ryan, D. H. (1991). *J. Appl. Phys.*, **70**, 6006.
- Libsch, J. F., Both, E., Beckman, G. W., Warren, D., and Franklin, R. J. (1950). *Trans. AIME*, **188**, 287.
- Lipson, H., Shoenberg, D., and Stupart, G. V. (1941). *J. Inst. Met.*, **67**, 333.
- Liu, N. C., Stadelmaier, H. H., and Schneider, G. (1987). *J. Appl. Phys.*, **61**, 3574.
- Makarov, E. S., and Vinogradov, S. I. (1956). *Kristallografiya*, **1**, 634.
- Martin, D. L., and Geisler, A. H. (1952). *Trans. ASM*, **44**, 461.
- Marusin, E. P., Bodak, O. I., Tsokol', A. O., and Fundamenskii, V. S. (1985). *Sov. Phys. Crystallogr.*, **30**, 338.
- Massalski, T. B. (ed.) (1992). *Binary Alloy Phase Diagrams*. ASM International, Materials Park, OH.

- Masumoto, H. (1936). *Sci. Rep. Tôhoku Imp. Univ. (Honda)*, 388.
- McCurrie, R. A., and Hawkrigde, D. G. (1972). *Philos. Mag.*, **25**, 753.
- Menth, A. (1976). *AIP Conf. Proc.*, No. 29, 600.
- Mitra Ghemawat, A., Foldeski, M., Dunlap, R. A., and O'Handley, R. C. (1989). *IEEE Trans. Magn.*, **25**, 3312.
- Moreau, J. M., Paccard, L., Nozières, J. P., Missell, F. P., Schneider, G., and Villas-Boas, V. (1990). *J. Less-Common Met.*, **163**, 245.
- Nachman, L. F., and Buehler, W. J. (1955). *Nav. Ord. Rep.*, 4130, December.
- Nesbitt, E. A. (1965). *J. Appl. Phys.*, **40**, 1259.
- Nesbitt, E. A., and Wernick, J. H. (1973). *Rare Earth Permanent Magnets*. Academic Press, New York, pp. 95–145.
- Nesbitt, E. A., Willens, R. H., Sherwood, R. C., Buehler, E., and Wernick, J. H. (1968). *Appl. Phys. Lett.*, **12**, 3361.
- Oesterreicher, H., Parker, F. T., and Misroch, M. (1977). *Appl. Phys.*, **12**, 287.
- Ohashi, K., Yokoyama, T., Osugi, R., and Tawara, Y. (1987). *IEEE Trans. Magn.*, **23**, 3101.
- Pearson, W. B. (1972). *The Crystal Chemistry and Physics of Metals and Alloys*. Wiley-Interscience, New York, p. 648.
- Petersen, J. F., Aydin, M., and Knudsen, J. M. (1977). *Phys. Lett. A*, **62**, 192.
- Potter, H. H. (1929). *Proc. Phys. Soc. London*, **41**, 135.
- Potter, H. H. (1931). *Philos. Mag.*, **12**(7), 255.
- Puzei, I. M. (1960). *Phys. Met. Metall. USSR*, **9**(2), 103.
- Rani, R., Hegde, H., Navarathna, A., Chen, K., and Cadieu, F. J. (1992). *IEEE Trans. Magn.*, **28**, 2835.
- Rathenau, G. W., and Snoek, J. L. (1941). *Physica*, **8**, 555.
- Ray, A. E. (1974). *Cobalt*, No. 1, 3.
- Raynor, G. V., and Rivlin, V. G. (1988). *Phase Equilibria in Ternary Alloys*, Part 4. Institute of Metals, London, pp. 268–283.
- Rogl, P. (1984). In *Handbook on the Physics and Chemistry of Rare Earths*, Vol. 6 (eds K. A. Gschneidner and L. Eyring). North-Holland, Amsterdam, pp. 335–523.
- Sagawa, M., Fujimura, S., Togawa, N., Yamamoto, H., and Matsuura, Y. (1984a). *J. Appl. Phys.*, **55**, 2083.
- Sagawa, M., Fujimura, S., Yamamoto, H., Matsuura, Y., and Hiraga, H. (1984b). *IEEE Trans. Magn.*, **20**, 1584.
- Sagawa, M., Hirosawa, S., Yamamoto, H., Fujimura, S., and Matsuura, Y. (1987). *Jpn J. Appl. Phys.*, **26**, 785.
- Sagawa, M., Hirosawa, S., Yamamoto, H., Matsuura, Y., Fujimura, S., Tokuhara, H., and Hiraga, K. (1986). *IEEE Trans. Magn.*, **22**, 910.
- Sanchez, J. L., Garcia, S., Suarez, N., Diaz, S., Leccabue, F., Panizzieri, R., Bocelli, G., and Calestani, G. (1989). *J. Magn. Magn. Mater.*, **79**, 249.
- Satya Murthy, N. S., Begum, R. J., Somanathan, C. S., and Murthy, M. R. L. N. (1969). *J. Appl. Phys.*, **40**, 1870.
- Schnitzke, K., Schultz, L., Wecker, J., and Katter, M. (1990). *Appl. Phys. Lett.*, **57**, 2853.
- Schultz, L., and Katter, M. (1991). In *Supermagnets, Hard Magnetic Materials* (eds G. J. Long and F. Grandjean). Kluwer, Dordrecht, pp. 227–259.
- Schultz, L., Schnitzke, K., and Wecker, J. (1990a). *Appl. Phys. Lett.*, **56**, 868.
- Schultz, L., Schnitzke, K., Wecker, J., and Katter, M. (1990). *IEEE Trans. Magn.*, **26**, 1373.
- Schultz, L., Schnitzke, K., Wecker, J., Katter, M., and Kuhr, C. (1991). *J. Appl. Phys.*, **69**, 6339.
- Sellmyer, D. J., Ahmed, A., Muench, G., and Hadjipanayis, G. (1984). *J. Appl. Phys.*, **55**, 2088.
- Sheng, L., Zhibul, L., Guowei, Z., Xiedi, P., Wei, J., and Wenwang, H. (1987). *IEEE Trans. Magn.*, **23**, 3095.
- Sherwood, R. C., Nesbitt, E. A., Wernick, J. H., Bacon, D. D., Kurtzig, A. J., and Wolfe, R. (1971). *J. Appl. Phys.*, **42**, 1704.
- Six, W., Snoek, J. L., and Burgers, W. G. (1934). *Ingenieur*, **49**, E195.
- Smit, H. H. A., Thiel, R. C., and Buschow, K. H. J. (1988). *J. Physique*, **F18**, 295.
- Stäblein, H. (1982). In *Ferromagnetic Materials*, Vol. 3 (ed. E. P. Wohlfarth). North-Holland, Amsterdam, pp. 441–602.
- Stadelmaier, H. H. (1969). In *Developments in the Structural Chemistry of Alloy Phases* (ed. B. C. Giessen). Plenum Press, New York, pp. 141–180.
- Stadelmaier, H. H. (1984). *Z. Metallk.*, **75**, 227.
- Stadelmaier, H. H., and El-Masry, N. A. (1985). In *Proc. 4th International Symposium on Magnetic Anisotropy and Coercivity in Rare Earth-Transition Metal Alloys* (ed. K. J. Strnat), Dayton, OH, p. 613.
- Stadelmaier, H. H., Henig, E.-Th., Schneider, G., and Petzow, G. (1988). *Z. Metallk.*, **79**, 316.
- Stadelmaier, H. H., Jang, T. S., and Henig, E.-Th. (1991). *Mater. Lett.*, **12**, 295.
- Stadelmaier, H. H., and Liu, N. C. (1989). *U.S. Pat.*, 4 849 035.
- Stadelmaier, H. H., and Park, H. K. (1981). *Z. Metallk.*, **72**, 417.
- Stadelmaier, H. H., Schneider, G., Henig, E.-Th., and Ellner, M. (1986). *J. Less-Common Met.*, **115**, L11.
- Stadelmaier, H. H., Schneider, G., Henig, E.-Th., and Ellner, M. (1991). *Mater. Lett.*, **10**, 303.
- Stadelmaier, H. H., and Schöbel, J.-D. (1969). *Monatsh. Chem.*, **100**, 224.
- Strnat, K. J. (1978). *J. Magn. Magn. Mater.*, **7**, 351.
- Strnat, K. J. (1988). In *Ferromagnetic Materials*, Vol. 4 (eds E. P. Wohlfarth and K. H. J. Buschow). North-Holland, Amsterdam, p. 131.
- Strnat, K. J., and Strnat, R. M. W. (1991). *J. Magn. Magn. Mater.*, **100**, 38.
- Stroink, G., Stadnik, Z. M., Viau, G., and Dunlap, R. A. (1990). *J. Appl. Phys.*, **67**, 4463.
- Sun, H., Otani, Y., Coey, J. M. D., Meckison, C. D., and Jakubovics, J. P. (1990). *J. Appl. Phys.*, **67**, 4659.
- Tarschisch, L. (1933). *Z. Kristallogr.*, **A86**, 423.

- Underhill, E. M. (ed.) (1952). *Permanent Magnet Handbook*. Crucible Steel Co., Pittsburgh, PA.
- Vogel, R. (1947). *Z. Metallk.*, **38**, 97.
- Voroshilov, Yu. V., Kripyakevich, P. I., and Kuz'ma, Yu. B. (1970). *Kristallografiya*, **15**, 934.
- Wang, Y., Hadjipanayis, G. C., Kim, A., Liu, N. C., and Sellmyer, D. J. (1990). *J. Appl. Phys.*, **67**, 4954.
- Wang, Y. Z., and Hadjipanayis, G. C. (1991). *J. Appl. Phys.*, **70**, 6009.
- Wecker, J., Katter, M., Schultz, L., and Schnitzke, K. (1990). In *Proc. 6th International Symposium on Magnetic Anisotropy and Coercivity in Rare Earth-Transition Metal Alloys* (ed. S. G. Sankar), Carnegie-Mellon University, Pittsburgh, PA, p. 94.
- Werner, F. E., and Jaffee, R. I. (1992). *J. Mater. Eng. Perform.*, **1**, 227-234.
- Wernick, J. H., Haszko, S. E., and Romanow, W. J. (1961). *J. Appl. Phys.*, **32**, 2495.
- Yamaguchi, A., Tanaka, Y., Yanagimoto, K., Sakaguchi, J., and Kato, N. (1989). *J. Jpn Met. Soc.*, **28**, 422.
- Yamamoto, H. (1972). *US Pat.*, 3 661 567.
- Yang, Y.-c., Zhang, X.-d., Ge, S.-l., Pan, Q., Kong, L.-s., Li, H., Yang, J.-l., Zhang, B.-s., Ding, Y.-f., and Ye, C.-t. (1991). *J. Appl. Phys.*, **70**, 6001.
- Yoshimoto, N., Sakurai, J., and Komura, Y. (1983). *J. Magn. Mater.*, **31-34**, 137-139.

This chapter was originally published in 1995 as Chapter 14 in *Intermetallic Compounds*, Vol. 2: *Practice*, edited by J. H. Westbrook and R. L. Fleischer.

Chapter 4

Semiconductor Applications

Katashi Masumoto

*The Research Institute for Electric and Magnetic Materials,
2-1-1 Yagiyama Minami, Taihaku-ku, Sendai 982-0807, Japan*

Akinori Katsui

*School of High-Technology for Human Welfare, Department of Materials Science and Technology,
Tokai University, 317 Nishino, Numazu, Shizuoka 401-0321, Japan*

Takashi Matsuoka

*NTT Basic Research Laboratories, Nippon Telegraph and Telegraph Corporation, 3-1 Wakamiya
Morinosato, Atsugi, Kanagawa 243-0198, Japan*

1. Introduction

Generally, semiconducting compounds have a diamond structure or one of its derivatives as a basis (see Parthé, Chapter 14 of Volume 1). This structure has two types of positions: the f.c.c. positions and the b.c.c. positions of half the octants. Figure 1 shows the related zinc blende structure, wurtzite structure, and chalcopyrite structure. The zinc blende structure is the one in which cations lie in the f.c.c. positions and anions lie in the b.c.c. positions with equivalent coordination. A ternary compound with a diamond structure may be obtained by substituting only cations or by substituting both cations and vacancies into the tetrahedral sites and octahedral sites of the f.c.c. lattice. Figure 2 is a diagram showing an example of the induction to higher-order semiconducting compounds with the diamond structure. In this arrangement, each of the compounds must have a positive valence of four on average (Pamplin, 1964). This requirement also applies to all of the ternary to multinary compounds having a diamond or similar structure described in this chapter. Thus Figure 2 shows that Ge, GaAs, ZnFeAs₂, and CuGaGe₂As₄ are all possible adamantane compounds.

Many of the semiconducting compounds show a variety of optical phenomena, such as luminescence, laser beam emission, and nonlinear optical effects, none of which is present in pure silicon. Many of these compounds have charge carriers with higher electron mobilities than silicon. Furthermore, there is a wide selection of materials from the same groups of compounds in constructing ternary and quaternary solid solutions of the diamond structure. Therefore, it is possible to change the fundamental properties of a semiconductor, such as the forbidden band gap, mobility, and lattice constant, over a usefully wide range. The result is a flexibility in material design for a variety of applications. There is more and more cut-throat competition in the development of compound semiconductors.

Table 1 as an example shows a comparison of materials used in some important compound semiconductor light-emitting diodes (LEDs). Many of the materials are compounds of two or more kinds of elements. A much higher level of material preparation technology is needed to construct useful devices from these compound semiconductors than is needed for an elemental semiconductor. The quality of presently available commercial materials is not yet sufficiently

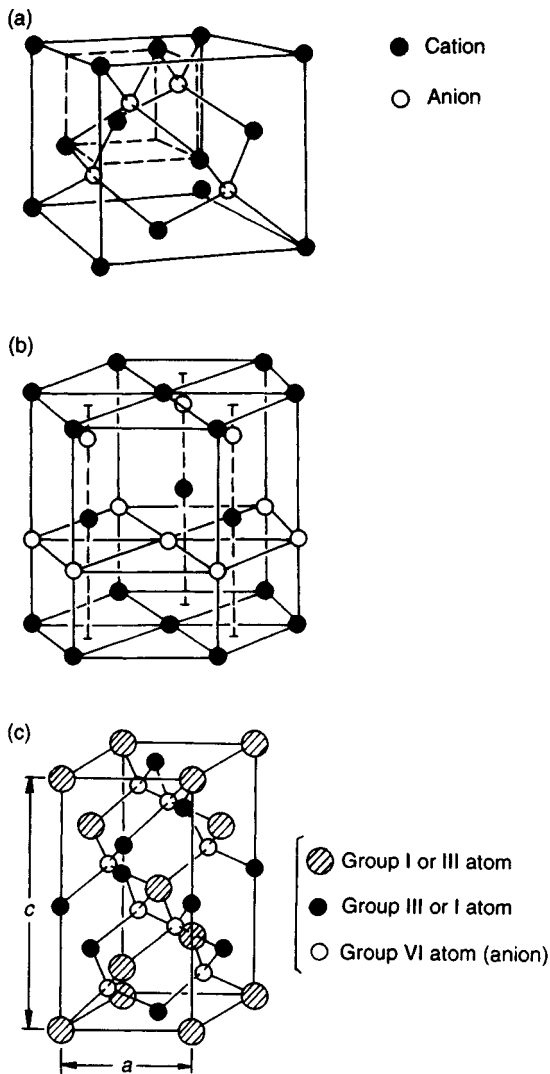


Figure 1. Crystal structures of (a) zinc blende (B3, cF8), (b) wurtzite (B4, hP4) and (c) chalcopyrite (E1₁, tI16)

high for obtaining the required properties as semiconductors, although their prices are extremely high. Yet there is more and more demand for compound semiconductor devices in all kinds of industries; therefore, material preparation technology is advancing steadily into the first stages of commercial production.

The III-V semiconducting compounds are in the most advanced stage of research and development, as a result of long-term studies of their physicochemical and electronic properties. They are now the most promising electronic materials. Particularly advanced materials in

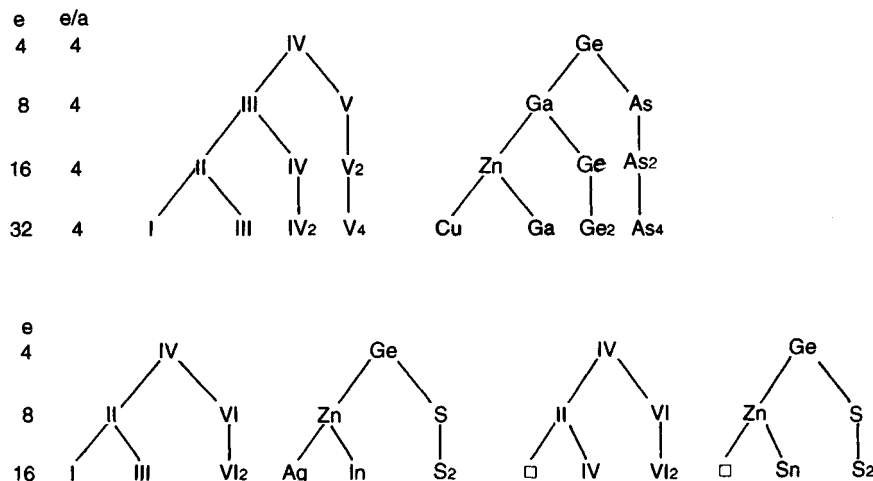
this field are optoelectronic semiconductors based on GaP, GaAs, and InP and magnetoelectronic semiconductors based on InSb and InAs. In the future, higher functionality and improved properties of these compounds will be needed.

There has been rapid and extensive progress in the technologies of preparing semiconducting compounds and manufacturing applied electronic devices. Recent developments in the techniques of crystal growth via the vapor phase have been remarkable. Particularly, molecular beam epitaxy (MBE) and metal organic vapor-phase epitaxy (MOVPE) make it possible to stack one layer of atoms onto another. Such deposition of different semiconductors, having different widths of their forbidden bands, serves to form an artificial 'superlattice'* having a width potentially equivalent to, or less than, the de Broglie wavelength. It is further possible, by repeated deposition of dissimilar lamellae, to make a modulated lamellar 'superlattice' with a controlled and varied potential period. This technique for depositing very thin atomic layers makes it possible to attain heterojunctions between structures of different lattice constants. Thus, we now have more degrees of freedom in the combination of semiconducting materials to form a new type of 'superlattice', namely the 'strained superlattice'. One new proposal is that, without a periodic change in potential but with a periodic change in another physical property (for example, the effective mass), it might be possible to form both a quantum well and a 'superlattice'.

Using advanced techniques of crystal growth and materials processing, we can change the spatial distribution of impurity atoms at short (atomic scale) intervals, even in a semiconducting material with a forbidden band gap. This leads to a change in the spatial distribution of electric charges, and hence to the formation of a periodic change in potential to produce a 'superlattice'. It has also been found possible to form buried layers of compounds, e.g. semiconducting CoSi₂, by high-dose ion implantation followed by annealing. Silicide layers formed by this mesotaxy process are single crystal, aligned with the substrate, with smooth, abrupt interfaces and excellent electrical characteristics (Celler and White, 1992).

In summary, starting with the conventional technique for forming a simple heterojunction, the advanced technology for producing a quantum well and many

*Quotes are used here to distinguish this type of material from the superlattice of the metallurgist, an ordered array of atoms formed from a disordered binary (or higher) solid-solution alloy.

^aCommercially available.

2. Compound Semiconductors for Device Applications

* 2.1 Group II–VI Semiconducting Compounds

Group II–VI semiconductors are binary compounds and their solid solutions, consisting of Group IIB elements (Zn, Cd, Hg) and Group VIB elements (O, S, Se, Te), e.g. ZnSe, ZnS and (Hg, Cd)Te, are typical.

2.1.1 ZnSe and ZnS

The forbidden band gaps E_g of Zn chalcogenides are 2.26 eV for ZnTe, 2.67 eV for ZnSe and 3.7 eV for ZnS, all at 300 K. Their mutual solid solutions exist over all compositions, and thus E_g of Zn chalcogenides can change continuously from the yellow region to the violet region. Attention has especially centered around ZnSe and ZnS as materials for light-emitting device applications in the blue region.

ZnSe and ZnS possess a phase transition between the zinc blende type and wurtzite type. The transition temperatures are 1698 K and 1297 K for ZnSe and ZnS, respectively (Klakov *et al.*, 1976).

ZnS has a high equilibrium dissociation pressure (3.7×10^2 kPa) at the melting point T_m (2103 K). The T_m (1793 K) and dissociation pressure (53 kPa) of ZnSe are not as high. However, the vapor pressures of Zn, S and Se are exceedingly high in comparison with the compounds. Consequently, it is difficult to grow large, high-quality single crystals of ZnSe and ZnS from the melt. The vapor-growth method has been intensively studied to avoid these problems. High-purity ZnSe single crystals including few twin boundaries have been grown by means of the sublimation method (Fujita *et al.*, 1979).

As-grown crystals are high-resistance n-type, and an anneal in the melt or under the vapor pressure of Zn is essential for low resistivity. Epitaxial thin-film growth has been achieved using liquid-phase epitaxy (LPE), vapor-phase epitaxy (VPE), MOVPE and MBE. Among these alternatives, the MOVPE and MBE methods have been intensively examined because of the nonequilibrium character of film growth. Since ZnSe and ZnS wafers for epitaxial growth are not commercially available, GaAs (mismatch of 0.27% for ZnSe) and GaP (0.77% for ZnS) are very frequently employed as substrates. The epitaxial growth temperature is 350 to $\sim 500^\circ\text{C}$.

Undoped films are highly resistive (specific resistivity ρ above $10^6 \Omega \text{ cm}$), and the photoluminescence (PL) spectra generally show strong near-band edge emission and a weak self-activated emission.

Formation of a p–n junction leads to realization of high injection efficiency in LED applications, and hence conduction-type conversion is needed. However, control of conduction type by means of impurity doping has proven unachievable in Group II–VI semiconductors, except for CdTe. The reason still remains unclarified.

For n-type films, iodine is useful as a donor species, and the carrier concentration can be controlled in the range 10^{16} – 10^{19} cm^{-3} (Shibata *et al.*, 1988). The resistivities of films doped with $1 \times 10^{19} \text{ cm}^{-3}$ iodine atoms decreased to as little as $1.3 \times 10^{-3} \Omega \text{ cm}$ at room temperature. These doped films showed a strong blue PL at 300 K. For p-type films, nitrogen (Ohki *et al.*, 1988), phosphorus (Bhargava, 1982), lithium (Nishizawa, 1986; Yasuda *et al.*, 1988; Cheng *et al.*, 1988) and oxygen (Akimoto *et al.*, 1989) have been examined as acceptor species. Recently, a nitrogen-doping technique using a high-frequency plasma cell was established. Furthermore, a radio-frequency plasma gas cell was installed into an MBE chamber and low-resistance p-type films were grown on a GaAs substrate by plasma-assisted doping with nitrogen (Park *et al.*, 1990; Ohkawa, 1990). Still further, a laser diode (LD) with a (Zn, Cd)Se/ZnSe quantum-well structure has been manufactured, and laser emission with a wavelength of 494 nm at 300 K was observed by electric current injection (Jeon *et al.*, 1991; Haase *et al.*, 1991).

2.1.2 (Hg, Cd)Te

The narrow band gap semiconductor (Hg, Cd)Te is a solid solution of the Group II–VI semiconductors HgTe and CdTe. The band gap changes continuously from HgTe (-0.3 eV at 0 K) to CdTe (1.6 eV at 0 K).

The terminal compound CdTe generally shows no phase transition. As-grown crystals, grown from a melt with a Te-rich composition, proved to be p-type and to contain a high concentration of Cd vacancies (Triboulet and Marfaing, 1977). By annealing under Cd vapor pressure, the crystals become low-resistance n-type (Triboulet, 1981).

Epitaxial film growth has also been studied. CdTe, (Cd, Zn)Te and (Cd, Mn)Te have been used as substrates. Undoped (Hg, Cd)Te films formed by the LPE method contained 10^{16} – 10^{17} cm^{-3} Hg vacancies and showed p-type conduction. By annealing under Hg vapor pressure, the films were converted to n-type conduction. Both conduction types could also be produced by impurity doping.

(Hg, Cd)Te has been developed as a material for an infrared detector in the range 1–20 μm . Furthermore, (Hg, Cd)Te has high electron mobility and forms an

insulating native oxide of high quality in the film form; it is therefore highly useful for electrical applications.

A 'superlattice' of modulated CdTe/HgTe and ZnTe/HgTe structure is highly desirable for high-speed devices, such as Gunn diodes and hot-electron transistors. In an (Hg, Cd)Te/HgTe/(Hg, Cd)Te structure with a double barrier type, single quantum well, a negative resistance attributed to a resonance tunnel effect was found (Reed *et al.*, 1987). The peak to valley ratio was 1.4:1, comparable with that of AlGaAs/GaAs.

2.2 Group III-V Semiconducting Compounds

Group III-V semiconductors are binary compounds and their solid solutions consist of Group IIIB elements (B, Al, Ga, In) and Group VB elements (N, P, As, Sb). Table 2 shows some fundamental characteristics of Group III-V semiconductors. Practical interest has been most intensively centered on GaAs, InP, and the solid solutions (Al, Ga)As, (In, Ga)As, and (In, Ga) (As, P).

GaAs and InP melt congruently; however, they have high dissociation pressures. Hence, pressures above atmospheric pressure are required over the melt to maintain a stoichiometric composition during the growth process. The pressures are 100 and 2.7×10^3 kPa for GaAs ($T_m = 1511$ K) and InP ($T_m = 1335$ K), respectively.

These crystals usually contain high concentrations of compositional defects. Thus, growth of perfect single crystals of large diameter has been investigated by means of horizontal Bridgman (HB), liquid-encapsulated Czochralski (LEC), and vertical-gradient freezing (VGF) methods. Point defects, diffusion mechanisms, and superlattice disordering in GaAs-based materials have been reviewed in depth by Tan *et al.* (1991). Cr, oxygen and native point defects form deep acceptor levels in GaAs (Hobgood *et al.*, 1982; Martin *et al.*, 1980).

In InP, transition metal elements such as Fe (Mizuno and Watanabe, 1975; Kamada *et al.*, 1984) and Ti (Iseler, 1986; Katsui, 1988) form deep levels. The deep levels compensate the residual carriers electrically, and as a result the crystals become semi-insulating with ρ above $5 \times 10^6 \Omega \text{ cm}$.

The semi-insulating crystals are useful as substrates for optoelectronic integrated circuits (OEICs), capable of reducing floating capacitance and providing electrical isolation for devices.

Recent practical interest has been greatly centered on OEICs. Furthermore, marked advancement in the MOVPE and MBE methods and in the sophistication of small-scale, high-resolution processing techniques have enabled producers to propose various multi-functional or high-performance devices. A voluminous and excellent secondary literature exists dealing with Group III-V semiconductors and their applications (for example, Willardson and Beer, 1975–1992).

2.3 Group IV-IV Semiconducting Compounds

SiC, one of the Group IV-IV semiconductors, possesses crystal polymorphism (Marshall *et al.*, 1974). Hexagonal α -SiC is an indirect transition type semiconductor having a band gap E_g of about 3.0 eV at 300 K. It is useful as a material for LEDs in the blue region. Low-resistance n-type and p-type films are grown by doping with nitrogen and aluminium, respectively. The blue emission is probably due to a donor-acceptor (D-A) emission in the n-type layer.

High-quality α -SiC single crystals have recently been grown by an improved Reigh method and a sublimation method (Tairov and Tsvetkov, 1981). A p-n junction has been formed in these crystals by a rotational dipping method (Ikeda *et al.*, 1979). First, a p-type layer was

Table 2. Fundamental properties of Group III-V compound semiconductors

| Properties | GaAs | InP | InAs | InSb | AlN | BN (cubic) |
|---|----------------------------|-----------------------|------------------------|------------------------|---------------------|-------------|
| E_g (eV) at 300 K | 1.43 | 1.35 | 0.36 | 0.18 | 5.9 | 8.0 |
| Transition type | Direct | Direct | Direct | Direct | Direct | Indirect |
| Recombination coefficient ($\text{cm}^2 \text{s}^{-1}$) | 7.21×10^{-10} | 1.26×10^{-9} | 8.5×10^{-11} | 4.58×10^{-11} | | |
| Hall mobility μ_e ($\text{cm}^2 \text{V}^{-1} \text{s}^{-1}$) | | | | | | |
| 300 K | 8500 | 4500 | 33 000 | 80 000 | 14 (μ_b) | 0.2 (500 K) |
| 77 K | | 4.5×10^4 | 1.5×10^5 | 1×10^6 | | |
| Surface recombination velocity (cm s^{-1}) | 2×10^7 | 1×10^3 | | | | |
| Dielectric constant (C/N) | $\sim 2.7 \times 10^{-12}$ | | 1.14×10^{-12} | 2.35×10^{-12} | 5×10^{-12} | |
| Relative permittivity ϵ/ϵ_0 | 12.9 | 12.1 | 12.5 | 18.7 | | |
| Thermal conductivity ($\text{W cm}^{-1} \text{deg}^{-1}$) | 0.455 | 0.68 | 0.273 | 0.166 | 3.2 | 13 |
| Melting point (K) | 1511 | 1343 | 1215 | 798 | ~ 2723 | > 2973 |
| Hardness (kg mm^{-2}) | 750 | 540 | 380 | 220 | 1200 | 7300–10 000 |

grown on the crystals by immersion in an Si melt doped with Al, and then an n-type layer was formed by introducing nitrogen gas into the melt.

LEDs with a central wavelength of 475 nm, an external quantum efficiency of 2×10^{-4} , a maximum luminous intensity of 12 mcd at an operational current of 20 mA and continuous room-temperature operation times above 5000 h have been developed (Koga *et al.*, 1985).

For an SiC LED, since the band gap of α -SiC is larger than the energy of photoemission, reabsorption of emitted light in the LED interior is negligibly small.

In cubic β -SiC, undoped n-type films with a carrier concentration of 10^{16} – 10^{17} cm $^{-3}$ have been grown on a two inch diameter Si wafer by means of chemical vapor deposition (CVD).

Just as with α -SiC, β -SiC is chemically and structurally stable to high temperatures and is highly thermally conductive. Diodes and transistors operable at high temperatures and high electric power have been studied.

* 2.4 Group IV–VI Semiconducting Compounds

Table 3 shows some fundamental properties of Group IV–VI semiconductors. (Pb, Sn)Te compounds which form a complete solid-solution series of the Group IV–VI semiconductors PbTe and SnTe are direct transition type semiconductors.

The crystal structure of (Pb, Sn)Te is f.c.c., NaCl-type B1 (cF8). The band gap of (Sn $_x$ Pb $_{1-x}$)Te at 77 K decreases linearly with increasing x from 0.22 eV for the terminal compound PbTe, becomes zero at $x=0.4$, and again increases to 0.27 eV for the other terminal compound SnTe at $x=1$ (Paker and Johnson, 1981).

As-grown, undoped (Pb, Sn)Te crystals are p-type, owing to high concentrations of Pb and/or Sn vacancies.

The n-type crystals are obtained by annealing as-grown crystals in a metal-rich atmosphere, so that the Pb and/or Sn vacancies are compensated. Furthermore, Pb and/or Sn interstitials may be generated (Paker and Johnson, 1981). The n-type conversion is also achieved by doping with Sb, Cd or In. Tl is used as a dopant for p-type crystals (Antcliffe and Wrobel, 1970).

(Pb, Sn)Te is mechanically soft, similar to aluminum metal. Plastic deformation readily occurs and low-angle boundaries are easily formed. Efforts have been made to grow bulk single crystals without low-angle boundaries (Kinoshita and Sugii, 1983).

Recent studies have been made of epitaxial thin-film growth by means of LPE using a Te solvent and MBE.

(Pb, Sn)Te is promising as a material for variable wavelength LDs and for photodetectors for the wavelength region 5–30 μ m. Although (Pb, Sn)Te has the same band gap as the Group II–VI semiconductor (Hg, Cd)Te, (Pb, Sn)Te has a larger effective electron mass and a smaller energy loss owing to nonradiative recombination; therefore, it is more useful for device applications.

LDs with homojunctions and double hetero junctions (DH) have been studied (Tomasett and Fonstad, 1974; Horikoshi *et al.*, 1982). In DH-type structures, the laser oscillation temperature is below about 80 K.

A 'quantum well' in semiconductors signifies a quantum-mechanical well of a certain potential energy, and within it carriers, electrons or holes, are two-dimensionally confined. A single quantum well is the most fundamental structure, and consists of an extremely thin well layer sandwiched between barrier layers. A quantum well may also be formed such that a light beam is confined in it, as well as electrons. Then, their confinement becomes highly effective in a multiple quantum-well (MQW) structure, and therefore the upper

Table 3. Fundamental properties of Group IV–VI compound semiconductors and semimetals

| Properties | PbS | PbSe | PbTe | SnS | SnSe | SnTe |
|--|---------|--------|--------|--|----------|-----------|
| Lattice constant (nm) | 0.59362 | 0.6147 | 0.6461 | $a = 0.599$, $b = 0.434$, $c = 1.120$ | 59.9 | 62.98 |
| Density (g cm $^{-3}$) | 7.59 | 8.15 | 8.25 | 5.08 | 6.18 | 6.51 |
| Volume dilatation coefficient (10^{-6} K $^{-1}$) | 20 | 20 | 18–20 | | | 21 |
| Specific heat (J g $^{-1}$ K $^{-1}$) | 0.14 | 0.14 | 0.15 | 0.19 | 0.18 | 0.18 |
| Thermal conductivity (W m $^{-1}$ K $^{-1}$) | 2.5 | 1.6 | 2.0 | | | 20 |
| Permittivity ϵ | | | 428 | | | |
| ϵ_0 | | | 32.6 | | | 35.9 |
| Vickers hardness (kg mm $^{-2}$) | | | 30 | | | 62 |
| Melting point (K) | 1349 | 1076 | 1190 | 1154 | 1133 | 1079 |
| Band gap (eV) at 77 K | 0.30 | 0.22 | 0.22 | -1.08^a | -0.9^a | -0.27^a |
| Effective mass | 0.2 | 0.27 | 0.22 | | 0.15 | 0.256 |

^aIn these semimetals a negative band gap implies an overlap of the conduction and valence bands.

temperature limit can be expected to be raised in LDs provided with the MQW structure. Pulse oscillation at 204 K was demonstrated in an MQW laser with a quantum-well layer of (Pb, Sn)Te and a barrier layer of Pb(Se, Te), which was capable of emitting at a wavelength of 6 μm (Shinohara *et al.*, 1985). However, even in a simple DH-type laser of wavelength 3.27 μm structured by (Pb, Cd) (S, Se)/PbS/(Pb, Cd) (S, Se), pulse oscillation operation at 200 K was observed (Koguchi *et al.*, 1987).

2.5 Group V–VI Semiconducting Compounds

Bi_2Se_3 , Bi_2Te_3 and Sb_2Te_3 compounds have a layered structure with a rhombohedral unit cell (C33, hR5). The physical and mechanical properties of these compounds are very anisotropic arising from the hexagonal symmetry of the crystal. Solid solutions of these narrow band gap semiconductors have been utilized for thermoelectric devices (Lovett, 1977; Uemura and Nishida, 1988; see also Vedernikov, Chapter 20 in this volume).

The figure of merit Z for evaluating thermoelectric materials is given by $\alpha^2\sigma/\kappa$, where α is the thermoelectromotive force, σ is the electrical conductivity and κ is the thermal conductivity. Some n-type and p-type thermoelectric materials are prepared with Bi-rich and Sb-rich solid solutions, respectively. The optimum Z value is attained by controlling the electron and hole concentrations with halogens and tellurium, respectively, as dopants. Commercial thermoelectric materials are commonly made with a uniaxial solidification technique in which the a axis is grown as the preferred direction since it has better thermoelectric properties than the c -axis (Uemura and Nishida, 1988). The Z value of the material oriented along the a axis is about $3.0 \times 10^{-3} \text{ K}^{-1}$. In order to increase the mechanical strength, however, the Z value of most commercial materials is suppressed to $2.0\text{--}2.6 \times 10^{-3} \text{ K}^{-1}$ by allowing some misorientation of the a axis.

Since Bi_2Te_3 crystals with the layered structure show pronounced mechanical cleavage on the c plane, the uniaxially solidified polycrystalline samples and the single crystals are readily broken along the solidification direction and the c plane. It was found that the mechanical strength of Bi_2Te_3 can be improved by powder metallurgy techniques without spoiling the thermoelectric properties. Despite the fact that the thermoelectric power and electrical resistivity of the sintered materials are varied, optimization is again realized by controlling the composition of the alloying element and the dopant and by increasing the phonon thermal resistivity owing to grain boundary scattering. Recently, anisotropic sintered

materials of Bi_2Te_3 have been fabricated by the hot-pressing technique (Ohsugi *et al.*, 1989). A maximum figure of merit for n-type $\text{Bi}_{1.85}\text{Te}_{2.85}\text{Se}_{0.15}$ of up to $3.7 \times 10^{-3} \text{ K}^{-1}$, perpendicular to the pressing direction, has been achieved, which is much higher than that of single crystals (Kaibe, 1989; Kaibe *et al.*, 1989).

These sintered materials are quite suitable for very small thermomodule applications, for example, for building cooling modules for optical communication devices and equipment for semiconductor processing, etc.

2.6 Transition Metal Silicide Semiconductors

*

Transition metal silicides, which have been investigated mainly as refractory materials, have interesting physical and chemical properties owing to the continuous changes in the valences of the transition metal atoms.

CrSi_2 , MnSi_{2-x} ($0.273 \geq x \geq 0.250$) and $\beta\text{-FeSi}_2$ are semiconductors developed as thermoelectric conversion materials for use at temperatures above 1200 K (see Vedernikov, Chapter 20 in this volume). Their heat-resistant properties are attractive, even though the thermoelectric power of these materials is not as large as that of the chalcogenide thermoelectric materials, and their electrical conductivities are comparatively high.

Of all the silicides, a degenerate semiconductor of p-type CrSi_2 with a hole concentration of 10^{20} cm^{-3} has superior heat resistance and is used for a high-performance thermoelectric leg (Nishida, 1972). Also, nonstoichiometric MnSi_{2-x} is a p-type, degenerate semiconductor (Nishida, 1972; Kawasumi *et al.*, 1981). It is noted that $\beta\text{-FeSi}_2$ becomes p-type by doping with Mn and/or Al (Nishida, 1973) and n-type with Co atoms. These materials have found use in high-performance, high temperature applications (Ware and McNeill, 1964).

On the other hand, the thermoelectric performance of the semimetal CoSi (its conduction and valence bands overlap by about 0.02 eV) is inferior to that of the silicides mentioned above; it is an n-type material with a comparatively large thermoelectric power (Asanabe *et al.*, 1964). When this material is combined with p-type CrSi_2 , one can obtain a $\text{CoSi}\text{--}\text{CrSi}_2$ thermocouple. As with the previously mentioned silicides, including FeSi_2 , mass production technology is established (Tokushima *et al.*, 1972; Uemura and Nishida, 1988), and developmental research on these materials is now in progress for thermoelectric generator applications. Since the electric power of these thermocouples is sufficient for power supplies for safety devices for gas and petroleum combustion instruments and so on, various ideas have been proposed in this field.

Note that since these materials are useful for application at higher temperatures with material costs much lower than those of the chalcogenides, special applications are possible, such as high-temperature controllers for combustion and chemical reaction instruments or furnaces and for thermoelectric generators that utilize waste heat.

Mesotaxially formed, buried layers of silicides have also been investigated. Such patterned layers of CoSi_2 have been used as gates for permeable-base transistors, and have been proposed for application as buried collector contacts for high-speed bipolar transistors, as ground planes for microstrip lines, and as mirrors in GaAs-Si modulators. In addition to CoSi_2 , Ti, Fe, Cr, Ni, and Y silicides have also been formed by mesotaxial implantation (Celler and White, 1992).

2.7 Ternary Semiconducting Compounds

As ternary compounds, Group II₂-III-VI₄ (defect chalcopyrite type), Group I₃-V-VI₄ (famatinite), and Group I₂-II-VII₄ (stannite) are known (see Parthé, Chapter 14 in Volume I). Chalcopyrite-type compounds have been most intensively studied of all ternary semiconducting compounds. They are expressed by the molecular formulae I-III-VI₂ and II-IV-V₂, and have the same tetragonal structure with $c/a \approx 2$ as chalcopyrite CuFeS_2 (E1₁, tI16) (Shay and Wernick, 1975). High-quality single crystals of 1 cm³ have been grown by the traveling heater method (Sugiyama *et al.*, 1989) and by the gradient freezing method (Ando and Katsui, 1981).

The principal features of chalcopyrite-type compounds are birefringence and a large, nonlinear optical constant. Typical compounds are AgGaS_2 , AgGaSe_2 , ZnGeP_2 and CdGeAs_2 . These compounds with a wide band gap and large lattice distortion show a degeneracy of the refractive index at a specified wavelength (Lotspeich, 1979). Recently, optical filters were prepared utilizing this property (Horinaka *et al.*, 1989).

Chalcopyrite-type semiconductors are direct transition type. Among them, CuAlS_2 and CuGaS_2 , belonging to the I-III-VI₂ compounds, have E_g above 2 eV and thus show potential for use in light-emitting devices in the visible region. The conduction type of as-grown crystals is usually highly resistive p-type, the resistivity of which can be decreased by annealing under a constituent chalcogen atmosphere.

High-quality, impurity-doped, heteroepitaxial films have been studied by means of MOVPE using cyclopentadienyl(triethylphosphine)copper(I) (CpCuTEP) as a Cu source material (Hara *et al.*, 1987) in a closed-tube halide VPE method with chloride sources and MBE.

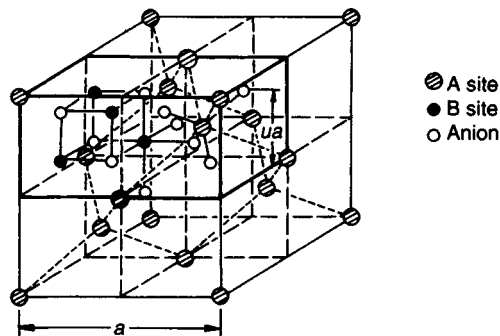


Figure 3. Spinel structure H1_1 (cF56) (unit cell of A sites). The heavy lines define a subcell which is one fourth of the unit cell of A sites

Recent interest has focused on CuInSe_2 as a material for a high conversion efficiency, thin-film solar cell without optical degradation. CuInSe_2 has an E_g of about 1.0 eV at room temperature and a high absorption coefficient, above $1 \times 10^5 \text{ cm}^{-1}$. The efficiency of solar cells with polycrystalline CuInSe_2 films, produced mainly by means of selenization and vacuum evaporation methods, exceeds 14% (Michell *et al.*, 1988; Basol and Kapur, 1990). Development of CuInSe_2 solid solutions and tandem structures with amorphous Si are in progress to realize conversion efficiencies above 20%.

2.8 Ferromagnetic Semiconducting Compounds

There are many kinds of magnetic semiconductors; most are binary and ternary compounds. The attention of many researchers has focused on a group of ferromagnetic chromium chalcogenide-based ternary compounds represented by MCr_2X_4 , where M stands for a nonmagnetic metal, such as Cd or Hg, and X is S or Se. They, like ferrite, are of spinel structure (H1_1 , cF56), as shown in Figure 3. The portion of the structure defined by the thick solid lines corresponds to one fourth of the unit cell in the spinel structure. All M ions lie at A sites, each of which is a lattice point at the center of a tetrahedron of anions. The Cr ions all lie at B sites, each of which is a lattice point at the center of an octahedron of anions. Neighboring pairs of Cr ions are ferromagnetically bonded.

Table 4 lists the properties of major chromium chalcogenide-based ternary compounds. Compounds having Cu atoms at A sites are metallic conductors and not ferromagnetic; compounds having Zn atoms at A sites are antiferromagnetic. Although these compounds are not ferromagnetic, they are listed in Table 4 because a comparison of ferromagnetic materials with nonferromagnetic

Table 4. Properties of chromium chalcogenide based ternary compounds

| Compound | Lattice constant a (Å) (1 Å = 0.1 nm) | u parameter ^a | Magnetic moment (4.2 K) (μ_B per molecule) | Curie point T_C (K) | Asymptotic Curie point θ (K) | Resistivity ρ (room temperature) (Ω cm) | Magnetic type | Conduction mode |
|-----------------------------------|---|-------------------------------|--|--|---|---|-------------------|-----------------|
| CdCr ₂ O ₄ | 8.596 | 0.396 | | Antiferromagnetic, Néel point $T_N = 9$ K | -83 | | Antiferromagnetic | |
| CdCr ₂ S ₄ | 10.239 | 0.375 | 5.55 | 86 | +152 | $\sim 10^3$ | Ferromagnetic | Semiconductor |
| CdCr ₂ Se ₄ | 10.745 | 0.383 | 5.94 | 121 | +204 | $\sim 10^4$ | Ferromagnetic | Semiconductor |
| HgCr ₂ S ₄ | 10.244 | 0.392 | 5.35 | 36 | +137 | | Ferromagnetic | Semiconductor |
| HgCr ₂ Se ₄ | 10.743 | 0.390 | 5.64 | 110 | +192 | | Ferromagnetic | Semiconductor |
| MnCr ₂ S ₄ | 10.108 | 0.387 | 1.27 | 80 | -12 ± 10 | $\sim 10^9$ | Ferrimagnetic | Semiconductor |
| FeCr ₂ S ₄ | 9.989 | 0.385 | 1.6 | 192 | -234 ± 14 | ~ 20 | Ferrimagnetic | Semiconductor |
| CoCr ₂ S ₄ | 9.916 | 0.382 | 2.4 | 235 | -390 ± 40 | $\sim 10^3$ | Ferrimagnetic | Semiconductor |
| CuCr ₂ S ₄ | 9.822 | 0.381 | 4.58 | 420 | +390 | $\sim 10^{-4}$ | Ferromagnetic | Metallic |
| CuCr ₂ Se ₄ | 10.337 | 0.380 | 4.94 | 460 | +465 | $\sim 10^{-4}$ | Ferromagnetic | Metallic |
| CuCr ₂ Te ₄ | 11.137 | 0.379 | 4.93 | 365 | +400 | $\sim 10^{-4}$ | Ferromagnetic | Metallic |
| ZnCr ₂ O ₄ | 8.328 | 0.387 | | $T_N = 16$ K | -392 | | | Semiconductor |
| ZnCr ₂ S ₄ | 9.983 | 0.385 | | $T_N = 18$ K | +18 | | Antiferromagnetic | Semiconductor |
| ZnCr ₂ Se ₄ | 10.443 | 0.384 | | $T_N = 23$ K | +115 | | Antiferromagnetic | Semiconductor |

^aThe u parameter gives the lattice site of the anion (ideally $u = 0.375$, see Figure 3).

materials, both having the same crystal structure, is of significance in understanding the chromium chalcogenide-based magnetic semiconductors.

With the above exceptions, chromium chalcogenide ternary compounds are both ferromagnetic and semiconducting, and they show unique conducting behavior as general magnetic materials. These compounds have been the objects of numerous studies on their electrical, magnetic, and optical properties. A combination of these properties seems promising for new electronic devices and is of worldwide interest from the viewpoints of physicochemical qualities and applications. Ferromagnetic semiconductors containing Cd or Hg atoms at the A sites can be doped with impurities to exhibit p-type or n-type conduction. These materials have charge carriers with the largest mobilities among all the magnetic materials. An appropriate chemical treatment makes the magnetic anisotropy of these compounds less significant and forces them to have a narrow microwave absorption width. Thus, we may be able to find new fields for their application.

CdCr_2Se_4 is a material that has been studied as a thin film for p-n junction elements (Wen *et al.*, 1968). HgCr_2Se_4 and CdCr_2Se_4 are promising materials for tunable semiconductor lasers for the mid-infrared region (Masumoto and Koguchi, 1976, 1982; Koguchi and Masumoto, 1978; Takahashi *et al.*, 1983). The wavelength of their laser oscillations changes with ambient temperature and applied magnetic field; the rate of change is about 10 times that of IV-VI semiconducting compounds. For example, the optical absorption edge of HgCr_2Se_4 is 0.83 eV (1.49 μm) at 300 K; it sharply decreases with decreasing temperature (a phenomenon known as the red shift), reaching 0.28 eV (4.43 μm) at 4.2 K (Harbeke *et al.*, 1968; Lehmann and Emmenegger, 1969). At the Curie temperature (about 120 K), the edge is further decreased by 10% with the application of a 10 kG magnetic field (Lehmann and Emmenegger, 1969).

3. Electrical Applications

3.1 Materials with High Electron Mobility

Si has the following characteristics: (i) its electron mobility is relatively high; (ii) high-purity and high-perfection single-crystal wafers up to eight inches in diameter are commercially available; (iii) insulating SiO_2 is quite compatible with Si and is highly useful for diffusion masking and passivation; (iv) its strength is high; and (v) its E_g is moderate for integration with other materials.

These characteristics make Si highly suitable for integrated electronic applications. Although Si at present is certainly in the very large scale integration (VLSI) age, attempts to realize with compound semiconductors better integrated circuits (ICs) than those with Si have been increasingly made.

In materials for high-speed device applications, high electron mobility and high saturation carrier velocity are required. Table 5 shows a comparison of characteristics among high-mobility Group III-V semiconductors. The narrower the band gap and the smaller the effective mass, the higher is the electron mobility. Saturation velocity has the same trend as the mobility. The mobility of carriers is affected by various scattering mechanisms, and generally scattering by optical phonons is predominant in compound semiconductors.

GaAs, InP, InSb and InAs show high electron mobilities and high saturation velocities relative to Si. They therefore are suitable for high-speed device applications. In GaAs, semi-insulating crystals are commercially available, and thus low power consumption is expected, as well as high-speed operation. Both InSb and InAs have higher electron mobility than GaAs. However, conduction in both of these semiconductors, owing to their band gaps at 300 K, is intrinsic and, hence, low temperatures are needed for operation with a high margin of reliability.

There are two conceptions in the further development of high-speed integrated circuits using compound semiconductors. One direction aims at speeds above those of Si ICs, and the other direction is toward Si/VLSI devices resistant to radiation damage and with low power consumption for space development applications. In the latter case speed is sacrificed. In the former, as well as in GaAs metal Schottky field effect transistors (MESFETs), the IC being at an LSI level, superhigh-speed devices such as the high electron mobility transistor (HEMT), the heterojunction bipolar transistor (HBT), the permeable-base transistor (PBT), the static inductance transistor (SIT), and the metal insulator semiconductor field effect transistor (MISFET) are objectives.

3.2 GaAs MESFET ICs

The driving force for GaAs FET IC developments is the exploitation of electron mobilities several times larger than that of Si by direct circuit integration on a semi-insulating substrate using ion implantation and extension of recently developed, ultrahigh-resolution processing techniques to Group III-V semiconductors.

Table 5. Property comparison of high electron mobility semiconductors

| Property | InSb | InAs | GaSb | InP | GaAs | Ge | Si |
|--|--------------------|--------------------|----------------------|-------------------|-------------------------------|----------------------|----------------------|
| E_g (eV) 300 K | 0.18 | 0.36 | 0.67 | 1.35 | 1.43 | 0.665 | 1.107 |
| 77 K | 0.228 | 0.41 | 0.80 | 1.40 | 1.47 | 0.7343 | 1.1532 |
| Lattice constant (nm) | 0.64787 | 0.6058 | 0.6095 | 0.58687 | 0.5653 | 0.5658 | 0.54198 |
| Electron affinity (eV) | 4.59 | 4.9 | 4.06 | 4.38 | 4.07 | 4.13 | 4.01 |
| Electron mass ^a m/m_0 | | | | | | | |
| m_e | 0.0139 | 0.024 | 0.041 | 0.0810 | 0.0667 | 0.0815 | 0.1905 |
| m_h | 0.32 | 0.41 | 0.26 | 0.56 | 0.71 | 0.32 | 0.50 |
| Hall mobility at 300 K ($\text{cm}^2 \text{V}^{-1} \text{s}^{-1}$) | | | | | | | |
| μ_e | 80 000 | 33 000 | 4000 | 4500 | 8500 | 3800 | 1450 |
| μ_h | 450 | 450 | 1420 | 150 | 435 | 1800 | 500 |
| μ_e ($\text{cm}^2 \text{V}^{-1} \text{s}^{-1}$) at 77 K | 1×10^6 | 1.5×10^5 | | 4.5×10^4 | | 3.6×10^4 | 2.4×10^4 |
| Saturation drift velocity v_m (cm s^{-1}) | 5.2×10^7 | 3.2×10^7 | $< 6 \times 10^6$ | 2.3×10^7 | $1.7\text{--}2.0 \times 10^7$ | 6×10^6 | 1×10^7 |
| Saturation field E_m (V cm^{-1}) | 5.6×10^2 | 4×10^3 | | 1.2×10^4 | 5.2×10^3 | 4×10^3 | 2×10^4 |
| Intrinsic carrier concentration | | | | | | | |
| n_i (cm^{-3}) 300 K | 2×10^{16} | 1×10^{15} | 2.7×10^{12} | 1.4×10^7 | 1.2×10^7 | 1.8×10^{13} | 1.2×10^{10} |
| 77 K | 3.8×10^9 | 3.5×10^3 | | | | | |

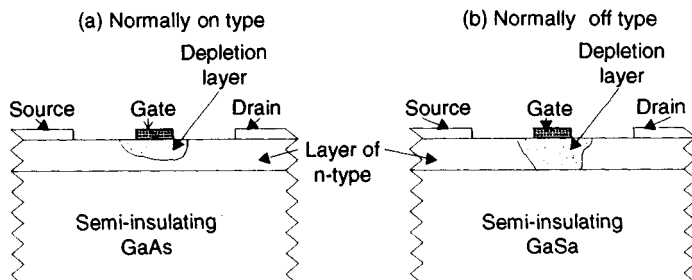
Currently under development are MESFETs, metal oxide semiconductor (MOS) FETs, junction-type FETs and so on, the FET being a fundamental device for GaAs ICs. Because of the underdeveloped planar techniques for p–n junctions, the leading device type is the MESFET.

Studies of GaAs ICs started in 1970, at which time the Si LSI was developed. By 1974, the normally-on GaAs IC was proposed. In 1977 and 1978, integrated circuits and normally-off ICs were produced, respectively. Since then, remarkable progress in the degrees of integration and speed achieved has been made yearly.

A MESFET is a transistor with a structure which is formed from a Schottky gate electrode and source and drain ohmic electrodes on an n-type semiconductor layer. A metal–semiconductor ohmic contact is used as a gate electrode in the MESFET, instead of a p–n junction. The operational function is such that the gate input signal changes the spread of the Schottky contact depletion layer, and thus changes the thickness of the

channel layer, which provides the conductance between the source and drain. Figure 4 shows the two typical structures of MESFETs. There are normally-on elements (depletion type) and normally-off elements (enhancement type) in fundamental circuit constructions of MESFETs. In the normally-on type, the current is cut off by applying a negative electric field. On the other hand, in the normally-off type, the source and drain pinch off at the built-in voltage and are turned ‘on’ by a positive voltage.

Although normally-on types operate at very high speed, the power consumption is large, the circuit is complex, the occupied area is large, and hence they are unsuitable for integration. Normally-off types have simple circuit construction and small power consumption, and thus are suitable for high integration. However, normally-off types possess several problems still to be solved: the manufacturing conditions are severe, the logic amplitude is small, the limitation on the pinch-off voltage is strict and the switching speed is rather low. Developments of GaAs FET ICs are making

**Figure 4.** Fundamental structures of the two MESFET types

steady progress through a reiterative process of experimental production and evaluation.

A serious problem on the performance side of the GaAs MESFET LSI is that, compared with the Si LSI, the speed is not as high as expected. Furthermore, there is a problem of low yield. Uniformity of characteristics is important for LSI, and hence reliable achievement of a high-quality, semi-insulating GaAs substrate is necessary.

3.3 New High-speed Devices

Superhigh-speed devices based on new operational principles have been proposed as a result of marked progress with heterojunction techniques and high-resolution processing techniques. Here, HEMTs, HBTs, PBTs, SITs and MISFETs are introduced.

3.3.1 HEMTs

A modulated, doped GaAs/AlGaAs heterojunction is a junction formed from undoped GaAs and AlGaAs heavily doped with an n-type impurity. In single heterojunctions and in a 'superlattice' using modulated, doped GaAs/AlGaAs, the mobility, especially at low temperatures, is greatly increased compared to GaAs

of a nearly equal carrier concentration (Dingle *et al.*, 1978).

Since in such a junction as GaAs/Al_{0.3}Ga_{0.7}As the electron affinity of GaAs ($E_g = 4.07$ eV) is larger than that of Al_{0.3}Ga_{0.7}As ($E_g = 3.75$ eV), electrons supplied from the donor in n-type AlGaAs flow to the GaAs side and are accumulated in quite a narrow region of the heterojunction, which then forms a two-dimensional electron gas (Dingle *et al.*, 1978). Conduction electrons are spatially isolated from the donor and are less scattered by ionized and neutral impurities; therefore, the mobility is exceedingly high (Hiyamizu and Mimura, 1981).

The HEMT is a superhigh-speed device utilizing a single, modulation-doped heterojunction (Mimura *et al.*, 1980). Fundamental to the HEMT is a heterojunction gate. Figure 5 shows the structure and schematic band diagram near the gate of the MESFET and the heterojunction gate FET. In the MESFET, the channel layer must have impurity concentrations of about 10^{16} cm^{-3} in order to switch the channel and to obtain the required channel current. Consequently, subsequent impurity scattering caps the electron mobility at the channel. On the other hand, in heterojunction types impurity concentrations in the channel are below 10^{15} cm^{-3} . A heterojunction gate with high impurity concentrations is constructed by forming a layer with a larger band gap

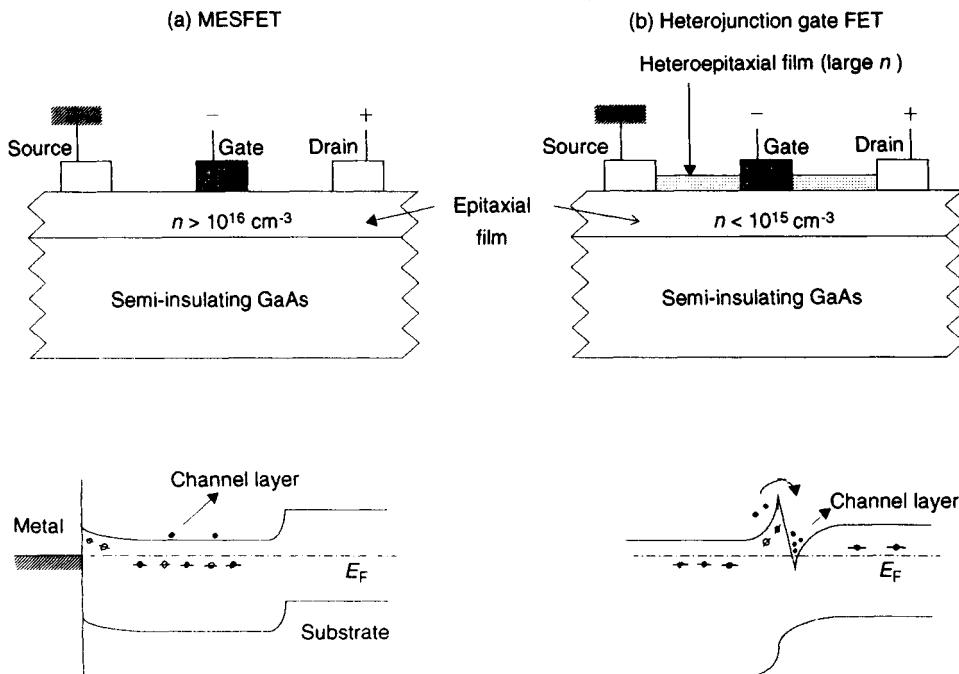


Figure 5. Comparison of MESFET and heterojunction gate FET (upper, structures; lower, schematic band diagrams near the gates)

and smaller electron affinity than the channel. A sufficient supply of the required electrons is obtained from the high-concentration layer.

In the HEMT structure, the low-field electron mobility is $8 \times 10^3 \text{ cm}^2 \text{ V}^{-1} \text{ s}^{-1}$ at 300 K, twice that of the GaAs MESFET, and the saturation velocity is $1.5\text{--}1.9 \times 10^7 \text{ cm s}^{-1}$; hence the current gain cutoff frequency f_T in switching is high. For example, f_T was 80 GHz at a gate length of $0.25 \mu\text{m}$, twice that of a GaAs MESFET with the same gate length (Abe *et al.*, 1987).

As materials for HEMTs, AlGaAs/InGaAs/GaAs (Chao *et al.*, 1987) and InAlAs/InGaAs/InP (Henderson, 1987) have also been studied.

3.3.2 HBTs

The concept of the HBT is defined in Shockley's patent (Shockley, 1948). With the advancement of heterojunction technology and ion implantation technology, devices have since been experimentally produced and their performance confirmed.

The features of the HBT are a high degree of freedom in structural design and high speed, because movements of electrons and holes are separately controlled (Kroemer, 1982).

Injection of minority carriers from base to emitter is so restricted, compared to homojunction bipolar transistors, as to allow doping with high concentrations of carriers. Thus, base resistance, base thickness and conductance between base and collector decrease, and the design of transistors with high speed and excellent high-frequency characteristics can be realized.

Recently, n-p-n-type (Beneking and Su, 1981) and p-n-p-type (Su *et al.*, 1981) bipolar transistors of homojunction or heterojunction types using GaAs with AlGaAs have been examined. Also, an HBT with an f_T of 105 GHz and a maximum oscillation frequency f_{MAX} of 55 GHz was developed through improvements in device structures and processing (Ishibashi, 1987).

A review article dealing with recent HBT studies has been published (Sugeta and Ishibashi, 1990).

3.3.3 PBTs and SITs

In both PBT (Bozler and Alley, 1980) and SIT (Nishizawa *et al.*, 1975) devices there is a vertical FET, as is expected for superhigh-frequency operation.

The PBT has the same structure as a base-embedded SIT (Alley *et al.*, 1980; Vojak *et al.*, 1983), and consists of a grating made from a thin film of tungsten which is embedded in an epitaxial GaAs layer. The electrons flow from emitter to collector through slits in the metal

film. The tungsten grating is used as a gate, and a gate length of about $0.1 \mu\text{m}$ is easily attainable. In a theoretical comparison of PBT, MESFET and HEMT devices with very short gate lengths, an f_{MAX} above 500 GHz was projected in PBTs for an effective gate length of $0.15 \mu\text{m}$ (Das, 1987).

The structure of an SIT is fundamentally the same as that for a PBT but the dimensions and the impurity concentrations of the active layer differ from those of the PBT. In an SIT, the distance between source and gate is extremely short, and the structure has a sufficiently small resistance R_s between source and gate that the product of R_s and mutual conductance G_m is $\ll 1$ (Sugeta, 1986). Furthermore, the impurity concentration is so low that the whole active layer is depleted at the gate voltage.

The SIT is also useful for high electric power applications (Nishizawa, 1986).

3.3.4 MISFETs

The electron saturation drift velocity of InP is 1.5 times as large as that of GaAs. Theoretical (Frey and Wada, 1979) and experimental studies of high-speed InP FETs have been made.

To realize an MESFET in InP is difficult, owing to the small potential barrier of the Schottky junctions in the n-type layer. In an InP MIS-type structure, an electron accumulation layer and an electron inversion layer can be easily formed at the insulating film-InP interface (Lile *et al.*, 1978), and hence InP is suitable for MISFET applications. This situation is quite in contrast to the case of GaAs (Meiners, 1978).

The largest factor in the realization of high-speed InP MISFETs is the formation of a high-quality gate-insulating film. Enhancement-type MISFETs using SiO_2 , Si_3N_4 , P_3N_5 or anodic Al_2O_3 as the gate-insulating film have been investigated. The channel layer was directly formed on a semi-insulating substrate surface in InP, and an effective mobility of about $3000 \text{ cm}^2 \text{ V}^{-1} \text{ s}^{-1}$ was attained for an Al_2O_3 /native oxide double-gate structure.

A problem common to InP MISFETs is the drift of the drain current. Recently, drain current drift below $\pm 10\%$ of the initial value was attained (Hasegawa, 1984). From this result, it was speculated that the drift is probably owing to interface levels being distributed energetically and spatially below a conduction band.

Furthermore, enhancement-type MISFETs using InGaAs have been studied and an effective mobility of $1500 \text{ cm}^2 \text{ V}^{-1} \text{ s}^{-1}$ was obtained using plasma oxidation of Al_2O_3 as the gate film.

Chapter 5

Superconductor Applications

Z. J. John Stekly and Eric Gregory

Intermagetics General Corporation, 6 Eastern Road, Acton, MA 01720, USA

1. Introduction—Characteristics of A15 Superconductors

When certain materials are cooled below a critical temperature T_c , their electrical resistance drops to zero and they carry electrical current with no power dissipation and no heating. This phenomenon is termed superconductivity and is a result of a small attraction between some of the conduction electrons. This attraction occurs through interaction with the positive ion lattice. The effect is very weak and is easily destroyed by thermal agitation. This is why all superconductors require a cryogenic environment. Most practical superconducting devices operate in liquid helium (4.2 K), although some of the so-called 'high-temperature superconductors' can operate in liquid nitrogen (77 K) and even maintain a measure of superconductivity above 100 K.

Superconductors are used both in electronic circuitry and in bulk applications, most of which are based on high-field electromagnetic coils. To understand the use of superconductors in such devices, one must understand the relationship between superconductivity and magnetism.

Above a certain critical field H_c , superconductivity is destroyed and the material then behaves normally. Superconductivity is also destroyed, even in the absence of an external magnetic field, when the current flowing through the superconductor reaches a value J_c at which its associated magnetic field exceeds the critical value.

Many pure metals are what are termed type I superconductors and these, when cooled below T_c , totally expel magnetic flux and are unable to carry significant currents at even moderate fields. Some metals, alloys,

and many compounds exhibit a different behavior to that described above. When the magnetic field exceeds a value of H_{c1} , the flux can penetrate into the bulk of the material in the form of fluxoids (individual units of flux surrounding local normal regions) until a much higher magnetic field H_{c2} is reached, where the fluxoids overlap and the material goes normal. In an ideal material with no imperfections in the field region between H_{c1} and H_{c2} , transport currents would normally cause the fluxoids to move and the material would go normal prematurely resulting in low critical current densities J_c . However, grain boundaries, dislocations, and other imperfections can pin the fluxoids and enable a high J_c to be obtained in these type II materials even at high magnetic fields.

From the above, it can be seen that T_c and H_{c2} are physical characteristics of a given composition, but J_c is more dependent on the structural properties and history of the material.

Under changing magnetic fields, the fluxoids tend to move and thus generate heat. If the filaments of the superconductor are small and surrounded closely by material of high thermal conductivity, i.e. Cu or Al, heating of the superconductor is minimal and the material remains in the superconducting state; hence the need for fine filaments in a high-conductivity metal matrix.

Although the phenomenon of superconductivity was discovered by Onnes (1911), it was not until 50 years later that the first practical 'high-field', 8 T magnet was prepared by Kunzler *et al.* (1961). It was wound from wire made of the intermetallic A15 (cP8) compound Nb_3Sn . Many of the superconducting devices that have been made since the 1960s have employed a ductile

solid-solution alloy of Nb-Ti. This material, however, can only be used to generate, and/or operate in, fields up to 11 T, even when the temperature is reduced to 1.8 K. For fields above this value and for higher-temperature operation, other superconducting materials are required. Before the advent of high- T_c oxide superconductors, discovered by Bednorz and Müller (1986), these materials were generally A15 (cP8) compounds of the type A_3B .

In the manufacture of practical high-field superconductors, the aim is to optimize simultaneously H_{c2} , T_c , J_c^* and mechanical behavior. This must be done in material which is in either a tape or wire form and hence suitable for winding into coils. Tapes have been, and are being, manufactured for limited applications but the most widely used product form is wire. Almost all practical superconductors that are made as wire consist of a composite of fine, twisted, superconducting filaments in a nonsuperconducting matrix. Also in the composite is a material of high thermal and electrical conductivity which provides stabilization against transients which may otherwise drive the superconductor into the normal state. These composites have properties dependent on the superconductor itself (intrinsic properties) and those more related to the structure and constitution of the composite (extrinsic properties). While these are, of course, interrelated, they will be dealt with separately in this discussion. The intrinsic superconducting properties of the A15 compounds will be dealt with first. Later sections will be devoted to the fabrication and properties of the multifilamentary composites.

2. Intrinsic Properties

2.1 Structure

In the A_3B structure the B atoms, which can be either transition or nontransition metals, are arranged on a body-centered cubic (b.c.c.) lattice and the A atoms, which are always transition metals, are in pairs each of which straddles the center of a face of the cube. This arrangement results in orthogonal chains of closely spaced A atoms running through the crystal structure. It is believed that these chains lead to the good superconducting properties of many of the materials. As a consequence, it is important that their continuity is maintained if the highest superconducting properties are

to be achieved. For this reason, stoichiometry and order in the structure are important. This does not mean that single crystals or highly textured polycrystals are a necessity as they are in some oxide superconductors. This is owing to a difference in coherence length ξ . In Nb_3Sn , ξ is greater than the grain boundary width, and this is not the case in the oxide materials.

Of the more than 70 compounds showing the A15 structure, more than 50 show superconducting properties (Table 1). Several are metastable, however, and can only be produced by physical vapor deposition (PVD), chemical vapor deposition (CVD), high-pressure techniques or fast-quenching techniques. Until the advent of the oxide superconductors, as reported by Bednorz and Müller (1986), the compound with the highest identified critical temperature $T_c = 23$ K was Nb_3Ge , as noted by Gavalier (1973).

Table 1. Superconducting transition temperatures of binary A15 phases

| Nontransition elements | T_c (K) | Transition elements | T_c (K) |
|------------------------|-----------|---------------------|-----------|
| Ti_3Sb | 6.5 | Ti_3Ir | 4.2 |
| | | Ti_3Pt | 0.5 |
| $Zr_{80}Sn_{20}$ | 0.92 | | |
| $Zr-Pb$ | 0.76 | Zr_3Au | 0.9 |
| $Zr_{-3}Bi$ | 3.4 | | |
| $V-Al$ | 14 | $V_{29}Re_{71}$ | 8.4 |
| V_3Ga | 15.9 | $V_{30}Os_{50}$ | 5.7 |
| V_3Si | 17.0 | $V_{65}Rh_{35}$ | ~1 |
| $V_{-3}Ge$ | 6 | $V_{63}Ir_{37}$ | 1.7 |
| $V_{-3}Ge$ | 11 | $V_{-3}Pd$ | 0.08 |
| $V_{-79}Sn_{-21}$ | 3.8 | V_3Pt | 3.7 |
| $V_{77}As_{23}$ | 0.2 | $V_{76}Au_{24}$ | 3 |
| $V_{76}Sb_{24}$ | 0.8 | | |
| Nb_3Al | 19.1 | $Nb_{75}Os_{25}$ | 1.0 |
| Nb_3Ga | 20.7 | $Nb_{75}Rh_{25}$ | 2.6 |
| $Nb_{-3}In$ | 9.2 | $Nb_{72}Ir_{28}$ | 3.2 |
| $Nb_{82}Si_{18}$ | 4.4 | Nb_3Pt | 11 |
| $Nb-Si$ | 11-17 | $Nb_{-3}Au$ | 11.5 |
| $Nb-Ge$ | 17 | | |
| $Nb-Ge$ | 23 | $Ta_{85}Pt_{15}$ | 0.4 |
| Nb_3Sn | 18 | $Ta_{-80}Au_{20}$ | 0.55 |
| $Nb-Sb$ | 2 | | |
| $Nb_{-3}Bi$ | 3 | $Cr_{72}Ru_{28}$ | 3.4 |
| | | $Cr_{73}Os_{27}$ | 4.7 |
| $Ta_{-3}Ge$ | 8 | $Cr_{78}Rh_{22}$ | 0.07 |
| $Ta_{-3}Sn$ | 8.3 | $Cr_{82}Ir_{18}$ | 0.75 |
| $Ta_{-3}Sb$ | 0.7 | | |
| | | $Mo_{40}Tc_{60}$ | 13.4 |
| Mo_3Al | 0.58 | $Mo_{-65}Re_{-35}$ | ~15 |
| Mo_3Ga | 0.76 | $Mo_{75}Os_{25}$ | 13.1 |
| $Mo_{77}Si_{23}$ | 1.7 | $Mo_{78}Ir_{22}$ | 8.5 |
| $Mo_{77}Ge_{23}$ | 1.8 | $Mo_{82}Pt_{18}$ | 4.6 |
| | | $W_{-60}Re_{-40}$ | 11 |

* H_{c2} is the upper critical field of the superconductor, T_c is the critical temperature of the superconductor, and J_c is the current-carrying capacity of the superconductor.

2.2 Phase Diagrams of A15 Compounds

It can be seen from Table 1 that the compounds of niobium and vanadium exhibit the highest values of T_c , and consequently these have been studied most widely (Flükiger, 1981). Figure 1 shows the areas of stability of the A15 compounds in the Nb–Ga, Nb–Al and Nb–Ge binary systems. It is obvious that the stoichiometric composition is stable only near melting at the eutectic or peritectic temperature. In contrast the V–Ga system, where the A15 compound forms by ordering of the V-rich solid solution rather than by a peritectic reaction (Figure 2), shows considerable stability on both sides of V_3Ga stoichiometry.

The binary system which has been investigated most comprehensively is Nb–Sn because of its wide usage. While there is some disagreement on the shape of the single-phase A15 field at low temperatures, the generally accepted diagram at elevated temperatures is shown in Figure 3. It has become common practice to prepare the stoichiometric A15 compound in the solid state by the introduction of the B element from a copper matrix. The copper does not enter into the bulk structure but appears to be present in the grain boundaries, where it slows down grain growth but does not appear to lower T_c as reported by Smathers and Larbalestier (1983).

It was reported by Benz (1966) that while Nb_3Sn tape was produced in the past by immersing niobium strip into molten tin (V_3Ga tape is produced by a similar method), the multifilamentary wire is frequently

produced from a bronze matrix. The latter can be prealloyed or formed immediately prior to the formation of Nb_3Sn , as in the internal-tin process.

The above discussion concerned binary systems; and, while no true ternary compounds of the A15 type are known to exist, it is possible to stabilize the A15 structure in some cases by adding a third element. One such stabilized structure is $Nb_3Al_{0.75}Ge_{0.25}$, which has the highest H_{c2} of all A15 compounds (43.5 T). Many different elements have been added to Nb_3Sn to control properties, processing, or microstructure; the additives most frequently employed commercially are Ta (Livingston, 1978) and Ti (Tachikawa *et al.*, 1991). These elements increase the normal-state resistivity faster than they cause a reduction in T_c and the result is an increase in the high-field J_c . These third elements may also have other effects such as changing the kinetics of diffusion and refining the grain structure.

It is generally agreed that the primary pinning centers in the A15 compounds are the grain boundaries, as described by Livingston (1978), and they are particularly effective at low fields. Above a reduced magnetic field h ($h = H/H_{c2}$) of 0.6, the pinning force F_p has a field dependence shown by the equation

$$F_p = J_c H = [(H_{c2}^*)^{5/2} / A k^2] h^{1/2} (1 - h)^2$$

where J_c is the superconductor critical current density and H is the applied magnetic field. H_{c2}^* is obtained by extrapolation of a $J_c^{1/2} H^{1/4}$ versus H curve, A is a

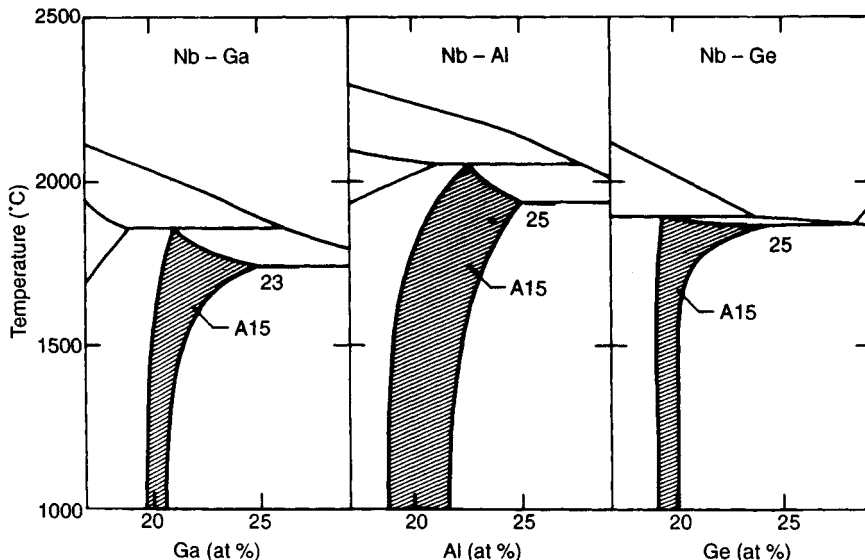


Figure 1. Phase diagrams showing the locations of the A15 phases in the Nb–Ga, Nb–Al and Nb–Ge binary systems (by permission of ASM International)

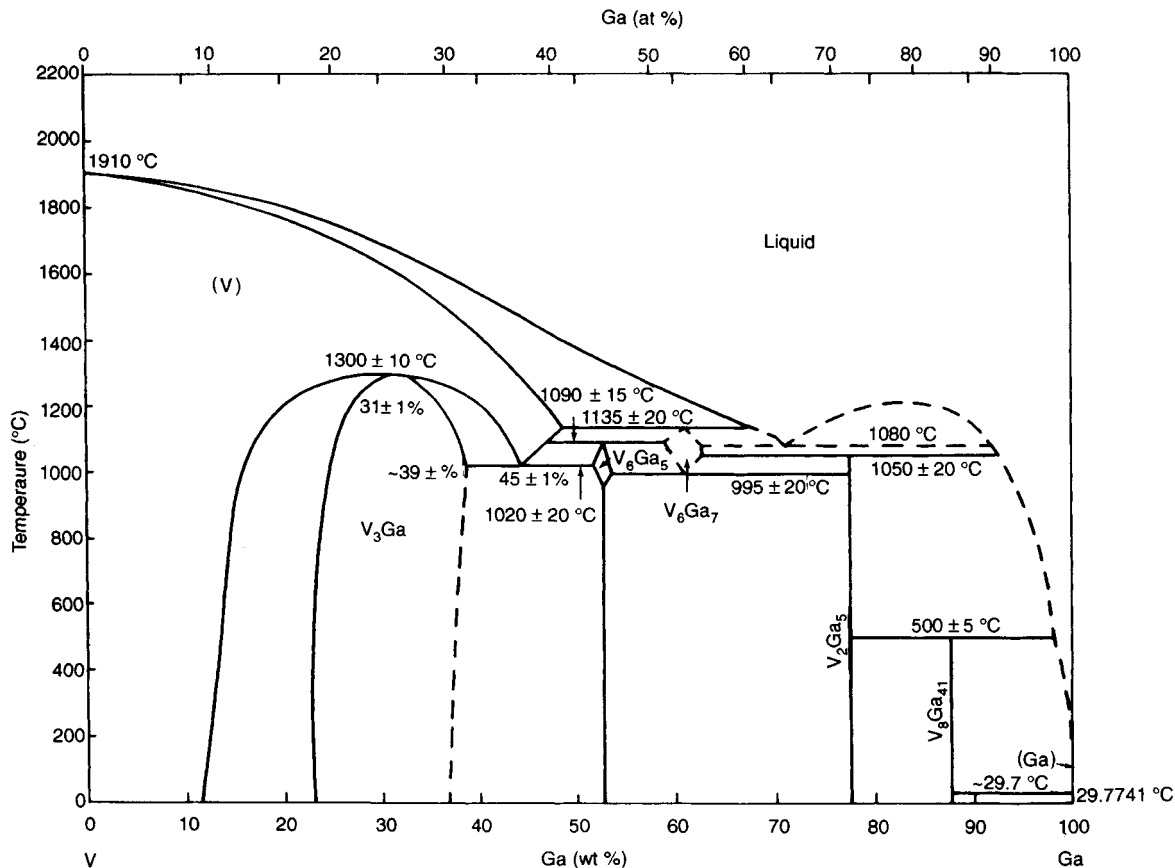


Figure 2. Phase diagram for the V-Ga system (by permission of ASM International)

constant and k is the ratio of the magnetic field penetration to the coherence length for the superconductor (Ginsberg-Landau parameter). The maximum pinning force occurs at $h=0.25$, and the general effect of the alloying elements that increase H_{c2} is to reduce $F_{p,max}$. This results in a crossover in the plots of J_c against field. The alloyed material has a lower J_c at lower fields and a higher one at higher fields (see Figure 4).

2.3 Strain Effects

As reported by Ekin (1984), the elastic strain sensitivity of B_{c2}^* ($\mu_0 H_{c2}$) and T_c in A15 compounds is an intrinsic property of the superconducting material and depends very little on reaction conditions, configuration or metallurgical processing. Figure 5 shows the effect of strain on the B_{c2} of a number of different A15 compounds. The most commonly used A15 material

Nb₃Sn has one of the greatest elastic strain sensitivities. While Nb₃Al is less sensitive to strain, it is, nevertheless, quite sensitive.

The third and fourth element additions to Nb₃Sn do not lessen the strain sensitivity of the critical field of this superconductor. The addition of 1.5 at% Ti leaves it unchanged while the addition of 7.5 wt% Ta makes the critical field slightly more sensitive to strain. Importantly, the additives do lessen the strain sensitivity of J_c at a given magnetic field. This is because the maximum value of the bulk average upper critical field (B_{c2m}) is enhanced and the further the operating field is from B_{c2m} , the less is the effect of the strain on J_c . Additional effects of strain such as prestrain and the irreversible strain limit are mainly a function of conductor configuration and processing and will be discussed under extrinsic properties.

In this discussion we will only deal with those A15s that have combinations of high H_{c2} and high T_c and

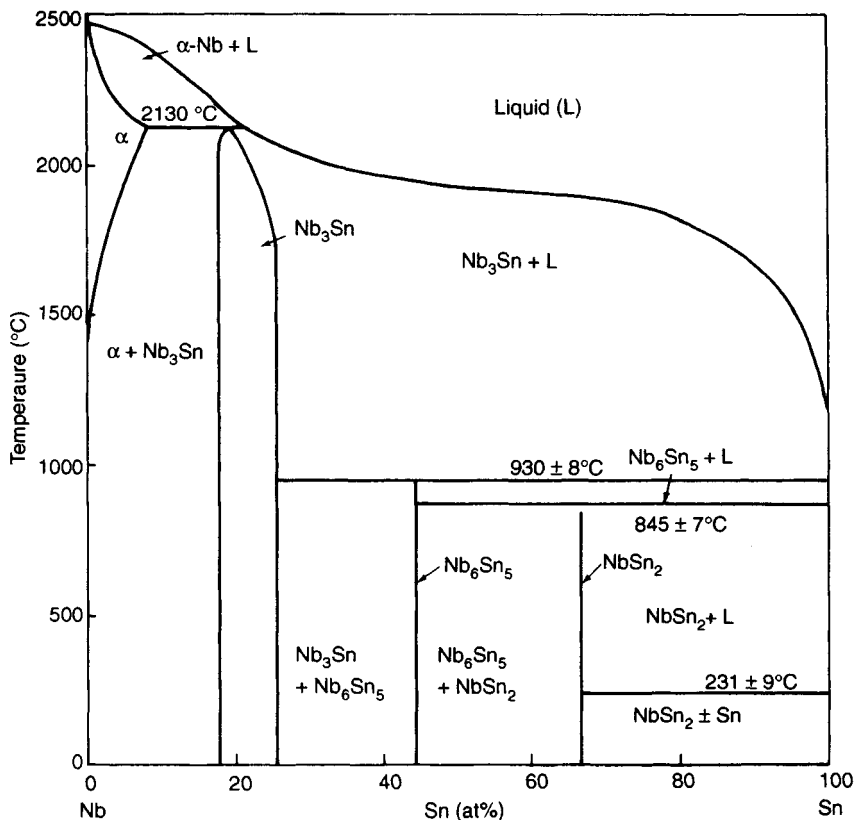


Figure 3. Phase diagram for the Nb-Sn binary system (by permission of ASM International)

can be fabricated into practical superconductors. These are Nb₃Sn, (Nb, Ti)₃Sn and (Nb, Ta)₃Sn, and to a lesser extent V₃Ga, Nb₃Al, Nb₃Ge and Nb₃(Al, Ge).

3. Extrinsic Properties

Once an A15 compound with an adequate B_{c2} and T_c , both essentially intrinsic properties, has been selected, much of the effort to make a practical superconductor is devoted to fabrication techniques and the optimization of the current-carrying capability J_c and mechanical properties. It is important to realize that B_{c2} and T_c can, however, be changed, depending on the conditions involved in the formation of the Nb₃Sn.

Before considering the details of the fabrication techniques used, we will discuss some of the factors concerned with the formation of Nb₃Sn and the effect of these on properties. These effects are of a general nature and apply, in some manner, to all the fabrication techniques used.

3.1 Nb₃Sn Formation and Superconducting Properties

The approach most frequently used for the formation of Nb₃Sn, its ternaries and V₃Ga in wire or tape form has been the solid-state diffusion process from a bronze matrix. This matrix can either be a pre-alloyed bronze (the bronze process, see below) or a higher-tin bronze formed by diffusion of Sn into Cu immediately prior to the A15 formation (the internal-tin process).

In the case of Nb₃Sn, the rate of formation of the layer of compound is measurable at 550 °C, but temperatures in the range 650–750 °C are most frequently used for commercial heat treatment. The superconducting properties that result from such heat treatment are affected significantly by the interaction of a number of variables. These variables include the duration and temperature of the heat treatment, the initial Sn concentration in the matrix, the ratio of available Sn to Nb, the Nb filament size, and the presence

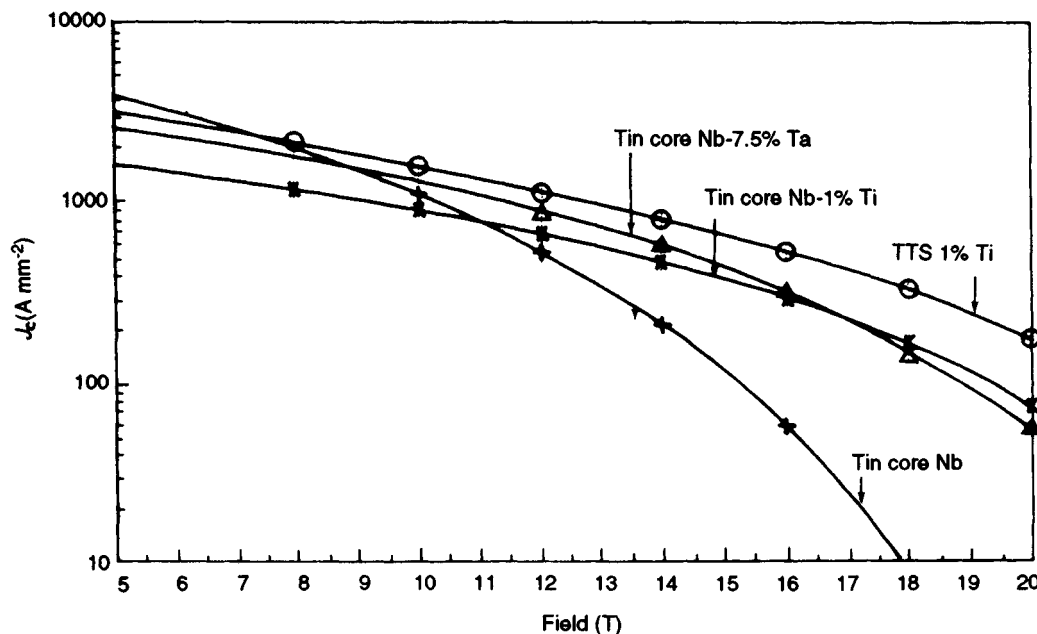


Figure 4. Comparison of J_c versus field curves for various Nb_3Sn -based superconducting materials. Various amounts of Ta and Ti are added to the Nb prior to reaction. There are four curves for a tin core in a niobium conductor and one for a tubular tin source (TTS) surrounding a central array of niobium rods (by permission of IGC)

of dopants in the filaments and/or the matrix. The formation conditions for Nb_3Sn and how they affect both J_c and T_c have been discussed in detail for many years (Suenaga *et al.*, 1975; Suenaga, 1985; Suenaga and Clark, 1980).

T_c is primarily related to the stoichiometry of the Nb_3Sn layer although, as will be seen below, it is significantly depressed by compressive stress. The time to reach the maximum value of T_c decreases as the temperature at which the Nb_3Sn is formed increases. T_c varies across the layer thickness in the early stages of the reaction, and this variation is greatest at low heat-treatment temperatures. After the Nb has been completely reacted, a uniform T_c is obtained. A high T_c may also be desirable to secure maximum J_c properties at fields greater than 10 T. Although large grains are usually present when a high T_c is obtained, grain size is thought to be unimportant, as pinning is controlled by the flux-line lattice in this field region and not by grain boundaries.

When measurements are made at low fields and 4.2 K, the change in T_c does not significantly affect J_c . At low fields, grain boundaries are the primary source of pinning, and the lower treatment temperatures lead to smaller grain sizes and improved pinning. The critical current density J_c in the conductors frequently exhibits

a peak as a function of reaction time at each temperature, and the locus of the peak increases monotonically with increased time and decreased temperature of reaction (Martin *et al.*, 1979).

J_c can be increased by increasing the tin content in the bronze. The amount of required bronze is thus reduced, resulting in a decrease in the bronze to niobium ratio. For a given duration and temperature of heat treatment, this increase in tin content will cause faster diffusion and thus lead to the formation of more Nb_3Sn . The maximum amount of tin that can be introduced into copper without causing the appearance of a second phase is 14 wt%, and this second phase causes fabrication problems when the prealloyed-bronze approach is used. The internal-tin approach, which does not call for the formation of the high-tin bronze until the end of wire fabrication, does not suffer from this restriction on the amount of tin that can be introduced.

One phenomenon which takes place in the formation of Nb_3Sn by the diffusion method is that of the development of Kirkendall porosity (Smigelskas and Kirkendall, 1947). It was pointed out some time ago by Easton and Kroege (1979) that, in the prealloyed-bronze approach, increasing the reaction time causes degradation of J_c at smaller strains. This effect was said to offset the improvement of J_c due to increased

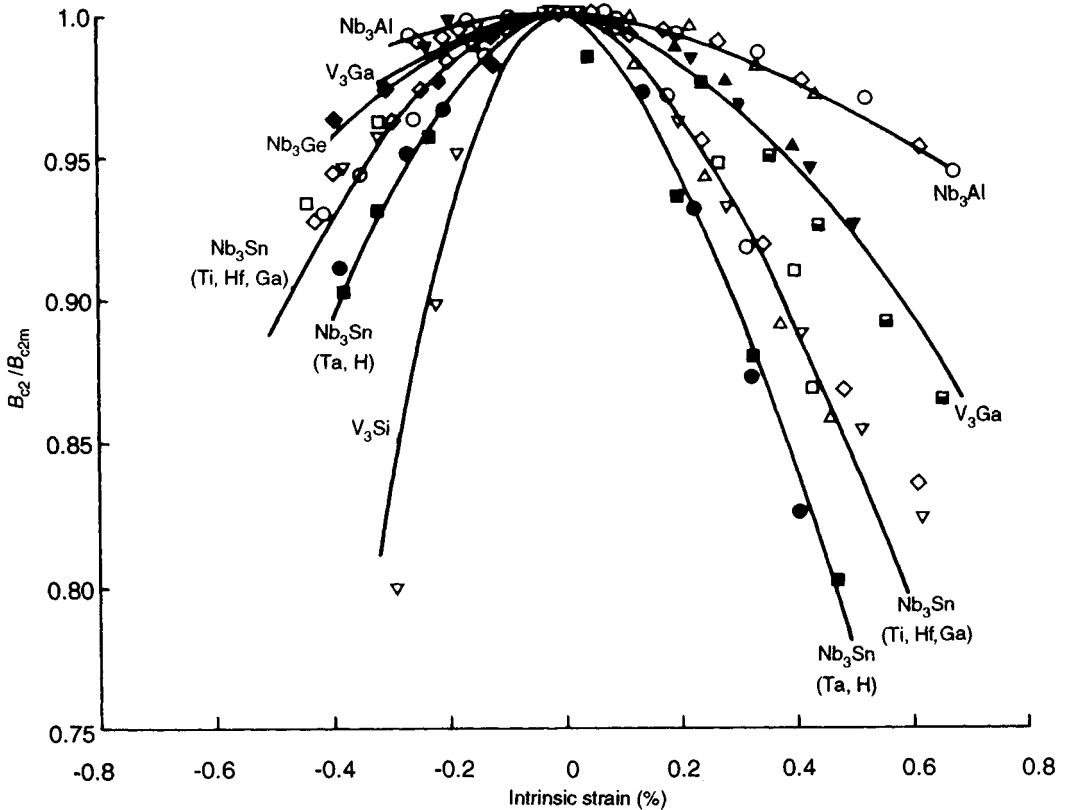


Figure 5. Effect of uniaxial strain on the upper critical field of practical A15 superconductors. B_{c2}^* has been normalized by its maximum (nearly strain-free) value B_{c2m}^* . Binary Nb_3Sn is represented by the same curve as for Nb_3Sn (Ti, Hf, Ga) (by permission of ASM International)

layer thickness. The effect has been somewhat ignored since that time as it was assumed to have only a minor effect on properties. In the internal-tin process, however, owing to the fact that copper and tin are also interdiffusing during the heat treatment of the material, the Kirkendall voids are greater in number and size under certain conditions. The possible effects of this porosity on electrical and mechanical properties have been examined recently and methods have been proposed for its reduction and elimination (Gregory *et al.*, 1991a, 1992a,b). Some of these results are referred to in the section on mechanical properties.

The importance of fine filaments for increasing the overall J_c , particularly at low fields, is more critical in the case of the prealloyed-bronze approach than in the internal-tin method, where a higher percentage of tin is present in the matrix. However, in both methods, in order to maximize the Nb–matrix interface, the filaments of Nb are made as small as is conveniently feasible, even if this is not required for reasons of

stability or losses. The filament size that is most frequently made commercially is between 2 and 8 μm , and the resulting conductors therefore contain very large numbers of filaments.

In addition to having fine filaments twisted* to reduce losses, a practical superconductor composite cable must also contain a normal metal with high electrical conductivity to provide an alternate current path should the superconductor suddenly enter the normal state. This path is usually provided by high-purity copper which is separated from the filament-containing area by a diffusion barrier made from vanadium, niobium or, preferably, tantalum. The matrix surrounding the filaments still contains a significant amount of tin after reaction to form Nb_3Sn and, therefore, has a relatively high resistance. This area, together with that of the

*Twisting reduces losses because the voltage difference between wires becomes sinusoidal, which has zero average.

diffusion barrier, is generally referred to as the non-copper area and is the area which is used to calculate the current densities.

3.2 Mechanical Properties

One of the problems of the high-purity copper stabilizer material is that since the last operation carried out on the composite material is a high-temperature (650–700 °C) heat treatment, the stabilizer is in the fully annealed soft condition. It therefore allows most of the stresses and strains imposed on the composite during magnet winding and service operation to be carried by the relatively brittle non-copper portion of the conductor. In an effort to minimize this effect, an attempt has been made recently to replace some of the copper stabilizer

by dispersion-hardened copper (Gregory *et al.*, 1991b). This hardened copper increases the overall strength of the conductor, increases the amount of precompression to which the Nb₃Sn is subjected, and also increases ϵ_m and ϵ_{irrev} (ϵ_m is the strain where J_c is a maximum and ϵ_{irrev} is the irreversible strain).

During the early development of multifilamentary superconductors, the breaking strain was examined and found to be considerably in excess of that of tape conductors. Experiments on the effect of mechanical deformation on J_c and T_c showed that at low strains J_c increased and it was not until strains of about 0.5–1.0% that degradation of current-carrying properties occurred (Randall *et al.*, 1975). It was also shown by Luhman and Suenaga (1977) that Nb₃Sn wires had their critical temperature raised markedly after the

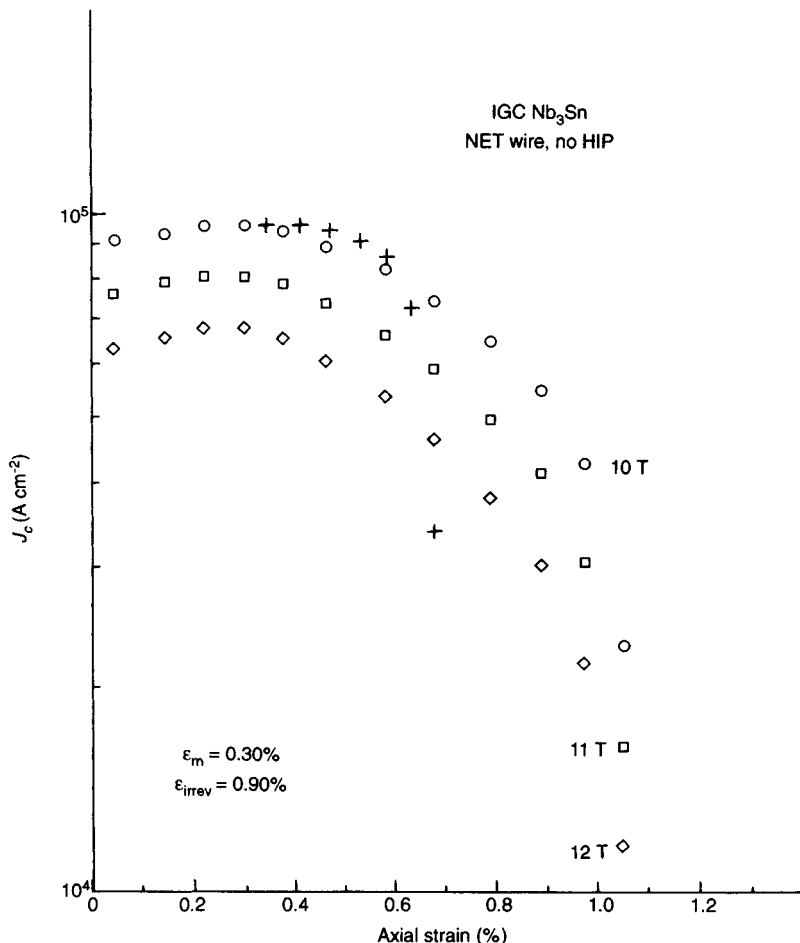


Figure 6. J_c versus axial strain for a 19 sub-element wire at various fields (wire not subjected to HIP). The quantity ϵ_{irrev} is the irreversible strain and ϵ_m is the strain where J_c is a maximum (NET=Next European Torus, a large fusion machine). Plus signs, where different from the circles, show the effects of unloading the strain (by permission of IGC)

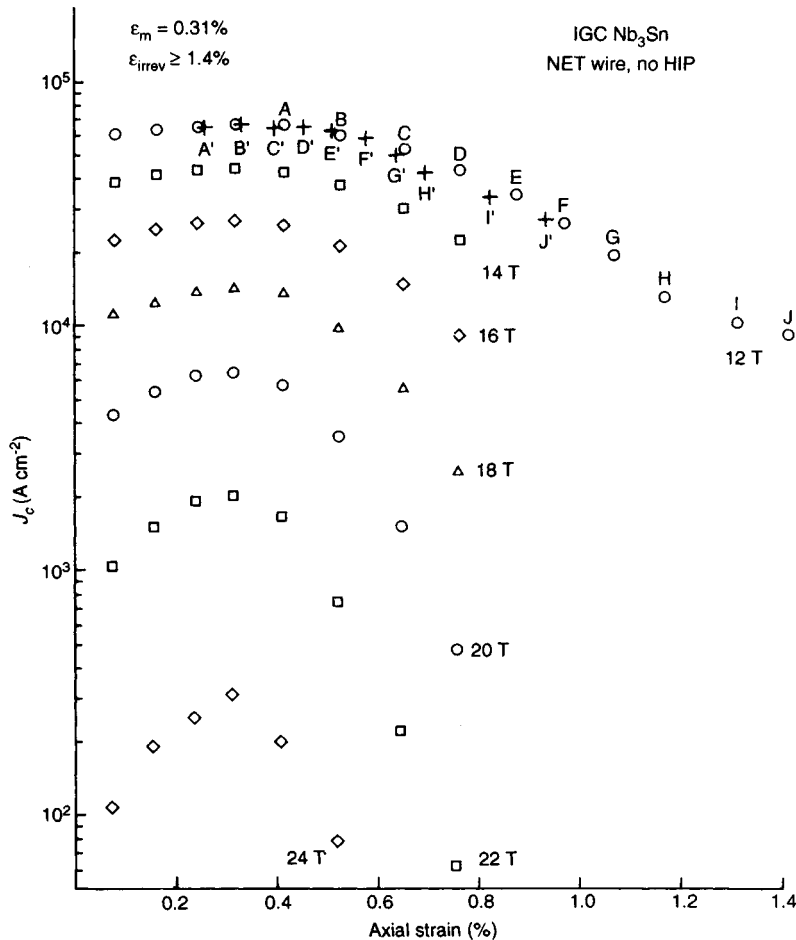


Figure 7. J_c versus axial strain for a 19 sub-element wire at various fields (wire subjected to HIP) A–J refers to values with increasing strain, A'–J' refers to values after the corresponding strain has been removed (by permission of IGC)

removal of the bronze cladding. This resulted from the release of the compressive stresses induced in the Nb_3Sn when the bronze contracted onto it during cooling from the formation temperature.

From a practical point of view, the effects of strain on the J_c values of multifilamentary Nb_3Sn conductors have been discussed by Ekin (1984) in terms of: (1) compressive prestrain ϵ_m ; (2) irreversible strain ϵ_{irrev} ; and (3) elastic strain sensitivity on the upper critical field $B_{c2}(\epsilon)$ and the peak pinning force $F_p(\epsilon)$. The last of these has already been discussed under intrinsic properties and will not be discussed further here.

Figure 6 shows a typical set of J_c versus strain curves at varying fields for modern materials. It is important to realize that these curves are highly dependent on

conductor configuration and processing. There are, as measured in tensile tests, indications that hot isostatic pressing (HIP) of the 19 subelement material at 580 °C doubles the intrinsic irreversible strain after the conductor has received final heat treatment (Figure 7) (Gregory *et al.*, 1992a,b). Investigations are being carried out to determine the extent to which HIP improves J_c , 'n' and reliability of properties along the length of the wire. Also, work is being carried out to determine the extent to which wires and cables can be handled after HIP at intermediate temperatures without creating permanent damage.

¹The natural logarithm of the slope of the resistivity versus current curve at the superconducting to normal transition.

3.3 Practical Fabrication Methods for Nb_3Sn , $(\text{Nb}, \text{Ti})_3\text{Sn}$ and $(\text{Nb}, \text{Ta})_3\text{Sn}$

As reported by Kunzler *et al.* (1961), the 1961 8 T magnet was wound with an Nb_3Sn conductor made from Nb and Sn powders in an Nb tube, but this manufacturing process was not developed commercially. After other attempts to make coils from stranded Nb_3Sn wires by the 'wind and react' approach, Rosner and Benz (1965) reported that most of the commercial conductors for high-field applications were fabricated in the form of tapes. These were made either by chemical vapor deposition (CVD) (Hanak *et al.*, 1964) or surface diffusion techniques (Benz, 1966). Reaction temperatures above 930 °C were used in these approaches in order to avoid the formation of compounds other than Nb_3Sn (see Figure 3). Since the thickness of the reacted layer, and of the tape as a whole, was small, it was possible to bend them after reaction without significant damage. In this way 'react and wind' techniques could be used, and for several years many high-field magnets were constructed using Nb_3Sn and V_3Ga tapes made by the surface diffusion technique as described by Markewicz *et al.* (1977), and many of these magnets are still in daily operation.

Physical vapor deposition (PVD), plasma spraying, rapid-quenching methods and other techniques have been used to prepare Nb_3Sn (Adam *et al.*, 1977), Nb_3Ge (Gavaler, 1973), Nb_3Al (Takeuchi *et al.*, 1987; Tachikawa *et al.*, 1989), $\text{Nb}_3(\text{Al}, \text{Ge})$ and other compounds in tape form on a small scale. While interesting properties have been obtained, few of these tapes have been used on a commercial scale. In addition to the high cost of fabrication and the problems involved in scale-up, the product form produced, i.e. tape, is not ideally suited for use in devices for AC or pulsed applications. Fine, twisted, multifilamentary wires are a more widely accepted product form than tape, since they are less limiting to the applications of the devices in which they are used.

Several different techniques have been tried since the original powder-in-tube and stranded wire techniques were used. Some of these that involve powder metallurgy (P/M) have been described by Hemachlam and Pickus (1977), Schultz *et al.* (1979), Flükiger *et al.* (1979), and Hecker *et al.* (1988); and others, e.g. the 'in situ' process, have been described by Tsuei (1973) and Roberge and Fihey (1977). None of these processes has, as yet, been used commercially to produce significant quantities of these materials.

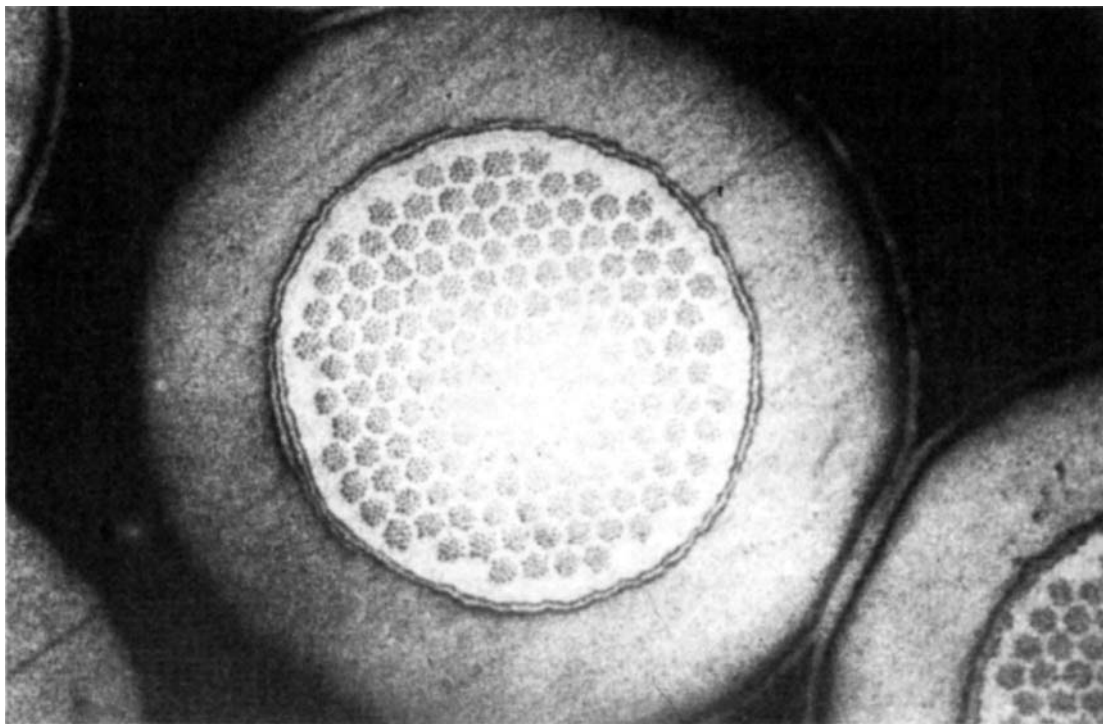


Figure 8. Cross section of bronze-processed material. The 0.7 mm strand contains 2869 filaments in a copper matrix that occupies 66% of the space (by permission of Westinghouse)

The earliest multifilamentary technique used to produce relatively large quantities of material was the bronze process described by Kaufman and Pickett (1971) and Tachikawa (1970). This process can be used to produce both Nb_3Sn and V_3Ga composites by stacking either Nb or V rods in a Cu-14 wt% Sn or a Cu-18 wt% Ga matrix, respectively. These assemblies are then extruded, processed to some intermediate size, and restacked, reextruded and drawn to form fine wires (Hillman, 1981). When the wire is at a final size, the Sn, or the Ga, in the bronze is reacted with the micron-sized filaments to form Nb_3Sn or V_3Ga , respectively. Since the bronzes, even when largely depleted of the alloying elements after reaction, have low electrical and thermal conductivity, high-purity copper must be added to the composite to provide the necessary stability. To maintain the high purity of the copper stabilizer, a barrier of either Nb, V, or preferably Ta is incorporated to prevent interdiffusion. Figure 8 shows a cross section of such a bronze material.

One of the drawbacks of the bronze process is that the matrix work-hardens rapidly, so that many intermediate annealing steps are required to avoid wire breakage. These anneals not only increase the cost of the material but also frequently lead to prereaction of the Sn with the Nb, or the Ga with the V, causing the formation of compound at the filament-matrix interface, which can create distortion and ductility problems. While this compound formation is not the primary source of filament nonuniformity ('sausaging'), it could well contribute to the low J_c values in some of the earlier bronze materials. The Sn and Ga levels in the bronzes are limited to the values given above in order to maintain a single phase in the matrix and thus ensure ductility. This fact has a significant effect on the J_c that can be obtained in the material inside the barrier i.e. the 'non-copper' area. This is the area used when current densities are reported in the A15 composite conductors, as mentioned above. In recent reports, the J_c in the bronze-processed materials has been increased by adding Ge to the matrix, as reported by Tachikawa *et al.* (1991). One of the largest applications of bronze-processed material in the US was the CCIC (cabled conductor in conduit) conductor made by Airco for the Westinghouse large coil in the fusion Large Coil Task (LCT) (Dresner *et al.*, 1988).

In order to increase the amount of available tin and still maintain ductility, several fabrication methods involving coprocessing of copper and tin were developed in an effort to replace the bronze approach. One of the first was the external diffusion method. Gregory (1992) reported that niobium was processed in a copper matrix

in much the same manner as multifilamentary Nb-Ti superconducting composites. When the Nb-Cu composite had been reduced to a fine size, it was coated with tin, given a low-temperature diffusion heat treatment and then reacted to form Nb_3Sn (Suenaga and Sampson, 1972). The drawbacks to this process were that it was only applicable to fine wires, and problems were encountered from the agglomeration of tin into local areas on the wire and the formation of porosity in the composite owing to Kirkendall effects (Smigelskas and Kirkendall, 1947). Attempts were made to avoid these effects (Cogan *et al.*, 1983) by controlling heat treatments and altering the plating procedures, but the external-tin process was not adopted as a commercial fabrication method.

In its place, a series of internal-tin diffusion processes were developed, yielding a variety of different conductor configurations (Hashimoto *et al.*, 1974, 1978; Petrovich and Zeitlin, 1978; Schwall *et al.*, 1983; Smathers *et al.*, 1988). All these processes do not require the repeated anneals needed in the bronze method, and the product is free from prereaction.

Schwall *et al.* (1983) describe the process as developed by IGC Advanced Superconductors Inc., shown schematically in Figure 9. It requires the production of two components, a composite tube and a stabilizer tube. The composite tube (which contains many filaments) is made by the conventional assembly and extrusion techniques used for composite superconductors (Gregory, 1992). This tube is filled with a high-Sn alloy and drawn down to a suitable size for restacking. The stabilizer tube includes an Nb or Ta barrier, and the amount of Cu is varied depending on the application. Recently this process has undergone considerable modification to increase the piece length, improve the J_c for given AC losses and improve reliability and reproducibility of properties (Gregory *et al.*, 1990, 1991a,b; Summers *et al.*, 1991; Kanithi *et al.*, 1989).

The result of this work is a 'tin-core' conductor of the type shown (before reaction heat treatment) in Figure 10. This is a conductor which has been developed for the International Experimental Reactor (ITER) program. The filaments in the strand are Nb 7.5 wt% Ta and the barrier is Ta backed by Nb.

Figure 11 shows schematically a modification of the internal-tin process involving the use of a tubular tin source (TTS). The cross section of a conductor made by this process is shown in Figure 12 (before the reaction heat treatment). This conductor exhibits a high current density, as described by Ozeryansky and Gregory (1991), but in its present design it can only be used in small diameters (<0.5 mm), although work is under way to produce larger-diameter conductors with a range of

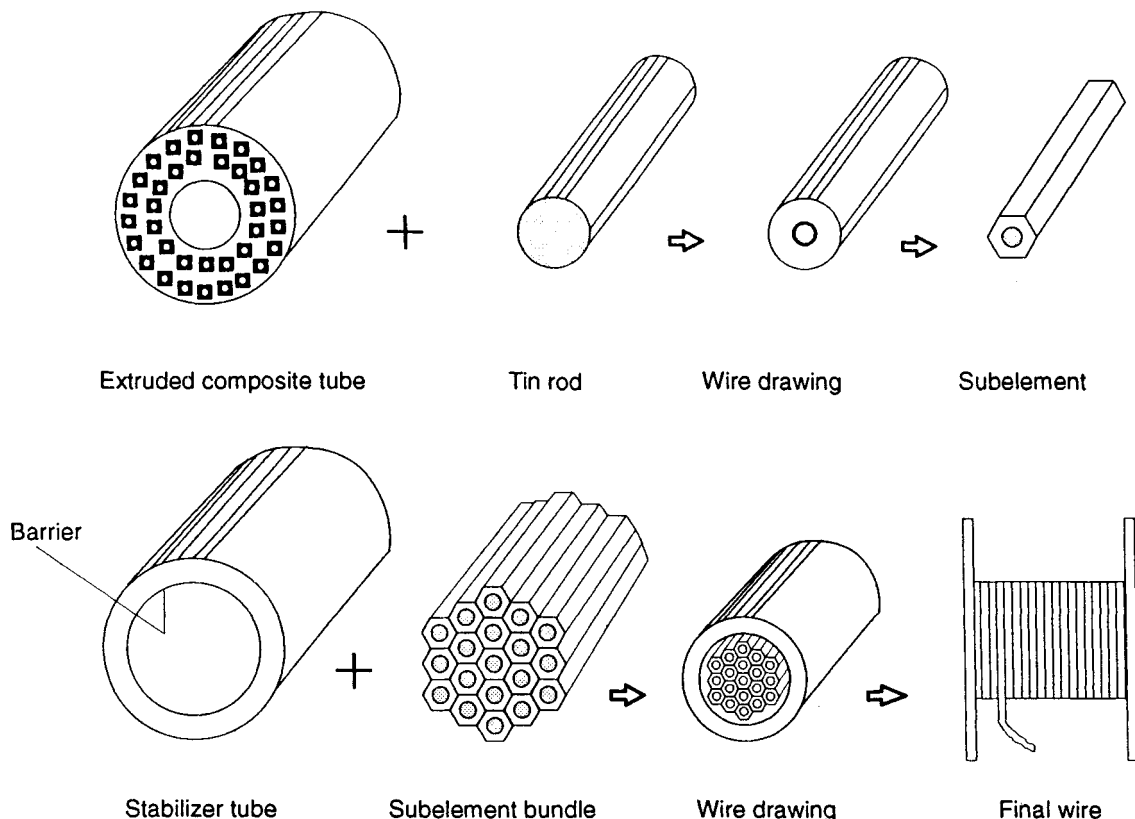


Figure 9. Fabrication steps in the tin-core internal-tin process for making Nb_3Sn (by permission of IGC)

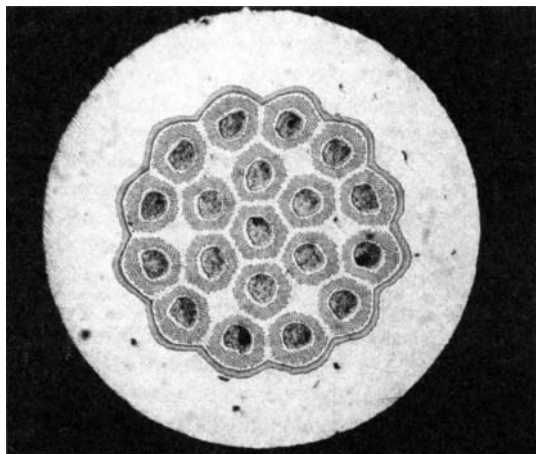


Figure 10. Cross section of ITER conductor with 19 sub-elements. The wire diameter is 0.78 mm. The copper occupies 60% of the cross section. The barrier layer is tantalum (by permission of IGC)

different copper percentages, lower losses and better reliability.

The new conductor designs offer promise for <20 T applications. Typical properties of the two different conductor configurations (Figures 10 and 12) are shown in Figure 4 and Table 2. It has been reported by Gregory *et al.* (1992a,b) that the use of Nb and Nb-7.5 wt% Ta in the filaments results in material with improved piece length when compared with material made from Nb-1.3 wt% Ti. Figure 4 clearly shows the advantage of the third element when high J_c values at high fields are required. No data are yet available on TTS material made with Nb-7.5 wt% Ta filaments, but it is expected that it, like the Ti-containing material, will show considerably higher J_c values than the tin-core designs. The heat treatments on the two alloyed tin-core materials shown in Figure 4 were slightly different, and it is unknown at the present time whether the crossover at around 16 T is as a result of this fact or because of the filament composition.

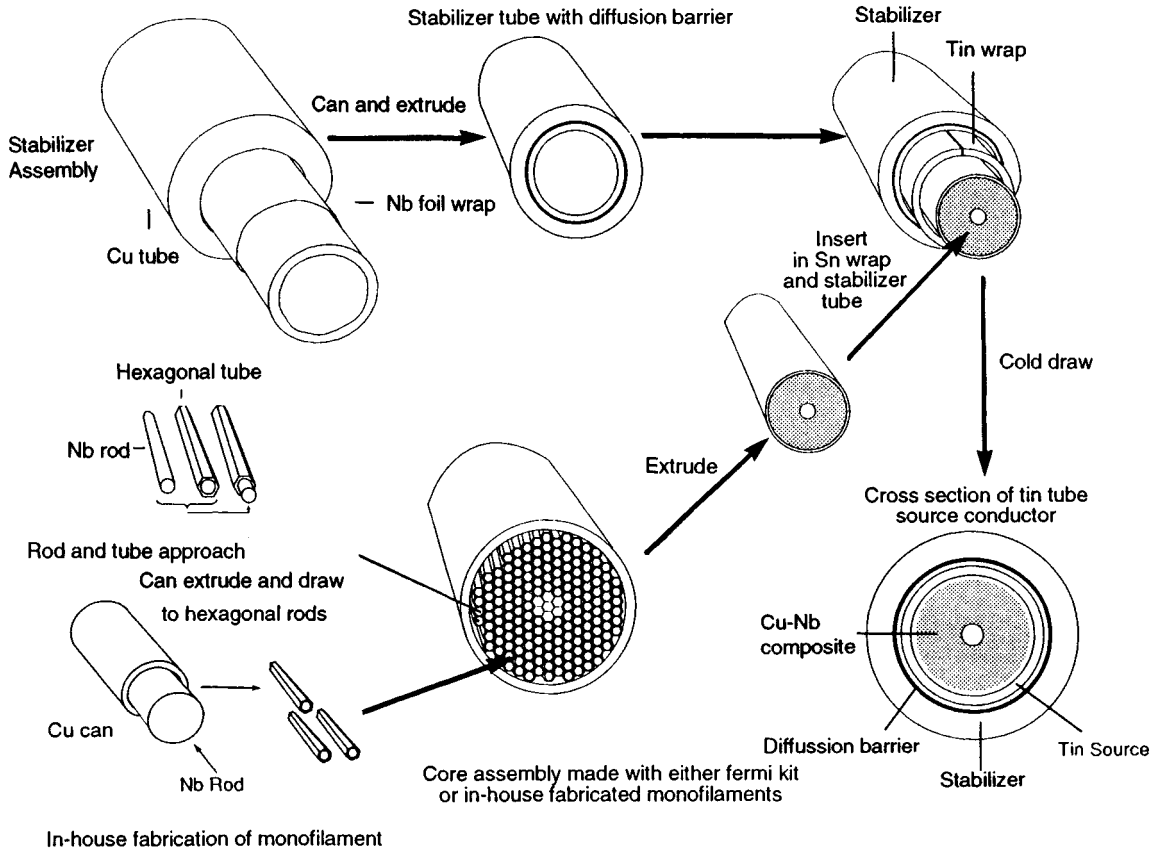


Figure 11. Fabrication steps in the TTS internal-tin process for making Nb₃Sn (by permission of IGC)

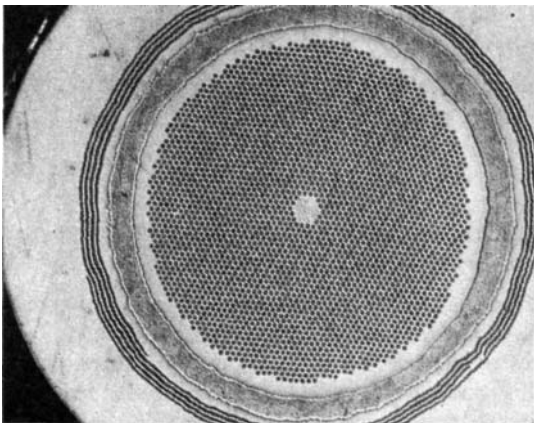
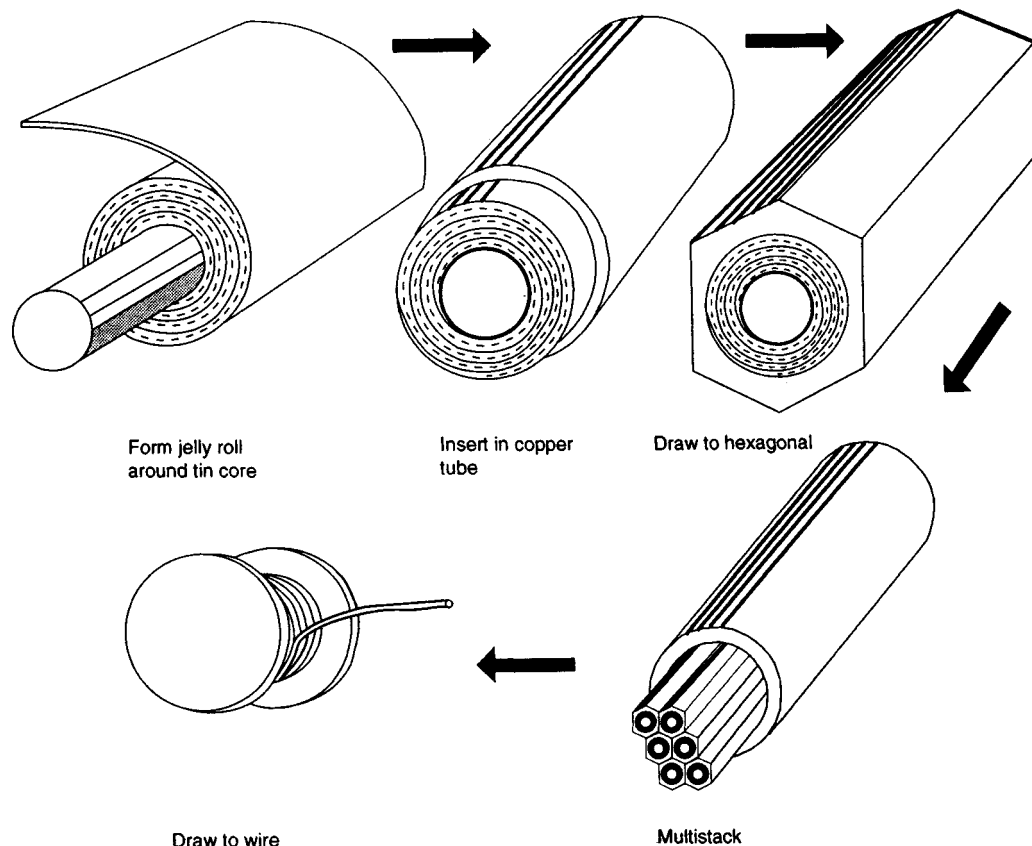


Figure 12. Cross section of a TTS conductor. The wire diameter is 0.5 mm, surrounded by multilayers of niobium (by permission of IGC)

A variation of the bronze process reported by McDonald (1981, 1983) and McDonald *et al.* (1983) originally consisted of rolling expanded Nb (or Nb alloy) foil into a 'jelly roll' (MJR). This material suffered from the same drawbacks as all the early bronze-processed material. It led, however, to the tin-core MJR (Smathers *et al.*, 1988). The expanded metal Nb-1.3 wt% Ti sheet is wound on to a tin rod core and copper is interleaved in place of the bronze in the original process. A barrier layer separates each jelly roll from the surrounding copper. Many tin-core MJR units are restacked to reduce the tin diffusion distances. The process is shown schematically in Figure 13, and Figure 14 shows the cross section of an 18 subelement conductor. A design similar to this was used in the US DPC (demonstration poloidal coil) which was tested in the Tokai Japan Demonstration Poloidal Coil Test (Hoenig and Steeves, 1989).

Table 2. Comparison of current density J_c for various Nb₃Sn fabrication processes

| Field (T) | J_c (A mm ⁻²) | | | | |
|--------------|-----------------------------|---------------|--------------------------|--------------------------|---------------------|
| | Low-loss tin core (Nb) | Tin core (Nb) | Tin core (Nb-7.5% Ta) | Tin core (Nb-1.0% Ti) | TTS (Nb-1.0% Ti) |
| 8 | 1120 | | | 1154 | 2112 |
| 10 | 650 | 1100 | | 940 | 1552 |
| 12 | 350 | 550 | 877 | 650 | 1115 |
| 14 | 140 | 200 | 585 | 442 | 780 |
| 16 | | 62 | 324 | 332 | 532 |
| 18 | | 10 | 135 | 163 | 328 |
| 20 | | | 63 | 70 | 169 |

**Figure 13.** Fabrication steps in the tin-core MJR internal-tin process for making Nb₃Sn (by permission of IGC)

4. General—Applications of A15 Superconductors

A15 (cP8) materials have higher critical temperatures and higher critical magnetic fields than Nb-Ti, the most ductile, solid-solution, low-temperature superconductor material that has seen the widest use (Stekly, 1990a,b, 1991). The main reason for this is that A15 superconductors are more brittle and, as a consequence, more

difficult to use. Of the A15 superconducting materials, Nb₃Sn has seen far wider use than the others.

Most applications use a conductor that is wound into the required geometry. This conductor can range from a simple tape, a single monolithic conductor (round or rectangular), a many-strand cable (round or rectangular), to a complex cable conductor within a structural conduit providing mechanical support for

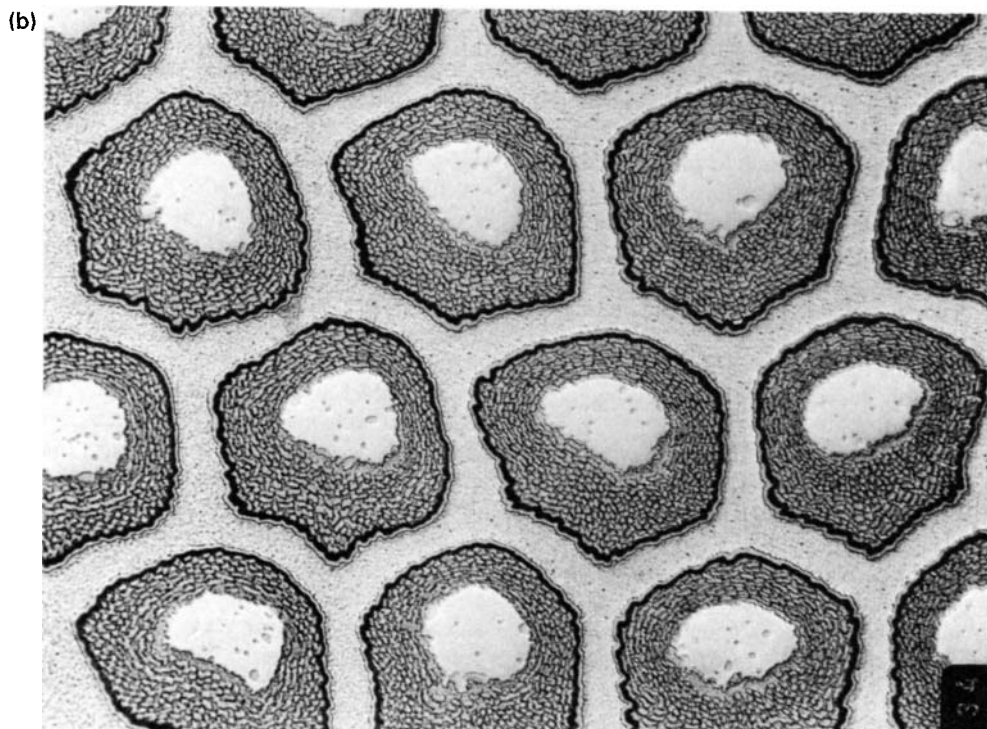
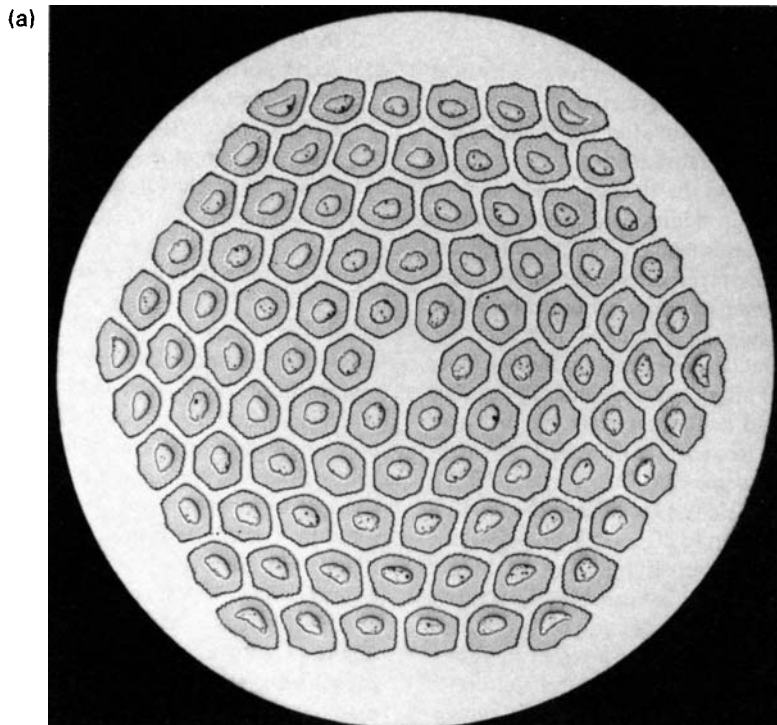


Figure 14. Cross-section of a tin-core MJR internal-tin conductor; (a) $\times 100$, (b) $\times 1000$ (by permission of Teledyne Wah Chang)

the cable as well as a vacuum-tight passage for helium flow.

In general, the A15 superconductors formed by heat treatment are brittle. In making devices, both fabrication after reaction as well as reaction after fabrication have been used. For devices fabricated after reaction, conductors must withstand the stresses and strains of the fabrication process in addition to those resulting from cool-down to operating temperature and energizing to rated conditions with potentially significant magnetic forces. For devices reacted after fabrication, appropriate survivable electrical insulation is required. Alternatively, electrical insulation and/or epoxy to hold the assembly together may be added after reaction. Most applications involve coils of wound conductors. At one extreme, Nb_3Sn has been used to generate over 20 T in small-bore solenoids. On a somewhat larger scale, Nb_3Sn coils form part of high-field test facilities in the 10–13 T range with bore sizes of up to 60 cm. At a comparable scale, Nb_3Sn coils form the external part of hybrid magnet facilities that eventually are capable of generating 45 T. In these, Nb_3Sn superconducting coils are used to generate a background field for a resistive, room-temperature insert which in turn produces the major fraction of the field and requires large electrical power.

At the other extreme are the very large high-field Nb_3Sn coils used for magnetic fusion research. Here, large background magnetic fields are required to confine and control a plasma long enough for thermonuclear reactions to take place. These represent by far the largest-scale application of Nb_3Sn technology. In each of the applications, the form of conductor is determined by the following major considerations.

- (1) Enough superconductor needs to be used to carry the current, with a margin sufficient for all expected operating conditions.
- (2) The superconductor must be subdivided into fine filaments to:
 - (a) stabilize superconductor currents;
 - (b) provide low losses under time-varying conditions; and
 - (c) minimize magnetic field distortions owing to superconductor magnetization.
- (3) A normally conducting matrix, usually copper or aluminum, is used to:
 - (a) stabilize the current in the superconductor under all expected conditions; and
 - (b) provide for safe voltages/temperatures during quench (uncontrolled growth of a resistive region).

- (4) Appropriate selection must be made of conductor form: tape, wire monolith and cable.
- (5) A supporting structure, in the form of a cable component, an enclosing conduit and a distributed element which supports individual turns or as a separate component, must be provided in cases where magnetic forces are high.

5. Comparison with Other Superconductors

Until the discovery of the ceramic, high critical temperature superconductors with critical temperatures approaching 120 K, the A15 superconductors with critical temperatures in the 18–23 K range were the only option. Ceramic, high critical temperature materials are brittle (like A15 superconductors); their availability in conductor form has so far been limited, and until recently, current-carrying capacity in conductor configurations has been low when compared with lower critical temperature superconductors. Their availability and performance have now improved significantly. Figure 15 compares the superconductor current-carrying capacities of selected short samples and coils of various materials. Solid-solution Nb–Ti, because of its ductility and ease of use, has been widely used as a superconductor. At 4 K it is limited to fields of 9–10 T. At 1.8 K, Nb–Ti can be used to 12–13 T. Nb_3Sn (4 K) has usable current density up to 18–20 T. Also shown for comparison is a 20 T Nb_3Sn coil, reported by Markiewicz *et al.* (1992a), operating at 2 K.

Data from several sources for bismuth strontium calcium copper oxide (BSCCO) at 77 K, 20 K and 4 K are shown in Figure 15 (Motowidlo *et al.*, 1992; Motowidlo, 1992). While the current-carrying capacity decreases rapidly with magnetic field at 77 K, data at 4 K and 20 K potentially indicate that the high- T_c materials will carry more current than Nb_3Sn (at 4 K) at fields above about 14 T. Comparison of current-capacity at 4 K of small samples of BSCCO conductors and small coils made with the same material (at 4 K) indicates a decrease of about a factor of four (Haldaar, 1992; Sato, 1991, 1992; Walker *et al.*, 1992).

Nb_3Sn , and to a smaller extent V_3Ga and Nb_3Al , have been used at high fields and at temperatures above the 4 K required for Nb–Ti. Nb_3Sn has also been considered for cases where heating owing either to steady heat sources or transient operation results in temperatures too close to the critical for Nb–Ti. Ability to absorb heat is an important advantage Nb_3Sn has in

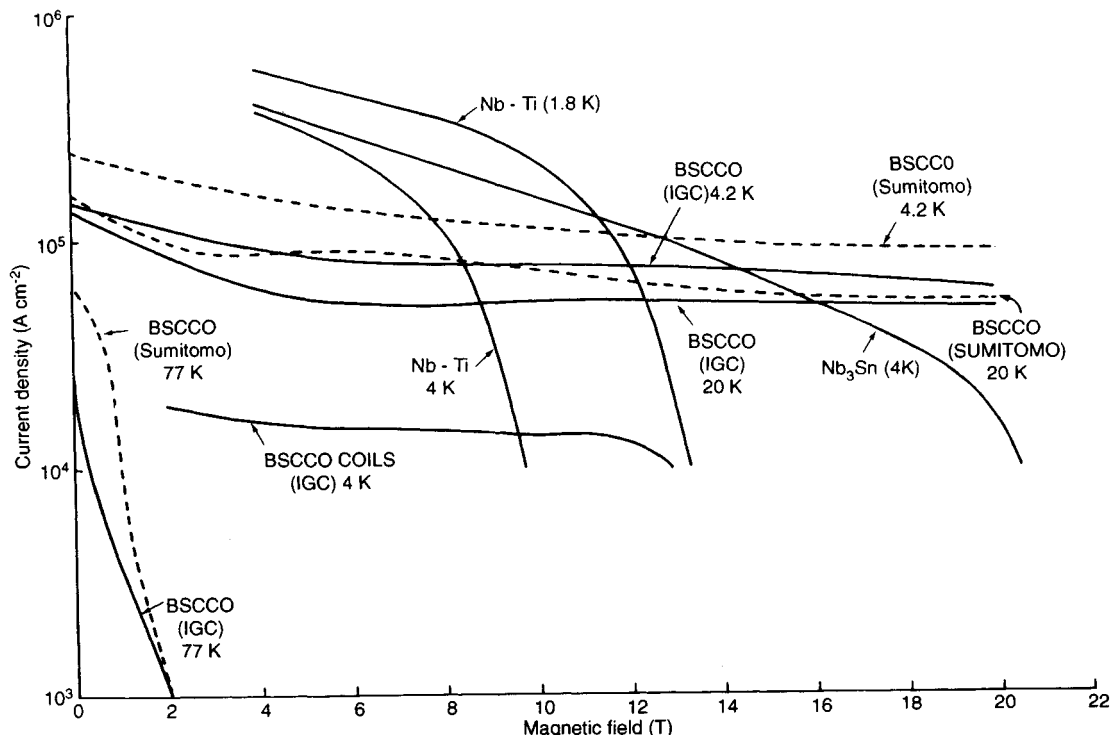


Figure 15. This figure compares the superconductor current-carrying capacity of Nb_3Sn at 4 K with that of other low and high critical temperature superconductors. The curves for Nb-Ti, the most commonly used superconductor, are shown at 4 K and 1.8 K. Data for bismuth strontium calcium copper oxide (BSCCO) from two sources are shown at 77 K, 20 K, and 4.2 K (by permission of IGC)

this regard. The confidence in and database on Nb_3Sn are extensive; and in view of these factors, use of the ceramic superconductors will depend initially on their availability and then on their performance in devices. The coil-winding technology developed for Nb_3Sn tapes should be directly applicable to the high- T_c materials where tape conductors are being developed. Hein and Gubser (1981) is a good review of work carried out in the 1970s while Lampman and Zorc (1992) is a good general reference for various superconductors and their properties.

6. High-field Magnets

Small bore diameter, high-field magnets, usually for research on superconductors, solid-state experiments or physics experiments are typical applications of A15 superconductors. Figure 16 shows a 17.5 T (31 mm bore

diameter) superconducting system reported by Markiewicz *et al.* (1977). The system was built by Intermagnetics for the Japanese National Research Institute for Metals, where it was used for over eight years (Tachikawa *et al.*, 1985a,b). The figure shows a typical high-field magnet system. The Nb_3Sn coil with V_3Ga inset (removed) is shown in the center of the picture. Also shown for illustration is the support structure (right) on which both coils are normally suspended. The vacuum-insulated cryostat suitable for 4.2 K operation is shown on the left. This system is unique in several respects. It gave for many years the highest magnetic field produced using superconductors alone. It also represents application of an A15 superconductor other than Nb_3Sn . Because V_3Ga is able to carry significant current at higher magnetic fields than Nb_3Sn , it was used for the high-field insert. The Nb_3Sn coil was made by using an Nb tape dipped in molten tin, reacted to form Nb_3Sn , then reinforced with stainless steel tape and stabilized

Chapter 6

Magnetostriction: Materials and Applications

Rodney D. Greenough and Michael P. Schulze

Department of Applied Physics, University of Hull, Hull HU6 7RX, UK

1. Introduction

The term magnetostriction should strictly be reserved to describe the change in dimensions of a magnetic material as it undergoes magnetization, and often the distinction between 'magnetostriction' and 'magnetoelasticity' is, unfortunately, not made; confusion between them occurs, especially with amorphous materials in which the response to the application of stress produces large changes in the magnetization because of the high magnetoelastic coupling, whereas dimensional changes generated during magnetization are usually quite small. The distinction between the two terms is that magnetoelasticity can be seen in a variety of different responses, not only as a magnetostrictive dimensional change but also in the ' ΔE effect' (a change in an elastic modulus with the state of magnetization) or stress-induced magnetic anisotropy, for example. Its origin can be due to an interplay of either the magnetic exchange energy or ionic energy, which depends on the strength and symmetry of localized crystal fields, with the elastic bonding energy of the material.

There is also a need to distinguish between magnetoelastic coupling, as described for instance in the Kittel (1949) formation of magnetostriction, and magnetomechanical coupling, although their fundamental origins are the same. Whereas the former describes the interatomic coupling of the magnetic and elastic energies within a single crystal structure, gauged by the magnetoelastic coupling coefficients B_1 and B_2 (Lee, 1955), the magnetomechanical coupling is more empirical and gauges the efficiency in the conversion of input energy density $\frac{1}{2} \mu H^2$ to elastic energy density

$\frac{1}{2} E \epsilon^2$ (where E is the Young's modulus and ϵ is the elastic strain for an isotropic body), or vice versa. Magnetomechanical coupling like magnetoelastic coupling can be anisotropic, in keeping with the crystal structure, but it is also influenced by the frequency of excitation, metallurgical condition of the sample, the manner in which it is housed or even its geometry. Magnetoelasticity is a term used frequently by physicists, whereas magnetomechanical coupling is an engineering term.

The purpose of this chapter is to review research conducted since the early 1960s on magnetoelastic metals, alloys and compounds and to show how materials with optimum magnetostrictive properties can be employed in devices whose extraordinary magnetomechanical coupling efficiencies can generate large displacements even under substantial loads.

It is beyond the scope of this chapter to include advances made with amorphous materials such as iron-transition metal (TM) or nickel-transition metal compounds and rare earth-transition metal (RE-TM) compounds. These have been reviewed by Luborsky (1980) and are now finding novel applications in noncontact torque sensors, accelerometers and pressure transducers (i.e. passive transducers). Crystalline, highly magnetostrictive intermetallics, such as the RE-Fe compounds, for instance, are more suited to actuation or sonar projectors (active transducers), and these are the subject of this chapter. In crystalline materials, the anisotropic magnetostriction is of principal interest; volume magnetostrictive effects are usually much smaller, isotropic and normally only observed in large applied fields.

The anisotropic magnetostrictive strains in a cubic single crystal are given by

$$\frac{dl}{l} = \frac{3}{2} \lambda_{100} \left(\alpha_1^2 \beta_1^2 + \alpha_2^2 \beta_2^2 + \alpha_3^2 \beta_3^2 - \frac{1}{3} \right) + 3 \lambda_{111} (\alpha_1 \alpha_2 \beta_1 \beta_2 + \alpha_2 \alpha_3 \beta_2 \beta_3 + \alpha_3 \alpha_1 \beta_3 \beta_1) \quad (1)$$

where α and β are the direction cosines of magnetization and strain measurement, respectively, and λ_{100} and λ_{111} are the magnetostriction constants relating to the strains along the $\langle 100 \rangle$ and $\langle 111 \rangle$ axes relative to the demagnetized state.

The anisotropy energy is given by

$$E_a = K_1 (\alpha_1^2 \alpha_2^2 + \alpha_2^2 \alpha_3^2 + \alpha_3^2 \alpha_1^2) + K_2 (\alpha_1^2 \alpha_2^2 \alpha_3^2 + \dots) \quad (2)$$

where K_1 and K_2 are the anisotropy constants. These relationships are considered in more detail by Chikazumi (1964) and Jiles (1991).

For polycrystalline cubic materials the average strain measured at an angle θ to the magnetic moment is given by

$$\frac{dl}{l} = \frac{3}{2} \lambda_s \left(\cos^2 \theta - \frac{1}{3} \right) \quad (3)$$

where λ_s is the polycrystalline magnetostriction coefficient and is related to the single-crystal coefficients by

$$\lambda_s \approx \frac{2}{5} \lambda_{100} + \frac{3}{5} \lambda_{111} \quad (4)$$

An ideal demagnetized state is often difficult, if not impossible, to achieve in practice; so strain measurements are often made by applying a magnetic field in two different directions—usually parallel and then perpendicular to the strain measurement direction—and the difference $\lambda_{\parallel} - \lambda_{\perp}$ is used as an unambiguous measure of the magnetostriction of the material without reference to any 'demagnetized' state.

2. History of Magnetostrictive Materials

The following description of the advances made in magnetostrictive materials puts their present performance in perspective; only relatively recently have their properties been developed to the extent that they are attractive for a variety of applications, some of which are briefly reviewed in Section 7.3 of the present chapter.

For comparative purposes, the magnetostriction coefficients for some single-crystal elements and early polycrystalline alloys are given in Table 1, together with

anisotropy coefficients which indicate the relative field strengths required to generate maximum strains. In the 1950s nickel or alloys containing nickel were the most promising magnetostrictive candidates for applications because of their relatively high strains and low magneto-crystalline anisotropies. Even in the 1970s such materials were still considered for sonar generators (Davies, 1977) or ultrasonic cleaning transducers in industry (Bulat, 1974). Meanwhile, piezoelectrics which could be operated more efficiently at higher frequencies became increasingly popular. To avoid high operating voltages, magnetostrictive ferrites were considered, and their potential for transducers was reviewed by van de Burgt and Stuijts (1963). Cobalt ferrite, for instance, develops larger strains than metallic alloys and has higher electrical resistivity, thus reducing eddy current losses; but these advantages are outweighed by brittleness, structural imperfections and the large fields necessary to overcome high magnetocrystalline anisotropy (Table 1).

Present-day magnetostrictive intermetallic materials have overcome many of these earlier difficulties and drawbacks. They have been developed from fundamental research conducted on the rare-earth elements in the 1960s, described by Rhyne and Legvold (1965) and Clark *et al.* (1965). With highly anisotropic 4f electron orbitals (Figure 1), three elements in particular—terbium, dysprosium and samarium—in single-crystal form are noted for their huge magnetostrictive strains that are at least an order of magnitude greater than any of the 3d metallic alloys (Table 2). These remain the largest magnetic strains ever recorded, but these elements are of little value for transducers because of their low Curie temperatures T_C (Table 2). As a result of research conducted by Clark and coworkers at the Naval Research Laboratories and Verhoeven and coworkers at the Ames Laboratories

Table 1. Single-crystal magnetostriction coefficients λ_{100} and λ_{111} and anisotropy coefficients for some 3d transition elements and cobalt ferrite; λ_s is the magnetostriction coefficient from some polycrystalline transition metal alloys and heat-treated nickel

| Single crystal | $10^6 \lambda_{100}$ | $10^6 \lambda_{111}$ | $10^3 K_1$ | Reference |
|--|----------------------|----------------------|------------|---|
| Fe | 20.7 | -21.2 | 47 | Lee (1955) |
| Ni | -45.9 | -24.3 | -59 | Lee (1955) |
| $\text{Co}_{0.8}\text{Fe}_{2.1}\text{O}_4$ | 515 | 45 | 1700 | Bozorth and Walker (1952) |
| Polycrystalline | $10^6 \lambda_s$ | | | |
| 45 Permalloy | 120 | — | | US National Defense Research Council (1946) |
| 2V Permendur | 150 | | | |
| Ni (heat treated) | 300 | | | |

(Iowa State University), rare earth-iron intermetallics REFe_2 have been developed that at room temperature maintain a substantial fraction of the magnetostriction from the RE ions because their Curie temperatures are several hundred degrees higher. It is on these compounds that much attention is now focused because of their potential for applications. A range of other RE-Fe compositions has been studied, and magnetostriction data for REFe_3 , $\text{RE}_6\text{Fe}_{23}$ and $\text{RE}_2\text{Fe}_{17}$ are given by Clark (1980), but none of these compositions

generates magnetostrictive strains larger than those in ReFe_2 compounds.

3. Magnetostriction

The choice of material for a magnetostrictive application depends on its fundamental response to applied fields and temperature. How the best performance is engineered from actual material is described after the

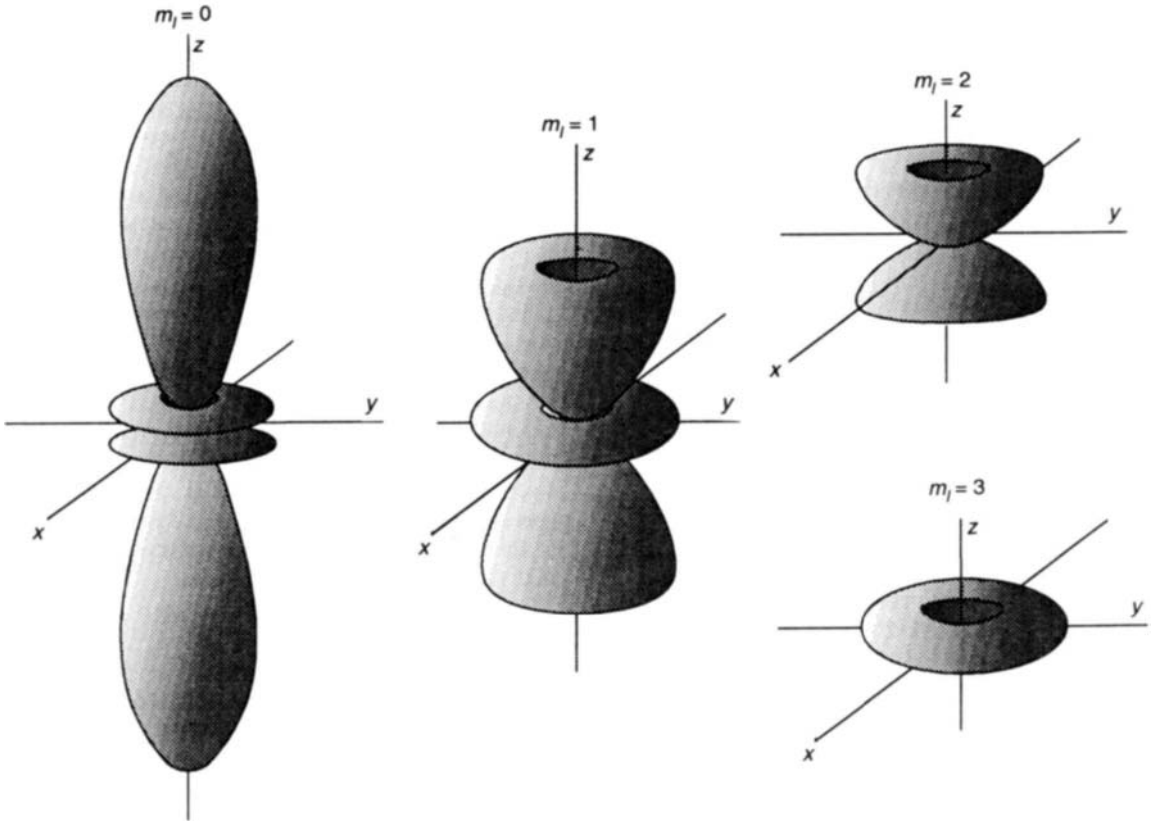


Figure 1. Anisotropy of the rare-earth 4f electron wave functions

Table 2. Magnetostriction in single crystals of dysprosium and terbium at low temperatures ($T < T_C$) measured along particular crystal axes; magnetostriction as values of $\frac{2}{3}(\lambda_{\parallel} - \lambda_{\perp})$ from polycrystalline REFe_2 compounds at room temperature, and associated values for the Néel temperature T_N and Curie temperature T_C

| | Magnetostriction ($\times 10^6$) | T_C (K) | T_N (K) | Reference |
|-------------------|------------------------------------|-----------|-----------|----------------------------|
| Dy | 6000 (<i>a</i> axis) | 87 | 179 | Clark <i>et al.</i> (1965) |
| Tb | 7000 (<i>b</i> axis) | 221 | 230 | Rhyné and Legvold (1965) |
| TbFe ₂ | 2500 (polycrystalline) | 700 | — | Clark (1980) |
| DyFe ₂ | 650 (polycrystalline) | 635 | — | |
| SmFe ₂ | – 2500 (polycrystalline) | 676 | — | |

present discussion of the more fundamental aspects of magnetostrictive behavior.

3.1 Atomic Theory

The difficulties in formulating fundamental theories for magnetostriction on an atomic scale are reflected in the small number of publications in the field. Before calculations can commence for itinerant electron systems (3d transition metals and alloys), detailed information is needed on the band structure and density of states as well as on their strain dependences. Only in recent times have such calculations been attempted for iron by Ohta and Shimizu (1982) and Tatebayashi *et al.* (1986). With localized moments, precise single-ion calculations can be made, for instance, to predict the magnitude and temperature dependence of the anisotropy and magnetostriction from the Co^{2+} ion in ferrites (Slonczewski, 1961); but such detailed analyses have yet to be conducted for rare-earth systems. For rare earths, a point charge model has been described by Clark (1980), and work by Callen and Callen (1963, 1965) is frequently employed to analyze the temperature dependence of magnetostriction for single-ion systems. However, specific calculations for the magnetostrictive effects arising from individual rare-earth ions in RE-Fe compounds would be invaluable in the pursuit of even better magnetostrictive performance, i.e. larger strains in smaller applied fields over wider temperature ranges. At present, the anisotropy of the 4f orbitals and the point charge model adequately explain the signs of the anisotropies and magnetostrictions from Dy or Tb ions in RE-Fe compounds at room temperature (Table 3). The magnetostriction is not necessarily of the same sign as the anisotropy, because the former depends on the strain dependence of the magnetoelastic energy.

In the absence of detailed theoretical work, advances in magnetostrictive materials made since the 1970s have depended on experimental data with, in the main, qualitative analyses. It is beyond the scope of the present work to review all such data and only a few are now described to illustrate how present-day magnetostrictive materials evolved.

Table 3. Predicted polarities of magnetostriction and anisotropy in TbFe_2 and DyFe_2 (after Clark, 1980)

| | TbFe_2 | DyFe_2 |
|----------------------------|-----------------|-----------------|
| Magnetostriction λ | + | + |
| Anisotropy $K_1 + K_2/11$ | – | + |
| K_2 | + | – |

3.2 Magnetostriction in Rare-earth Compounds

3.2.1 RE-Fe Compounds

Room-temperature magnetostriction data have been reported by Clark (1980) for a variety of RE-Fe compositions. The addition of iron to the REs raises the Curie temperature near to or above room temperature (Table 2), enabling the exceptional magnetostrictive properties of the RE ions to be harnessed for practical purposes. For example, the field dependences of the strains in TbFe_2 , TbFe_3 , $\text{Tb}_6\text{Fe}_{23}$ and $\text{Tb}_2\text{Fe}_{17}$ measured by Clark (1974) and Abbundi and Clark (1978) in polycrystalline materials are compared in Figure 2. Clearly the largest strains are seen in TbFe_2 . The magnetostrictions in REFe_2 , where RE = Tb, Sm, Dy, Er, Tm or Ho, are compared in Figure 3, which shows how effectively Tb, in particular, can generate strains as large as ~ 2500 p.p.m. even in polycrystalline material. These field-dependent data also illustrate a problem associated with the magnetocrystalline anisotropy in that impractically large fields ($\sim 2000 \text{ kA m}^{-1}$) are needed to generate the strains. One solution to the problem would be to use single-crystal materials so that the full strain represented by the room-temperature magnetostriction coefficient λ_{111} (~ 2450 p.p.m.; Clark, 1980) could be realized. However, with the magnetocrystalline anisotropy and magnetostriction from Tb ions in TbFe_2 being of opposite sign (Table 3), a reduction in the former can be achieved without necessarily causing a simultaneous reduction in the latter.

3.2.2 Terfenol-D

The magnetocrystalline anisotropies of TbFe_2 and DyFe_2 are of opposite sign (Table 3), and work by Clark (1974) showed that combining the two to form a pseudobinary compound of the form $\text{Tb}_{1-x}\text{Dy}_x\text{Fe}_2$ lowers the overall magnetic anisotropy. With the specific composition $\text{Tb}_{0.27}\text{Dy}_{0.73}\text{Fe}_2$ the minimum anisotropy is achieved near room temperature (Figure 4) when the positive and negative anisotropies of the Tb and Dy ions almost, but not totally, cancel each other. However, since the magnetostrictions of the two constituent compounds are of the same sign, a substantial fraction of the magnetostriction in TbFe_2 is retained and strains ~ 1600 p.p.m. can be generated in fields as low as $\sim 800 \text{ kA m}^{-1}$ (Figure 5). This composition is frequently referred to as Terfenol-D (Ter derived from terbium, Fe to represent the iron content, nol for the Naval Ordnance Laboratories (USA) at which the

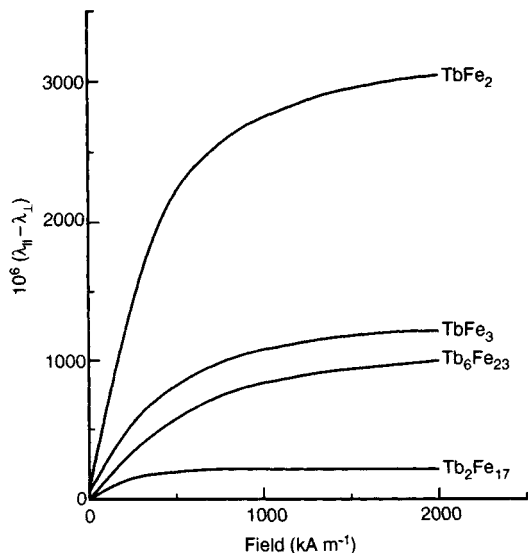


Figure 2. Field dependences of the magnetostrictions in polycrystalline samples of terbium-iron compounds at room temperature (after Clarke, 1980; Abbundi and Clark, 1978)

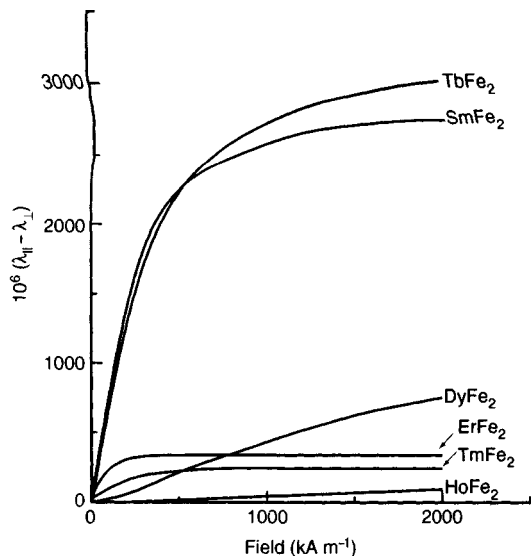


Figure 3. Comparison of the magnetostrictions at room temperature in polycrystalline REFe₂ compounds (after Clark 1974; Koon *et al.*, 1974)

pioneering work was conducted, and D to denote the dysprosium); and it is this compound which formed the basis of future developments that produced material particularly suited to applications.

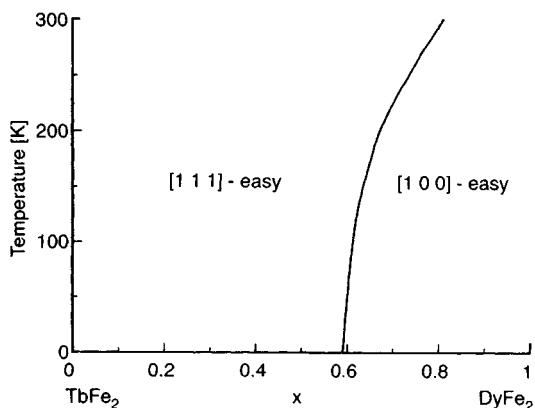


Figure 4. TbFe₂ magnetic anisotropy phase diagram depicting the changes in magnetocrystalline anisotropy as a function of temperature and composition in the range Tb_{1-x}Dy_xFe₂ (after Atzmony *et al.*, 1973)

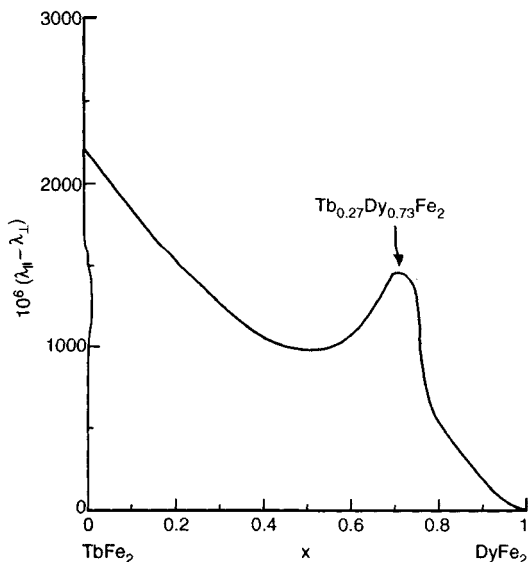


Figure 5. Magnetostriction developed in Tb_{1-x}Dy_xFe₂ with an applied field of 800 kA m⁻¹ showing a maximum in magnetostrictive strain when the magnetocrystalline anisotropy energy is a minimum for the composition Tb_{0.27}Dy_{0.73}Fe₂ (after Clark, 1974)

3.3 Temperature Dependence of Magnetostriiction

In Re-Fe compounds the temperature dependence of magnetostriction is dominated by the behavior of the rare-earth ions, usually following the single-ion behavior described by Callen and Callen (1963, 1965). Experimental data below room temperature (Clark, 1980;

Abbundi and Clark, 1978) show that the temperature dependences for λ_{111} measured from single-crystal TbFe₂ and TmFe₂ follow the $\hat{f}_{5/2} [L^{-1}(m)]$ law, the reduced hyperbolic Bessel function of the inverse Langevin function $L(x) = \coth x - 1/x$, where m is the reduced magnetization $M(T)/M(0)$ (Callen and Callen, 1963, 1965). The full strains are realized at low temperatures, reaching ~ 4500 p.p.m. in TbFe₂ and ~ 3500 p.p.m. in TmFe₂. At room temperature the strains in TbFe₂ and SmFe₂ are the largest of all the heavy RE-Fe compounds because they have the highest Curie temperatures.

Temperature effects in the pseudobinary compound Tb_{1-x}Dy_xFe₂ are influenced by the competing anisotropies of DyFe₂ and TbFe₂, and a moment reorientation occurs near room temperature. The temperature for this reorientation depends on the precise composition, and there are phase diagrams (Atzmony *et al.*, 1973; Sato *et al.*, 1986) that indicate the temperature at which one or the other of the two crystal axes [111] and [100] becomes the 'easy' axis (Figure 4).

Above room temperature, experimental data for $\lambda_{\parallel} - \lambda_{\perp}$ obtained from partially textured TbFe₂ and Tb_{0.27}Dy_{0.73}Fe₂ show a decrease in accordance with the $\hat{f}_{5/2} [L^{-1}(m)]$ behavior for a single-ion system. For the latter composition as the temperature increases, a greater proportion of the magnetostriction is due to the TbFe₂ content compared to that of the DyFe₂ (Clarke and Crowder, 1985).

These inherent physical properties can impose a limitation on the range of temperatures over which Terfenol-D can be used in devices. The lower limit is set by the spin reorientation, whilst the decrease in strains described by the $\hat{f}_{5/2} [L^{-1}(m)]$ law above room temperature restricts high-temperature operation to temperatures less than $\sim 180^{\circ}\text{C}$. Attempts continue to be made to enhance the high-temperature performance by the addition of other 3d transition elements (Co or Mn) (Clark *et al.*, 1991), but present indications are that an alternative solution will have to be sought if substantial increases are to be obtained.

Recently, the magnetostrictions of rare-earth alloys without iron have been examined at liquid nitrogen temperatures. In Tb_{1-x}Dy_x ($0.33 \leq x \leq 0.5$) single crystals, the strains reach levels of ~ 6000 p.p.m. (Clark *et al.*, 1992).

3.4 Field Dependence of Magnetostriction

From a practical point of view, one important goal is to achieve the largest strains with the minimum applied field and with that in mind, it is useful to study how the

magnetostrictive strains develop in relation to the magnetization processes that take place when a field is applied. Magnetization arising from 180° domain wall movement is not accompanied by a magnetostrictive deformation; the less energetically favorable processes, such as other domain wall movements or rotations of the magnetization, both of which generate the macroscopic magnetostrictive strains, tend to occur at higher fields. Separation of 180° wall displacements from these other processes would be ideal because the limits of applied field, between which the optimum magnetostrictive response $d\lambda/dH$ ($=d_{33}$, the 'd coefficient') occurs, would then be well defined and associated with just one part of the magnetization curve. In practice it is unusual for such well-defined responses to occur, and for most magnetization curves they tend to overlap. The following section describes the way that Terfenol-D can be engineered to produce the best magnetostrictive response from the smallest applied field.

4. Binary REFe₂ Compounds

4.1 Preparation

The REFe₂ binary and pseudobinary compounds crystallize into a cubic Laves phase C15 (cF24) structure (Figure 6). (The Laves phases and related structures are discussed in the chapter by Gladyshevskii and Bodak, Volume 1). The phase diagrams for the binary terbium-iron (Dariel and Atzmony, 1976) and dysprosium-iron (van der Groot and Buschow, 1970) systems are very similar, the former being shown in Figure 7. In the absence of specific phase diagrams for ternary compounds, binary diagrams often provide sufficient guidelines for the formation of pseudobinary compounds such as Tb_{1-x}Dy_xFe₂, where $x = 0.7$ or 0.73 and $y \approx 2.0$.

Examination of the phase diagram indicates that the intermediate REFe₂ phase is formed at ~ 67 at% Fe in a peritectic reaction. For the pseudobinary (Dy,Tb)Fe₂ compound, as the temperature is lowered from the melt, a series of reactions occurs to give DyFe₃ or Tb₆Fe₂₃ and TbFe₃, followed by the formation of REFe₂. According to McMasters *et al.* (1986), it is possible to produce metastable REFe₂ at temperatures slightly higher than the peritectic in order to bypass the undesirable segregation of the REFe₃ phase. At the peritectic temperature an unstable intermediate phase is formed from an RE-rich melt. The core of the initial crystallization is iron rich but, with concentration gradients, the grain boundaries are RE rich. The results

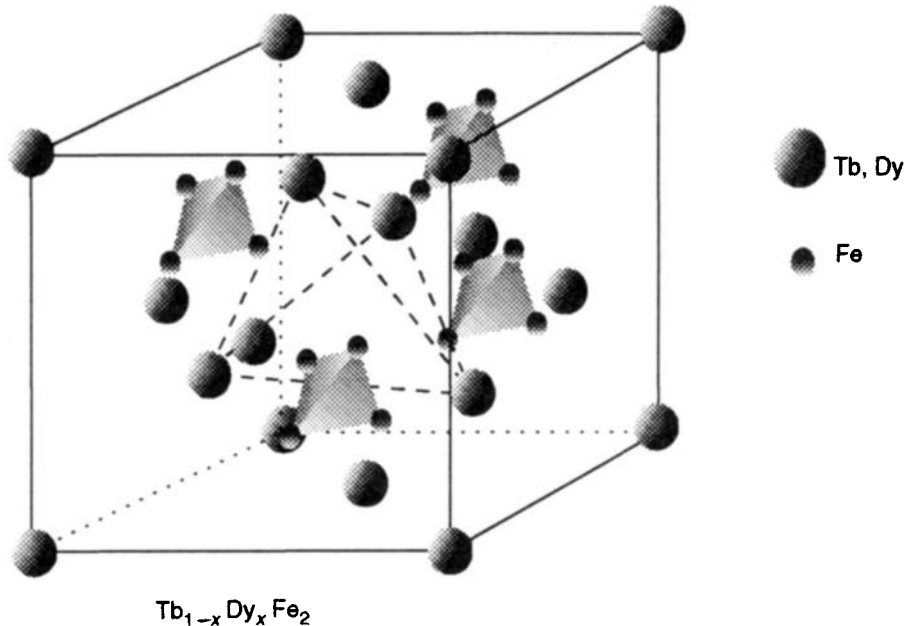


Figure 6. Rare earth-iron Laves phase crystal structure (C15, cF24)

of phase separation are illustrated in Figure 8, where micrographs from arc-melted polycrystalline samples show the RE-rich regions near the grain boundaries and at the other extreme the occurrence of REFe_3 . Provided the preparation techniques are correct, REFe_2 grain growth can be achieved.

The two production techniques usually employed are contained, free-float zone melting using a quartz crucible (Pfann, 1952) or, if constraints imposed by crucible size are to be avoided, Bridgman growth (Verhoeven *et al.*, 1987) using a boron nitride crucible with a platinum sheet liner to avoid reaction between the RE and boron nitride (Laudise, 1970). The Czochralski method can also be employed (McMasters *et al.*, 1986), and with a slow speed and sufficient heat flow it can produce material with lower internal stress and fewer dislocations (Bi *et al.*, 1992).

4.2 Metallurgy

It has been shown by Verhoeven *et al.* (1987) that the dendritic growth in $\text{Tb}_{0.3}\text{Dy}_{0.7}\text{Fe}_2$ is primarily along a $\langle 11\bar{2} \rangle$ direction in $\{111\}$ sheet planes, but the reason why the $\langle 111 \rangle$ direction is not a growth direction is not fully understood. Efforts to produce $\langle 111 \rangle$ -oriented material would be rewarded, because the resultant magnetostrictive strains would exceed those seen in

$\langle 11\bar{2} \rangle$ -oriented material. The ideal platelike structure is depicted in Figure 9 and a micrograph of a section cut from a rod of $\text{Tb}_{0.27}\text{Dy}_{0.73}\text{Fe}_{1.95}$, prepared by Etrema Products (USA), illustrates how well the lamellae form in practice (Figure 10). This method of observing the structure is clearly destructive; but, because structure plays such an important role in the magnetostrictive response, a technique has been developed which can test samples, typically 250 mm long, without recourse to sectioning (Schulze, 1990). The grain orientation is examined by monitoring the flux distribution at each point along the rod axis, and local deviations in AC (alternating current) permeability indicate the regions of grain misorientation or the presence of voids or cracks. The importance of grain orientation will be discussed further in Section 5 in relation to the optimization of material performance for devices.

5. Properties of Terfenol-D for Devices

Having considered some fundamental aspects of magnetostriction in RE-Fe compounds, attention is now turned to their macroscopic properties and an examination of the principles behind the use of Terfenol-D in working devices.

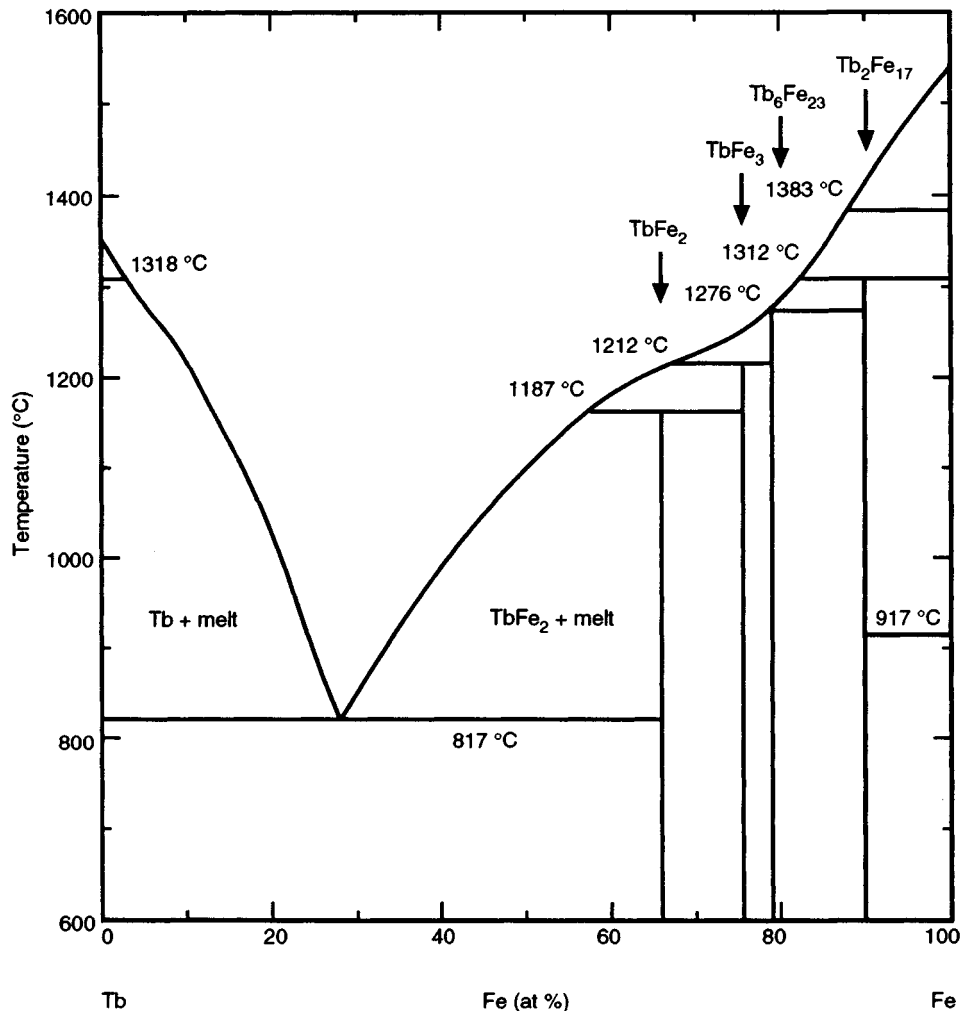


Figure 7. Binary terbium-iron phase diagram (after Dariel *et al.*, 1976)

5.1 Magnetomechanical Coupling

Transduction efficiency is gauged by the magnetomechanical coupling coefficient k and through the equations of state it can be related to physically measurable parameters. Following the analysis for piezoelectric materials given by Mason (1960), adapted by Davies (1977) for magnetostrictive materials, if ϵ represents strain, σ the stress, and B and H the magnetic induction and field, respectively, then

$$dB = \left(\frac{\partial B}{\partial H} \right)_{\sigma} dH + \left(\frac{\partial B}{\partial \sigma} \right)_{H} d\sigma$$

$$\therefore dB = \mu_{\sigma} dH + d^* d\sigma \quad (5)$$

and

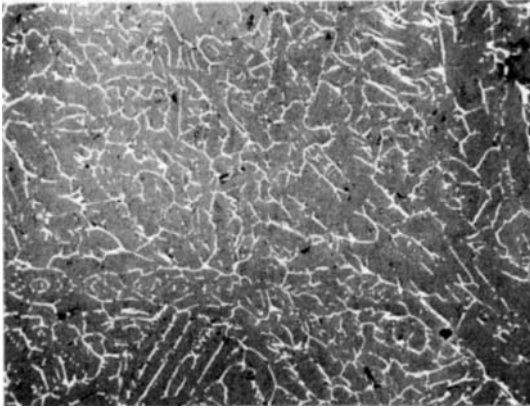
$$d\epsilon = \left(\frac{\partial \epsilon}{\partial H} \right)_{\sigma} dH + \left(\frac{\partial \epsilon}{\partial \sigma} \right)_{H} d\sigma$$

$$\therefore d\epsilon = d dH + S_H d\sigma \quad (6)$$

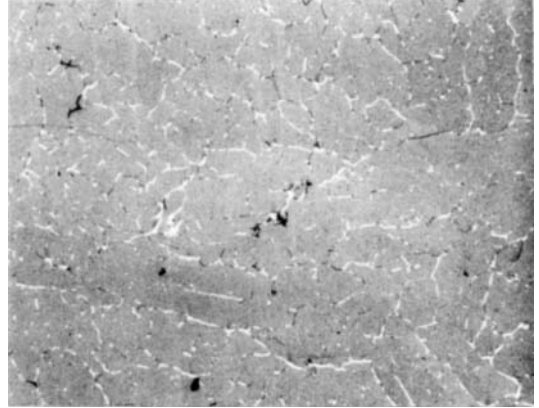
where the permeability at constant stress

$$\mu_{\sigma} = \left(\frac{\partial B}{\partial H} \right)_{\sigma}$$

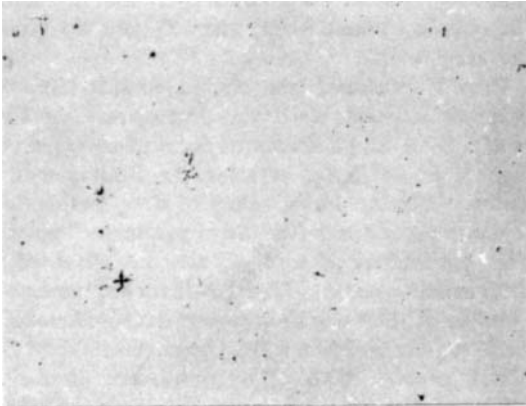
$$d^* = \left(\frac{\partial B}{\partial \sigma} \right)_{H}$$



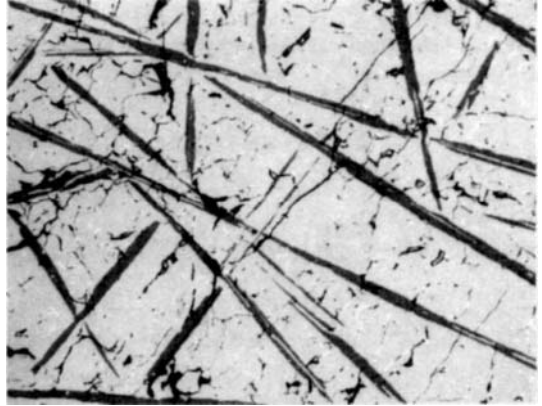
$y = 1.7$



$y = 1.95$



$y = 1.975$



$y = 2.1$

Figure 8. Segregation in as-cast polycrystalline RE-Fe compounds with the composition $\text{Tb}_{0.27}\text{Dy}_{0.7}\text{Fe}_y$. With $y = 1.7$ the light areas are regions of RE-rich phase; for $y = 2.1$ the gray linear regions are Fe-rich REFe_3 and the dark areas are voids developed during specimen preparation

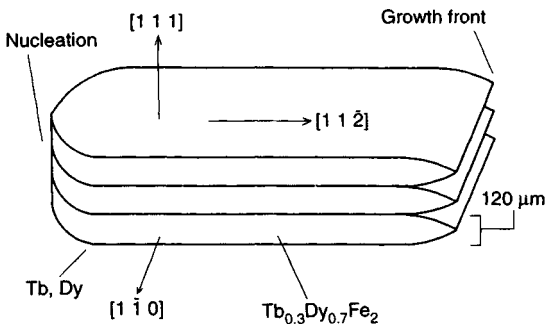


Figure 9. Ideal structure of a grain-oriented, pseudobinary terbium-dysprosium-iron compound

$$\text{and } d = \left(\frac{\partial \epsilon}{\partial H} \right)_\sigma$$

are the piezomagnetic strain coefficients and the elastic compliance at constant field

$$S_H = \left(\frac{\partial \epsilon}{\partial \sigma} \right)_H$$

Now

$$d\sigma = \left(\frac{\partial \sigma}{\partial B} \right)_\epsilon dB + \left(\frac{\partial \sigma}{\partial \epsilon} \right)_B d\epsilon$$

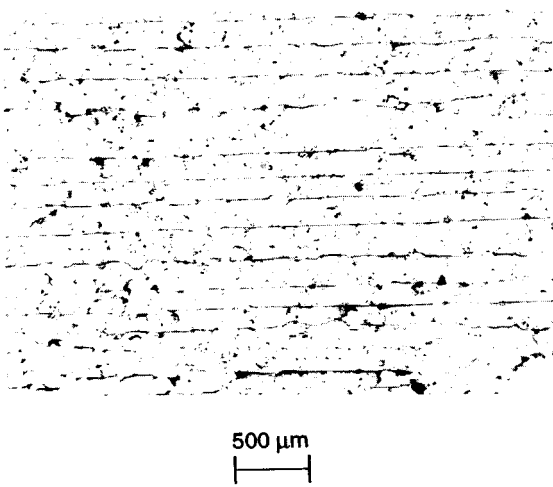


Figure 10. Micrograph of the lamellae in grain-oriented Tb_{0.27}Dy_{0.73}Fe_{1.95}

$$\therefore d\sigma = -\lambda dB + E_B d\epsilon \quad (7)$$

and

$$dH = \left(\frac{\partial H}{\partial B} \right)_\epsilon dB + \left(\frac{\partial H}{\partial \epsilon} \right)_B d\epsilon$$

$$\therefore dH = \frac{1}{\mu_\epsilon} dB - \lambda d\epsilon \quad (8)$$

where the magnetoelastic coefficient

$$\lambda = - \left(\frac{\partial \sigma}{\partial B} \right)_\epsilon = - \left(\frac{\partial H}{\partial \epsilon} \right)_B$$

$$\frac{1}{\mu_\epsilon} = \left(\frac{\partial H}{\partial B} \right)_\epsilon$$

where μ_ϵ is the permeability at constant length, and

$$E_B = \left(\frac{\partial \sigma}{\partial \epsilon} \right)_B$$

is Young's modulus at constant induction.

From equations (5) and (6)

$$d dB - \mu_o d\epsilon = (dd^* - \mu_o S_H) d\sigma \quad (9)$$

and

$$S_H dB - d^* d\epsilon = (S_H \mu_o - dd^*) dH \quad (10)$$

Comparing equations (9) and (10) with equations (7) and (8)

$$\mu_o = \mu_\epsilon / (1 - k^2) \quad (11)$$

and

$$E_B = E_H / (1 - k^2) \quad (12)$$

where

$$k^2 = dd^* / \mu_o S_H \quad (13)$$

Equations (11) and (12) demonstrate the consequences of magnetomechanical coupling; the permeability when the material is free to expand or contract is the same as that in the clamped state (i.e. constant length) when $k=0$, otherwise the permeability is changed owing to the interaction between the applied stress and magnetic induction (cf. $(\partial B / \partial \sigma)_H$ in equation 5). Likewise, the modulus of elasticity is modified by a contribution from the coupling unless $k=0$, when E_B and E_H become indistinguishable.

Provided the material is not subjected to large field or stress variations $d \approx d^*$, as demonstrated by Clark *et al.* (1990), and a simplified form of equation (13), namely $k^2 = d^2 / \mu_o S_H$, offers a practical method to measure k by obtaining values of d , μ_o and S_H from separate experiments (the 'three parameter' method). The parameters d and μ_o can be obtained by differentiating static λ - H and B - H curves, respectively (Abell *et al.*, 1986), or by applying small oscillatory AC fields superimposed on a DC (direct current) bias field (Clark *et al.*, 1990). The compliance S_H can be measured directly either from the velocity of sound

$$v = \left(\frac{E_H}{\rho} \right)^{1/2} \quad (14)$$

where ρ is the density, or from the resonant frequency f_R for a particular geometry. In a cylindrical bar of length l , for instance, the longitudinal resonance occurs when

$$f_R = \frac{1}{2l} \left(\frac{E_H}{\rho} \right)^{1/2} \quad (15)$$

Separate measurements of d , μ_o and S_H are time consuming and an alternative method to measure the coupling uses magnetomechanical resonance by measuring the resonant and antiresonant frequencies f_R and f_A . From equations (12) and (15)

$$k_{33}^2 = \frac{\pi^2}{8} (1 - f_R^2 / f_A^2) \quad (16)$$

where a geometrical shape factor $\pi^2/8$ is introduced (Mason, 1960) for a cylindrically shaped sample and k_{33} is the coupling of the longitudinal vibrational mode with an excitation applied parallel to the rod length. Values for f_R and f_A can be measured as a function of the applied DC bias field by monitoring the resonance through the electrical impedance (Savage *et al.*, 1975). Resonance frequencies are typically in the kilohertz range and, provided a correction is made for eddy current effects, these coupling values are generally in agreement with the 'three parameter' results (Schulze, 1990).

Although discussion of the coupling is incomplete until consideration is given to its stress dependence, it is worth noting at this stage just how good Terfenol-D is compared with its predecessors. For instance, in a nickel alloy (e.g. Permendur) $k_{33} \approx 0.5$, whereas values as large as 0.8 have been measured in Terfenol-D (Schulze, 1990). This represents an efficiency of 64% in energy conversion—equal to or better than most piezoelectric materials.

5.2 Pressure Response of λ , d_{33} and k_{33}

Owing to the magnetoelastic response of magnetostrictive materials, their states of magnetization are susceptible to applied stress so that the maximum strains generated in an applied field λ_m , the rate of increase in strain with applied field d_{33} and the coupling coefficient k_{33} are not only field dependent but also pressure dependent. The first observations of the effects of pressure on the magnetostriction in Terfenol-D and related compounds were reported by Clark and Savage (1983) for $\text{Tb}_{0.27}\text{Dy}_{0.73}\text{Fe}_{1.95}$, Clark *et al.* (1988) for $\text{Tb}_{0.3}\text{Dy}_{0.7}\text{Fe}_{1.9}$ and Clark *et al.* (1983) for $\text{Tb}_{0.5}\text{Dy}_{0.5}\text{Fe}_{1.95}$. For the composition $\text{Tb}_{0.3}\text{Dy}_{0.7}\text{Fe}_{1.95}$, grain oriented with the $[11\bar{2}]$ axes of the crystalline plates, the applied uniaxial pressure and field all parallel to the rod axis, an anomalously large jump in the magnetostriction occurs at a particular field strength for each level of pressure (known as the 'burst' effect). An example in Figure 11 shows the sudden increase in 'd coefficient' with the application of pressure. Jenner *et al.* (1990) reported the corresponding pressure dependence of the optimum coupling coefficient which mirrors the field and pressure dependences of the permeability, 'd coefficient' and elastic compliance in accordance with equation (13); typical data for $\text{Tb}_{0.3}\text{Dy}_{0.7}\text{Fe}_{1.95}$ are shown in Figure 12. For the same sample the relationship between applied field and applied pressure to obtain either optimum coupling or optimum 'd coefficient' is shown in Figure 13.

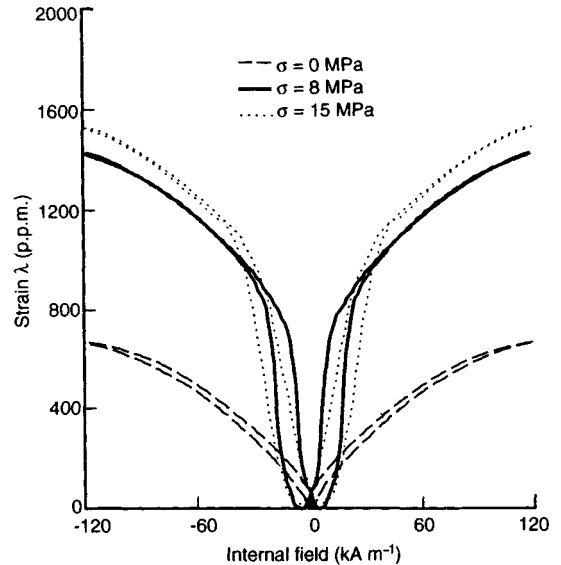


Figure 11. Magnetostriction in grain-oriented $\text{Tb}_{0.3}\text{Dy}_{0.7}\text{Fe}_{1.95}$, measured along the growth axis with the field and uniaxial pressures applied parallel to the $[11\bar{2}]$ axes, illustrating a sharp increase in $d\lambda/dH$ ('d coefficient') in the ranges 0–8 MPa

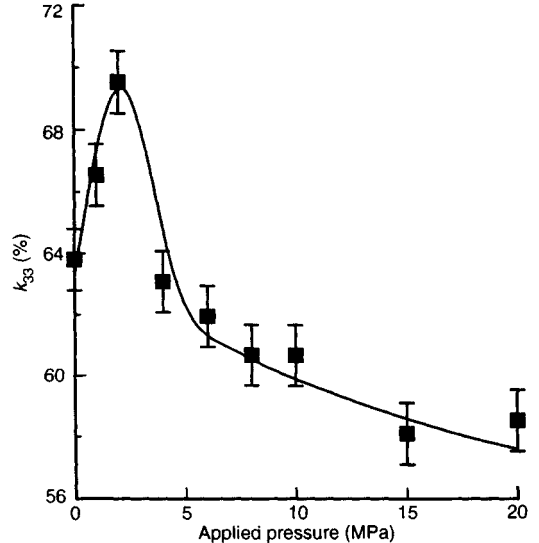


Figure 12. Pressure dependence of the optimum magneto-mechanical coupling coefficient k_{33} in the grain-oriented $\text{Tb}_{0.3}\text{Dy}_{0.7}\text{Fe}_{1.95}$

It is apparent that to operate Terfenol-D efficiently in a device, a choice may have to be made between these two. For instance, to produce the largest strains with the smallest increases in applied field (thereby minimizing

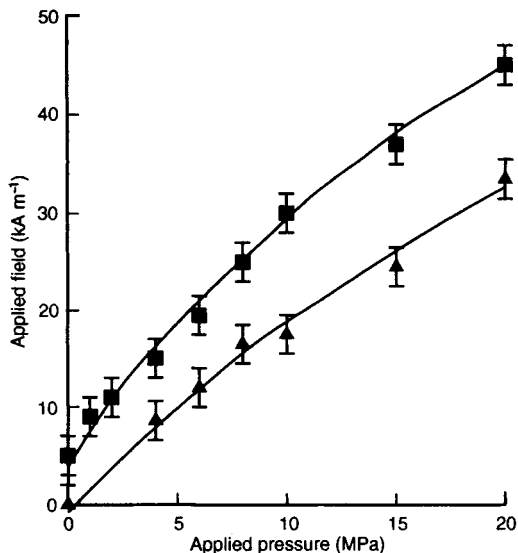


Figure 13. Applied fields and pressures required to achieve either optimum coupling k_{33} (■) or optimum 'd coefficient' d_{33} (▲) in grain-oriented $\text{Tb}_{0.3}\text{Dy}_{0.7}\text{Fe}_{1.95}$

power requirements), the field and pressure to obtain optimum 'd coefficient' would have to be chosen.

To explain the 'burst' effect, the associated magnetization processes have been analyzed. Symmetry arguments show that no magnetic strains are realized by 180° domain wall movements, and the generation of magnetostrictive strains depends on an effective rotation of magnetization M by the movement of domain walls, other than 180° walls, or by rotation of the direction of magnetization which exists within each single domain. With such rotations, Clark *et al.* (1984) predict that the magnetostriction develops at a rate proportional to M^2 in $\text{Tb}_{0.27}\text{Dy}_{0.73}\text{Fe}_{1.95}$, and departures from this behavior are attributed to structural imperfections. The 'burst' effect anomaly in $\text{Tb}_{0.3}\text{Dy}_{0.7}\text{Fe}_{1.9}$ was explained (Clark *et al.*, 1988) by crystallographic twinning, but more recent work by Jiles and Thielke (1993) is based on a three-dimensional anisotropic rotational model used previously to map the anisotropic energy surfaces (Thielke and Jiles, 1991, 1992). By minimizing field and anisotropy energies, the model predicts both a sudden increase in strain at a critical field strength and the negative strains which have been observed at low field strengths (Schulze *et al.*, 1992). It also shows that these features in the predicted λ - H curves depend on the initial distribution of moments amongst the various $\langle 111 \rangle$ axes prior to the application of a field along the $[11\bar{2}]$ axis. Provided that distribution can be regulated (for instance, by the

application of a uniaxial prestress) so that the moments preferentially lie along the $\langle 111 \rangle$ axes normal to the rod axis, the subsequent magnetostrictive response can be maximized.

5.3 Frequency Response

Terfenol-D, being a metallic material with electrical conductivity $\sigma \approx 1.6 \times 10^6 \Omega^{-1} \text{m}^{-1}$, suffers from induced eddy currents in AC fields. Macroscopic screening currents (i.e. the skin effect) prevent full field penetration and cause an apparent reduction in permeability. Experimental data (Figure 14) obtained from a region of the magnetization curve which is relatively free from domain wall movement agree with skin effect predictions calculated in accordance with the geometry of the measured sample (Greenough and Schulze, 1990). This effect and the associated losses can be minimized by laminating the Terfenol-D, and it is predicted by Butler (1988) that the operational frequency can be raised to $\sim 80 \text{ kHz}$ for 1 mm thick laminations. However, if magnetization is proceeding mainly by domain wall movement (for instance, in the low-field region of the magnetization curve; Figure 15), then a significant level of 'anomalous loss' occurs due to localized eddy currents near the walls, especially at high frequencies when the domain wall velocities increase, presenting the same problems to the Terfenol-D user as those already encountered by electrical transformer designers. There are few experimental data for Terfenol-D at high frequencies and little attention has been given to the corresponding mechanical response speed even if the input magnetic energy levels are maintained. Such information is essential if successful high-speed actuation is to be achieved.

6. Recent Developments

6.1 Magnetic Annealing

The effect of magnetic annealing of Terfenol-D was first investigated by Verhoeven *et al.* (1989), who showed that raising the temperature above the Curie temperature and cooling in the presence of a magnetic field ($\sim 740 \text{ kA m}^{-1}$) caused the maximum magnetostrictive strains subsequently measured at room temperature to be increased. Recently Galloway *et al.* (1993a, b) have demonstrated that in $\text{Tb}_{0.3}\text{Dy}_{0.7}\text{Fe}_{1.95}$ magnetic annealing can lead to an increase in magnetic anisotropy and with selected annealing conditions d_{33} increases fivefold at pressures as low as 2 MPa (Figure 16). This enhancement of magnetostrictive

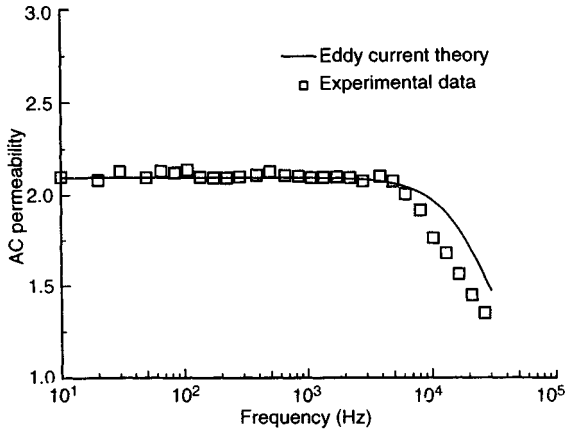


Figure 14. Experimental data for the apparent AC permeability of a 6 mm diameter rod of $\text{Tb}_{0.23}\text{Dy}_{0.73}\text{Fe}_{1.95}$ as a function of frequency in an applied DC bias field of 15 kA m^{-1} compared with skin effect calculations (Greenough and Schulze, 1990)

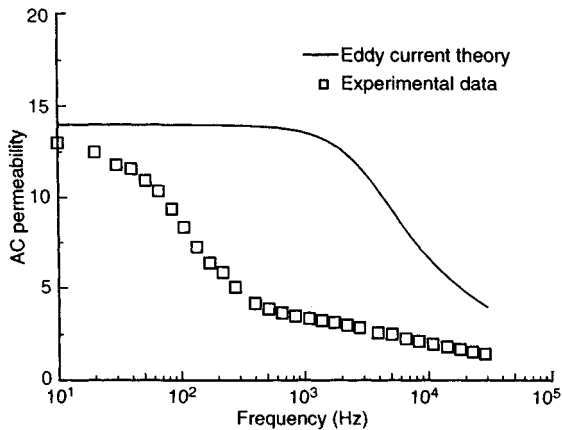


Figure 15. Experimental data for the apparent AC permeability of a 6 mm diameter rod of $\text{Tb}_{0.23}\text{Dy}_{0.73}\text{Fe}_{1.95}$ as a function of frequency in zero applied DC bias field compared with a calculated macroscopic eddy current effect (Greenough and Schulze, 1990)

performance at low pressures is because the induced anisotropy, like an applied uniaxial prestress, encourages moments to populate preferentially those $\langle 111 \rangle$ axes which subsequently generate the greatest strains. By altering the annealing conditions, the 'd coefficient' can be reduced in magnitude but it is then relatively insensitive to the prestress level. These responses to magnetic annealing lend support to the predictions of the three-dimensional anisotropy model. If regulation of the annealing conditions can, as the experimental data indicate, control the pressure dependence of the

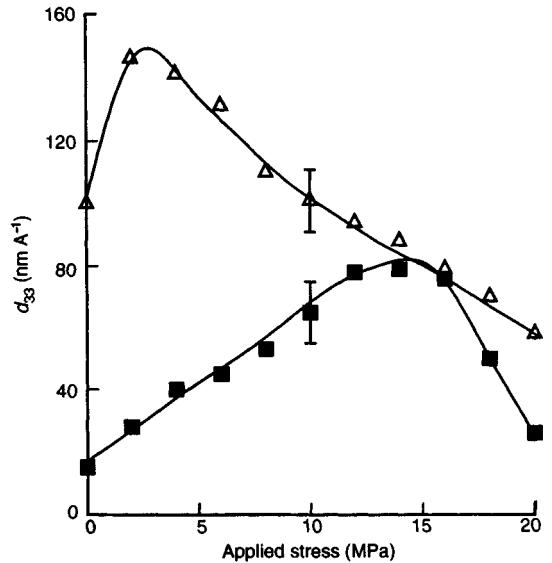


Figure 16. Pressure dependence of d_{33} in $\text{Tb}_{0.3}\text{Dy}_{0.7}\text{Fe}_{1.95}$ before (■) and after (△) magnetic annealing (Galloway *et al.*, 1993a, b)

'd coefficient', then magnetostrictive response may be tailored according to the requirements of a particular application.

6.2 Composites

As an alternative to laminating, which is a feasible but not a particularly easy process, a composite containing granular Terfenol-D embodied in a nonconducting matrix could be advantageous. This has been achieved by Sandlund and Cedell (1992) while maintaining a significant level of magnetostriction ($\sim 1000 \text{ p.p.m.}$) (Figure 17). With the added advantage of being machinable into different shapes, such material should have a much higher frequency response than the parent Terfenol-D compound. One disadvantage at the present time is that the carefully engineered and controlled magnetization process that produces such high 'd coefficients' in grain-oriented Terfenol-D no longer prevails in the relatively randomly oriented grains of a composite, and larger fields are required. However, the piezomagnetic strains produced are accompanied by a lower sensitivity to stress.

7. Magnetostrictive Actuators

The production of RE-Fe compounds is sufficiently well developed for devices to be constructed and these are

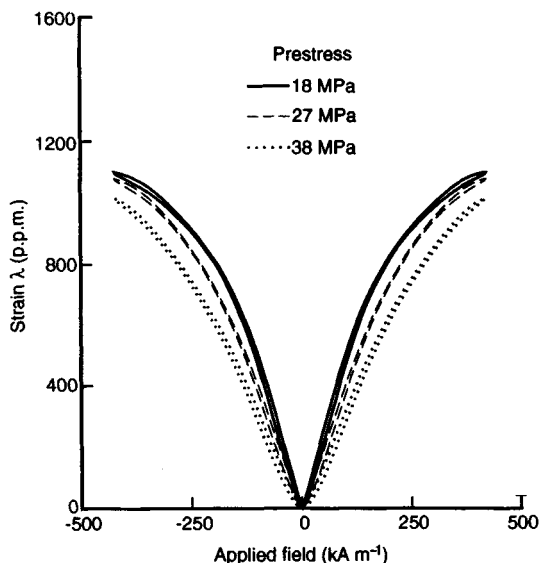


Figure 17. Field and pressure dependence of the magnetostriction in a powdered Terfenol-D composite (Sandlund and Cedell, 1992)

finding a wide variety of applications. It is beyond the scope of this chapter to provide a comprehensive survey of all the known applications to date or to give a full technical description of how such devices are designed. Usually each actuator is constructed to meet individual specifications which define the required displacement, load, speed, physical size, power consumption, etc. With information on the field and pressure dependences of λ , d_{33} and k_{33} in Terfenol-D, as described in previous sections, actuators can be built which typically require ≤ 10 W of electrical power and generate 100 to 200 μm of movement with loads of ~ 35 kg from a rod of Terfenol-D ~ 6 mm in diameter and 150 mm long.

7.1 Operating Principles

Efficient operation (i.e. in terms of minimizing the power requirements) is usually achieved with a combination of fields from permanent magnets and a solenoid. A typical isopressure strain versus field curve in Figure 18 illustrates the role of permanent magnets in generating a DC bias field H_b , upon which a dynamic (slowly varying DC or AC) field from a solenoid is superimposed to generate a corresponding strain.

7.2 Actuator Design and Control

Several actuator designs have been published, and they can be found in the proceedings of conferences held

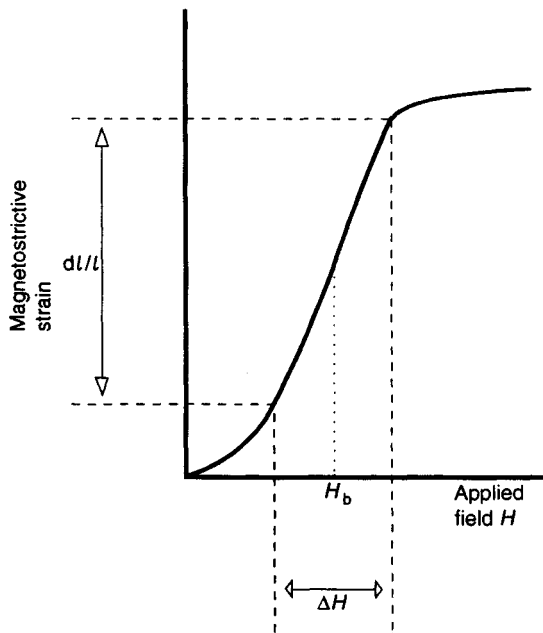


Figure 18. Typical variation of magnetostrictive strain as a function of applied field at constant pressure, illustrating the dynamic field variations about a DC bias field H_b and the corresponding strain of $d\lambda/l$

recently (Section 10.2, Tyren, 1988; Lenz, 1990; Borgmann and Lenz, 1992) but experience has shown that the same actuator design cannot be employed for every application. Terfenol-D is reactive; so its magnetomechanical performance changes in accordance with the working conditions, for instance when static or dynamic loads are varying; and, for regulated movement in such circumstances, some element of automatic feedback control may be necessary. Furthermore, different samples of Terfenol-D with the same nominal composition tend to have slightly different magnetomechanical performances which, together with nonlinearities and hysteresis, can be catered for by an 'intelligent' control system.

7.3 Applications

Three specific applications of Terfenol-D actuators are as follows.

7.3.1 Sonar

Early piston or folded-horn transducers (Meeks and Timme, 1977; Smith and Logan, 1977) contained relatively low-grade Terfenol-D ($k_{33} \approx 0.6$, $d_{33} \approx 80 \text{ nm A}^{-1}$)

compared with material presently available ($k_{33} \approx 0.7$, $d_{33} \approx 180 \text{ nm A}^{-1}$). Studies of Terfenol-D under high-drive conditions show that it is more attractive for low-frequency sonar devices than its piezoelectric counterpart PZT (lead zirconate titanate) (Moffett *et al.*, 1991a, b) and transducers based on Terfenol-D are now commercially available. For instance, omnidirectional, resonant, flextensional transducers have been designed to work in the 300 Hz to 5 kHz band, resonating at 550 Hz. The source level at 550 Hz is $\sim 200 \text{ dB re } 1 \mu\text{Pa at } 1 \text{ m}$ (Asea Brown Boveri, EB Seatech, Sweden), and a typical frequency response is shown in Figure 19. Another design has been published by Butler and Ciosek (1980) which contains an octagonal arrangement of Terfenol-D rods with a circumferential resonant mode at 775 Hz, delivering acoustic powers of $\sim 350 \text{ W}$. The performance of resonant devices has been studied by Claeysen *et al.* (1991) and strain amplitudes of $\sim 2440 \text{ p.p.m.}$ (peak to peak) were measured at resonance. A model of a complete device predicts its performance and also yields d_{33} , k_{33} , E_H and μ_o values for the Terfenol-D drive element by analyzing the electrical impedance of the device as a function of frequency (Claeysen, 1989).

7.3.2 Fuel Injection Valve

A design by Dyberg (1986) produces movement which regulates a diesel engine valve with injection pressures of $\sim 600 \text{ bar}$, operating at a frequency of $\sim 12 \text{ Hz}$.

7.3.3 Active Vibration Control

The load-bearing capabilities of Terfenol-D, coupled with its large magnetostriction and high transduction efficiency, present an unrivaled opportunity for active vibration control. Effort has concentrated on devising control systems which take vibration sensor signals to regulate the actuator (Reed, 1988; Hiller *et al.*, 1989) and, in particular, self-adaptive controllers which maintain optimum system performance even though the characteristics of the actuator may change owing to variations in load during operation (Parvinmehr *et al.*, 1989; 1992; Adaptive Control Systems, 1990).

8. Summary

Progress in magnetostrictive intermetallics has made a great leap forward following the initial discovery of huge magnetostrictions in the rare-earth elements. Since the first research-grade RE-Fe compounds were prepared,

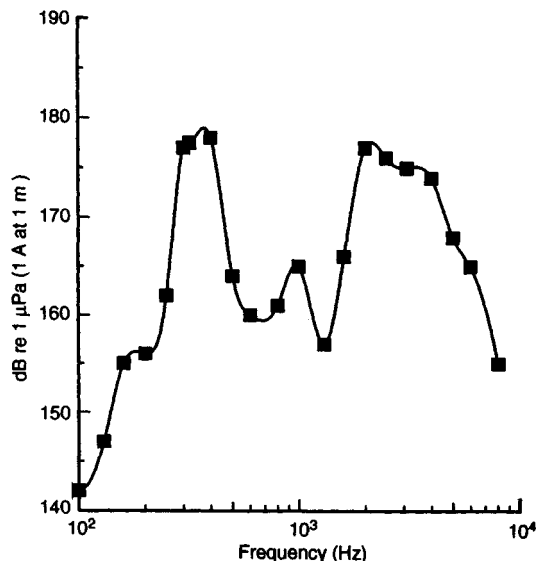


Figure 19. Output from a resonant Terfenol-D sonar transducer (reproduced by permission of Asea Brown Boveri)

processing technology has improved, so that high-quality Terfenol materials with sufficiently reproducible properties are now available in quantities for devices to be constructed. The exceptional magnetostrictive strains, transduction efficiency and load-bearing capability offer great potential in a wide variety of applications, many of which have yet to be realized in practice.

The present work has attempted to review the progress from fundamental research to device applications—a process which has taken about 30 years—and much credit for that progress is due to A. E. Clark and co-workers in the USA, as evident from the number of publications cited herein. Obviously not every contribution can be recognized in this review, but it is hoped that sufficient information has been given for readers to pursue any other aspects of the subject which have had to be omitted.

9. Acknowledgements

The authors are grateful to the staff at the University of Hull and all members of the magnetics research group past and present who made a contribution to this work, but especially to Judy Slator who had the unenviable task of turning illegible writing into a professional manuscript. Their thanks also go to Stuart Abell for the use of the micrographs shown in Figure 8.

10. References

10.1 Specific

- Abbundi, R., and Clark, A. E. (1978). *J. Appl. Phys.*, **49**, 1969.
- Abell, J. S., Butler, D., Greenough, R. D., Joyce, V., and Pitman, K. C. (1986). *J. Magn. Magn. Mater.*, **62**, 6.
- Adaptive Control Systems, DRA Defence Research Agency. (1990). *UK. Pat. Appl.*, 89310286.3.
- Atzmony, V., Dariel, M., Bauminger, E., Lebenbaum, D., Nowik, I., and Offer, S. (1973). *Phys. Rev. B.*, **7**, 4220.
- Bi, Y. J., Hwang, A. M. H., and Abell, J. S. (1992). *J. Magn. Mater.*, **104**, 1471.
- Bozorth, R. M., and Walker, J. G. (1952). *Phys. Rev.*, **88**, 1209.
- Bulat, T. J. (1974). *Ultrasonics*, **12**, 59.
- Butler, J. L. (1988). *Application Manual for the Design of Magnetostrictive Transducers*. Edge Technologies Inc., Iowa, USA, Section III, p. 28.
- Butler, J. L., and Ciosek, S. J. (1980). *J. Acoust. Soc. Am.*, **67**(5), 1809.
- Callen, E., and Callen, M. B. (1963). *Phys. Rev.*, **129**, 578.
- Callen, E., and Callen, M. B. (1965). *Phys. Rev.*, **139**, A446.
- Chikazumi, S. (1964). *Physics of Magnetism*. Wiley, New York.
- Claeyssens, F. (1989). PhD thesis, INSA, Lyon, France.
- Claeyssens, F., Colombani, D., Tessereau, A., and Ducros, B. (1991). *IEEE Trans. Magn.*, **27**(6), 5343.
- Clark, A. E. (1974). *AIP Conf. Proc.*, No. 18, 1015.
- Clark, A. E. (1980). In *Ferromagnetic Materials* (ed. E. P. Wohlfarth). North Holland, Amsterdam, Vol. 1 Chapter 7, 531.
- Clark, A. E., and Crowder, D. N. (1985). *IEEE Trans. Magn.*, **21**(5), 1945.
- Clark, A. E., DeSavage, B., and Bozorth, R. M. (1965). *Phys. Rev.*, **138**, A216.
- Clark, A. E., and Savage, H. T. (1983). *J. Magn. Magn. Mater.*, **31–34**, 849.
- Clark, A. E., Savage, H. T., and Spano, M. L. (1984). *IEEE Trans. Magn.*, **20**(5), 1443.
- Clark, A. E., Spano, M. L., and Savage, H. T. (1983). *IEEE Trans. Magn.*, **19**(5), 1964.
- Clark, A. E., Teter, J. P., and McMasters, O. D. (1988). *J. Appl. Phys.*, **63**(8), 3910.
- Clark, A. E., Teter, J. P., and Wun-Fogle, M. (1991). *J. Appl. Phys.*, **69**(8), 5771.
- Clark, A. E., Teter, J. P., Wun-Fogle, M., Moffett, M., and Lindberg, J. (1990). *J. Appl. Phys.*, **67**(9), 5007.
- Clark, A. E., Wun-Fogle, M., and Restorff, J. B. (1992). *IEEE Trans. Magn.*, **28**(5), 3156.
- Dariel, M. P., Halthuis, J. T., and Pickus, M. R. (1976). *J. Less-Common Met.*, **45**, 91.
- Davies, Jr, C. M. (1977). *US Navy J. Underwater Acoust.*, **27**(1), 39.
- Dyberg, J. (1986). In *Proc. 1st International Conference on Giant Magnetostrictive Alloys and Their Impact on Actuator and Sensor Technology, Marbella, Spain*. (ed. C. Tyren), Terfenol AB, Lund, Sweden.
- Galloway, N., Greenough, R. D., Schulze, M. P., and Jenner, A. G. I. (1993a). *J. Magn. Magn. Mater.*, **119**, 107.
- Galloway, N., Greenough, R. D., Schulze, M. P., and Thoeke, J. B. (1993b). Presented at *INTERMAG Conference*, Houston, (Unpublished).
- Greenough, R. D., and Schulze, M. P. (1990). *IEEE Trans. Magn.*, **26**(5), 2586.
- Hiller, M. W., Bryant, M. D., and Umegaki, J. (1989). *J. Sound Vib.*, **133**(3), 364.
- Jenner, A. G. I., Greenough, R. D., Wilkinson, A. J., and Parvinmehr, A. (1990). *IEEE Trans. Magn.*, **26**(5), 2589.
- Jiles, D. C. (1991). *Introduction to Magnetism and Magnetic Materials*. Chapman and Hall, London.
- Jiles, D. C., and Thoeke, J. B. (1993). *J. Magn. Magn. Mater.* (in press).
- Kittel, C. (1949). *Rev. Mod. Phys.*, **21**, 555.
- Koon, N. C., Schindler, C., Williams, C., and Carter, F. (1974). *J. Appl. Phys.*, **45**, 5389.
- Laudise, R. A. (1970). *The Growth of Single Crystals*. Prentice Hall, Englewood Cliffs, NJ, Chapter 5.
- Lee, E. W. (1955). *Rep. Prog. Phys.*, **18**, 184.
- Luborsky, F. E. (1980). In *Ferromagnetic Materials* (ed. E. P. Wohlfarth). North Holland, Amsterdam, Chapter 6.
- Mason, P. W. (1960). *Piezoelectric Crystals and Their Application to Ultrasonics*, 5th edn. Van Nostrand, New York, Chapter 5, p. 66.
- McMasters, O. D., Verhoeven, J. D., and Gibson, E. D. (1986). *J. Magn. Magn. Mater.*, **54–57**, 849.
- Meeks, M. B., and Timme, R. W. (1977). *J. Acoust. Soc. Am.*, **62**, 1158.
- Moffett, M. B., Clark, A. E., Wun-Fogle, M., Lindberg, J. F., Teter, J. P., and McLaughlin, E. A. (1991a). *J. Acoust. Soc. Am.*, **89**(3), 1448.
- Moffett, M. B., Powers, J. M., and Clark, A. E. (1991b). *J. Acoust. Soc. Am.*, **90**(2), 1184.
- Ohta, Y., and Shimizu, M. (1982). *J. Phys. F.*, **12**, 1045.
- Parvinmehr, A., Greenough, R. D., Wilkinson, A. J., and Jenner, A. G. I. (1989). In *Proc. IFAC Symposium on Adaptive Systems in Control*, Vol. II, p.547.
- Parvinmehr, A., Wilkinson, A. J., and Greenough, R. D. (1992). In *Proc. 5th IMA Conference on Control Theory*. Oxford University Press, Oxford, pp. 199–204.
- Pfann, W. G. (1952). *Trans. AIME*, **194**, 747.
- Reed, R. S. (1988). In *Proc. 59th Shock and Vibration Symposium*, Albuquerque, NM, Vol. 4.
- Rhyne, J. J., and Legvold, S. (1965). *Phys. Rev.*, **138**, A507.
- Sandlund, L., and Cedell, T. (1992). In *Proc. 3rd International Technology Transfer Congress, 'Actuator '92'* (eds H. Borgman and K. Lenz), VDI/VDE, Bremen, Germany.
- Sato, K., Isikawa, Y., Mori, K., Clark, A. E., and Callen, E. (1986). *J. Magn. Magn. Mater.*, **54–57**, 875.
- Savage, H. T., Clark, A. E., and Powers, J. M. (1975). *IEEE Trans. Magn.*, **11**(5), 1355.
- Schulze, M. P. (1990). PhD thesis, University of Hull, UK.
- Schulze, M. P., Greenough, R. D., and Galloway, N. (1992). *IEEE Trans. Magn.*, **28**(5), 3159.
- Slonczewski, J. C. (1961). *Phys. Rev.*, **122**(5), 1367.
- Smith, R. R., and Logan, J. C. (1977). *US Navy J. Underwater Acoust.*, **27**(1), 175.

- Tatebayashi, T., Ohtsuka, S., Ukai, T., and Mori, N. (1986). *J. Magn. Magn. Mater.*, **54–57**, 973.
- Thoelke, J. B., and Jiles, D. C. (1991). *IEEE Trans. Magn.*, **27**(16), 5352.
- Thoelke, J. B., and Jiles, D. C. (1992). *J. Magn. Magn. Mater.*, **104–107**, 1453.
- US National Defense Research Council, Division 6 13. (1946). DDC No. T1669.
- van de Burgt, C. M., and Stuijts, A. L. (1963). *Ultrasonics*, **1**, 199.
- van der Groot, A. S., and Buschow, K. H. J. (1970). *J. Less-Common Met.*, **21**, 151.
- Verhoeven, J. D., Gibson, E. D., McMasters, O. D., and Baker, H. H. (1987). *Metall Trans.*, **18A**, 223.
- Verhoeven, J. D., McMaster, O. D., Ostenson, J. E., and Gibson, E. D. (1989). *J. Appl. Phys.*, **66**(2), 772.

10.2 General

- Borgman, H., and Lenz, K. (1992). *Proc. 3rd International Technology Transfer Congress, 'Actuator '92'*. VDI/VDE, Bremen, Germany.
- Lenz, K. (1990). *Proc. 2nd International Technology Transfer Congress, 'Actuator '90'*. VDI/VDE, Bremen, Germany.
- Tyren, C. (ed.) (1988). *Proc. 2nd International Conference on Giant Magnetostriuctive and Amorphous Alloys for Sensors and Actuators*, Marbella. Sensglas Terfenol AB, Lund, Sweden.

This chapter was originally published in 1995 as Chapter 17 in *Intermetallic Compounds*, Vol. 2: *Practice*, edited by J. H. Westbrook and R. L. Fleischer.

Chapter 7

Optical Applications

M. Wendy England and Edward T. Arakawa

Life Sciences Division, Oak Ridge National Laboratory, Oak Ridge, TN 37831-6123, USA

1. Introduction

The chapter in the first edition of this book (Roberts, 1967) on the electronic properties and applications of intermetallic compounds (IMCs) provides a very good starting point for this overview of the optical applications of IMCs. Most of the basic processes being utilized today were either routine, or being researched, at that time. The main improvement since then is in the incredible degree of sophistication now achieved in some of the applications. The IMCs in use in 1967 were mainly metal-metal or metal-metalloid semiconductor compounds chosen for the values of their energy gaps and carrier mobilities. Modifications to their optical and electrical characteristics were obtained by doping samples with specified distributions of impurities. Photodetectors, photovoltaic cells, photon sources utilizing electroluminescence, and the then recent discovery of GaAs injection lasers are described by Roberts (1967). Thus GaAs was already recognized as an important IMC for optical applications. As will be seen in this chapter, it remains extremely important, playing an integral role in many of today's products which depend on, or involve, the optical properties of an IMC. Relatively recently, in an effort to improve the performance of these types of devices, the materials characteristics desired for specific applications have frequently been obtained by choosing suitable ratios of components in ternary, quaternary, or multicomponent materials. Except in special cases, these intermetallic materials are not simple binary or ternary compounds but alloys of IMCs. Their optical applications are included in this chapter since their use provides a logical extension to the work described by Roberts (1967).

Section 2 of this chapter describes some systems which depend directly for their operation on the optical properties (reflectance, transmittance, absorbance and/or refractive index) of the material used in the construction of the system. There is relatively little in the literature on this topic for the true IMCs. Applications involving some carbides (e.g. SiC, TiC), sulfides (e.g. ZnS, MoS₂, As₂S₃) and oxides (e.g. ZnO, LiNbO₃, LiTaO₃), which are not true metal-metal compounds but which are used extensively and are often cited along with IMCs, are thus included.

Section 3 describes simple, single-stage devices involving interactions of photons and electrons (and/or holes). When these devices involve intermetallic semiconducting compounds, their operation depends on their intrinsic and/or extrinsic semiconducting properties. This makes some overlap with Chapter 15 by Masumoto *et al.* (1993) on semiconductors inevitable. Similarly, with photoelectric effects, there will be some overlap with other chapters.

Section 4 covers the most rapidly expanding field, that of integrated circuits and their dependence for successful operation on the optical properties of the component IMCs. The basic operations are those identified in the late 1960s, but over the years technological improvements have led to products with capabilities not even dreamt of at that time. Improvements in material fabrication and in product design have led to improved efficiencies, both in systems designed for photon detection and in systems designed for the production of photons, in particular production of coherent photons. Optical interconnects in integrated circuits allow incredibly short switching times. The end results are devices with very fast response times, high efficiency,

and, where applicable, an extremely high power, well-collimated, coherent output. In addition, all of these features can be achieved from devices that are highly miniaturized compared with those available in the late 1960s. In many instances, integrated circuits may involve several types of devices in a remarkably small volume of a doped and/or structured IMC or network of such compounds.

Relatively few of the many optical materials in use today are true IMCs. Of those optical materials in use that are true IMCs, some have been chosen for other desirable properties rather than for 'ideal' optical properties. For example, Testardi *et al.* (1973) prepared films of Mo_5Ru_3 and W_3Ru_2 on sapphire substrates. These IMC films are electrical conductors with Knoop hardness values comparable to sapphire. In addition, they exhibit good acid corrosion resistance, have high scratch resistance, and show excellent adhesion to their sapphire substrates. Reflectivity measurements for a range of photon energies from the infrared (IR) to the ultraviolet (UV) were obtained in order to assess their possible use as mirrors. Reflectivity, normalized to that for aluminum at the same wavelength, ranges from $\sim 57\%$ at $0.2\ \mu\text{m}$ to $\sim 90\%$ at $12\ \mu\text{m}$ for the Mo_5Ru_3 films and from $\sim 33\%$ to $\sim 72\%$ for the W_3Ru_2 films over the same wavelength range (the reflectance of Al is greater than 90% over most of this wavelength range). Although their reflectance values are not as high as are achievable for conventional mirrors maintained under ideal conditions, they are viable mirror materials for use in adverse conditions. The optical, and other, properties of the IMCs that result in their use in specific applications will be stressed in this chapter. To do this, each application is illustrated using a few examples. No attempt has been made to make this chapter a comprehensive review of every IMC that has been used in each optical application.

As a brief historical background (for more details see Westbrook, 1977) we note that some of the mirrors made for general use as early as 1800 BC were made of Cu–Sn alloys of various compositions. These bronze mirrors, the standard product for thousands of years, were supplanted by a better product based on another IMC when the Venetians in 1505 AD perfected the process of coating large flat glass plates with an Sn–Hg amalgam. This process held sway for nearly 400 years until the introduction of the silver nitrate chemical reduction process and, more recently, the general use of vacuum evaporation of Al, Au and other metals for making large mirrors.

In publications describing optical properties and/or their use, the terminology used to identify the energy

or wavelength of the photons depends on the region of the electromagnetic spectrum and, to a lesser extent, the preference of the individual scientist. The energy E and wavelength λ of a photon are related by the expression

$$E = 1.24/\lambda$$

where E is in electron volts (eV) and λ is in micrometers (μm). When quoting from publications the choice made by the author(s) has been adhered to, except that the units for λ have been converted into MKS units where necessary.

Finally, it should be pointed out that our chief concern is with the types of optical devices which incorporate IMCs and closely related materials. Emphasis is on the basic mechanisms involved in the way each device operates. The crystal structures of the component materials are not given, as this information is not relevant in most cases and, furthermore, is readily available elsewhere. When the intrinsic energy gap, which depends on crystal structure, is relevant for the operation of the device its value is given. Similarly, crystal orientation is included only when the optical properties are orientation dependent. In general, only the properties of the IMC which need to be known for reproducibility of the optical properties, and thus the operation of the device in which it is used, are given in this chapter.

2. Applications Based Principally on Optical Properties

The optical properties of a material can be utilized in a number of ways. IMCs individually have optical properties that make them appropriate choices for use in specific optical wavelength regions. When acceptable optical characteristics are combined with other properties, such as low density and/or resistance to radiation damage, IMCs emerge as very important in today's highly technological society. Basic systems employing IMCs that depend for their operation principally on the optical properties of the IMC component are described in this section. These systems depend on interrelated properties such as reflectance, transmittance, absorbance and/or refractive index, as described in the first edition of this book. Changes in any of these properties owing to, for example, changes in temperature or changes of composition by means of selective doping, are also utilized.

2.1 Reflectors

Silicon carbide (SiC) and titanium carbide (TiC) are both used in the construction of mirrors designed for use in harsh environments and/or where weight is an important factor. SiC has been shown to compare favorably with other materials for the construction of large mirrors for space-based, lightweight optical telescopes. Of the selection of traditional and less traditional materials studied, SiC has a high stiffness combined with minimal weight, a high thermal conductivity, and high strength (Miroshnikov, 1992). In addition, SiC has a low thermal expansion coefficient, high thermal shock resistance, and is a hard, radiation-resistant material. Solid SiC is usually porous and, without special treatment, unsuitable for optical surfaces (Goela *et al.*, 1991). For an extremely lightweight SiC mirror, Wakugawa (1991) designed an SiC foam core covered with SiC layers. The mirror surface could be formed by chemical vapor deposition (CVD). CVD SiC may be machined and polished to the desired shape and optical quality. Using this technique, a lightweight mirror can be obtained that is resistant to gravitational sag and has a relatively low thermal mass that facilitates uniform cooling.

For various land-based hostile environments, where the weight of the optical components may not be a factor, CVD SiC films are used extensively. CVD SiC performs well on optical components used for the manipulation of synchrotron radiation. CVD SiC can be used as a reflector at wavelengths that extend from the visible to the X-ray region. It can withstand high X-ray fluxes without surface degradation or excessive thermal distortion. Similarly, CVD SiC can be used in laser systems involving high-intensity IR, visible, or UV radiation. In the applications already mentioned, the high thermal conductivity of the SiC enables heat to be efficiently conducted away from the optical surface. In addition, CVD SiC is a stable phase at temperatures from -190 to 1350°C . Thus CVD SiC can be used in situations where the optics must be able to withstand high temperatures and/or changes of temperature.

The optical constants of SiC, TiC, and WC are reported by Yanagihara *et al.* (1986) in the soft X-ray region from 80 to 1200 eV and by Rife and Osantowski (1981) in the extreme ultraviolet (XUV) region from 40 to 150 eV. Figure 1 shows the reflectance as a function of incidence angle for polished CVD SiC. These data, obtained for photon energies of 350, 500, 700 and 1000 eV, are reproduced from Yanagihara *et al.* (1986). Numerical values for the optical constants of SiC, TiC, and WC are also given by these authors.

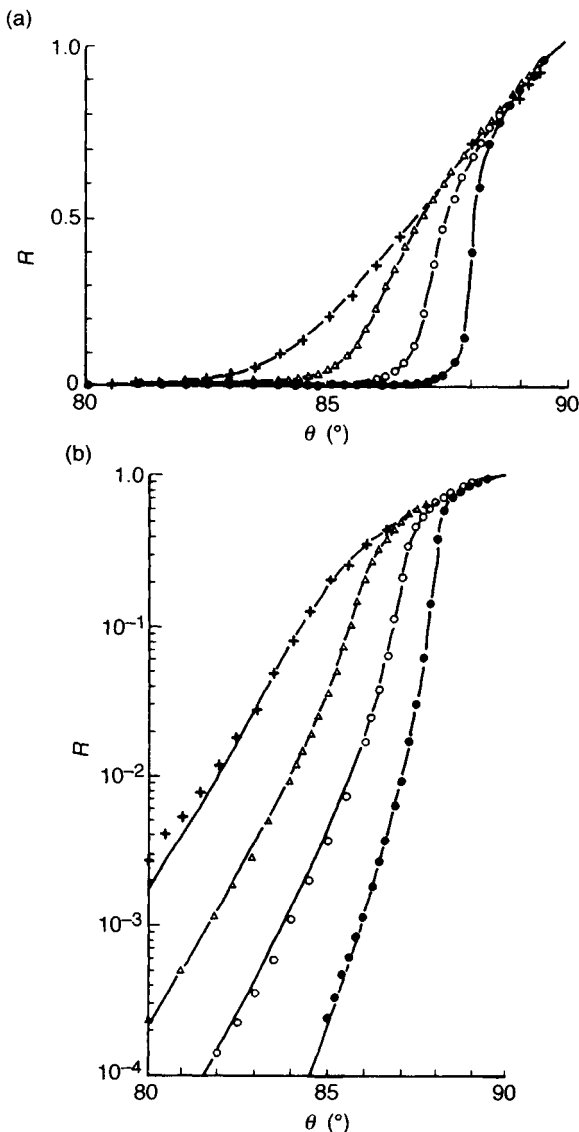


Figure 1. Measured reflectance as a function of incidence angle (deviation from normal incidence) for polished CVD SiC at $h\nu = 1000$ eV (\bullet), 700 eV (\circ), 500 eV (Δ), and 350 eV ($+$). Part (a) is on a linear scale and part (b), showing the same data, is on a semilogarithmic scale (from Yanagihara *et al.*, 1986)

The preparation of CVD SiC and measurements of its properties (other than its optical properties) of interest for optics applications in severe environments are described by Goela *et al.* (1991). The use of various materials, including SiC, to make mirrors for optical telescopes is discussed by Miroshnikov (1992). The use

of a superpolished SiC mirror, in combination with an MgF_2 coupler for the high-power operation of an argon excimer laser, is described by Kurosawa *et al.* (1991). They report a reflectance for SiC at 126 nm as high as 47% and a threshold damage fluence of 1 J cm^{-2} . For comparison, the reflectance for Al at the same wavelength of 126 nm is as high as 80% but its threshold damage fluence of 0.24 J cm^{-2} is much lower. Fella and Holleck (1991) describe the production of metastable $\text{Ti}_{0.5}\text{Si}_{0.5}\text{C}$ coatings. These coatings, in the TiC–SiC system, were optimized with respect to adhesion, composition and microstructure, giving a high potential for good wear-protective coatings for highly stressed surfaces. Optical properties are not discussed, but are presumably comparable to those of SiC and TiC. Knotek and Löffler (1991) discuss the use of vapor-deposition technology combined with laser surface-treatment technology to produce both amorphous and crystalline SiC coatings. Annealing of SiC coatings at $\sim 1000^\circ\text{C}$ can only be achieved by means of heating the exposed surface, rather than the whole system, owing to the high reactivity of silicon with metal substrates. A recent book on CVD materials (Galasso, 1991) devotes a whole chapter to CVD SiC, and also covers the CVD of many other high-temperature, wear-resistant materials.

The deterioration of vacuum ultraviolet (VUV) reflecting surfaces owing to the formation of IMCs has been studied by Hunter *et al.* (1971) and Hunter *et al.* (1972). Gold diffraction gratings, overcoated with Al + MgF_2 to increase their efficiency in the VUV, were found to suffer a severe loss in efficiency within six months to a year after coating. At a wavelength of 121.6 nm, for example, the reflectance could drop from 50 to 2%. Deterioration of the surface resulted from interdiffusion of Au and Al. A number of IMCs result, the most important being Au_2Al and AuAl_2 , this latter compound having a lavender tint which has been referred to in solid-state electronics as the 'purple plague'. The interdiffusion of Au and Al can be effectively eliminated by the use of thin dielectric layers, such as SiO_2 , between the grating and the overcoating material. If the mirror surface is to be Al, the barrier layer is more effective if a thin layer of Cr is deposited between the Al and the SiO_2 . Extensive observations are presented by Hunter *et al.*, including the results of some preliminary studies involving the interdiffusion of Pt and Al. Barrier layers are also discussed by de Reus in Chapter 29 of this volume.

2.2 Filters

All intermetallic semiconductors can be considered in a simple sense to act as filters. A window, or thin-film

sample, transmits low-energy photons while absorbing some higher-energy photons. The energy at which the sample begins to absorb depends on the value of the intrinsic energy gap in the semiconductor or on the presence of impurities in the sample.

The physics of antireflection coatings on an optical component are well known (see Chopra, 1969). With a single-layer coating, zero reflectance can only be obtained for a single wavelength λ where the thickness of the coating layer is $\lambda/4$ and the refractive index of the thin-film coating layer is between the values for the substrate and the medium in which the observation is being made. As an example of this, in the 8 to $15 \mu\text{m}$ region of the IR, single-layer evaporated $\lambda/4$ ZnS coatings have been used on Si and Ge (Cox and Hass, 1958). In a similar manner, single-layer thin films can be used to give an enhanced reflection. To yield greater versatility, multilayer antireflection coatings (antireflecting stacks) and multilayer reflection coatings (reflecting stacks) have been used for many years. These consist of alternately high (H) and low (L) refractive index films, each of thickness $\lambda/4$.

Transmission interference filters consist of two selectively reflecting stacks separated by a spacer layer, arranged in such a way that their central reflectance maxima are suitably displaced. Such interference filters may have high transmission over a fairly narrow bandwidth. Multilayer thin-film interference filters have been reported which utilize ZnS (Weinberger *et al.*, 1982) or ZnSe (Smith *et al.*, 1984) for the spacer layer. The Fabry–Perot-type interference filters studied by Smith *et al.* had the general construction HLHL... (mHH)... LHLH, where H indicates a $\lambda/4$ thickness of high-index material (ZnSe), L indicates a $\lambda/4$ layer of low-index material (ThF_4) and m is an integer. The high–low stacks act as high-reflection mirrors around the thicker mHH spacer. Transmission data for reflecting stacks which consisted of three HL periods and $m=4$ are shown in Figure 2. In this work ZnSe was chosen as the material for the spacer for subsequent development of a high-speed switching device based on the room-temperature, visible-wavelength, optical bistability which can be obtained using ZnSe interference filters (see Section 2.4).

Horinaka *et al.* (1985) and Yamamoto *et al.* (1986) have reported the construction of an optical bandpass filter using AgGaSe_2 . Single-crystal AgGaSe_2 is optically active and birefringent, and also happens to have a specific wavelength at which an optical isotropy occurs. An optical bandpass filter with a polarizer–[100] AgGaSe_2 –analyzer sandwich structure was constructed, as illustrated in Figure 3 taken from

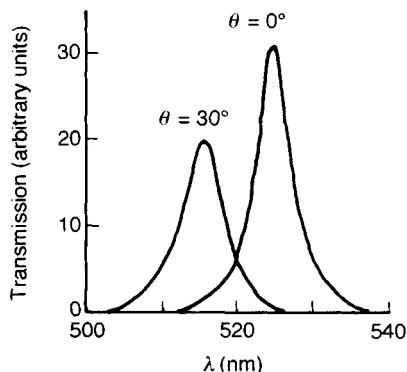


Figure 2. Low-power transmission characteristics of a ZnSe interference filter for two angles of incidence (from Smith *et al.*, 1984)

Yamamoto *et al.* (1986). The peak in the transmission occurs at 811 nm, i.e. the wavelength at which the birefringence happens to be zero. Values of the thickness of the AgGaSe_2 and the required value of ϕ , the rotation angle from the [100] axis in the (001) plane, were calculated from the measured value of optical activity for transmission at 811 nm. The observed bandwidth agrees with theory in both cases shown in Figure 3. Yamamoto *et al.* also demonstrated that the

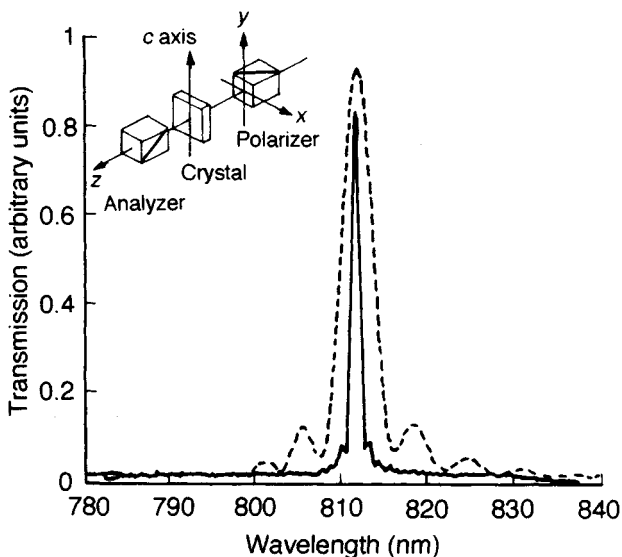


Figure 3. Transmission spectra of AgGaSe_2 bandpass filters with a Cross-Nicol configuration of polarizer and analyzer. The solid line is for a crystal of thickness 3.28 mm and $\phi = 38^\circ$, showing a bandwidth of 1.1 nm. The broken line is for a crystal of thickness 0.76 mm and $\phi = 0^\circ$, showing a bandwidth of 4.5 nm (from Yamamoto *et al.*, 1986)

central wavelength of the filter could be changed. For filters using mixed crystals of $\text{AgGa}(\text{S}_x\text{Se}_{1-x})_2$ ($x = 0.1, 0.3, 0.5$ and 0.7) the central wavelength, measured in electron volts, increased linearly with increase in x , as predicted by Horinaka (1985).

In an approach geared to industrial applications, Granqvist (1990) discusses window coatings for the future. 'Smart windows' would be designed with coatings of chromogenic materials, capable of adjusting their transmittance in response to dynamic conditions of photon flux and its inclination. In many parts of the world such windows could be very energy efficient. Doped metal oxides have been used in preliminary studies, but doped oxide semiconductor (IMC) coatings show promising properties. Physical structuring of the coatings, to increase efficiency at a given angle of incidence, is also being considered.

2.3 X-Ray Masks

X-ray lithography requires the construction of masks that have desired optical properties and that are resistant to radiation damage. The membrane used to carry the stepper mask in X-ray lithography must be transparent to the X-ray radiation. In addition, it must provide enough optical transparency and minimal scattering in the visible region in order to allow mask alignment with a precision of ~ 50 nm. Its modulus of elasticity must be high and its thermal expansion coefficient low. In addition it must be optically flat. SiC has these properties, and extensive research has gone into methods of fabricating good SiC membranes. Boily *et al.* (1991) describe the production of SiC membranes for X-ray masks by laser ablation deposition. This method has the advantage of producing, in a very simple manner, pure stoichiometric (1:1) SiC films that are free of hydrogen. Self-supporting SiC membranes, $2.5 \mu\text{m}$ thick and 1 inch in diameter, have been fabricated on an Si wafer. These membranes had an optical transparency at 633 nm of 40%, which is adequate for mask alignment. There are some indications (Klages, 1991) that thin diamond films may make even better X-ray masks and that CVD diamond thin-film technology is being developed (Klages, 1991; Galasso, 1991).

2.4 Optical Switches Dependent on the Photorefractive Effect

The photorefractive effect, which occurs in some optically transparent materials, consists of a change in the refractive index of the material owing to the action of light. In some experimental systems, involving the

transmission of high radiation densities, the effect has been termed 'optical damage', although the system is not permanently changed or 'damaged', returning to its original condition when the radiation source is removed. As an example, the photorefractive effect in a lithium niobate waveguide prevents its widespread use at a wavelength of $0.63\ \mu\text{m}$ (Balagurov *et al.*, 1986). In other systems the photorefractive effect has been deliberately utilized, as in optical switches. An understanding of this effect is of fundamental importance in many of today's applied optical technologies, including optical information processing, parallel signal processing, holography, fiber optics and integrated optics. Several basic studies of the photorefractive effect have been undertaken. As examples, theoretical and experimental studies have been conducted using As_2S_3 (Balagurov *et al.*, 1986) and GaAs (Piccari and Scotti, 1989). Both studies reported changes in refractive index of $\leq 7 \times 10^{-4}$.

The ZnSe interference filters discussed in Section 2.2 can be used as room-temperature switches for visible light. Smith *et al.* (1984) reported that their room-temperature interference filters incorporating ZnSe spacers exhibited reproducible bistable operation at $514\ \text{nm}$ with adequate stability to demonstrate truly steady-state operation. The intrinsic nonlinearity in ZnSe, necessary for bistable operation, results from thermally induced refractive index changes. Switching times of a few milliseconds were achieved using $514\ \text{nm}$ wavelength radiation at an irradiance of $\sim 250\ \text{W cm}^{-2}$. The spacer thickness of 2λ ($m=4$, see Section 2.2) resulted in a dominance of the nonlinearity in the filters studied. With appropriate initial detuning, bistable operation was obtained and external switching between transmission states demonstrated. The switching times of a few milliseconds result from the fact that the nonlinearity is thermally induced. Smith *et al.* (1984) predicted the faster switching times that are now achievable and the use of these devices in two-dimensional arrays of all-optical logic elements and novel display devices. Two years later, Bigot *et al.* (1986) reported nanosecond switching of bistable ZnSe interference filters at room temperature. This result was achieved by using a continuous-wave (CW) argon laser at $514.5\ \text{nm}$ to maintain the device near its threshold and a pulsed laser to induce the switching. In one case, an XeCl excimer laser at $308\ \text{nm}$ was used that delivered pulses of $0.2\ \text{mJ}$ for $15\ \text{ns}$ to the sensitive region of the interference filter. In another case, a frequency-tripled yttrium aluminum garnet (YAG) laser at $355\ \text{nm}$ delivered pulses of $0.2\ \text{mJ}$ for $30\ \text{ps}$. The dynamics of the switching in this case are represented in Figure 4.

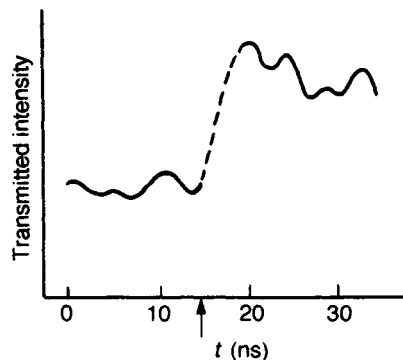


Figure 4. Dynamic response of a bistable ZnSe interference filter at room temperature to a $30\ \text{ps}$ YAG pulse for a $2\ \text{ns}$ time base. The arrow indicates the arrival of the pulse (from Bigot *et al.*, 1986)

The measured rise time was $4\ \text{ns}$, which corresponded to the temporal resolution of the experimental setup. These observations represented an important step in the development of optical processing devices. In the same year Jin *et al.* (1986) reported the simultaneous optical bistable switching of adjacent pixels on ZnSe and ZnS interference filters. Pattern recognition was demonstrated in these experiments.

An optical NOR gate, constructed by Ojima *et al.* (1986), consisted of a GaAs/AlGaAs multiple quantum-well (MQW) crystal (see Section 3.6) sandwiched between two dielectric mirrors. This is the geometry utilized in a fixed-space Fabry-Perot interferometer or etalon. Two diode lasers (see Section 3.8) were employed as the probe and pump light sources. The MQW consisted of 180 periods of $5.8\ \text{nm}$ thick GaAs wells and $9.6\ \text{nm}$ thick $\text{Al}_{0.4}\text{Ga}_{0.6}\text{As}$ barriers. The free-exciton absorption peak was at $825\ \text{nm}$; so, a diode laser with that peak wavelength was selected for the pump laser. When the pump light pulse is absorbed, the free-exciton absorption is saturated and the index of refraction is decreased at the probe wavelength. This shifts the Fabry-Perot transmission peak to shorter wavelengths and decreases its transmission at the probe wavelength. In this way, stable optical NOR gate operation was obtained by utilizing the optical bistability of GaAs/AlGaAs MQW etalons and two diode lasers. These switches are inherently faster than those in which the change in refractive index is thermally induced. Also, the fact that diode lasers can be used as light sources has made GaAs optical-logic gates attractive for optical signal processing, since the various components can be fabricated on the same substrate. Mishina *et al.* (1992) have studied ultrafast optical nonlinearities in type II

AlGaAs/AlAs MQW structures and their applicability to ultrafast switching devices. Weegels *et al.* (1992) have proposed a mechanism based on light-activated band structure modifications in pseudomorphic heterostructures that can be employed in light-activated optical switches or all-optical modulators. From preliminary experiments and model calculations, they predict an all-optical modulation with a contrast ratio of 27:1.

2.5 Slab Waveguides

Optical waveguides are used extensively in applications such as optical switching, optical computing, communications, and integrated circuits.

Pitt (1984) presented a case study to illustrate the use of thin films in optical waveguiding devices. Thin films are frequently used in integrated optics as the medium in which the optical energy is guided. Pitt stresses that the optical quality of films used in this way must be high to minimize optical energy losses. The film material, the way the film is manufactured, and the geometries employed are all important to the successful operation of any device which depends for its operation on slab or thin-film waveguides. A description of an integrated acousto-optic spectrum analyzer for radar applications is presented by Pitt to illustrate the basic principles involved. The component frequencies in an electromagnetic signal pulse may be determined electronically using an array of narrow-band filters or by some sort of acousto-optic, electro-optic or surface acoustic wave device. An integrated acousto-optic analyzer has the advantage of being fast, small and lightweight—all properties of importance in military and other applications. Basically, coherent light from a laser is introduced into a planar waveguide. The input electromagnetic pulse, to be analyzed, is converted to an analogous acoustic wave signal which is then made to travel across the laser beam. The different frequencies in the acoustic wave propagate across the interaction region as compression/rarefaction gratings in the waveguide material. The different effective gratings diffract the laser light beam at angles which relate to the frequency components propagating across the interaction region. Hence the signal can be analyzed from its resultant spatial distribution. The optical waveguide is a piezoelectric single crystal of LiNbO_3 doped with Ti by diffusion from one surface. The maximum refractive index increase, over that of the LiNbO_3 , is at the Ti- LiNbO_3 interface. Most of the energy of the laser beam is confined to this surface, and there is a strong interaction with the perturbation owing to the acoustic surface wave. Pitt describes the

advantages, and disadvantages, of various experimental setups. Most systems use LiNbO_3 ; but a ZnO thin film, which is cheaper than LiNbO_3 , can be used where lower performance can be tolerated.

Mentzer *et al.* (1985) discuss the design and fabrication of GaAs optical waveguides for use in integrated optical circuits operating at IR wavelengths. The doping distributions required in some circuit components were achieved by Mentzer *et al.* by ion implantation. This method allowed precise control of dopant profiles, which could not be achieved by diffusion or any other techniques at that time. Thus by choosing a suitable dopant profile, any desired spatial variation of refractive index could be obtained. The process described depends upon the compensation of free carriers in crystalline GaAs by means of suitable doping. The presence of free carriers in a semiconductor lowers the refractive index relative to that in the pure material (see also Section 2.4). Thus a knowledge of the refractive index as a function of both wavelength and free-carrier concentration in the crystal is critical in the design of ion-implanted waveguides. An analysis of the interrelationship of these quantities is given by Mentzer *et al.* for GaAs in the IR wavelength region well below the fundamental absorption edge. Losses in optical waveguides owing to scattering, absorption, and radiation, must be considered when designing systems for specific applications. These losses are discussed for GaAs. Taking all aspects into account, the design of proton-implanted GaAs, low-loss, single-mode, planar waveguides for use in the IR is described. Such optical waveguides are an integral part of present-day devices involving integrated optics (see Section 4).

Laser fabrication of structures on the surfaces of waveguides is another way of maximizing the transmission of light through waveguiding structures. Willner *et al.* (1989) used laser-induced etching to fabricate rib waveguides on a GaAs/AlGaAs heterostructure system. The etched GaAs has a lower effective index of refraction than the rest of the system. In one experiment they etched two trenches $\sim 12\ \mu\text{m}$ apart and of various trench depths d from 0.1 to $1.2\ \mu\text{m}$ in a $2\ \mu\text{m}$ thick GaAs layer on an $\text{Al}_{0.3}\text{Ga}_{0.7}\text{As}$ substrate. The refractive index was lowered in the region of the trenches enough to confine IR radiation ($1.5\ \mu\text{m}$ wavelength from a single-mode laser) to the central region between the trenches. Figure 5 shows their results for the measured transmitted optical intensity as a function of the depth of the etched trenches. This illustration shows the principles involved. In conventional rib waveguides employing multiple-rib structures the trenches can be shallower for comparable

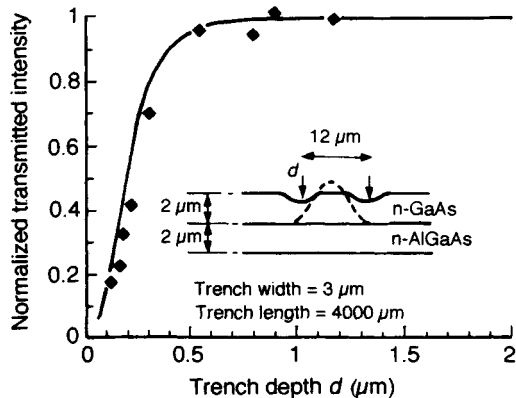


Figure 5. Transmitted light intensity as a function of trench depth d in a $12\ \mu\text{m}$ wide guide. Theoretical values are given by the solid line and the measured values by \blacklozenge (from Willner *et al.*, 1989)

efficiencies. Salathé *et al.* (1979) have given a detailed account of the fabrication of mesa-type waveguides in AlGaAs structures by laser-induced etching.

Bierlein and Vanherzele (1989) describe the properties and new applications of potassium titanyl phosphate (KTP). They show that low-loss optical waveguides can be formed in KTP. Several electro-optic and nonlinear optical devices have been fabricated which show that KTP is superior to many other materials for some optical waveguide applications.

2.6 Optical Coupling

Efficient optical coupling between the various components of a system is a basic requirement for successful optical applications of IMCs. Applications include optical switching, optical computing, and monolithic optical and electrical circuit integration. A proper design of such systems requires a knowledge of the refractive indices of the materials over a wide wavelength range. Chiang *et al.* (1991) have developed a method suitable for the direct measurement of the high refractive indices encountered in semiconductor waveguides. As an example of their technique, they present the effective refractive indices of single-mode GaAs/AlGaAs slab waveguides. The method is suitable for many single-mode slab waveguide geometries, but not for ridge waveguides. It is particularly applicable for buried waveguides and high refractive index waveguides that cannot be measured by prism couplers.

Willner *et al.* (1989), using techniques described in Section 2.5, demonstrated optical coupling between waveguides. Etched features can be varied smoothly

across the surface of a GaAs waveguide by controlling the power of the laser producing the etching. This procedure was used to fabricate a compact waveguide coupler. The trench depth was varied gradually in the vicinity of the two waveguides to be coupled, minimizing the excitation of higher-order modes or back reflections. Controlled laser-etching techniques were also used to fabricate two-level waveguides in a single-step process.

Holman and Skinner (1985) describe a proposed cooperative program designed to develop guided-wave optoelectronic manufacturing technology. They make it clear that this work would include optical fibers. The technologies that allow IR wavelength radiation to be guided in a slab waveguide can be adapted to a geometry that might be termed a fiber. Among other things they discuss single-mode versus multi-mode fiber technology, with an advantage of the single-mode systems being the ability to make high-speed and low-voltage optical switching components for those systems. They stress the need to enhance optoelectronic component reliability by incorporating fault tolerance in the design of systems. An optoelectronic component is considered to be fault tolerant if, upon a fault being detected, the component automatically switches to a redundant or alternative mode of operation. An example is given of a fault-tolerant optical signal repeater. In a conventional repeater the optical input signal is detected by a photodiode and then an amplified signal is retransmitted by a laser into an optical fiber output channel as illustrated in Figure 6(a). Figure 6 also demonstrates how a measure of fault tolerance can be achieved by placing a guided-wave electro-optical circuit between the input and output optical fibers. In the normal mode of operation illustrated in Figure 6(b), the optical input signal is directionally coupled, or switched, through several stages before the regenerated, optical output signal exists via the output optical fiber. When a problem occurs in the repeater, a fault-detection channel allows fault-activated optical bypass of the switches, such that the input signal passes directly from the input optical fiber to the output optical fiber of the repeater, as shown in Figure 6(c). The optical signal repeater is transparent in failure and is able to operate during failure in a properly power-budgeted, closed-loop network topology. It is obvious that any technology which utilizes the switching of optical signals between different channels will be very dependent on efficient optical coupling. The materials chosen by Holman and Skinner in 1985 for applications of guided-wave electro-optical switching circuits were inorganic single crystals based on LiNbO_3 and the III-V semiconducting alloys based on GaAs.

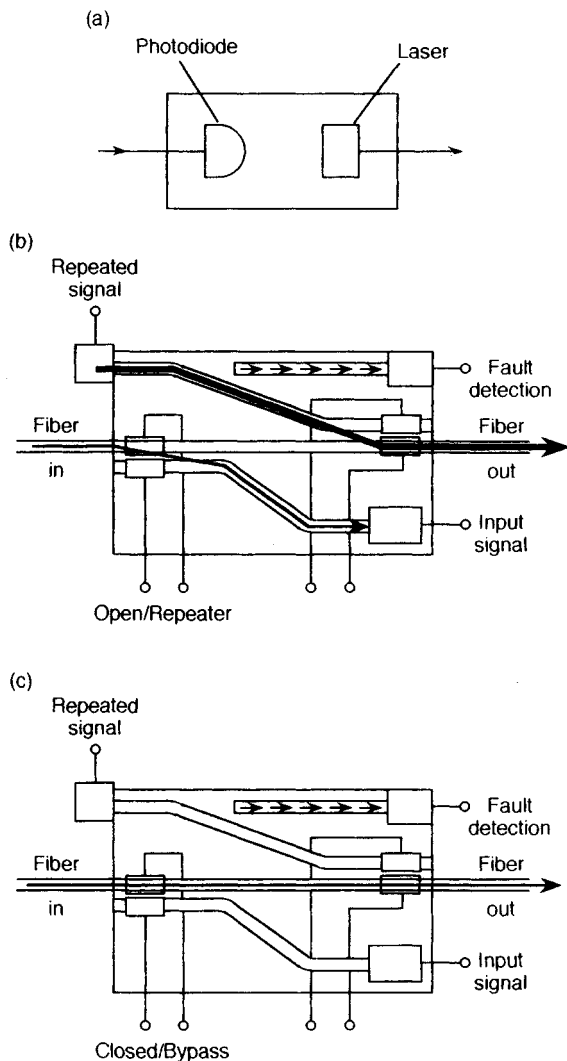


Figure 6. Fault-tolerant performance of an optoelectronic component using an electro-optical circuit: (a) conventional repeater concept; (b) repeater mode with laser operating and power on; and (c) bypass mode with laser burnout or power off (from Holman and Skinner, 1985)

2.7 Diffraction Gratings

The usefulness of slab waveguiding structures can be greatly enhanced by the fabrication of periodic structures on selected surfaces. If the periodicity is chosen correctly, the structure serves as a diffraction grating, allowing radiation to be coupled into and out of the waveguide. Varying the period, or line spacing, across the face of a grating can increase its usefulness.

Gratings with variable periods are called chirped gratings. Suzuki and Tada (1980) describe one method of fabricating chirped gratings on GaAs optical waveguides. Their method is based on the interference of two spherical laser beams after spatial filtering by pinholes. Details are given for the fabrication of uniform, symmetric chirped and antisymmetric chirped gratings. Chirped gratings with small variations in the period were fabricated on GaAs thin-film optical waveguides. The profiles and patterns of the chemically etched corrugations were found to be quite uniform, as shown in photomicrographs obtained by scanning electron microscopy (SEM). The periodic variations of their chirped gratings were measured to an accuracy of better than one in 10^4 and good agreement was obtained between measured and calculated values. They predicted that GaAs optical waveguides with chirped gratings would be useful for optical devices, such as filters and distributed feedback lasers.

Sawtooth diffraction gratings have also been fabricated in GaAs. Deep diffraction gratings with a low pitch (grooves mm^{-1}) are frequently employed in high-performance spectroscopic instruments operating at high orders. The fabrication of uniform gratings over a large area, by purely chemical etching, is difficult because reaction and diffusion rates are sensitive to temperature and agitation of the etching solution. Carrabba *et al.* (1986) developed a photoelectrochemical method of fabricating sawtooth gratings in *n*-GaAs (short for *n*-type* GaAs). They used polished single crystals of (100)-oriented *n*-doped GaAs, patterned along the [011] and [011] directions. Positive photoresist was spin coated onto the polished (100) surface of the crystal which was then mounted in an electrochemical cell. Photoelectrochemical etching of the patterned crystal surface was achieved using uniform illumination from a 100 W Xe arc lamp (200 to 300 mW cm^{-2}). The time evolution of the photocurrent in the circuit was used to monitor the etching process. SEM photographs showing cross sections of the grooves photoelectrochemically etched in the [011] direction are shown in Figure 7 at three

*In an intrinsic semiconductor the conductivity is controlled by the value of the energy gap E_g . The presence of certain types of impurities and/or imperfections will result in an impurity-derived conductivity in addition to the intrinsic conductivity. In *n*-type material the impurity-derived conductivity is owing to electrons. A heavily doped *n*-type material may be labeled n^+ -type. Similarly, when the impurity-derived conductivity is owing to 'holes' the material is termed *p*-type or p^+ -type. A *p*-*n* junction occurs when a semiconductor crystal has been treated in such a way that it contains both *p*-type and *n*-type regions separated by a very thin internal boundary. The interface between the different regions is called a *p*-*n* junction.

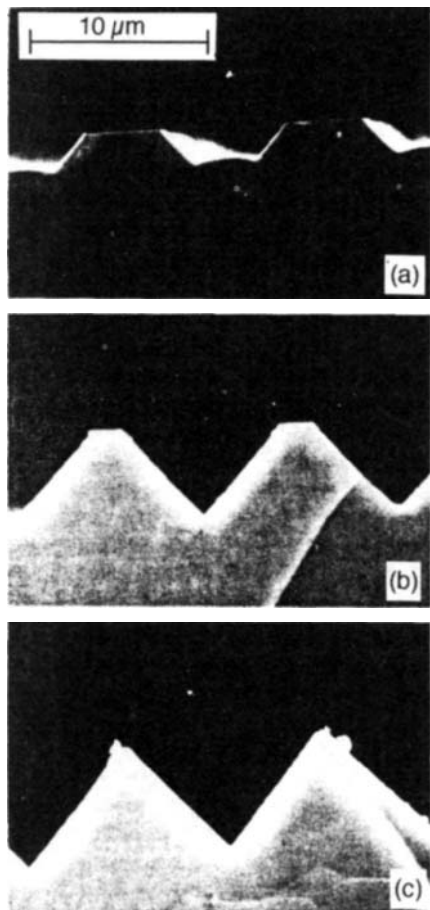


Figure 7. Scanning electron micrographs showing cross sections of grooves photochemically etched in the (100) n-GaAs [011] direction at three different stages of development (from Carrabba *et al.*, 1986)

stages of development. This grating had a groove spacing of $10\ \mu\text{m}$ and a groove depth of $7.14\ \mu\text{m}$. The gratings produced by Carrabba *et al.* were characterized by exceptional smoothness. When using this technique, precise control of the etching depth is obtained by monitoring the total coulombs passed, while the rate of etching is controlled by the light intensity. Controlling groove geometry during photoetching will permit the fabrication of a wide variety of new structures for use in integrated electrooptics.

2.8 Optical Modulators

A whole range of optical modulators is commercially available, including modulators consisting of LiNbO_3

or LiTaO_3 waveguides. Polarized laser light is passed into the modulator along the axis of the waveguide. When an electric field is applied perpendicular to the axis of the waveguide, the Pockels effect occurs, i.e. the refractive index of the material of the waveguide changes linearly with the electric field intensity. Phase modulation is achieved by changing the optical path length through the waveguide. Thus phase modulation of a light beam is achieved simply by modulating the applied electric field. Amplitude modulation involves a guided-wave interferometer. The input waveguide is split into two independent sections and then recombined into a single output waveguide. The phase difference between the two interferometer arms produces amplitude modulation of the output beam.

Canit and Chazalviel (1987) describe the use of a ZnSe photoelastic modulator in the IR wavelength region below $\sim 15\ \mu\text{m}$. This device can be used in situations requiring the modulation of large-diameter or large-aperture light beams and with high-intensity laser beams. The system is easy to build and highly reliable. Furthermore, for high-frequency (50 kHz) light chopping it has an advantage over Pockels cell birefringent modulators, which required small-aperture beams. As shown in Figure 8, the basic design consists of a photoelastic element (P) of polycrystalline ZnSe which is mechanically excited by two piezoelectric transducers (PZT type, made of lead titanate and zirconate) glued to P at the centers of two opposite faces. The transducers, driven by an electric field applied in the vertical direction, oscillate along the axis of the ZnSe sample producing shear stresses such that P resonates in the fundamental $\lambda/2$ longitudinal bulk mode. The dynamic stress and strain are also shown in Figure 8. This system achieves an optical retardation of λ at a wavelength of $6.5\ \mu\text{m}$. Canit and Chazalviel also describe a similar but more complicated design. Depending on the actual design, they report optical retardations of up to $\lambda/4$ at $15\ \mu\text{m}$ and $\lambda/2$ at $11.6\ \mu\text{m}$. These systems can be used as polarization modulators as well as intensity modulators, e.g. for CO_2 lasers.

2.9 Polarization Rotation

Polarization rotation is an important effect in integrated optics. It was demonstrated in the early 1980s (see Shani *et al.*, 1991) in both LiNbO_3 and III-V waveguides using periodic electrodes in conjunction with the electro-optic effect and in LiNbO_3 using etched SiO_2 films to apply a periodic stress, thus changing the index via the photoelastic effect. Shani *et al.* (1991) have proposed, and demonstrated, a new method. They produce

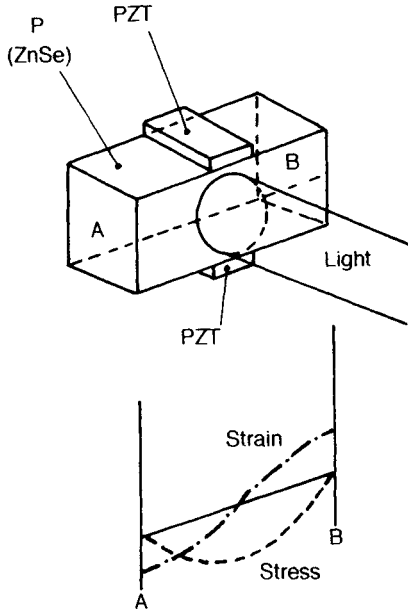


Figure 8. ZnSe photoelastic modulator (P) showing the transducers (PZT) and the incident light beam that is to be modulated or analyzed. The relative stress and strain pattern in the ZnSe is also shown (adapted from Canit and Chazalviel, 1987)

polarization rotation by loading a ribbed InP waveguide in a periodic asymmetric way. They obtained complete $TE \leftrightarrow TM^{\dagger}$ conversion (rotation of the transverse electric field by 90°), with only 2 to 3 dB excess loss, in a 3.7 mm long waveguide, and 80% rotation in a 0.3 mm long waveguide. Polarization rotation of less than 1% was obtained in a straight regular waveguide, without the periodic loading.

2.10 Pyro-optical Sensors

Reproducible changes with temperature in any of the optical properties of a material may be used to measure temperature and/or temperature changes. As an example, Li *et al.* (1991) have shown that MoS_2 is a potential candidate material for pyro-optical sensors. The temperature sensitivities of both the reflectance and the refractive index of MoS_2 were measured by ellipsometric techniques. A wavelength corresponding to a photon energy of 2.02 eV was found to give maximum sensitivity for the particular material and techniques employed. The temperature range covered

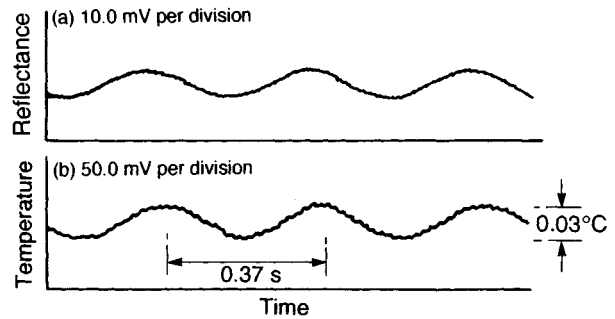


Figure 9. (a) Modulation of the reflectance of a single crystal of MoS_2 subjected to a 2.7 Hz temperature modulation (b) of $0.03^{\circ}C$ (adapted from Li *et al.*, 1991)

was from room temperature to $\sim 100^{\circ}C$. Within this temperature range, temperature changes of $\leq 0.01^{\circ}C$ could be detected by monitoring the reflectance. As shown in Figure 9, reflectance measurements could be used accurately to track 2.7 Hz temperature modulations of $0.03^{\circ}C$. The sensitivity demonstrated by Li *et al.* illustrates what is possible. In practice, pyro-optical sensors would be designed and calibrated to fulfill the needs of special applications.

2.11 IMC Optical Materials

It can be seen from this section that the optical properties of IMCs lead to the same types of devices for the IR region as those made out of glass or other 'transparent' materials for use in the visible region of the electromagnetic spectrum. In addition, some IMCs have physical and thermal properties that make them attractive for use under harsh conditions, such as high-temperature environments on earth or radiation fields in outer space. When these properties are associated with acceptable optical properties, IMCs are found to have many applications. Several authors discuss the development of materials, including IMCs, for the rapidly advancing fields of modern optics and information processing (Hilton and Cronin, 1986; Miroshnikov, 1992), guided-wave optoelectronic manufacturing technology (Holman and Skinner, 1985), photonic device applications (Kolinsky, 1992) and material design for severe service applications (Okamura, 1991). Okamura, for example, projects the use of Ti-Al-based and Nb-Al-based IMCs in aerospace and energy-production applications. Workshops are held on selected IMCs, for example mercury cadmium telluride and related compounds (Freeman, 1991). Whole books have been devoted to GaAs (e.g. Howes and Morgan, 1985; Ferry, 1985)

[†]TE = transverse electric field, TM = transverse magnetic field.

and CVD materials (Galasso, 1991). These accounts of new materials and technologies point the way from the devices discussed in this section to devices that depend for their operation on the dynamic interaction between photons and electrons and/or holes.

3. Single-Stage Applications Based on Photon–Electron Interactions

The optical applications of IMCs also include devices where the process of primary importance for their operation involves the interaction of individual photons and electrons within the IMC. Devices that are activated by incident photons are primarily of two types: those in which the photons produce an electric current in a circuit that includes the IMC, and those in which the incident photons interact with the electrons in the IMC resulting in an output light beam with characteristics different than those of the incident beam. When the first type of device is used to detect or to measure the intensity of light, it is generally termed a photodetector. The quantity recorded may be photoconductivity in the IMC or photoemission from the IMC. When, on the other hand, it is used to convert solar energy into useful energy the first type of device is termed a photovoltaic or solar cell. Light-emitting diodes and lasers, which utilize photoluminescence, and some all-optical switches are examples of the second type of device. In addition, some light-emitting diodes and lasers utilize electroluminescence. Applications of each type of device are given in this section.

3.1 Photodetectors

The material used in any device for the efficient detection of incident photons must be photosensitive over the part of the electromagnetic spectrum being studied. If a wide spectrum is to be covered, several different systems, each using a relevant photosensitive material, must be used. This scenario is considered by Ovsyuk and Svtashev (1992). The IMCs listed, with their photosensitive regions of the electromagnetic spectrum, are: lead sulfide and indium arsenide (0.1 to 3.5 μm); lead telluride, lead selenide, indium antimonide, and $\text{Cd}_{0.3}\text{Hg}_{0.7}\text{Te}$ (3.0 to 5.5 μm); $\text{Cd}_{0.2}\text{Hg}_{0.8}\text{Te}$ and PbSnTe (5.0 to 14.0 μm); and gallium arsenide (3 to 50 μm). A general review of optical sensors developed in the (former) USSR for use from the far IR to the visible region is given by Khryapov *et al.* (1992). Cadmium and mercury telluride solid solutions ($\text{Cd}_x\text{Hg}_{1-x}\text{Te}$) are their usual starting

materials for IR detectors. They show that, by choosing a suitable value for x , photodetectors can be optimized for any desired spectral range between 1.5 and 16 μm . Fast photodiodes, employing InGaAsP/InP heterostructures, have been developed for the 1.1 to 1.7 μm spectral range. Cooled photodiodes based on InSb and InAs have been developed for the 3 to 5 μm and 2 to 3 μm spectral ranges, respectively. Parameters for these diodes are reported for a temperature of 77 K. Lead chalcogenide photodetectors, in use since the mid-1940s, are still being actively developed. Pankratov (1992) gives a review of non-selective thermal radiation detectors used in the (former) USSR in various parts of the IR region. One device, termed by Pankratov a pyroelectric detector, and used in pyroelectric arrays, is based on a single crystal of lithium tantalate. In the example given, each individual detector, or element, in the array was 0.5×0.5 mm and the distance between elements was 0.1 mm. Another device, termed a thermoelectrical detector, depends on the anisotropic properties of single-crystal CdSb . The sensitivity of this detector depends on the geometry employed, ranging from 100 to 200 V K^{-1} at temperatures of 70 to 290 K and 350 to 750 V K^{-1} at 290 to 420 K. More details are available in the references quoted by Pankratov. Photocathodes, depending on photoemissive materials for their operation, have been studied extensively for many years (see for example the text by Sommer, 1968). Many IMCs, as well as their alloys, are used as photocathodes. The most widely used is Cs_3Sb which has a high quantum yield in the visible region of the spectrum.

The importance of HgCdTe systems is evidenced by the existence of a series of workshops on the physics and chemistry of these and related systems (Freeman, 1991). Continuously varying, direct gap semiconducting characteristics are seen as the $\text{Hg}_{1-x}\text{Cd}_x\text{Te}$ system goes through the full alloy range ($x = 0$ to 1). Since the direct energy band gap E_g varies from 0 to 1.6 eV, detectors can be tailored to be sensitive in a specific energy range. One example, taken from Ovsyuk and Svtashev (1992), of the preparation of a photodiode, formed out of $\text{Hg}_{1-x}\text{Cd}_x\text{Te}$ and designed to be sensitive in the wavelength range from 6 to 14 μm , is illustrated in Figure 10. The spectral response of this photodiode is shown in Figure 11. Since the electron diffusion length in narrow-gap semiconductors is large, the diode consisted of a p-type layer on an n-type substrate. In anticipation of using this type of photodiode in arrays of photosensitive elements, this geometry was chosen to provide effective electrical insulation between each element of the array. In addition, a passivating coating

Chapter 8

Magneto-Optical Applications

William A. McGahan

Center for Microelectronic and Optical Materials Research, Department of Electrical Engineering,
University of Nebraska at Lincoln, NE 68508-0511 USA

1. Introduction

Magneto-optical (MO) effects were first discovered by Faraday nearly 150 years ago in experiments on glass samples placed between the pole faces of a magnet (Mattis, 1988), yet only relatively recently have these effects found practical applications. The first proposal for MO-based data storage by Mayer (1958) launched a period of intense study of MO effects in various materials, with the promising goal of high-density optical storage based on thermomagnetic writing and readout via the polar Kerr effect. MO data storage offers two distinct advantages over other techniques. First, the areal density of stored data can be very large, as it is limited primarily by the wavelength of the laser used to read and record the bits. The compact disk is a good example of the type of storage densities achievable with optical data storage systems. The second advantage is that the read/write head in the MO disk drive never physically contacts the disk. Thus the fatal 'head crash' associated with conventional magnetic disk storage never occurs in the MO system. Also, the MO storage technique provides removable disks capable of storing more data than a typical conventional hard drive. The greatest disadvantage associated with MO recording is very slow random access times. As a result, MO systems are most commonly used for archival data storage, with typical applications being the storage of satellite images, CAT scans, etc. In this chapter, we review the phenomenology and physical origins of the Kerr and Faraday effects, which are the most important first-order MO effects for data storage and other device applications. We also outline the principal materials

requirements for MO storage media, and discuss the properties of various intermetallic compounds (IMCs) with respect to these requirements. We would point out that the discovery by Chaudhari *et al.* (1973) of amorphous rare-earth/transition metal alloys all but ended research on IMCs for direct use as storage media, and the amorphous class of materials dominates the MO media market today. However, the properties of the IMCs are still at least of academic interest, and the fact that several IMCs (MnBi, PtMnSb, for example) exhibit very large Kerr effects at room temperature has led to continuing research into this interesting class of materials.

2. Phenomenological Description of Magneto-Optical Effects

Michael Faraday discovered in 1845 that linearly polarized light undergoes a rotation of the polarization plane when transmitted through a magnetized medium if the light propagates along the direction of the magnetization (Mattis, 1988). Towards the end of that century, Kerr found that a similar rotation of the polarization vector occurs when linearly polarized light is reflected at normal incidence from the surface of a magnetized material. The Faraday and Kerr effects are the most important MO effects in terms of storage and device applications, and we review the phenomenology of these effects in this section. The following is by no means a complete review, and the interested reader is referred to the many reviews in the literature (Bloomberg and Connell, 1988; Meiklejohn, 1986; Parker, 1987; McGahan *et al.*, 1992a, b) for more details.

We consider the geometry shown in Figure 1. The sample is assumed to be infinitely thick, and to extend infinitely in the x and y directions. A linearly polarized beam of light propagating along the z direction strikes the surface of the sample, which reflects part of the beam and transmits the rest into the bulk of the sample. When the material is isotropic and unmagnetized, the polarization of the reflected and transmitted beams is identical to that of the incident beam, and only the amplitudes of the reflected and transmitted components are altered by the material. The presence of magnetization in the material leads to an alteration of the polarization state of the reflected and transmitted components as well. We will discuss the physical reasons for this in the next section, and present the phenomenology for tracing these effects in this section.

In order to describe the amplitude and polarization state of the incident, reflected, and transmitted beams we will employ the Jones vector formalism. This formalism is valid for all angles of incidence, but we will only consider the special case of normal incidence. Since the electric field of the incident and reflected beams is perpendicular to the direction of propagation of the beam, two unit vectors in the plane perpendicular to the wave vector of the light are required to describe any possible polarization of the beam. For the case of normal incidence, we can choose any two orthogonal vectors which lie in the plane perpendicular to the wave vector of the light. We will choose these vectors to lie along the x and y axes, and give them the labels \hat{p} and \hat{s} , corresponding to the plane of incidence (p) and the direction perpendicular to the plane of incidence (s).

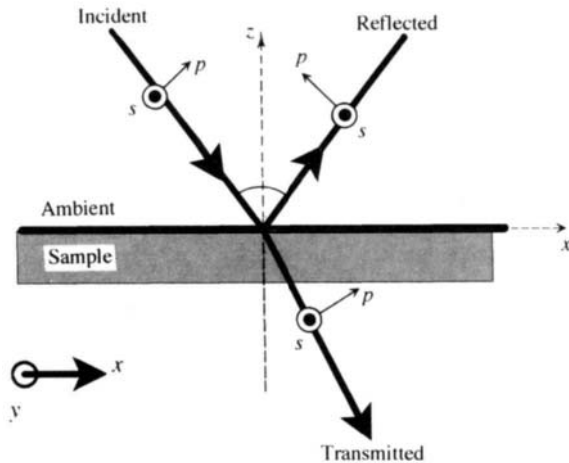


Figure 1. Geometry for consideration of optical reflection and the Kerr and Faraday effects

These labels are chosen in accordance with the oblique incidence case, where the incident and reflected wave vectors define the plane of incidence (containing the x axis in this case). Any arbitrary polarization can be written as a two-component vector, where the components are the projections of the electric field of the light beam along the p and s directions. These components are in general complex, as the relative phase as well as the magnitude of the two components determines the polarization state of the beam.

Within this framework, we will now consider the reflection of light from the surface of a semi-infinite material, as depicted in Figure 1. It can be easily shown that for a perfectly smooth surface, the reflected and transmitted electric fields are given in terms of the incident fields by the following equations (Azzam and Bashara, 1989)

$$\begin{pmatrix} \tilde{E}_p \\ \tilde{E}_s \end{pmatrix}_{\text{reflected}} = \begin{pmatrix} \tilde{r}_p & 0 \\ 0 & \tilde{r}_s \end{pmatrix} \begin{pmatrix} \tilde{E}_p \\ \tilde{E}_s \end{pmatrix}_{\text{incident}} \quad (1)$$

$$\begin{pmatrix} \tilde{E}_p \\ \tilde{E}_s \end{pmatrix}_{\text{transmitted}} = \begin{pmatrix} \tilde{t}_p & 0 \\ 0 & \tilde{t}_s \end{pmatrix} \begin{pmatrix} \tilde{E}_p \\ \tilde{E}_s \end{pmatrix}_{\text{incident}} \quad (2)$$

where \tilde{E}_p and \tilde{E}_s represent the (complex) components of the electric fields along the p and s directions, respectively, \tilde{r}_p and \tilde{r}_s are Fresnel reflection coefficients for the surface, and \tilde{t}_p and \tilde{t}_s are Fresnel transmission coefficients for the interface. The Fresnel coefficients are given (for normal incidence) in terms of the complex index of refraction \tilde{n} of the medium by the following equations (Azzam and Bashara, 1989)

$$\tilde{r}_p = \frac{\tilde{n} - 1}{\tilde{n} + 1} \quad \tilde{r}_s = \frac{1 - \tilde{n}}{1 + \tilde{n}} = -\tilde{r}_p \quad (3)$$

$$\tilde{t}_p = \tilde{t}_s = \frac{2}{\tilde{n} + 1} \quad (4)$$

Note that for the present case, in which there is no sample magnetization, the matrices which relate the reflected and transmitted electric fields to the incident field are diagonal. Furthermore, it can be shown that regardless of the choice of basis vectors (p and s directions, in this case), these matrices will always be diagonal at normal incidence. As a direct consequence of the diagonal nature of these matrices, an incident beam which is linearly polarized will always yield reflected and transmitted beams which have the same linear polarization as the incident beam, albeit with different amplitudes.

When the sample is magnetized along the z direction, the Jones matrices for reflection and transmission at the surface are no longer diagonal (for reasons which will be discussed in the next section) and have the form

$$[\mathbf{J}]_r = \begin{pmatrix} \tilde{r}_p & \tilde{k} \\ \tilde{k} & \tilde{r}_s \end{pmatrix} \quad [\mathbf{J}]_t = \begin{pmatrix} \tilde{t}_p & \tilde{u} \\ \tilde{u} & \tilde{t}_s \end{pmatrix} \quad (5)$$

where \tilde{k} and \tilde{u} are small (complex) off-diagonal components, and $[\mathbf{J}]_r$ and $[\mathbf{J}]_t$ are the Jones matrices for reflection and transmission at the surface of the sample, respectively. For the case of linearly polarized incident light, these off-diagonal components lead to a small alteration of the reflected and transmitted polarizations from the incident linear polarization. The reflected and transmitted polarizations in this case become slightly elliptical, with the major axis of the ellipse rotated away from the original linear polarization by a small angle θ , as shown in Figure 2. This small angle is the polar Kerr rotation, and the ratio of the minor to the major axis of the resultant polarization ellipse is termed the polar Kerr ellipticity. The label 'polar' refers to the fact that the sample magnetization is assumed to lie along the sample normal. There are two other orientations for which the Kerr effect can be measured, in which the sample magnetization lies along the x or y axis, referred to as the longitudinal and equatorial Kerr effects. These effects are generally much smaller than the polar Kerr effect, and are much less commonly measured. The rotation angle and ellipticity of the reflected beam are often combined into a single complex quantity $\tilde{\psi} = \theta + i\eta$, which is given by (in the small-angle approximation)

$$\tilde{\psi} = \frac{\tilde{r}_p}{k} = -\frac{\tilde{r}_s}{k} \quad (6)$$

At normal incidence, the off-diagonal Fresnel coefficients are given by (Sokolov, 1967)

$$\tilde{k} = \frac{-i\tilde{n}\tilde{Q}}{(1+\tilde{n})^2} \quad (7)$$

where \tilde{Q} is the magneto-optical Voigt parameter, defined fundamentally in the next section. We can combine equations (7) and (3) to yield a useful expression for the Kerr effect in reflectance from the surface of a bulk sample magnetized perpendicular to the sample surface

$$\tilde{\psi} = \frac{-i\tilde{n}\tilde{Q}}{(1-\tilde{n}^2)} = \frac{\tilde{\epsilon}_{xy}}{\sqrt{\tilde{\epsilon}_{xx}}(1-\tilde{\epsilon}_{xx})} \quad (8)$$

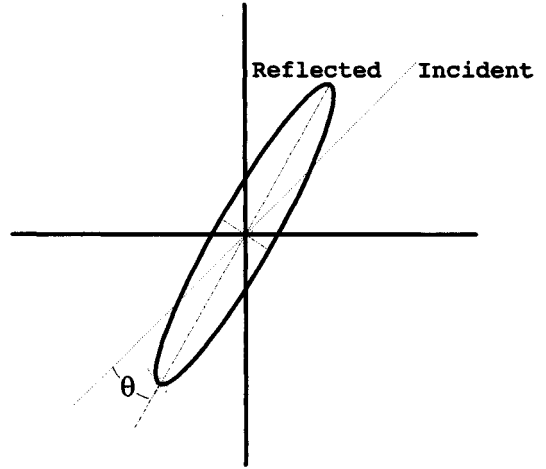


Figure 2. The incident and reflected polarization states for the nonzero polar Kerr effect

where we have shown the formula in terms of the complex index of refraction \tilde{n} and the Voigt parameter \tilde{Q} as well as in terms of the diagonal ($\tilde{\epsilon}_{xx}$) and off-diagonal ($\tilde{\epsilon}_{xy}$) terms of the dielectric tensor. We will clarify the relationship between these quantities in the next section.

There are several interesting consequences of the above functional form for the complex Kerr effect. First, the Voigt parameter \tilde{Q} will be shown in the next section to be linear in the magnetization, such that a reversal in the direction of the magnetization (from $+z$ to $-z$) yields a change in the sign of the Voigt parameter and hence a change in sign of both the Kerr ellipticity and rotation. Hence, by measuring the position of the major axis of the polarization ellipse of the reflected beam with respect to the original linear polarization, we can determine whether the sample magnetization is up or down with respect to the sample surface normal. This is the principle by which bits (small domains) of up and down magnetization are read optically in magneto-optical memories, as the transitions between regions of up and down magnetization can be detected by the associated change in sign of the polar Kerr effect. Second, the Kerr effect is a linear function of the Voigt parameter (and hence the magnetization), but depends on the complex index of refraction of the material as well, and in a somewhat more complicated manner. As a result, fundamental studies of MO effects in materials require both optical (ellipsometry, reflectance, transmittance) and MO (Kerr rotation and ellipticity) measurements (McGahan *et al.*, 1991, 1992a, b; Hansen and Krumme, 1984).

A second important magneto-optical effect, the Faraday effect, occurs when a beam of linearly polarized light propagates through a material which has a non-zero component of the magnetization along the direction of propagation of the beam. If the material is isotropic and unmagnetized, the beam will retain the same linear polarization at all times as it propagates through the material. When magnetized, the material induces a rotation of the polarization axis as well as a small ellipticity, and these effects are cumulative as the beam propagates through the material. If the material is transparent, i.e. there is no absorption ($k=0$), there will be no induced ellipticity and the polarization axis of the beam will only be rotated as the beam propagates through the material. The total rotation is proportional to the length of material through which the beam has propagated, and is also proportional to the component of the magnetization along the wave vector of the beam. As a result, reversal of the magnetization will induce a change in sign of the rotation of the propagating beam. The Faraday effect has been used with nearly transparent films for optical data storage, but is more commonly used in integrated optical devices and polarization modulators. Specifically, the Faraday rotation and ellipticity of a linearly polarized beam of light due to passage through a sample of thickness l , neglecting surface reflection effects, is given by (Sokolov, 1967)

$$\theta_F + i\eta_F = \frac{-i\pi l \tilde{Q}}{\lambda_0} - \frac{\pi l \epsilon_{xy}}{\lambda_0 \sqrt{\epsilon_{xx}}} \quad (9)$$

where λ_0 is the wavelength of the light *in vacuo*. We will not consider the Faraday effect further, as IMCs are by nature strongly optically absorbing, and applications of these compounds involve the Kerr effect.

The above discussions are valid for the cases of the normal incidence polar Kerr effect and the Faraday effect for beams propagating along the direction of the magnetization. However, real magneto-optical storage structures, for example, usually consist of multilayer stacks in which only one or two of the layers are magneto-optically active. The other layers are used for optical enhancement of the Kerr rotation and optimization of the thermal properties of the stack, and can serve to protect the MO layer from oxidation. For the case of reflection from multilayer stacks at normal incidence, equations (5) are still valid, but equations (8) are not, and it becomes somewhat involved to evaluate the dependence of the Jones matrix elements on the indices of refraction, Voigt parameters, and thicknesses of the individual layers and the substrate. The reader is

referred to the literature for details on the calculation of the optical and magneto-optical response of multilayered systems and for systems illuminated at oblique angles of incidence (Smith, 1965; Parker, 1987; Gamble and Lissberger, 1988; McGahan and Woollam, 1989; Visnovsky, 1991).

3. Physical Origins of Magneto-Optical Effects

The Faraday effect occurs when light propagates in a magnetized material, and the Kerr effect occurs when light is reflected from the surface of a magnetized material, yet both effects have the same physical origin. Consider a specimen having cubic crystalline symmetry. In this case Neumann's principle indicates that due to the invariance of the crystal under all symmetry operations in the cubic group, all physical properties of the crystal must be equivalent along any direction, i.e. the material is isotropic. If the material is magnetized (for simplicity the magnetization is taken to be uniform and along the z direction), the cubic symmetry of the crystal is broken and at best we can expect rotational symmetry about the axis of the magnetic field (z axis). In this case we may invoke Neumann's principle to show that invariance under rotations about the z axis requires the following general form for the dielectric tensor (as well as any second-rank tensor associated with a physical property of the material) (see Burns, 1985, for a thorough discussion)

$$\vec{\epsilon} = \begin{bmatrix} \epsilon_{xx} & -\epsilon_{xy} & 0 \\ \epsilon_{xy} & \epsilon_{xx} & 0 \\ 0 & 0 & \epsilon_{zz} \end{bmatrix} \quad (10)$$

The dielectric tensor $\vec{\epsilon}$ relates the displacement field \vec{D} in the material to the applied electric field \vec{E} via the relation

$$\vec{D} = \vec{\epsilon} \vec{E} = \vec{E} + 4\pi \vec{P} \quad (11)$$

where \vec{P} is the electrical polarization vector in the material. We note that the off-diagonal elements are equal in value and opposite in sign, which is required for symmetry under reversal of the magnetization direction. Since the diagonal elements are unchanged by reversal of the magnetization and the off-diagonal elements change sign, we can develop these quantities as power series in the magnetization M . The off-diagonal series is usually truncated after the first term, such that ϵ_{xy} is nominally linear in the magnetization.

The diagonal elements are assumed to be independent of the magnetization, although the second-order term leads to the (very small) Voigt effect. The elements of the dielectric tensor are related to the complex index of refraction \tilde{n} and Voigt parameter \tilde{Q} in the following manner

$$\tilde{n} = \sqrt{\tilde{\epsilon}_{xx}} \quad \tilde{Q} \equiv \frac{i\tilde{\epsilon}_{xy}}{\tilde{\epsilon}_{xx}} \quad (12)$$

The cubic material under discussion can be shown from symmetry considerations to exhibit an isotropic dielectric tensor in the absence of a magnetic field, such that the off-diagonal elements are all zero and the diagonal elements are equal. In this case the displacement, polarization, and applied electric field vectors are collinear, and linearly polarized light will retain its polarization state when reflected at normal incidence from a planar surface of the material or when transmitted through the material in any direction.

When the material is magnetized and the dielectric tensor has the form shown in equation (10), the displacement, polarization, and applied electrical field vectors are no longer collinear, as the off-diagonal components of $\vec{\epsilon}$ mix the x and y components of the fields. This can be understood in a classical sense as being due to the Lorentz force on the atomic electrons as they move in the presence of the field \vec{M} . In the absence of magnetization, the electrons experience only the force due to the electric field $e\vec{E}$, which is always in the direction of the applied field \vec{E} . The response of the electrons to the applied field, which determines the polarization \vec{P} (and hence the displacement field \vec{D}), is always in the direction of \vec{E} and all the fields are collinear. When a magnetic field is present, the moving electrons are deflected by the Lorentz force $e\vec{v} \times \vec{M}$ in addition to the electrical force $e\vec{E}$, and do not generally move along the direction of \vec{E} such that \vec{P} , \vec{E} , and \vec{D} are no longer collinear.

In order to understand the consequences of this we must recall that the wave equation for \vec{E} yields three equations (one for each spatial dimension) which are coupled if the dielectric tensor is not diagonal. If we perform the coordinate transformation to the principal axis system in which the dielectric tensor is diagonal, the equations are uncoupled, and we find a separate solution for the component of \vec{E} along each of the principal axes. Each component propagates with an index of refraction equal to the square root of the corresponding principal (diagonal) element of the (diagonalized) dielectric tensor. For a cubic material with no magnetization, the dielectric tensor is already diagonal, the three principal solutions are along the x ,

y , and z axes, and all three waves propagate with the same index of refraction. This is the *isotropic* case, as a wave of arbitrary polarization state retains that state when propagating in any direction in the material.

The material becomes *anisotropic* when magnetized, as diagonalizing equation (10) yields three solutions corresponding to right-circularly and left-circularly polarized light and z -polarized light. The right-circularly and left-circularly polarized waves propagate with different indices of refraction and are reflected and transmitted differently by the material. In the non-magnetized case, a linearly polarized wave would be resolved into its components along the Cartesian axes, each of which propagates with the same index of refraction, and the propagating components would add at any point to form the same linear polarization. In the magnetized case, the linearly polarized wave must be resolved into its left-circularly and right-circularly polarized and z components. These waves then propagate with different indices of refraction $\tilde{n}_{\pm} = \tilde{n}_0(1 \pm \frac{1}{2}\tilde{Q})$, where \tilde{n}_0 is the isotropic (no magnetization) index of refraction and the $+$ and $-$ subscripts denote right-circularly and left-circularly polarized light, respectively (McGahan and Woollam, 1989). As a result, both the amplitude and phase of each wave change differently, and the component waves do not add at further points in space to form the same linear polarization again. For this reason, the simple Jones matrix is no longer diagonal, as mentioned in the previous section, because at normal incidence the reflected beam contains a polarization component orthogonal to the original linear polarization.

To look further at the microscopic origins of the Kerr and Faraday effects, we must abandon the classical approach and adopt the methods of quantum mechanics to consider the absorption of polarized light by solids. Our goal is to calculate, for a given solid, the diagonal (optical) and off-diagonal (magneto-optical) components of either the dielectric tensor $[\tilde{\epsilon}]$ or the optical conductivity tensor $[\tilde{\sigma}]$, whose elements are related to those of the dielectric tensor by (Burns, 1985)

$$\sigma_{ij} = \frac{i\omega}{4\pi}(1 - \tilde{\epsilon}_{ij}) \quad (13)$$

To do this, we first (in principle) solve Schrödinger's equation for the electrons in the solid with a Hamiltonian appropriate to the solid under illumination, and then evaluate the required tensor elements from the matrix elements of the dipole operator. Unfortunately, while the general mechanics of this approach have been known for many years (Argyres, 1955; Bennett and Stern, 1965;

Pershan, 1967; Erskine and Stern, 1973), the numerical evaluation of magneto-optical effects from the results of electronic band structure calculations is exceedingly difficult, and only very recently have methods been developed which yield reasonable results (Oppeneer *et al.*, 1991; Maurer *et al.*, 1992).

Within the semiclassical approximation for the electromagnetic field of the illuminating light, the one-electron Hamiltonian appropriate for electrons in an arbitrary solid illuminated by monochromatic light can be written as follows (Argyres, 1955)

$$\mathcal{H} = \mathcal{H}_0 + \mathcal{H}' + \mathcal{H}'' \quad (14)$$

where

$$\mathcal{H}_0 = \frac{1}{2m} \vec{p}^2 + V(\vec{r}) \quad (15)$$

$$\mathcal{H}' = \frac{1}{2mc^2} [\vec{\nabla} V(\vec{r}) \times \vec{p}] \cdot \vec{s} \quad (16)$$

$$\mathcal{H}'' = \frac{e}{mc} \vec{A}(\vec{r}, t) \cdot \vec{p} \quad (17)$$

We will specifically treat the case of magnetically ordered materials, as in this case we can neglect the interaction of the electrons with any reasonable applied magnetic field. For the case of nonmagnetic materials, a term representing this interaction must be included to yield any magneto-optical effects. The first term (\mathcal{H}_0) in the above Hamiltonian is the standard one-electron Hamiltonian for electrons in solids, where m is the electron mass, \vec{p} is the momentum operator, and $V(\vec{r})$ is an effective potential due to all of the other electrons in the solid as well as the nuclear cores. This effective potential can be found in a number of ways, and the reader is referred to the literature on electronic structure calculations for details (Skriver, 1984, for example). The second term (\mathcal{H}') represents the interaction of the orbital angular magnetic moment of the electron with its own spin moment, where c is the speed of light and \vec{s} is the spin of the electron. The third term represents the interaction of the electron with the electromagnetic fields due to the illuminating light, where e is the electronic charge and $\vec{A}(\vec{r}, t)$ is the vector potential appropriate for the electromagnetic disturbance. The second and third terms are usually small compared to the first, so the general procedure most often used is to solve Schrödinger's equation for the first term of the above Hamiltonian and treat the second and third terms as perturbations. The calculation of electron

eigenstates and eigenenergies in solids for even the first term of the Hamiltonian is difficult, and the reader is again referred to the literature for details (Skriver, 1984).

Let us assume that we have obtained solutions to the above Hamiltonian, such that the bound eigenstates of electrons in the solid, as well as the associated energies, are known. This information is sufficient in principle to calculate all elements of the dielectric tensor via the following procedure. We know from diagonalization of the dielectric tensor earlier in this section that the two allowed polarizations in the solid, for the assumed cylindrical symmetry about the axis of magnetization, are right-circularly and left-circularly polarized light. All other polarizations (linear, for example) must be described as linear combinations of these two basis polarizations. We then determine appropriate vector potentials \vec{A}_{\pm} for the right (+) and left (−) circular polarizations, and use them to calculate the matrix elements of the kinetic momentum operator $\vec{\pi}_{\pm}$, where (Bennett and Stern, 1965)

$$\vec{\pi}_{\pm} = \vec{p} + \frac{e}{c} \vec{A}_{\pm}(\vec{r}) + \frac{\hbar}{4mc} [\vec{\sigma} \times \vec{\nabla} V(\vec{r})] \quad (18)$$

in which \hbar is Planck's constant divided by 2π and $\vec{\sigma}$ is the Pauli spin operator. The final term, which represents spin-flip transitions between electronic states, was shown by Misemer (1988) to yield usually negligible contributions to the matrix elements, and is often neglected as a result. The elements of the optical conductivity tensor are then given in terms of the matrix elements of $\vec{\pi}$ as follows (Bennett and Stern, 1965)

$$\text{Re}\{\sigma_{xx}(\omega)\} = \frac{\pi e^2}{\hbar \omega m^2 V} \sum_{\beta}'' \sum_{\alpha}' |\langle \beta | \pi_x | \alpha \rangle|^2 \cdot [\delta(\omega_{\beta\alpha} - \omega) + \delta(\omega_{\beta\alpha} + \omega)] \quad (19)$$

$$\text{Im}\{\sigma_{xx}(\omega)\} = \frac{-2e^2 \omega}{\hbar m^2 V} \sum_{\beta}'' \sum_{\alpha}' \frac{|\langle \beta | \pi_x | \alpha \rangle|^2}{|\omega_{\beta\alpha}|(\omega_{\beta\alpha}^2 - \omega^2)} \quad (20)$$

$$\text{Re}\{\sigma_{xy}(\omega)\} = \frac{e^2}{2\hbar m^2 V} \sum_{\beta}'' \sum_{\alpha}' \left[\frac{|\langle \beta | \pi_- | \alpha \rangle|^2}{(\omega_{\beta\alpha}^2 - \omega^2)} - \frac{|\langle \beta | \pi_+ | \alpha \rangle|^2}{(\omega_{\beta\alpha}^2 - \omega^2)} \right] \quad (21)$$

$$\Im\{\sigma_{xy}(\omega)\} = \frac{\pi e^2}{4\hbar\omega m^2 V} \sum_{\beta} \sum_{\alpha}' \left\{ |\langle\beta|\pi_-|\alpha\rangle|^2 \cdot [\delta(\omega_{\beta\alpha} - \omega) + \delta(\omega_{\beta\alpha} + \omega)] - |\langle\beta|\pi_+|\alpha\rangle|^2 \cdot [\delta(\omega_{\beta\alpha} - \omega) + \delta(\omega_{\beta\alpha} + \omega)] \right\} \quad (22)$$

In the above expressions, β denotes unoccupied (final) states, α denotes occupied (initial) states, π_+ and π_- are the appropriate kinetic momentum operators for right-circularly and left-circularly polarized light, respectively, $\hbar\omega_{\beta\alpha}$ is the energy difference between states β and α and $\hbar\omega$ is the energy at which the conductivity tensor is evaluated. Note that only first-order, interband transitions are included in the above treatment. Clearly, the off-diagonal component σ_{xy} is zero unless the dipole matrix elements for right-circularly and left-circularly polarized light differ. This will happen when the electronic states are altered by spin-orbit coupling, as this provides the mechanism for differing absorption of the two allowed polarization states. A large degree of spin-orbit coupling is known to lead often to large MO effects (e.g. MnBi), but the size of the MO effect in a given material has been shown by the numerical studies of Misemer (1988) to have a complicated dependence on the degree of spin-orbit coupling present in that material, as well as on the exchange splitting of the various states involved, and no set rules for the prediction of materials with large MO effects exist.

The above equations for the conductivity tensor are simple in form, but are very difficult to evaluate numerically. Oppeneer *et al.* (1991) have provided a detailed discussion of these difficulties. Note that any discussion of MO properties in terms of specific electronic transitions should be based on analysis of the off-diagonal elements of either the dielectric or conductivity tensor, as the more commonly used Kerr rotation and ellipticity are functions of both the diagonal and off-diagonal elements of these tensors, and can be more difficult to interpret, particularly if the optical constants (diagonal elements) exhibit significant dispersion in the spectral region of interest. It is possible to use MO measurements to gain information about the electronic band structure and specific electronic transitions in a material provided optical and MO effects can be separated (Hansen and Krumme, 1984; Erskine and Stern, 1973; Bennett and Stern, 1965). As a specific example, Erskine and Stern (1973) used measurements of the optical and magneto-optical response of single-crystal gadolinium to determine the energy of the unfilled 4f (spin down) levels above the Fermi level in this metal. They also estimated (from analysis of their measurements) the unoccupied and total d-shell

bandwidth, and the positions of the peaks in the density of states of the d bands with respect to the Fermi level.

4. Materials Requirements for Magneto-Optical Applications

The primary magneto-optical application for IMCs is erasable optical data storage, based on the use of a focused laser to create small domains thermomagnetically in a thin MO film and the use of the same laser operating at lower power to detect the polar Kerr rotation due to the written domains of up and down magnetization. Unfortunately, materials used for this application are subject to very stringent requirements, which very few of the IMCs meet. At the time of the first proposal of MO data storage, however, the amorphous class of metallic alloys which currently dominate the MO storage market were undiscovered, and IMCs were the most promising known class of materials. As a consequence, most of the initial search for MO recording materials was confined to IMCs. In particular, the discovery of large polar Kerr effects in MnBi prompted the first proposal of MO data storage (Mayer, 1958), and most of the early research subsequently centered on this and other Mn-based compounds which could be grown with perpendicular magnetic anisotropy.

In this section, we briefly review the materials requirements for magneto-optical data storage. A detailed discussion of these requirements and other design requirements for MO storage media can be found in the review by Bloomberg and Connell (1988).

First, the material must be magnetically ordered at room temperature in order to retain stable domains which are written thermomagnetically. Useful MO storage materials are either ferromagnetic or ferri-magnetic, such that Curie point or compensation point writing can be performed. Curie point writing is performed by heating a small area of the material above its Curie point and allowing it to cool in an external field, large enough to orient the cooling region but small enough not to affect the unheated portion of the disk. In compensation point writing, the material is heated above its compensation point, such that the direction of the total magnetization in that area is reversed. The interested reader may consult Chapter 40 by Kouvel in Volume 1 of this work for details on the compensation and Curie points for magnetic materials.

Second, the material should exhibit a reasonably large polar Kerr effect. This criterion must be used with caution, as in storage applications the magneto-optical material is generally incorporated in multilayered

structures to enhance the MO signal. Mansuripur (1986) has shown that a valid figure of merit (FOM) for optically absorbing MO materials when used in interference-based enhancement multilayers is

$$\text{FOM} = \frac{|\epsilon_{xy}|}{\text{Im}(\epsilon_{xx})} \quad (23)$$

This figure of merit reflects the fact that the ability of a material to transfer energy from the original linear polarization to the perpendicular polarization, as represented by the magnitude of the off-diagonal dielectric tensor element, is of prime importance for MO recording media. Unfortunately, measurements of the off-diagonal tensor elements are difficult to perform, and are rather scarce in the literature. On the other hand, there is an abundance of Kerr rotation measurements, so the Kerr rotation or the product of the Kerr rotation and the reflectance (a valid figure of merit if there are no optical enhancement layers) is most often quoted as being indicative of the usefulness of a material for MO storage applications. Also, although the above figure of merit favors materials with low optical absorption, some degree of absorption is required for sufficient energy transfer from the writing laser to the disk to take place during the thermomagnetic write process. In summary, equation (23) is the most accurate estimator for a material's usefulness for MO recording, but the most difficult to measure. The product of the reflectance and the Kerr rotation is a less accurate but still very useful estimator, and is commonly used to compare materials in the literature. Finally, the Kerr rotation alone for a bulk material is only indirectly related to the ability of that material to function as an MO storage media, and provides only a rough means of comparing materials.

A third important materials requirement is the existence of strong perpendicular magnetic anisotropy in thin films of the material. This is necessary in order to form domains of up and down magnetization with respect to the surface of the film, which is desirable for denser data storage. Also, in-plane magnetized films would require a read process based on the longitudinal Kerr effect, which is considerably smaller than the polar Kerr effect. Related magnetic requirements, stated in the review of Greidanus and Zeper (1990), are that the magnetization in the film can be reversed thermomagnetically with available diode laser powers and magnetic field strengths, such that the Curie or compensation temperature should be $< 300^\circ\text{C}$ and the required switching field be $< 50\text{ kA m}^{-1}$. Also, a square or nearly square hysteresis loop in the perpendicular orientation is required for consistent switching and maximal remanent Kerr rotation, and the

coercivity of the material at room temperature should be high to prevent accidental erasure of data. This is a very difficult requirement for IMCs to meet, as the demagnetizing field for thin films tends to force the easy axis of magnetization to be in the plane of the film, and a large degree of perpendicular anisotropy is required to maintain out-of-plane magnetization. Even when perpendicular domains can be achieved in IMCs, the coercive force required to reverse the magnetization tends to be small. Amorphous rare-earth/transition metal (RE/TM) based alloys provide high coercivity and square hysteresis loops in the perpendicular orientation, which is very difficult to achieve with IMCs.

In order to reduce readout noise, it is very important to be able consistently to produce small ($\sim 1\text{ }\mu\text{m}$) domains thermomagnetically in thin films of the material. The storage film must then be either epitaxially grown or have grains of much less than $1\text{ }\mu\text{m}$ in size. Domain walls tend to be pinned at grain boundaries, hence polycrystalline films tend to sustain very jagged domains which lead to increased readout noise. This is one reason why the current class of amorphous rare-earth/transition metal based alloys dominates the current MO media market, as the amorphous materials provide a myriad of pinning sites for the domains, and will retain very small, uniform domains.

Also, as the MO disk will be rewritten many times, it is important that the material properties do not change significantly after many thermal cycles. This was a problem in the first MO disk systems based on MnBi, which may undergo a structural phase transition after repeated thermal cycling.

Finally, the material should be stable over long periods of time against oxidation and corrosion. This has been a difficult problem with the current amorphous RE/TM alloys, which are very reactive and difficult to protect from oxidation and corrosion. There are other materials requirements which are not critical, but desirable from the production standpoint, such as minimal cost, ease of deposition, and speed of deposition.

To conclude this section, we would point out that there are very few true IMCs which are useful for MO recording applications, and at the present time the market is dominated by the amorphous rare-earth transition metal alloys, due to the superior properties of these materials.

5. Magneto-Optical Properties of Intermetallic Compounds

In this section, we will review the research to date on the magneto-optical properties of IMCs. This section

is divided into subsections for manganese-based, cobalt-based, and iron-based binary IMCs, a subsection devoted to other magneto-optically active IMCs, and a subsection on ternary and pseudo-binary IMCs. Finally, we will briefly describe the related amorphous alloys which currently are the cornerstone of the MO recording media market. Much of the following data for IMCs are taken from the reviews of Buschow *et al.* (1983) and Buschow (1988). We quote from the first:

... there is a general lack of information on the magneto-optical properties of magnetic metallic systems (although magnetic properties are well known). Furthermore, no simple models seem to exist that relate these properties to other physical properties, even in the case of the few materials for which magneto-optical data are available ...

This was published in 1983, and since that time the predominance of MO studies on amorphous alloys, multilayers, compositionally modulated structures, and substituted garnet films has accompanied a diminished interest in the MO properties of IMCs. As a result, much of the existing data are found in the paper of Buschow *et al.* (1983), who adopted:

... a 'poor man's approach' to the problem: We have prepared all alloys and intermetallics that are known from the literature to be ferro- or ferrimagnetic above room temperature and have measured their Kerr rotation and their room temperature magnetization.

This approach is common in the MO research community, and is very useful for identifying materials which are potential optical recording candidates. A more fundamental study would involve measurements of the optical properties of these materials as well, such that the diagonal and off-diagonal elements of the dielectric or conductivity tensor, which can sometimes be interpreted in terms of individual electronic transitions via equations (19) to (22), could be calculated from the measurements. This requires a much more complicated experiment, however, and very few measurements of the optical and magneto-optical constants of materials exist in the literature (McGahan *et al.*, 1991, 1992a, b; Hansen and Krumme, 1984; Bains *et al.*, 1992).

In the following sections, we do not attempt a thorough tabulation of all known MO measurements on IMCs. Rather, we present illustrative results, explanations of the properties of each class of materials (when possible), and an extensive list of references which the reader may consult for details. Also, in the interests of brevity we do not include details as to the crystal structure and magnetic properties of each material, as

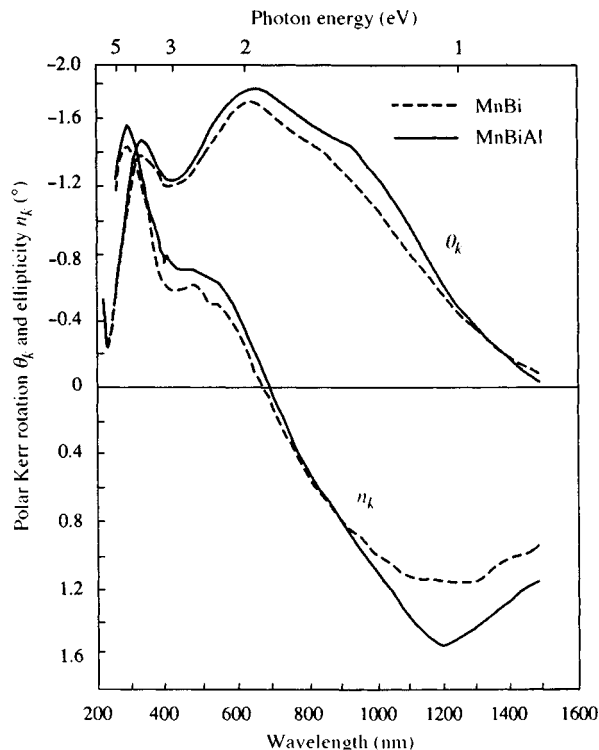


Figure 3. The polar Kerr rotation and ellipticity of MnBi and MnBiAl thin films (after Di *et al.*, 1992 by permission of Elsevier Science Publishers BV)

this information is presented in other chapters of this work.

5.1 Manganese-based Binary Compounds

There are relatively few ferromagnetic Mn-based IMCs (as compared to, say, the iron compounds), yet these materials have played a very important role in the development of MO recording technology and provide the greatest potential of any true IMCs for future MO applications. In particular, the compound MnBi was the first material used for MO recording, and still receives attention due to its large Kerr effect. In addition to MnBi, several other Mn-based IMCs exhibit perpendicular anisotropy, such that much of the early search for MO recording materials centered on Mn-based materials.

The most useful of the Mn-based binary alloys is probably MnBi. The polar Kerr rotation and ellipticity of both MnBi and MnBiAl thin films, from Di *et al.* (1992), are shown in Figure 3. The large peak in the Kerr rotation at 1.8 eV is attributed to transitions from Mn3d to (Mn4p, Bi6p) states, and the peak at 3.3 eV is attributed

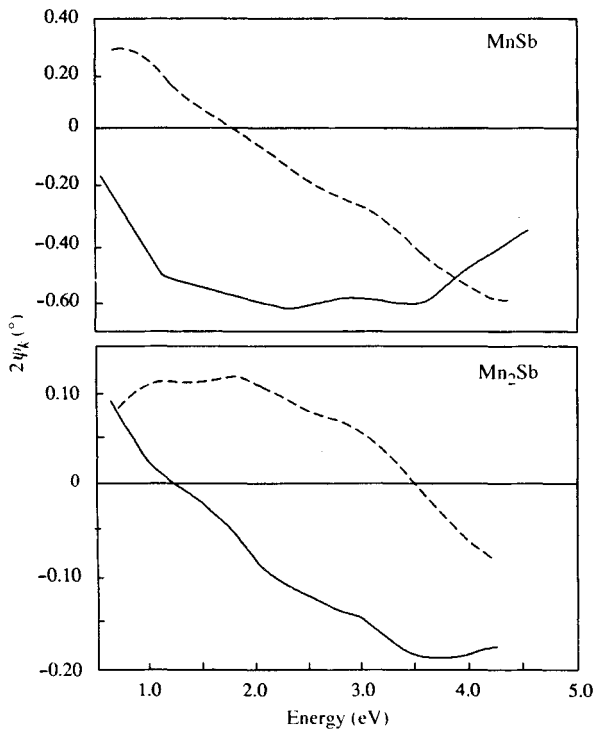


Figure 4. Polar Kerr rotation and ellipticity spectra for MnSb and Mn₂Sb (from Buschow, van Engen, and Jongebreur, 1983. Reproduced by permission of Elsevier Science Publishers BV). Note that twice the Kerr rotation (solid line) and ellipticity (dashed line) are plotted

to both Mn3d to (Mn4p, Bi6p) and Bi6p to Bi6d inter-band transitions. The large size of the Kerr effect in this compound has been attributed to the large degree of spin-orbit coupling in the Bi atoms (Misemer, 1988). Unfortunately, MnBi undergoes a structural phase

transition near its Curie temperature, which precludes repeated thermal cycling of the film. Substitutions of Ti (Feldtkeller, 1972), Al (Di *et al.*, 1992), and rare earths (Fang *et al.*, 1992) were attempted in order to stabilize the MnBi structure, with some success. Other magnetically ordered Mn compounds were also studied prior to the discovery of the current class of amorphous alloys. MnAs (Stoffel and Schneider, 1970), Mn₅Ge₂ (Sawatzky, 1971a), and MnSb (Sawatzky, 1971b) were all studied as potential MO media. The Kerr spectra of MnSb and Mn₂Sb are shown in Figure 4, as measured by Buschow *et al.* (1983). Comparison of the three spectra in Figures 3 and 4 illustrates the variety of spectral features encountered in Mn compounds, and there are no common features which can be linked to the presence of Mn in the particular compound. As a result, little is understood concerning the specific transitions which contribute to the MO effects in the Mn-based binary compounds. Data for some Mn-based binary compounds are listed in Table 1.

5.2 Cobalt-Based Binary Intermetallic Compounds

Very few magneto-optical studies of cobalt-based binary IMCs, other than those of Buschow *et al.* (1983) and Buschow (1988), exist in the literature. Stoffel (1968) measured the complex indices of refraction and Voigt parameters of Nd₂Co₁₇ and NdCo₅ and found that the magnitude of \tilde{Q} decreased with increasing rare-earth content. They concluded that $|\tilde{Q}|$ was proportional to the total magnetization in these compounds, and not to a sublattice magnetization. The compound UCo₅ was studied by Brändle *et al.* (1990), who measured optical reflectivity over the spectral range 0.03–12 eV and the polar Kerr effect from 0.6 to 4.5 eV on

Table 1. Manganese-based binary compounds

| Alloy or compound | SB symbol | Pearson symbol | Saturation magnetization (A m ² kg ⁻¹) | Kerr rotation (633 nm) (°) | Kerr rotation (830 nm) (°) |
|----------------------------------|-----------------|----------------|---|----------------------------|----------------------------|
| 'Mn ₂ Ga' | L1 ₀ | tP4 | >36 | 0.01 | 0.01 |
| Mn ₂₃ Y ₆ | D8 _a | cF116 | 33 | 0.00 | 0.00 |
| Mn ₂₃ Gd ₆ | D8 _a | cF116 | 45 | 0.00 | 0.00 |
| Mn ₃ In | D8 ₃ | cP52 | 0.7 | 0.00 | 0.00 |
| MnNi ₃ | L1 ₂ | cP4 | 27 | 0.00 | 0.00 |
| MnV | B2 | cP2 | 0.1 | 0.00 | <0.01 |
| Mn ₂ Sn | B8 ₂ | hP6 | 4.0 | 0.00 | 0.00 |
| MnNi | L1 ₀ | tP4 | 0.3 | <0.01 | <0.01 |
| MnPt ₃ | L1 ₂ | cP4 | 14.9 | 0.00 | 0.00 |
| Mn ₅ Ge ₂ | D8 _g | oI28 | 5 | -0.01 | 0.01 |
| MnSb | B8 | hP4 | 99 | -0.29 | -0.27 |
| Mn ₂ Sb | C38 | tP6 | 29 | -0.04 | -0.01 |

Table 2. Cobalt-based binary compounds (source: Buschow, van Engen, and Jongebreur, 1983)

| Alloy or compound ^a | SB symbol | Pearson symbol | Saturation magnetization (A m ² kg ⁻¹) | Kerr rotation (633 nm) (°) | Kerr rotation (830 nm) (°) |
|------------------------------------|------------------|----------------|---|----------------------------|----------------------------|
| Co | A3 | hP2 | 156 | -0.35 | -0.39 |
| Co ₂ Mg | C14 | hP12 | 55 | -0.33 | -0.34 |
| CoZn | A13 | cP20 | 39 | -0.12 | -0.12 |
| Co ₃ Si | D0 ₁₉ | hP8 | 47 | -0.13 | -0.14 |
| Co ₁₁ Zr ₂ | f.c.c. | — | 72 | -0.15 | -0.17 |
| Co ₂₃ Zr ₆ | D8 _a | cF116 | 49 | -0.09 | -0.10 |
| Co ₇ Hf | — | tP32 | 74 | -0.20 | -0.23 |
| Co ₂₃ Hf ₆ | D8 _a | cF116 | — | -0.11 | -0.13 |
| 'Co ₉ Mo ₂ ' | D0 ₁₉ | hP8 | 35 | -0.09 | -0.11 |
| CoPd | — | — | 78 | -0.19 | -0.17 |
| CoPt | L1 ₀ | tP4 | 30 | -0.33 | -0.36 |
| Co ₁₇ Y ₂ | — | hP38 | 131 | -0.24 | -0.29 |
| Co ₅ Y | D2 _d | hP6 | 130 | -0.14 | -0.14 |
| Co ₇ Y ₂ | — | hR18 | 61 | -0.10 | -0.11 |
| Co ₃ Y | — | hR12 | 15 | -0.09 | -0.09 |
| Co ₁₃ La | D2 ₃ | cF112 | 130 | -0.26 | -0.36 |
| Co ₃ La | D2 _d | hP6 | 90 | -0.11 | -0.10 |
| Co ₇ La ₂ | — | hP36 | 55 | -0.08 | -0.07 |
| Co ₁₇ Gd ₂ | — | hR19 | — | -0.28 | -0.35 |
| Co ₃ Gd | D2 _d | hP6 | — | -0.11 | -0.14 |

^aSee also CoFe, Co₃Fe and CoFe₃ in Table 3.

polycrystalline and single-crystal samples. They found a maximum polar Kerr rotation of about -0.3° at ~ 3.0 eV, and concluded that U did not contribute to the Kerr effect in UCo₅.

Data for other cobalt-based binary compounds are listed in Table 2, abridged from Buschow *et al.* (1983). These measurements are restricted to compounds which are ferromagnetic or ferrimagnetic at room temperature,

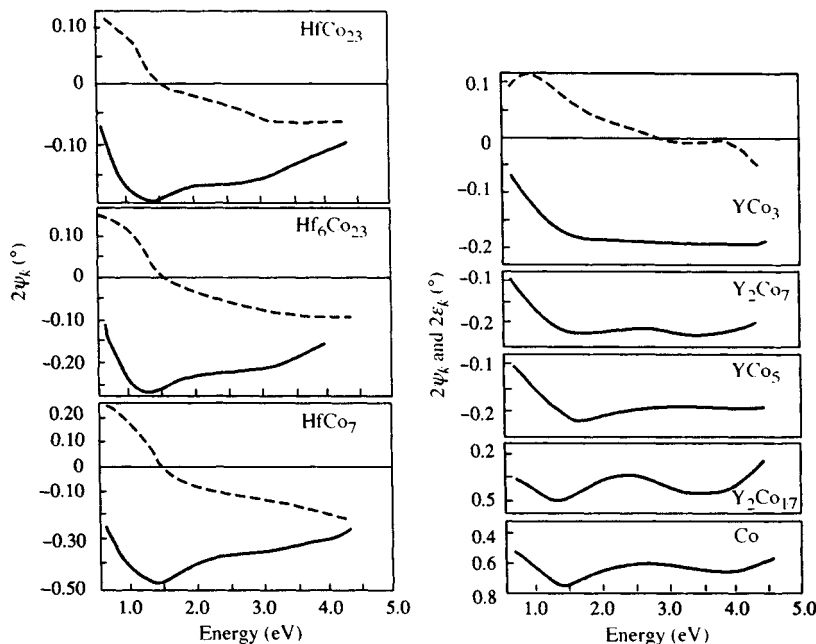


Figure 5. Polar Kerr rotation (solid line) and ellipticity (dashed line) for several Hf-Co and Y-Co compounds (after Buschow, van Engen, and Jongebreur, 1983. Reproduced by permission of Elsevier Science Publishers BV)

and we have only tabulated those with measured Kerr rotations $>0.1^\circ$. Also, the spectra measured by Buschow *et al.* (1983) for Hf-Co and Y-Co compounds are shown in Figure 5. Note the peak in the Kerr rotation at *ca* 1.3–1.4 eV which occurs for all spectra. Buschow *et al.* (1983) attribute this peak, as well as the lesser peak (most obvious in the pure cobalt spectrum) around 3.9 eV, to d-p transitions involving d electrons at the top of the majority spin band and at the bottom of the minority spin band, respectively. They interpret shifts in these peaks upon alloying or compounding with s-type or p-type metals as being due to hybridization at the bottom of the 3d band.

5.3 Iron-Based Binary Intermetallic Compounds

In addition to the comprehensive study of Buschow *et al.* (1983), there have been several investigations of other binary iron-based IMCs. Sawatzky (1971c) measured the specific polar Faraday rotations and absorption coefficients of polycrystalline films of Fe_3Si_3 at room temperature. The films were found to have an easy axis of magnetization in the plane of the film, however, and a recording figure of merit about one fourth that of MnBi. Stoffel (1969) measured the Voigt parameters and coercivities of polycrystalline FeRh strips above the first-order phase transition at 75 °C over the spectral range 400–900 nm, and found the maximum value of $|\tilde{Q}|$ to be about one fourth that of the maximum for iron and cobalt in the same spectral range. Katayama and Hasegawa (1981) and Mukimov *et al.* (1985) have studied the Laves phase C15 (*cF24*) RFe_2 compounds where $\text{R} = \text{Gd}, \text{Tb}, \text{Dy}, \text{Ho}, \text{and Er}$. Mukimov *et al.* (1985) measured the equatorial Kerr effects of polycrystalline samples of these materials as well as the isomorphous YFe_2 over the spectral range 0.5–5.0 eV. Using these results and reflectivity measurements, they extracted the absorptive (real) part of the off-diagonal element of the dielectric tensor, which is reproduced as Figure 6. Note the feature in these data ~ 1.6 eV, common to most Fe compounds, and that the change of sign seen for the yttrium compound as opposed to the other three is due to a reversal of the direction of the sublattice spins in the material, as it lies on the opposite side of its compensation at room temperature. This reversal of sign in the MO properties of materials as their temperature moves through the compensation temperature is commonly seen in ferrimagnetic materials (McGahan *et al.*, 1992a, b). For comparison, the polar Kerr rotation measurements of Katayama and Hasegawa (1981) for these materials are shown in Figure 7. They interpreted the large negative peak at ~ 290 nm

(~ 4 eV) as being due to transitions between 4f and 5d states of the rare-earth atoms. It is interesting to note that this strong spectral feature does not appear in the data of Mukimov, which should be more fundamentally related to transition matrix elements, and serves to illustrate the difficulties in directly interpreting Kerr measurements in terms of electronic structure without first eliminating the dependence of the Kerr effect on the optical constants of the material. Finally, Ferguson and Romagnoli (1969) measured the transverse Kerr effects of GdFe_2 films, a compound which was subsequently found not to exist, such that their results probably pertain to iron-poor $\text{Gd}_2\text{Fe}_{17}$ alloys (Buschow, 1988).

The bulk of MO measurements on binary iron-based IMCs have been performed by Buschow *et al.* (1983). Their data for the room-temperature magnetization and Kerr rotation at 633 and 830 nm (1.96 and 1.5 eV) for a variety of Fe-based compounds are listed in Table 3. Also, spectra from Buschow *et al.* (1983) for three iron-titan compounds, as well as bulk iron, are shown in Figure 8. The negative peak in the Kerr rotation at ~ 1.1 eV is seen to remain relatively unchanged for the various

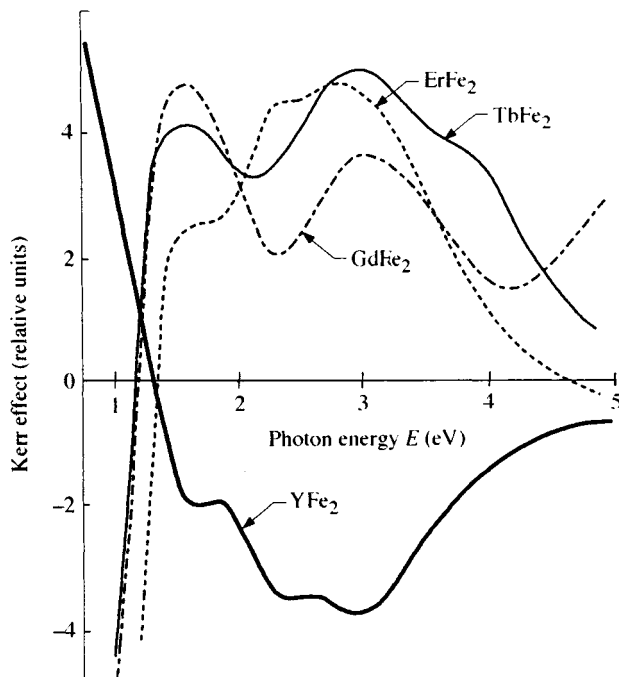


Figure 6. The absorptive (real) part of the off-diagonal dielectric tensor element $\tilde{\epsilon}_y$ for a series of cubic Laves phase RFe_2 compounds (after Mukimov, Sharipov, and Ernazarova, 1985. Reproduced by permission of Akademie-Verlag GmbH)

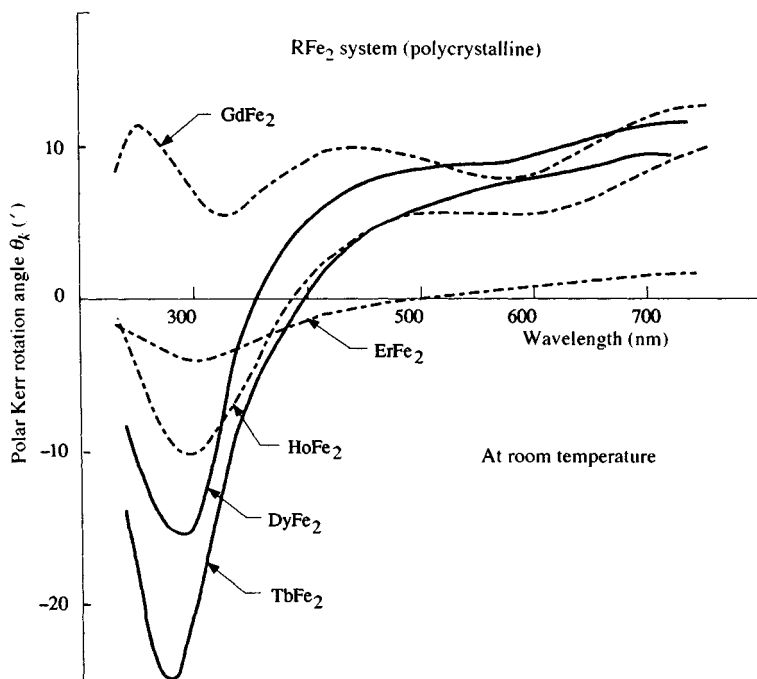


Figure 7. Polar Kerr rotation spectra for several RFe_2 cubic Laves phase compounds (after Katayama and Hasegawa, 1981. Reproduced by permission of the Institute of Materials)

Fe–Sn compounds, while the higher energy end of the spectrum is significantly altered. They observed similar behavior in the Fe–Al and Fe–Ga systems, and offer a similar interpretation for the low energy peak as that given for the cobalt-based compounds. The peak is thought to be due to transitions from the top of the majority 3d band, and they suggest that the intensity

of the peak provides a measure of the 3d band splitting in the given material.

5.4 Other Binary Intermetallic Compounds

Several binary compounds which are not based on manganese, iron, or cobalt have also been investigated.

Table 3. Iron-based binary compounds (source: Buschow, van Engen, and Jongebreur, 1983)

| Alloy* or compound | SB symbol | Pearson symbol | Saturation magnetization ($A \cdot m^2 \cdot kg^{-1}$) | Kerr rotation (633 nm) ($^\circ$) | Kerr rotation (830 nm) ($^\circ$) |
|--------------------|------------------|----------------|--|-------------------------------------|-------------------------------------|
| Fe | A2 | cI2 | 213 | –0.41 | –0.52 |
| Fe_3Al | D0 ₃ | cF16 | 156 | –0.39 | –0.48 |
| ' Fe_7Ga_3 ' | L1 ₂ | cP4 | 147 | –0.45 | –0.56 |
| ' Fe_2Ga ' | A2 | cI2 | 92 | –0.39 | –0.45 |
| Fe_3Ga_2 | A2 | cI2 | 101 | –0.34 | –0.44 |
| Fe_3Ga_4 | Monoclinic | mC42 | 24 | –0.16 | –0.19 |
| Fe_3C | D0 ₁₁ | oP16 | 100 | –0.21 | –0.24 |
| Fe_3Si | L2 ₁ | cF16 | 138 | –0.32 | –0.36 |
| Fe_3Si_3 | D8 ₈ | hP16 | 76 | –0.17 | –0.25 |
| Fe_3Ge | D0 ₁₉ | hP8 | 133 | –0.41 | –0.44 |
| Fe_3Sn | D0 ₁₉ | hP8 | 126 | –0.31 | –0.38 |
| Fe_3Sn_2 | Monoclinic | m*40 | 69 | –0.24 | –0.29 |
| Fe_2Se | C14 | hP12 | 52 | –0.17 | –0.17 |
| Fe_2Hf | C14 | hP12 | 45 | –0.32 | –0.35 |
| ' Fe_2Co ' | A2 | cI2 | 234 | –0.42 | –0.46 |
| ' $FeCo$ ' | A2 | cI2 | 230 | –0.54 | –0.60 |
| ' $FeCo_3$ ' | A2 | cI2 | 200 | –0.48 | –0.58 |
| ' $FeNi_3$ ' | A1 | cF4 | 108 | –0.23 | –0.17 |
| Fe_3Pt | L1 ₂ | cP4 | 108 | –0.52 | –0.58 |
| $FePt$ | L1 ₀ | tP4 | 42 | –0.32 | –0.39 |

*Alloy compositions shown in quotes were not heat-treated sufficiently to reach their equilibrium ordered structures.

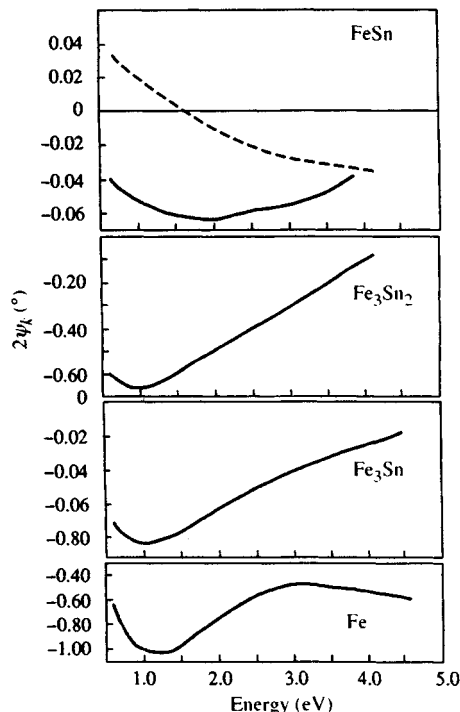


Figure 8. Polar Kerr rotation spectra for several Fe-Sn compounds (after Buschow *et al.*, 1983. Reproduced by permission of Elsevier Science Publishers BV). The polar Kerr ellipticity is shown as the dashed line for FeSn

Comstock and Lissberger (1970) measured the specific Faraday rotations and absorption coefficients of CrTe films, and found a figure of merit for this material of about one fourth that of MnBi. Atkinson (1977) measured the complex indices of refraction and Voigt parameters of Cr_3Te_4 films at six wavelengths between 405 and 615 nm, and used these results to predict a maximum signal to noise ratio for the MO read process which was about one tenth that predicted for MnBi. Recently, Sato *et al.* (1992) have measured the reflectivity from 0.3 to 23 eV and the polar Kerr rotation and ellipticity from ~ 0.5 to 3.0 eV on single crystals of Cr_3Te_4 , from which they extracted the elements of the conductivity tensor. They found qualitative agreement with predictions from band-structure calculations, and concluded that the chromium d electrons are not localized in Cr_3Te_4 , and that this compound should be described with an itinerant electron magnetic model.

Perhaps the most interesting classes of materials (many which are not truly intermetallic) are the cerium-based and uranium-based compounds. CeSb exhibits the largest Kerr rotation of any known material ($> 15^\circ$ near

0.4 eV) (Schoenes and Reim, 1985). CeTe (Schoenes, 1987), UTe (Reim, 1986; Schoenes and Brändle, 1991), and many other U and Ce compounds have been shown to exhibit very large Kerr effects as well. A proposed explanation for these giant MO effects is that the orbital angular momentum in these materials is not quenched (Lim *et al.*, 1991), such that light may couple directly to the orbital moment of the electrons, rather than indirectly via the weak spin-orbit interaction. Although these materials do not in general order magnetically at room temperature, considerable theoretical work has been devoted to them, and the reader is referred to the review by Reim (1986) for details.

5.5 Ternary Intermetallic Compounds

There is a large number of pseudobinary and ternary IMCs which are magnetically ordered at room temperature, several of which have attracted attention as potential MO recording media. Sawatzky and Street (1973) found MnGaGe films to have nearly square hysteresis loops in the perpendicular orientation with a coercive field of ~ 1.5 kOe for an 800 Å polycrystalline film. They measured the polar Faraday rotation of this material as well, and demonstrated that (at the time) MnGaGe was a promising MO medium. Sherwood *et al.* (1971) demonstrated Curie point writing on MnAlGe films with an argon ion laser in 1971, and observed the written patterns via the polar Faraday effect. Katsui (1976) measured the Faraday rotations of thin (300–500 Å) films of MnCuBi coated with SiO_2 , and found square hysteresis loops in the perpendicular orientation with large (~ 2.5 kOe) coercivities. In 1990, van Engelen and Buschow measured the Kerr spectra from 0.5 to 4.6 eV of the $\text{YFe}_{10}\text{T}_2$ series, with T = Cr, Mo, W, and Si, as well as the $\text{RFe}_{10}\text{Si}_2$ series, where R = Lu, Tb, Dy, Gd, Nd, Er, and U, and concluded from their measurements that the 4f-electron systems have relatively little influence on the Kerr spectra, with the exception of the U compound, in which the 5f and 3d sublattices were postulated to interact strongly enough to induce a magnetic moment on the U atoms at room temperature, leading to a contribution to the Kerr effect from the U sublattice as well. In 1988, van Engelen *et al.* also found this to be the case for the compounds UMn_2Si_2 and UMn_2Ge_2 .

A ternary compound which has recently attracted considerable interest is Cl_b (cF12) PtMnSb. Van Engen *et al.* (1983a, b) found this material to exhibit the largest-known room-temperature Kerr rotation ($> 2.5^\circ$ at 1.72 eV). PtMnSb is a half-metallic ferromagnet, a term derived from the fact that the minority spin bands exhibit

Table 4. Some ternary compounds (source: Buschow, 1988)

| Compound | SB symbol | Pearson symbol | Saturation magnetization ($\text{A m}^2 \text{kg}^{-1}$) | Kerr rotation (633 nm) ($^\circ$) | Kerr rotation (830 nm) ($^\circ$) |
|-------------------------------|-----------------|----------------|--|-------------------------------------|-------------------------------------|
| $\text{LaCo}_{11}\text{Si}_2$ | D_{23} | cF112 | 77 | -0.18 | -0.21 |
| MnAlGe | C_{38} | tP6 | 40 | -0.02 | -0.02 |
| Fe_2NiAl | L_{21} | cF16 | 117 | -0.25 | -0.30 |
| Fe_2MnAl | L_{21} | cF16 | 52 | -0.12 | -0.14 |
| Fe_2CrAl | L_{21} | cF16 | — | -0.11 | -0.12 |
| Co_2FeAl | L_{21} | cF16 | 138 | -0.37 | -0.42 |
| Fe_2NiGa | L_{21} | cF16 | 55 | -0.15 | -0.15 |
| Fe_2CoGa | L_{21} | cF16 | 120.9 | -0.41 | -0.47 |
| Fe_2CrGa | L_{21} | cF16 | 42.5 | -0.18 | -0.20 |
| Co_2FeGa | L_{21} | cF16 | 116.8 | -0.41 | -0.49 |
| Co_2MnGa | L_{21} | cF16 | 87.5 | -0.14 | -0.15 |
| Co_2HfSn | L_{21} | cF16 | 19.8 | 0.15 | 0.00 |
| Co_2FeSi | L_{21} | cF16 | 139.8 | -0.33 | -0.34 |
| Co_2FeGe | L_{21} | cF16 | 124.2 | -0.43 | -0.51 |
| Fe_2CoGe | L_{21} | cF16 | 118.2 | -0.35 | -0.39 |
| Co_2FeIn | L_{21} | cF16 | — | -0.44 | -0.58 |
| Ru_2FeSn | L_{21} | cF16 | 33 | -0.14 | -0.08 |
| PdMnSb | C_{1b} | cF12 | 53 | -0.14 | -0.14 |
| PtMnSb | C_{1b} | cF12 | 54 | -0.93 | -0.76 |
| PtFeSb | F0_1 | cP12 | 20 | -0.06 | -0.06 |
| PtMnSn | C_{1b} | cF12 | 30 | -0.14 | -0.11 |
| FeNiIn | B8_2 | hP6 | 23.3 | -0.12 | -0.12 |
| FeCoGe | B8_2 | hP6 | 43.2 | -0.15 | -0.15 |
| FeCoSn | B8_2 | hP6 | 34.6 | -0.10 | -0.11 |

a gap at the Fermi energy, which the majority spin bands do not. PtMnSb is then metallic with respect to the majority spin electrons, and semiconducting with respect to the minority spin electrons. This material has also been studied structurally by Attaran and Grundy (1989), and the complex indices of refraction and Voigt parameters have been measured over the spectral range 350–800 nm (1.55–3.54 eV) by Bains *et al.* (1992) on 250 nm thick films of PtMnSb on glass substrates.

A very large number of ternary IMCs has been studied by Buschow *et al.* (1983) and Buschow (1988). Data for the room-temperature magnetization and polar Kerr rotation for some of these compounds taken from Buschow's review are listed in Table 4. Other than the efforts of Buschow and coworkers (1983, 1988) to interpret spectra of some of these compounds in terms of charge-transfer spectra (van Engen *et al.*, 1983a, b) and previous theoretical work mentioned for PtMnSb , there has been very little systematic research aimed at understanding the MO properties of ternary (and binary) IMCs.

We conclude the summary of MO properties of true IMCs by noting that of all the compounds mentioned, MnBi and PtMnSb are certainly the most likely to find future applications in MO storage. Prior to the discovery of the amorphous rare-earth/transition metal alloys,

MnBi was a leading candidate for MO storage applications, and the very large Kerr effects displayed by both these materials has led to continued research into these systems. A typical example is the work of Kawanabe and Naoe (1991) on Pt-MnSb multilayers. This system had been previously found to exhibit strong perpendicular anisotropy (Kawanabe and Naoe, 1988), which bulk PtMnSb does not, and was found to exhibit a Kerr rotation of 0.83° at 1.97 eV. Similar innovative approaches to the preparation of materials based on IMCs hold some promise for the development of better MO media in the future.

5.6 Amorphous Alloys

Even though the materials considered in this section are not IMCs *per se*, they deserve mention here, as this class of materials currently dominates the MO media market completely. Many binary and ternary amorphous alloys of rare-earth and transition metals exhibit significant MO effects and perpendicular anisotropy. For example, TbFeCo can be sputtered as an amorphous thin film over a wide range of compositions, which allows the alloy ratios to be adjusted to optimize the compensation temperature of the alloy for the thermomagnetic write process. Recently, solid solutions of cobalt and platinum

have been grown which exhibit perpendicular magnetic anisotropy and large polar Kerr effects in the blue region of the spectrum, attractive for future MO drives based on shorter-wavelength diode lasers.

Amorphous metallic alloys offer a number of important advantages over crystalline compounds as MO recording media. First, the amorphous nature of the material provides pinning sites for the thermomagnetically written domains, such that very small ($<1\ \mu\text{m}$), uniform domains can be produced, which reduces the readout noise considerably. Second, the properties of the alloy can be directly controlled by varying the alloy composition, a luxury which is not available in many crystalline compounds. Third, many of the RE/TM amorphous alloys exhibit very strong perpendicular magnetic anisotropy in thin-film form, such that square hysteresis loops with large coercivities can be obtained at room temperature. Also, by selecting the proper alloy ratio, the compensation points of these films can be positioned at will near room temperature, such that low-power diode lasers are sufficient to write domains thermomagnetically. Finally, the amorphous RE/TM alloys display a reasonably strong polar Kerr effect. We do not present data for these materials here, but refer the interested reader to the literature for details (Bloomberg and Connell, 1988; Greidanus and Zeper, 1990; Hansen, 1990).

The primary drawback of the amorphous RE/TM alloys is that they are very reactive, in general, and must be carefully protected by non-oxide dielectric coatings in order to remain stable for any period of time. Also, they tend to be difficult to produce, such that sputtering targets of the alloyed material (most commonly a TbFeCo-based alloy) are very expensive.

6. Summary

In this chapter, we have reviewed the phenomenological and physical principles of first-order magneto-optical effects, and summarized research to date on the magneto-optical properties of intermetallic compounds. Amorphous alloys currently dominate the MO market, but it may be possible that intermetallic or related compounds may constitute the next generation of MO recording materials. For example, Weller (1992) has recently shown that solid solutions of Co and Pt exhibit large Kerr rotations and significant perpendicular anisotropies over a small range of compositions around 70% Pt, i.e. near CoPt_3 . Also, while the crystalline (or polycrystalline) nature of true intermetallics rules out many applications for these materials due to grain

boundary noise in the readout process, fundamental studies of intermetallic compounds have been and will continue to be of great benefit in understanding the factors leading to large MO effects in materials.

7. Acknowledgements

The author would like to thank NASA Lewis (NAG-3-95) and the NSF (DMR 8918889) for financial support.

8. References

- Argyres, P.N. (1955). *Phys. Rev.*, **97**(2), 334.
- Atkinson, R. (1977). *Thin Sol. Films*, **47**, 177.
- Attaran, E., and Grundy, P. J. (1989). *J. Magn. Magn. Mater.*, **78**, 51.
- Azzam, R. M. A., and Bashara, N. M. (1989). *Ellipsometry and Polarized Light*, 2nd edn. North Holland, Amsterdam, p. 272.
- Bains, G. S., Carey, R., Newman, D. M., and Thomas, B. W. J. (1992). *J. Magn. Magn. Mater.*, **104-107**, 1011.
- Bennett, H. S., and Stern, E. A. (1965). *Phys. Rev. A*, **137**(2), 448.
- Bloomberg, D., and Connell, G. A. N. (1988). In *Magnetic Recording*, Vol. 2 (eds C. D. Mee and E. D. Daniel). McGraw-Hill, New York, p. 305.
- Brändle, H., Schoenes, J., Hulliger, F., and Reim, W. (1990). *J. Magn. Magn. Mater.*, **83**, 29.
- Burns, G. (1985). *Solid State Physics*. Academic Press, New York, p 87.
- Buschow, K. H. J. (1988). In *Ferromagnetic Materials*, Vol. 4 (eds E. P. Wohlfarth and K. H. J. Buschow). Elsevier, Amsterdam, pp. 493-595.
- Buschow, K. H. J., van Engen, P. G., and Jongebreur, R. (1983). *J. Magn. Magn. Mater.*, **38**, 1.
- Chaudhari, P., Cuomo, J. J., and Gambino, R. J. (1973). *Appl. Phys. Lett.*, **22**, 337.
- Chen, D., Aagard, R. L., and Liu, T. S. (1970). *J. Appl. Phys.*, **41**(3), 1395.
- Chen, D., Gondo, Y., and Blue, M. D. (1965). *J. Appl. Phys.*, **36**(3), 1261.
- Chen, D., Otto, G. N., and Schmit, F. M. (1973). *IEEE Trans. Magn.*, **9**(2), 66.
- Comstock, R. L., and Lissberger, P. H. (1970). *J. Appl. Phys.*, **41**(3), 1397.
- de Groot, R. A., Mueller, F. M., van Engen, P. G., and Buschow, K. H. J. (1984). *J. Appl. Phys.*, **55**(6), 2151.
- Dekker, P. (1976). *IEEE Trans. Magn.*, **12**(4), 313.
- Di, G. Q., Iwata, S., Tsunashima, S., and Uchiyama, S. (1992). *J. Magn. Magn. Mater.*, **104-107**, 1023.
- Erskine, J. L., and Stern, E. A. (1973). *Phys. Rev. Lett.*, **30**, 1329.

- Fang, R.-Y., Dai, D.-S., Zhang, S., Long, P., Ma, T.-J., Dai, C., and Zhang X.-X. (1992). *J. Magn. Magn. Mater.*, **104–107**, 1031.
- Feldtkeller, E. (1972). *IEEE Trans. Magn., Proc. 1972 Intermag Conf.*, p. 481.
- Ferguson, P. E., and Romagnoli, R. J. (1969). *J. Appl. Phys.*, **40**(3), 1236.
- Gamble, R., and Lissberger, P. H. (1988). *J. Opt. Soc. Am.*, **5**, 1533.
- Greidanus, F. J. A. M., and Zeper, W. B. (1990). *MRS Bull.*, **15**(4), 31.
- Hansen, P. (1990). *J. Magn. Magn. Mater.*, **83**, 6.
- Hansen, P., and Krumme, J. P. (1984). *Thin Sol. Films*, **114**, 69.
- Katayama, T., and Hasegawa, K. (1981). In *Proc. 4th Int. Conf. on Rapidly Quenched Metals*, Sendai. The Japan Institute of Metals, Sendai, p. 915.
- Katsui, A. (1976). *J. Appl. Phys.*, **47**(8), 3609.
- Kawanabe, T., and Naoe, M. (1988). *J. Physique*, **C8**, 1783.
- Kawanabe, T., and Naoe, M. (1991). *J. Magn. Soc. Jpn.*, **15**(S1), 53.
- Lewicki, G., and Guisinger, J. E. (1973). *J. Appl. Phys.*, **44**(5), 2361.
- Lim, S. P., Price, D. L., and Cooper, B. R. (1991). *IEEE Trans. Magn.*, **27**(4), 2648.
- Mansuripur, M. (1986). *Appl. Phys. Lett.*, **49**(1), 19.
- Mattis, D. C. (1988). *The Theory of Magnetism I*. Springer-Verlag, Berlin, p. 15.
- Maurer, T., Sticht, J., Oppeneer, P. M., Herman, F., and Kübler, J. (1992). *J. Magn. Magn. Mater.*, **104–107**, 1029.
- Mayer, L. (1958). *J. Appl. Phys.*, **29**, 1454.
- McGahan, W. A., Chen, L. Y., Woollam, J. A., Sequeda, F., and Do, H. (1992a). *Appl. Phys. Commun.*, **11**(4), 549.
- McGahan, W. A., He, P., Woollam, J. A., and Sequeda, F. O. (1992b). *Appl. Phys. Commun.*, **11**(4), 375.
- McGahan, W. A., He, P., Chen, L. Y., Bonafede, S., Woollam, J. A., Sequeda, F., McDaniel, T., and Do, H. (1991). *J. Appl. Phys.*, **69**(8), 4568.
- McGahan, W. A., and Woollam, J. A. (1989). *Appl. Phys. Commun.*, **9**(1/2), 1.
- Meiklejohn, W. H. (1986). *Proc. IEEE*, **74**(11), 1570.
- Misemer, D. K. (1988). *J. Magn. Magn. Mater.*, **72**, 267.
- Mukimov, K. M., Sharipov, Sh. M., and Ernazarova, L. A. (1985). *Phys. Stat. Sol. (B)*, **127**, K129.
- Oppeneer, P. M., Sticht, J., and Herman, F. (1991). *J. Magn. Soc. Jpn.*, **15**(S1), 73.
- Parker, M. R. (1987). In *SPIE 31st Annual International Technical Symposium on Optical and Optoelectronic Applied Science and Engineering*, San Diego.
- Pershan, P. S. (1967). *J. Appl. Phys.*, **38**(3), 1482.
- Reim, W. (1986). *J. Magn. Magn. Mater.*, **58**, 1.
- Sato, K., Aman, Y., and Hongu, H. (1992). *J. Magn. Magn. Mater.*, **104–107**, 1947.
- Sawatzky, E. (1971a). *J. Appl. Phys.*, **42**(4), 1706.
- Sawatzky, E. (1971b). *IEEE Trans. Magn., Proc. 1971 Interimag Conf.*, p. 377.
- Sawatzky, E. (1971c) *IEEE Trans. Magn., Proc. 1971 Interimag Conf.*, p. 374.
- Sawatzky, E., and Street, G. B. (1973). *J. Appl. Phys.*, **44**(4), 1789.
- Schoenes, J. (1987). *J. Magn. Soc. Jpn.*, **11**(S1), 99.
- Schoenes, J., and Brändle, H. (1991). *J. Magn. Soc. Jpn.*, **15**(S1), 213.
- Schoenes, J., and Reim, W. (1985). *J. Less-Common Met.*, **112**, 19.
- Sherwood, R. C., Nesbitt, R. A., Wernick, J. H., Bacon, D. D., Kurtzig, A. J., and Wolfe, R. (19971). *J. Appl. Phys.*, **42**(4), 1704.
- Skriver, H. L. (1984). *The LMTO Method*. Springer Series in Solid State Sciences, Vol. 41. Springer-Verlag, New York.
- Smith, D. O. (1965). *Opt. Acta*, **12**, 13.
- Sokolov, A. V. (1967). *Optical Properties of Metals*. Elsevier, Amsterdam.
- Stoffel, A. M. (1968). *J. Appl. Phys.*, **39**(2), 563.
- Stoffel, A. M. (1969). *J. Appl. Phys.*, **40**(3), 1238.
- Stoffel, A. M., and Schneider, J. (1970). *J. Appl. Phys.*, **41**(3), 1405.
- van Engelen, P. P. J., and Buschow, K. H. J. (1990). *J. Magn. Magn. Mater.*, **84**, 47.
- van Engelen, P. P. J., de Mooij, D. B., and Buschow, K. H. J. (1988). *IEEE Trans. Magn.*, **24**, 1728.
- van Engen, P. G., Buschow, K. H. J., and Erman, M. (1983a). *J. Magn. Magn. Mater.*, **30**, 374.
- van Engen, P. G., Buschow, K. H. J., Jongebreur, R., and Erman, M. (1983b). *Appl. Phys. Lett.*, **42**, 202.
- Visnovsky, S. (1991). *J. Magn. Soc. Jpn.*, **15**(S1), 67.
- Weller, D. Private communication.

This chapter was originally published in 1995 as Chapter 19 in *Intermetallic Compounds*, Vol. 2: *Practice*, edited by J. H. Westbrook and R. L. Fleischer.

Chapter 9

Thermoelectric and Electrical Applications

Marat V. Vedernikov

A. F. Ioffe Physico-Technical Institute, Russian Academy of Sciences, 194021 St Petersburg, Russia

1. Introduction

The first edition of *Intermetallic Compounds* contained an excellent chapter by Cadoff (1967) entitled 'Thermoelectric Properties'. It was an adequate survey of the current research into the thermoelectric (TE) power conversion and thermoelectric materials at the time. The achievements it summarized included the development of the theory of TE energy conversion, of several basic TE materials (using $A_2^V B_3^{VI}$ and $A^{IV} B^{VI}$ compounds), of the simplest theory of the transport properties of semiconductors, a few proposals for the improvement of TE properties, and a description of the first industrial TE devices. But the TE energy conversion method still did not enjoy wide recognition. For the topic of intermetallic compounds this field was of considerable importance, since the above mentioned basic TE materials could be classed as intermetallics (in the general sense of this term). Since the late 1960s the situation has changed essentially. Indeed, various TE devices have now found broad application in many areas of technology; several very important practical applications have taken place; the quality of the originally used materials has improved noticeably; new basic TE materials capable of operating in both higher and lower temperature ranges have been developed; and it was shown that the simplest theoretical models are not sufficient to account in detail for the transport properties observed in the most promising TE materials. And, as is also important, we have witnessed the appearance of a large number of publications on all aspects of thermoelectricity, including original papers, reviews, and monographs.

The present review is an attempt at a successive survey of the major aspects of TE applications with a view of giving the reader a general idea of the problems involved. However, taking into account the existence of good monographs, by necessity the fundamentals will be covered only briefly. For a more detailed analysis one can be referred to the classic pioneering work of Ioffe (1957), a concise account of all aspects of thermoelectricity by Rowe and Bhandari (1983), a detailed treatment of thermoelectric and thermomagnetic cooling by Goldsmid (1986), and the recent general review by Wood (1988) with a particular emphasis on the high-temperature TE materials for space use. The last three publications list practically all the relevant bibliography. We shall deal in more detail with the results obtained since the late 1960s in the above mentioned areas. We shall discuss the problems associated with the improvement of TE efficiency in energy conversion devices and with the use of intermetallic compounds for this purpose. Note also that the expanding production and application of TE devices since the 1970s has initiated organization of regular international conferences on thermoelectricity. Starting from 1976, they were hosted by Professor K. R. Rao at the University of Texas at Arlington; in 1987 the first European conference was convened; then they were combined and are presently held annually in different cities under the auspices of the International Thermoelectric Society. The conference proceedings provide a practically complete overview of current studies and development of new TE materials and new TE devices; they report on thermoelectric measurements and, to a lesser extent, on the physics of TE and, more

generally, on the transport properties of materials. References to conference proceedings (1976–1992) can be found in Section 9.

Practical application of TE phenomena is based primarily on the use of certain intermetallic compounds as active TE materials. Electrically conducting intermetallics have not yet found any other electrical application in technology. We shall discuss this point briefly after a survey of their TE applications.

The conclusion of this chapter offers some comments on prospective uses of the intermetallics for thermoelectric and electrical applications.

2. Thermoelectricity: Physical Phenomena and Terminology

Thermoelectric phenomena arise in electrical circuits made up of two or more unlike conductors. The simplest thermoelectric circuits consisting of two different conducting materials A and B are shown in Figure 1. The circuit in Figure 1(a) does not contain an electromotive force (e.m.f.) source; however, if a temperature difference ΔT is created between contacts 1 and 2 then a thermoelectromotive force E_{AB} will appear in the circuit. This is the so-called 'Seebeck effect' discovered in 1821. If the sense of ΔT is reversed, the electromotive force E_{AB} will likewise reverse its sign. When an external voltage source E generates an electric current I in the TE circuit in the absence of an external temperature difference ΔT (Figure 1b), then a temperature difference will appear between contacts 1 and 2. This is accompanied by liberation on one contact of a certain heat, and by absorption on the other of an equal amount of what is called Peltier heat Q_{AB} . This effect was discovered by Peltier in 1834. If the current sense is reversed, the hot and cold contacts will interchange places.

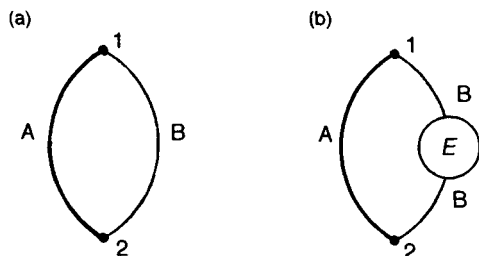


Figure 1. The simplest thermoelectric circuits (a) without external voltage source and (b) with external voltage source E

The thermoelectric properties of materials are characterized by the Seebeck coefficient S (also called the thermopower) and the Peltier coefficient Π . These coefficients relate the voltage E and heat Q generated in a TE circuit with the actions responsible for their appearance

$$\begin{aligned} E_{AB} &= S_{AB} \Delta T \\ Q_{AB} &= \Pi_{AB} I \end{aligned} \quad (1)$$

The subscripts A and B in equations (1) indicate that the thermopower and the Peltier heat arise and can be measured only on a pair of conductors A and B. Thus the coefficients S_{AB} and Π_{AB} are relative quantities characterizing the properties of material A with respect to material B, and vice versa. Soon after the discovery of TE phenomena, Thomson (Lord Kelvin) analyzed them theoretically from the thermodynamic viewpoint and predicted the existence of the third TE effect which subsequently was given his name. The Thomson effect consists in the liberation or absorption of additional heat (Thomson heat Q_{Th}) in a conductor when a current I goes through it in the presence of a temperature difference ΔT , i.e. $Q_{Th} = \mu I \Delta T$, where μ is the Thomson coefficient. Being very small, this effect has not found any application and therefore will not be considered here. It is remarkable, however, that in contrast to the Seebeck and Peltier effects, the Thomson coefficient μ can be defined for a single conductor; in other words, one can experimentally determine both μ_A and μ_B . The theory of Thomson yields the following relations connecting the three thermoelectric coefficients

$$\begin{aligned} \Pi_{AB} &= S_{AB} T \\ \mu_A - \mu_B &= (dS_{AB}/dT)T \end{aligned} \quad (2)$$

The second of these relations permits determination of the absolute value of the Seebeck coefficient for a given single conductor

$$S_A = \int_0^T \frac{\mu_A}{T} dT$$

This offers the possibility of introducing not only relative TE characteristics for a pair of conductors but also inherent TE coefficients for each material as well, with $S_{AB} = S_A - S_B$, $\Pi_{AB} = \Pi_A - \Pi_B$. As follows from Thomson's relations, it is sufficient to measure experimentally one of the three TE coefficients, the other two being readily calculated after that. One usually measures S , since electrical measurements are much simpler and can be done with a higher precision than

the thermal ones. S is expressed in VK^{-1} (more frequently μVK^{-1}), Π in WA^{-1} or V (usually μV) and μ in VK^{-1} .

3. Thermoelectric Applications: Principles

As we have seen in the preceding section, by passing a heat flux through a TE circuit one can generate a voltage across it, while a flow of electric current produces a heat flux through it. Thus TE circuits can, in principle, serve as converters of thermal into electrical energy or electrical into thermal energy. They can be used to design specific devices of practical interest. The simplest TE device is a thermoelement or thermocouple. Figure 2(a) presents a thermoelement connected as a thermoelectric generator (TEG), and Figure 2(b) shows a thermoelectric heat pump or thermoelectric cooler (TEC). The converter consists essentially of rods (or legs) A and B made of TE materials (it should be noted that the term 'TE materials' is presently being replaced by 'thermoelectrics', by which one understands the material in which thermoelectric energy conversion takes place). The legs A and B are connected by a metallic strap K_1 , and the other leg ends are provided with straps K_2 used to connect the thermoelement into the external circuit. The thermoelement is placed on an insulating base D of a high thermal conductivity material.

When connected in the TEG arrangement, a heat flux q is supplied to the upper junction K_1 , its temperature increasing ('hot junction' with the temperature T_{hot}).

The heat passes through the thermoelement and q_{dis} is dissipated through base D. The temperature of the 'cold junction' K_2 is $T_{\text{cold}} < T_{\text{hot}}$. Part of the heat flux is converted into electrical energy, generating a current in the external circuit, the useful power being released in the load resistor R . In the TEC arrangement, object F to be cooled is connected with the working (upper) junction. The current from the external source E is passed in such a direction as to cool the working junction to the temperature T_{cold} . The temperature of the lower junctions will increase up to $T_{\text{hot}} > T_{\text{cold}}$, the heat being dissipated from the insulating base D.

Since the efficiency of the TE conversion is relatively low, a single thermoelement may not be capable of providing the required output electric power (TEG) or temperature decrease (TEC). These parameters can be improved by properly combining thermoelements in thermoelectric modules (see Figure 3). The modules can be single stage (Figure 3a) and multistage or cascade (Figure 3b). In the TEG arrangement, cascading permits one to achieve efficient generator operation at a high temperature difference $T_{\text{hot}} - T_{\text{cold}}$ (in each stage one uses the thermoelectric most suited for the given temperature interval). In the case of the TEC, cascading provides a substantially deeper cooling, the number of thermoelements in a stage increasing toward higher temperatures (see Figure 3b).

The most important parameter characterizing a thermoelement is its energy conversion coefficient. For the TEG it is called the efficiency η , and for the TEC it is the coefficient of performance ϵ . They can be presented in the following form

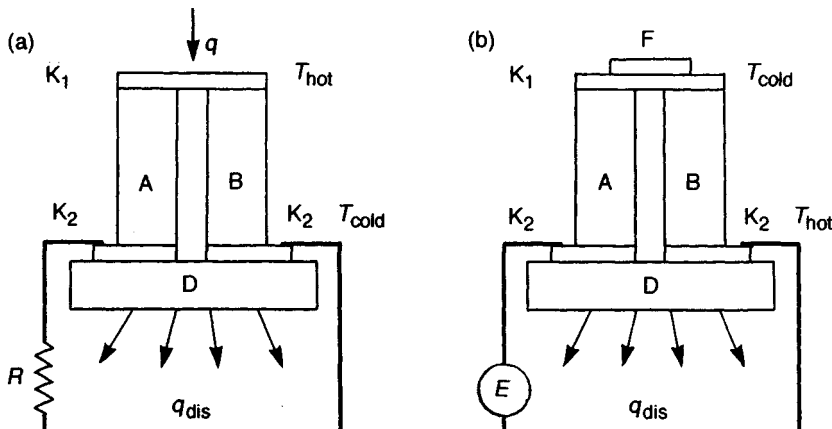


Figure 2. Thermoelement (thermocouple) (a) connected as a thermoelectric generator and (b) connected as a thermoelectric heat pump (cooler)

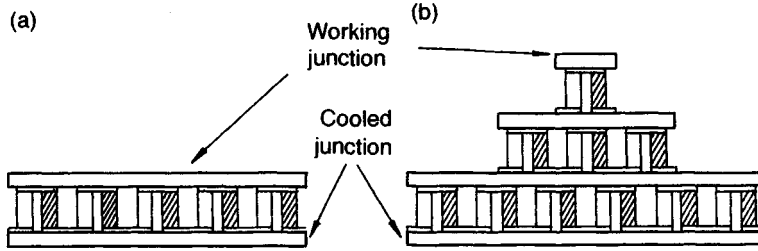


Figure 3. Thermoelectric modules: (a) single-stage module; and (b) multistage (cascade) cooling module

$$\eta = \frac{T_{\text{hot}} - T_{\text{cold}}}{T_{\text{hot}}} \frac{(1 + ZT_{\text{mean}})^{1/2} - 1}{(1 + ZT_{\text{mean}})^{1/2} + T_{\text{cold}}/T_{\text{hot}}} \quad (3)$$

$$\epsilon = \frac{T_{\text{cold}}}{T_{\text{hot}} - T_{\text{cold}}} \frac{(1 + ZT_{\text{mean}})^{1/2} - T_{\text{hot}}/T_{\text{cold}}}{(1 + ZT_{\text{mean}})^{1/2} + 1} \quad (4)$$

$$Z = \frac{S^2 \sigma}{\chi} \quad (5)$$

Here $T_{\text{mean}} = (T_{\text{hot}} + T_{\text{cold}})/2$, S is the thermopower, and σ and χ are the electrical and thermal conductivity, respectively. The values of σ and χ are assumed to be equal for both legs, and S has different signs but the same value. Parameter Z depends on thermoelectric material properties only; it is called the thermoelectric figure of merit, and its dimension is K^{-1} . The greater the figure of merit of a material, the higher is the efficiency of conversion. It is very important to understand that efficiency depends on a particular combination of transport properties S , σ and χ only, and not on any one separately. So the parameters S , σ , χ and Z are often called collectively the thermoelectric properties of a material.

The expressions for η and ϵ represent products of two multipliers. The first of them (the thermodynamic term) describes the thermal conversion cycle involved, the second (thermoelectric term) being determined (through Z) by a combination of the thermoelectric properties. The thermodynamic term is the greater, the greater is the ΔT at the thermoelement (for the TEG). The thermoelectric term is more complex in structure and should apparently have an optimum at certain values of the three transport properties. To find this optimum, consider the qualitative dependence of the transport properties of a solid on the carrier concentration (see Figure 4). The concentration increases from left to right, so that in the left-hand part of the graph it corresponds to dielectrics (region D), and in the right-hand part to metals (region M), with semiconductors and semimetals lying in between (SC, SM). The magnitude of the

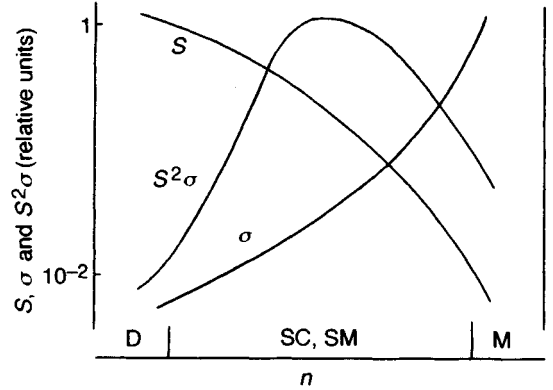


Figure 4. Qualitative dependence of transport properties of solids on current carrier concentration n

thermoelectric power parameter $S^2 \sigma$ in regions D and M is small owing to the smallness of σ and S , respectively. At the same time, at medium concentrations where neither σ nor S is small, $S^2 \sigma$ increases. Of the two additive components of the thermal conductivity, electronic and lattice, the lattice term is more essential for TE conversion (see below). However, since the lattice thermal conductivity does not depend strongly on carrier concentration, the dependence of the figure of merit Z on concentration will be about the same as that of $S^2 \sigma$, i.e. it should have a maximum in the region of degenerate semiconductors and semimetals. These are the characteristics that are typical of many intermetallic compounds and, hence, it is among the latter that one could possibly find efficient thermoelectrics.

4. Thermoelectric Applications: Practice

4.1 Basic Areas of TE Application

4.1.1 Thermocouples—TE Thermometers

The thermoelectromotive force generated in a TE circuit depends only on the conductor material and the

temperature difference between the contacts. The voltage across a thermocouple can be readily measured with high accuracy. Therefore thermoelements can be used for high-precision measurements of temperature differences. By fixing the temperature of one junction we can transform the thermoelement into a TE thermometer. Among its merits are high accuracy and reliability and applicability over a very broad temperature range. Being more than 100 years old, TE thermometry retains its potential for science and technology.

4.1.2 TEGs—Thermoelectric Generators

The Seebeck effect was used to generate electrical energy already in the 19th century (primarily under laboratory conditions); however, it was later replaced by more efficient means. Only after World War II did development and production of modern TEGs become justified owing to a substantial improvement of the quality of thermoelectrics and the appearance of a market for such generators in various areas of technology. A TEG is capable of converting into electric power heat of any origin, e.g. organic fuel combustion, nuclear reactors, radioactive isotope heat sources, solar heat, or the heat given off by any warm object (in particular, even the human body). The TEG is a solid-state converter; it does not emit any noise, and does not require regular servicing. It can be used to construct an autonomous, service-free electric power supply wherever there is a heat source. TEGs find application as power supplies for gas pipelines and radio relay links, spacecraft in deep and near-earth space, sea buoys and other remote land-based and sea-based recording and signaling objects, in instrument making, and in military and civilian equipment. Since even the best known thermoelectrics have a relatively low TE conversion efficiency, the output power of the present-day TEGs lies in the range 10^{-3} – 10^4 W.

4.1.3 Thermoelectric Radiation Detectors

Detection and measurement of radiant energy is a major area of instrumentation engineering where radiation detectors are used. An essential place among them is occupied by TE detectors based on thermocouples. A radiation flux incident on the detector receiver area is absorbed and heats it. From the amount of heating one can readily derive the radiation flux. The receiver plate is connected with a thermocouple or (more frequently) a thermocouple array, its voltage being calibrated in units of radiation flux. Thermoelectric detectors are

non-selective in radiation frequency, do not need a power supply, do not require cooling, and are simple and reliable. As thermoelectric material one can use both metals and semiconductors. Since the main requirement a TE converter should meet is high sensitivity, it must have a small mass. Therefore metallic thermocouples are made of thin wires, and semiconductor ones of thin films. To increase the sensitivity still more, individual elements are connected in batteries of tens and hundreds series-connected thermocouples.

4.1.4 Thermoelectric Coolers and Conditioners

Owing to the Peltier effect, a thermoelement can operate as a heat pump, the heat being transferred to either junction, depending on the actual current direction. As a result, it can be employed both as a cooler (TEC) and as a conditioner, i.e. a device intended to maintain the temperature at a given level. With no movable parts, these devices are noiseless, compact, reliable, and easily controllable by purely electrical means. In all these respects the TE coolers possibly surpass coolers of all other types. Their principal shortcoming is the fairly low conversion efficiency (with the thermoelectrics available today), which makes the method expensive and economically hardly feasible for large operating volumes. However, for small-scale cooling technology the method has gained wide recognition in many areas of application, which keep growing steadily, from consumer goods to military devices, instrumentation, medicine, computers, car equipment, etc. A new interest has arisen recently in connection with the problem of the holes in the ozone layer, the growth of which is associated with freon emissions into the atmosphere. Thermoelectric cooling does not require freon for its operation. TE cooling is undoubtedly a major area of present thermoelectric application which exceeds the others by far in production volume.

The main, and practically the only, thermoelectric materials of industrial significance for TECs are materials based on $A_2B_3^{VI}$ compounds (Bi_2Te_3 and the corresponding solid solutions). They are useful for TEC operation near room temperature. A single-stage module is capable of lowering the temperature by 70 K (at zero heat load at the working junction). A module with four to six stages can lower the temperature by 120–130 K from 300 K at the hot junction. The temperature range 350–200 K is routine for TECs since suitable active materials are available, and the industrial technology of module production and very accurate heat calculation techniques for these TECs have been developed. As will be seen in Section 5, cooling to still lower temperatures

represents a much more difficult problem and poorly developed, primarily because of the lack of thermoelectrics of suitable efficiency for this range.

4.2 Characteristic Examples of Applications

A thermoelectric generator with a radioactive heat source was developed for operation on the surface of the moon. Several such generators were taken to the moon by American astronauts during the Apollo project (see Figure 5). Generators of 73.6 W output electric power operated successfully as a power supply for instrumentation for several years. The active leg material is based on $A^{IV}B^{VI}$ compounds (like PbTe).

A thermoelectric generator with a radioactive heat source was developed as a power supply for deep-space missions. Electric generators with 155 W output were employed with extraordinary success on the American spacecraft Voyager where they provided support for operation of all instrumentation, as well as information

transmission to the earth during the many-years flight to Jupiter, Saturn, Neptune, and Uranus. The legs materials are Si-Ge alloys.

A thermoelectric generator utilizing the heat from a nuclear reactor will be used as a power supply for space platforms. Model SP-100 (Figure 6) consisting of a nuclear reactor and an extension TE generator (with the heat transferred from the reactor to the TEG by a liquid-metal carrier) is of modular design and can supply electric power of 10–100 kW, depending on the number of modules used. Space platforms designed for various projects are planned to be launched by the USA in the 1990s. The TEG legs will be made of Si-Ge alloys.

Organic fuel based TE generators have been used as power supplies for gas pipelines and radio relay links located in remote areas. Gas pipelines need power supplies for operation of the corrosion protection systems and for testing and control instrumentation. On radio relay stations, intermediate amplifiers have to be powered. The best energy source for remote areas is a

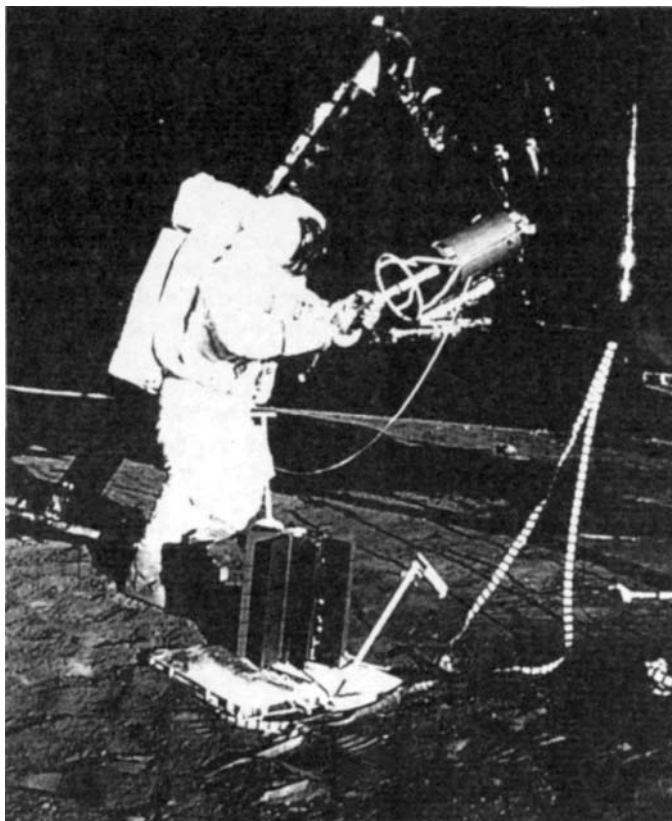


Figure 5. Apollo lunar surface experimental package powered by a SNAP-27 thermoelectric generator (reproduced by permission of NASA and the Jet Propulsion Laboratory)

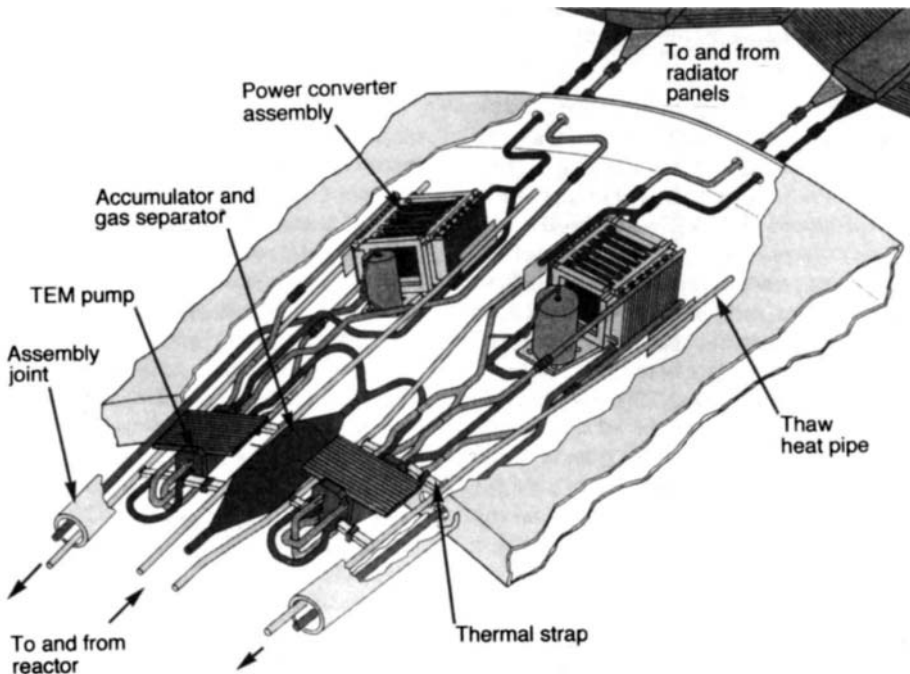
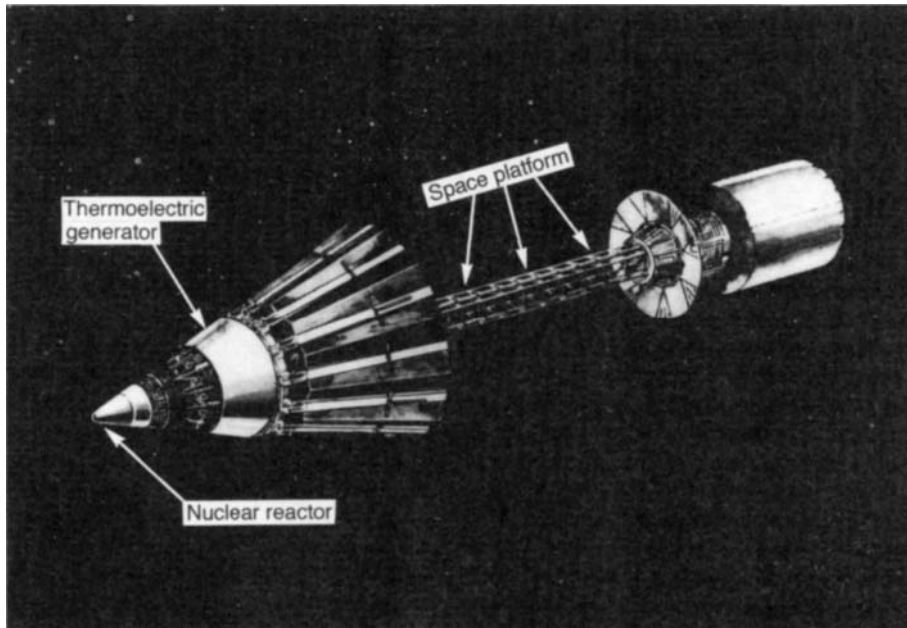


Figure 6. The power converter assembly for the SP-100 project to power a space platform (reproduced by permission of G. Stapfer of the Jet Propulsion Laboratory)

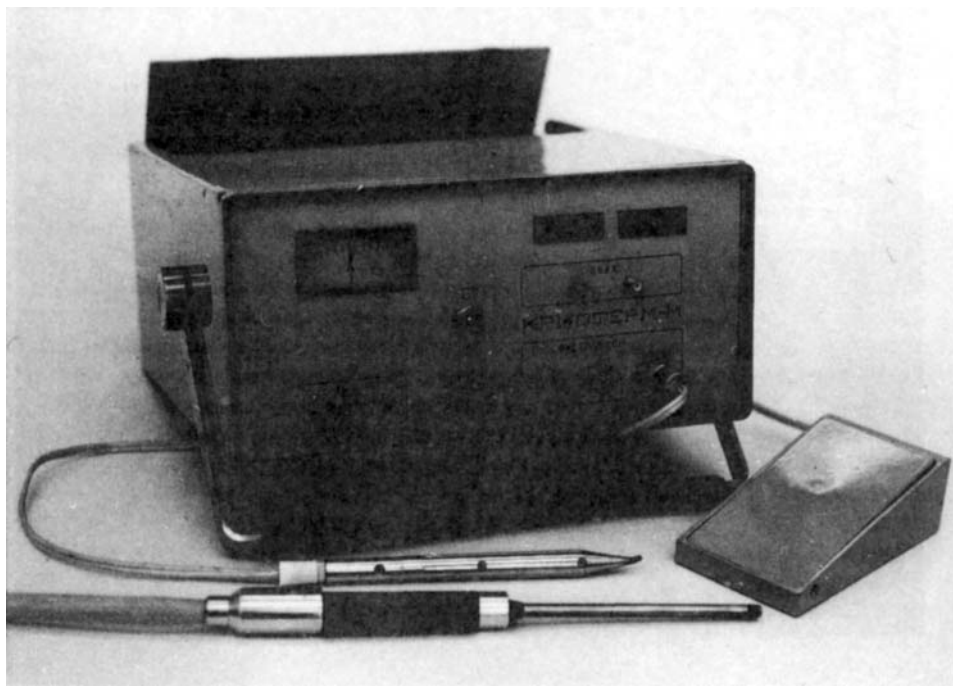


Figure 7. A commercial unit 'Cryotherm', a thermoelectric cryoextractor with cooling element, power supply and remote-control pedal (reproduced by permission of Informelectro, 1985, Moscow)

TEG operating on liquid or gas fuel, since it is capable of functioning for long times without servicing. The TEGs of this kind use $A_2^V B_3^{VI}$ compounds (like $Bi_2 Te_3$) as material for the legs. Such generators of output power 100–200 W are produced in Russia and Canada.

Thermoelectric coolers are used for IR photoelectric detectors. IR detectors presently find wide use in civilian and military applications, most of them requiring deep cooling to suppress the inherent noise so as to reach the desired sensitivity. The best way here is to employ a miniature single-stage or multistage TE cooler capable of reducing the sensor temperature by 40 K or more. The legs are made of $A_2^V B_3^{VI}$ compounds (like $Bi_2 Te_3$).

Thin, thermoelectrically cooled probes are used for cryosurgery. A miniature TE cooler is mounted on the end of such a probe, a commercial version of which is shown in Figure 7. It is brought into contact with the desired piece of tissue and, after the power is turned on, cools rapidly down to a temperature substantially below 0 °C. The tissue freezes onto the probe and can be removed together with it. This method was successfully used in cataract surgery to remove opaque, crystalline lenses from human eyes. For the active material of the cooler legs, $A_2^V B_3^{VI}$ compounds are used (like $Bi_2 Te_3$).

To keep precooled food and beverages cold, only small amounts of heat have to be removed if the thermal insulation is good. With small refrigerator volumes (~20 l), this can be done with only one TE cooling module consuming a few tens of watts. Such a small refrigerator can be made shockproof and very reliable, and is extremely useful in a car. The module leg material is usually $A_2^V B_3^{VI}$ (like $Bi_2 Te_3$). Such refrigerators are mass produced in a number of countries.

An analysis carried out in France shows that for the climatic conditions prevailing in that country the most practical method of railroad-coach air conditioning (from the viewpoints of comfort, reliability, and serviceability) is based on the use of the TE air conditioner. Such a coach was built and passed successfully through long-term testing. However, at the conversion efficiency reached (the active leg material is a type $Bi_2 Te_3$ compound) the TE method appears to be too expensive for this purpose.

5. Thermoelectrics (TE Materials)

5.1 Requirements for Thermoelectric Materials

Materials suitable for the fabrication of thermoelement legs are increasingly designated at present by a new term,

thermoelectrics. A natural requirement for thermoelectrics is the capability for thermoelectric conversion with the desired efficiency in a given temperature interval. While usually one looks for a material with a high figure of merit Z , in some applications there may be a demand for a maximum output voltage or maximum current in the TEG operation. This will require a thermoelectric with a combination of transport properties different from that needed to obtain a high Z . We discuss the conditions determining the Z of a material in the next section.

There are also other requirements associated with the specific features of thermoelectric conversion and with the thermoelement operating conditions. Indeed, the conversion efficiency is the higher, the larger is the temperature difference across the thermoelement and, hence, the higher is the hot-junction temperature (in the case of TEGs) (see equation 3). Thus the best choice would be thermoelectrics capable of operating at high temperatures and with a high temperature drop across them. Materials with low operating temperatures also find areas of application, since there are many fairly low temperature heat sources. One should also take into account that the material with the highest mean value of Z over a given temperature interval is the most efficient, not necessarily the one with the maximal Z in the same interval.

The conditions under which a thermoelement operates dictate the requirements for stability with respect to temperature cycling, for matching with the linear expansion coefficient of the strap plate materials (Figure 2) and for resisting the diffusion of active impurities into the thermoelectric. Another essential requirement is that the thermoelectric be machinable and consist of inexpensive and nontoxic components.

5.2 Elements of the Standard Theory of TE Materials

Underlying the present-day growth of thermoelectrics applications is the idea of Ioffe, expressed as far back as 1930, that semiconductors (a new class of materials at that time) are inherently capable of providing a higher thermoelectric figure of merit than metals. It is for nondegenerate semiconductors considered in the free-electron approximation that the theory of TE properties connecting Z with the microscopic parameters of a material was developed. Today this theory, which may be considered as standard or basic, permits one to understand qualitatively the physics underlying these phenomena and to make some estimations, while not being able to account for all the complexity of the behavior of the high-efficiency thermoelectrics.

The most definite estimate can be obtained if one considers the carriers[†] in a thermoelectric as obeying the classical Maxwell–Boltzmann statistics (which is correct for nondegenerate semiconductors). Note that the figure of merit Z enters into equations (3) and (4) for the thermoelement efficiency only in the combination ZT , which may be called the dimensionless figure of merit. Theory yields for this quantity the following expression (valid for one current carrier species and one energy band with the simplest quadratic dispersion law)

$$ZT = \frac{[\mu^* - (r + 5/2)]^2}{(\beta \exp \mu^*)^{-1} + (r + 5/2)} \quad (6)$$

Here $\mu^* = \mu/k_B T$ is the reduced Fermi energy, k_B is the Boltzmann constant, and r is the exponent in the expression for the carrier relaxation time $\tau \approx E^r$ if one accepts for τ a power-law dependence on energy E . Thus ZT depends on the carrier energy spectrum (through μ^* which in this model is related directly with the carrier concentration n) and on the conduction mechanism (through r which is different for different mechanisms of scattering, from acoustic and optical phonons, ionized impurities, etc.). Finally, the last parameter in equation (6) determining ZT is the dimensionless material parameter β

$$\beta = \text{constant} \times (u/\chi_L)(m^*)^{3/2} T^{5/2} \quad (7)$$

Here u is the carrier mobility, m^* is the carrier effective mass and χ_L is the lattice heat conductivity. One can analyze equation (6) to find the maximum value of ZT as a function of μ^* and, hence, of n . One comes to the conclusion that the optimum value of n providing the maximum ZT is about 10^{19} cm^{-3} . This concentration is too high to consider the electron gas nondegenerate; however, more rigorous calculations taking into account the degree of degeneracy yield similar results. Thus the maximum of efficiency in Figure 4 should be placed at concentrations of $10^{19} - 10^{20} \text{ cm}^{-3}$. These concentrations are indeed typical of heavily doped semiconductors and semimetals, as predicted in the qualitative analysis in Section 3. To operate within a fairly broad temperature interval, such a semiconductor should have this concentration already at fairly low temperatures, possibly starting from 0 K. Then in the operating interval all impurities will already be ionized, and the concentration will not change with increasing temperature till intrinsic conduction sets in. Thus in the operating region where impurity conduction prevails,

[†]The fundamentals of electrical and thermal conductivity in intermetallics are reviewed in Chapters 41 and 44 in Volume 1 by Braunovic and by White respectively.

a heavily doped semiconductor will behave as a metal, i.e. its electrical conductivity will decrease with temperature. As will be seen in the next section, this is indeed the case for real high-efficiency thermoelectrics. The greater is β , the greater is ZT ; however, as evident from equation (7), β increases substantially with increasing temperature. Therefore ZT increases with heating too, till the onset of intrinsic conduction results in a decrease of S and an increase of the electronic thermal conductivity χ_{el} owing to the contribution of the minority carriers, when ZT decreases. The examples presented in the next section support this prediction as well, namely that the function ZT usually passes through a maximum. The threshold of the onset of intrinsic conduction is naturally higher, the broader is the band gap. This is why operation at high temperatures requires the use of broader band gap semiconductors. Besides, the optimum concentration mentioned earlier was evaluated for room temperature, while in the general case $n_{opt} \approx T^{3/2}$, so that in high-temperature materials the concentration should be higher. Note also that in our model the thermopower is connected intimately with concentration, so that one can easily calculate its optimum value corresponding to the maximum of ZT ; $S_{opt} = 172 \mu V K^{-1}$.

As follows from equation (7), β is greater, the greater are m^* and the ratio u/χ_L . The latter conclusion is based on the simplifying assumption that in the thermal conductivity of a real thermoelectric, where $\chi = \chi_L + \chi_{el}$, one may safely neglect the electronic component. While in actual fact the electronic component does affect the conversion efficiency, its influence is relatively small since it is connected rigidly with the electrical conductivity through the Wiedemann–Franz law. The conclusion that χ_L decreases at a constant u is very essential, since it is this approach that permitted Ioffe to propose one of the most effective methods to increase Z , namely by using solid solutions based on high-efficiency thermoelectrics. The band structure of a solid solution closely resembles that of the starting material. Therefore by proper doping one can usually maintain the value of $S^2\sigma$ constant within certain limits. As for the lattice thermal conductivity of a solid solution, it always decreases with alloying because of the additional scattering, in some cases by as much as a few times. As will be seen in the next section, most high-efficiency thermoelectrics are solid solutions of either elemental semiconductors (or semimetals) or of intermetallic compounds.

5.3 Real Thermoelectrics

A typical feature of thermoelectrics is a strong temperature dependence of their transport properties.

Therefore each of them has a sufficiently high figure of merit only in a limited temperature interval. Because of this, one usually divides thermoelectrics into low-temperature (for use below 500 K), medium-temperature (400–900 K) and high-temperature (above 800 K) materials. The materials belonging to the last two groups are primarily employed only in TEGs, whereas the low-temperature materials are used in both generators and in coolers. The number of types of materials used actively in practice is presently narrowed down to one in each class. We shall give below brief characteristics of these principal materials and data on their TE properties (S , σ , χ , Z) as a function of temperature. These data relate to high-efficiency systems, but not necessarily to materials with record-high parameters. They will illustrate the above general description and should give an idea as to what degree the transport coefficients may vary for a fixed figure of merit. A comparison with this set of data may turn out to be useful when analyzing the possible application of intermetallics as thermoelectrics.

5.3.1 Low-Temperature Thermoelectrics Using $A_2^V B_3^{VI}$ Compounds

The basic compound is Bi_2Te_3 (see Figure 8 for a partial phase diagram). The materials used in practice are solid solutions with the structurally isomorphous compounds Sb_2Te_3 and Bi_2Se_3 and are thus

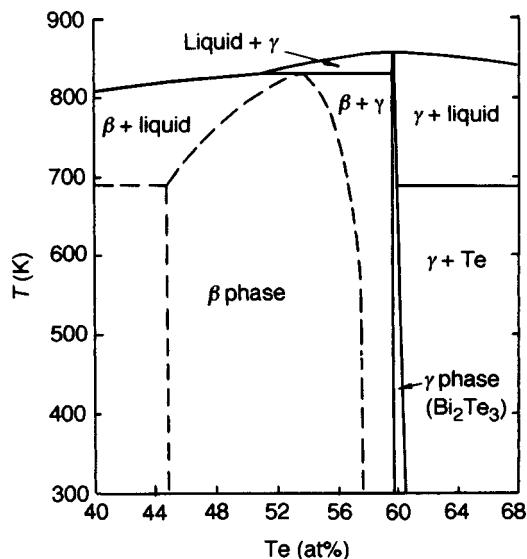


Figure 8. Partial phase diagram of the Bi–Te system (data from Glatz, 1965)

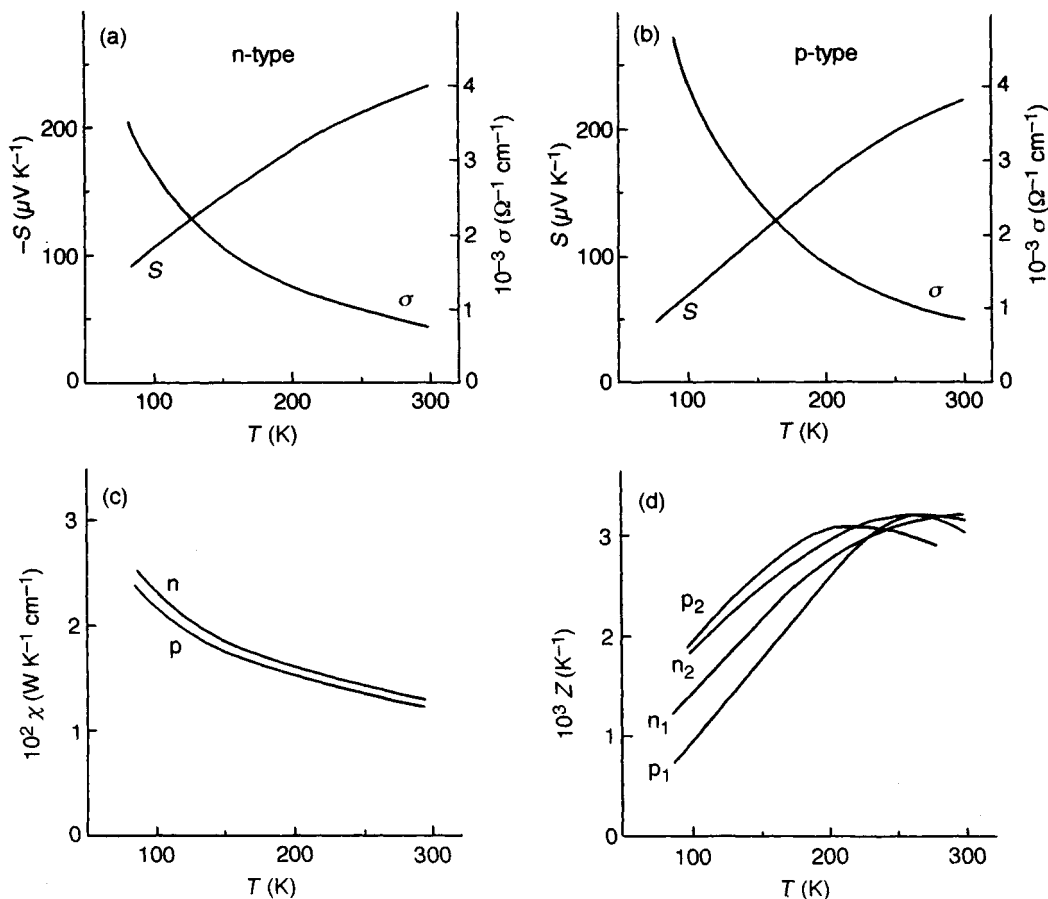


Figure 9. Temperature dependence of the thermoelectric properties of low-temperature thermoelectrics based on $A_2^{V}B_3^{VI}$ compounds: (a) thermopower S and electrical conductivity σ for n-type material ($Bi_2Te_{2.7}Se_{0.3}$); (b) S and σ for p-type material ($Bi_{0.5}Sb_{1.5}Te_3$); (c) thermal conductivity χ for the same materials of n-type and p-type; and (d) figure of merit Z for the same materials of n-type and p-type (symbols n_1 , p_1) and other materials optimized for lower temperatures (symbols n_2 , p_2) (data from A. F. Ioffe Physical-Technical Institute)

represented by the general formula $(Bi, Sb)_2(Te, Se)_3$. They are of rhombohedral structure (C33 Bi_2STe_2 , hR5) and are essentially anisotropic in their mechanical and transport properties. The crystals are layered and easily cleave along the basal planes. The highest value of Z is obtained when the long axis of a cylindrical sample lies in the basal plane, with the temperature gradient and electric current directed along this axis. The parameters S , σ , χ and Z presented in Figure 9 were measured along this direction. The melting point of Bi_2Te_3 is 848 K. The material is prepared by direct melting of the components in quartz ampoules. Samples for use in scientific work or in applications are fabricated from this material by ceramic techniques or by zone leveling with subsequent cutting in the desired direction.

Bi_2Te_3 is a semiconductor with many-valley conduction and valence bands and a narrow band gap of 0.15 eV. This narrow gap implies the onset of intrinsic conduction at fairly low temperatures and a working temperature limit of 450 K. The band gap of Bi_2Se_3 is considerably broader, so that materials in which it is used are capable of stable operation up to 600 K. The material can be made n-type or p-type by using a nonstoichiometric composition (excess of tellurium) and doping it with electrically active impurities (halogens and metals). The carrier concentrations in the materials whose properties are shown in Figure 9 lie in the range 10^{18} – 10^{20} cm $^{-3}$. By properly varying the solid-solution composition and impurity content one can control the temperature dependence of the transport properties over

a fairly broad range. This approach is used in the optimization if one intends to increase Z in the working temperature interval or to shift the maximum of Z toward lower or higher temperatures. Figure 9 presents the properties of a pair of materials of n-type and p-type optimized for use in coolers operating close to room temperature. Shown in Figure 9(d) are the characteristics of materials optimized for applications at 150 K and lower (curves n_2 and p_2).

5.3.2 Low-Temperature Thermoelectrics: Bi-Sb Alloys

As seen from Figure 9 the efficiency of Bi_2Te_3 -based materials drops dramatically below 200 K. Only one efficient thermoelectric is presently available for operation at temperatures below 150 K, namely bismuth-rich Bi-Sb solid solutions. It is only possible to produce n-type materials in this alloy system. As Yim and Amith (1972) reported, the highest efficiency is observed in $\text{Bi}_{0.85}\text{Sb}_{0.15}$. Figure 10 presents the parameters of an undoped alloy of this composition. Doping with metallic impurities (Sn, Pb, Te) affects the carrier concentrations and transport properties of the alloys. This thermoelectric is remarkable in many respects: (i) its figure of merit Z is not only very high but increases with decreasing temperature; and (ii) the figure of merit increases in a magnetic field: for the composition mentioned above, Z increases at 77 K from $6.5 \times 10^{-3} \text{ K}^{-1}$ in a zero field up to $11 \times 10^{-3} \text{ K}^{-1}$ at 0.15 T.

In contrast to Bi_2Te_3 , this thermoelectric represents not an intermetallic compound but rather an elemental Bi-based solid solution. In its electronic band structure, Bi is not a semiconductor but a semimetal. Like Bi_2Te_3 , it has a rhombohedral structure (A7 As, hR2) and is markedly anisotropic. It is most efficient in the thermoelectric sense in the direction along the trigonal c axis. It is to this direction that the data presented in Figure 10 refer.

5.3.3 Medium-Temperature Thermoelectrics Based on $\text{A}^{\text{IV}}\text{B}^{\text{VI}}$ Compounds

The basic compound is PbTe, the only compound formed in the system (Figure 11). As thermoelectrics one can use PbTe proper, its analogs PbSe, PbS and SnTe, or their solid solutions. Having an f.c.c. structure (B1 NaCl, cF8), they are isotropic in their transport properties. The melting point of PbTe is 1190 K. These materials are prepared by direct melting of the components in quartz ampoules with subsequent preparation of ceramic samples by hot-powder pressing.

PbTe and its analogs are semiconductors. The band gap in PbTe is 0.3 eV, which is considerably greater than the band gaps in the low-temperature materials. As a result, the $\text{A}^{\text{IV}}\text{B}^{\text{VI}}$ -based materials become efficient at higher temperatures. By deviation from stoichiometry and doping one can produce both n-type and p-type materials. The typical active impurities used are the halogens (donors) and alkali metals (acceptors). For the materials shown in Figure 12 the carrier concentration is 10^{19} – 10^{20} cm^{-3} . Complex combinations of the solid-solution components and impurities were proposed

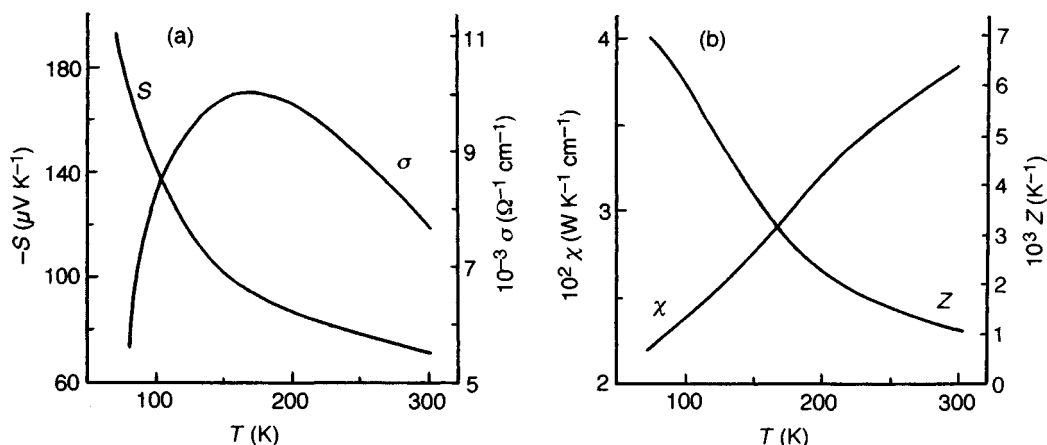


Figure 10. Temperature dependence of the thermoelectric properties along the trigonal c axis of solid solution $\text{Bi}_{0.85}\text{Sb}_{0.15}$ (a low-temperature, n-type thermoelectric material): (a) thermopower S and electrical conductivity σ ; and (b) thermal conductivity χ and figure of merit Z (data from A. F. Ioffe Physical-Technical Institute)

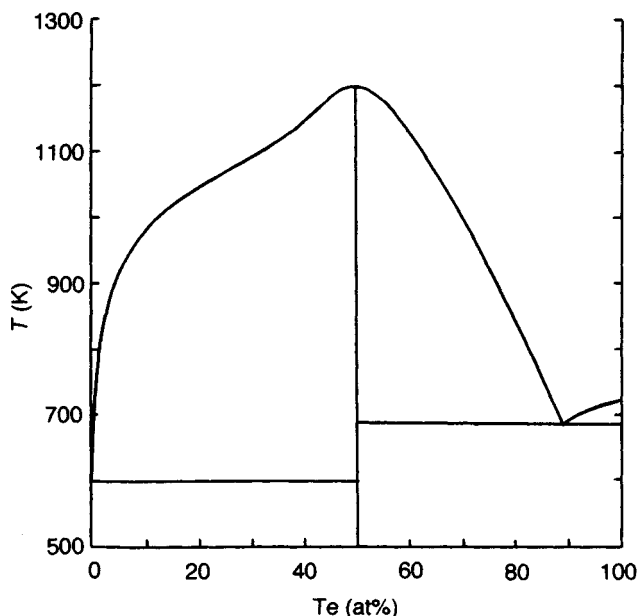


Figure 11. Phase diagram of the Pb-Te system (data from Lin *et al.*, 1989)

to obtain high-efficiency materials. As p-type material, GeTe was also used.

5.3.4 High-Temperature Thermoelectrics: Si-Ge Alloys

Silicon and germanium are the classical materials of semiconductor electronics used in the form of high-purity single crystals, i.e. samples with a very low carrier concentration compared with the concentrations optimal for thermoelectric applications. The required concentration can be reached, however, by heavy doping. Nevertheless, even doped Si and Ge have a low Z , since their thermal conductivity is too high. Si and Ge are capable of dissolving in one another without limit, the thermal conductivity of the alloys dropping so strongly in the process that they become promising for TE applications. Silicon surpasses germanium in melting point (1693 versus 1231 K, respectively) and band gap width (1.15 versus 0.65 eV), and is more stable at high temperatures. Therefore Si-rich solid solutions are preferable for use in high-temperature applications, the $\text{Si}_{0.7}\text{Ge}_{0.3}$ composition (Figure 13) being the most efficient. This material can operate at temperatures of up to 1200 K. By proper doping one can obtain both n-type and p-type materials (doping with boron produces

p-type, and with phosphorus, n-type). The maximum efficiency is reached at carrier concentrations close to $1.5 \times 10^{20} \text{ cm}^{-3}$. A thermoelement made of such materials and with the hot and cold junctions maintained at 1200 and 300 K, respectively, provides a conversion efficiency of 10%. As found recently, doping Si-Ge not with phosphorus but with phosphorus and gallium in the proportion corresponding to the compound GaP increases the solubility of P in Si-Ge. This markedly improves the figure of merit of the n-type leg.

Si, Ge, and their solid solutions, being of cubic symmetry (A4 diamond (C), cF8), have isotropic transport properties. The materials used in applications are obtained by zone leveling or hot-powder pressing.

6. General Discussion of the Art in TE Applications

6.1 State of the Art

The preceding sections have presented, albeit briefly, the fundamentals of thermoelectric conversion, the principles of converter design, the main areas of TE applications, and a few concrete examples of important applications. Finally, basic information on all thermoelectrics of

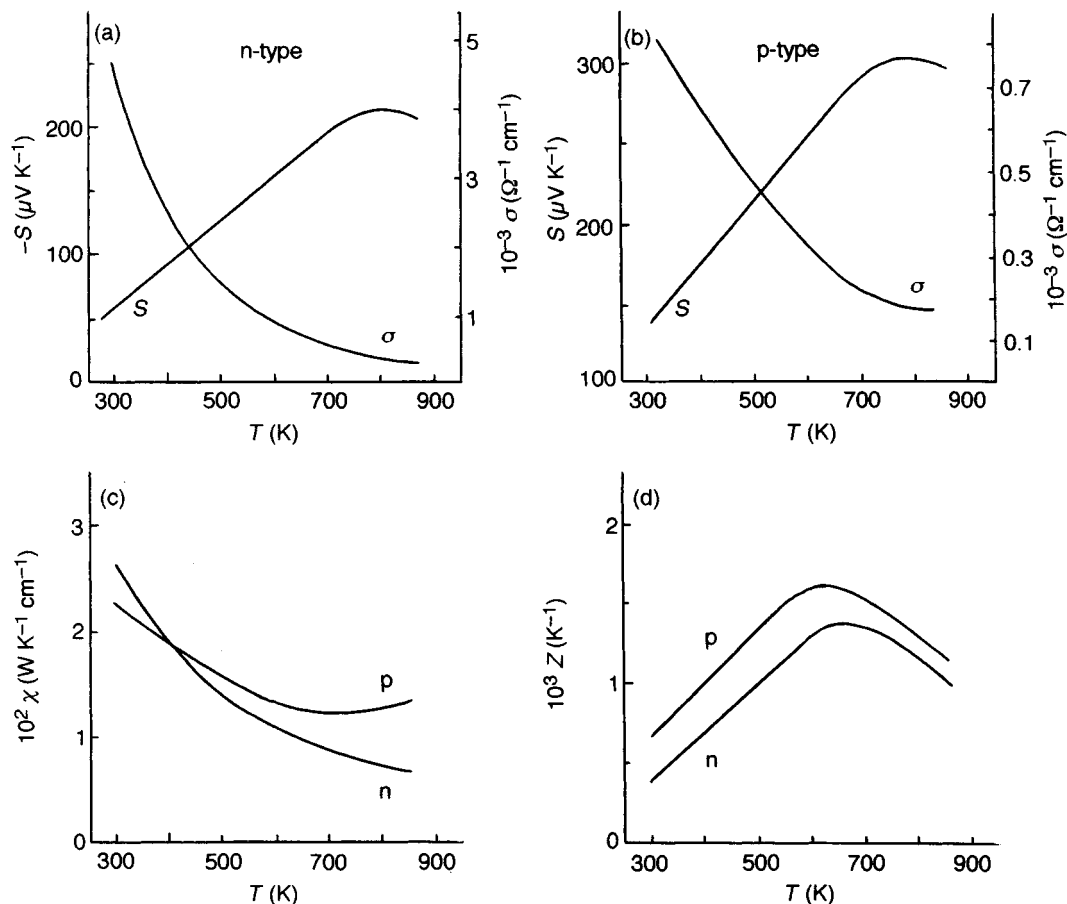


Figure 12. Temperature dependence of the thermoelectric properties of medium-temperature thermoelectrics based on $A^{IV}B^{VI}$ compounds: (a) thermopower S and electrical conductivity σ for n-type material (doped PbTe); (b) S and σ for p-type material (doped PbTe); (c) thermal conductivity χ for the same materials of n-type and p-type; and, (d) figure of merit Z for the same materials of n-type and p-type (data from A. F. Ioffe Physical-Technical Institute)

practical significance and some aspects of the simple microscopic theory have been given. We now make a general evaluation of the state of the art in this area and discuss the potential for further development, in particular the investigation of intermetallics.

On the whole, it may be said that the development of the TE conversion problem has achieved a certain stage of completeness. Indeed, fairly efficient thermoelectrics have been developed owing to our capabilities for scientific prediction, the reliable methods of calculation for various TE converters and the technology for mass production presently available. A market for TE devices has appeared as a result of improvements in TE efficiency and a growing recognition of the potential inherent in this new class of energy converters in

many areas of engineering, particularly in high-tech applications. This market is now substantial and keeps growing. While in the earlier stages thermoelectricity was used on a small scale, in the 1980s the areas of TE cooling and radiation detectors began attracting many customers. On the whole, thermoelectric cooling based exclusively on the use of the $A_2B_3^{VI}$ compounds is today the leading commercial application. And it is these same compounds that are more often employed in TE generators too. Therefore the $A_2B_3^{VI}$ -based solid solutions may be considered as the most important thermoelectrics of today.

Regrettably, TE applications are characterized not only by obvious achievements but by difficulties as well. Most significantly, the figure of merit of present-day

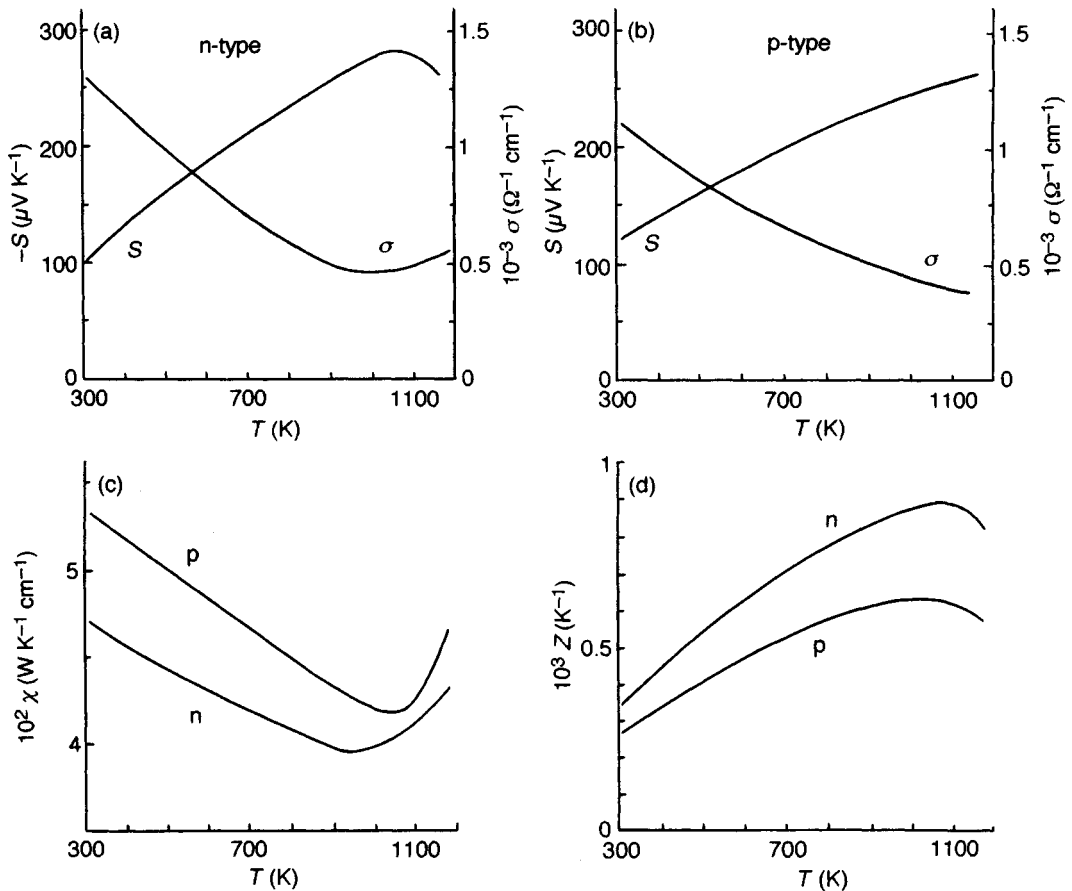


Figure 13. Temperature dependence of the thermoelectric properties of solid-solution $\text{Si}_{0.7}\text{Ge}_{0.3}$ (a high-temperature thermoelectric material): (a) thermopower S and electrical conductivity σ for n-type material; (b) S and σ for p-type material; (c) thermal conductivity χ for the same materials of n-type and p-type; and (d) figure of merit Z for the same materials of n-type and p-type (data from Dismukes *et al.*, 1964)

thermoelectrics remains fairly low. The best of the low-temperature, medium-temperature and high-temperature materials reach only a level of $ZT \approx 1.0$, which restricts TE applications to the domain of low-power devices, and rather expensive ones at that.

6.2 Prospects of a Broadening of TE Applications: Significance of Intermetallic Compound Studies

Viewed from a purely technical standpoint, the not-yet-exploited potential of TE conversion appears very promising, if one recalls what was said in Section 4. To cite an example, consider the idea of Ioffe of incorporating TE panels into the walls of houses and

industrial buildings for their automatic heating or cooling through a controlled heat exchange with the outside air, or for the conversion into electrical energy of part of the heat dissipated by numerous domestic and industrial objects. It has been pointed out, however, that this project would hardly be feasible economically with the presently available thermoelectrics. The efficient thermoelectrics described in Section 5 were known as far back as the early 1960s and have since been studied thoroughly. And while the behavior of these materials is still not fully understood, many experts believe that their figures of merit will not be increased much above the presently reached level. Nevertheless, further studies aimed at improving the available materials are important since they may lead to the development of more economical devices.

To assess the prospects for a substantial increase of Z and for discovery of revolutionary new thermoelectrics, let us analyze the theoretical treatment of the TE figure of merit presented in Section 5, basing the argument on what we know today. On the one hand, it should be noted that the simplest theory provides a few essential qualitative conclusions which retain their basic significance and offer guidelines for a search for new thermoelectrics. These are the existence of an optimum concentration, of its high value, and of its extension toward high operating temperatures; the need for using materials with a degenerate electron gas; the role of the band gap; and the need for minimizing the lattice thermal conductivity.* On the other hand, a search for materials with a high mobility and a high effective mass would hardly be productive, since theory is presently not developed to the stage where it could predict these parameters quantitatively. Such factors as the type of chemical bonding, the scattering mechanism involved, extent of the band non-parabolicity, the variation of the effective mass with temperature (all of which appeared significant in the earlier stages of research) do not attract interest any more, since it gradually became clear that among efficient thermoelectrics there are no materials with a simple band structure (i.e. one energy band and a quadratic dispersion law). Furthermore, the degree of degeneracy is high, and there are always several coexisting bonding types and scattering mechanisms. As a rule, these are materials with complex lattice defect structures. Determination of the electronic band structure of such materials and of their transport properties requires invoking much more complex models, which can be solved only by numerical calculation. This approach is still not very well developed. Actually, it should be noted that the transport coefficients of a solid are structurally much more complex than, say, the optical or magnetic parameters which are determined by the band structure. In the theoretical and experimental investigation of the electronic spectra of solids considerable progress has been made. At the same time the transport properties depend both on the band structure and the carrier-scattering processes, which are still poorly understood. Two more considerations are in order here: (i) a thorough understanding of the figure of merit requires an equally clear understanding of the three transport coefficients; and (ii) one of the coefficients, namely the thermal conductivity, is an essentially more

complex parameter since it involves both the electronic and the lattice processes. We find ourselves in a peculiar situation where one cannot rely on quantitative estimates based on the standard theory, and at the same time a more realistic approach also fails to yield reliable results. Therefore modern solid-state theory is not yet capable of predicting the limiting values of Z for thermoelectrics. It should, however, be pointed out that the present-day theory cannot impose any constraints on the increase of Z above the level currently reached. Therefore, on the one hand, one should continue to develop the theory of the transport properties and, on the other, it is necessary to carry out systematic experimental investigations, aimed not only at finding new materials but also at experimentally determining the behavior of the transport properties as a function of various factors.

The primary subject of these studies should be intermetallic compounds. Indeed, among the four most efficient thermoelectrics described above, two represent solid solutions of elemental semiconductors and semimetals, and the other two are solid solutions of intermetallics. No other elemental substance can claim the place of a thermoelectric, with the exception of doped boron. Practically, only when chemical compounds are formed can one calculate new types of bond energies and crystal structures, some of which could be favorable for the manifestation of high

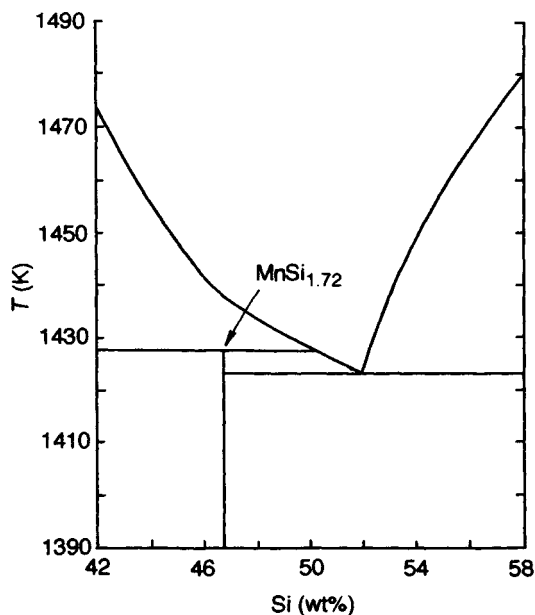


Figure 14. Partial phase diagram of the Mn-Si system (data from Morokhovets, Elagina, and Abrikosov, 1966)

*On the latter topics, the reader may wish to refer to the chapters in Vol. 1 by Singh (6), Pintschovius (7), Braunovic (41) and White (44).

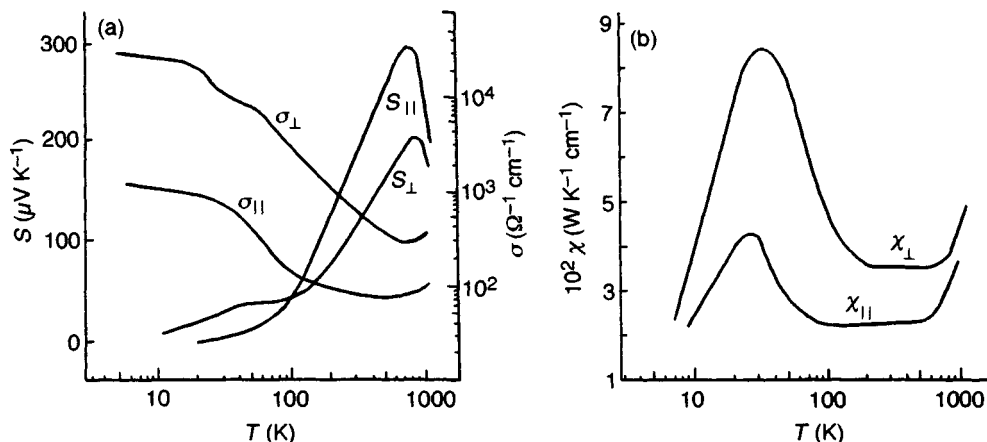


Figure 15. Temperature dependence of the thermoelectric properties of a single crystal of $\text{MnSi}_{1.72}$, a highly anisotropic p-type thermoelectric material (for two principal crystallographic directions relative to the tetragonal axis): (a) thermopower S and electrical conductivity σ ; and, (b) thermal conductivity χ (data from A. F. Ioffe Physical-Technical Institute)

thermoelectric figures of merit. But a practical thermoelectric material has also to be a sufficiently good conductor, and it is more probable that among all kinds of compounds intermetallics will be such good conductors. Some work has been carried on in the investigation of potential thermoelectrics in recent years, although it cannot be considered as sufficient. The most interesting materials with high figures of merit turned out to be Cu_2Se -type selenides which surpass $\text{A}^{\text{IV}}\text{B}^{\text{VI}}$ -based materials in the medium-temperature range. Unfortunately one is forced to renounce the possibility of their practical application till their diffusive and mechanical properties are improved. Transition metal silicides are another interesting and promising group of materials.* They are formed from cheap components and can be used in air at high temperatures. Some of them are very interesting for their physics and for potential applications arising from one peculiarity: anisotropy of properties. For example, the higher silicide of manganese, $\text{MnSi}_{1.72}$ (tP120) (see Figure 14 for a partial phase diagram), shows anomalously high anisotropy of the thermopower over an unusually wide temperature range (Figure 15). The figure of merit of this silicide is high enough that it can be considered as a potential competitor to the Si-Ge alloys. Other potential high-temperature materials, such as rare-earth chalcogenides, boron and some borides, have been under investigation too. This topic is considered in detail in the review by Wood (1988).

In the early book by Ioffe (1957) metals were considered as having absolutely no potential as TE

conversion materials. However, such an opinion is correct only for simple (normal) metals with very low thermopower. But the general situation of the thermopower of metals is significantly more complicated; an overview of this subject is given in the book by Blatt *et al.* (1976). Even some pure transition metals and their alloys can have sufficiently high thermopower: it is possible to select a couple of such metallic alloys whose thermopowers reach values around $100 \mu\text{V K}^{-1}$. It is of interest to note in this connection that it is possible in some cases to increase the figure of merit of a metallic thermocouple by using for one leg an alloy with the ordered structure of an intermetallic compound. Vedernikov *et al.* (1969) showed that in the alloy system Pd-U the solid solution of composition $\text{Pd}_{88.9}\text{U}_{11.1}$ orders to form the tetragonally distorted f.c.c. compound Pd_8U below 1000 K. Thermopower and electrical conductivity increase in the ordered state; the value of thermopower achieved is more than $30 \mu\text{V K}^{-1}$, which is the maximum positive thermopower for metallic alloys.

7. Electrical Applications

Electrically conducting materials are primarily used as conductors (materials with a low electrical resistivity), as heaters (materials with a high resistivity) and as electronic resistors (materials with a high resistivity and a low temperature coefficient of resistivity). Intermetallics certainly cannot compete against pure

*See also Chapter 15 by Masumoto, Katsui, and Matsuoka.

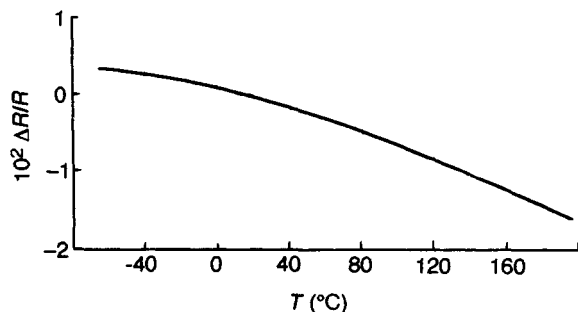


Figure 16. Temperature dependence of the relative change of electrical resistivity $(R_T - R_{20^\circ\text{C}})/R_{20^\circ\text{C}}$, of the alloy NG45F, based on the intermetallic compound NiMn (Molotilov, 1974)

metals as low-resistivity materials. Carbides are widely used in heaters designed for long-term operation in air without special protection. The most popular in this class is silicon carbide, SiC. Molybdenum disilicide, MoSi₂, is also employed in heaters; it sustains higher temperatures than SiC. In a previous part of this chapter such silicides were considered as intermetallics. Both these materials have been known for a long time, and relevant information can be found in reference books.* Apparently there is no current systematic basic research in connection with the development of this type of material.

For electronic resistors one uses metallic alloys and composite materials. The latter materials use as the conducting component metal silicides, primarily those of chromium of various compositions. There is an interesting Russian reference (Molotilov, 1974) to the development of a resistive alloy, NG45F, based on the intermetallic NiMn (L1₀AuCu, tP4) with small additions of V and Fe. After a special heat treatment, the alloy reaches a resistivity of 200 μΩ cm with a temperature coefficient of $-10 \times 10^{-5} \text{ K}^{-1}$ to $3 \times 10^{-5} \text{ K}^{-1}$ in the range 20–200 °C, and a thermopower of 1 μV K⁻¹ with respect to copper (see Figure 16). A thin wire of 0.03–0.05 mm diameter can be manufactured from this alloy. No further progress in this direction has been reported, however.†

8. Conclusion

Of the two points to be considered here we first estimate the situation with the electrical applications treated

*Electrical properties and applications of silicides are extensively reviewed by Kumar in Chapter 10 of this volume.

†The use of intermetallics as resistors, conductors, contacts, and integrated circuit materials in various specialized applications is reviewed in the chapter by Westbrook in this volume.

briefly in the preceding section. Technology certainly needs better materials for heaters and resistors. But this is a rather old problem, and it seems that no fresh scientific idea has been offered in this field for a long time. It may be recommended to the researchers studying intermetallics and similar compounds (such as carbides, nitrides, and silicides) to focus their attention on the magnitude of the electrical resistivity of the material under investigation and its temperature dependence, but only provided that the heat resistance of the material is high enough for present applications.

The situation is radically different with the thermoelectric applications. Here science has provided a solid foundation for the use of the known thermoelectrics in technology. This is not the end of the road, however. Theoreticians have yet to propose theoretical and numerical methods which would permit high-accuracy interpretation of the energy spectra and transport properties of materials with high carrier concentrations and complex crystal types and band structures. Solid-state physicists and materials scientists are faced with a complex investigation of the transport properties of new groups of high-conductivity materials, with particular emphasis on the effect of impurities and the formation of solid solutions. This research should be directed primarily at those intermetallic compounds the transport properties of which are not yet sufficiently known. One should bear in mind that an increase of the dimensionless figure of merit ZT by as much as 20–30% would be a noticeable gain for TE conversion, and an increase of ZT up to 2, over a considerable temperature interval, would have a pronounced effect on energetics and refrigerator technology. Note also that present-day solid-state theory has not revealed the existence of any criterion making such an increase of ZT impossible. The current growing interest in the problems of energy saving and ecology will provide an impetus to TE-based power conversion and cooling. Beside the main problem of looking for more efficient materials, the development of cheaper, nontoxic compounds, technologically suitable for module fabrication, should not be overlooked. On the other hand, a careful study of the transport properties could provide materials scientists with a better understanding of intermetallics, because these properties are highly sensitive to the structure, stress, and defect state of the material.

We have considered only the basic issues of the topic ‘thermoelectric applications’. Among the related subjects which we could not cover here are such problems as the anisotropy of the thermoelectric properties and anisotropic thermoelements,

galvanomagnetic cooling, thin thermoelectric films and miniaturization of converters, and the effect of the degree of dispersion in ceramic materials on TE properties.

9. References

- Blatt, F. J., Schroeder, P. A., Foiles, C. L., and Greig, D. (1976). *Thermoelectric Power of Metals*. Plenum Press, New York.
- Cadoff, I. (1967). In *Intermetallic Compounds* (ed. J. H. Westbrook). John Wiley & Sons, Inc., New York, Chapter 26, p. 517.
- Dismukes, J. P., Ekstrom, L., Steigmeier, E. F., Kudman, I., and Beers, D. S. (1964). *J. Appl. Phys.*, **35**, 2899.
- Glatz, A. C. (1965). *J. Electrochem. Soc.*, **111**, 1204.
- Goldsmid, H. J. (1986). *Electronic Refrigeration*. Pion, London.
- Ioffe, A. F. (1957). *Semiconductor Thermoelements and Thermoelectric Cooling*. Infosearch, London.
- Lin, Y.-C., Hsieh, K.-C., Sharma, R. C., and Chang, Y. A. (1989). *Bull. Alloy Phase Diagr.*, **10**, 340.
- Molotilov, B. V. (ed.) (1974). *Precision Alloys Handbook*. Metallurgy, Moscow, p. 266 (in Russian).
- Morokhovets, M. A., Elagina, E. I., and Abrikosov, N. Kh. (1966). *Neorg. Mater.*, **2**, 650 (in Russian).
- Rao, K. R. (ed.) (1976). *Proc. International Conference on Thermoelectric Energy Conversion*, University of Texas at Arlington. IEEE, New York, 76CH1156-9 REG 5.
- Rao, K. R. (ed.) (1980). *Proc. 3rd International Conference on Thermoelectric Energy Conversion*, University of Texas at Arlington. IEEE, New York, 80CH1546-1 REG 5.
- Rao, K. R. (ed.) (1982). *Proc. 4th International Conference on Thermoelectric Energy Conversion*, University of Texas at Arlington. IEEE, New York, 82CH1763-2.
- Rao, K. R. (ed.) (1984). *Proc. 5th International Conference on Thermoelectric Energy Conversion*, University of Texas at Arlington.
- Rao, K. R. (ed.) (1986). *Proc. 6th International Conference on Thermoelectric Energy Conversion*, University of Texas at Arlington.
- Rao, K. R. (ed.) (1988). *Proc. 7th International Conference on Thermoelectric Energy Conversion*, University of Texas at Arlington.
- Rowe, D. M. (ed.) (1988). *Proc. 1st European Conference on Thermoelectrics*. Peter Peregrinus, London.
- Rowe, D. M. (ed.) (1992). *Proc. 10th International Conference on Thermoelectrics*. Babrow Press, Cardiff, UK.
- Rowe, D. M., and Bhandari, C. M. (1983). *Modern Thermoelectrics*. Holt, Reinhart and Winston, London.
- Scherrer, H., and Scherrer, S. (eds) (1989). *Proc. 8th International Conference on Thermoelectric Energy Conversion*, Institut Nationale Polytechnique de Lorraine, Nancy, France.
- Vedernikov, M. V., Terekhov, G. I., Sinyakova, S. I., and Ivanov, O. S. (1969). *Metals*, No. 4, 191 (in Russian).
- Vining, C. (ed.) (1990). *Proc. 9th International Conference on Thermoelectrics (USA)*. Jet Propulsion Laboratory, Pasadena, CA.
- Wood, C. (1988). *Rep. Prog. Phys.*, **51**, 459.
- Yim, W. M., and Amith, A. A. (1972). *Solid-State Electron.*, **15**, 1141.

This chapter was originally published in 1995 as Chapter 20 in *Intermetallic Compounds*, Vol. 2: *Practice*, edited by J. H. Westbrook and R. L. Fleischer.

Addendum

This addendum includes new references of the same character as earlier and some general remarks on new ideas in the field of thermoelectric materials.

There is as yet no special journal on thermoelectrics or thermoelectric energy conversion. This is why anyone who is interested in exploring the whole spectrum of thermoelectric studies should resort to the annual proceedings of the International Conference on Thermoelectrics, references to which are listed (Rao, 1992; Matsuura, 1994; Mathiprakasam and Heenan,

1994; Vedernikov, 1995; IEEE, 1996; IEEE, 1997; IEEE, 1998). Another helpful and universal source of knowledge on thermoelectrics and related problems is the *CRC Handbook of Thermoelectrics* (Rowe, 1995). This is a collection of 55 monograph chapters by international experts on many aspects of this subject.

As to new ideas, recent years are remarkable in the several suggestions which have been supported by USA government grants. Of course, these suggestions assume a very strong increase of the ZT parameter (see

Section 6.1 of the foregoing paper). This support gave rise to a significant upsurge in basic research on thermoelectrics in the USA. It is impossible to explain here in detail these new directions; we shall only name them. The first direction is a new way to decrease the lattice thermal conductivity in some materials with a high power parameter $S^2\sigma$ (see Section 3 of the foregoing paper). The best result is achieved with the so-called skutterudite crystallographic structure (CoSb_3 type): some ZTs higher than 1 are realized. Another current direction is an investigation of different materials of very complicated crystalline structure with anomalously low thermal conductivity. Their thermal conductivity can come nearer to that of amorphous solids, but $S^2\sigma$ is still too low at present. In both cases, powerful new approaches to materials design and synthesis are being applied, namely combinatorial screening and pressure tuning of materials parameters. Lastly, the third direction is a basically new approach to thermoelectric conversion by use of artificial one- and two-dimensional materials of nanometric scale. According to this concept, thermoelectric properties could be modified strongly in such wires and thin films at a characteristic size of 1–50 nm. Detailed information can be found in the proceedings listed and in references Mahan *et al.* (1997) (short popular review), Mahan (1998) (physical review), Tritt *et al.* (1997, 1998), Tritt (1999), and Di Salvo (1999).

The author's personal estimation of the present situation is as follows: the situation for users of thermoelectric devices is the same as was described in the foregoing paper; the situation may change due to the ideas mentioned but not earlier than a few years hence; however, this probability is not great because of the significant physical uncertainty of the ideas.

References

- DiSalvo, F. J. (1999) *Science*, **285**, 703.
- IEEE (1996) *Proc. 15th International Conference on Thermoelectrics*. (Passadena, CA, USA). Institute of Electrical and Electronics Engineers Catalog Number 96TH8169, USA.
- IEEE (1997) *Proc. 16th International Conference on Thermoelectrics*. (Dresden, Germany). IEEE Catalog Number 97TH8291, USA.
- IEEE (1998) *Proc. 17th International Conference on Thermoelectrics*. (Nagoya, Japan). IEEE Catalog Number 98TH8365, USA.
- Mahan, G., Sales, B., and Sharp, J. (1997) *Physics Today*, **50**(3), 42.
- Mahan, G. D. (1998) *Solid State Physics*, Vol. 51, ed. Ehrenreich, H. and Spaepen, F. Academic Press, p. 81.
- Mathiprakasam, B., and Heenan, P. (eds.) (1994) *Proc. 13th International Conference on Thermoelectrics*. American Institute of Physics Conf. Proc. N316, N.Y., USA.
- Matsuura, K. (ed.) (1994) *Proc. 12th International Conference on Thermoelectrics*. The Institute of Electrical Engineers of Japan, Tokyo, Japan.
- Rao, K. R. (ed.) (1992) *Proc. 11th International Conference on Thermoelectrics*. The University of Texas at Arlington, Texas, USA.
- Rowe, D. M. (ed.) (1995) *CRC Handbook of Thermoelectrics*. CRC Press. Boca Raton.
- Tritt, T. M., Mahan, G., Lyon, H. B. Jr., and Kanatzidis, M. G. (eds.) (1997) 'Thermoelectric Materials—New Directions and Approaches'. *Mater. Res. Soc. Proc.* Vol. 478.
- Tritt, T. M., Lyon, H. B. Jr., Mahan, G., and Kanatzidis, M. G. (eds.) (1998) 'Thermoelectric Materials 1998—The Next Generation Materials for Small-Scale Refrigeration and Power Generation Applications', *Mater. Res. Soc. Proc.* Vol. 545.
- Tritt, T. M. (1999) *Science*, **283**, 804.
- Vedernikov, M. V. (ed.) (1995) *Proc. 14th International Conference on Thermoelectrics*. A. F. Ioffe Physical-Technical Institute, St. Petersburg, Russia.

Chapter 10

Diffusion Barriers

Roger de Reus

Mikroelektronik Centret, Ørstedes Plads, DTU, Bldg 345-East, DK-2800 Lyngby, Denmark

1. Introduction

The function of a diffusion barrier is to separate two materials physically and thus prevent interdiffusion of these materials. Over the past few years the term diffusion barrier has been almost inseparable from microelectronics. The continuous scaling down of feature sizes in microelectronics brings the physical limits of miniaturization closer and closer, demanding reliable processing and performance of films with thicknesses and lateral dimensions of only several tens of nanometers.

That shrinking dimensions in microelectronics necessitate diffusion barriers becomes clear from the following example. In an interfacial reaction limited process the penetration depth x is proportional to time: $x \propto t$. If for a given system 1 mm is penetrated in 10 years, 100 nm are penetrated in approximately 9 h. However, a more likely failure mechanism is a diffusion-limited reaction. Now, x is given by $x = \sqrt{Dt}$, in which D is the diffusion constant. If for a given system 1 mm is penetrated in 10 years ($D \approx 3 \times 10^{-15} \text{ m}^2 \text{ s}^{-1}$, which is a realistic value), a simple calculation shows that 1 μm is penetrated in 5 min, and 100 nm in 3 s.

The obvious solution to this problem is to separate the overlayer O from the substrate S by a diffusion barrier X. In the S/O sample configuration (Figure 1a) S and O can easily interact, whereas this interaction is hindered in the configuration S/X/O (Figure 1b).

Several requirements would have to be met for a diffusion barrier. If the structure is used as a contact, one would like to optimize the electrical conductivity perpendicular to the layer across the interfaces, and

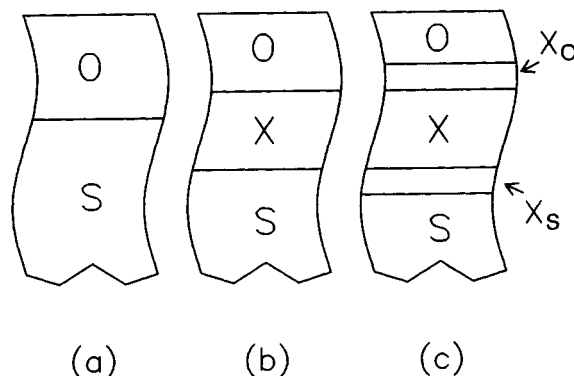


Figure 1. Principle of a diffusion barrier. (a) An overlayer O in direct contact with the substrate S. Interdiffusion of O and S can easily take place. (b) Insertion of a diffusion barrier X will limit direct interdiffusion of O and S. (c) A practical example of an elaborate diffusion barrier. Additional layers X_s and X_o are inserted between S and X and between X and O, respectively. In this engineering approach each interface is tailored to meet specific requirements

control the stability and reproducibility of the barrier height, the ideality factor, and the contact resistivity. If the structure serves as an interconnect, the electrical conductivity parallel to the layer, the carrier concentrations, the carrier mobilities, and electromigration are important parameters. A typical engineering approach is to separate the functions and add layers at the interfaces to optimize the performance of the structure, as shown in Figure 1(c). Examples are a contacting layer X_s between substrate and diffusion barrier, and a layer X_o to improve adhesion of the overlayer to the barrier.

It is important to realize that an arbitrary multilayer system is almost always in a nonequilibrium situation. The Gibbs free energy of a system will always be lowered by intermixing in compound-forming systems. In other words, a diffusion barrier cannot prevent interdiffusion, only retard the degradation process. However, special cases of immiscible compounds or epitaxial growth may reduce surface energy and favor layered structures at the cost of decreased mixing entropy. Enhanced lifetimes of over 10 years can be achieved by applying diffusion barriers, justifying their usage and resulting in commercial products of high quality.

Intermetallic compounds are important to the subject of diffusion barriers, not only because they may form inadvertently by reaction/diffusion of the S and O layers, but also because their high stability, limited solid solubility, slow diffusion rates, and compatibility with the S and/or O layers make them attractive intentional barriers. They also may play a critical role as contacting layers. The purpose of this chapter is to offer practical guidelines which help in understanding the stability of thin-film diffusion barriers. Semi-empirical models are presented to predict which phase forms first and the subsequent phase formation sequence, to predict the stability of amorphous metal alloys, and to predict the reactions of metal alloys with semiconductor substrates. The prediction of trends in phase formation is important, because this is a common mechanism of failure. An overview of relevant thin-film reactions available from the literature to date is given. No claim is made that these data are complete. Apart from intermetallic systems, attention is paid to interstitial compounds, which form an important group of diffusion barriers since they are very inert. The reliability of data presented here should be considered carefully. As will be shown later in this chapter, small amounts of impurities may have a tremendous impact on reaction temperatures and reaction products. Most articles on thin-film reactions do not take these effects into consideration. In general, the deposition process will determine to a large extent the properties of thin films. Characteristics with respect to properties of thin-film diffusion barriers and processing will be addressed in Section 7.

Examples of binary couples used throughout this chapter (Al-Ni, Ni-Zr, etc.) usually relate to laboratory experiments and serve to explain the semi-empirical models presented here. In practice, Ti-W, TiSi₂ and other refractory silicides in combination with TiN and WN are applied as diffusion barriers for electrical contacts in microelectronics.

Although the reader may get the impression that diffusion barriers are only applied in microelectronics,

this is not the case. Just as for solderings on micro-electronic components, thin-film barriers may be used to increase the wettability or adhesion of braze alloys in macroscale joining operations. The barrier may also prevent diffusion of unwanted components of the braze alloy into the substrate surface, but this is usually not a point of primary concern. Other fields of application may be the improvement of fiber composites. Coating of the fibers with suitable materials will preserve the mechanical properties of the fibers by preventing interdiffusion and compound formation with the matrix material. Especially in the case of metal matrix composites, the reactivity will pose problems in stabilizing these structures. However, the problem is not as delicate as in microelectronics, where metallic impurity levels of 10^{10} at. cm⁻³ can be disastrous. (In comparison, the atomic density of Si is 5×10^{22} at cm⁻³.)

The high reactivity and preparation temperatures of the new class of oxide superconductors require diffusion barriers as well if integration with semiconductor technology is desired. To date, more than five years after the discovery of several high- T_c compounds with superconducting transition temperatures above the boiling point of nitrogen, no commercial products based on high- T_c superconductivity are yet available on a large scale. The majority of diffusion barriers in this area are oxides and are thus beyond the scope of this treatise on intermetallic compounds.

As will be clear from the above, this chapter only partially covers the area of thin-film diffusion barriers, and places major emphasis on their role in microelectronics. Fundamental issues on thin-film diffusion barriers will be addressed that are relevant both to microelectronics and to other application areas. Many of the points raised here will be of general interest for metallurgists. Suggestions for further reading are given in Section 8 of this chapter.

2. Types of Diffusion Barriers

Below the Tammann temperature, which is one half to two thirds of the melting point of a solid (in K) (Tammann and Mansuri, 1923), atomic diffusion may be dominated by diffusion via surface or line defects, e.g. grain boundaries or dislocations, rather than by bulk processes (Balluffi and Blakely, 1975; Gupta *et al.*, 1978). Realistic values for diffusion constants are shown in Figure 2, where Arrhenius plots are given for various types of diffusion. Most diffusion barriers aim to eliminate diffusion along extended defects. The following

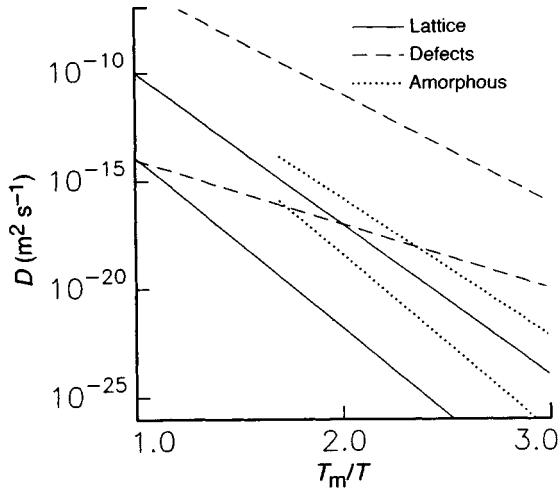


Figure 2. Approximate ranges of diffusion constants D for various diffusion mechanisms in metallics as an inverse function of homologous temperature (the temperature T (in K) is scaled to the melting temperature T_m of the solid). It is observed that diffusion along extended defects dominates at low temperatures (the region between the dashed lines). Diffusion in amorphous alloys (between the dotted lines) is slower, but limited in temperature range because of crystallization. The slowest type of diffusion is lattice diffusion (between the solid lines)

classification of diffusion barriers can be made, based on their principle of operation.

- (i) Stuffed barriers: fast diffusion paths, such as grain boundaries and other extended defects, are stuffed with foreign atoms and diffusion is blocked.
- (ii) Inert barriers: reactions with adjacent materials are minimized.
- (iii) Sacrificial barriers: control of the interfacial reactions allows partial consumption of the barrier without 'short circuiting' the substrate and overlayer.

Several examples of the stuffed barrier type in thin films exist. Elemental metal films, while some can be made amorphous at cryogenic temperatures, are usually polycrystalline at room temperature or above. Grain boundary diffusion is therefore to be expected, even if the adjacent overlayer or substrate material is insoluble in the barrier. However, both good and poor results were reported with tungsten barrier films for aluminum metallization (Bartur and Nicolet, 1981; van Gurp and Reukers, 1979; Ting and Wittmer, 1982), and it was suggested that decoration of the grain boundaries by impurities effectively blocks these fast diffusion paths (Kattelus and Nicolet, 1988). Sinke and co-workers (1985) showed this for TiN. The performance of Si/TiN/Al

structures was strongly enhanced by exposure of the TiN to oxygen before depositing the Al overlayer. Also, incorporation of oxygen in the TiN barrier layer improved the stability of the structure. The impurity concentrations are around several at%, which is typically the amount of impurities needed to stuff the grain boundaries. A disadvantage of the stuffed barrier type is that many properties, such as electrical conductivity, can be strongly influenced by changes at the grain boundaries. Although many experiments point to the existence of stuffed barriers, detailed evidence is not presented.

Inert barriers rely on their low reactivity to minimize interdiffusion. The ultimate diffusion barrier does not react with either substrate or overlayer and eliminates grain boundary diffusion totally. Epitaxial, single-crystal thin films may fulfil these criteria. The diffusivity is similar to lattice diffusion, which is the slowest type of diffusion (see Figure 2). The feasibility of single-crystal diffusion barriers is shown by the following experiment (Tu and Rosenberg, 1972). Pb and Au react readily at a few hundred degrees. Pb/Ag/Au sandwich structures were annealed at 200 °C for more than 48 h. In the case of a polycrystalline Ag layer the C16 (tI12) Pb₂Au intermetallic compound had formed. In the specimens where the Ag layer was a single crystal no reactions were observed. Clearly, mass transport along the grain boundaries was effectively blocked.

Amorphous alloys may also be classified as inert barriers owing to the absence of grain boundaries and they have many other attractive properties. Such properties include high wear and corrosion resistance, low magnetic losses, flexible structure, and, of course, no grain boundary diffusion. Amorphous alloys usually are less dense than bulk materials and the diffusion constants are somewhat higher than for lattice diffusion, but much lower than for diffusion along defects (see Figure 2). The definition of 'amorphous' is sometimes debated. Here, an amorphous alloy is one which exhibits atomic order on the scale of no more than one unit cell. Experimentally this means that only broad halos are observed in diffraction patterns, and an exothermic heat effect is measured at the crystallization temperature. Elemental metals do not normally exist in the amorphous state at room temperature, but crystallization temperatures of around 1000 °C for binary amorphous metal alloys are not uncommon (see Section 4). Although metastable, amorphous alloys are potential candidates for diffusion barriers.

A sacrificial type of barrier is partially consumed during processing. Thin adjacent films usually react in a laterally uniform fashion. For the barrier structure

S/X/O depicted in Figure 1(b), reaction may occur between substrate and barrier (interface S/X), or between barrier and overlayer (interface X/O), or at both interfaces. If the reaction rates are known, the overlayer and substrate materials may effectively be kept separated under controlled conditions. Practical cases of this type of barrier will not be discussed in this chapter, but a semi-empirical model to predict the phase formation sequence will be presented in Section 3.

Finally, without going into detail, another type of barrier with interest for microelectronic applications should be mentioned. The so-called driving force barrier (Ho, 1982) minimizes deleterious effects on device integrity from external driving forces. Two examples will be given. Firstly, an intermediate film of fine-grained Pb–In–Au was shown to disperse the stress in lead alloy Josephson junctions and thus reduce hillock growth caused by thermal cycling (Huang *et al.*, 1980; Murakami, 1979). Secondly, significant improvement in the electromigration resistance of Al(Cu) interconnecting lines was obtained by incorporating aluminum-rich compound barriers such as D_{022} (tI8) Al_3Ti or Al_3Hf (Howard *et al.*, 1978). Complete void linkage between the top and bottom Al(Cu) layers in the Al(Cu)/ Al_3Ti /Al(Cu) line is blocked and the electromigration lifetime is improved by more than an order of magnitude.

3. Prediction of the Phase Formation Sequence: The Effective Heat of Formation Model

Thin-film reactions are typical examples of non-equilibrium processes. For example, in the case of silicide formation, only one compound phase forms at a particular interface (Nicolet and Lau, 1983), which is unlike equilibrium systems where simultaneous formation of a number of phases can lead to the lowest free energy state of the system. Obviously, it will be of great interest to be able to predict the first-phase formation and phase formation sequence, especially in the case of diffusion barriers. One of the first rules by Walser and Bené (1976) states that

The first compound nucleated in planar binary reaction couples is the most stable congruently melting compound adjacent to the lowest-temperature eutectic in the bulk equilibrium phase diagram.

To predict subsequent phase formation in metal–silicon systems, the above rule was extended using the smallest temperature difference between the liquidus and the peritectic (or peritectoid) point as a measure of stability

when the compounds between the first phase and the remaining element are all noncongruently melting (Tsaur *et al.*, 1981). The Walser–Bené rule was subsequently extended to metal–metal systems by relaxing the requirement that the first phase to form needs to be congruently melting (Bené, 1982). Later, Ronay (1983) predicted first-phase formation taking into account the central eutectic, diffusing species, and interfacial free energy. Very recently, the wealth of information which can be obtained from equilibrium phase diagrams, in combination with the ‘ordered Cu_3Au rule’ (d’Heurle and Gas, 1986), was used to predict first-phase formation and the sequence of phase formation in the Al–Ni system (d’Heurle and Ghez, 1992a, b). None of the above-mentioned rules, however, made direct use of thermodynamic data. The effective heat of formation concept, proposed by Pretorius (Pretorius, 1984, 1990; Pretorius *et al.*, 1990, 1991, 1992; Li *et al.*, 1992), enables the calculation of heats of formation as a function of concentration and has been successfully applied in many cases, such as silicide and aluminide systems. Pretorius *et al.* (1993) have recently written an extensive review article on the effective heat of formation model. The model will now be explained.

The driving force for a process to take place is the change in Gibbs free energy

$$\Delta G^\circ = \Delta H^\circ - T\Delta S^\circ$$

which can be approximated by the change in enthalpy ΔH° , since the product of temperature T and change in entropy ΔS° is small during solid-state formation of ordered compounds. Neglecting activation and nucleation barriers, it should be possible to use heats of formation to predict phase formation, since a system would always want to go to its lowest free energy state. As mentioned before, phase formation at an interface during solid-state interaction is a nonequilibrium process. Therefore, standard rules in equilibrium thermodynamics cannot be applied to predict phase formation at the interface. The elements at the growth interface intermix at an (at this point unknown) effective concentration. This effective concentration will differ from the physical concentration at the growth interface, since the actual concentration will be affected during solid-state reaction by many factors, such as lowest eutectic, impurities, atomic mobility, diffusing species, etc. The term effective concentration is similar to the effective concentration used in solution chemistry, where an activity coefficient links the effective and the true concentrations which can differ greatly.

If a compound A_{1-x}B_x is to be formed at an effective concentration x' of element B, element B will

be the limiting element in the reaction if $x' < x$. If ΔH° is the heat of formation of the compound phase $A_{1-x}B_x$ with x the compound concentration of the limiting element B, the heat released during compound formation will be dictated by the effective concentration of the limiting element and the concentration of the limiting element in the compound to be formed. An effective heat of formation $\Delta H'$ can therefore be defined as

$$\Delta H' = \Delta H^\circ \left(\frac{\text{effective concentration of limiting element}}{\text{compound concentration of limiting element}} \right)$$

$$= \Delta H^\circ \left(\frac{x'}{x} \right)$$

As an example, let us consider the solid-state interaction between Al and Ni in which Al_3Ni ($\Delta H^\circ = -38 \text{ kJ mol}^{-1}$; Hultgren *et al.*, 1973) is formed.* Assume an arbitrarily chosen effective Ni concentration $x' = 0.15$ at the Al/Ni interface. It is clear that in this case all effectively available Ni atoms will be consumed at the interface to form the D_{011} (oP16) Al_3Ni compound and Al atoms will be in excess. So, Ni is the limiting element. Its compound concentration is $x = 0.25$. The effective heat of formation is given by

$$\Delta H' = \Delta H^\circ (0.15/0.25) = -22.8 \text{ kJ mol}^{-1}$$

The effective concentration expresses the availability of the limiting element at the growth interface. The excess atoms should be regarded as being available for formation of the next increment of the compound at the moving interface. The effective heat of formation can be looked upon as the maximum heat released during formation of a given compound at a given effective concentration at the growth interface.

A graphic representation is obtained by constructing effective heats of formation diagrams, as shown in Figure 3(b) for the Al-Ni system. For each compound the most negative values for $\Delta H'$ occur when the effective concentration matches the compound concentration. In that case $\Delta H' = \Delta H^\circ$. The diagrams are thus easily constructed by plotting the heat of formation ΔH° (expressed in kJ per mole of atoms) of each compound at its stoichiometric concentration and subsequently triangulating these points with the end points of the concentration axis.

*Note that the Al-Ni system is only a model system for discussion purposes, but it is representative for most of the Al-transition metal systems. Aluminum-rich compounds are effective barriers, as mentioned in Section 2.

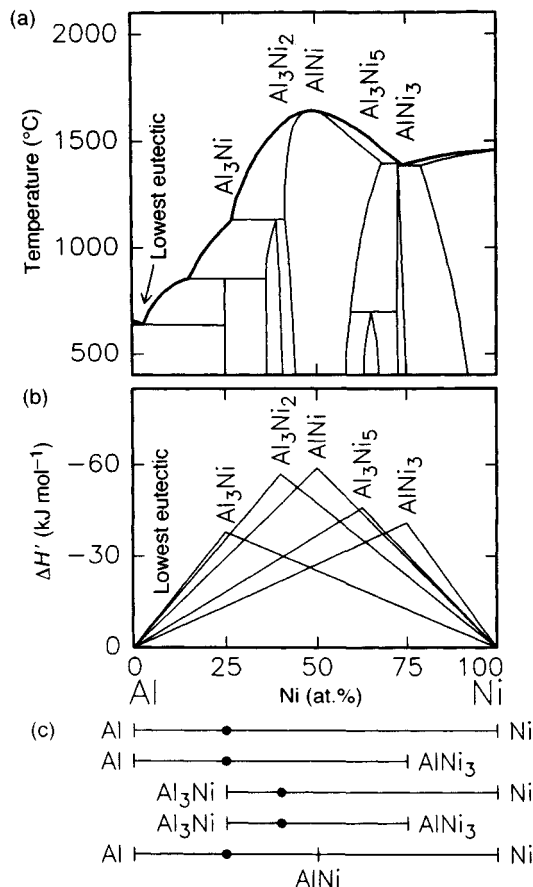


Figure 3. Application of the effective heat of formation rule to the Al-Ni system. (a) The Al-Ni phase diagram (redrawn after Massalski, 1986) shows the positions of the intermetallic compounds and the lowest eutectic. (b) The effective heat of formation ($\Delta H'$) diagram for compound phase formation. Each triangle represents the energy released for a particular Al-Ni intermetallic compound per mole of atoms as a function of concentration (ΔH° values were obtained from Hultgren *et al.* (1973), except for the Al_3Ni_5 compound, for which ΔH° was calculated using the macroscopic atom model; see de Boer *et al.* (1988)). (c) Various sample structures for which phase formation and decomposition have been studied. The first phase formed in each case is indicated by the filled circle on the concentration axis.

To predict phase formation using the effective heat of formation concept, it is necessary to know what the effective concentrations are of the two reacting species at the growth interface. As argued before, the effective concentrations of the reactants are likely to differ greatly from the true concentrations and cannot be calculated. It is well known, however, that for a large variety of systems with a given structure and bond type, the activation energy for solid-state interdiffusion is directly

proportional to the melting point of the solid (Brown and Ashby, 1980; Gjostein, 1973). Assuming that the pre-exponential factor in the diffusion coefficient does not vary over several orders of magnitude, the activation energy determines the mobility. The greatest mobility of the atoms and the most effective mixing at a reaction interface are therefore expected to take place at the composition of the deepest eutectic (or liquidus) of the binary system. The effective concentrations of the interacting atoms at a growth interface are therefore chosen to be those of the lowest-temperature eutectic or liquidus. If a eutectic is absent in the phase diagram, an arbitrary, but nonzero, concentration close to the lowest liquidus is chosen. Note that the same criterion was used in the Walser-Bené phase formation rule (Walser and Bené, 1976). In Figure 3(a) the phase diagram of Al-Ni (Massalski, 1986) is shown. The lowest eutectic at 2.7 at% Ni is indicated in the figure. This value is chosen as the effective concentration of Ni during reaction with Al. Inspection of the Al-Ni effective heat of formation diagram shows that at this concentration Al_3Ni is the phase with the most negative $\Delta H'$. So, formation of Al_3Ni is expected. This is also the first phase that is found to form experimentally (Baglin and d'Heurle, 1976; Colgan *et al.*, 1985; Howard *et al.*, 1978; Köster *et al.*, 1980). The rule for first-phase formation states (Pretorius *et al.*, 1990, 1991) that

The first compound phase to form during metal-metal interaction is the phase with the most negative effective heat of formation ($\Delta H'$) at the concentration of the lowest temperature eutectic (liquidus) of the binary system.

The next step is the application of the effective heat of formation concept to predict the phase formation sequence. Again, the Al-Ni system will be used as an illustration. For the case of a thin Al film on a thick Ni substrate, a stage during interaction will be reached where all the Al will be consumed during first-phase Al_3Ni formation. Ni will be the remaining element. At this point, the effective Al concentration at the $\text{Al}_3\text{Ni}/\text{Ni}$ interface cannot be maintained at its initial value and has to decrease, thus moving to the right of the effective heat of formation diagram (see Figure 3) until a concentration slightly higher than 25 at% Ni is reached. At this concentration the diagram shows that the Al_3Ni_2 compound will be the most favorable phase to form, since it exhibits the most negative $\Delta H'$ value at that concentration. After consumption of all the Al_3Ni , the effective concentration of the atoms at the reacting interface is expected to move further to the

right until AlNi becomes the most likely phase to form. The next phase to form would be Al_3Ni_5 , but this phase has not been observed experimentally in diffusion couples. The absence of this phase in thin-film reactions is attributed to a high nucleation barrier (d'Heurle and Ghez, 1992b). Finally, AlNi₃ will be formed. The effective heat of formation rule for the phase formation sequence in metal-metal systems is thus formulated (Pretorius *et al.*, 1993) as follows

After first-phase formation in metal-metal binary systems, the effective concentration moves in the direction of the remaining element and the next phase to form at the growth interface is the next phase richer in the unreacted element.

Phase decomposition can be predicted using the effective heat of formation concept as follows. As for the case of first-phase formation, mixing at an interface will always be controlled by the lowest eutectic. The effective concentration will be expected to be as close as possible to that of the lowest eutectic within the concentration range of the two interacting phases. This will be so even if the eutectic composition lies outside this range. Phases will react with each other to form the phase with the most negative effective heat of formation ($\Delta H'$) and a compound concentration as close as possible to that of the just-determined effective concentration. Phases with concentrations outside those of the interacting (stable) phases cannot be formed, since their formation can only lead to an increase in free energy.

As an example of phase decomposition let us look at the Al-Ni system again. After constructing the effective heat of formation diagram and locating the lowest-temperature eutectic (liquidus), several test structures are depicted in Figure 3(c). The first structure, Al/Ni, has been discussed before while predicting first-phase formation. The effective concentration for mixing at the Al/Ni interface is expected to be the concentration of the lowest eutectic. At this composition, Al_3Ni exhibits the most negative $\Delta H'$ and is the phase expected to form, as indicated by the dot on the concentration axis. As shown in Table 1, this is in agreement with the experimentally observed phase. For the case of Al/ AlNi_3 , mixing at the interface is again expected to occur at the concentration of the lowest eutectic, resulting in Al_3Ni formation, as observed. For the case of $\text{Al}_3\text{Ni}/\text{Ni}$, the composition of the lowest eutectic lies outside the concentration range defined by the $\text{Al}_3\text{Ni}/\text{Ni}$ sample structure. Now, the effective concentration will be as close as possible to the Al_3Ni concentration. Since no Al is available to form more Al_3Ni , the phase expected

Table 1. Formation of aluminide phases in the Al–Ni system for couples with several sample structures. The predicted phase was obtained using the effective heat of formation rule in conjunction with the lowest melting point eutectic of the binary system. The experimentally observed phases are from Colgan *et al.* (1985)

| Sample | Predicted phase | Observed phase |
|--------------------------------------|---------------------------------|---------------------------------|
| Al/Ni | Al ₃ Ni | Al ₃ Ni |
| Al/AlNi ₃ | Al ₃ Ni | Al ₃ Ni |
| Al ₃ Ni/Ni | Al ₃ Ni ₂ | Al ₃ Ni ₂ |
| Al ₃ Ni/AlNi ₃ | Al ₃ Ni ₂ | Al ₃ Ni ₂ |
| Al/AlNi/Ni | Al ₃ Ni | Al ₃ Ni |

to form is Al₃Ni₂. The Al₃Ni/AlNi₃ sample is expected to behave similarly to the previous sample structure. Regardless of whether Al₃Ni is in contact with AlNi₃ or Ni, the Al₃Ni₂ phase is expected to form, since it is the compound closest to the deepest eutectic within the concentration range of the reacting phases at the interface. Finally, the Al/AlNi/Ni trilayer structure is considered. Here, phase formation may occur at two interfaces. The effective heat of formation approach, however, predicts Al₃Ni at the Al/AlNi interface to be the first phase to form, since this is the phase with the most negative $\Delta H'$ at the concentration of the lowest eutectic. For all sample structures discussed, the effective heat of formation model correctly predicts the initial phase formation (see Table 1). This in contrast to the efforts of Colgan *et al.* (1985), who also used thermodynamics to predict phase formation and decomposition in these structures, but in none of the cases is their prediction successful.

The effective heat of formation model has been applied successfully in many cases, e.g. silicide phase formation sequences, and has been used to explain how the presence of impurities such as oxygen or small amounts of gold can alter the phase formation sequence during nickel and cobalt silicide formation, respectively (Pretorius, 1984, 1990). It has also been useful in explaining why CoSi formation is dominant at low temperatures while the formation of Co₂Si becomes significant at higher temperatures during ion-beam mixing in the Co–Si system (Xia *et al.*, 1989). Correct phases were predicted for thin-film aluminide formation for almost all systems which could be verified from the literature, and also for the exceptional case of Al–Au, in which the lowest-temperature eutectic lies at the Au-rich side of the phase diagram (Pretorius *et al.*, 1990, 1991). Furthermore, the model has been extended to Cu-metal (Li *et al.*, 1992) and Au-metal (Pretorius *et al.*, 1992) systems.

It should be noted that activation and nucleation barriers are not taken into account in the effective heat of formation approach. For the case of silicide formation, this can be anticipated by excluding the formation of noncongruently melting phases (Tsaur *et al.*, 1981; Pretorius, 1984, 1990). In general, the formation of compounds characterized by large unit cell dimensions containing a large number of atoms may be suppressed (Pretorius *et al.*, 1991). Also, special cases of first-phase formation, such as the formation of metastable crystalline phases or solid-state amorphization reactions, will not be predicted, simply because $\Delta H'$ values of these phases will be less favorable than $\Delta H'$ values of equilibrium phases at almost any composition, and special experimental conditions must be fulfilled in order to form these types of phases.

In fact, unlike the Walser–Bené rules (Walser and Bené, 1976; Bené, 1982), which are rather empirical, the effective heat of formation rule makes direct use of thermodynamic data and there is in effect a quantitative reason for the relatively broad margin of its success.

4. Stability of Amorphous Metal Alloys

The absence of grain boundaries, which act as fast diffusion paths at moderate temperatures, makes amorphous diffusion barriers suitable to overcome this type of failure mechanism. One serious constraint, however, is that amorphous alloys are metastable. Although the temperature at which the amorphous-to-crystalline phase transformation takes place (T_x) is not an intrinsic materials property, it is a key parameter to determine the stability of an amorphous alloy. Measured values of T_x can vary considerably, depending not only on the way crystallization is induced (e.g. ramp annealing versus isochronal annealing), but also on the detection method (e.g. resistivity measurements versus diffraction techniques). In Table 2 an overview is given of the highest reported values of T_x for amorphous binary transition metal alloys of stated composition.

The description of general trends in the behavior of T_x is essential in order to predict the stability of amorphous alloy systems when experimental information is lacking. An attractive approach is the macroscopic atom model, introduced and extended by Miedema and coworkers and recently described by de Boer *et al.* (1988). In the macroscopic atom picture, energy considerations are cast in terms of contact interactions that take place at the interface between dissimilar atoms. By assigning only two coordinates, ϕ^* , the chemical potential for electronic charge, and n_{ws} , the electron density at the boundaries of the Wigner–Seitz cell,

Table 2. Crystallization temperatures T_x of binary transition metal alloys. The highest reported temperatures to date for known systems are listed. For this compilation, no distinctions were made with regard to preparation method or the method used to determine T_x . Compositions shown are for the alloys as prepared; there is no implication as to the stoichiometry of equilibrium or metastable compounds which may form on crystallization

| Alloy | T_x (K) | References | Alloy | T_x (K) | References |
|-----------------------------------|-----------|--|-----------------------------------|-----------|--|
| Ag ₅₀ Cu ₅₀ | 360 | Wang (1981) | Ir ₄₅ Ta ₅₅ | 1283 | Davis <i>et al.</i> (1978) |
| Ag ₅₀ Ni ₅₀ | <300 | Mayer <i>et al.</i> (1981) | Ir ₂₅ W ₇₅ | <350 | van der Kolk (1988) |
| Au ₂₅ Co ₇₅ | 470 | Mayer <i>et al.</i> (1981) | La ₆₉ Ni ₃₁ | 443 | Buschow (1982) |
| Au ₄₀ Fe ₆₀ | 813 | Wang (1981) | Mo ₉ Nb ₉₁ | 75 | Collver and Hammond (1978) |
| Au ₂₂ La ₇₈ | 453 | Buschow (1982) | Mo ₅₀ Ni ₅₀ | 900 | Liu <i>et al.</i> (1983) |
| Au ₅₀ Ni ₅₀ | <300 | Mayer <i>et al.</i> (1981) | Mo ₃₀ Re ₇₀ | 1020 | Collver and Hammond (1978) |
| Au ₃₅ Ti ₆₅ | 670 | Liu <i>et al.</i> (1983) | Mo ₈₂ Rh ₁₈ | 155 | Wang (1981) |
| Au ₃₅ Zr ₆₅ | 820 | de Reus <i>et al.</i> (1991) | Mo ₅₅ Ru ₄₅ | 800 | Collver and Hammond (1978), Liu <i>et al.</i> (1983) |
| Co ₅₀ Cu ₅₀ | <300 | Mayer <i>et al.</i> (1981) | Mo ₁₅ Zr ₈₅ | 910 | Collver and Hammond (1978) |
| Co ₄₀ Hf ₆₀ | 823 | Wang (1981) | Nb ₄₅ Ni ₅₅ | 920 | Liu <i>et al.</i> (1983), Wang (1981) |
| Co ₅₀ La ₅₀ | 473 | Wang (1981) | Nb ₅₀ Pd ₅₀ | 850 | van der Kolk <i>et al.</i> (1989b) |
| Co ₅₀ Mo ₅₀ | 1170 | Hung <i>et al.</i> (1986b), Liu <i>et al.</i> (1983) | Nb ₄₀ Rh ₆₀ | 1093 | Wang (1981) |
| Co ₅₀ Ta ₅₀ | 1120 | Hung <i>et al.</i> (1986b) | Nb ₅₀ Zr ₅₀ | 750 | Collver and Hammond (1978) |
| Co ₇₈ Ti ₂₂ | 873 | Buschow (1982) | Ni ₄₃ Ta ₅₇ | 1020 | Hung <i>et al.</i> (1986c), Hung <i>et al.</i> (1986b) |
| Co ₅₅ W ₄₅ | 1070 | Wang <i>et al.</i> (1989) | Ni ₄₈ Ti ₅₂ | 822 | Buschow (1983) |
| Co ₄₀ Y ₆₀ | 642 | Wang (1981) | Ni ₃₆ W ₆₄ | 920 | Zhu <i>et al.</i> (1984b) |
| Co ₉₀ Zr ₁₀ | 833 | Wang (1981) | Ni ₃₁ Y ₆₉ | 591 | Colinet <i>et al.</i> (1987) |
| Cr ₅₀ Cu ₅₀ | <350 | Shin <i>et al.</i> (1983), Payne and Clemens (1992) | Ni ₆₅ Zr ₃₅ | 886 | Sakata <i>et al.</i> (1982) |
| Cr ₄₃ Ni ₅₇ | <300 | Hung <i>et al.</i> (1986b) | Os ₄₅ Ta ₅₅ | 1220 | van der Kolk (1988) |
| Cr ₅₀ Pd ₅₀ | <350 | Minemura <i>et al.</i> (1988) | Os ₃₀ W ₇₀ | 1220 | van der Kolk (1988) |
| Cr ₅₀ Ti ₅₀ | 920 | Blatter and von Allmen (1985) | Pd ₄₀ Ta ₆₀ | 1050 | van der Kolk <i>et al.</i> (1989b) |
| Cu ₅₆ Hf ₄₄ | 831 | Wang (1981) | Pd ₄₀ Ti ₆₀ | 750 | Thompson and Politis (1987) |
| Cu ₅₀ Mo ₅₀ | 280 | Brekkeker <i>et al.</i> (1987) | Pd ₅₀ V ₅₀ | 570 | van der Kolk <i>et al.</i> (1989b) |
| Cu ₂₀ Ta ₈₀ | 1070 | Nastasi <i>et al.</i> (1985) | Pt ₅₀ Ti ₅₀ | 720 | Hung and Mayer (1986) |
| Cu ₆₅ Ti ₃₅ | 700 | Sakata <i>et al.</i> (1982) | Pt ₁₈ W ₈₂ | 1070 | de Reus and Saris (1990) |
| Cu ₄₄ V ₅₆ | 280 | Brekkeker <i>et al.</i> (1987) | Pt ₂₂ Zr ₇₈ | 768 | Buschow (1982) |
| Cu ₅₀ W ₅₀ | 450 | Nastasi <i>et al.</i> (1985), Wang (1981) | Re ₇₅ Ta ₂₅ | 1220 | van der Kolk (1988) |
| Cu ₉₀ Zr ₁₀ | 877 | Buschow (1984a) | Re ₅₃ W ₄₇ | 1070 | Denier van der Gon <i>et al.</i> (1987) |
| Fe ₄₀ Hf ₆₀ | 866 | Wang (1981) | Rh ₄₅ Ta ₅₅ | 1118 | Wang (1981) |
| Fe ₇₀ Mo ₃₀ | 870 | Huang <i>et al.</i> (1989) | Rh ₃₀ Zr ₇₀ | 758 | Buschow (1982) |
| Fe ₅₀ Pt ₅₀ | <300 | Battaglin <i>et al.</i> (1986) | Ru ₅₀ Ti ₅₀ | 450 | Cheng <i>et al.</i> (1985) |
| Fe ₆₃ Ti ₃₇ | 930 | Scheuer <i>et al.</i> (1989) | Ru ₃₅ W ₆₅ | 1070 | Denier van der Gon <i>et al.</i> (1987) |
| Fe ₅₀ W ₅₀ | 1150 | Wang (1981) | Ru ₂₅ Zr ₇₅ | 670 | Cheng <i>et al.</i> (1985) |
| Fe ₅₀ Y ₅₀ | 741 | Wang (1981) | Ta ₅₀ Ti ₅₀ | <500 | Capio and Williams (1987) |
| Fe ₈₇ Zr ₁₃ | 882 | Altounian <i>et al.</i> (1986), Buschow (1984a) | Ta ₃₇ W ₆₃ | 210 | Collver and Hammond (1987) |
| Hf ₃₆ Ni ₆₄ | 923 | Buschow (1984b) Wang (1981) | V ₅₀ Zr ₅₀ | 870 | de Reus and Saris (1990), Weeber and Bakker (1987) |
| Hf ₄₇ V ₅₃ | 808 | Buschow (1982) | W ₄₀ Zr ₆₀ | 1170 | Zhu <i>et al.</i> (1984b) |
| Ir ₅₅ Nb ₄₅ | 1133 | Wang (1981) | | | |

to each transition element, it is possible to separate all those binary alloys with negative heats of formation from those with positive values. Adjustment of the magnitude of the heat of formation to known experimental values enables the prediction of values for all those systems that have not yet been measured. The physics underlying the macroscopic atom model is supported by ample experimental evidence (Miedema, 1992). In nonscientific terms: atoms in an alloy will adapt to each other. Enthalpy effects are related to surface energies and are determined by the differences in ϕ^* (giving rise to a dipole energy) and n_{ws} (which requires transfer of electrons to higher-energy

levels in order to obtain a continuous electron density) of the constituent atoms. The concentration of the alloy and the molar volumes of its constituents determine the contact areas between its constituent atoms. In a dilute alloy $A_{1-x}B_x$, a vacancy at normal sites of the minority constituent B can be looked upon as a pure A vacancy with the size of a B atom. In concentrated alloys the contact of both constituents will be sensed. Although the model is primarily empirical, its general applicability has stimulated several theoretical discussions (Alonso and Girifalco, 1978a, b; Chelikowsky and Phillips, 1978; Hodges, 1979; Williams *et al.*, 1980; Pettifor, 1987)

on the validity of its physics. In the context of this section, the macroscopic atom model is merely a tool to assess thermodynamic data, which in their turn are used to predict the stability of amorphous alloys.

First of all, it should be pointed out that the heat of compound formation and T_x do not correlate. This has been shown convincingly (Buschow, 1982). However, for many binary systems a correlation between T_x and the formation enthalpy $\Delta H_{V\text{small}}$ of cavities the size of the smaller constituent was found

$$T_x = 7.5 \Delta H_{V\text{small}} \text{ (K)}$$

with the proportionality factor of 7.5 in units of K mol kJ⁻¹. The background of this so-called Buschow model is that crystallization occurs when the smaller constituent of the alloy becomes mobile. This happens at a temperature T_x which is proportional to the activation energy for the diffusion process represented by $\Delta H_{V\text{small}}$. In the macroscopic atom model formation enthalpies are related to surface energies. Thus, the enthalpy of vacancy formation is related to the surface energy of a hole. Such a hole is partially surrounded by A atoms and partially by B atoms, and values of ΔH_V are calculated as follows

$$\Delta H_{VA} = (1 - f_B^A) \Delta H_{IV}^A + f_B^A (V_A/V_B)^{5/6} \Delta H_{IV}^B \text{ (kJ mol}^{-1}\text{)}$$

ΔH_{IV}^A and ΔH_{IV}^B are the monovacancy formation enthalpies for pure A and B, respectively, and V_A and V_B are the molar volumes. The power 5/6 in the scaling factor $(V_A/V_B)^{5/6}$ is a compromise between two considerations. On the one hand, volume changes of the vacancy as compared to the pure metal will influence the contact area of the vacancy with its surrounding atoms and therefore the exponent should be greater than 2/3. On the other hand, it is known that in a pure metal monovacancies generally attract each other. So, the exponent must be smaller than unity. The degree to which A atoms are surrounded by B atoms, f_B^A , is dependent on the degree of order in the system. In regular liquids or solid solutions of composition $A_{1-x}B_x$ this value is given by

$$f_B^A = c_B^s$$

where c_B^s represents the surface concentration of B atoms and is defined as

$$c_B^s = x V_B^{2/3} / [(1-x) V_A^{2/3} + x V_B^{2/3}]$$

For ideally ordered phases, f_B^A is given by

$$f_B^A = c_B^s [1 + 8(c_A^s c_B^s)^2]$$

whereas it has been shown (Weeber and Bakker, 1987) that for amorphous alloys the calculation of f_B^A by

$$f_B^A = c_B^s [1 + 5(c_A^s c_B^s)^2]$$

agrees well with experimental data, assuming some degree of order in amorphous alloys with a negative heat of formation.

In Figure 4(b) the measured values of T_x as well as the predicted values by the Buschow model (solid line, $T_x = 7.5 \Delta H_{N_i}$) are given as a function of composition for the Ni-Zr system. Although the values predicted by the Buschow model agree well with the experimental data, the background of the model (mobility of the smaller constituent) is in contradiction with observations of solid-state amorphization in which an amorphous alloy forms by diffusion of the smaller constituent. Crystallization via a diffusion-controlled process requires collective motion of both constituents (Schwarz and Johnson, 1983; Barbour *et al.*, 1987; Thomas *et al.*, 1988). The Buschow model was therefore modified and T_x was correlated with the formation enthalpy of cavities the size of the larger constituent (Barbour *et al.*, 1987; de Reus and Saris, 1990)

$$T_x = 4.7 \Delta H_{V\text{large}} \text{ (K)}$$

Again, the proportionality factor is in units of K mol kJ⁻¹. The prediction for the Ni-Zr system following this formula is represented by the dashed line in Figure 4(b). The large size difference between the Ni and Zr atoms, and hence the large difference between the formation enthalpies of cavities the size of Ni and Zr atoms, results in rather similar predictions of T_x following either the Buschow model or the modified model. However, for the case where $\Delta H_{V\text{small}} \approx \Delta H_{V\text{large}}$, the predictions of T_x differ significantly. For such a system, as can be seen in Figure 5 for Os-W, the Buschow model overestimates T_x with more than 500 K, whereas $T_x = 4.7 \Delta H_{V\text{large}}$ predicts the correct values.

The correlation between crystallization temperature and the enthalpy of cavity formation is only valid if crystallization occurs via long-range diffusion. Typically, this is true if more than one phase is present after crystallization (phase separation) or if the crystallization product consists of a phase with a complicated crystal structure. Then, crystallization requires atomic diffusion of both constituents over more than one atomic distance. Since the species with the larger size and the larger ΔH_V will be the slower diffusant, this species

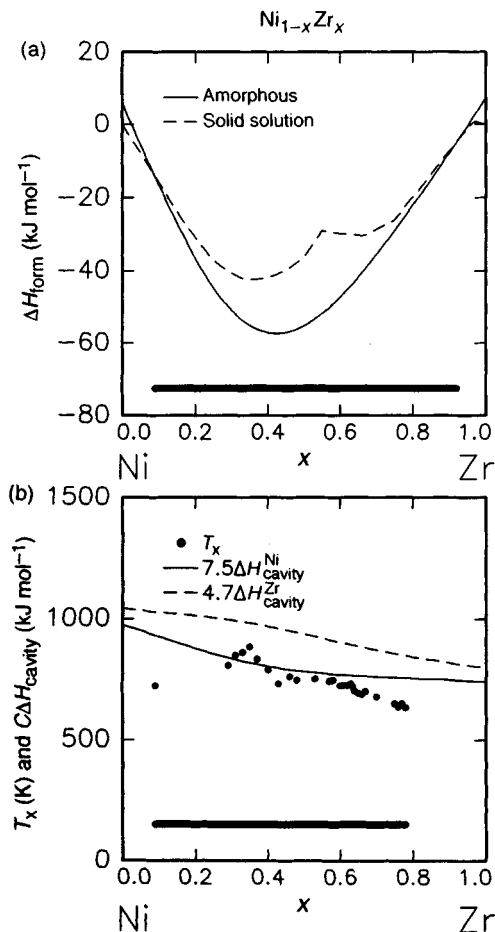


Figure 4. Prediction of crystallization temperatures of amorphous Ni_{1-x}Zr_x alloys. (a) Heat of phase formation ΔH_{form} for the amorphous phase and the solid solution. The solid bar indicates the composition range over which the amorphous phase is thermodynamically more stable than the solid solution. (b) Crystallization temperatures T_x of melt-spun a-Ni_{1-x}Zr_x alloys (from Buschow, 1984a). The predicted values of T_x according to Buschow ($T_x = 7.5\Delta H_{\text{cavity}}^{\text{Ni}}$) and the modified Buschow model ($T_x = 4.7\Delta H_{\text{cavity}}^{\text{Zr}}$) are indicated. See text for a description of the proportionality constant, C . The solid bar represents the composition range of amorphous phase formation and corresponds closely to the solid bar in (a)

will determine the relaxation time of the diffusion process. In fact, in many cases this is the experimental parameter which is measured: T_x is the temperature at which a detectable amount of interdiffusion occurs in a certain time interval.

Crystallization via a polymorphic transition does not require diffusion. If an amorphous alloy crystallizes into a single solid solution, the constituent atoms only need

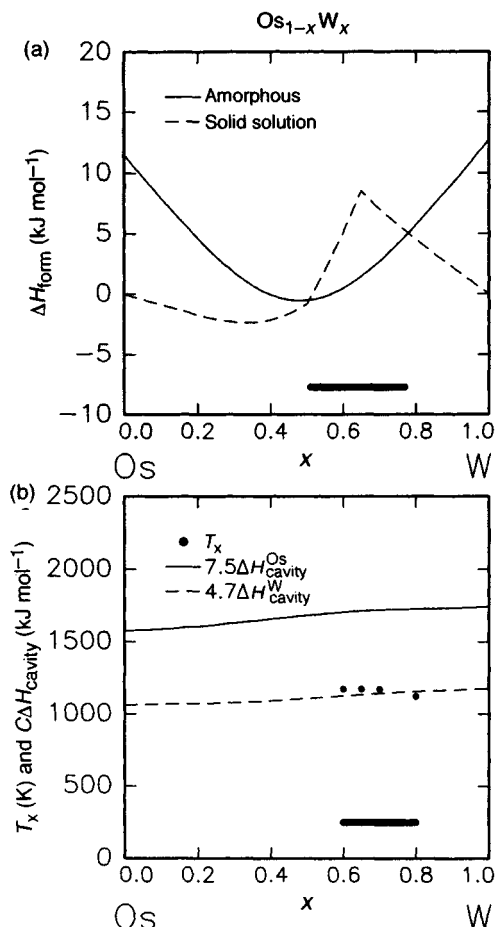


Figure 5. As in Figure 4 but for the system Os-W. (a) Heat of formation of the amorphous phase and of the solid solution. The composition range of a 'stable' amorphous phase is represented by the solid bar. (b) Experimentally determined values of T_x for vapor-quenched a-Os_{1-x}W_x (from van der Kolk, 1988). Since the heats of cavity formation are very similar for both constituents, the values of T_x as predicted by Buschow ($T_x = 7.5\Delta H_{\text{cavity}}^{\text{Os}}$) and the modified Buschow model ($T_x = 4.7\Delta H_{\text{cavity}}^{\text{W}}$) are very different, and in favor of the latter. As for the Ni-Zr system, the solid bar representing the composition range of amorphous phase formation is in good agreement with the predicted range indicated by the solid bar in (a)

to relocate at a normal lattice position. Such a process can take place at low temperatures. Examples are the systems Ru-W and Re-W, whose crystallization temperatures (ranging from -200 to 800 °C) show a strong dependence as a function of composition (Collver and Hammond, 1978; Denier van der Gon *et al.*, 1987). The low values of T_x were found if crystallization occurred into solid solutions. It is clear that the

relationship between T_x and $\Delta H_{\nu_{\text{large}}}$ is not valid in these cases. One should compare the relative stability of the amorphous alloy and the solid solution of the same composition. In the macroscopic atom model (de Boer *et al.*, 1988; Loeff *et al.*, 1988; van der Kolk *et al.*, 1988) the formation enthalpy of an amorphous alloy is calculated by

$$\Delta H^{\text{am}} = \Delta H^{\text{chem}} + 0.0035 \bar{T}_m \text{ (kJ mol}^{-1}\text{)}$$

in which \bar{T}_m is the averaged melting temperature of the solids (in kelvin) and the constant 0.0035 is in $\text{kJ K}^{-1} \text{mol}^{-1}$. The term comprising \bar{T}_m compares to the heat of fusion for liquids and reflects the disordered nature of the amorphous alloy. The chemical contribution for a binary alloy $A_{1-x}B_x$ is determined by

$$\Delta H^{\text{chem}} = (1-x)f_B^A \Delta H_{A \text{ in } B}^{\text{sol}} \text{ (kJ mol}^{-1}\text{)}$$

The degree to which A atoms are surrounded by B atoms, f_B^A , was described above. Values of $\Delta H_{A \text{ in } B}^{\text{sol}}$, the solution enthalpy of A in B, are tabulated in de Boer *et al.* (1988). The formation enthalpy of the solid solution is given by

$$\Delta H^{\text{ss}} = \Delta H^{\text{chem}} + \Delta H^{\text{elastic}} + \Delta H^{\text{structural}} \text{ (kJ mol}^{-1}\text{)}$$

The chemical term ΔH^{chem} was discussed before. $\Delta H^{\text{elastic}}$ is the elastic contribution which arises from the size mismatch of the constituents. It reflects the energy it requires to occupy equivalent lattice sites in the solid solution. The structural contribution $\Delta H^{\text{structural}}$ is the energy associated with the simple hexagonal close-packed (h.c.p.), face-centered cubic (f.c.c.) and body-centered cubic (b.c.c.) crystal structures. This term is determined as a function of the average number of valence electrons of the metal alloys. $\Delta H^{\text{structural}}$ is approximately zero if the average number of valence electrons per atom of the alloy is around 4.2 or 6.7. These values correspond to the transitions from h.c.p. to b.c.c. and from b.c.c. to h.c.p. crystal structures, respectively. Extensive descriptions and tables for $\Delta H^{\text{elastic}}$ and $\Delta H^{\text{structural}}$ can be found elsewhere (de Boer *et al.*, 1988; Loeff *et al.*, 1988; van der Kolk *et al.*, 1988).

Once ΔH^{ss} and ΔH^{am} are known it can be determined whether the amorphous alloy is more stable than the solid solution by assessing whether

$$\Delta H^{\text{am}} - \Delta H^{\text{ss}} < 0$$

If so, crystallization of the amorphous alloy into the solid solution cannot occur and the relationship between

T_x and $\Delta H_{\nu_{\text{large}}}$ is expected to be valid (Loeff *et al.*, 1988; de Reus and Saris, 1990). In the concentration range where $\Delta H^{\text{am}} - \Delta H^{\text{ss}} > 0$ the solid solution will be the more stable phase and low values of T_x are expected. It should be noted that the chemical term in the calculation of $\Delta H^{\text{am}} - \Delta H^{\text{ss}}$ is cancelled if the same degree of (dis)order in the amorphous alloy and the solid solution is assumed. The calculations of ΔH^{am} and ΔH^{ss} for the systems Ni–Zr and Os–W are displayed in Figures 4(a) and 5(a), respectively. (Note that, in actuality, both these systems form intermetallics at equilibrium; see Massalski, 1986.) The bars in the lower parts of these figures represent the regions where $\Delta H^{\text{am}} - \Delta H^{\text{ss}} < 0$ and high crystallization temperatures are expected. The predicted concentration ranges correspond remarkably well with those determined by experiment, represented by the bars in Figures 4(b) and 5(b). Thin films of $\text{Os}_{1-x}\text{W}_x$ with compositions slightly outside the range $0.6 \leq x \leq 0.8$ were crystalline as deposited at room temperature (van der Kolk, 1988). Several other alloy systems show the same features and it was therefore suggested that the concentration range given by $\Delta H^{\text{am}} - \Delta H^{\text{ss}} < 0$ can also be used to predict the range of amorphous alloy formation (van der Kolk *et al.*, 1988).

It should be emphasized that in this model only metastable phases are compared. The existence of two-phase regions or of compounds with complicated crystal structures in the equilibrium phase diagram does not necessarily imply high crystallization temperatures. Primary crystallization to another metastable state may result. The number of equilibrium compounds merely indicates the sign and size of the heat of formation of the system, which is independent of T_x , as mentioned before (Buschow, 1982). A few examples will clarify this.

Chromium and copper are immiscible, even in the liquid state. The Cr–Cu system exhibits a large positive heat of formation and it can be calculated that $\Delta H^{\text{am}} - \Delta H^{\text{ss}} > 0$ over the entire composition range. Sputter deposition of $\text{Cr}_{1-x}\text{Cu}_x$ at an arbitrary composition results in a single-phase solid solution (Payne and Clemens, 1992) that is a metastable state. According to van der Kolk *et al.* (1988), this was to be expected. Solidification from the gas phase in the sputter deposition process does not result in an amorphous phase, but in another metastable crystalline phase. This is in contrast to the equilibrium state according to the phase diagram. Vacuum annealing at $10^\circ\text{C min}^{-1}$ to 500°C leads to the equilibrium state by phase separation of Cr and Cu.

The equilibrium phase diagram of the Re–W system contains the compounds $\sigma\text{-ReW}(\text{D8}_b, \text{tP30})$ and $\chi\text{-Re}_3\text{W}(\text{A12, c158})$ (Massalski, 1986). So, amorphous

Re–W alloys in the concentration range 25–50 at% Re should reach thermodynamic equilibrium by forming the above-mentioned compounds. However, amorphous $\text{Re}_{41}\text{W}_{59}$ crystallized into a single-phase solid solution of Re in b.c.c. W at 200 °C (Denier van der Gon *et al.*, 1987). At the composition of 41 at% Re, $\Delta H^{\text{am}} - \Delta H^{\text{ss}} \approx 6$ (kJ mol⁻¹). Crystallization occurs at a relatively low temperature into another metastable phase. Crystallization of amorphous $\text{Re}_{53}\text{W}_{47}$ into σ -ReW occurred at 800 °C. It should be remarked that at a composition of 53 at% Re $\Delta H^{\text{am}} - \Delta H^{\text{ss}} \approx 3$, i.e. slightly positive but within the uncertainty of ± 4 (kJ mol⁻¹) of the macroscopic atom model.

Once more, these examples stress the fact that a general approach enables the prediction of trends, but not of exact values. Furthermore, one has to deal with metastable phases and cannot rely on the equilibrium phase diagram. Crystallization of amorphous alloys frequently leads to the discovery of new metastable compounds.

The above first-order thinking has also been applied to ion-beam mixing of binary metal systems (de Reus *et al.*, 1991). ΔH_{Vsmall} (in kJ mol⁻¹) was related to T_c , the critical temperature at which radiation-stimulated diffusion sets in, by

$$T_c = 4.0\Delta H_{\text{Vsmall}} \text{ (K)}$$

Below T_c , ion-beam mixing is roughly independent of temperature. Above T_c , a strong enhancement of the mobility of the smaller constituent is expected. This results in an effective mixing of the two components. This does not necessarily lead to the formation of equilibrium compounds, but rather may lead to the formation of metastable phases, such as amorphous alloys or extended solid solutions. However, above T_{eq} , which is related to ΔH_{Vlarge} (in kJ mol⁻¹) by

$$T_{\text{eq}} = 3.8\Delta H_{\text{Vlarge}} \text{ (K)}$$

the larger constituent can migrate over large distances and equilibrium phases will form. For systems with similar ΔH_{Vsmall} and ΔH_{Vlarge} the temperatures for radiation-stimulated diffusion and equilibrium phase formation will coincide. The composition dependence of phase formation during ion-beam mixing has not been investigated.

As mentioned in the introduction of this section, a large spread in the experimental data on T_x consequently makes it difficult to give a general and accurate description of this parameter. The rather naïve picture formed by correlating a critical temperature for diffusion

to cavity formation enthalpy, without taking nucleation effects into account, cannot be interpreted as other than as a rough estimate of the crystallization temperature. However, use of this correlation, in combination with the predictions of concentration ranges for which $T_x = 4.7\Delta H_{\text{Vlarge}}$ is valid if $\Delta H^{\text{am}} - \Delta H^{\text{ss}} < 0$, is a very convenient way to predict T_x for alloys for which experimental data do not exist.

5. Interactions between Binary Alloys and Semiconductor Substrates

Much knowledge is obtained from thermal reactions of transition metal films with Si (Tu and Mayer, 1978; Nicolet and Lau, 1983). Recently, an effort was made to develop a coherent picture of interactions between binary metallic alloys and Si, Ge–Si, and GaAs (Hung, 1992). This type of study directly relates to the growing requirement for reliable contacts in integrated devices. Interactions between Si and binary alloys involve only three elements and are reasonably well understood. When compound substrates such as GaAs are involved, the increased number of compounds observed after reacting with metallic alloys makes a general understanding much more complicated. The effective heat of formation model is used to explain special cases of phase formation.

5.1 Single-element Films on Si

All transition metals form compounds with silicon. The trend in thin-film reactions of transition metals with silicon is as follows. Late transition metals and noble metals (Ni, Pd, Pt) are the moving species in silicidation reactions and form metal-rich silicides as a first phase at temperatures between 200 and 400 °C. As shown in Figure 6(a) for the Ni–Si system, phases more rich in Si form at higher temperatures. The reactions are commonly laterally uniform, yielding sharp interfaces. Around 600 °C Si becomes mobile as well. The formation of phases, such as NiSi_2 , which have to overcome a nucleation barrier usually results in jagged interfaces.

In the reaction between silicon and refractory metals, Si is the moving species and common reaction temperatures are 500 °C or above, yielding Si-rich phases. A typical example is given in Figure 6(b) for Si–Zr. ZrSi_2 forms as the first and only phase around 700 °C.

The above-mentioned reactions are consistent with the effective heat of formation model presented in Section 3.

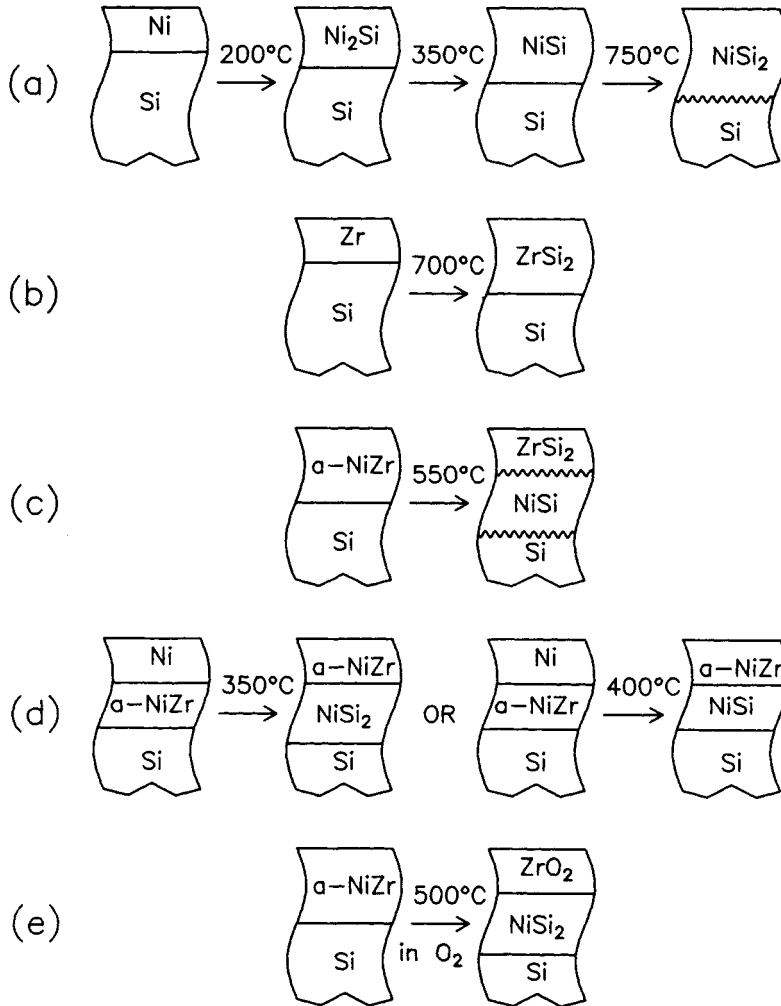
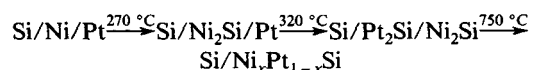


Figure 6. Silicidation reactions in the Ni-Zr-Si system upon vacuum annealing. (a) Between 200 and 350 °C Ni_2Si forms in the reaction between Si and Ni. Between 350 and 750 °C NiSi forms. At 750 °C NiSi_2 forms. The interface between NiSi_2 and the Si substrate is faceted. (b) Zr and Si react at around 700 °C to form ZrSi_2 . (c) Amorphous Ni-Zr reacts with Si at 550 °C. An inner layer of NiSi and an outer layer of ZrSi_2 form. The interfaces are rough. (d) At 350 °C Ni is able to diffuse slowly through amorphous Ni-Zr. Epitaxial NiSi_2 forms. At 400 °C the mobility of Ni is higher and NiSi forms. (e) In a controlled oxygen atmosphere Zr is extracted from the amorphous Ni-Zr and ZrO_2 forms at the surface. The Ni released forms an inner layer of NiSi_2 which is epitaxial with the Si substrate

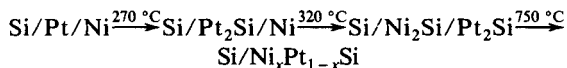
5.2 Bilayers on Si

The study of reactions of bilayers with Si is necessary to understand multilevel metallization schemes. If both layers are near-noble metals, first the silicide of the metal adjacent to the Si substrate will be formed around 300 °C. Subsequently, the outermost metal layer will diffuse through the silicide just formed and react with Si at the substrate interface. Inversion of the sequence

of metals of the bilayer inverts the order of compound formation. At high temperatures, when all atoms become substantially mobile, ternary monosilicides may be formed. The following reactions were observed in the Pt-Ni-Si system (Finstad, 1978)



and



The formation of ternary monosilicides in Si/Pt/Pd and Si/Ni/Pd structures was also suggested (Finstad and Nicolet, 1979). Upon vacuum annealing of bilayers of Ni/Co and Co/Ni on Si in the temperature range 475–550 °C, the monosilicides NiSi and CoSi form. The original order of the metals is inverted. After consumption of the pure metals a mixture of the isomorphous disilicides NiSi₂ and CoSi₂ is formed at the NiSi/CoSi interface (Finstad *et al.*, 1986). Note that the disilicides grow at much lower temperatures than in the binary systems Si/Ni and Si/Co.

Crystallographic data of metal disilicides show four main types of structure: C54 (TiSi₂), C49 (ZrSi₂), C40 (CrSi₂), and C11 (MoSi₂) (Nicolet and Lau, 1983). When two disilicides have different crystal structures, limited solubilities are usually observed. When two disilicides are isomorphous, solid solutions over the entire composition range may form, as shown above. A compilation of bulk solubility data for disilicides is given in Hung (1992).

For bilayers consisting of a near-noble and a refractory metal deposited on Si two possibilities exist. If the inner layer is a near-noble metal, the near-noble silicide forms first. After the near-noble metal is consumed, an outer layer of the refractory metal silicide forms at higher temperatures. Examples are Si/Pd/V (Mayer *et al.*, 1979), Si/Pd/Cr (Olowolafe *et al.*, 1976), and Si/Pd/Ti (Finstad and Nicolet, 1980). If the refractory metal is adjacent to the substrate and the near-noble metal is the outer layer, the metal layers may react with each other prior to silicidation. For the structure Si/V/Pd, V acts as a diffusion barrier up to 450 °C. At 500 °C, V and Pd interact to form binary intermetallics which then enter silicidation reactions. The final, lateral, inhomogeneous structure at this temperature is Si/Pd₂Si/(Pd₂Si + VSi₂) (Mayer *et al.*, 1979). Mo and Co are immiscible upon annealing, and Si/Mo/Co structures react at 550 °C to form Si/MoSi₂/Co. After consumption of the Mo, CoSi rapidly grows on top of the MoSi₂. Eventually, an Si/MoSi₂/CoSi₂ structure is formed (Wang *et al.*, 1988). The onset of reaction in Si/Ta/Cu structures was observed around 600 °C and the compounds TaSi₂ and Cu₃Si were detected (Kolawa *et al.*, 1991a).

The ternary Ni₄Ti₄Si₇ is formed during annealing of Si/Ti/Ni between 500 and 600 °C (see Figure 31 in Chapter 11 by Villars, Volume 1). Before formation of the ternary, the Ti/Ni bilayer intermixed at lower temperatures, forming the intermetallics Ni₃Ti and NiTi₂ (Setton *et al.*, 1987; Setton *et al.*, 1989).

In the case where both metals of the bilayer are refractory metals, Si will always be the moving species in the silicidation reactions. The refractory silicides will grow sequentially, starting from the inner layer. The initial reaction at the Si interface is determined by the reaction temperature of Si with the adjacent refractory metal. This has been shown for Si/Mo/W and Si/W/Mo structures (Baglin *et al.*, 1980; d'Heurle *et al.*, 1982). The isomorphous MoSi₂ and WSi₂ compounds which form during annealing of these structures are well separated and intermix only after annealing at temperatures of 900 °C or higher.

5.3 Solid Solutions on Si

The reaction temperatures of solid solutions with Si are summarized in Table 3. Alloying of two near-noble metals increases the reaction temperature, because the metal alloys, which are the moving species in the reactions, are more strongly bonded in the metal matrix (i.e. interaction effects occur, as evidenced by low-temperature ordering of the solid solutions) and a higher activation energy for the reaction is to be expected. Similar to the bilayer structures, initially well-separated silicides form in Si/Ni–Co structures (d'Heurle *et al.*, 1985). This is most likely due to a difference in mobility of the metals, which can be deduced from the individual reaction temperatures with Si as well. In Si/Pt–Ni structures, NiSi is the first phase formed around 350 °C (Ottaviani *et al.*, 1982; Nava *et al.*, 1982). After annealing at 700 °C, the ternary monosilicide Pt_xNi_{1-x}Si was observed.

Silicides of near-noble metals and those of refractory metals have different crystal structures and exhibit limited mutual solubility. Annealing of solid solutions consisting of a near-noble and a refractory metal on Si substrates commonly results in layer structures with an inner layer of the near-noble metal silicide and an outer layer of the refractory metal silicide (Ottaviani *et al.*, 1980). The combination of a high mobility of the near-noble metal and the low solubilities of the silicides explains the observed phase separation phenomena (Hung, 1992). This effect has been studied extensively with the goal of producing a shallow silicide contact. When a refractory-metal-rich alloy is used, only a small amount of Si will be consumed in the formation of the near-noble metal silicide and a shallow contact is accomplished. The remaining alloy film is enriched in the refractory metal component and serves as a diffusion barrier.

As can be seen from Table 3, it is commonly observed that the reaction temperature of an alloy consisting of

Table 3. Reaction temperatures of binary solutions consisting of transition metals with Si. The three parts of the table (separated by blank lines) refer to the following constituent combinations of the alloy: near-noble metals only, a combination of a near-noble and a refractory metal, and refractory metals only. T_r^A and T_r^B are the reaction temperatures between Si and pure A and pure B, respectively. T_r^{AB} is the reaction temperature between Si and the solid solution A(B) or B(A) at a composition of $A_{100-x}B_x$. Compositions shown are for alloys as prepared; there is no implication of stoichiometry of a crystalline phase

| Alloy $A_{100-x}B_x$ | T_r^A (°C) | T_r^B (°C) | T_r^{AB} (°C) | References |
|---|-----------------|-----------------|--------------------|--|
| Pt _{18/45} Ni _{82/55} | 200 | 200 | 350 | Ottaviani <i>et al.</i> (1982), Nava <i>et al.</i> (1982) |
| Ni _{5/95} Co _{95/5} | 200 | 350 | 450 | d'Heurle <i>et al.</i> (1985) |
| Pd ₈₀ V ₂₀ | 100 | 600 | 300 | Mayer <i>et al.</i> (1979) |
| Pd ₁₀ V ₉₀ | 100 | 600 | 500 | Mayer <i>et al.</i> (1979) |
| Pd ₈₀ W ₂₀ | 100 | 650 | 400 | Olowolafe <i>et al.</i> (1979), Eizenberg <i>et al.</i> (1985) |
| Pd ₃₀ W ₇₀ | 100 | 650 | 500 | Olowolafe <i>et al.</i> (1979), Eizenberg <i>et al.</i> (1985) |
| Pd ₇₀ Ta ₈₀ | 100 | 650 | 400 | van der Kolk <i>et al.</i> (1989a) |
| Pt ₉₀ Cr ₁₀ | 200 | 450 | 300 | Tu <i>et al.</i> (1980) |
| Pt ₁₀ Cr ₉₀ | 200 | 450 | 450 | Tu <i>et al.</i> (1980) |
| Pt ₅₀ V ₅₀ | 200 | 600 | 500 | Hung <i>et al.</i> (1988a) |
| Pt ₈₀ W ₂₀ | 200 | 650 | 500 | Eizenberg and Tu (1982) |
| Pt ₂₀ W ₈₀ | 200 | 650 | 600 | Eizenberg and Tu (1982) |
| Ni ₈₀ Cr ₂₀ | 200 | 450 | 300 | Rozgonyi <i>et al.</i> (1991) |
| Ni ₅₇ Cr ₄₃ | 200 | 450 | 350 | Hung <i>et al.</i> (1986c) |
| Ni ₂₀ Cr ₈₀ | 200 | 450 | 400 | Appelbaum <i>et al.</i> (1984) |
| Ti _{80/30} W _{20/70} | 500 | 650 | 700 | Harris <i>et al.</i> (1976), Gas <i>et al.</i> (1986) |
| Ti _{15/10} W _{85/90} | 500 | 650 | > 1100 | Gas <i>et al.</i> (1986) |
| Ti _{20/80} V _{80/20} | 500 | 600 | 600 | Appelbaum and Eizenberg (1984) |
| Ti _{50/10} Ta _{50/90} | 500 | 650 | 500 | Capio and Williams (1987) |
| Mo ₈₅ W ₁₅ | 525 | 650 | 500 | Olowolafe <i>et al.</i> (1986) |
| Ta ₈₀ W ₂₀ | 650 | 650 | 750 | Appelbaum <i>et al.</i> (1983), Gas <i>et al.</i> (1987) |
| Ta _{80/50} V _{20/50} | 650 | 600 | 750 | Appelbaum and Eizenberg (1984) |
| Ta ₂₀ V ₈₀ | 650 | 600 | 650 | Appelbaum and Eizenberg (1984) |
| Cr _{76/13} V _{24/87} | 450 | 600 | < 1200 | Long and Mahan (1990) |
| Cr ₉₃ Ta ₇ | 450 | 650 | 500 | Palmstrøm <i>et al.</i> (1983) |
| Cr ₇₇ Ta ₂₃ | 450 | 650 | 600 | Palmstrøm <i>et al.</i> (1983) |
| Cr ₃₀ Ta ₇₀ | 450 | 650 | 700 | Palmstrøm <i>et al.</i> (1983) |

a refractory and a near-noble metal with Si is between the reaction temperatures of the pure constituents with Si. This behavior is not understood in detail (Mayer *et al.*, 1979; d'Heurle, 1985; d'Heurle and Gas, 1986). The observation of the monosilicides NiSi and PtSi as the first growing phases instead of Ni₂Si and Pt₂Si in Si/Pt₉₀Cr₁₀ (Tu *et al.*, 1980), Si/Pt₈₀W₂₀ (Eizenberg and Tu, 1982), Si/Ni₆₀Cr₄₀ (Appelbaum *et al.*, 1984), and Si/Ni₈₀Cr₂₀ (Rozgonyi *et al.*, 1991) structures is not surprising if the effective heat of formation model is borne in mind. The mobility of the near-noble metal in the alloy is reduced as compared to the mobility in the pure metal. Therefore, the effective concentration is shifted from metal rich toward silicon rich, in favor of monosilicide formation. PdSi only forms above 750 °C when pure Pd is deposited on Si, and the formation of Pd₂Si is not affected when Pd₈₀V₂₀ (Mayer *et al.*, 1979) or Pd₈₀W₂₀ (Olowolafe *et al.*, 1979) on Si is annealed. In the case of Si/Ni₈₀Cr₂₀ the structure Si/NiSi/a-Cr-Si-Ni/Ni_{80-x}Cr_{20-y} forms at 300 °C (Rozgonyi *et al.*, 1991). Nickel

monosilicide is formed in the reaction between Si and the Ni which is supplied through a very thin amorphous ternary alloy. Above 350 °C Ni₂Si is also observed.

Refractory metal disilicides are frequently observed upon annealing of Si/metal structures. Four main types of structure exist (see also Section 5.2), and the behavior of disilicide systems can reasonably well be predicted on the basis of crystal chemistry and isomorphy. Isomorphy of two disilicides indicates large or even complete mutual solubility.

Reactions in the Si/Ti-W system have been investigated extensively by Gas *et al.* (1986). Ti-W reacts with Si around 700 °C if the Ti concentration is greater than 30 at%. The reaction products are a hexagonal solid solution of W in TiSi₂ and the low-temperature phase of WSi₂. After annealing at 950 °C the tetragonal, high-temperature WSi₂ phase is also detected. W-rich alloys (Ti₁₀W₉₀ and Ti₁₅W₈₅) do not react with Si up to temperatures of 1100 °C. The sluggish reaction with Si has also been noticed for other W-rich alloys.

Other alloys forming nonisomorphous silicides on Si that have been investigated are Ta-W (Appelbaum *et al.*, 1983; Gas *et al.*, 1987) and Ti-V (Appelbaum and Eizenberg, 1984). WSi_2 -TaSi₂ showed complete solid solubility at low temperatures and an increasingly broad miscibility gap above the transition of WSi_2 to the tetragonal form (Gas *et al.*, 1987). In Si/Ti₅₀Ta₅₀ structures Ta₅Si₃ was found upon annealing (Capio and Williams, 1987).

The isomorphous disilicides forming in Mo-W, Ta-V, Cr-V, and Cr-Ta show complete solubility in bulk and powder metallurgy experiments. Similar results are reported for thin films on Si (Olowolafe *et al.*, 1986; Appelbaum and Eizenberg, 1984; Long and Mahan, 1990), except for CrSi₂-TaSi₂, in which system a miscibility gap exists and macroscopic phase separation of the silicides is observed (Palmstrøm *et al.*, 1983).

5.4 Amorphous Alloys on Si

Amorphous phases are entirely homogeneous and eliminate diffusion along the fast, short-circuit diffusion paths offered by grain boundaries and dislocations. Although amorphous alloys are metastable, crystallization temperatures are frequently above 700 °C (see Table 2), which is above the temperatures involved in post-metallization device processing. Therefore, amorphous metal alloys are attractive alternatives as diffusion barriers in metallization schemes. The stability against surrounding materials will in many cases determine the

success of an amorphous diffusion barrier. The interactions between amorphous metallic alloys and Si are the subject of this section.

An overview of the reaction temperatures of amorphous metal alloys with Si is given in Table 4. The temperatures T_r^{AB} indicate when substantial reaction between the alloy and Si occurs. The reactions between Si and amorphous alloys consisting of a near-noble and a refractory metal are very similar to the reactions between Si and binary crystalline solid solutions. The reaction temperature is higher than the reaction temperature of Si with the pure near-noble metal. A satisfactory relationship between the reaction temperature of the amorphous alloy and that of its refractory constituent was shown, suggesting that the initial stage of reaction is Si-diffusion limited (Hung *et al.*, 1986a). Usually the alloy remains amorphous up to the reaction temperature. The near-noble constituent is locked in the amorphous matrix of the alloy and first becomes available for the reaction with Si when Si becomes mobile and breaks up the amorphous alloy. At these high temperatures the near-noble constituent rapidly diffuses toward the Si interface. In combination with the fact that the near-noble and refractory silicides formed usually exhibit a miscibility gap, this results in a layered structure. The near-noble silicide is found next to the Si and the refractory silicide at the surface. A typical example is given in Figure 6(c) for amorphous Ni₄₀Zr₆₀ (a-Ni-Zr). No interdiffusion was observed after annealing for 30 min at 500 °C. At 600 °C ZrSi₂ is observed at

Table 4. Crystallization temperatures T_x of amorphous binary transition metal alloys and reaction temperatures with Si. T_r^{A} and T_r^{B} are the reaction temperatures of Si with pure A and pure B, respectively. T_r^{AB} is the reaction temperature of Si with the alloy A_{100-x}B_x. Compositions shown are for the alloys as prepared; there is no implication as to the stoichiometry of equilibrium or metastable compounds which may form on crystallization

| Alloy A _{100-x} B _x | T_x (°C) | T_r^{A} (°C) | T_r^{B} (°C) | T_r^{AB} (°C) | References |
|--|---------------|--------------------------|--------------------------|---------------------------|------------------------------------|
| Co ₅₀ Mo ₅₀ | 850 | 350 | 525 | 550 | Hung <i>et al.</i> (1986b) |
| Co ₅₀ Ta ₅₀ | 800 | 350 | 650 | 650 | Hung <i>et al.</i> (1986b) |
| Co ₅₅ W ₄₅ | 850 | 350 | 650 | 650 | Wang and Mayer (1989) |
| Co ₆₀ W ₄₀ | 850 | 350 | 650 | ≤ 550 | Reader <i>et al.</i> (1991) |
| Co ₆₀ Zr ₄₀ | 540 | 350 | 650 | 500 | Duchateau <i>et al.</i> (1991) |
| Cu ₂₀ Ta ₈₀ | 750 | 250 | 650 | 650 | Saris <i>et al.</i> (1985) |
| Fe ₃₇ W ₆₃ | 700 | 450 | 650 | 650 | Suni <i>et al.</i> (1983b) |
| Ir ₄₅ Ta ₅₅ | 900 | 350 | 650 | 825 | de Reus <i>et al.</i> (1990a) |
| Ni ₅₅ Nb ₄₅ | 600 | 200 | 550 | 525 | Wang and Mayer (1989) |
| Ni ₄₃ Ta ₅₇ | 700 | 200 | 650 | 650 | Hung <i>et al.</i> (1986b) |
| Ni ₄₈ Ti ₅₂ | 550 | 200 | 500 | 550 | Hung and Mayer (1986) |
| Ni ₃₆ W ₆₄ | 650 | 200 | 650 | 625 | Zhu <i>et al.</i> (1984c) |
| Ni ₄₀ Zr ₆₀ | 500 | 200 | 650 | 550 | de Reus <i>et al.</i> (1990d) |
| Pd ₃₀ Ta ₇₀ | 725 | 100 | 650 | 625 | van der Kolk <i>et al.</i> (1989a) |
| Pt ₅₀ Ti ₅₀ | 720 | 200 | 500 | 550 | Hung and Mayer (1986) |
| Pt ₁₈ W ₈₂ | 800 | 200 | 650 | 825 | de Reus (1990) |
| W ₄₀ Zr ₆₀ | 900 | 650 | 650 | 700 | So <i>et al.</i> (1986) |

the surface and NiSi next to the Si substrate (de Reus *et al.*, 1990d). It should be noted that, for the Ni–Zr alloy mentioned, the crystallization temperature of self-supporting thin films is around the reaction temperature with Si. In general, an upper limit of the reaction temperature is given by the crystallization temperature of the amorphous alloy.

Exceptions to the general reaction mechanism as mentioned above exist. Limited reaction at 500 °C by out-diffusion of the near-noble component into Si was observed for Si/Ni₃₆W₆₄ (Zhu *et al.*, 1984c) and for Si/Pd₅₀Ta₅₀ (van der Kolk *et al.*, 1989a). At temperatures between 600 and 650 °C the reaction between Si and amorphous Pd_{1-x}Ta_x (0.4 < x < 0.9) proceeds as expected. The final structure upon annealing is Si(100)/Pd₂Si/TaSi₂.

Although a number of ternary silicides have been found in the bulk, these ternaries were not observed in comparable thin-film systems. For example, Ta₃Ni₂Si and TaNiSi exist, but the reaction between Si and Ni₄₃Ta₅₇ leads to the formation of the layered NiSi/TaSi₂ structure (Hung *et al.*, 1986a). Ternaries were reported upon reacting Si with amorphous Pt₅₀Ti₅₀ and, similar to the Si/Ti/Ni bilayer structure, with amorphous Ni₄₈Ti₅₂ (Hung and Mayer, 1986). Both amorphous alloys crystallized before the reaction with Si set in. Similarly, amorphous Pd₆₅Er₃₅ crystallized at 350 °C, but reaction with the Si substrate did not occur until 650 °C (Ottaviani *et al.*, 1983).

Amorphous Co–W on Si forms the structure Si/CoSi₂/Si–Co–W/a–Co–W (Reader *et al.*, 1991) upon annealing below 550 °C. The CoSi₂ shows a strong epitaxial relationship with the single-crystal Si substrate. The unusually low formation temperature of CoSi₂ can again be explained using the effective heat of formation model. The limited availability of Co at the Si interface results in an effective concentration in favor of disilicide formation instead of monosilicide formation. After annealing at temperatures of 600 °C or higher the structure Si/CoSi₂/(CoSi₂ + WSi₂) was observed.

Most of the alloys in Table 4 are thermodynamically unstable when in contact with Si. The formation enthalpy of the near-noble silicide is greater than that of the amorphous alloy. So, decomposition of the amorphous alloy to form a near-noble silicide and the pure refractory metal is thermodynamically favored, but limited kinetically, as explained before. However, the high heats of formation and crystallization temperatures above 900 °C of Ir–Ta alloys (> 55 at% Ta) make this system exceptional. The reaction of amorphous Ir₄₅Ta₅₅ with Si is exothermic only if both Ir and Ta silicides form. This does not happen at the temperature

at which the refractory silicide TaSi₂ usually forms (650 °C), but first around 850 °C, close to the crystallization temperature (de Reus *et al.*, 1990a). Crystalline Ir–Ta of the same composition reacts at a substantially lower temperature of 700 °C.

Furthermore, amorphous Pt₁₈W₈₂ alloys exhibit extremely high reaction temperatures of over 800 °C with Si (de Reus, 1990). Pt and W were codeposited to a thickness of 300 Å by electron beam evaporation onto Si(001) and NaCl substrates. The Si substrates were etched in a 3% buffered HF solution prior to deposition. The NaCl substrates were dissolved in deionized water and the a–Pt–W films were mounted onto molybdenum transmission electron microscopy grids prior to annealing in a vacuum better than 10^{–5} Pa. The self-supporting a–Pt₁₈W₈₂ films crystallized at 800 °C (de Reus and Saris, 1990). In Figure 7 Rutherford backscattering spectra are shown for as-deposited and annealed Si/Pt₁₈W₈₂ structures (de Reus, 1990). The surface channels for Si, Pt, W, and O are indicated. No changes are observed in the structure after annealing at 800 °C. Pt and W signals, which overlap, are observed at the surface channels of Pt and W. The Si signal is observed at lower energies than the surface channel because the substrate is covered by the Pt–W film. During annealing at 850 °C, reaction occurred. Si is found at the sample surface and Pt and/or W have penetrated into the substrate. X-ray diffraction confirms the existence of PtSi and WSi₂ in the reacted sample. In all samples some oxygen is detected at the sample surface. The formation enthalpy of amorphous Pt₁₈W₈₂ is very low, so the thermodynamic driving force for the reaction with Si is large and not limited as in the Ir–Ta system discussed before. A Pt₂₀W₈₀ solid solution, which is of almost the same composition, reacts with Si at around 600 °C (Eizenberg and Tu, 1982) (see also Table 3). Apparently a kinetic barrier exists in the Si/a–Pt₁₈W₈₂ system up to very high temperatures. Aging of the amorphous Pt–W alloys for one day in air results in a decrease of the reaction temperature with Si of approximately 50 °C. This may indicate that impurities such as oxygen or water influence the reaction temperature; this knowledge is important from an application point of view. It is clear that kinetics play a determining role in the superior stability against Si of amorphous Ir₄₅Ta₅₅ and Pt₁₈Ta₈₂. However, a clear picture of the reaction mechanism does not exist.

Ni–Zr and Co–Zr belong to a special class of amorphous alloys which form by solid-state interdiffusion. The asymmetry in diffusivity of the constituents allows interdiffusion but no compound formation. Ni and Co are the moving species in the

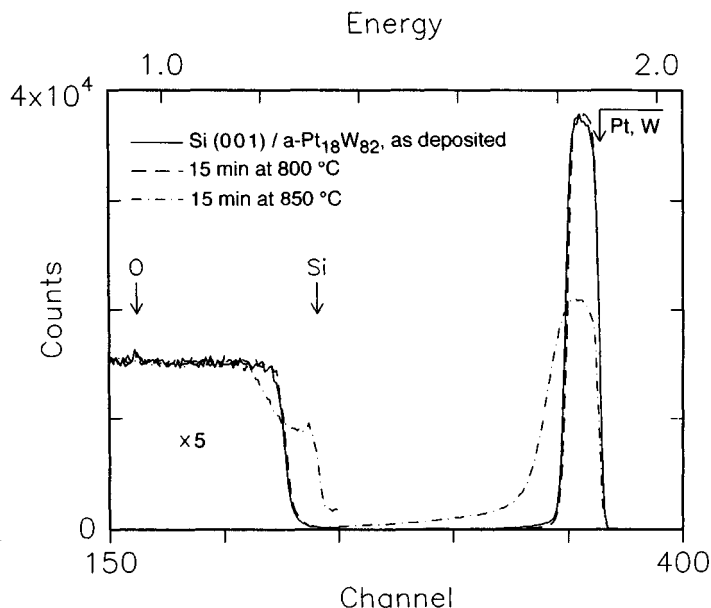


Figure 7. The 2 MeV $^4\text{He}^+$ Rutherford backscattering spectra of vacuum-annealed Si(001)/a-Pt₁₈W₈₂ sample structures before and after reacting. The sample tilt was 7°, the scattering angle 120°. Surface channels are indicated by arrows. No reactions between the Si substrate and the Pt-W overlayer were observed below 800 °C

solid-state amorphization reaction around 350 °C. Ni-Zr on Si is thermodynamically stable if only nickel monosilicide is formed, and it does not react until Si becomes mobile and both NiSi and ZrSi₂ form (see above and Figure 6c). However, the presence of an Ni layer at the surface changes the thermodynamics of the system. Now Ni can diffuse through the amorphous Ni-Zr and react with Si. This does not require decomposition of the amorphous Ni-Zr. The low diffusivity of Ni through the amorphous alloy toward the Si substrate results in the formation of epitaxial NiSi₂ at 350 °C (see Figure 6d). At 400 °C the mobility of Ni is increased. This promotes the availability of Ni at the interface and increases the effective Ni concentration, resulting in NiSi formation (de Reus *et al.*, 1990d). The order of Ni silicide formation is completely reversed as compared to the Si/Ni system shown in Figure 6a.

In a controlled oxygen ambient, amorphous Ni-Zr decomposes at 500 °C. The formation of ZrO₂ is a highly exothermic process and Zr oxidizes at the surface, thus releasing Ni. This Ni rapidly diffuses to the Si interface and forms epitaxial NiSi₂ (see Figure 6e).

For amorphous Co₆₀Zr₄₀ similar effects are observed. Reaction with Si occurs at 500 °C and CoSi₂ forms at the interface (Duchateau *et al.*, 1991). This reaction is

exothermic and a Co 'supply' at the surface is not necessary. Annealing at temperatures above 600 °C results in the structure Si/CoSi₂/(ZrSi₂ + CoSi₂).

The formation of CoSi₂ upon annealing of Si/Co at 700 °C in NH₃ is retarded by a thin nitride layer at the interface. Similar to Ni-Zr, annealing of Si/a-Co-Zr in NH₃ results in a layered structure of Si/CoSi₂/(CoSi₂ + ZrSi₂)/ZrN. Nitriding of Zr takes place at the sample surface and epitaxial CoSi₂ forms at the Si interface. The formation of ZrSi₂ is observed as well. Apparently, the activation barrier for the reaction between amorphous Co-Zr and N₂ is too high, since no reactions were observed upon annealing Si/a-Co-Zr in N₂ ambient.

Rapid thermal annealing of Ti-Co/Si structures (Ti-Co alloy or multilayer) at 900 °C for 10 s in pure N₂ results in the formation of Si(111)/CoSi₂/Ti-Co-Si (Hsia *et al.*, 1991).

Amorphous alloys offer an intriguing possibility to control phase formation. Both the process temperature and the pressure of reactive environments make it possible to control the 'release rate' of constituent metals at the Si interface and thus influence the effective concentration. These processes result in the formation of phases which are not observed in Si/metal structures under the same conditions.

5.5 Interactions with Other Semiconductor Substrates

Ohmic and Schottky (rectifying) contacts are fundamental components for GaAs devices. Reviews on Ohmic and Schottky contact materials have been published elsewhere (Murakami, 1990; Sands *et al.*, 1990; Hung, 1992). Mechanical, metallurgical, and electrical stabilities of metals on GaAs are major issues in GaAs device processing whenever temperatures greater than 850 °C are involved. A summary of the reactions with metallic thin films following the overview by Hung (1992) will be appropriate here.

Most pure metals react with GaAs between 500 and 600 °C, which makes them unsuitable as contact material. The final phases are metal-gallium and metal-arsenic compounds. Ti-W solid solutions, which proved to be successful on Si, react with GaAs at temperatures between 700 and 800 °C, mainly by inward Ti diffusion. Reproducibility problems seem to occur at elevated temperatures, resulting in mixed reports (Yokoyama *et al.*, 1982; de Potter *et al.*, 1989; Sadler and Eastman, 1983). An increase of the stability was observed for silicided (> 850 °C) (Yokoyama *et al.*, 1982; Gill *et al.*, 1985) and nitrided (Geissberger *et al.*, 1987) Ti-W films.

The stability against GaAs of the following amorphous alloys has been reported. Ni₆₀Nb₄₀ reacts with GaAs via Ni diffusion at 400 °C, which is 250 °C below the crystallization temperature (Doyle *et al.*, 1983; Thomas *et al.*, 1987). Although Ni₆₀Ta₄₀ crystallizes on SiO₂ at 750 °C, the formation of Ni₂GaAs is observed to set in between 400 and 450 °C. A final structure of GaAs/NiGa/Ta(Ni)As is observed after annealing at 600 °C (Lahav and Eizenberg, 1984; Lahav and Eizenberg, 1985; Lahav *et al.*, 1986, 1987). Amorphous Cu-Ta diffusion barriers between GaAs and Au show interfacial reactions between GaAs and Cu at 500 °C (Oh *et al.*, 1986, 1987a,b, 1988).

The gallides and arsenides formed in the reactions between GaAs and pure metals are an extremum of the tie line with GaAs in the ternary phase diagram of the metal-GaAs system and therefore may form thermally stable contacts to GaAs. The following intermetallics have been tested: NiGa (Guivar'c *et al.*, 1987), CoGa (Palmstrøm *et al.*, 1989), RhGa (Guivar'c *et al.*, 1988), PtGa₂, PtGa, Pt₂Ga (Sadwick *et al.*, 1989; Kim *et al.*, 1990), and AuGa₂ (Lince *et al.*, 1986). The simple B1 (cF8) and B2 (cP2) structure type compounds, such as NiGa and CoGa, tend to grow epitaxially on GaAs, which provides substantial technological advantages over polycrystalline solid-solution metallizations with respect to thermal stability, interface

uniformity, and barrier height. However, the experimental results indicate that the materials mentioned above are hardly compatible with the process requirements for self-aligned structures which require the gate metallization to undergo an n⁺ implant activation anneal above 850 °C. For instance, although no evidence for reaction was found in GaAs(001)/AuGa₂ structures below the melting point of AuGa₂ (491.4 °C) and a certain degree of alignment with the substrate was observed, annealing between 300 and 400 °C caused the film to break up and coalesce into highly rectangular crystallites (Lince *et al.*, 1986). The best results were reported for PtGa₂ and PtGa, which were found to be stable against annealing in pure N₂ up to 800 °C and 600 °C, respectively (Kim *et al.*, 1990).

The formation enthalpies of Al-Ga and Al-As compounds are relatively low. Since most aluminides exhibit large heats of formation, the application of Al-containing alloys for direct contacts to GaAs may be advantageous. Successful application of WAL_x for self-aligned gates has been reported (Kwok, 1986). Some Ga out-diffusion was observed after annealing GaAs/Ni₅₀Al₅₀ structures for 30 min at 800 °C (Hung, 1992). Most promising results were obtained for the system GaAs/Pt-Al (Blanpain *et al.*, 1990). Rapid thermal annealing of GaAs/Al₆₄Pt₃₆ in an N₂ ambient for 20 s at 950 °C resulted in some As at the sample surface, but the layer structure maintains its integrity even after annealing at 1000 °C. Arsenic out-diffusion and formation of AlAs were observed for Al-Pt alloys richer in Al than Al₂Pt. Gallium out-diffusion was observed for alloys richer in Pt than AlPt, resulting in the formation of PtGa.

Epitaxial NiAl films were obtained by postannealing at 850 °C of Ni/Al bilayers with an AlN capping layer on GaAs (Sands, 1988).

Furthermore, the stability against GaAs of Ta-Si, W-Si (Yokoyama *et al.*, 1986; Callegari *et al.*, 1987; Tseng *et al.*, 1983; Kao *et al.*, 1989; Lau *et al.*, 1985; Basile *et al.*, 1991), Cr-Si (Huang and Yang, 1991), and W-N (Yamagishi, 1984; Yamagishi and Miyauchi, 1985; Geissberger *et al.*, 1986; Uchitomi *et al.*, 1986) has been investigated.

AuGa₂ films grown by molecular beam epitaxy (MBE) on GaSb(001) were the subject of an investigation by Lince and Williams (1985, 1986).

The first phase to form in Ge(001)/Cr reactions is Cr₄Ge₃ (Hong and Mayer, 1990). Both Cr and Ge are mobile during reaction. In the Ge/Pt system, PtGe, Pt₂Ge₃, and PtGe₂ are successively formed above 400 °C (Marshall *et al.*, 1985). This last reference also points out the parallels between silicide and germanide formation.

The reactions between Pt and amorphous $\text{Si}_{50}\text{Ge}_{50}$ (Hong and Mayer, 1989) and between Pt and single-crystal $\text{Si}_{0.8}\text{Ge}_{0.2}$ (Kanaya *et al.*, 1990) proceed rather similarly. Around 300 °C Pt diffuses into the Si–Ge, and a uniform layer consisting of Pt_2Si and Pt_2Ge forms. Above 400 °C PtSi and GeSi were observed. Between 450 and 500 °C macroscopic phase separation occurs, resulting in an outer layer of PtSi. Ni and $\text{Si}_{50}\text{Ge}_{50}$ react to form $\text{Ni}_2(\text{Si}_{50}\text{Ge}_{50})$ at 300 °C and a layer structure Si/NiSi/Ni($\text{Si}_{50}\text{Ge}_{50}$) at 400 °C (Thompson *et al.*, 1988). The formation of ternary solid solutions has also been suggested in the reaction between Si–Ge and Ti (Thomas *et al.*, 1989, 1990).

The near-noble metals Pt and Ni appear to be the moving species in the reaction with Si–Ge at low temperatures, resulting in a uniform, mixed metal–Si–Ge layer. At higher temperatures both Si and Ge become mobile and layer phase separation is observed. Compositional changes in the unreacted Si–Ge alloy are not uncommon. In general, the heat of formation of a silicide is large compared to the heat of formation of its counterpart germanide. This favors the dissociation of the germanide into the silicide. For instance, this decomposition was shown for Si/GePt (Hong, 1991) and Si/NiGe (Li *et al.*, 1990).

Similar to the Si/Pt–Ti system, in which the ternary silicide PtTiSi was observed (Ottaviani *et al.*, 1982; Nava *et al.*, 1982), the reaction of PtTi with $\text{Si}_{50}\text{Ge}_{50}$ sets in at around 550 °C; and a uniform mixture of PtTiGe forms at the sample surface, whereas Ge accumulation near the interface was observed (Hong, 1991).

The fact that most silicides are more stable than their counterpart germanides implies that the most Si-rich silicides will be thermodynamically stable against Si–Ge in the absence of ternary phase formation. Indeed, at temperatures as high as 800 °C only some local intrusion of PtSi with $\text{Si}_{50}\text{Ge}_{50}$ was observed (Hong *et al.*, 1991). Furthermore, Pd_2Si in contact with Si–Ge is stable against annealing up to 750 °C (Hong *et al.*, 1990).

Finally, no detectable reactions were observed between AlPd and Si or Ge at 720 °C. AlPd is therefore expected to be stable against Si–Ge as well. Experimentally, the Si(111)/ $\text{Si}_{50}\text{Ge}_{50}$ /AlPd structure was shown to be stable against annealing up to at least 700 °C for 30 min (Hong and Mayer, 1990).

6. Diffusion Barriers in Metallization Schemes

Many of the diffusion barriers reported in the literature consist of single-layer or multilayer elemental films. Commonly used metallization schemes on Si include

Ti/Pt/Au, Cr/Au, Ta/Al, and Ta/Cr/Al. These structures will form compounds at low temperatures and react with Si upon further annealing. Aluminides formed in such processes form good diffusion barriers against Al diffusion (with lifetimes of $> 10^4$ h at 250 °C) and, acting as a driving force barrier, improve the electromigration resistance. Furthermore, introduction of oxygen during the deposition of the elemental layers, or at the interface of two adjoining layers, usually results in more effective diffusion barriers. However, more chemically and thermally stable materials are desired.

Application of binary solid solutions will increase the chemical stability. As shown in Table 3, Pd–W reacts with Si between 400 and 500 °C. Upon annealing Si/Pd–W/Al structures Pd becomes mobile and reacts at both interfaces to form Pd_2Si and Al_4Pd (Eizenberg *et al.*, 1985). W remains intact, but forms WSi_2 and Al_{12}W at higher temperatures. The extent of reaction and the magnitude of the reaction temperature depend on alloy composition. In the case of $\text{Pd}_{80}\text{W}_{20}$, Al penetrates the alloy below 400 °C. In a $\text{Pd}_{20}\text{W}_{80}$ alloy, the stability of the contact is preserved even following annealing at 550 °C for 30 min. The W-rich surface layer acts as a sacrificial barrier but will eventually fail if the Al overlayer is much thicker than the barrier.

Solid solutions of W_{94}Re_6 and $\text{W}_{70}\text{Ti}_{30}$ sandwiched between Si and Al fail at 550 °C and < 500 °C, respectively (Lange *et al.*, 1991). Exposure to air before deposition of the Al overlayer improved the stability of the $\text{W}_{70}\text{Ti}_{30}$ to 550 °C. This suggests that W–Ti acts as a barrier with stuffed grain boundaries.

In a more detailed study it was shown that Si/ $\text{SiO}_2/\text{W}_{80}\text{Ti}_{20}/\text{Al}$ fails at 475 °C (Dirks *et al.*, 1990). The W–Ti alloy, which exhibited a columnar-like structure, was exposed to air prior to sputter deposition of the Al. The thin oxide at the interface appears not to influence the reaction of W and α -Ti with Al, during which Al-rich W and Ti compounds form.

Near-noble silicides generally fail as a diffusion barrier between silicon and aluminum at temperatures between 200 and 400 °C by phase formation of Al-rich compounds. Refractory metal silicides show compound formation around 500 °C, but fail by diffusion of Al at temperatures of 400 °C (Wittmer, 1984).

Copper is interesting as an interconnect because of its lower electrical resistivity than that of Al. However, it is a deep-level donor and a fast diffuser in Si, and thus diffusion barriers are required. The application of CoSi_2 , CrSi_2 , or TiSi_2 as a diffusion barrier between Si and Cu fails at 300 °C by Cu_3Si formation (Olowolafe *et al.*, 1990). Later in this section more studies on diffusion barriers in Cu metallization will be reported.

Index

Note: Figures and Tables are indicated [in this index] by *italic page numbers*

| <u>Index terms</u> | <u>Links</u> | | |
|--|--------------|-----|----|
| A | | | |
| A15 superconductors | 17 | 83 | |
| applications | 96 | 98 | 99 |
| characteristics | 83 | | |
| comparison with other superconductors | 98 | | |
| extrinsic properties | 87 | | |
| fabrication methods | 92 | | |
| intrinsic properties | 84 | | |
| mechanical properties | 90 | | |
| phase diagrams | 85 | 87 | |
| strain effects | 86 | 89 | |
| structure | 84 | | |
| transition temperatures listed | 84 | | |
| Abundance of elements, semiconductors | 75 | | |
| Acoustoelectric devices | 73 | | |
| Acousto-optic spectrum analyzer | 145 | | |
| Active vibration controllers | 135 | | |
| Ag-Al-Mn system, magnetic properties | 36 | 37 | |
| Ag-Au-Pb sandwich structures | 209 | | |
| Ag-Ga-Se system, optical applications | 142 | | |
| Ag-Mg system | 22 | | |
| Ag-Pd alloys, temperature coefficient of resistivity | 9 | | |
| Air-conditioning applications | 194 | | |
| Al-As-Ga system, optical applications | 144 | 153 | |
| Al-Co-Fe-Ni system | 31 | 35 | |
| <i>see also</i> Alnico alloys | | | |
| Al-Co-Ta system, diffusion barriers | 231 | | |
| Al-Fe-Ni system, magnetic properties | 36 | | |

| <u>Index terms</u> | <u>Links</u> | | | | |
|--|---------------------|-----|-----|-----|----|
| Alfenol [magnetic material] | 34 | | | | |
| Al-Fe-Si system | 35 | | | | |
| Al-Fe system, magnetic properties | 34 | | | | |
| Al-Ga-In-N system, in light-emitting devices | 79 | | | | |
| Al-Ge-Mn system, magnetic properties | 37 | | | | |
| Al-Mg system | 25 | | | | |
| AlMn magnets, fabrication of | 37 | 45 | | | |
| Al-Mn system, magnetic properties | 36 | 37 | 45 | | |
| Al-Nb system, phase diagram | 85 | | | | |
| Al-Ni system | | | | | |
| phase diagram | 211 | | | | |
| phase-formation sequence prediction | 210 | 211 | 212 | | |
| Alnico [magnetic] alloys | 31 | 33 | 35 | 36 | 46 |
| Aluminum alloys, temperature dependence of resistivity | 25 | | | | |
| Aluminum-gold alloys | 142 | | | | |
| Aluminum nitride, as semiconductor | 55 | | | | |
| Amalgams, applications | 140 | | | | |
| Amorphous alloys | | | | | |
| crystallization of | 213 | 216 | 222 | 229 | |
| temperatures listed | 214 | | | | |
| as diffusion barriers | 209 | 213 | 222 | 229 | |
| magneto-optical applications | 183 | | | | |
| stability of | 213 | | | | |
| Amorphous phases, thermodynamics | 217 | | | | |
| Anisotropic magnetostriction | 121 | | | | |
| Anisotropy | | | | | |
| magnetocrystalline | 3 | 5 | 31 | 32 | 33 |
| | 34 | 122 | 124 | | |
| magneto-optical effects | 173 | 176 | | | |
| Anisotropy coefficients [for permanent magnets] | 33 | | | | |
| Antiferromagnetism | 1 | 4 | | | |
| in chromium chalcogenides | 59 | | | | |

Index terms**Links**

| | | | | | |
|--------------------------------------|-----|-----|-----|-----|-----|
| Antiphase boundaries (APBs) | | | | | |
| electrical resistivity affected by | 12 | | | | |
| scattering by | 12 | | | | |
| Antireflection coatings | 142 | | | | |
| Arsenides | 225 | | | | |
| As-Ga-In-P system | | | | | |
| in light-emitting devices | 64 | | | | |
| optical applications | 152 | 158 | 159 | | |
| AsNi structure type | 37 | | | | |
| Atomic-layer epitaxy (ALE) | 154 | | | | |
| AuCu structure type | 36 | | | | |
| Au-Cu-Zn system | 140 | | | | |
| Au-In optical recording film | 163 | | | | |
| Au-Sn system | 25 | | | | |
| Avalanche photodetectors/photodiodes | 67 | 69 | 70 | 152 | 157 |

B

| | | | | | |
|--|-----|-----|-----|--|--|
| Bandgap energy | | | | | |
| in light-emitting devices | 79 | 156 | 159 | | |
| relationship with lattice constants, in light-emitting devices | 79 | | | | |
| Bandpass [optical] filters | 142 | | | | |
| Barrier layers | 142 | | | | |
| <i>see also</i> Diffusion barriers | | | | | |
| B-Co-Zr system | 37 | | | | |
| Beam transport magnets [in particle accelerators] | 109 | | | | |
| B-Fe-Nd system | 46 | | | | |
| magnetic properties | 42 | | | | |
| Bi-Cu-Mn system, magneto-optical applications | 182 | | | | |
| Bi-Mn system, magnetic properties | 37 | | | | |
| Bi-Pb alloys, grain-boundary flux pinning in | 23 | | | | |
| Birefringence | 58 | | | | |
| Bi-Sb-Se-Te system, thermoelectric applications | 196 | | | | |

Index terms**Links**

| | | | |
|--|-----|-----|-----|
| Bi-Sb system, thermoelectric applications | 198 | | |
| Bismanol [magnetic material] | 37 | | |
| Bismuth chalcogenides, as semiconductors | 57 | | |
| Bismuth strontium calcium copper oxide (BSCCO) superconductors | 98 | | |
| comparison with other superconductors | 99 | | |
| Bismuth telluride | | | |
| temperature coefficient of resistivity | 9 | | |
| thermoelectric applications | 196 | 197 | |
| Bi-Te system | | | |
| phase diagram | 196 | | |
| thermoelectric applications | 197 | | |
| Bloch's theory of metals | 8 | | |
| Boron nitride, as semiconductor | 55 | | |
| Bragg-Williams approximation | 11 | | |
| Brazing alloys, diffusion barriers used | 208 | | |
| Bridgman [single-crystal growth] method | 55 | 127 | |
| Bronze process [for fabrication of superconductors] | 88 | 93 | |
| Buried heterostructure (BH) lasers | 64 | 66 | |
| Buried layers [of silicides] | 58 | | |
| ‘Burst’ effect anomaly, in magnetostrictive materials | 131 | 132 | |
| Buschow model | 215 | | |
| C | | | |
| C15 structure | 127 | | |
| Cable-in-conduit superconductors | 93 | 105 | 112 |
| Cadmium telluride, in nuclear radiation detectors | 74 | | |
| Carbides | | | |
| electrical applications | 204 | | |
| as magnetic materials | 42 | 43 | |
| vacancy concentration dependence of resistivity | 21 | | |
| Cd-Hg-Te system, optical applications | 150 | | |
| Cd-Se-Zn system, light-emitting devices | 54 | 67 | 160 |

| <u>Index terms</u> | <u>Links</u> | | | | |
|--|---------------------|-----|-----|-----|-----|
| Ce-Co-Cu system, magnetic properties | 41 | | | | |
| Cerium-based compounds, magneto-optical effects | 182 | | | | |
| Chalcopyrite [mineral name], structure | 52 | | | | |
| Chalcopyrite-type compounds | 58 | | | | |
| Chemical composition, electrical conductivity affected by | 19 | | | | |
| Chemical vapor deposition (CVD) | 56 | 92 | 141 | 232 | |
| Chirped [diffraction] gratings | 147 | | | | |
| Chromium chalcogenide based ternary compounds, as semiconductors | 58 | | | | |
| Chromium silicides, as semiconductors | 57 | | | | |
| Coatings | | | | | |
| antireflection | 142 | 143 | | | |
| for windows | 143 | 167 | | | |
| Cobalt-based binary compounds, magneto-optical applications | 178 | | | | |
| Cobalt borides, magnetic properties | 35 | | | | |
| Cobalt ferrite | 122 | | | | |
| Cobalt-lanthanide [magnetic] compounds | 40 | | | | |
| Cobalt silicides, as semiconductors | 57 | 58 | | | |
| Co-Cr-Fe system | 35 | | | | |
| Co-Cu-Fe-Sm-Zr system | 41 | | | | |
| Co-Cu-Ni system, magnetic properties | 35 | 36 | | | |
| Co-Cu-Sm system, magnetic properties | 41 | | | | |
| Coercivity | 32 | | | | |
| Co-Fe alloys, magnetic properties | 35 | | | | |
| Co-Fe-V system, magnetic properties | 36 | | | | |
| Coherent-potential approximation (CPA) | 10 | | | | |
| Coincidence-site lattice (CSL) [grain-boundary structure] model | 20 | | | | |
| Collective electron theory | 2 | 15 | | | |
| Communications systems applications | 64 | 70 | 71 | 74 | 145 |
| | 146 | 160 | | | |
| Compensation [magnetization] point | 4 | | | | |
| Compensation point writing | 175 | | | | |

Index terms**Links**

| | | | |
|---|-----|-----|-------|
| Composites | | | |
| diffusion barriers used | 208 | | |
| magnetostrictive materials | 133 | | |
| Compositional superlattices | 157 | | |
| Computer disk drive read/write heads | 46 | 169 | |
| Computers, optically based | 74 | | |
| Concentric circle grating surface-emitting (CCGSE) lasers | 163 | | |
| Conductors | 203 | | |
| Continuous Electron Beam Accelerator Facility (CEBAF) | 108 | | |
| Copper, in metallization schemes | 226 | 239 | |
| Copper-gold alloys, electrical resistivity | 11 | | |
| Copper-palladium alloys, temperature dependence of electrical resistivity | 14 | | |
| Copper-tin alloys, optical applications | 140 | | |
| Co-Pr-Sm system, magnetic properties | 41 | | |
| Core losses [in electric motors] | 45 | | |
| Co ₅ R structure type | 38 | | |
| Co-Sm compounds, magnetic properties | 40 | 44 | |
| Co-W amorphous alloys, reactions with silicon | 223 | | |
| Co-Zr amorphous alloys, reactions with silicon | 224 | | |
| Cr-Cu system, phase separation in | 217 | | |
| Critical current density [superconductors] | | | |
| factors affecting | 88 | | |
| strain effects | 90 | 91 | |
| Cryosurgery applications | 194 | | |
| Crystal-field interactions | 3 | | |
| Crystallization | | | |
| of amorphous alloys/phases | | | |
| temperatures | 216 | | |
| temperatures listed | 214 | 222 | 229 |
| Crystal structures | | | |
| illustrated | 52 | 58 | |
| of semiconductors | 51 | 54 | 57 58 |

| <u>Index terms</u> | <u>Links</u> | | | | |
|--|---------------------|-----|----|----|----|
| Cu-Fe-Ni system, magnetic properties | 35 | | | | |
| Cunico [magnetic material] | 35 | | | | |
| Cunife [magnetic material] | 35 | | | | |
| Curie point/temperature | | | | | |
| ferromagnetic semiconducting compounds | 59 | 60 | | | |
| magnetic materials | 34 | 36 | 37 | 38 | 40 |
| | 41 | 42 | 43 | 44 | 45 |
| magneto-optical materials | 176 | | | | |
| magnetostrictive materials | 123 | | | | |
| Curie point writing | 175 | 182 | | | |
| Curie-Weiss law/regime | 3 | | | | |
| Cu ₂ Sb structure type | 37 | | | | |
| Cu ₇ Tb structure type, magnetic properties | 38 | | | | |
| Czochralski [single-crystal growth] technique | 55 | 127 | | | |

D

| | | | | | |
|--|-----|-----|-----|-----|--|
| Data storage applications | 169 | 172 | 175 | | |
| Degenerate semiconductors | 57 | | | | |
| Demonstration Poloidal Coil | 95 | | | | |
| Density, semiconductors/semimetals | 56 | | | | |
| Density of states (DOS), and superconductivity | 18 | | | | |
| Depletion-layer conversion devices | 73 | | | | |
| Diamond structure | 51 | | | | |
| Diamond X-ray masks | 143 | | | | |
| Dielectric constant, semiconductors | 55 | 73 | | | |
| Dielectric tensor | 173 | | | | |
| Diffraction gratings | 147 | | | | |
| Diffusion barriers | 207 | | | | |
| amorphous alloys as | 209 | 213 | 222 | 229 | |
| applications | 89 | 208 | 233 | | |
| in composites | 208 | | | | |
| effect of impurities | 213 | 232 | | | |

Index terms**Links**Diffusion barriers (*Continued*)

| | | | | | |
|--------------------------|-----|-----|--|--|--|
| in metallization schemes | 226 | | | | |
| preparation and use | 232 | | | | |
| principles | 207 | | | | |
| requirements | 207 | | | | |
| in superconductors | 89 | | | | |
| tandem | 231 | | | | |
| types | 208 | | | | |
| driving force barrier | 210 | | | | |
| inert barrier | 209 | | | | |
| sacrificial barrier | 209 | | | | |
| stuffed barrier | 209 | 229 | | | |

Diffusion processes

| | | | | | |
|----------------------------------|-----|----|--|--|--|
| amorphous phases formed by | 223 | | | | |
| superconductors fabricated using | 92 | 93 | | | |

Diode lasers

| | | | | |
|----|----|-----|-----|-----|
| 53 | 54 | 56 | 64 | 66 |
| 74 | 75 | 150 | 159 | 167 |

Directionally solidified materials, magnetic materials

45

Disilicides

219

Dislocation resistivity models

25 26

Dislocations, electrical conductivity affected by

24

Distributed feedback (DFB) lasers

66 67

Domain wall pinning

176

Double heterojunction/structure light-emitting devices

56 64 66 158 159

Driving-force barriers

210

Dy-Fe-Tb system

| | | | | | |
|---------------------------|-----|-----|-----|--|--|
| ‘burst’ effect anomaly in | 132 | | | | |
| magnetic annealing of | 132 | | | | |
| magnetostriction in | 124 | | | | |
| frequency effects | 132 | 133 | | | |
| pressure effects | 131 | 133 | | | |
| metallurgy | 127 | 129 | 130 | | |

see also Terfenol-D

Index terms**Links****E**

| | | | | | |
|---|-----|-----|-----|-----|-----|
| Effective concentration | 210 | | | | |
| Effective heat of formation, definition | 211 | | | | |
| Effective-heat-of-formation model | 210 | | | | |
| Elastic compliance | 129 | | | | |
| Elastic strain sensitivities, A15 superconductors | 86 | | | | |
| Electrical applications | 203 | | | | |
| Electrical behavior | 7 | | | | |
| Electrical conduction | | | | | |
| in intermetallic compounds | 11 | | | | |
| effect of chemical composition | 19 | | | | |
| effect of dislocations | 24 | | | | |
| effect of grain boundaries | 20 | | | | |
| effect of impurities and vacancies | 20 | | | | |
| effect of magnetic species | 14 | | | | |
| effect of ordering | 11 | | | | |
| in metals | 8 | | | | |
| Electrical conductivity | | | | | |
| factors affecting | 9 | | | | |
| temperature dependence | 203 | 204 | | | |
| of thermoelectric materials | 197 | 198 | 200 | 201 | 203 |
| Electrical resistivity | | | | | |
| calculation of | 10 | | | | |
| effect of antiphase boundaries | 12 | | | | |
| effect of order | 12 | 14 | | | |
| magnetic disorder component | 10 | | | | |
| models | 8 | 11 | | | |
| phase transitions studied | 7 | | | | |
| Electrical steels | 45 | | | | |
| Electrical-to-mechanical energy conversion | 46 | | | | |
| Electricity generators | 113 | 189 | 191 | 192 | |
| Electric power transmission lines | 112 | 114 | | | |

| <u>Index terms</u> | <u>Links</u> | | | |
|---|---------------------|-----|-----|-----|
| Electroluminescence | 150 | 156 | | |
| Electronics applications | 55 | 58 | 60 | 115 |
| Electron mobility | 60 | 72 | | |
| Electron-phonon coupling | 18 | | | |
| Electron-photon interactions, applications based on | 150 | | | |
| Energy conversion | | | | |
| efficiency of | 189 | | | |
| photovoltaic | 150 | 155 | | |
| thermoelectric | 187 | | | |
| Energy density [for permanent magnets] | 32 | | | |
| Energy product [for permanent magnets] | 34 | | | |
| progress in development | 46 | 46 | | |
| Enthalpy of formation | | | | |
| of aluminides | 225 | | | |
| of amorphous alloys | 217 | | | |
| of solid solutions | 217 | | | |
| Exchange energy | 2 | | | |
| F | | | | |
| Fabry-Perot interference filters | 142 | | | |
| Fabry-Perot interferometer | 144 | | | |
| Fabry-Perot lasers | 66 | 67 | | |
| Faraday effect | 169 | 172 | 182 | |
| Fault-tolerant optoelectronic components | 146 | 147 | | |
| Fe-Nd compounds, magnetic properties | 44 | | | |
| Fe-Nd-Ti system, magnetic properties | 43 | | | |
| Fermi energy | 8 | | | |
| Fermi level | 8 | | | |
| Fermi velocity | 8 | | | |
| Ferrimagnetism | 1 | 4 | | |
| Ferrites | 45 | 122 | | |

| <u>Index terms</u> | <u>Links</u> | | | | |
|--|---------------------|-----|-----|-----|-----|
| Ferromagnetic materials | | | | | |
| electrical resistivity | 10 | | | | |
| hysteresis loop | 32 | | | | |
| Ferromagnetic moment | 4 | | | | |
| Ferromagnetic-paramagnetic transition | 13 | 15 | | | |
| Ferromagnetic semiconducting compounds | 58 | | | | |
| Ferromagnetism | 1 | 3 | | | |
| Fe ₇ R structure type | 44 | | | | |
| Fe ₁₇ R ₅ structure type | 44 | | | | |
| Fe-Sm compounds, magnetic properties | 44 | | | | |
| Fe-Sm-Ti alloys, magnetic properties | 43 | 44 | | | |
| Fe-Sm-V alloys, magnetic properties | 43 | 44 | | | |
| Fe-Sm-Zr compounds, magnetic properties | 44 | | | | |
| Fe-Sn system, magneto-optical properties | 182 | | | | |
| Fe-Tb system, magnetic properties | 45 | | | | |
| Field-effect transistors (FETs) | 60 | 63 | 75 | | |
| Figures of merit | | | | | |
| magnetic materials | 46 | | | | |
| magneto-optical materials | 176 | | | | |
| superconductors | 98 | 99 | | | |
| thermoelectric materials | 57 | 190 | 195 | 196 | 197 |
| | 198 | 200 | 201 | | |
| factors affecting | 202 | 204 | 206 | | |
| Filters | 58 | | | | |
| optical | 142 | | | | |
| Fine-filament superconductors | 89 | 98 | | | |
| V-VI compounds | | | | | |
| semiconductors | 57 | | | | |
| thermoelectric materials | 191 | 194 | 196 | 200 | |
| Floating-zone (FZ) method | 127 | | | | |
| IV-IV compounds, semiconductors | 53 | 55 | 76 | 78 | |

Index terms**Links**

IV-VI compounds

| | | | |
|--------------------------|-----|-----|-----|
| semiconductors | 53 | 56 | 78 |
| thermoelectric materials | 192 | 198 | 200 |

Fresnel coefficients 170 171

Frustration [magnetic phenomenon] 4

Fuel injection valves 135

G

Ga-Ge-Mn system, magneto-optical applications 182

Ga-In-N system, in light-emitting devices 79

Gallides 225

Gallium arsenide

in Hall devices 72

in light-emitting devices 64

optical applications 139 145 146 147 153

optoelectronic applications 158

reactions with metallic thin films 225

as semiconductor 55 60

Gallium nitride

in light-emitting devices 80

properties 80

Galvanomagnetic coefficients 9

Ga-Nb system, phase diagram 85

Gauge parameter [for piezoresistive devices] 73

Ga-V superconductors, magnetic applications 99 100

Ga-V system, phase diagram 86

Ge-Nb system, phase diagram 85

Ge-Ni-Si system 226

Ge-Pt-Si system 226

Germanium-based semiconductors 61

Ge-Si system

optical applications 153

Index terms**Links**

| | | | |
|--|-----|-----|-----|
| Ge-Si system (<i>Continued</i>) | | | |
| thermoelectric applications | 199 | 201 | |
| Ginsberg-Landau parameter | 86 | | |
| Grain boundaries | | | |
| A15 compounds | 85 | | |
| electrical conductivity affected by | 20 | | |
| Grain-boundary hardening | 22 | | |
| electrical properties affected by | 22 | | |
| Grain-boundary phase transformations | 21 | | |
| Grain-boundary pinning | 23 | 85 | |
| Grain orientation, in magnetostrictive materials | 127 | 131 | |
| Guided-wave optoelectronics | 148 | | |
| Gunn diodes | 55 | | |
| H | | | |
| Hall devices | 72 | | |
| Hall effect | 9 | | |
| Hall mobility [semiconductors] | 55 | 61 | |
| Hard magnets | 5 | 31 | 33 |
| Hardness | | | |
| grain-boundary | 22 | | |
| of semiconductors | 55 | 56 | |
| Heaters, materials used | 203 | 204 | |
| Heat pumps | 189 | 191 | 194 |
| Heavy-fermion compounds | | | |
| magnetically ordering compounds | 1 | | |
| magnetic properties | 3 | | |
| Heterodyne receiver | 71 | | |
| Heterojunction bipolar transistors | 60 | 63 | |
| Heterojunction phototransistors | 163 | | |
| Heterojunctions | 52 | 62 | |

Index terms**Links**

| | | | |
|---|-----|-----|--------|
| Heusler alloys | | | |
| electrical properties | 16 | | |
| magnetic properties | 1 | 31 | 36 |
| Hexaferrites | 46 | | |
| Hg-Sn system | 140 | | |
| High-electron-mobility transistors (HEMTs) | 60 | 62 | |
| High-field magnets | 83 | 99 | |
| High-temperature superconductors | 83 | | |
| and electron-phonon interaction | 18 | | |
| grain-boundary effects | 24 | | |
| High-temperature thermoelectrics | 199 | | |
| Hot-electron transistors | 55 | | |
| Hot isostatic pressing (HIP) | 91 | | |
| Hume-Rothery phases, electrical resistivity | 19 | | |
| Hybrid magnet facilities | 103 | | |
| Hysteresis loops | 32 | | |
| for ferromagnetic materials | 32 | | |
| magnetization | 5 | | |
| rectangular/square | 32 | 35 | 182 |
| I | | | |
| Impurities, electrical conductivity affected by | 20 | | |
| Indium compounds | | | |
| in Hall devices | 72 | | |
| in magnetoresistive devices | 72 | | |
| optical applications | 150 | | |
| as semiconductors | 55 | 61 | 63 |
| Inert barriers | 209 | | |
| Infrared detectors | 54 | 151 | 194 |
| Integrated-circuit applications | 60 | 61 | 74 |
| optical components | 139 | 164 | |
| Integrated optical devices | 55 | 71 | 75 172 |

Index terms**Links**

| | | | | |
|---|-----|-----|-----|-----|
| Intensity modulators | 148 | | | |
| Interdiffusion, amorphous phases formed by | 223 | | | |
| Interference filters | 142 | 143 | | |
| as optical switches | 144 | | | |
| Internal-tin processes [for fabrication of superconductors] | 88 | 93 | 96 | 97 |
| International Thermonuclear Experimental Reactor (ITER) program | 93 | 94 | 106 | 107 |
| Interstitial compounds, as diffusion barriers | 227 | 228 | | |
| Intrinsic coercivity | 32 | | | |
| Intrinsic resistivity | 10 | | | |
| Ion-beam mixing | 218 | 232 | | |
| Iron-based binary compounds, magneto-optical applications | 180 | | | |
| Iron-lanthanide [magnetic] compounds | 42 | | | |
| Iron-nickel alloys, magnetic properties | 34 | | | |
| Iron-rare-earth compounds | | | | |
| crystal structure | 127 | | | |
| magnetic properties | 44 | | | |
| magneto-optical measurements | 180 | 181 | | |
| magnetostriction in | 123 | 124 | 124 | 125 |
| temperature dependence | 125 | 125 | | |
| metallurgy | 127 | 129 | 130 | |
| phase diagrams | 126 | 128 | | |
| preparation of | 126 | 129 | | |
| Iron silicides, as semiconductors | 57 | | | |
| Iron-terbium compounds | | | | |
| magnetic properties | 45 | | | |
| magnetostriction in | 123 | 124 | 125 | |
| Iron-terbium system, phase diagram | 128 | | | |
| Ir-Ta amorphous alloys, reactions with silicon | 223 | | | |
| Isoperm [magnetic material] | 34 | 35 | | |

J

| | | | | |
|---|-----|-----|-----|--|
| Japanese National Research Institute for Metals, magnet systems | 99 | 100 | 100 | |
| Josephson-junction technology | 115 | | | |

Index terms**Links****K**

| | | | | | |
|----------------------------------|-----|-----|-----|-----|-----|
| Kerr effect | 169 | 171 | | | |
| Kerr rotation | 176 | 178 | 179 | 181 | 183 |
| Kerr spectra | | | | | |
| cobalt-based binary compounds | 179 | | | | |
| iron-based binary compounds | 181 | 182 | | | |
| manganese-based binary compounds | 177 | 178 | | | |
| Kinetics, ordering/disordering | 14 | | | | |
| Kirkendall porosity/voids | 88 | 89 | 93 | | |

L

| | | | | | |
|---|-----|-----|-----|-----|-----|
| Lamellar microstructure, magnetostrictive materials | 130 | | | | |
| Lanthanide-transition metal compounds, magnetic properties | 38 | | | | |
| Large Coil Task (LCT) program | 93 | 104 | | | |
| Large Hadron Collider (LHC) | 109 | | | | |
| Laser-based switches | 162 | 163 | | | |
| Laser diodes (LDs) | 53 | 54 | 56 | 64 | 66 |
| | 74 | 75 | 150 | 159 | 167 |
| optically pumped | 160 | 161 | | | |
| Laser-induced etching | 145 | | | | |
| Lattice parameters | | | | | |
| relationship with bandgap energy, in light-emitting devices | 79 | | | | |
| semiconductors | 56 | 61 | | | |
| Lattice resistivity | 10 | | | | |
| Laves phases | | | | | |
| as magnetic materials | 38 | 45 | | | |
| magneto-optical effects | 180 | 181 | | | |
| Lead chalcogenides | | | | | |
| optical applications | 150 | | | | |
| as semiconductors | 56 | | | | |
| Lead telluride, thermoelectric applications | 198 | | | | |
| Light-emitting devices | 64 | | | | |

| <u>Index terms</u> | <u>Links</u> | | | | |
|--|---------------------|-----|----|----|----|
| Light-emitting diodes (LEDs) | 51 | 53 | 54 | 55 | 56 |
| | 58 | 64 | 65 | 74 | 75 |
| | 150 | 158 | | | |
| Linear-combination-of-atomic-orbitals (LCAO) methods, applications | 21 | | | | |
| Liquid-phase epitaxy (LPE) | 54 | 56 | | | |
| Long-range ordering, effect on electrical resistivity | 11 | | | | |
| Loop shearing, magnetic materials | 33 | | | | |
| Lorentz forces | 46 | 173 | | | |
| Low-temperature thermoelectrics | 196 | | | | |
| M | | | | | |
| McDonald jelly-roll (MJR) process [for superconductors] | 95 | 96 | | | |
| cross section of conductor | 97 | | | | |
| Machinable permanent magnets | 45 | | | | |
| Magnesium alloys, electrical resistivity | 19 | | | | |
| Magnet characteristics | 32 | | | | |
| Magnetically levitated transport | 111 | 113 | | | |
| Magnetically soft alloys | | | | | |
| applications | 45 | | | | |
| properties | 33 | | | | |
| Magnetic annealing | 34 | 132 | | | |
| Magnetic applications | 31 | | | | |
| Magnetic disorder, as resistivity component | 10 | | | | |
| Magnetic disordering temperature | 4 | | | | |
| Magnetic exchange interactions | 2 | | | | |
| indirect exchange | 2 | | | | |
| Magnetic fusion research | 98 | 103 | | | |
| Magnetic materials | | | | | |
| applications | 45 | | | | |
| composition notation | 33 | | | | |
| Magnetic oxides | 45 | | | | |

| <u>Index terms</u> | <u>Links</u> | | | | |
|----------------------------------|---------------------|-----|-----|----|----|
| Magnetic properties | 1 | | | | |
| hard/permanent magnets | 33 | | | | |
| intrinsic properties | 3 | | | | |
| magnetically soft alloys | 33 | | | | |
| units used | 32 | | | | |
| Magnetic refrigerators | 189 | | | | |
| Magnetic resonance imaging (MRI) | 109 | 112 | | | |
| image | 113 | | | | |
| Magnetic structures | 5 | | | | |
| Magnetization intensity | 32 | | | | |
| Magnetocrystalline anisotropy | 3 | 5 | 31 | 32 | 33 |
| | 34 | 122 | 124 | | |
| Magnetoelastic coefficient | 130 | | | | |
| Magnetoelastic coupling | 121 | | | | |
| Magnetoelectronic semiconductors | 52 | | | | |
| Magnetomechanical coupling | 121 | 128 | | | |
| Magnetomechanical resonance | 130 | | | | |
| Magneto-optical applications | 169 | | | | |
| materials requirements | 175 | | | | |
| Magneto-optical effects | | | | | |
| phenomenological description | 169 | | | | |
| physics | 172 | | | | |
| Magneto-optical properties | 176 | | | | |
| amorphous alloys | 183 | | | | |
| cobalt-based binary compounds | 178 | | | | |
| iron-based binary compounds | 180 | | | | |
| manganese-based binary compounds | 177 | | | | |
| ternary compounds | 182 | | | | |
| Magnetoresistive coefficients | 9 | | | | |
| Magnetoresistive devices | 16 | 72 | 73 | | |

| <u>Index terms</u> | <u>Links</u> | | |
|--|---------------------|-----|-----|
| Magnetostriction | 34 | 121 | |
| atomic theory | 124 | | |
| factors affecting choice of material | 123 | | |
| frequency response | 132 | | |
| magnetic-field effects | 125 | 126 | 134 |
| pressure response | 131 | 134 | |
| temperature dependence | 125 | | |
| Magnetostriction constants | 122 | | |
| Magnetostrictive actuators | 133 | | |
| applications | 134 | | |
| design and control | 134 | | |
| operating principles | 134 | | |
| Magnetostrictive materials | | | |
| applications | 134 | | |
| historical background | 122 | | |
| rare-earth compounds | 124 | 126 | |
| Magnetostrictive response | 126 | | |
| Magnets | | | |
| high-field | 99 | | |
| hybrid facilities | 103 | | |
| Magnons | 11 | | |
| Manganese-based binary compounds, magneto-optical applications | 177 | | |
| Manganese silicides | | | |
| as semiconductors | 57 | | |
| thermoelectric properties | 203 | | |
| Matthias profiles | 17 | | |
| Matthiessen's rule | 10 | | |
| Mechanical alloying, magnetic materials prepared by | 42 | 43 | |
| Mechanical properties, superconductors | 90 | | |
| Mechanical-to-electrical energy conversion | 46 | | |
| Medium-temperature thermoelectrics | 198 | | |

| <u>Index terms</u> | <u>Links</u> | | | |
|--|---------------------|-----|----|-----|
| Melting temperatures | | | | |
| semiconductors/semimetals | 54 | 55 | 56 | 199 |
| thermoelectric materials | 197 | 199 | | |
| Melt spinning [processing technique], magnetic materials prepared by | 42 | 44 | | |
| Mercury iodide, in nuclear radiation detectors | 74 | | | |
| Mesotaxial implantation | 58 | | | |
| Metal-insulator semiconductor field-effect transistors (MISFETs) | 60 | 63 | | |
| Metallization [in integrated circuits], diffusion barriers in | 226 | 239 | | |
| Metalloids, in rare-earth-transition-metal magnetic compounds | 39 | | | |
| Metal organic chemical vapor deposition | 154 | | | |
| Metal organic vapor-phase epitaxy | 52 | 54 | | |
| Metal Schottky field-effect transistors (MESFETs) | 60 | 74 | | |
| Microhardness testing | 22 | | | |
| Microstructures, Dy-Fe-Tb system | 129 | | | |
| Miedema's model | 213 | | | |
| Mirror Fusion Test Facility | 105 | | | |
| Mirrors | 140 | 141 | | |
| Mischmetal alloys | 41 | | | |
| Mismatch [in semiconductors] | 54 | | | |
| Mn-Pt-Sb compounds, magneto-optical applications | 182 | | | |
| Mn-Si system | 203 | | | |
| phase diagram | 202 | | | |
| Mn ₁₂ Th structure type | 39 | 43 | | |
| Mn ₂₃ Th ₆ structure type | 43 | | | |
| Models, electrical resistivity | 8 | 11 | 25 | 26 |
| Modulation-doped heterojunctions/structures | 62 | 157 | | |
| Modulators | | | | |
| optical | 70 | 148 | | |
| photoelastic | 148 | 149 | | |
| Molecular-beam epitaxy (MBE) | 52 | 153 | | |
| Molecular-field theory | 15 | | | |

Index terms**Links**

| | | | | | |
|--|-----|-----|-----|-----|-----|
| Molybdenum disilicide | | | | | |
| in heaters | 205 | | | | |
| optical applications | 149 | | | | |
| Monolithic integration | 70 | | | | |
| Mo-Ru system, optical applications | 140 | | | | |
| Mo-Si-W system | 220 | | | | |
| MOVPE | 79 | | | | |
| Multifilamentary superconductors | 90 | 92 | 93 | 102 | 103 |
| Multiple-compound [diffusion] barriers | 231 | | | | |
| Multiple quantum-well (MQW) modulators | 69 | 70 | | | |
| Multiple quantum-well (MQW) structure | | | | | |
| in laser diodes | 80 | | | | |
| in semiconductors | 56 | 144 | 157 | 158 | 167 |
| N | | | | | |
| Nb-Sn superconductors | | | | | |
| applications | 98 | 99 | 110 | 116 | |
| comparison with other superconductors | 98 | | | | |
| fabrication techniques | 92 | | | | |
| mechanical properties | 90 | | | | |
| properties affected by formation processes | 87 | | | | |
| in thermonuclear fusion research coils | 103 | | | | |
| Nb-Sn system | 85 | | | | |
| phase diagram | 87 | | | | |
| Nb-Ti superconductors | 96 | 98 | 99 | 103 | 109 |
| | 110 | 114 | | | |
| compared with other superconductors | 99 | | | | |
| Nearly-free-electron theory | 11 | | | | |
| Néel temperature | 4 | 59 | 123 | | |
| Neumann's principle | 172 | | | | |
| Neutron diffraction/scattering, magnetic structures determined using | 2 | | | | |
| NG45F [resistive] alloy | 204 | | | | |

Index terms**Links**

| | | |
|---|-----|-----|
| Ni-Si-Pd system | 220 | |
| Ni-Si-Pt system | 219 | |
| Ni-Si-Ti system | 220 | |
| Ni-Si-Zr system, silicidation reactions | 218 | 219 |
| Ni-Ti system, shape-memory films | 164 | |
| Nitrides, as magnetic materials | 42 | 44 |
| Ni-Zr amorphous alloys, reactions with silicon | 223 | |
| Ni-Zr system, crystallization temperatures | 215 | 216 |
| N-Si-Ta amorphous alloys, as diffusion barriers | 231 | |
| N-Si-Ta system, diffusion barriers | 232 | 233 |
| N-Si-W system, diffusion barriers | 232 | |
| N-Ti-W system, diffusion barriers | 231 | |
| Nuclear magnetic resonance (NMR) spectrometry | 101 | 102 |
| Nuclear radiation detectors | 74 | |

O

| | | | | |
|---|-----|-----|-----|--------|
| Optical applications | 64 | 79 | 139 | |
| Optical bandpass filters | 142 | | | |
| Optical communications systems applications | 64 | 70 | 71 | 74 145 |
| | 146 | 160 | | |
| Optical computers | 74 | | | |
| Optical conductivity tensor | 173 | | | |
| Optical coupling | 146 | | | |
| Optical data storage applications | 169 | 172 | 175 | |
| Optical detectors | 67 | | | |
| Optical filters | 58 | 142 | | |
| Optical glass fibers | 74 | | | |
| Optical modulators | 70 | 148 | | |
| Optical NOR gate | 144 | | | |
| Optical recording media | 163 | | | |
| Optical signal repeaters | 146 | 147 | | |

Index terms**Links**

| | | | | |
|---|-----|-----|-----|-----|
| Optical signal storage/retrieval | 64 | 160 | | |
| Optical switches | 71 | | | |
| photoconductivity-dependent | 153 | | | |
| and photorefractive effect | 143 | | | |
| Optical waveguides | 145 | | | |
| Optoelectronic integrated circuits | 55 | 71 | 75 | 164 |
| Optoelectronic semiconductors | 52 | 64 | 150 | |
| Orbital quenching | 3 | | | |
| Order, and electrical resistivity | 12 | 14 | | |
| Ordered Cu ₃ Au rule | 210 | | | |
| Ordering, and magnetic permeability | 31 | | | |
| Os-W system, crystallization temperatures | 215 | 216 | | |
| Oxide superconductors | 84 | | | |

P

| | | | | |
|--------------------------------------|-----|-----|----|-----|
| Paramagnetic moment | 4 | | | |
| Particle accelerators | 108 | | | |
| Pattern-recognition applications | 144 | | | |
| Pb-Te system, phase diagram | 199 | | | |
| Pd-Si-V system | 220 | | | |
| Pd-U system | 203 | | | |
| Peltier effect | 188 | 191 | | |
| Permalloy [magnetic material] | 34 | 122 | | |
| Permanent magnets | 33 | 35 | | |
| applications | 46 | | | |
| machinable | 45 | | | |
| Permeability [of magnetic materials] | 32 | 33 | | |
| at constant length | 130 | | | |
| at constant stress | 128 | | | |
| Permeable-base transistors (PBTs) | 58 | 60 | 63 | |
| Permendur [magnetic material] | 35 | 36 | 45 | 122 |
| Permittivity, semiconductors | 55 | 56 | 73 | |

Index terms**Links**

| | | | | | |
|---|-----|-----|-----|----|-----|
| Phase decomposition | 212 | | | | |
| Phase diagrams | | | | | |
| Al ₅ compounds | 85 | 87 | | | |
| Al-Nb | 85 | | | | |
| Al-Ni | 211 | | | | |
| Bi-Te | 196 | | | | |
| Fe-Tb | 128 | | | | |
| Ga-Nb | 85 | | | | |
| Ga-V | 86 | | | | |
| Ge-Nb | 85 | | | | |
| Mn-Si | 202 | | | | |
| Nb-Sn | 87 | | | | |
| Pb-Te | 199 | | | | |
| Phase formation sequence, prediction of | 210 | 212 | | | |
| Phases, decomposition of | 212 | | | | |
| Phonon-electron coupling | 18 | | | | |
| Phonon resistivity | 10 | | | | |
| Photocathodes | 151 | | | | |
| Photoconductivity-dependent optical switches | 153 | | | | |
| Photodetectors | 56 | 68 | 70 | 78 | 150 |
| Photodiodes | 67 | 150 | 151 | | |
| Photoelastic modulators | 148 | 149 | | | |
| Photoluminescence | 156 | 157 | | | |
| Photoluminescence spectra | 157 | 158 | | | |
| Photon-electron interactions, applications based on | 150 | | | | |
| Photonic devices | 148 | | | | |
| Photorefractive effect | 143 | | | | |
| optical switches using | 143 | | | | |
| Photothyristors | 162 | 163 | | | |
| Phototransistors | 163 | | | | |
| Photovoltaic cells | 150 | 153 | 155 | | |
| <i>see also</i> Solar cells | | | | | |

| <u>Index terms</u> | <u>Links</u> | | | | |
|---|---------------------|-----|-----|----|----|
| Physical vapor deposition (PVD) | 232 | | | | |
| Piezomagnetic strain coefficients | 129 | | | | |
| Piezoresistive devices | 73 | | | | |
| Piezoresistive semiconductors, acoustoelectric properties | 73 | | | | |
| Pinning centers | 85 | | | | |
| Plasma-assisted doping | 54 | | | | |
| Platinum-based magnets | 36 | | | | |
| Pockels effect | 148 | | | | |
| Point defects, in semiconductors | 55 | | | | |
| Polarization | 32 | | | | |
| Polarization modulators | 148 | 172 | | | |
| Polarization rotation | 148 | | | | |
| Polymerically bonded magnets | 45 | | | | |
| Potassium titanyl phosphate (KTP) | 146 | | | | |
| Powder metallurgy techniques | 91 | 92 | | | |
| Power applications | 112 | | | | |
| Power-transmission lines | 112 | 114 | | | |
| Processing | | | | | |
| of diffusion barriers | 232 | | | | |
| melting methods, single-crystal growth | 55 | 127 | | | |
| of semiconductors | 54 | 55 | 56 | 57 | 75 |
| of superconductors | 87 | 92 | 96 | | |
| Pseudobinary compounds | 124 | 126 | 129 | | |
| Pseudogap | 14 | | | | |
| Pseudopotential methods | 11 | | | | |
| Pt-Si-Ti system | 226 | | | | |
| Pt-W amorphous alloys, reactions with silicon | 223 | 224 | | | |
| ‘Purple plague’ | 142 | | | | |
| Pyroelectric detectors | 151 | | | | |
| Pyro-optical sensors | 149 | | | | |
| PZT piezoelectric transducers | 148 | 149 | | | |

Index terms**Links****Q**

| | | | |
|--|-----|----|-----|
| Quantum-confined Stark effect | 70 | | |
| Quantum-mechanical calculations | | | |
| electrical conductivity | 9 | | |
| magneto-optical effects | 173 | | |
| Quantum wells [in semiconductors] | 55 | 56 | 156 |
| <i>see also</i> Multiple...; Single...quantum-well structure | | | |
| Quantum-well structure laser diode | 54 | 67 | |

R

| | | | |
|--|-----|-----|-----|
| Radiation detectors | 54 | 191 | |
| Radio-frequency cavities | 108 | | |
| Rapid-solidification methods, magnetic materials prepared by | 42 | | |
| Rare-earth compounds | | | |
| magnetic properties | 1 | 6 | |
| magneto-optical applications | 180 | 181 | 184 |
| magnetostriction in | 124 | | |
| with transition metals, magnetic properties | 38 | | |
| <i>see also</i> Iron-rare-earth compounds | | | |
| Rare-earth elements, electron wave functions | 123 | | |
| Rare-earth permanent magnets | 31 | 38 | |
| alloys of transition metals and lanthanides | 38 | | |
| alloying with metalloids | 39 | | |
| B-Fe-Nd compounds | 42 | 46 | |
| cobalt-samarium compounds | 40 | | |
| Fe ₇ R type | 44 | | |
| Fe ₁₇ R ₅ type | 44 | | |
| Fe ₃ Sm type | 44 | | |
| Fe ₂ Tb type | 45 | | |
| iron-samarium compounds | 42 | | |
| Mn ₁₂ Th structure type | 43 | | |
| properties | 33 | | |
| Rare-earth/transition metal alloys, magneto-optical applications | 176 | 179 | 181 |

Index terms**Links**

| | | | | |
|---|-----|-----|-----|-----|
| Reaction temperatures | | | | |
| amorphous alloys | | | | |
| with aluminum | 229 | | | |
| with silicon | 222 | | | |
| transition metals with silicon | 220 | | | |
| Red shift | 60 | | | |
| Reflectance, as function of incidence angle | 141 | | | |
| Reflectors | 140 | 141 | | |
| Refractive index | 171 | | | |
| Refractory-metal silicides | 57 | | | |
| Refrigerators | 189 | 191 | 194 | |
| Remanence [for permanent magnets] | 34 | 47 | | |
| Residual resistivity | 10 | | | |
| Resistivity anomaly | 13 | 15 | | |
| Resistors, electronic | 203 | 204 | | |
| Re-W system, crystallization temperatures | 216 | 217 | | |
| Roll anisotropy, in magnetically soft materials | 34 | | | |
| Rotating machinery, superconductors used | 114 | | | |
| Ruderman-Kittel-Kasuya-Yoshida (RKKY) interactions | 11 | | | |
| Rutherford backscattering spectrometry | 229 | | | |
| amorphous alloys | 223 | 224 | | |
| Ru-W system | | | | |
| crystallization temperatures | 216 | | | |
| optical applications | 140 | | | |
| S | | | | |
| Sacrificial barriers | 209 | | | |
| Saturation magnetization, values listed | 178 | 179 | 181 | 183 |
| Sawtooth diffraction gratings | 147 | | | |
| Schottky-type devices | 75 | 225 | | |
| Seebeck effect | 188 | 191 | | |
| Segregation, at grain boundaries, electrical conductivity affected by | 21 | 22 | | |

Index terms**Links**

| | | | | |
|--|-----|-----|-----|-----|
| Selenides, as thermoelectrics | 203 | | | |
| Semiconductor diode lasers | 150 | 159 | | |
| Semiconductor injection lasers | 160 | | | |
| Semiconductors | 19 | | | |
| applications | 51 | | | |
| grain-boundary effects | 24 | | | |
| interactions with binary alloys | 218 | | | |
| amorphous alloys on Si | 222 | | | |
| bilayers on silicon | 219 | | | |
| on GaAs | 225 | | | |
| single-element films on silicon | 218 | | | |
| solid solutions on Si | 220 | | | |
| thermoelectric applications | 197 | 198 | | |
| Semi-insulating crystals | 60 | | | |
| Semimetals | 57 | | | |
| Sendust [magnetic material] | 35 | | | |
| Separate-confinement heterostructure (SCH) laser diode | 80 | | | |
| Shape-memory films | 164 | | | |
| SiC-TiC system, optical applications | 142 | | | |
| Silicidation reactions | 218 | 219 | | |
| Silicides | | | | |
| chemical reactivity | 233 | | | |
| refractory-metal silicides | 57 | | | |
| as semiconductors | 57 | | | |
| semiconductors | 218 | | | |
| ternary silicides | 219 | 220 | 223 | 226 |
| as thermoelectrics | 203 | 204 | | |
| transition-metal silicides | 203 | | | |
| Silicon-based semiconductors | 60 | 61 | | |
| Silicon carbide | | | | |
| in heaters | 205 | | | |
| optical applications | 141 | | | |

Index terms**Links**

| | | | | |
|---|-----|-----|-----|---------|
| Silicon carbide (<i>Continued</i>) | | | | |
| as semiconductor | 55 | | | |
| in X-ray masks | 143 | | | |
| Silmanal [magnetic material] | 36 | 37 | | |
| Single quantum-well (SQW) structure, in light-emitting diodes | 80 | | | |
| Si-Pd-Pt system | 220 | | | |
| Si-Ti-W system | 221 | | | |
| Skutterudite crystal structure, thermoelectric materials | 206 | | | |
| Slab waveguides | 145 | | | |
| 'Smart' windows | 143 | 167 | | |
| Soft ferromagnets | 5 | | | |
| Soft magnets | 31 | 33 | 34 | |
| applications | 45 | | | |
| Solar cells | 58 | 78 | 150 | 153 |
| characteristics | 156 | | | |
| construction of | 154 | 155 | | |
| Sommerfeld theory | 8 | | | |
| Sonar transducers | 122 | 134 | | |
| SP-100 thermoelectric generator | 192 | 193 | | |
| Space-based applications | 141 | 151 | 167 | 192 193 |
| Specific electrical resistivity, listed for various metals | 22 | 26 | | |
| Specific heat, semiconductors/semimetals | 56 | | | |
| Spin-disorder scattering effect | 11 | 12 | 15 | |
| Spinel structure | 58 | | | |
| Spin-glass behavior | 1 | | | |
| Spin-orbit coupling, magneto-optical effects affected by | 175 | | | |
| Sputter-deposited films | | | | |
| diffusion barriers | 232 | | | |
| magnetic applications | 44 | 45 | | |
| optical applications | 163 | | | |
| Square hysteresis loops | 32 | 182 | | |
| Static inductance transistors (SITs) | 60 | 63 | | |

| <u>Index terms</u> | <u>Links</u> | | | | |
|---|---------------------|-----|-----|-----|-----|
| Stevens factor, second-order | 44 | | | | |
| Stoichiometry, electrical conductivity affected by | 19 | | | | |
| Strain gauges | 73 | | | | |
| Strain-induced resistivity change | 24 | | | | |
| Stuffed [diffusion] barrier | 209 | 229 | | | |
| Superconducting critical/transition temperature | 17 | | | | |
| factors affecting | 88 | | | | |
| as function of valence electrons per atom | 17 | 18 | | | |
| listed for various compounds | 84 | | | | |
| Superconducting quantum interference devices (SQUIDs) | 115 | | | | |
| Superconducting Super Collider (SSC) | 109 | | | | |
| Superconductivity | 16 | 83 | | | |
| effect of grain boundaries | 23 | | | | |
| effect of strain | 86 | | | | |
| Superconductors | 83 | | | | |
| applications | 96 | 98 | 102 | | |
| electronics | 115 | | | | |
| high-field magnets | 99 | | | | |
| hybrid magnet facilities | 103 | | | | |
| magnetically levitated vehicles | 111 | | | | |
| magnetic resonance imaging | 109 | | | | |
| NMR spectrometry | 102 | | | | |
| particle accelerators | 108 | | | | |
| power systems | 112 | | | | |
| thermonuclear fusion research | 103 | | | | |
| current-carrying capacity | 98 | 99 | | | |
| fabrication techniques | 87 | 92 | 96 | | |
| oxides as | 84 | | | | |
| ‘Superlattice’ [in semiconductors] | 52 | 55 | 62 | 153 | 157 |
| Supermagnets | 47 | | | | |

| <u>Index terms</u> | <u>Links</u> | | | | |
|---------------------------------|---------------------|-----|-----|-----|-----|
| Switches | | | | | |
| laser-based | 162 | 163 | | | |
| optical | 71 | 143 | 153 | | |
| Synchronous generators | 113 | | | | |
| T | | | | | |
| Tammann temperature | 208 | 232 | | | |
| Tandem [diffusion] barriers | 231 | | | | |
| Tape superconductors | 92 | 99 | | | |
| τ phase | 37 | | | | |
| Tellurides | | | | | |
| as semiconductors | 54 | | | | |
| as thermoelectric materials | 196 | 198 | | | |
| Terfenol-D | 124 | | | | |
| applications | 134 | | | | |
| composites | 133 | | | | |
| magnetic annealing of | 132 | | | | |
| properties | 127 | | | | |
| frequency response | 132 | | | | |
| magnetomechanical coupling | 128 | | | | |
| pressure response | 131 | | | | |
| temperature range limitation | 126 | | | | |
| Ternary compounds | | | | | |
| magneto-optical properties of | 182 | | | | |
| as semiconductors | 58 | 76 | | | |
| silicides | 219 | 220 | 223 | 226 | |
| Tevatron [particle accelerator] | 109 | | | | |
| Thermal conductivity | | | | | |
| semiconductors/semimetals | 55 | 56 | | | |
| thermoelectric materials | 197 | 198 | 200 | 201 | 203 |
| | 206 | | | | |
| Thermal radiation detectors | 150 | 151 | 191 | | |

| <u>Index terms</u> | <u>Links</u> | | | | |
|---|---------------------|-----|-----|-----|-----|
| Thermocouples | 189 | 190 | | | |
| Thermoelectric applications | 187 | | | | |
| conferences on | 187 | | | | |
| future developments | 201 | | | | |
| practice | 190 | | | | |
| principles | 189 | | | | |
| state of art | 199 | | | | |
| Thermoelectric circuits | 188 | | | | |
| Thermoelectric conversion materials | 57 | | | | |
| Thermoelectric coolers/conditioners | 189 | 191 | 194 | | |
| Thermoelectric devices | 57 | | | | |
| Thermoelectric figure of merit | 190 | 195 | | | |
| factors affecting | 195 | 202 | | | |
| temperature dependence | 196 | 197 | 198 | 200 | 201 |
| Thermoelectric generators | 189 | 191 | 192 | | |
| Thermoelectric heat pumps | 189 | 191 | 194 | | |
| Thermoelectricity, physics | 188 | | | | |
| Thermoelectric materials | | | | | |
| future applications | 201 | | | | |
| high-temperature thermoelectrics | 199 | | | | |
| literature sources | 205 | | | | |
| low-temperature thermoelectrics | 196 | | | | |
| medium-temperature thermoelectrics | 198 | | | | |
| requirements | 194 | | | | |
| theory | 195 | | | | |
| Thermoelectric power | 9 | | | | |
| Thermoelectric thermometers | 190 | | | | |
| Thermoelectromotive force, temperature dependence | 15 | 16 | | | |
| Thermonuclear fusion research | 98 | 103 | | | |
| Thermopower | 188 | 197 | 198 | 200 | 201 |
| | 203 | | | | |
| Thin-film photovoltaic cells | 155 | | | | |

| <u>Index terms</u> | <u>Links</u> | | | | |
|--|---------------------|-----|-----|-----|-----|
| Thomson effect | 188 | | | | |
| III-V compounds | | | | | |
| acoustoelectric devices | 73 | 74 | | | |
| diode lasers | 160 | | | | |
| Hall devices | 72 | | | | |
| in light-emitting devices | 79 | | | | |
| optical applications | 139 | 145 | 146 | 147 | 148 |
| | 153 | | | | |
| semiconductors | 52 | 53 | 55 | 74 | 75 |
| compared with silicon semiconductors | 75 | | | | |
| Tin amalgam coatings | 140 | | | | |
| Tin chalcogenides, as semiconductors | 56 | | | | |
| Titanium nitride, as diffusion barrier | 229 | | | | |
| Tokamaks | 104 | 106 | 107 | | |
| Transistor applications | 55 | 58 | 60 | | |
| Transition elements | | | | | |
| alloys with lanthanides, magnetic properties | 38 | | | | |
| electrical properties | 10 | | | | |
| Transition-metal compounds, magneto-optical applications | 184 | | | | |
| Transition-metal silicides | | | | | |
| semiconductors | 57 | 78 | | | |
| as thermoelectric materials | 203 | | | | |
| Transition-metal superconductors | 17 | | | | |
| Tubular tin source (TTS) superconductor | 93 | 95 | | | |
| Tunable lasers | 60 | | | | |
| II-VI compounds | | | | | |
| acoustoelectric devices | 73 | | | | |
| light-emitting devices | 54 | 64 | 79 | | |
| semiconductors | 53 | 54 | 76 | 78 | |

Index terms**Links****U**

| | | | |
|--|-----|----|----|
| Ultrasonic wave generation applications | 74 | | |
| Uniaxial anisotropy [of magnetic materials] | 32 | 34 | 35 |
| Uranium-based compounds, magneto-optical effects | 182 | | |

V

| | | | |
|---|-----|-----|--|
| Vacancies | | | |
| electrical conductivity affected by | 20 | 21 | |
| formation of, factors affecting | 215 | | |
| Valence electrons per atom, superconducting critical/transition temperature | | | |
| plotted against | 17 | 18 | |
| Vapor-phase deposition techniques | 142 | | |
| Vapor-phase epitaxy (VPE) | 54 | | |
| Vertical-cavity surface-emitting lasers (VCSELs) | 162 | 163 | |
| Vicalloy [magnetic material] | 36 | 45 | |
| Voigt parameter [for magneto-optical effects] | 171 | 173 | |

W

| | | | |
|--|-----|-----|--|
| Walser-Bené phase-formation rule | 210 | 212 | |
| compared with effective-heat-of-formation rule | 213 | | |
| Waveguide photodetectors | 68 | 70 | |
| Waveguides, optical | 145 | 157 | |
| Wiedemann-Franz law | 8 | 196 | |
| Window coatings | 143 | 167 | |
| Wurtzite structure | 52 | | |
| semiconductors | 79 | | |

X

| | | | |
|-------------|-----|--|--|
| X-ray masks | 143 | | |
|-------------|-----|--|--|

Index terms**Links****Z**

| | | | |
|---------------------------------------|-----|-----|-----|
| Zinc-blende structure | | | |
| crystal structure | 52 | | |
| semiconductors | 79 | | |
| Zinc chalcogenides, as semiconductors | 54 | 78 | |
| Zinc selenide, optical applications | 142 | 144 | 148 |